

IAEA TECDOC SERIES

IAEA-TECDOC-1819

Benchmark Analysis of EBR-II Shutdown Heat Removal Tests



IAEA

International Atomic Energy Agency

BENCHMARK ANALYSIS OF EBR-II
SHUTDOWN HEAT REMOVAL TESTS

The following States are Members of the International Atomic Energy Agency:

AFGHANISTAN	GEORGIA	OMAN
ALBANIA	GERMANY	PAKISTAN
ALGERIA	GHANA	PALAU
ANGOLA	GREECE	PANAMA
ANTIGUA AND BARBUDA	GUATEMALA	PAPUA NEW GUINEA
ARGENTINA	GUYANA	PARAGUAY
ARMENIA	HAITI	PERU
AUSTRALIA	HOLY SEE	PHILIPPINES
AUSTRIA	HONDURAS	POLAND
AZERBAIJAN	HUNGARY	PORTUGAL
BAHAMAS	ICELAND	QATAR
BAHRAIN	INDIA	REPUBLIC OF MOLDOVA
BANGLADESH	INDONESIA	ROMANIA
BARBADOS	IRAN, ISLAMIC REPUBLIC OF	RUSSIAN FEDERATION
BELARUS	IRAQ	RWANDA
BELGIUM	IRELAND	SAN MARINO
BELIZE	ISRAEL	SAUDI ARABIA
BENIN	ITALY	SENEGAL
BOLIVIA, PLURINATIONAL STATE OF	JAMAICA	SERBIA
BOSNIA AND HERZEGOVINA	JAPAN	SEYCHELLES
BOTSWANA	JORDAN	SIERRA LEONE
BRAZIL	KAZAKHSTAN	SINGAPORE
BRUNEI DARUSSALAM	KENYA	SLOVAKIA
BULGARIA	KOREA, REPUBLIC OF	SLOVENIA
BURKINA FASO	KUWAIT	SOUTH AFRICA
BURUNDI	KYRGYZSTAN	SPAIN
CAMBODIA	LAO PEOPLE'S DEMOCRATIC REPUBLIC	SRI LANKA
CAMEROON	LATVIA	SUDAN
CANADA	LEBANON	SWAZILAND
CENTRAL AFRICAN REPUBLIC	LESOTHO	SWEDEN
CHAD	LIBERIA	SWITZERLAND
CHILE	LIBYA	SYRIAN ARAB REPUBLIC
CHINA	LIECHTENSTEIN	TAJIKISTAN
COLOMBIA	LITHUANIA	THAILAND
CONGO	LUXEMBOURG	THE FORMER YUGOSLAV REPUBLIC OF MACEDONIA
COSTA RICA	MADAGASCAR	TOGO
CÔTE D'IVOIRE	MALAWI	TRINIDAD AND TOBAGO
CROATIA	MALAYSIA	TUNISIA
CUBA	MALI	TURKEY
CYPRUS	MALTA	TURKMENISTAN
CZECH REPUBLIC	MARSHALL ISLANDS	UGANDA
DEMOCRATIC REPUBLIC OF THE CONGO	MAURITANIA	UKRAINE
DENMARK	MAURITIUS	UNITED ARAB EMIRATES
DJIBOUTI	MEXICO	UNITED KINGDOM OF GREAT BRITAIN AND NORTHERN IRELAND
DOMINICA	MONACO	UNITED REPUBLIC OF TANZANIA
DOMINICAN REPUBLIC	MONGOLIA	UNITED STATES OF AMERICA
ECUADOR	MONTENEGRO	URUGUAY
EGYPT	MOROCCO	UZBEKISTAN
EL SALVADOR	MOZAMBIQUE	VANUATU
ERITREA	MYANMAR	VENEZUELA, BOLIVARIAN REPUBLIC OF
ESTONIA	NAMIBIA	VIET NAM
ETHIOPIA	NEPAL	YEMEN
FIJI	NETHERLANDS	ZAMBIA
FINLAND	NEW ZEALAND	ZIMBABWE
FRANCE	NICARAGUA	
GABON	NIGER	
	NIGERIA	
	NORWAY	

The Agency's Statute was approved on 23 October 1956 by the Conference on the Statute of the IAEA held at United Nations Headquarters, New York; it entered into force on 29 July 1957. The Headquarters of the Agency are situated in Vienna. Its principal objective is "to accelerate and enlarge the contribution of atomic energy to peace, health and prosperity throughout the world".

IAEA-TECDOC-1819

BENCHMARK ANALYSIS OF EBR-II SHUTDOWN HEAT REMOVAL TESTS

INTERNATIONAL ATOMIC ENERGY AGENCY
VIENNA, 2017

COPYRIGHT NOTICE

All IAEA scientific and technical publications are protected by the terms of the Universal Copyright Convention as adopted in 1952 (Berne) and as revised in 1972 (Paris). The copyright has since been extended by the World Intellectual Property Organization (Geneva) to include electronic and virtual intellectual property. Permission to use whole or parts of texts contained in IAEA publications in printed or electronic form must be obtained and is usually subject to royalty agreements. Proposals for non-commercial reproductions and translations are welcomed and considered on a case-by-case basis. Enquiries should be addressed to the IAEA Publishing Section at:

Marketing and Sales Unit, Publishing Section
International Atomic Energy Agency
Vienna International Centre
PO Box 100
1400 Vienna, Austria
fax: +43 1 2600 29302
tel.: +43 1 2600 22417
email: sales.publications@iaea.org
<http://www.iaea.org/books>

For further information on this publication, please contact:

Nuclear Power Technology Development Section
International Atomic Energy Agency
Vienna International Centre
PO Box 100
1400 Vienna, Austria
Email: Official.Mail@iaea.org

© IAEA, 2017
Printed by the IAEA in Austria
August 2017

IAEA Library Cataloguing in Publication Data

Names: International Atomic Energy Agency.
Title: Benchmark analysis of EBR-II shutdown heat removal tests / International Atomic Energy Agency.
Description: Vienna : International Atomic Energy Agency, 2017. | Series: IAEA TECDOC series, ISSN 1011-4289 ; no. 1819 | Includes bibliographical references.
Identifiers: IAEAL 17-01103 | ISBN 978-92-0-105517-0 (paperback : alk. paper)
Subjects: LCSH: Nuclear reactors — Shutdown. | Heat — Transmission — Mathematical models. | Fast reactors. | Sodium cooled reactors.

FOREWORD

At Argonne National Laboratory (ANL) in the 1950s, the Experimental Breeder Reactor I (EBR-I) generated the first useable amounts of electricity from liquid sodium cooled fast reactor (SFR) technology. In the 1980s, ANL conducted shutdown heat removal tests (SHRT) on EBR-II. ANL opened the experimental dataset to international collaboration in 2012 with the objective of improving the state of the art SFR codes by extending code validation to include comparisons against whole plant data. The IAEA launched the coordinated research project (CRP) Benchmark Analyses of EBR-II Shutdown Heat Removal Tests in 2012 to perform the code validation and to train the next generation of analysts and designers through international benchmark exercises. This publication documents the results and main achievements of the CRP.

A total of 19 organizations from 11 countries participated in the CRP and contributed to improving capabilities in SFR simulation through code verification and validation, with particular emphasis on shutdown heat removal phenomena. The focus of the CRP was the analyses of the SHRT-17 protected loss of flow and SHRT-45R unprotected station blackout tests. Both tests were initiated from full power and flow and were the most severe tests of their respective types performed during the SHRT programme. The benchmark was performed in two phases: initial blind and further simulations with updated models. The results of both phases are provided in this publication.

The IAEA expresses its appreciation to all participants in the CRP for their dedicated efforts leading to this publication. The IAEA extends its special thanks to L. Briggs (ANL) for coordinating this CRP and compiling this publication. The IAEA officer responsible for this publication was V. Kriventsev of the Division of Nuclear Power.

EDITORIAL NOTE

This publication has been prepared from the original material as submitted by the contributors and has not been edited by the editorial staff of the IAEA. The views expressed remain the responsibility of the contributors and do not necessarily represent the views of the IAEA or its Member States.

Neither the IAEA nor its Member States assume any responsibility for consequences which may arise from the use of this publication. This publication does not address questions of responsibility, legal or otherwise, for acts or omissions on the part of any person.

The use of particular designations of countries or territories does not imply any judgement by the publisher, the IAEA, as to the legal status of such countries or territories, of their authorities and institutions or of the delimitation of their boundaries.

The mention of names of specific companies or products (whether or not indicated as registered) does not imply any intention to infringe proprietary rights, nor should it be construed as an endorsement or recommendation on the part of the IAEA.

The IAEA has no responsibility for the persistence or accuracy of URLs for external or third party Internet web sites referred to in this publication and does not guarantee that any content on such web sites is, or will remain, accurate or appropriate.

CONTENTS

1.	INTRODUCTION.....	1
1.1.	OBJECTIVES OF THE COORDINATED RESEARCH PROJECT	1
1.2.	PROCEDURE FOR IMPLEMENTATION OF THE CRP	1
2.	DESCRIPTION OF EBR-II.....	3
2.1.	REACTOR	3
2.2.	CORE	3
2.3.	HEAT TRANSPORT SYSTEMS	5
2.3.1.	Primary heat transport system.....	5
2.3.2.	Intermediate heat transport system.....	6
2.3.3.	Water/steam system and turbines.....	6
2.4.	BASIC PLANT SPECIFICATIONS	6
3.	DESCRIPTION OF THE SHUTDOWN HEAT REMOVAL TESTS CONDUCTED IN 1984 AND 1986	7
3.1.	TEST DESCRIPTIONS.....	8
3.1.1.	SHRT-17.....	8
3.1.2.	SHRT-45R	8
3.2.	DESCRIPTION OF INSTRUMENTATION USED FOR THE TESTS	9
3.2.1.	Temperature measurements	9
3.2.2.	Flowmeters.....	10
3.2.3.	Instrumented subassembly XX09.....	11
3.2.4.	Instrumented subassembly XX10.....	12
3.2.5.	Fission power measurement.....	13
3.2.6.	Pressure measurements.....	13
3.3.	TEST RESULTS	13
3.3.1.	SHRT-17.....	13
3.3.2.	SHRT-45R	19
3.4.	INTERPRETATION OF THE EXPERIMENTAL DATA USED IN THE BENCHMARK EXERCISE	24
4.	BENCHMARK SPECIFICATIONS.....	34
4.1.	PLANT PARAMETERS	34
4.2.	CORE DATA	34
4.2.1.	Types of subassemblies	34
4.2.2.	Fuel properties.....	35
4.3.	PRIMARY CIRCUIT	37
4.4.	SHRT-45R NEUTRONICS BENCHMARK SPECIFICATION	38
4.5.	OUTPUT PARAMETERS TO BE CALCULATED	39
5.	DESCRIPTION OF SIMULATION CODES	41
5.1.	SYSTEMS ANALYSIS CODES	41
5.1.1.	CATHARE (IRSN)	41
5.1.2.	EBRDYN (IGCAR)	42
5.1.3.	FRENETIC (Politecnico di Torino)	42
5.1.4.	MARS-LMR (KAERI).....	43
5.1.5.	NETFLOW++ (U. of Fukui).....	43

5.1.6.	RELAP5-3D (ENEA, N.I.N.E., U. of Fukui)	43
5.1.7.	SAS4A/SASSYS-1 (Argonne, CIAE, TerraPower)	44
5.1.8.	SAC-CFR (NCEPU)	44
5.1.9.	SIMMER (KIT)	44
5.1.10.	SOCRAT-BN (IBRAE)	44
5.1.11.	SPECTRA (NRG)	45
5.1.12.	Super-COPD (JAEA)	45
5.1.13.	THACS (XJTU)	45
5.1.14.	TRACE (KINS, NRG, PSI)	46
5.2.	NEUTRONICS CODES	46
5.2.1.	DIF3D (Argonne)	46
5.2.2.	ERANOS (KIT, U. Fukui)	46
5.2.3.	MC ² -3 (Argonne)	46
5.2.4.	MCNP6 (ENEA)	46
5.2.5.	NJOY (U. Fukui)	47
5.2.6.	PARTISN (KIT)	47
5.2.7.	PHISICS (ENEA)	47
5.2.8.	SCALE6.1 (ENEA)	47
5.2.9.	SERPENT (Politecnico di Torino, PSI)	47
5.2.10.	TRAIN (KIT)	48
5.2.11.	VARI3D and PERSENT (Argonne)	48
5.3.	OTHER TYPES OF CODES	48
5.3.1.	ANSYS CFX (ENEA, NRG, U. of Fukui)	48
5.3.2.	ASFRE (JAEA)	48
5.3.3.	COBRA4i (TerraPower, U. of Fukui)	48
5.3.4.	STAR-CD (IGCAR)	49
5.3.5.	Thermo-Calc (Kyushu university)	49
6.	GENERAL DESCRIPTION OF CRP ANALYSIS APPROACH	49
6.1.	PHASE 1	49
6.2.	PHASE 2	50
7.	MODELS AND RESULTS	50
7.1.	CHINA INSTITUTE OF ATOMIC ENERGY (CHINA)	51
7.1.1.	Geometry/discretization	51
7.1.2.	Nuclear and thermo-physical data/correlations	51
7.1.3.	Thermal hydraulics methods and models	52
7.1.4.	Blind results	52
7.1.5.	Final results, data comparisons	53
7.2.	NORTH CHINA ELECTRIC POWER UNIVERSITY (CHINA)	60
7.2.1.	Geometry/discretization	60
7.2.2.	Nuclear and thermo-physical data/correlations	60
7.2.3.	Thermal hydraulics methods and models	61
7.2.4.	Blind results	63
7.2.5.	Final results, data comparisons	63
7.2.6.	Neutronics methods and models	70
7.2.7.	Neutronics results	71
7.3.	XI'AN JIAOTONG UNIVERSITY (CHINA)	72
7.3.1.	Geometry/discretization	72
7.3.2.	Nuclear and thermo-physical data/correlations	74

7.3.3.	Thermal hydraulics methods and models	75
7.3.4.	Blind results	78
7.3.5.	Final results, data comparisons	81
7.4.	IRSN (FRANCE).....	87
7.4.1.	Geometry/discretization.....	87
7.4.2.	Thermal hydraulics methods and models	87
7.4.3.	Blind results	89
7.4.4.	Final results, data comparisons	89
7.4.5.	Conclusions	91
7.5.	KIT (GERMANY)/KYUSHU UNIVERSITY (JAPAN)	92
7.5.1.	Geometry/discretization.....	92
7.5.2.	Nuclear and thermo-physical data/correlations.....	93
7.5.3.	Thermal hydraulics methods and models	94
7.5.4.	Blind results	97
7.5.5.	Final results, data comparisons	99
7.5.6.	Neutronics methods and models	108
7.5.7.	Neutronics results	110
7.6.	INDIRA GANDHI CENTRE FOR ATOMIC RESEARCH (INDIA).....	111
7.6.1.	Geometry/discretization.....	111
7.6.2.	Nuclear and thermo-physical data/correlations.....	112
7.6.3.	Thermal hydraulics methods and models	113
7.6.4.	Blind results	115
7.6.5.	Final results, data comparisons	118
7.7.	ENEA (ITALY).....	123
7.7.1.	Geometry/discretization.....	123
7.7.2.	Nuclear and thermo-physical data/correlations.....	125
7.7.3.	Thermal hydraulics methods and models	126
7.7.4.	Blind results	126
7.7.5.	Final CRP results and comparisons with the experimental data.....	130
7.7.6.	Neutronics methods and models	134
7.7.7.	Neutronics results	138
7.8.	NUCLEAR AND INDUSTRIAL ENGINEERING (ITALY).....	139
7.8.1.	Geometry/discretization.....	139
7.8.2.	Nuclear and thermo-physical data/correlations.....	140
7.8.3.	Thermal hydraulics methods and models	140
7.8.4.	Blind results	141
7.8.5.	Final results, data comparisons	143
7.8.6.	Neutronics methods and models	149
7.9.	POLITECNICO DI TORINO (ITALY)	150
7.9.1.	Geometry/discretization.....	150
7.9.2.	Nuclear and thermo-physical data/correlations.....	150
7.9.3.	Thermal hydraulics methods and models	151
7.9.4.	Blind results	153
7.9.5.	Final results, data comparisons	154
7.9.6.	Neutronics methods and models	160
7.9.7.	Neutronics results	161
7.10.	JAPAN ATOMIC ENERGY AGENCY (JAPAN)	162
7.10.1.	Geometry/discretization.....	162
7.10.2.	Nuclear and thermo-physical data/correlations.....	163
7.10.3.	Thermal-hydraulics methods and models.....	164
7.10.4.	Blind results	166

	7.10.5. Final results, data comparisons	167
7.11.	UNIVERSITY OF FUKUI (JAPAN)	175
	7.11.1. Geometry/discretization	175
	7.11.2. Nuclear and thermo-physical data/correlations	175
	7.11.3. Thermal hydraulics methods and models	176
	7.11.4. Blind results	179
	7.11.5. Final results, data comparisons	179
	7.11.6. Neutronics methods and models	188
	7.11.7. Neutronics results	189
7.12.	KOREA ATOMIC ENERGY RESEARCH INSTITUTE (REPUBLIC OF KOREA)	191
	7.12.1. Geometry/discretization	191
	7.12.2. Nuclear and thermo-physical data/correlations	192
	7.12.3. Thermal-hydraulics methods and models	193
	7.12.4. Blind results	194
	7.12.5. Final results, data comparisons	195
	7.12.6. Neutronics methods and models	205
7.13.	KOREA INSTITUTE OF NUCLEAR SAFETY (REPUBLIC OF KOREA)	205
	7.13.1. Geometry/discretization	205
	7.13.2. Nuclear and thermo-physical data/correlations	206
	7.13.3. Thermal hydraulics methods and models	207
	7.13.4. Blind results	208
	7.13.5. Final results, data comparisons	209
7.14.	NRG (NETHERLANDS)	213
	7.14.1. Geometry/discretization	213
	7.14.2. Nuclear and thermo-physical data/correlations	214
	7.14.3. Thermal hydraulics methods and models	215
	7.14.4. Blind results	218
	7.14.5. Final results, data comparisons	221
	7.14.6. Neutronics methods and models	227
7.15.	IBRAE-RAN (RUSSIAN FEDERATION)	227
	7.15.1. Geometry/discretization	227
	7.15.2. Nuclear and thermo-physical data/correlations	229
	7.15.3. Thermal hydraulics methods and models	230
	7.15.4. Blind results	231
	7.15.5. Final results, data comparisons	231
	7.15.6. Neutronics methods and models	233
7.16.	PAUL SCHERRER INSTITUTE (SWITZERLAND)	235
	7.16.1. Geometry/discretization and assumptions	235
	7.16.2. Results for SHRT-17 and SHRT-45R	236
	7.16.3. Neutronics model and results	243
7.17.	TERRAPOWER (USA)	247
	7.17.1. Geometry/discretization	247
	7.17.2. Nuclear and thermo-physical data/correlations	248
	7.17.3. Thermal hydraulics methods and models	250
	7.17.4. Blind results	251
	7.17.5. Final results, data comparisons	254
	7.17.6. Neutronics methods and models	260
7.18.	ARGONNE NATIONAL LABORATORY (USA)	260
	7.18.1. Geometry/discretization	260

7.18.2.	Nuclear and thermo-physical data/correlations.....	261
7.18.3.	Thermal hydraulics methods and models	261
7.18.4.	Blind results	263
7.18.5.	Final results, data comparisons	265
7.18.6.	Neutronics methods and models	270
7.18.7.	Neutronics results	271
7.19.	REACTIVITY FEEDBACK DATA PROVIDED FOR SHRT-45R.....	272
8.	SENSITIVITY AND/OR UNCERTAINTY ANALYSES	273
8.1.	KIT (GERMANY)/KYUSHU UNIVERSITY (JAPAN).....	273
8.1.1.	SHRT-17.....	273
8.1.2.	Neutronics benchmark.....	276
8.2.	ENEA (ITALY).....	280
8.3.	NUCLEAR AND INDUSTRIAL ENGINEERING (ITALY).....	282
8.4.	POLITECNICO DI TORINO (ITALY)	286
8.4.1.	SHRT-17.....	286
8.4.2.	SHRT-45R	287
8.5.	UNIVERSITY OF FUKUI (JAPAN).....	288
8.5.1.	Comparison between system codes.....	288
8.5.2.	Analysis of uncertainty due to cross-section covariances.	288
8.6.	KOREA ATOMIC ENERGY RESEARCH INSTITUTE (REPUBLIC OF KOREA).....	291
8.6.1.	MARS-LMR	291
8.7.	KOREA INSTITUTE OF NUCLEAR SAFETY (REPUBLIC OF KOREA).....	293
8.7.1.	Parametric study of instrumented subassembly steady state temperatures.....	293
8.7.2.	Effect of wire-wrapped fuel bundle correlations on the XX09 temperatures.....	294
8.8.	NRG (NETHERLANDS).....	296
8.9.	IBRAE-RAN (RUSSIAN FEDERATION)	297
8.10.	PAUL SCHERRER INSTITUTE (SWITZERLAND).....	299
8.11.	TERRAPOWER (USA).....	300
8.11.1.	Sensitivity to heat transfer correlations	300
8.11.2.	Sensitivity to pressure drop correlations	301
8.11.3.	Sensitivity to assumed fuel properties.....	302
8.12.	ARGONNE NATIONAL LABORATORY (USA).....	304
9.	QUALIFICATION PROCESS	306
9.1.	THE SCCRED METHODOLOGY	306
9.2.	RESULTS OF THE QUALIFICATION PROCEDURE	307
9.2.1.	The methodology.....	307
9.2.2.	Participants' results	316
9.3.	MAIN OUTCOMES FROM THE ANALYSIS.....	338
9.3.1.	Summary of the results	338
9.3.2.	Lessons learned	338
10.	OBSERVATIONS AND TRENDS WITHIN THE COLLECTIVE SET OF PARTICIPANT RESULTS	339
10.1.	GENERAL OBSERVATIONS.....	339

10.2.	SHRT-17	340
10.2.1.	Primary pump flowrate.....	340
10.2.2.	XX09 temperatures.....	341
10.2.3.	XX10 temperatures.....	341
10.3.	SHRT-45R.....	342
10.3.1.	Primary pump flowrate and fission power.....	342
10.3.2.	Z-Pipe inlet temperature	342
10.3.3.	XX09 and XX10 temperatures.....	344
11.	CONCLUSIONS AND RECOMMENDATIONS	344
11.1.	CONCLUSIONS FROM THE EBR-II BENCHMARKS STUDY	344
11.2.	LESSONS LEARNED FROM THE EBR-II BENCHMARKS STUDY.....	345
	APPENDIX I.....	347
	APPENDIX II	363
	APPENDIX III	369
	APPENDIX IV	393
	APPENDIX V	437
	APPENDIX VI.....	445
	REFERENCES.....	449
	ACRONYMS AND ABBREVIATIONS.....	459
	CONTRIBUTORS TO DRAFTING AND REVIEW	463

1. INTRODUCTION

1.1. OBJECTIVES OF THE COORDINATED RESEARCH PROJECT

Liquid sodium cooled fast reactor (SFR) technology development traces its beginnings to Argonne's Experimental Breeder Reactor I (EBR-I), which first generated useable amounts of electricity in December 1951. The succeeding decades saw construction and operation of experimental and prototype fast reactor facilities in the USA (EBR-I and -II, FERMI, and FFTF), the Russian Federation (BR-10, BOR-60, BN-350, and BN-600), the UK (DFR and PFR), France (RAPSODIE, PHENIX, and Superphénix), Germany (KNK and SNR-300), India (FBTR), and Japan (JOYO and Monju). A new generation of prototype fast reactors is now becoming available with the advent of CEFR in China, PFBR in India, and BN-800 in the Russian Federation [1].

SFRs represent a significant advance over established and evolutionary light water reactor designs in terms of efficient resource utilization, safety, reliability, management of high level waste, and non-proliferation. The demonstrated passive decay heat removal capability of SFRs has been of particular interest following the Fukushima accident.

The modelling and simulation tools that have been developed to support SFR design and safety analysis have originated in a range of countries, apply a variety of methodologies, and use many sources of data for validation and verification. Most of the data available for validating these tools have come from separate effects experiments.

The main objective of the Coordinated Research Project (CRP) is to perform the code validation by comparing the results of the SFR codes to whole plant data collected during the shutdown heat removal tests (SHRT) [2] conducted at ANL's EBR-II reactor during the 1980s. Analysis was done for the protected loss of flow test: SHRT-17 and, unprotected loss of flow test: SHRT-45R.

An additional objective of the CRP was training of the next generation of analysts and designers through international benchmark exercises.

1.2. PROCEDURE FOR IMPLEMENTATION OF THE CRP

The CRP was formally initiated in June 2012 and concluded in June 2016. The nineteen research organizations, representing eleven countries, that participated in the CRP are presented in FIG. 1.

Prior to the June 2012 initial research coordination meeting (RCM) at Argonne, Argonne prepared a detailed benchmark specification for the analyses of the SHRT-17 and SHRT-45R transients. In addition, Argonne prepared a neutronics benchmark specification for the SHRT-45R unprotected test. These specifications provided the necessary benchmark data for collaborative modelling and simulation benchmarking efforts within the international partnerships established through the CRP. The benchmark specifications were distributed to the participants at the first RCM and discussed at length. Questions and feedback on the specifications were provided to Argonne by the CRP participants over the next several months. Argonne addressed this input in revisions to both benchmarks that were issued in February 2013.



<p style="text-align: center;">China</p> <ul style="list-style-type: none"> • <i>China Institute of Atomic Energy (CIAE)</i> • <i>North China Electric Power University (NCEPU)</i> • <i>Xi'an Jiatong University (XJTU)</i> <p style="text-align: center;">France</p> <ul style="list-style-type: none"> • <i>Institut de Radioprotection et de Sûreté Nucléaire (IRSN)</i> <p style="text-align: center;">Germany</p> <ul style="list-style-type: none"> • <i>Karlsruhe Institute of Technology (KIT)</i> <p style="text-align: center;">Italy</p> <ul style="list-style-type: none"> • <i>Italian National Agency for New Technologies, Energy and Sustainable Economic Development (ENEA)</i> • <i>Nuclear and Industrial Engineering (N.I.N.E.)</i> • <i>Politecnico di Torino</i> <p style="text-align: center;">India</p> <ul style="list-style-type: none"> • <i>Indira Gandhi Centre for Atomic Research (IGCAR)</i> 	<p style="text-align: center;">Japan</p> <ul style="list-style-type: none"> • <i>Japan Atomic Energy Agency (JAEA)</i> • <i>Kyushu University</i> • <i>University of Fukui</i> <p style="text-align: center;">Republic of Korea</p> <ul style="list-style-type: none"> • <i>Korea Atomic Energy Research Institute (KAERI)</i> • <i>Korea Institute of Nuclear Safety (KINS)</i> <p style="text-align: center;">Netherlands</p> <ul style="list-style-type: none"> • <i>Nuclear Research and Consultancy Group (NRG)</i> <p style="text-align: center;">Russian Federation</p> <ul style="list-style-type: none"> • <i>Nuclear Safety Institute of the Russian Academy of Sciences (IBRAE-RAN)</i> <p style="text-align: center;">Switzerland</p> <ul style="list-style-type: none"> • <i>Paul Scherrer Institute (PSI)</i> <p style="text-align: center;">USA</p> <ul style="list-style-type: none"> • <i>Argonne National Laboratory</i> • <i>TerraPower</i>
---	--

FIG. 1. EBR-II benchmarks CRP participant organizations.

The recorded data were not distributed to the participants until after the second RCM, held at IAEA Headquarters in Vienna, Austria in November 2013. At this RCM, participants reported on their “blind” simulation results and discussed modelling problems encountered and possible solutions. Final “blind” results were due in February 2014, at which time Argonne provided all participants with the recorded data. Two additional RCMs were held to discuss progress on the simulations and compare results among the participants, as well as to discuss the uncertainty analysis and results qualification analysis that were being applied to the CRP simulation results by the participant team from N.I.N.E. The third RCM was held in March 2015 at ENEA offices in Bologna, Italy and the fourth and final RCM was held in April 2016 in Vienna. This final RCM also gave the participants an opportunity to discuss lessons learned during the CRP and to organize a special session covering the collective final simulation results from the CRP for the June 2017 IAEA FR-17 fast reactor conference.

The responsibilities of the host organization for the CRP were undertaken by Argonne as the organization that designed, built and operated EBR-II; conducted the SHRT series; and owns the data recorded during the series. Argonne served as a resource for the other participants on

EBR-II plant information and on the conduct of the two transients, and it also hosted the on-line archive for information, RCM presentations and documents for the CRP.

This report documents the model development work performed by CRP participants and presents the simulation results and comparisons with the recorded data. EBR-II, the SHRT-17 and SHRT-45R transients, and the benchmark specifications for these two transients are described in Sections 2–4. Sections 5–8 cover, for each participant group, the modelling work and the tools that were used, as well as presenting individual results and any sensitivity analyses performed. Sections 9 and 10 address the results as a whole, with Section 9 discussing the results qualification process applied to the results collectively and Section 10 presenting comparisons of the recorded data against the results taken as a whole.

2. DESCRIPTION OF EBR-II

Argonne began power operations of the Experimental Breeder Reactor II (EBR-II) in 1964 and continued until the reactor was shut down in 1994. EBR-II was operated initially to demonstrate the feasibility of a closed fuel cycle that required the addition of only uranium-238 to fuel the breeding process and allow for sustained operation. To achieve the intended fuel utilization, the initial EBR-II operating period was tied closely to research into pyrometallurgical reprocessing for irradiated nuclear fuel. This period lasted five years. Following the fuel cycle demonstration phase, the focus of EBR-II shifted for much of the next ten years towards irradiation experiments of advanced binary and ternary metal fuels and also advanced oxide fuels. During the last 15 years, EBR-II was used for experiments designed to demonstrate the importance of passive safety in liquid metal reactors (LMRs).

2.1. REACTOR

The EBR-II plant was designed and operated by Argonne National Laboratory for the US Department of Energy. EBR-II was rated for a thermal power of 62.5 MW(th) with an electric output of approximately 20 MW. It was a sodium cooled reactor that used metal fuel. At the time of the SHRT, the reactor was fueled with U-5Fs, a fissium fuel alloy uniquely developed and fabricated for EBR-II. The EBR-II plant was a pool design, with all major primary system components submerged in the primary tank, as illustrated in the simple primary system schematic given in FIG. 2.

2.2. CORE

The EBR-II reactor vessel grid plenum assembly accommodated 637 hexagonal subassemblies, which were installed in one of three regions: central core, inner blanket or outer blanket. The central core comprised the 61 subassemblies in the first five rows. Two of these positions contained safety rod subassemblies and eight positions contained control rod subassemblies. The remaining central core subassemblies were either driver fuel or experimental-irradiation subassemblies of varying types. Rows 6 and 7 formed what was called the inner blanket region. This region originally contained blanket subassemblies but was converted to driver and irradiation subassemblies in row 6 (known as the expanded core) and mostly stainless steel reflectors in row 7. The subassemblies in rows 8–16 formed the outer blanket region, with row 8 consisting of reflectors and rows 9–16 of blanket subassemblies, interspersed with a few reflectors.

For the SHRT transients, two instrumented subassemblies were inserted into core positions normally reserved for control rods. These two subassemblies were identified as XX09 and XX10 and were specifically designed with a variety of instrumentation to provide data for benchmark validation purposes. XX09 was a fueled subassembly that contained 59 fuel pins; in over one third of these pins, the standard spacer wires were replaced with spacer wire thermocouples that collectively recorded temperatures at four axial locations. XX10 was a non-fueled subassembly consisting of 18 pins, each wrapped with spacer wire thermocouples that collectively measured temperatures at four axial locations. Both subassemblies were also fitted with two inlet flowmeters. These two instrumented subassemblies thus provided detailed three-dimensional coolant temperature profiles that are useful in evaluating multidimensional subassembly models.

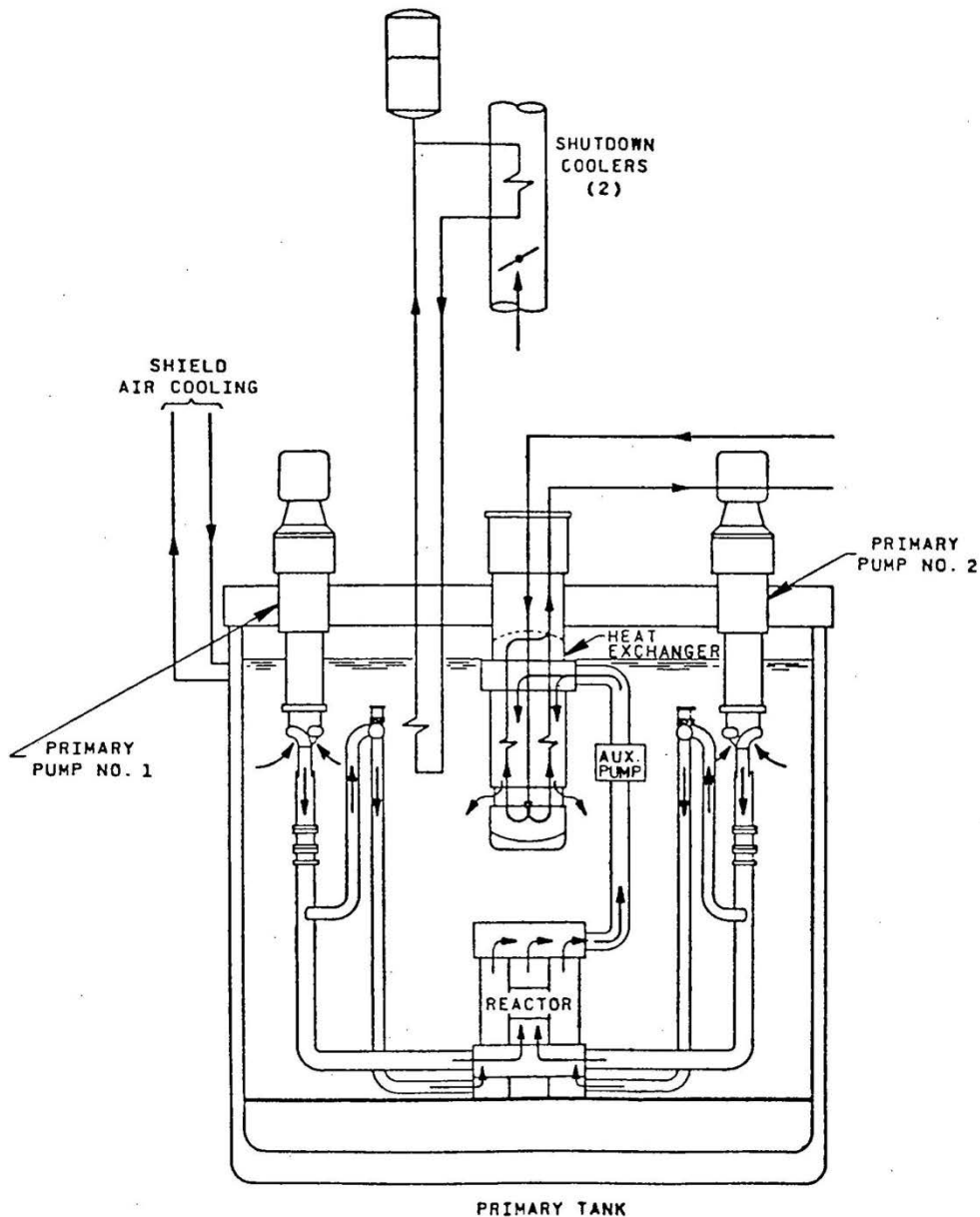


FIG. 2. EBR-II primary system components and sodium flow paths.

2.3. HEAT TRANSPORT SYSTEMS

The EBR-II plant included three cooling loops: a primary sodium loop, an intermediate sodium loop and a secondary steam loop. FIG. 3 shows a simple schematic of the primary, intermediate and steam systems.

2.3.1. Primary heat transport system

EBR-II was designed with two inlet plena, one high pressure and one low pressure. Two centrifugal primary pumps drew sodium from the primary tank pool and provided sodium to the two inlet plena for the core. Subassemblies in the inner core and extended core regions received sodium from the high pressure inlet plenum, accounting for approximately 85% of the total primary flow. The blanket and reflector subassemblies in the outer blanket region received sodium from the low pressure inlet plenum.

Hot sodium exited the subassemblies into a common upper plenum where it mixed before passing through the outlet pipe into the intermediate heat exchanger (IHX). The pipe feeding sodium to the IHX is referred to as the 'Z-Pipe'. Sodium then exited the IHX back into the primary sodium tank before entering the primary sodium pumps again. The shutdown coolers shown in FIG. 3 were not used during the transients analyzed in this CRP and so are not included in the benchmark model.

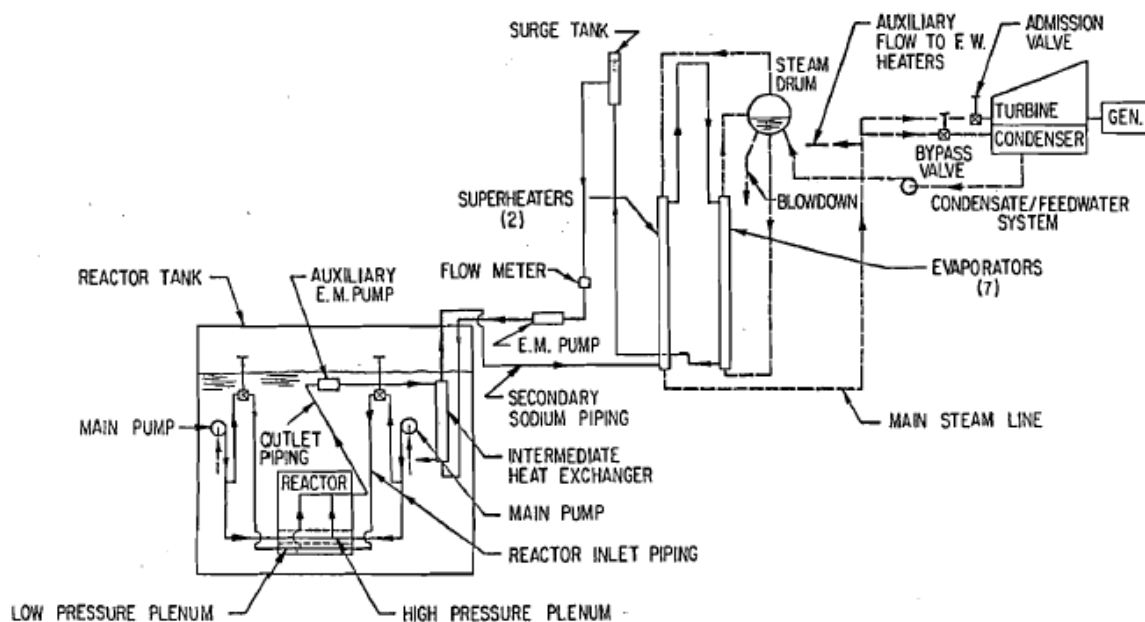


FIG. 3. EBR-II plant schematic.

The intermediate heat exchanger transferred heat from the radioactive primary system to the intermediate system and isolated the primary system from the water inventory in the steam plant. The IHX was a tube and shell design with single-wall straight tubes and was operated in the counterflow mode.

An electromagnetic auxiliary coolant pump was located on the exterior of the reactor outlet pipe. This pump operated in series with the main pumps and was available to provide coolant circulation for decay heat removal if the main pumps were to fail.

2.3.2. Intermediate heat transport system

The intermediate heat transport system also used sodium as the working fluid; unlike the primary system, however, the sodium was not radioactive. This loop transferred heat between the radioactive sodium in the primary loop and water in the steam system. Sodium in the intermediate loop was circulated by an electromagnetic pump upstream of the IHX. Sodium traveled from the IHX to the superheaters and then the evaporators, where its heat was transferred to the balance of plant. The colder sodium in the intermediate loop then traveled through a similar length of piping back to the pump and the IHX.

2.3.3. Water/steam system and turbines

The steam generator system consisted of two parallel superheaters and seven parallel evaporators, plus a conventional overhead steam drum. Steam flowed from the evaporators into the steam drum, then saturated steam flowed from the top of the steam drum downward through the superheaters and out to a conventional 20 MW(e) turbine generator system. A steam bypass system was also available to provide the option of absorbing all the energy produced by the reactor without generating electricity.

2.4. BASIC PLANT SPECIFICATIONS

The basic plant specifications are provided in TABLE 1 below:

TABLE 1. BASIC PLANT SPECIFICATIONS

Reactor type	Sodium cooled fast reactor
Thermal output	62.5 MW(th)
Electric output	20 MW(e)
Reactor grid positions	
Core	61
Inner blanket	66
Outer blanket	510
Total	637
Configuration	Hexagonal
Driver fuel subassemblies (s/a)	
No. of pins per core s/a	91
Length of fuel pin, 0 at.% burnup	34.3 cm
Composition	U-5Fs metal fuel
Uranium enrichment	67% U ²³⁵

Cladding and spacer wires	SS316
Plenum gas	Helium
Average core temperatures, °C	
Fuel	487
Steel	412
Coolant	393
Control/safety rods	
No. of control rods	8
No. of safety rods	2
Absorber material	B ₄ C
No. of pins per rod	61
Vertical travel	43.8 cm
Blanket fuel subassemblies	
No. of pins per blanket s/a	19
Length of pin	139.0 cm
Composition	Depleted uranium
Cladding	SS304

3. DESCRIPTION OF THE SHUTDOWN HEAT REMOVAL TESTS CONDUCTED IN 1984 AND 1986

In the 1970s, the role of EBR-II transitioned to new whole plant test programmes addressing anticipated off-normal conditions and severe accident initiators that might occur in future liquid metal reactor plants. Of particular interest are the shutdown heat removal tests, which demonstrated the potential for sodium cooled metal-fueled fast reactors to survive severe accident initiators with no core damage. The extensive data recorded for these tests provide an excellent basis for code and data verification, validation and qualification. These tasks are best accomplished within the framework of international benchmark simulations of the most severe of these tests, the SHRT-17 and SHRT-45R transients.

3.1. TEST DESCRIPTIONS

3.1.1. SHRT-17

On June 20, 1984 a full power loss of flow test in the SHRT series demonstrated the effectiveness of natural circulation in the EBR-II reactor. During this test the plant protection system was used to simultaneously scram the reactor. To initiate the SHRT-17 test, both primary coolant pumps and the intermediate loop pump were tripped to simulate a protected loss of flow accident beginning from full power and flow conditions. In addition, the primary system auxiliary coolant pump that normally had an emergency battery power supply was also turned off. The reduction in coolant flow rate caused reactor temperatures to rise temporarily to high, but acceptable levels as the reactor safely cooled itself down by natural circulation.

Prior to the start of SHRT-17, EBR-II was operated at full power and full flow for long enough that temperatures throughout the system had reached an equilibrium state. The full power operation was less than two hours in order to limit decay heat after scram. The control rod drives were active to allow control rod insertion at the start of the transient period.

The SHRT-17 transient was initiated by a trip of the primary and intermediate pumps. The reactor was also instantaneously scrammed. The primary pump trip mode was a breaker trip in which the power to the motor generator sets and the clutches was simultaneously lost. Each primary pump had its own controller and motor generator (M-G set). The flow coastdown was governed by the kinetic energy stored in the inertia of the M-G set. While the coastdown shapes for SHRT-17 were designed to be identical for the two primary pumps, intrinsic differences between the two pump drive units caused a difference in stop times. The auxiliary electromagnetic pump in the primary loop was turned off and did not receive power from battery backups as would actually occur during a total station blackout.

As the SHRT-17 test continued, the reactor decay power decreased due to fission product decay. After the start of the test, no automatic or operator action took place until the test had concluded. TABLE 2 summarizes the initial conditions and transient initiators for the SHRT-17 test.

TABLE 2. SHRT-17 TEST DESCRIPTION

Initial Power	57.3 MW
Initial Primary Coolant Flow Through Core	8500 gpm at 800°F
Initial Intermediate Coolant Flow	5615 gpm at 582°F
Initial Core Inlet Temperature	665°F
Primary and Intermediate Pump Coastdown Conditions	Power to motor generator sets removed
Control Rods	Full insertion at test initiation
Auxiliary EM Pump Conditions	Power to Auxiliary EM Pump removed

3.1.2. SHRT-45R

On April 3, 1986 a full power loss of flow test in the SHRT series demonstrated the effectiveness of passive reactivity feedback in the EBR-II reactor to bring the reactor to decay heat power. During this test the plant protection system was disabled to prevent initiation of a scram. To initiate the SHRT-45R test, both primary coolant pumps and the intermediate loop pump were tripped to simulate an unprotected loss of flow accident beginning from full power

and flow conditions. The reduction in coolant flow rate caused reactor temperatures to rise temporarily to high, but acceptable levels as the reactor safely terminated the fission process.

Prior to the start of SHRT-45R, EBR-II was operated at full power and full flow for long enough that the system had reached an equilibrium state. Just prior to test initiation, the control rod drives were deactivated to preclude control rod movement during the transient period. This action prevented insertion or withdrawal of the rods by the drive motors, but it did not affect the scram function.

The SHRT-45R transient was initiated by opening the breaker powering the motor generator set of each of the primary pumps and of the intermediate pump, thus removing the power supply to the pumps. The result was conditions that were similar to those that would occur during a station blackout. The auxiliary electromagnetic pump in the primary loop continued to receive power from its battery while the rectifier remained tripped, as would occur during a total station blackout.

As the SHRT-45R test continued, the reactor power decreased due to reactivity feedbacks. Once the test was initiated, no automatic or operator action took place until the test had concluded, at which point the reactor was scrammed. TABLE 3 summarizes the initial conditions and transient initiators for the SHRT-45R test.

TABLE 3. SHRT-45R TEST DESCRIPTION

Initial Power	60.0 MW
Initial Primary Coolant Flow Through Core	8972 gpm at 800°F
Initial Intermediate Coolant Flow	5475 gpm at 582°F
Initial Core Inlet Temperature	651°F
Primary and Intermediate Pump Coastdown Conditions	<ul style="list-style-type: none"> — Power to motor generator sets removed — Flow coastdown controlled by coupling and decoupling of motor generator set clutch — Approx. 95 seconds before pump stop
Control Rods	Insertion disabled
Auxiliary EM Pump Conditions	On battery

3.2. DESCRIPTION OF INSTRUMENTATION USED FOR THE TESTS

3.2.1. Temperature measurements

Thermocouples were by far the most widely available piece of instrumentation used in the EBR-II plant, along with a few resistance thermometers. Temperature data were recorded as follows:

- (a) Four thermocouples in the core inlet plena (three in the low pressure plenum and one in the high pressure plenum);
- (b) A set of 8 thermocouples arranged vertically on a probe that extended the height of the upper plenum and were located on the side opposite the Z-Pipe inlet;

- (c) Single thermocouples located at 21 different subassembly outlets – mostly drivers in rows 1–6, but also three reflectors in rows 7 and 9 and two blankets, one in row 12 and one in row 16;
- (d) A thermocouple at the Z-Pipe inlet (SHRT-45R only);
- (e) Two thermocouples at the IHX primary side inlet;
- (f) Four thermocouples on the IHX primary side above the bottom orifice plate;
- (g) Four thermocouples at the IHX primary side outlet;
- (h) One thermocouple at the IHX intermediate side outlet;
- (i) One thermocouple at the pump 1 inlet (SHRT-45R only);
- (j) Fourteen thermocouples in the primary sodium tank, installed at three different levels, to measure the bulk sodium temperature. Nine of the thermocouples were in the lower, stagnant part of the cold pool and five were near the top of the tank;
- (k) One thermocouple and one resistance thermometer at the IHX secondary inlet;
- (l) Two thermocouples and one resistance thermometer at the IHX secondary outlet.

In addition, for SHRT-45R, two thermocouple trees were installed in the cold pool. Each tree contained 32 thermocouples, ranging in axial position from 0.52 m. to 7.61 m. above the bottom of the primary tank. The trees were located diametrically opposite each other and near the tank wall; one tree was located between the two primary pumps, while the other was located between the IHX and primary pump 1.

Primary sodium thermocouples were known to lose calibration; EBR-II operators adjusted for this by comparing readings from all primary system instruments against the average reading during long isothermal periods.

3.2.2. Flowmeters

When EBR-II was built, two flowmeters were installed in each leg of the piping downstream of each primary pump. Each leg contained a Foster flow tube (ΔP flowmeter) and a permanent magnet, or electromagnetic (EM), flowmeter. Foster flow tubes are accurate to within 2% at full flow, but below about 25% of full flow, they become too inaccurate to use [3]. The electromagnetic flowmeters provide flow measurements with acceptable accuracy even down to low flow rates. The EM flowmeters could not be calibrated in water prior to installation in the sodium, so the Foster flow tubes were used to calibrate the EM flowmeters at full sodium flow once the EM flowmeters were installed in EBR-II, and the EM flowmeters were the primary instrumentation used to measure flow.

By the time that SHRT-17 was run, all four flowmeters in the piping following pump 1 had failed and could not be accessed to be replaced. The Foster flow tube in the high pressure plenum inlet piping from pump 2 had also failed, but both permanent magnet flowmeters and the Foster flowmeter in the low pressure piping were still operational.

Both types of flowmeters were also originally installed just upstream of the auxiliary pump in the Z-Pipe; however, the EM flowmeter had failed by the time SHRT-17 was conducted.

The intermediate loop included both an EM and a Foster flowmeter located just upstream of the intermediate loop pump, and both were still operating during the SHRT programme.

3.2.3. Instrumented subassembly XX09

XX09 was a fueled subassembly specifically designed with a variety of instrumentation to provide data for benchmark validation purposes. It contained 61 pin positions, of which 59 were driver fuel pins, and was located in a row 5 control rod position. The subassembly instrumentation recorded data representative of a driver subassembly. Two flowmeters, one above the other, and two thermocouples were located at the subassembly inlet, and another 22 thermocouples were positioned at five axial locations. These were spacer wire thermocouples that replaced the standard spacer wires in 22 fuel elements. Thirteen of these thermocouples were located at the top of the core to give a two dimensional radial temperature profile at that axial location. Two additional thermocouples recorded temperatures near the top of the control rod guide thimble that contained XX09. The XX09 instrument loading is illustrated in FIG. 4. The combined instrumentation gave a detailed transient temperature and flow profile of the subassembly.

Except for some minor modifications, the subassembly outer configuration was the same as a control rod. XX09 was coupled to an extension tube that traversed all the way up to the outside of the primary tank, providing a protected conduit for the instrument leads and permitting movement of the subassembly during fuel handling. Two of the 61 pin locations were replaced with hollow tubes used as conduits to permit passage of instrument leads.

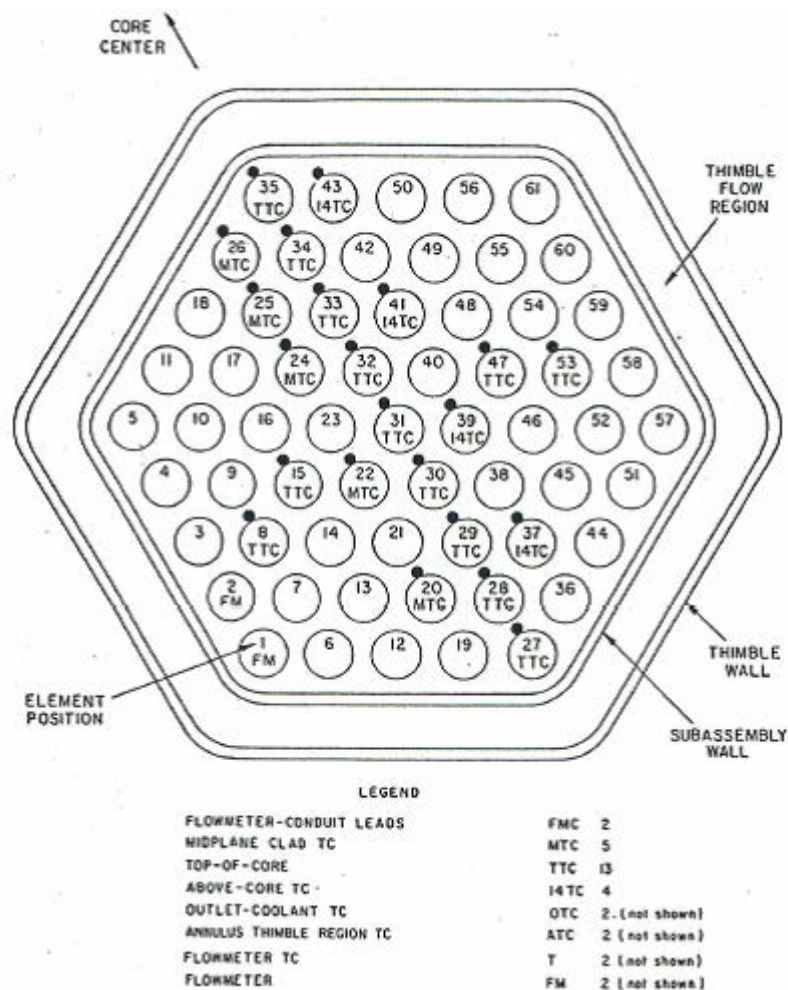


FIG. 4. XX09 instrumented subassembly instrument loading.

3.2.4. Instrumented subassembly XX10

XX10 was a non-fueled subassembly; like XX09, it was specifically designed with a variety of instrumentation to provide data for benchmark validation purposes. It contained 19 pin positions, of which 18 were steel pins, and was located in a row 5 control rod position. The subassembly instrumentation recorded data representative of a reflector subassembly. Two flowmeters, one above the other, and two thermocouples were located at the subassembly inlet, and another 20 thermocouples were positioned at four axial locations. These were spacer wire thermocouples that replaced the standard spacer wires on all 18 pins. Seven of these thermocouples were located at the top of the core and seven at a location above the core, giving a two dimensional radial temperature profile at both these axial locations. Two additional thermocouples recorded temperatures near the top of the control rod guide thimble. The XX10 instrument loading is illustrated in FIG. 5. The combined instrumentation gave a detailed transient temperature and flow profile of the subassembly.

Except for some minor modifications, the subassembly outer configuration was the same as a control rod. XX10 was coupled to an extension tube that traversed all the way up to the outside of the primary tank, providing a protected conduit for the instrument leads and permitting movement of the subassembly during fuel handling. Two thermocouples were attached to the extension tube and recorded sodium temperatures. One of the 19 pin locations were replaced with a hollow tube used as a conduit to permit passage of instrument leads.

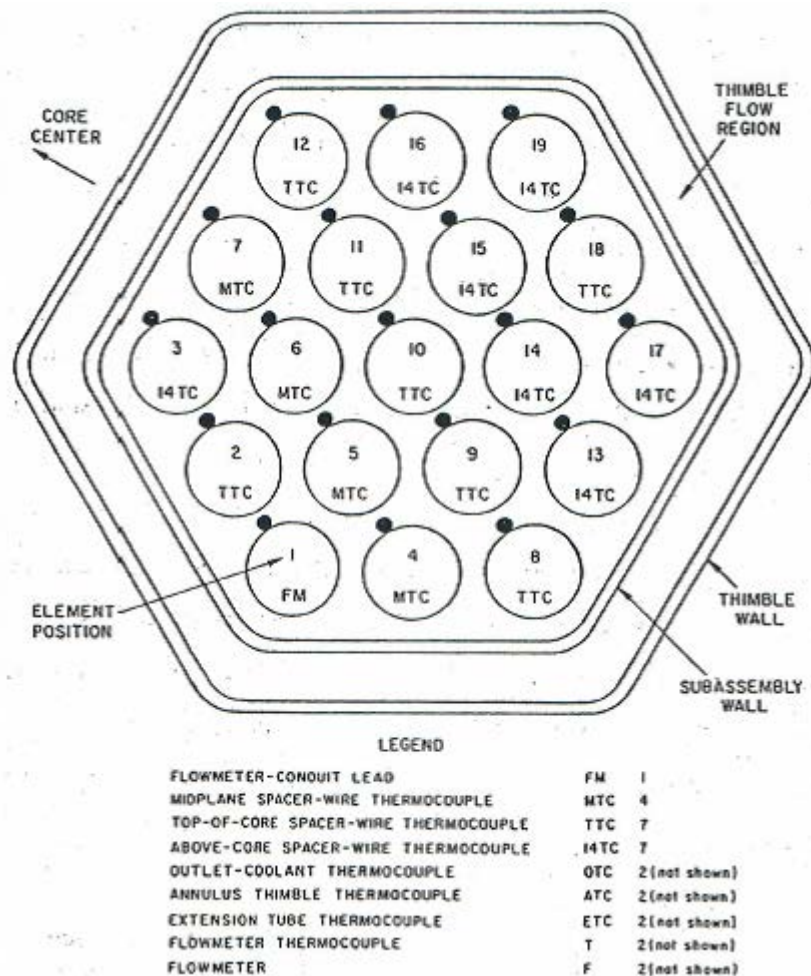


FIG. 5. XX10 instrumented subassembly instrument loading.

3.2.5. Fission power measurement

Two primary methods were used to measure EBR-II's core power level. The first method involved heat balance calculations based on coolant flow rates and temperatures. The second method measured the neutron flux intensity at several locations outside of the core. The heat balance calculations determined full power level based on total primary sodium flow rate and the temperature difference across the core. These were checked against heat balances across the intermediate sodium loop and the steam loop. Neutron flux intensity measurements were then used to measure fission power during the transients. These measurements were taken from three wide range instrument channels and two linear level channels.

3.2.6. Pressure measurements

All pressure measurements taken in EBR-II were calibrated such that at zero flow, the entire primary system measured a pressure of zero. In other words, the pressure drop due to gravity was calibrated out of the gauge pressure at all measurement locations. Only primary pump 1 discharge pressure measurements can be located for the SHRT-17 test; for the SHRT-45R test, data were recorded for primary pump 1 discharge pressure and in the upper plenum at the core outlet. The cover gas pressure was not measured but can be assumed to be the local atmospheric pressure.

3.3. TEST RESULTS

Sections 3.3.1 and 3.3.2 present the measured test data recorded by the data acquisition system during SHRT-17 and SHRT-45R, respectively. Of the available measurements described in Section 3.2, these measurements collectively represent the system behaviour during the two transients, and they were identified as the data best suited for comparison against the CRP participants' simulation results. Section 3.4 discusses the accuracy of these measurements and potential concerns for comparisons with systems code predictions. Section 10 compares the measured test data against the participants' final simulation results. These measurements represent an appropriate collection of parameters for comparison against results from the systems codes used by the benchmark participants.

3.3.1. SHRT-17

Primary system flow rates coasted down gradually during the first minute of SHRT-17 until the pumps stopped and natural circulation was established. Due to the rapid large negative reactivity insertion from the simultaneous control rod scram, fission power decreased much more quickly and the normalized power to flow ratio dropped to 0.2 after one second. The power to flow ratio then began to gradually increase as the core mass flow rate decreased faster than the heat generated by delayed neutrons and decay heat.

Over the first minute of the test, the normalized power to flow ratio continued to increase, exceeding the nominal value after forty seconds. Elevated core temperatures provided the necessary driving head to maintain relatively constant flow rates before the two pumps stopped at 42 and 51 seconds. The increased resistance of the stopped pumps caused flow rates to decrease again and the normalized power to flow ratio peaked at 2.4 after one minute.

As the system transitioned to natural circulation, the core outlet temperature remained elevated, and temperatures in the Z-Pipe began to increase. The core flow rate gradually

increased over the next few minutes and total power continued to decrease. Three minutes after the test began, the power to flow ratio decreased below its nominal value.

FIG. 6 illustrates mass flow rate measurements for the high and low pressure piping following pump #2 during the transition to natural circulation. These flow rates were measured with electromagnetic flowmeters as normalized flow rates and were renormalized to the initial flow rates specified in the benchmark. Because SHRT-17 was not representing station blackout conditions, the auxiliary EM pump in the Z-Pipe was disabled for the test. SHRT-17 flow rates were also lower than those during SHRT-45R due to lower system temperatures in the core, outlet plenum and Z-Pipe. After ten minutes, SHRT-17 flow rates were less than half of the SHRT-45R flow rates at ten minutes into that test. Analysis performed during the CRP suggests that after both pumps coasted down, they locked up due to the low flow rates. Locked pumps provide additional flow resistance that would further contribute to the lower flows measured during SHRT-17 than SHRT-45R.

FIG. 7 illustrates the power level during the SHRT-17 test. The neutron flux intensity measurements described in the previous section recorded the normalized fission power during the test. The American Nuclear Society (ANS) decay heat standard [4] was then used to calculate the initial fraction of power generated by decay heat at the start of the test. Then, decay heat generation during the test was calculated with the decay heat standard based on the fission power measurements.

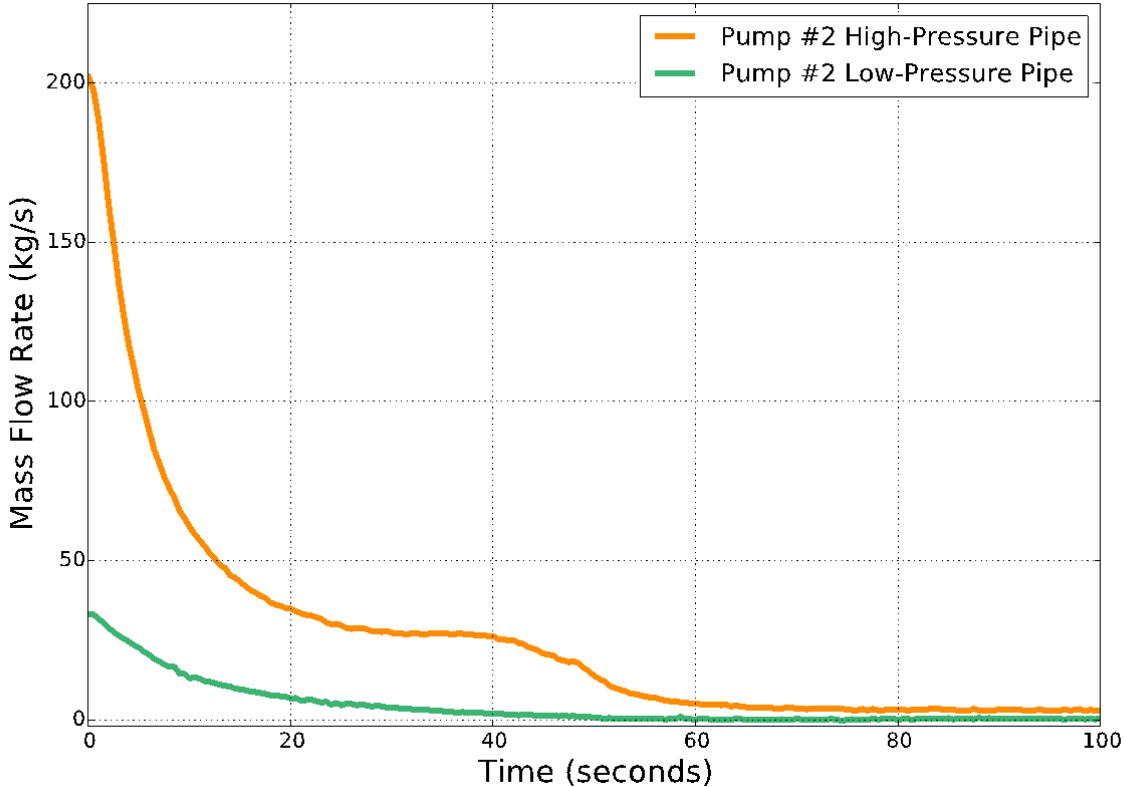


FIG. 6. SHRT-17 pump #2 high and low pressure mass flow rates.

The total power shown in FIG. 7 is the sum of the measured fission power and the calculated decay heat generation.

FIG. 8 illustrates the measured core inlet and outlet temperatures during SHRT-17. Because the pumps stopped during the loss of flow test, sodium in the cold pool was not well-mixed, and it took a long time for hot sodium leaving the IHX to propagate to the pump inlets. Consequently, temperatures in the inlet plena were nearly constant during the fifteen-minute test. It should be noted that the low pressure inlet plenum temperature shown in FIG. 8 is the average of the three thermocouple measurements from the plenum. All three low pressure inlet plenum thermocouples recorded very similar temperatures during the test.

The core outlet temperature decreased quickly at the beginning of the test following the control rod scram. Over the next two minutes the core outlet temperature increased due to the core flow rate decreasing faster than the total power level. The core outlet temperature peaked approximately one minute after the power to flow ratio peaked due to the heat capacity of the upper core structure and colder sodium already present in the outlet plenum. Although a thermocouple was installed at the Z-Pipe inlet, the measured core outlet temperature for SHRT-17 was not recorded by this instrument. It is believed that this measurement was a combination of several subassembly outlet temperature measurements, although the exact combination of those measurements is not known for certain. Section 3.4 discusses this further.

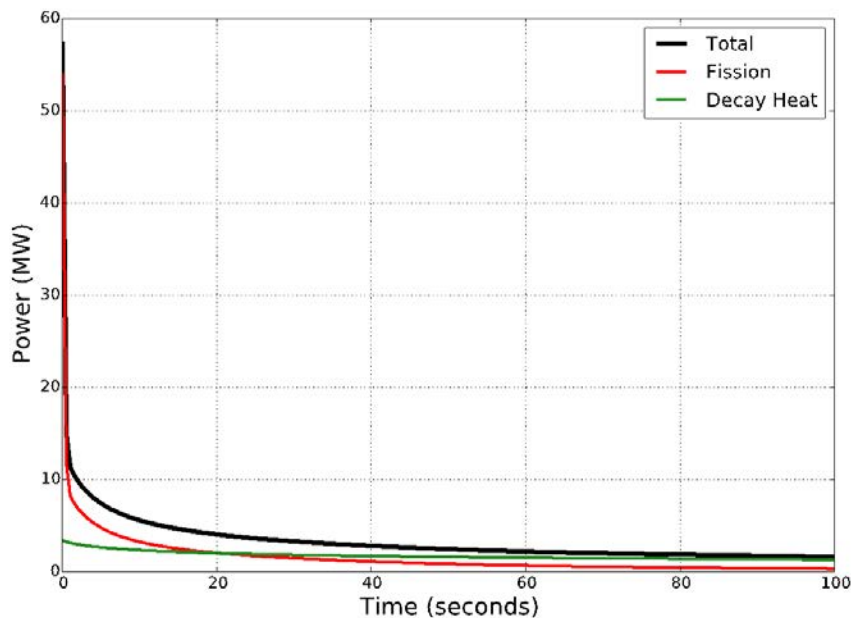


FIG. 7. SHRT-17 total power, fission power and decay heat.

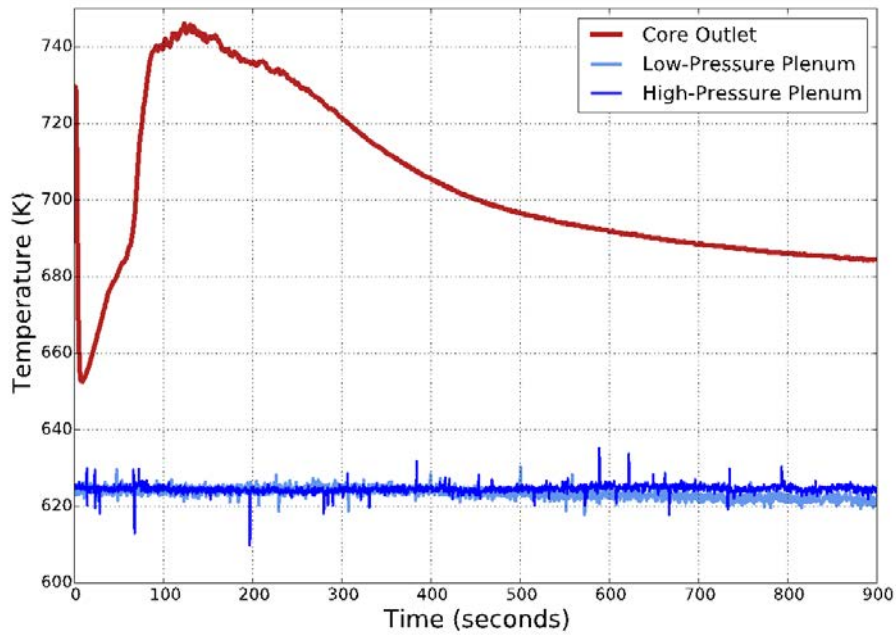


FIG. 8. SHRT-17 core inlet and outlet temperatures.

FIG. 9 illustrates the SHRT-17 measured primary and intermediate IHX temperatures. The primary side inlet temperature was measured by a thermocouple installed behind an impact baffle plate in the diffuser region at the top of the IHX. The primary side outlet temperature shown in FIG. 9 is the average of four temperatures measured just outside the IHX outlet window. The primary side inlet and outlet temperature measurements are considered to be unreliable representations of the average temperature of sodium entering and exiting the IHX. Section 3.4 discusses the IHX primary side temperature measurements further.

Intermediate side temperatures were measured by thermocouples installed within pipes upstream and downstream of the IHX. The reliability of these measurements has been verified by other temperatures measured further upstream and downstream within the intermediate system.

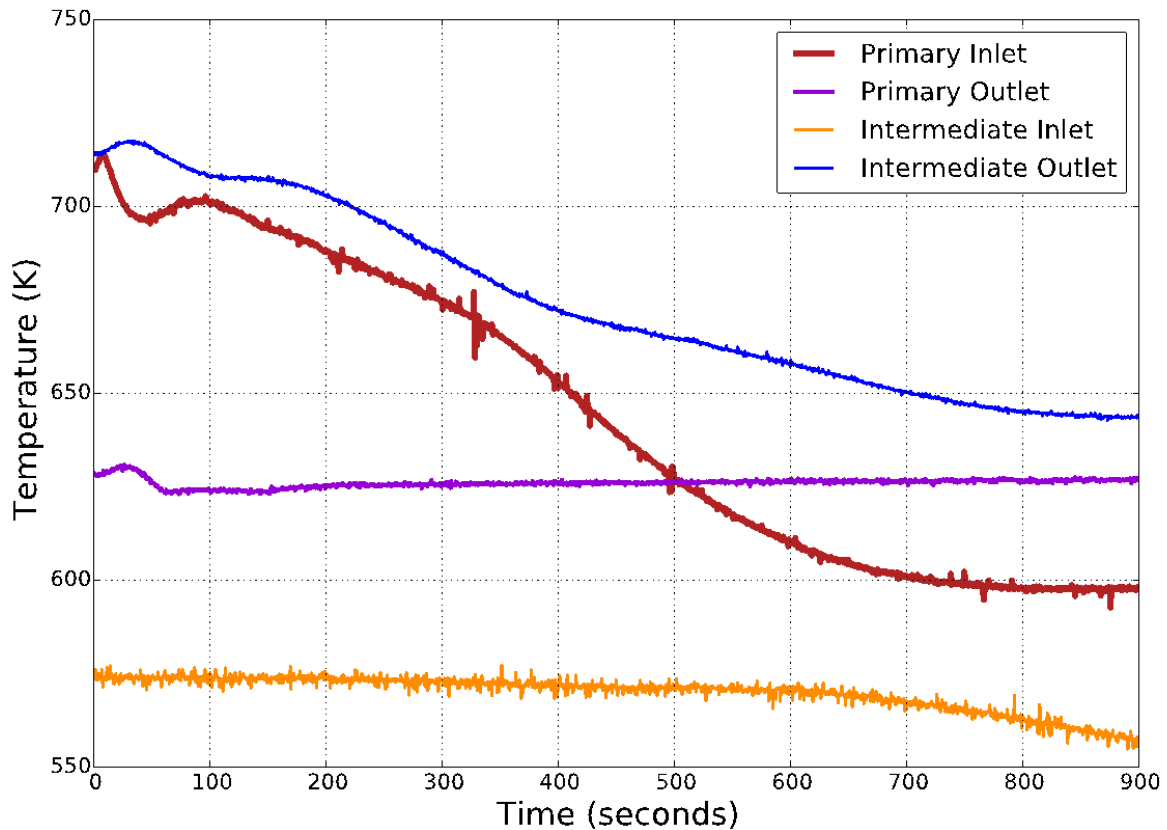


FIG. 9. SHRT-17 IHX temperatures.

FIG. 10 illustrates the flow rate and temperature measurements for the XX09 fueled instrumented subassembly during SHRT-17. The XX09 measured flow rate displayed a similar trend as the measured high pressure flow rate, reaching a minimum around sixty seconds before flow rates increased slightly as natural circulation was established.

Over the first 100 seconds, the thermocouples installed at the XX09 flowmeters at the bottom of the subassembly measured a temperature increase followed by a gradual decrease over the next 300 seconds. Neither of these temperature changes was recorded by the thermocouples in the inlet plena. It is believed that the temperature increase was due to gamma heating decreasing more slowly than the average core power level and undercooling as the core flow rate decreased. The flowmeter temperatures then began to decrease as gamma heating continued to decrease and natural circulation was established.

Within the pin bundle region of XX09, 22 thermocouples measured temperatures at one of three elevations: mid-core (MTC), top of core (TTC), and above core (14TC). Two thermocouples were installed at the outlet of the subassembly (OTC) and two more were installed at the top of the subassembly in the annular thimble region (ATC). Each of these 26 temperature measurements followed the power to flow ratio. Temperatures decreased very rapidly at the beginning of the transient before increasing to a maximum around 100 seconds. Temperatures began to decrease again after natural circulation was established and power continued to decrease. The TTC temperatures were higher than the 14TC, OTC and ATC temperatures due to the heat capacity of the above core structure.

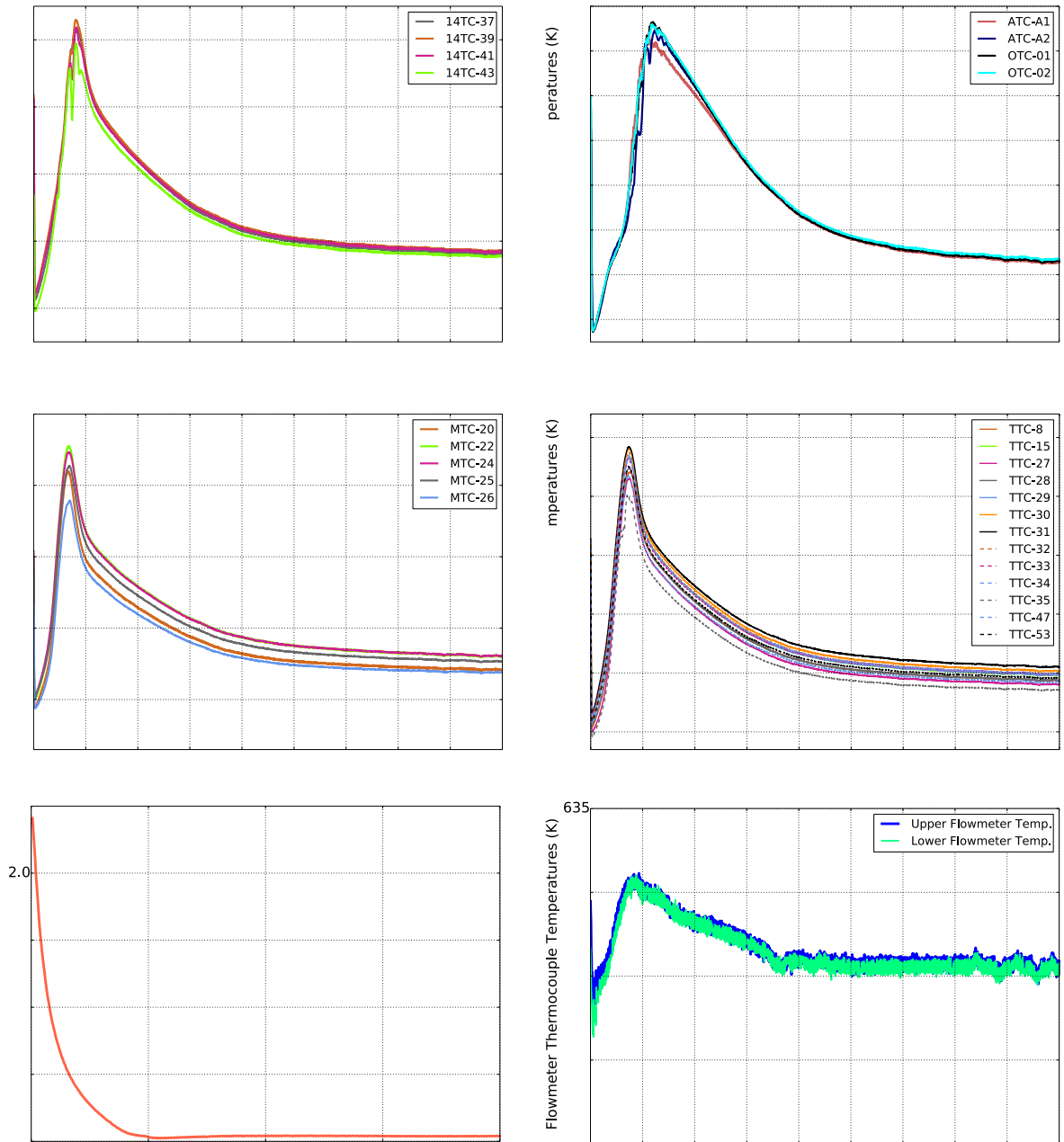


FIG. 10. SHRT-17 XX09 mass flow rate and temperatures.

FIG. 11 illustrates the flow rate and temperature measurements for XX10 during SHRT-17. Flowmeters and thermocouples were installed in similar locations in the XX10 non-fueled instrumented subassembly. The flow rate and temperature measurements for XX10 followed the same trends as XX09. While the initial power generated in XX09 was more than 25 times larger than the initial power generated in XX10, flow through XX09 was only 7 times larger. The lower power to flow ratio for XX10 resulted in lower peak temperatures than for XX09.

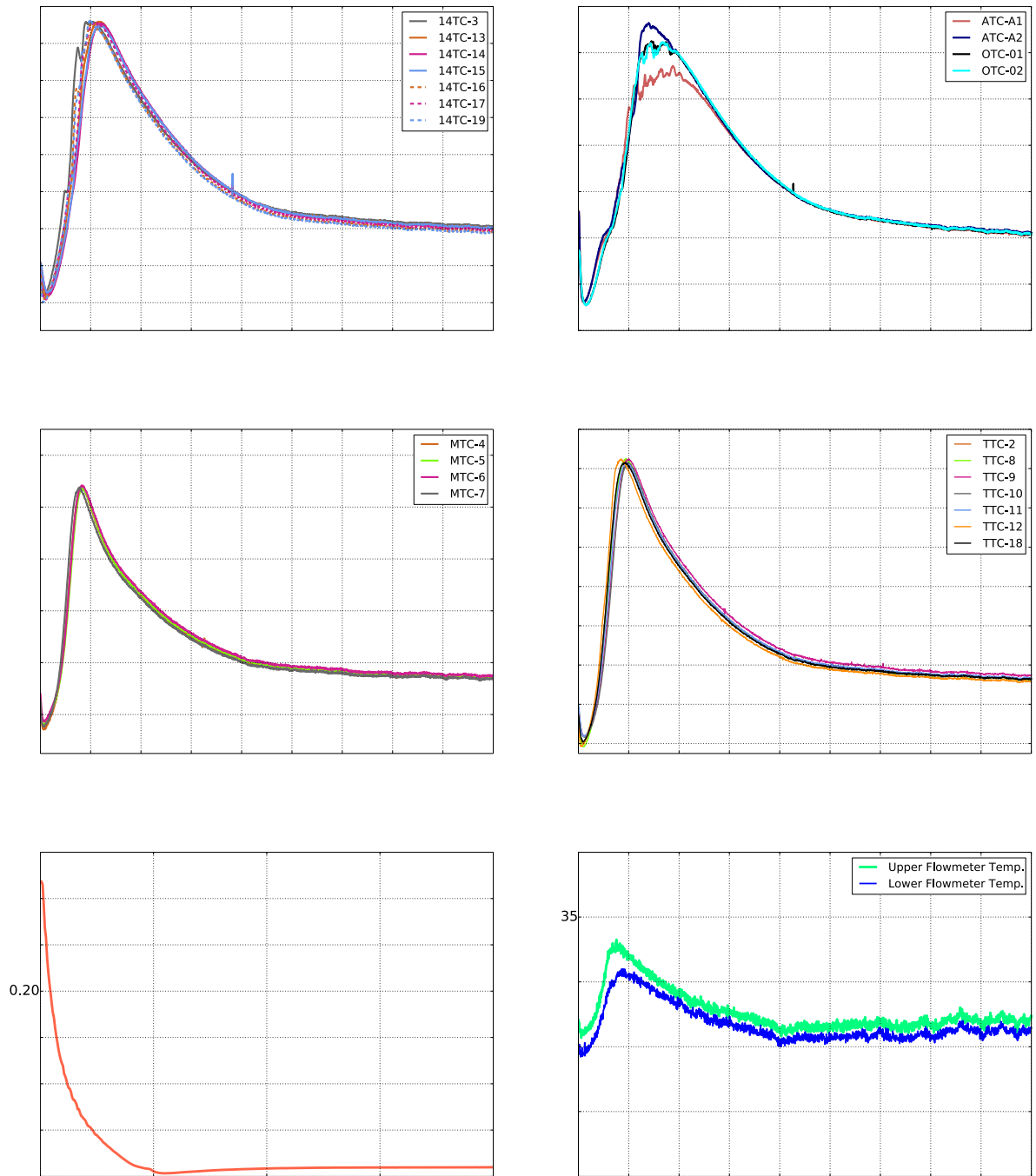


FIG. 11. SHRT-17 XX10 mass flow rate and temperatures.

3.3.2. SHRT-45R

Primary system flow rates coasted down gradually at the beginning of SHRT-45R after the pumps tripped. The two biggest differences between SHRT-45R and SHRT-17 were whether or not the control rods scrammed and the behaviour of the auxiliary EM pump, both of which contributed to higher flow rates for SHRT-45R. Because the control rods did not scram during the unprotected loss of flow test, power decreased more gradually and the power to flow ratio increased immediately at the start of the SHRT-45R test. The power to flow ratio peaked at

2.8 times the nominal value after one minute, producing higher temperatures in the core, upper plenum and Z-Pipe, which led to a larger driving head to help establish natural circulation. SHRT-45R represented a station blackout, so the auxiliary EM pump was left on battery power, providing a small head that also contributed to higher flow rates than for SHRT-17.

FIG. 12 illustrates the mass flow rate measurements for the high and low pressure piping for pump #2 during SHRT-45R. Due to the elevated temperatures at the beginning of the test, the pumps did not stop until 95 seconds into the test, after which the elevated temperatures in the system provided most of the driving head. Primary system flow rates remained relatively constant until 600 seconds into the test, when the current to the auxiliary EM pump was increased by 50% and flow rates increased by approximately 20%. The natural circulation flow rate during SHRT-45R was more than double the natural circulation flow rate during SHRT-17 because of the head provided by the auxiliary EM pump and the higher temperatures during the test. Additionally, the pumps may have locked up during SHRT-17 but not during SHRT-45R, so the flow resistance of the pumps would have been lower during the unprotected SHRT-45R test.

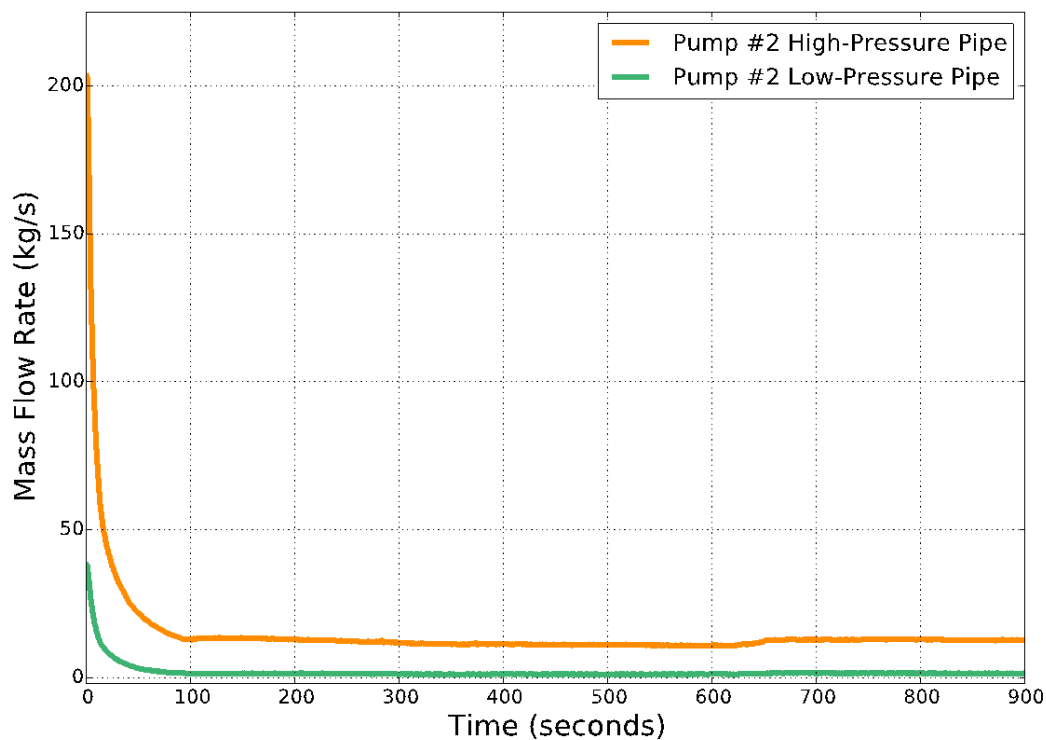


FIG. 12. SHRT-45R pump #2 high and low pressure mass flow rates.

With temperatures in the core increasing, the net reactivity quickly became negative, driving power down. After natural circulation was established, power continued to decrease due to the negative reactivity feedbacks. Based on the CRP participants' simulation results, the sodium density and radial core expansion reactivity feedback effects provided most of the negative reactivity. Axial core expansion also provided a negative reactivity feedback. The Doppler and control rod driveline effects were much smaller and did not play as significant a role in SHRT-45R as for other SFRs.

The power to flow ratio dropped below the nominal value around 400 seconds, as core flow rates were nearly constant but power was still decreasing gradually. The power to flow ratio stabilized at 0.8 times the nominal value around 600 seconds, just before the auxiliary EM pump current increased. Higher flow rates led to lower core temperatures and a small power increase. FIG. 13 illustrates the power level during the SHRT-45R test. As with SHRT-17, total power was the sum of the measured fission power and calculated decay heat. However, unlike SHRT-17, fission represented more than half of the total power for the entire test, hence the SHRT-45R natural circulation flow rates were more than double the SHRT-17 natural circulation flow rates.

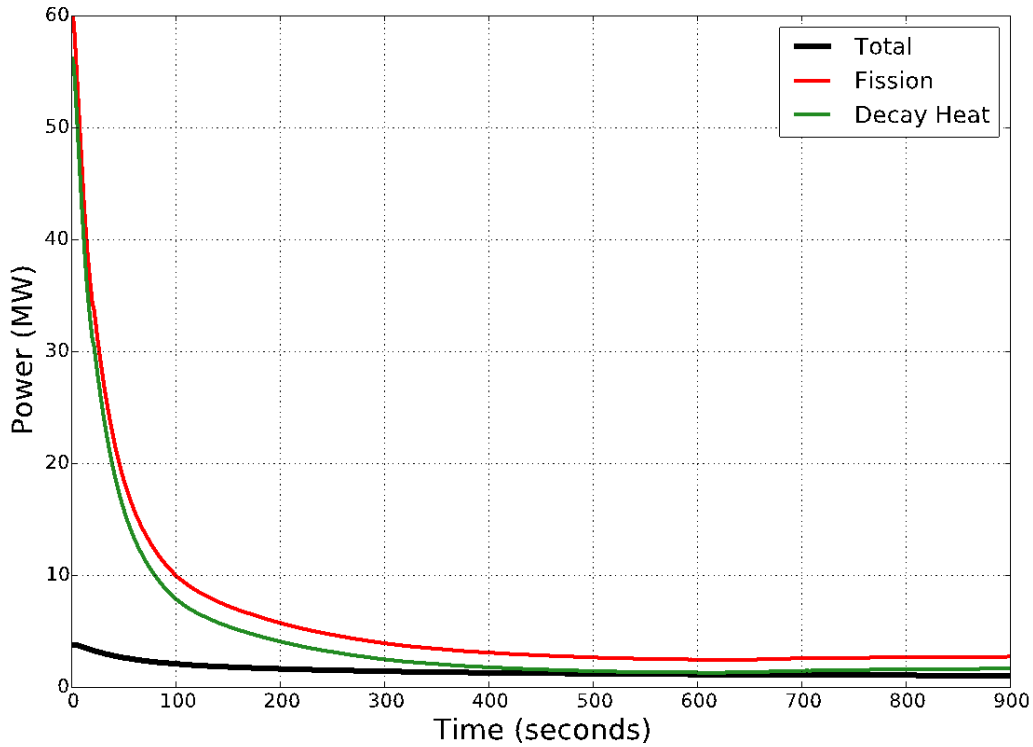


FIG. 13. SHRT-45R total power, fission power and decay heat.

FIG. 14 illustrates the measured core inlet and outlet temperatures during SHRT-45R. As with SHRT-17, a lack of mixing in the cold pool after the pumps tripped led to relatively flat temperatures in the high and low pressure inlet plena. The inlet plena temperatures began to diverge during the second half of the test due to increased stratification in the cold pool and because sodium in the low pressure inlet pipes was more exposed to the colder sodium at the bottom of the cold pool. The portion of the low pressure inlet pipes that traveled horizontally at the bottom of the cold pool was 63 cm longer than the horizontal portion of the high pressure inlet pipes at the bottom of the cold pool. Additionally, the high pressure inlet pipes were nearly twice as thick as the low pressure inlet pipes, providing greater insulation from the cold sodium.

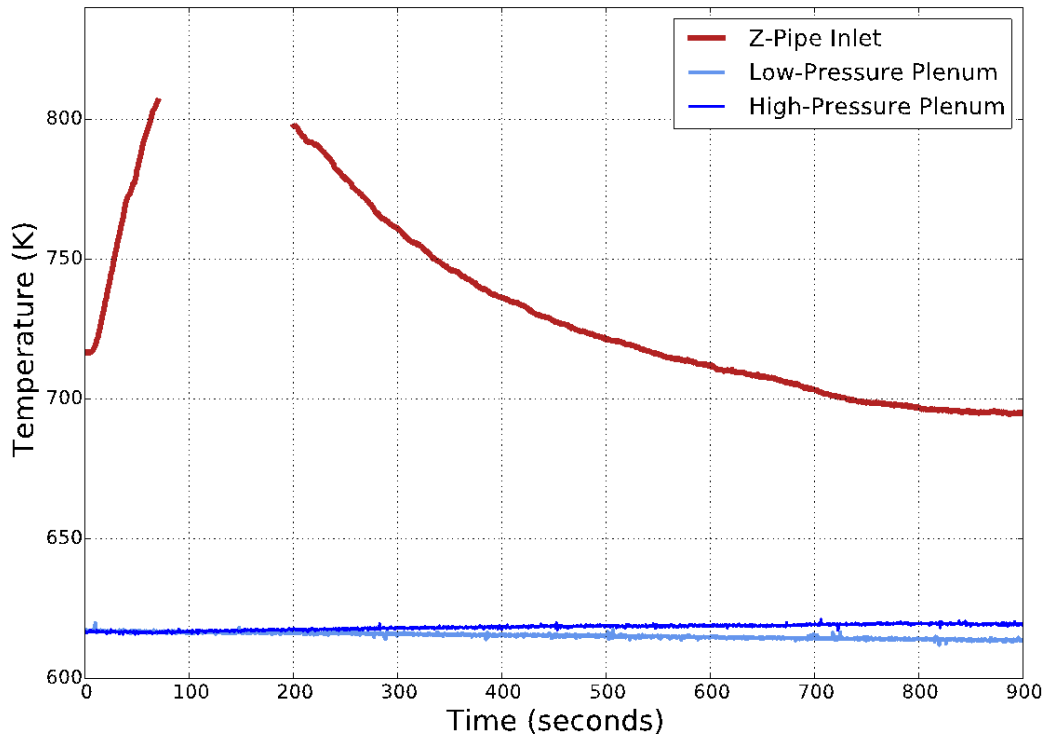


FIG. 14. SHRT-45R core inlet plena and Z-Pipe inlet temperatures.

Figure 14 also shows the Z-Pipe inlet temperature measurement for SHRT-45R. As the power to flow ratio increased, hotter sodium leaving the core mixed with the sodium already in the upper plenum before flowing into the Z-Pipe. The Z-Pipe inlet temperature continued to increase after the power to flow ratio began to decrease because the sodium leaving the core was still hotter than the average upper plenum temperature. There was an issue with the measured Z-Pipe inlet temperature between 75 and 200 seconds, which is discussed in the following section, that led to this data being removed for comparisons with simulation results. After 200 seconds, the Z-Pipe inlet temperature decreased for the remainder of the test as the power level continued to decrease.

FIG. 15 illustrates the SHRT-45R measured primary and intermediate IHX temperatures. The primary side inlet and intermediate side outlet temperatures followed the Z-Pipe inlet temperature, increasing during the first few minutes of the test and then decreasing as the power level continued to drop while flow was relatively constant. Heat lost through the Z-Pipe to the cold pool along with the position of the primary side inlet thermocouple contributed to lower temperatures at the IHX inlet than the Z-Pipe inlet. As with SHRT-17, the primary side temperature measurements are considered to be unreliable representations of the average temperature of sodium entering and exiting the IHX. Reasons why the primary side measurements were not as accurate as the intermediate side measurements are discussed in the following section.

FIG. 16 illustrates the flow rate and temperature measurements for the XX09 fueled instrumented subassembly during SHRT-45R. While the pumps were coasting down, the XX09 measured flow rate displayed a similar trend as the other flow measurements in the primary system. But after the pumps stopped around 100 seconds, the XX09 measured flow rate behaved differently from other flow measurements in the system, particularly the XX10

and pump #2 high pressure flow rates. Because of the large flow rate changes that were recorded by the XX09 flowmeter but not the other flowmeters, it is believed that the XX09 measured flow rate was not accurate for SHRT-45R after the first minute of the test. This is discussed further in Section 3.4.

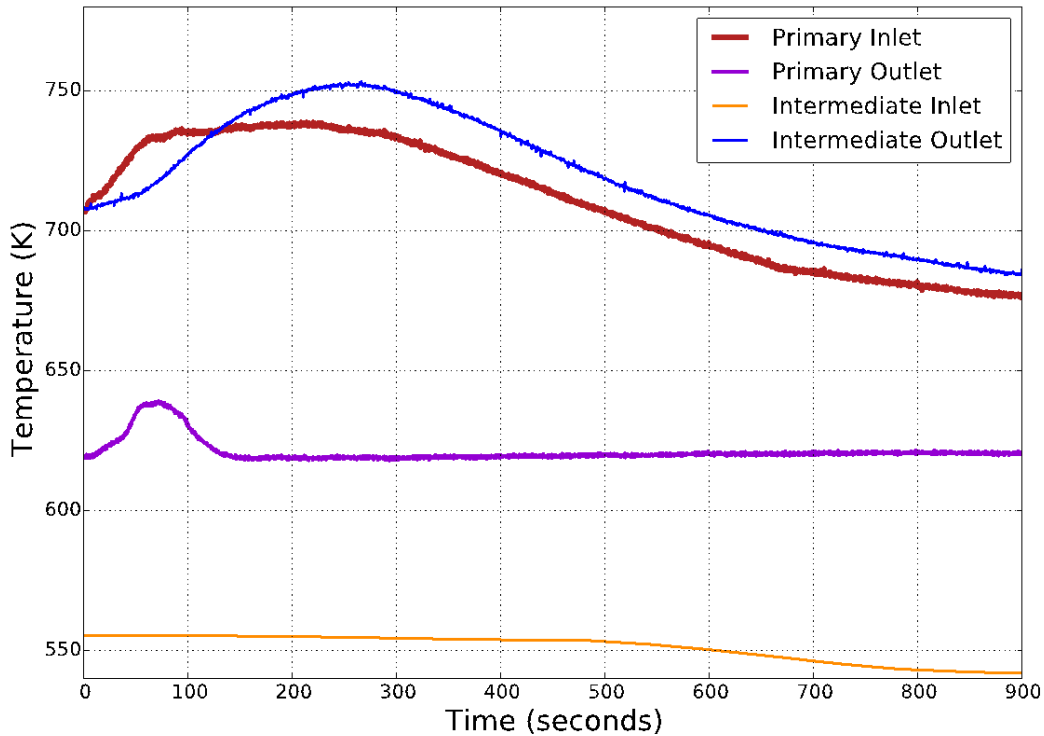


FIG. 15. SHRT-45R IHX temperatures.

Neither the XX09 flowmeter temperature nor the mid-core temperature measurements were available for SHRT-45R.

The TTC, 14TC, ATC and OTC thermocouples, which were installed at the top of or above the pin bundle region, all recorded temperatures that were very similar to the Z-Pipe inlet temperature. For each thermocouple type, the peak temperature was lower and occurred slightly later the higher up the thermocouple was installed. This was due to the heat capacity of the upper core structure drawing heat from the hotter sodium flowing out of the XX09 pin bundle region. At 650 seconds, all of these temperatures decreased due to the increased flow through the subassembly after the auxiliary pump head increased.

FIG. 17 illustrates the flow rate and temperature measurements for XX10 during SHRT-45R. The flow rate and temperature measurements for XX10 followed the same trends as XX09. Even though the core inlet temperature did not increase during SHRT-45R, the XX10 flowmeter thermocouples, which were installed at the bottom of the subassembly, recorded a 20 K increase. As with SHRT-17, this was likely caused by gamma heating and lower flow rates. The MTC, TTC, 14TC, ATC and OTC thermocouples all displayed very similar behaviour as the other temperature measurements described above. Due to the lower power to flow ratio in the non-fueled instrumented subassembly, lower peak temperatures were measured for XX10 than for XX09.

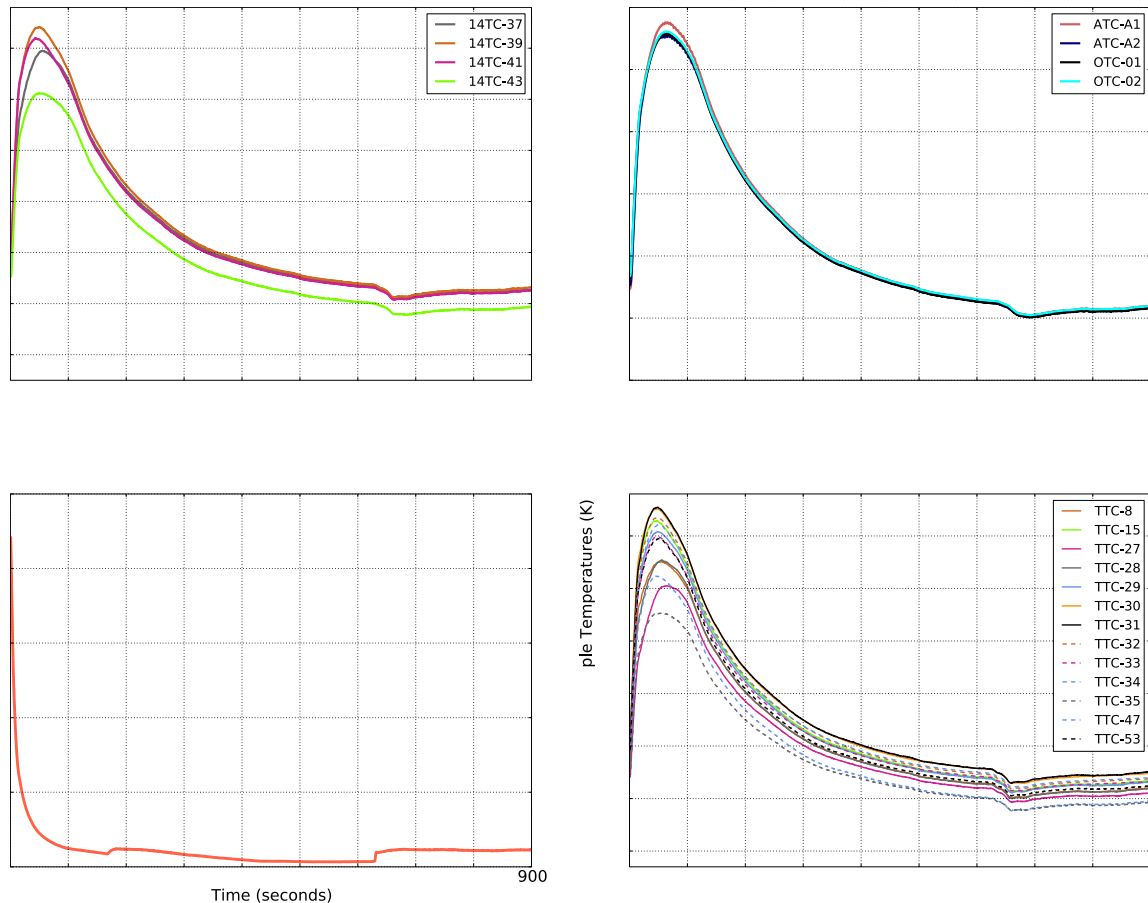


FIG. 16. SHRT-45R XX09 mass flow rate and temperatures.

3.4. INTERPRETATION OF THE EXPERIMENTAL DATA USED IN THE BENCHMARK EXERCISE

Throughout the CRP, the benchmark participants' simulation results were compared with the measurements described in the previous section to assess the status of their simulations. Section 10 discusses many of these comparisons and the participants' progress during the CRP. Large discrepancies between the simulation results and measured test data tended to suggest room for improvement, but this was not always the case. Most of the measurements accurately represented the SHRT-17 and SHRT-45R tests and were appropriate for comparison against systems code results. For a few, confidence was low that the measurements accurately represented the progression of the transients because an instrument was not installed in an ideal location or because it produced a suspicious measurement. The measurements described in the previous section are discussed below to identify which measurements were appropriate for these comparisons, which were heavily impacted by the location of the instrument, and which had a problem during one of the tests that made them inappropriate for the comparisons.

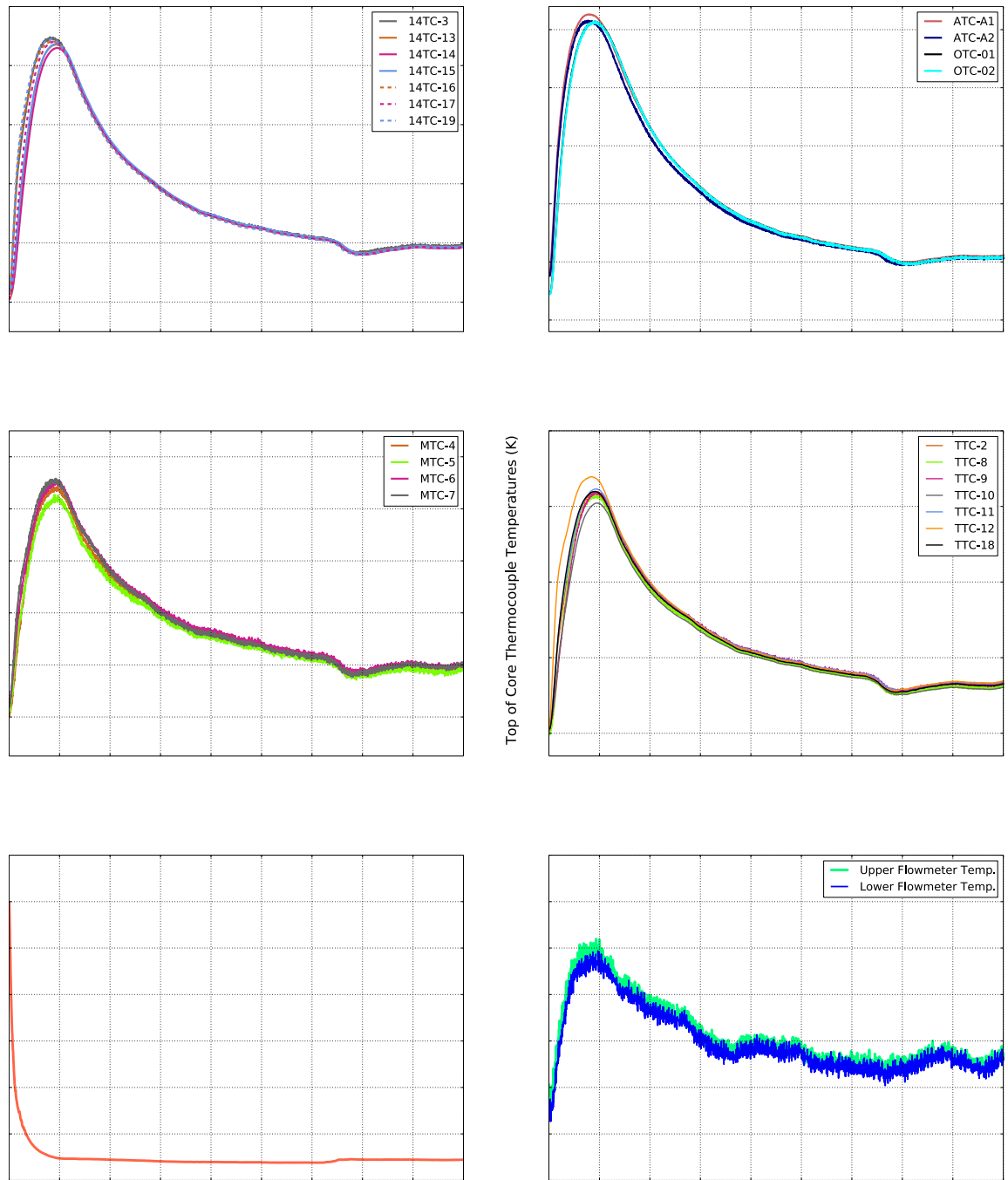


FIG. 17. SHRT-45R XX10 mass flow rate and temperatures.

The two most reliable flow measurements in the primary system were recorded in the high and low pressure piping for pump #2. Foster flow tubes and electromagnetic flowmeters were installed on both pipes. Because the Foster flow tubes measured a pressure difference, which is proportional to flow rate squared and then converted to mass flow rate, they were less accurate at low flow rates. Below 25% of the nominal flow rate, the Foster flow tubes were not considered to record accurate flow rates. Therefore, Foster flow tube measurements were not appropriate for the two loss of flow tests and were not compared with simulation results.

The current produced by sodium flowing through a magnetic field is proportional to mass flow rate, so electromagnetic flowmeters were better suited for low flows with reasonable accuracy. Whether there was a threshold at which the EM flowmeter accuracy dropped off or it gradually decreased at lower flow rates is not known. Therefore, flow measurements are treated with less confidence as they approach 1%. FIG. 18 illustrates the EM flow measurements for the pump #2 high and low pressure piping for both tests. The SHRT-45R high pressure flow rate is considered to be the most accurate because it remained above 5% of the nominal flow rate throughout the entire test. The SHRT-17 high pressure flow rate, on the other hand, decreased to as low as 1.5% before increasing to 2.5% once natural circulation was established.

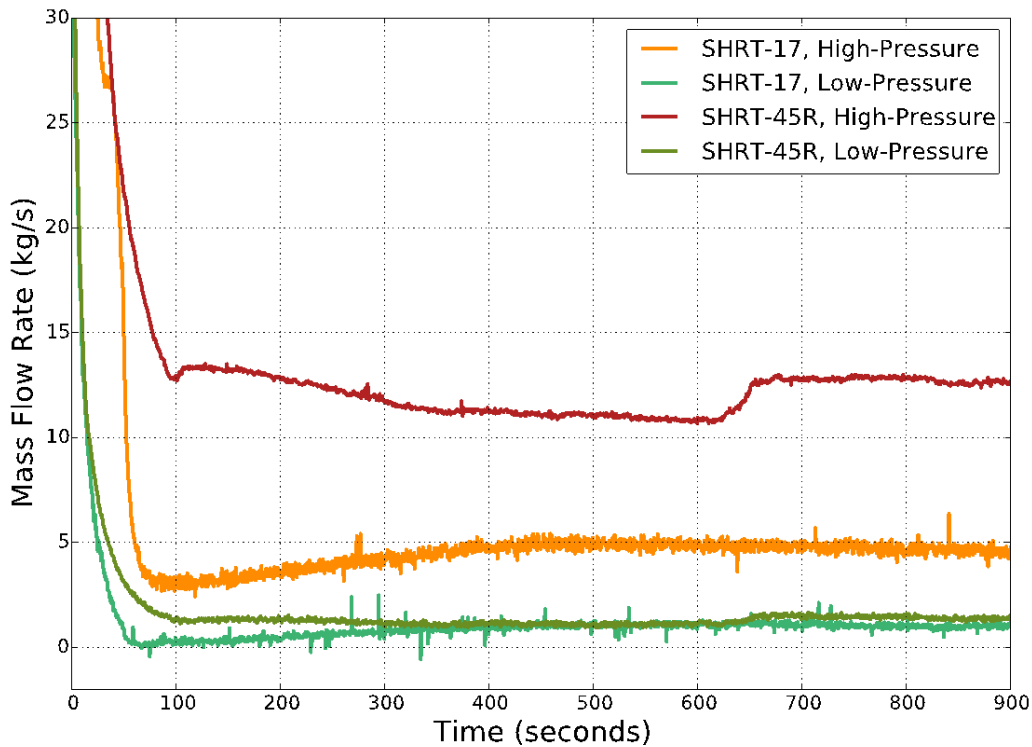


FIG. 18. SHRT-17 and SHRT-45R pump #2 high and low pressure mass flow rates.

For SHRT-17 and SHRT-45R, the low pressure flow rates were both approximately 3% ten minutes into the tests. The 2-to-1 ratio for the SHRT-45R to SHRT-17 high pressure flow rates was not maintained for the low pressure flow rates. In fact, the SHRT-17 low pressure flow rate was slightly higher than the SHRT-45R high pressure flow rate between 8 and 10 minutes. The head provided by the auxiliary EM pump for SHRT-45R should have produced a higher flow rate measurement, suggesting that the SHRT-45R low pressure flow rate measurement may have been too low.

FIG. 19 illustrates the temperature measurements from the high and low pressure inlet plena for both tests. Both temperature measurements are assumed to be very accurate for both tests. The biggest difference is increased noise for the SHRT-17 temperatures, but this is not believed to have affected the measurement accuracy. Unlike the IHX outlet temperature, which is discussed below, flat core inlet temperatures are consistent with the large volume of the cold pool and the lack of mixing after the pumps tripped.

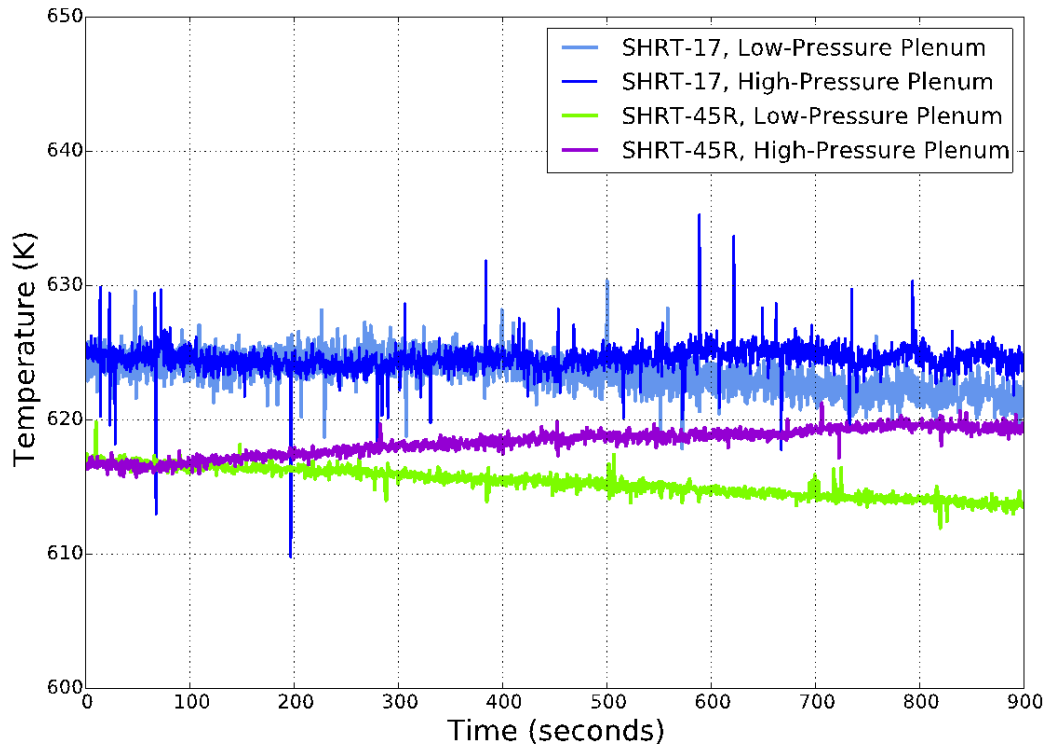


FIG. 19. SHRT-17 and SHRT-45R high and low pressure inlet plena temperatures.

FIG. 20 illustrates the core outlet temperature measurements for SHRT-17 and SHRT-45R. Originally, both measurements were thought to be from a thermocouple installed at the Z-Pipe inlet. However, evidence discussed below suggests that the measurement for SHRT-17 came from within the upper plenum flow baffle plate, which would account for the rapid temperature drop at the start of the test as opposed to the more gradual change for SHRT-45R due to flow mixing as sodium flowed through the upper plenum.

Except for the period between 75 and 200 seconds, the SHRT-45R Z-Pipe inlet temperature measurement is considered to be an accurate representation of the average core outlet temperature for two reasons. First, the flow baffle plate in the upper plenum mixed sodium discharged from the core subassemblies before it entered the Z-Pipe. Second, the thermocouple was installed along the midplane of the Z-Pipe, so it would not matter if stratification were established within the first few inches of the pipe. Unlike the SHRT-17 measurement, which registered very rapid temperature changes from only a handful of subassemblies, the SHRT-45R Z-Pipe inlet temperature reflected the average temperature of sodium discharged from the core.

The SHRT-45R data is not included in FIG. 20 between 75 and 200 seconds due to an instrumentation error. The data acquisition system recorded a constant temperature for most of this period, possibly due to saturation of the thermocouple, although this is only speculation. There was a short period before 200 seconds when the instrument produced an erratic temperature instead of a constant temperature, so that data was also neglected.

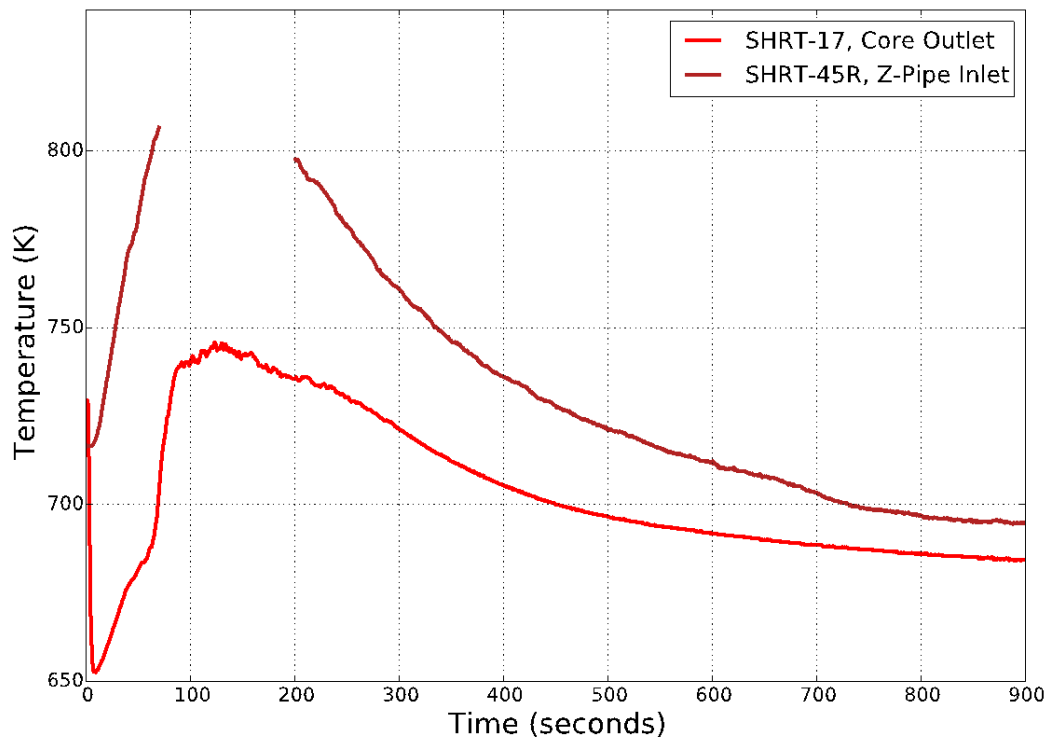


FIG. 20. SHRT-17 core outlet temperature and SHRT-45R Z-Pipe inlet temperature.

Returning to SHRT-17, the core outlet temperature measurement was likely a combination of temperatures measured at the outlets of 21 subassemblies. FIG. 21 illustrates these measurements along with the actual core outlet temperature measurement. A combination of these measurements matching the core outlet temperature measurement exactly could not be found, but at least one average of a subset of these temperatures was found to be within 5 degrees of the core outlet temperature measurement throughout the entire test.

Before it was realized that the Z-Pipe inlet temperature was not measured for SHRT-17, initial comparisons with simulation predictions of the Z-Pipe inlet temperature were poor. The exact nature of the SHRT-17 core outlet temperature could not be determined, so participants were not asked to provide an average upper plenum temperature for comparison. The measurement appears to be strongly weighted by the inner core subassembly outlet temperatures, and many participants did not discretize their upper plenum models sufficiently to capture this behaviour.

While the thermocouple at the Z-Pipe inlet captured the average temperature of sodium leaving the upper plenum, the thermocouple at the IHX inlet did not capture the average temperature of sodium leaving the Z-Pipe. FIG. 22 illustrates the Z-Pipe and IHX inlet temperature measurements for SHRT-45R. Although the Z-Pipe was designed to minimize heat losses to the cold pool, there was a 9.4 K difference between the two temperature measurements at steady state. Assuming that the measured IHX inlet temperature represented the average temperature of sodium leaving the Z-Pipe, 9.4 K would correspond to more than 5 MW lost to the cold pool. Heat balance calculations performed with intermediate sodium measurements upstream and downstream of the IHX confirmed that 60 MW were transferred from the primary sodium to the intermediate sodium. If these measurements are to be believed, and they were very similar to other temperatures measured further upstream and downstream of the IHX, then 5 MW simply could not have been lost through the Z-Pipe.

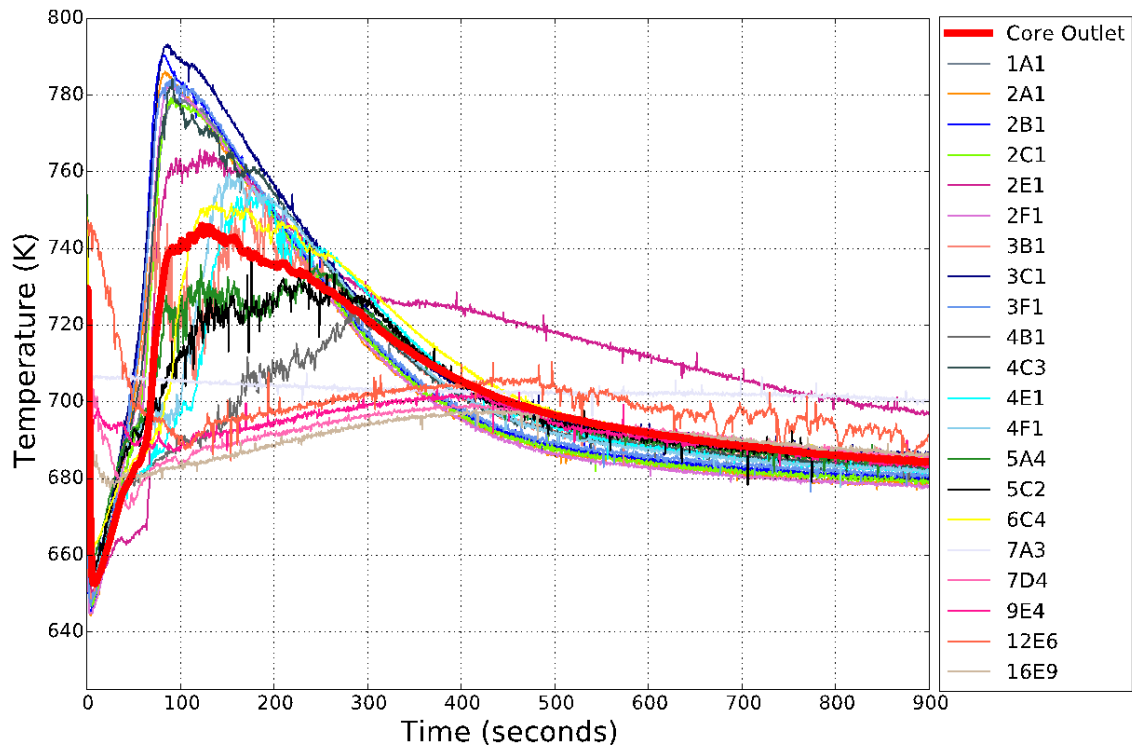


FIG. 21. SHRT-17 core outlet and subassembly outlet temperatures.

Additionally, some participants examined how large a temperature drop could be expected through the Z-Pipe. The Z-Pipe was a double-walled pipe with a sodium layer in between that was generally assumed to be stagnant. If the thermal resistance of only the outer pipe were considered, a temperature drop of at most 7 K would be expected along the Z-Pipe. Considering both walls of the Z-Pipe would reduce the maximum expected temperature to less than 4 K. Accounting for the resistance of the sodium layer and the film layer outside the Z-Pipe would reduce the temperature drop even further.

The reason the IHX inlet thermocouple did not capture the average temperature of sodium leaving the Z-Pipe, and therefore the average temperature of sodium entering the IHX, is the location in which it was installed. The thermocouple was installed behind a pair of impact baffle plates at the inlet of the IHX, next to one of the IHX tubes. The impact baffle plates isolated the thermocouple from the majority of sodium flowing through the IHX. In addition, heat transferred through the nearby IHX tubes meant that the sodium behind the impact baffle plates was likely colder than the rest of the sodium in the inlet of the IHX. Additionally, the thermocouple was installed below the midplane of the Z-Pipe, so if thermal stratification had developed in the pipe, the thermocouple would measure lower temperatures than the average Z-Pipe exit temperatures.

The location of the IHX inlet thermocouple also caused much slower measured temperature changes. Even though the Z-Pipe inlet temperature increased by approximately 100 degrees, and the Z-Pipe was relatively well insulated, the measured IHX inlet temperature increased by only 30 degrees. Because of the issues with this thermocouple at steady state and during the transient, confidence was very low that the IHX inlet thermocouple captured the general behaviour of sodium entering the IHX during either test.

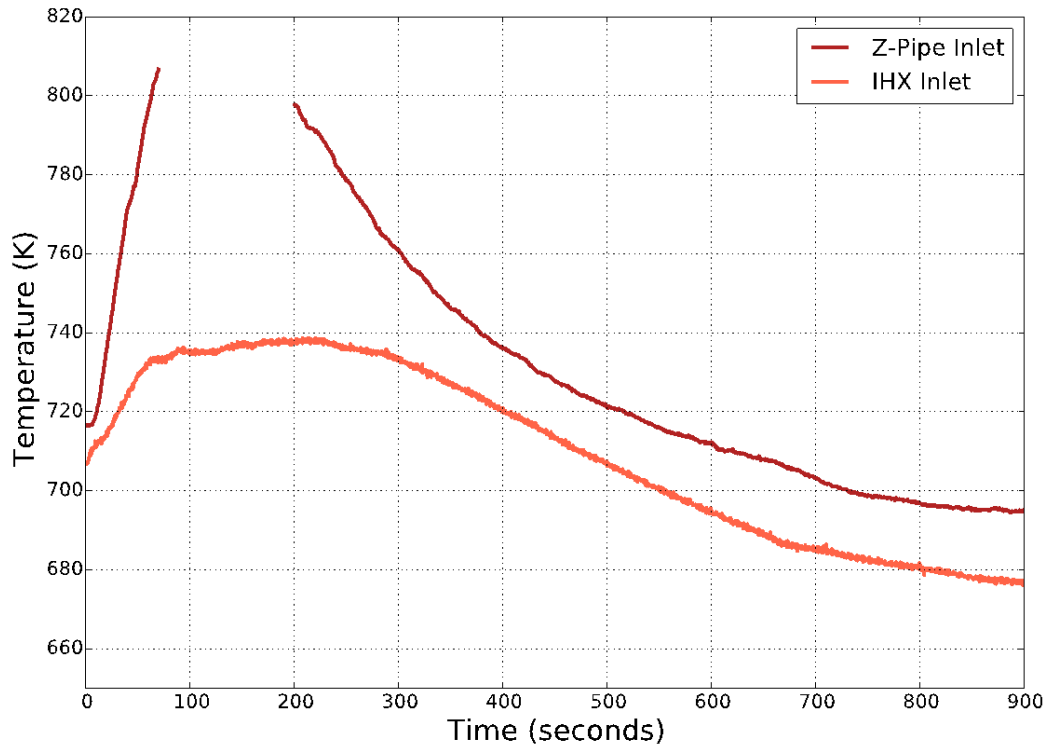


FIG. 22. SHRT-45R Z-Pipe inlet and IHX primary side inlet temperatures.

FIG. 23 illustrates the IHX primary side inlet and outlet temperature measurements for both SHRT-17 and SHRT-45R. As discussed above, analysis performed during the CRP led to low confidence in the IHX inlet temperature measurements. Additional analysis has led to doubts about the IHX outlet temperature measurements as well. Four thermocouples were installed at the approximate midplane of the IHX outlet window. FIG. 23 shows the average of these four measurements for the IHX outlet temperature. It should be noted that all four thermocouples recorded similar measurements for both tests.

Although the precise locations of these thermocouples are not known, old photographs of the IHX suggest they were approximately 2 inches outside the IHX tubes. Because they were located just outside the IHX in the cold pool, the IHX outlet thermocouples did not capture the average behaviour of sodium discharged from the IHX during low flow conditions. At nominal flow rates, the velocity of the sodium leaving the IHX was sufficient that it washed over the IHX outlet thermocouples.

But at low flow rates, sodium leaving the IHX was less likely to wash over the thermocouples. After the pumps finished coasting down during SHRT-45R, for example, hot sodium left the IHX at very low flow rates. That sodium was much hotter than the cold pool sodium, so buoyancy drove the IHX discharge sodium upward before it could wash over the IHX outlet thermocouples. FIG. 23 illustrates this with the IHX outlet temperature changing during the first 50 seconds of SHRT-17 and first 100 seconds of SHRT-45R before becoming relatively flat during the low flow portions of those tests.

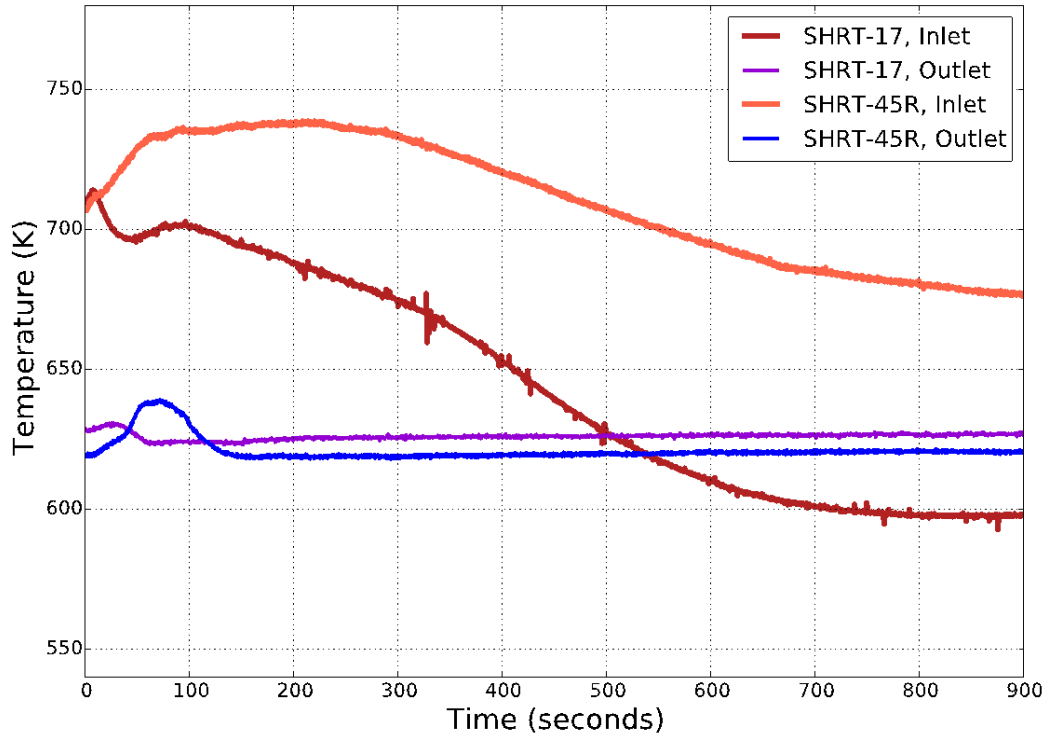


FIG. 23. SHRT-17 and SHRT-45R IHX primary side inlet and outlet temperatures.

Two thermocouple trees were installed in the cold pool to measure thermal stratification in the volume. These trees were available for SHRT-45R, but not SHRT-17. FIG. 24 illustrates the SHRT-45R IHX outlet temperature measurement, along with temperatures measured at several elevations within the cold pool from the thermocouple tree closest to the IHX. The IHX outlet was closest in elevation to the thermocouple at 4.41 meters. During the first 100 seconds of the transient, the flow rates were still high enough that sodium leaving the IHX washed over the IHX outlet thermocouples. However, after the pumps stopped, the measured outlet temperature gradually decreased to the temperature of sodium at that elevation in the cold pool.

FIG. 24 also helps illustrate why the core inlet temperatures were relatively flat for SHRT-45R. The pump inlets were at nearly the same elevation as the 5.78-meter thermocouple. The 5.78-meter temperature did not change much during SHRT-45R, only increasing by approximately 7 K. Because of the low flow rates, the pump inlet temperature would have changed even less than the 5.78-meter temperatures, which is consistent with the high pressure inlet plenum temperature for SHRT-45R increasing by approximately 4 K. Even though temperatures throughout the hot leg of the primary system increased very rapidly during SHRT-45R, the low flow rates and large size of the cold pool were responsible for relatively flat core inlet temperatures.

Except for the XX09 flowmeter thermocouple and MTC temperatures for SHRT-45R, which were unavailable for the test, the XX09 and XX10 temperature measurements were very reliable for both tests. All of the temperatures followed trends consistent with the other measurements. Most of the flow measurements are considered to be accurate as well, with the exception of the SHRT-45R XX09 flow measurement.

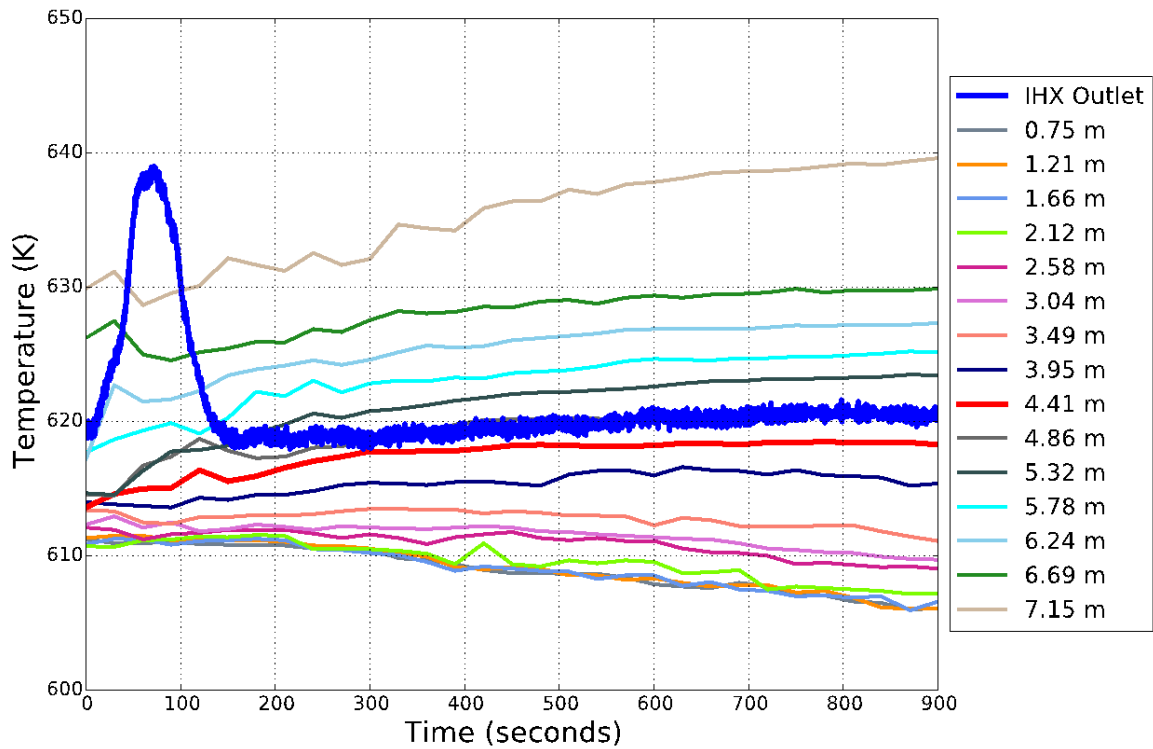


FIG. 24. SHRT-45R IHX primary side outlet and selected cold pool temperatures.

Figure 25 illustrates the XX09, XX10, and pump #2 high pressure flow rate measurements for SHRT-17, normalized to their initial values. XX09 and XX10 were fed by the high pressure inlet plenum, so the low pressure flow rate is not included in the figure. Each of the three measurements displays a similar coastdown before the pumps stopped. After the pumps stopped, the XX09 and high pressure flow rates are very similar. The XX10 flow rate is higher due to heat transfer from neighbouring subassemblies creating a buoyancy head within the instrumented subassembly.

FIG. 26 illustrates similar measurements for SHRT-45R. The high pressure flow rate and XX10 flow rate exhibited similar behaviour as for SHRT-17. But the XX09 flow measurement behaved in a significantly different manner from the other two measurements. This flow measurement decreased for a much longer period before suddenly increasing. There is no apparent reason why the XX09 flow rate would increase so drastically at 170 seconds when the other flow measurements did not. Then the flow rate decreased to approximately 2% while the other two flow rates remained above 5%. Finally, when the auxiliary EM pump current increased shortly after 600 seconds, the XX09 flow rate increased by a significantly larger amount than the other two flow rates. For these reasons, the XX09 flow rate for SHRT-45R is not considered to be accurate.

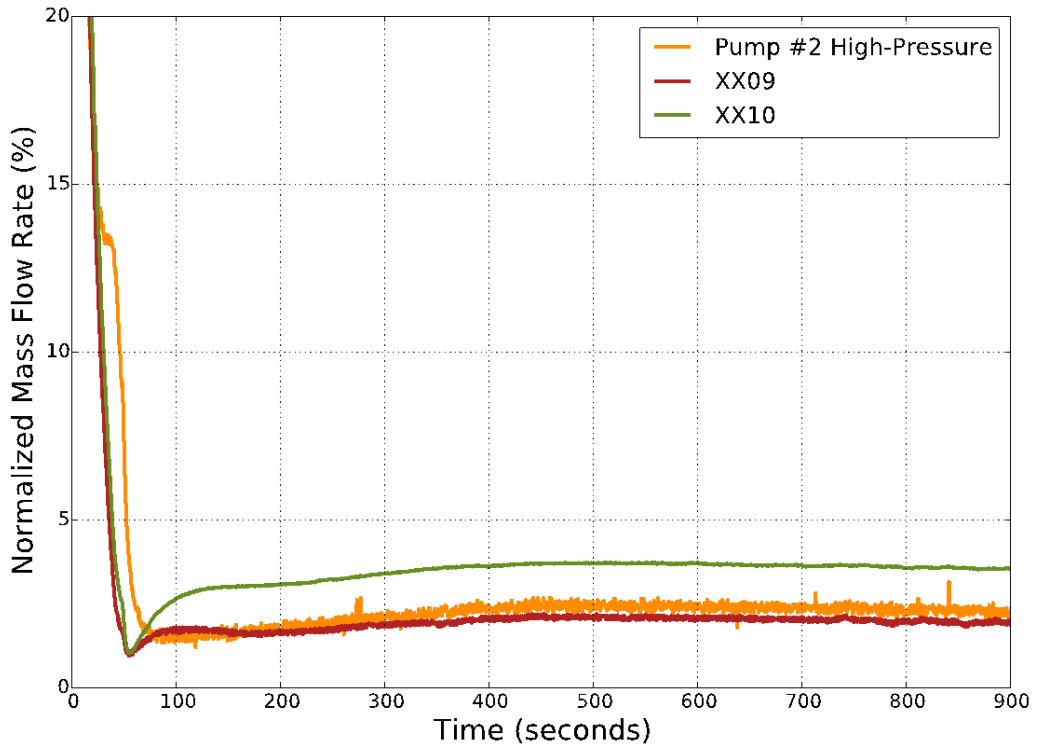


FIG. 25. SHRT-17 normalized mass flow rates.

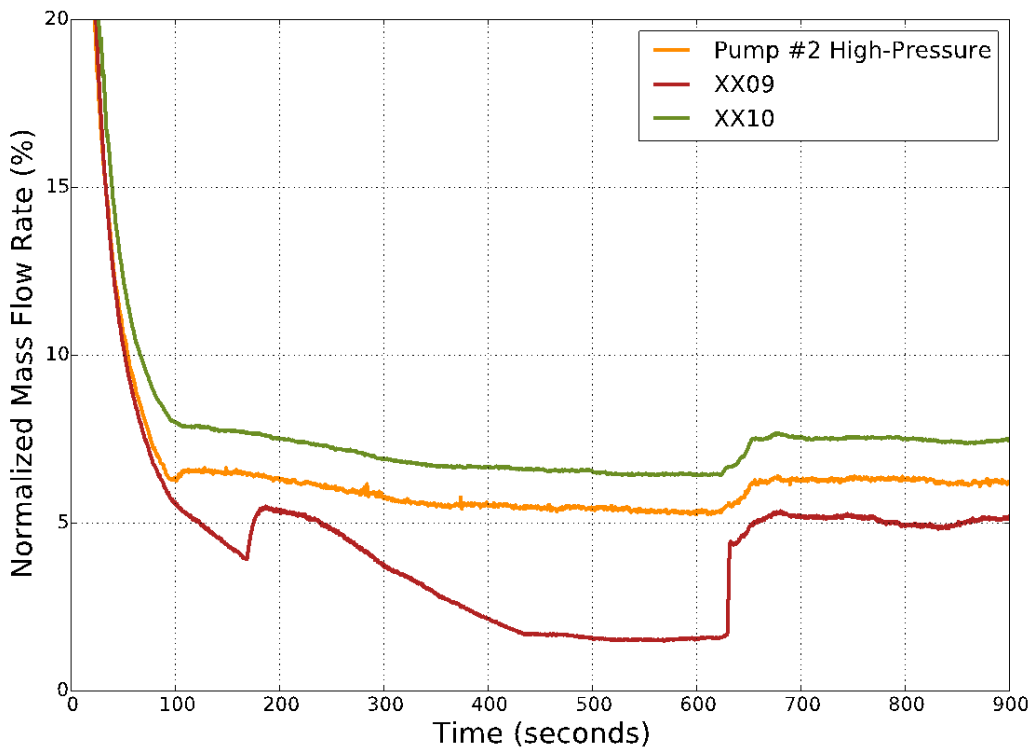


FIG. 26. SHRT-45R normalized mass flow rates.

4. BENCHMARK SPECIFICATIONS

4.1. PLANT PARAMETERS

The benchmark specifications for the SHRT-17 and SHRT-45R transients represent the subassemblies, inlet and outlet plena, primary circuit components and the primary circuit piping in significant detail. The reactor vessel, IHX, pumps and sodium piping are assumed to be the only components that displace sodium in the primary sodium tank.

Nominal design parameters are provided for the fuel elements and subassembly structure for all of the types of EBR-II drivers, dummy subassemblies, the two instrumented subassemblies, reflectors, blankets and the safety and control rods. Some simplifications were made to represent the upper and lower shield regions and the upper and lower adapters. Most details of the high pressure and low pressure inlet plena geometries are included. Limited available geometric information about the upper plenum internals meant that the baffles within the upper plenum could not be represented in detail.

All primary sodium piping dimensions are represented according to the as-built specifications. Each main primary sodium pump is modelled geometrically simply as a vertically oriented cylinder suspended from the primary tank cover. The auxiliary electromagnetic pump was attached around the outside of the reactor outlet pipe and so it did not affect the outlet pipe internal dimensions. The auxiliary pump was disabled for the SHRT-17 test and ran only on battery power for the SHRT-45R test, consistent with station blackout conditions.

The major dimensions of the IHX are included in the benchmark specifications. The tubes and downcomer pipe are represented using the as-built dimensions. The lower head and the annular space above the upper tubesheet are simplified to hemispherical plena.

Boundary conditions for the benchmark specification for both transients included the pump speeds of the two primary pumps, the intermediate sodium loop flow rate, and the sodium temperature at the intermediate loop inlet to the intermediate heat exchanger. Data were provided for the 15-minute duration of each test. For SHRT-17, the total power was also a boundary condition. For SHRT-45R, the auxiliary EM pump current was also a boundary condition. For participants who chose not to perform a neutronics analysis for SHRT-45R, the total power was provided as a boundary condition.

4.2. CORE DATA

4.2.1. Types of subassemblies

Several subassembly types were utilized during both transients. These included full drivers of several similar design types, partial drivers (drivers in which approximately half of the fuel elements were replaced with steel rods), 7-pin steel subassemblies, depleted uranium blankets, reflectors, experimental subassemblies, dummy subassemblies, control subassemblies, safety rod subassemblies and instrumented subassemblies. Driver subassemblies had 91 pins, control and safety subassemblies had 61 pins, blankets had 19 pins.

Each subassembly was composed of primarily three sections: upper adapter, centre hexagonal ducted section, and lower adapter or nozzle. The upper adapter for each subassembly was identical so that they could each be handled by the same fuel handling components. Different types of nozzles were used to prevent improper positioning of the subassembly on the reactor

grid. Also, different orifices were used to ensure appropriate amounts of coolant flow to each subassembly.

Driver subassembly centre hexagonal sections were composed of upper and lower shields/reflectors and a central fuel pin section. FIG. 27(a) shows a sample EBR-II Mark-II subassembly configuration. Each fuel pin consisted of sodium-bonded fuel pellets and an upper fission gas plenum. FIG. 27(b) shows an axial section schematic of the benchmark model of one of the driver subassembly types, the Mark-II AI core driver.

Each type of subassembly was modelled separately in the benchmark specifications. Simplifications were made in the benchmark specifications to the geometry of the upper and lower adapters and shield regions.

4.2.2. Fuel properties

For this benchmark specification, the linear thermal expansion of the U-5 wt % Fs fuel pins pre-irradiated in EBR-II is given as:

$$\frac{\Delta L(T)}{L_2} = \begin{cases} 1.62 \times 10^{-5}(T - 273), & T < 823\text{K} \\ 0.0089 + 5.7 \times 10^{-5}(T - 823), & 823\text{K} < T < 913\text{K} \\ 0.014 + 2.1 \times 10^{-5}(T - 273), & T > 913\text{K} \end{cases} \quad (1)$$

where

$\frac{\Delta L(T)}{L_2}$ = linear thermal expansion from a fixed temperature 273K to any temperature T, expressed as a fraction of length L_2 at the temperature 273K.

This correlation is independent of the fission content of the alloy. It was implemented in and tested with the SAS4A/SASSYS-1 code [5] for analysis of EBR-II transient tests.

The reference density which will be used for the U-5Fs fuel is $18.2 \times 10^3 \text{ kg/m}^3$ at 300K.

The heat capacity for U-5Fs fuel based on Argonne fuel properties work is

$$c_p(T) = a + bT + cT^2 \text{ kJ/kg-K}, \quad (2)$$

where a, b, and c are defined as follows:

$$\text{for } 273\text{K} < T < 833\text{K}, a = 0.13964, b = -1.9785 \times 10^{-5}, c = 3.1566 \times 10^{-7}$$

$$\text{for } 833\text{K} < T < 913\text{K}, a = 0.46364, b = -2.615 \times 10^{-4}, c = 0.0$$

$$\text{for } 913\text{K} < T < 1283\text{K (solidus)}, a = 2.40126, b = -3.5126 \times 10^{-3}, c = 1.4012 \times 10^{-6}$$

At both 833K and 913K there is a solid-to-solid phase transition. The associated enthalpy changes at these temperatures are:

$$T = 833\text{K}, \Delta h = 11.715 \text{ kJ/kg} \quad (3)$$

$$T = 913\text{K}, \Delta h = 8.368 \text{ kJ/kg} \quad (4)$$

It should be noted that these are very slow phase changes.

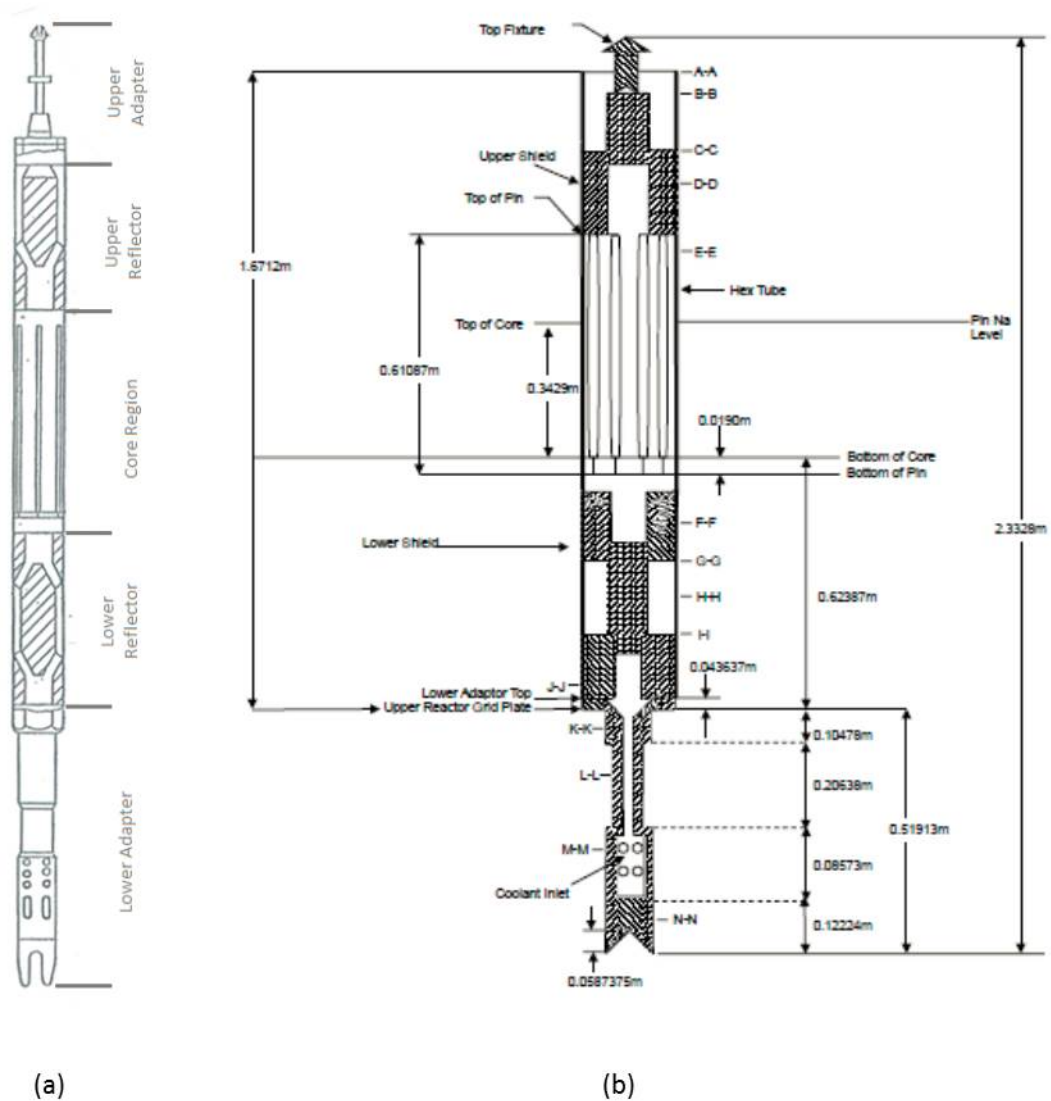


FIG. 27. (a) Sample Mark-II subassembly configuration, (b) Benchmark model of Mark-II AI core driver axial section.

The following correlation, which is independent of the fissium content of the alloy, is given for the thermal conductivity of U-5 wt % Fs fuel pins pre-irradiated in EBR-II.

$$k_s(T_c, U - xFs) = \begin{cases} 14.1 + 2.98 \times 10^{-2} T_c + 3.01 \times 10^{-6} T_c^2, & T_c < T_s \\ 56.0, & T_c > T_s \end{cases} \quad (5)$$

where

$k_s(T_c, U-5Fs)$ = thermal conductivity at temperature T_c °C of the solid (i.e., nonporous) U-5Fs alloy independent of the Fs content, W/m·°C,

T_s = solidus temperature of the U-5Fs alloy, and

x = weight per cent fissium.

The correlations for the thermal conductivity of the fully dense U-xFs alloy fuels are described by Eq. 5. However, the fuel develops fission gas-filled porosities during the steady state operation of the reactor. The bond sodium used in the fuel-cladding gap of U-xFs alloy fuel pins can also penetrate the fuel and fill some of the porosities of the fuel during this period. The gas-filled porosities tend to decrease the fuel thermal conductivity, whereas the sodium-filled porosities tend to increase it. These effects are considerable in the calculation of fuel temperature distribution. A formula is given below in Eq. 6 for the evaluation of these two effects. The formula is derived in [5] and is a generalization of a method for a single type of porosity.

The effective thermal conductivity k of the porous fuel can then be written in terms of the gas-filled volume porosity p_g and the sodium-filled volume porosity p_{Na}

$$\frac{k}{k_s} = 1 - p_g^{2/3} + \frac{p_{Na}^{2/3}}{\left(\frac{k_s}{k_{Na}}\right)p_{Na}^{1/3} + (1-p_{Na}^{1/3})} - p_{Na}^{2/3} \quad (6)$$

Equation 6 gives the effect of sodium- and gas-filled porosities on fully dense fuel thermal conductivity. It is noted that Eq. 6 satisfies two limiting conditions. First, in the absence of any logged sodium in the fuel, the ratio k/k_s equals the known reduction factor of $1 - p_g^{2/3}$. Second, if k_{Na} is set equal to k_s in Eq. 6, the last two terms on the right hand side cancel to make k/k_s again equal to $1 - p_g^{2/3}$, which is expected when the sodium and the fully dense fuel behave alike and the gas-filled porosity is the only nonconductive porosity in the material.

4.3. PRIMARY CIRCUIT

FIG. 28 and FIG. 29 below illustrate the locations and dimensions of the major components in the benchmark model of the primary sodium circuit. Simplified geometry is given for these components in the benchmark model. Some components in the EBR-II primary tank, such as the structure at the bottom of the primary tank, are assumed to occupy a negligible volume and are therefore not included in the benchmark model.

In these two figures, the blue piping represents the reactor outlet pipe, the green piping represents the high pressure inlet piping and the red piping represents the low pressure inlet piping. It is noted that FIG. 28 shows only one of the two primary pumps and its corresponding core inlet piping. The x-axis is along the direction from the axial centerline of the core to the axial centerline of the IHX and the z-axis is along the axial centerline of the reactor core.

The primary tank is the outer boundary of the primary sodium circuit and is modelled as a vertically oriented cylinder. It encompasses all of the major primary sodium components. The reactor vessel, intermediate heat exchanger and two primary sodium pumps are modelled as vertically oriented cylinders. Sodium piping is modelled as a series of straight pipes connected by pipe bends that, unless otherwise stated, have a bend radius equal to the pipe radius. The reactor vessel, IHX, pumps and sodium piping are assumed to be the only components that displace sodium in the primary sodium tank.

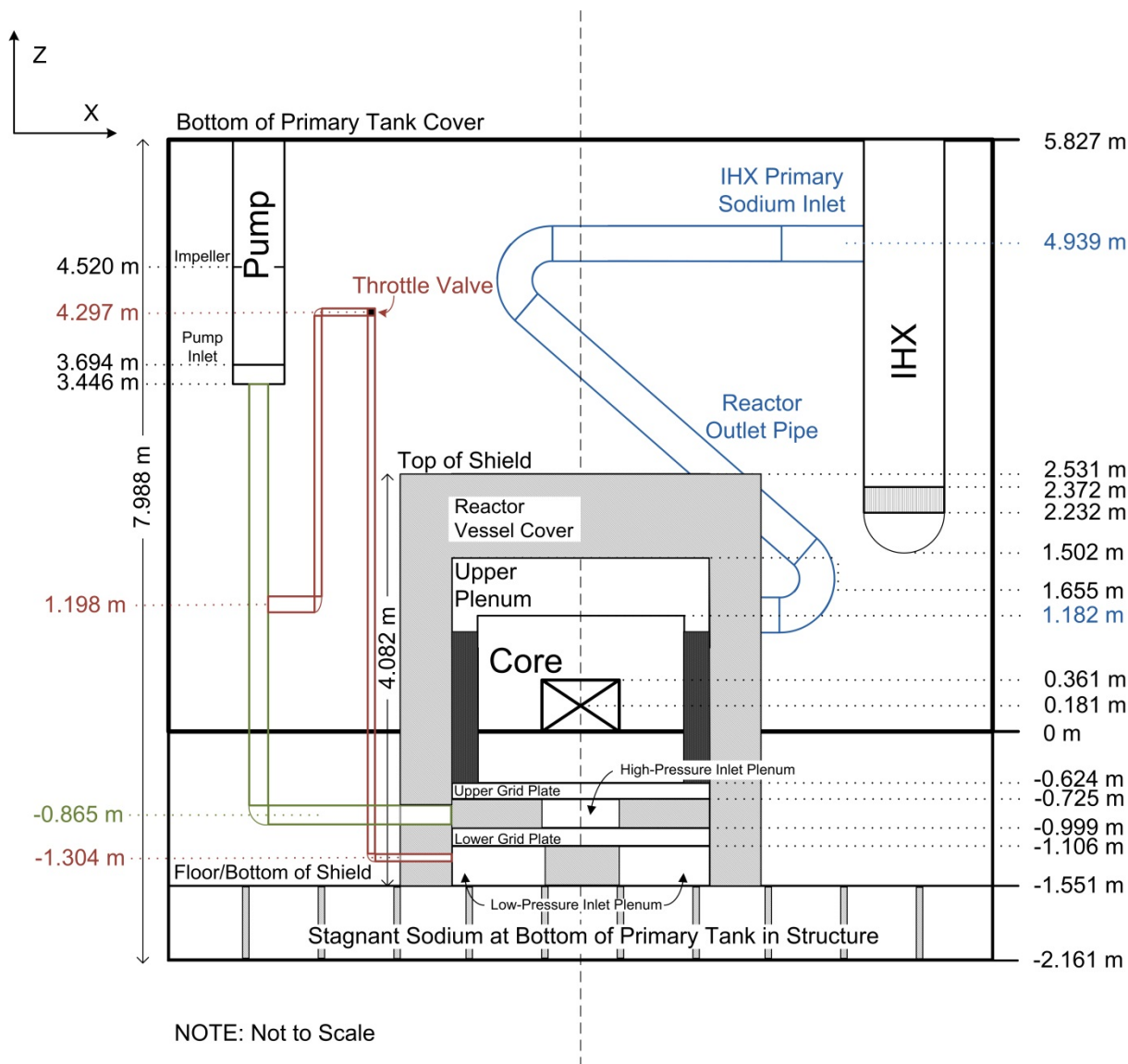


FIG. 28. Benchmark model of EBR-II primary vessel components: elevation view.

4.4. SHRT-45R NEUTRONICS BENCHMARK SPECIFICATION

A separate neutronics benchmark specification was developed to support the analysis of the SHRT-45R test. This specification provided the data needed to construct neutronics models of the SHRT-45R test, based on geometry and dimensions of the various types of EBR-II subassemblies and on the compositions of the fuel, coolant, cladding and structural materials at the beginning of SHRT-45R. CRP participants had the option of participating in the neutronics benchmark exercise and generating neutronics parameters to use in analysis of the SHRT-45R transient, or they could choose to use neutronics parameters provided by Argonne (see Section 7.19).

FIG. 30 presents a schematic of the core loading pattern that was used for run 138, the run in which SHRT-45R was conducted. This was not a fresh core, so the various driver and blanket subassemblies were partially depleted prior to initiation of the SHRT-45R transient. Isotopic fuel compositions for all core and blanket subassemblies were provided by Argonne to the

neutronics benchmark participants. Axial fuel swelling was accounted for in the calculation of these number densities.

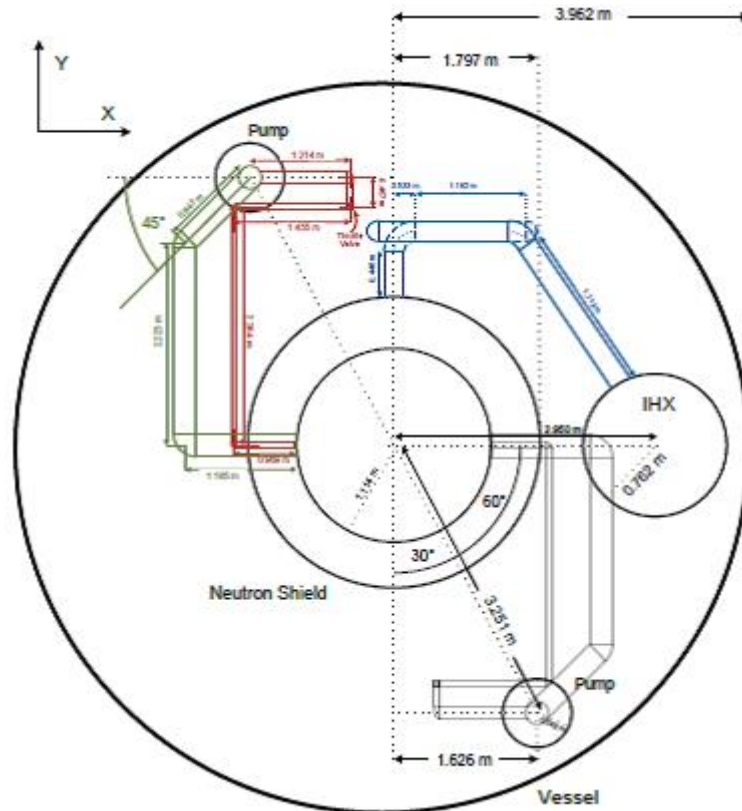


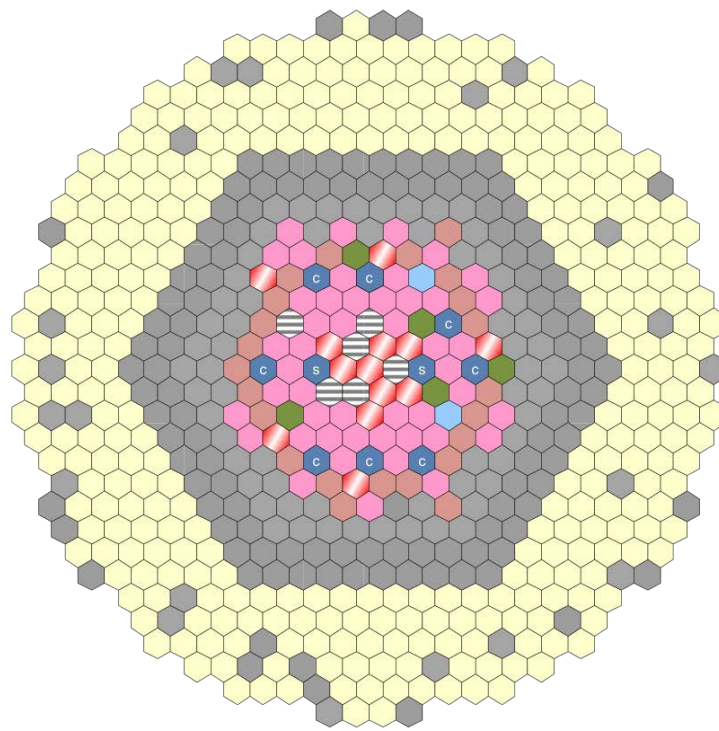
FIG. 29. Benchmark model of EBR-II primary vessel components: plane view.

4.5. OUTPUT PARAMETERS TO BE CALCULATED

Many measurements were recorded during the SHRT tests. The measurements best suited for comparison with the benchmark calculations are listed below. Several other calculated values are included that were not measured during the SHRT tests but are ideal for direct code-to-code comparisons among benchmark participants.

Those values that benchmark participants calculated during the transients are:

- (a) High pressure and low pressure inlet plena temperatures;
- (b) Z-Pipe inlet temperature;
- (c) IHX primary side inlet temperature;
- (d) Sodium mass flow rate at the primary sodium pumps;
- (e) IHX intermediate side outlet temperature;
- (f) XX09 and XX10 temperatures at the thermocouples locations;
- (g) XX09 and XX10 sodium mass flow rate;
- (h) Peak cladding temperature;
- (i) Peak fuel temperature;
- (j) Peak in-core coolant temperature;
- (k) Minimum margin to coolant boiling;
- (l) For SHRT-45R only: net reactivity, fission power and total power.



	Driver (47)		Control Rods (8)
	High-flow Driver (23)		Safety Rods (2)
	Half-worth Driver (13)		SST Dummy (6)
	Outer Blanket (330)		Experiments (5)
	SST Reflector (201)		Instrumented (2)

FIG. 30. Schematic of EBR-II subassembly core loading pattern for run 138.

SHRT-45R neutronics benchmark participants were expected to calculate the following parameters:

- (a) Core multiplication factor;
- (b) Effective delayed neutron fraction;
- (c) Power distribution of each subassembly, including fission and gamma heat;
- (d) Fission and decay heat power for the full 15 minutes of the transient, assuming a reactor scram at time=0;
- (e) Reactivity feedback coefficients:
 - (i) Axial expansion;
 - (ii) Radial expansion;
 - (iii) Sodium density;
 - (iv) Doppler;
 - (v) Control rod expansion

Additionally, two thermocouple trees were installed in the cold pool prior to the SHRT-45R test. The trees were diametrically opposite each other (see FIG. 31). As an option for those participants who wished to calculate more detailed cold pool temperature profiles, measurements from these thermocouple trees were made available for comparison with benchmark calculations. The two trees each had 32 thermocouples, spaced nine inches apart

axially, with the lowest thermocouple located about 0.5m. from the bottom of the primary tank. Measurements were taken every 30 seconds during the test. No thermocouple trees were installed in the cold pool for the SHRT-17 test.

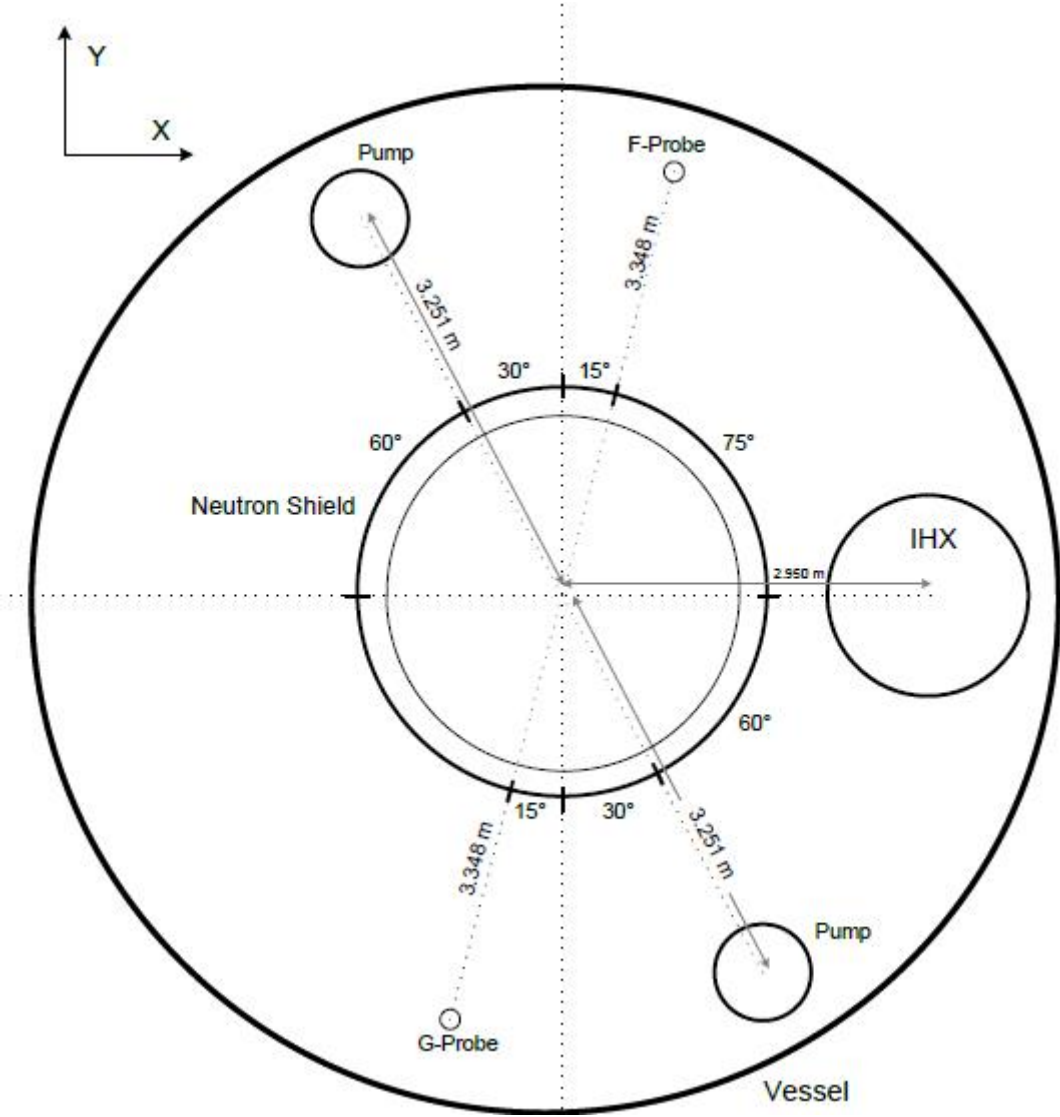


FIG. 31. Radial locations of F-Probe and G-Probe thermocouple trees.

5. DESCRIPTION OF SIMULATION CODES

5.1. SYSTEMS ANALYSIS CODES

5.1.1. CATHARE (IRSN)

The CATHARE systems analysis code has been co-developed by CEA, EDF, IRSN and AREVA since 1979. It is the reference code in France for PWR safety analysis. It has also been used for other light water reactor concepts (VVER, BWR, RBMK) and for experimental reactors applications.

CATHARE is a 6-equation code for two-phase flows (2 equations of mass balance, 2 equations of energy balance and 2 equations of momentum balance). The main variables are the pressure, the liquid and gas enthalpies, the liquid and gas velocities, the void fraction (and possibly mass fraction of incondensable gases). The aim of the code is to represent mechanical non-equilibrium and thermal non-equilibrium, at all flow regimes and all heat transfer regimes within the range of design and safety analysis. The code has a flexible modular structure allowing the representation of any kind of hydraulic circuit, from the analytical experimental facilities to the whole reactor power plant. The main hydraulic elements are axial (1-D), volumes (0-D) and a possibility of 3-D vessels. There are five main modules, with specific correlations and closure laws (1-D: axial; 0-D: volume, THREED or 3-D: PWR reactor vessel, BC: boundary condition and RG: double ended break). The code numerical scheme is fully implicit (1-D and 0-D) or semi-implicit (3-D), with an implicit thermal coupling between the walls and the fluid. The non-linear system is solved by a Newton-Raphson iterative method.

In the Generation IV framework, the standard version of the code (CATHARE_2v2.5_2) has integrated new developments for sodium cooled fast reactors (SFR), lead alloy cooled reactor (LFR), gas cooled reactors (GFR and high temperature reactors (HTR)), supercritical light water reactors and molten salt reactors.

For sodium applications, the main developments [6] are related to:

- (a) Physical properties of sodium (liquid and vapour);
- (b) Physical models: specific heat exchange correlations (Skupinski and Borishanskii heat exchange correlations), specific friction loss coefficient in the wire-wrapped fuel pins zone (Pontier's law [6]);
- (c) Update of the point-kinetics model (feedback effects due to diagrid expansion, wrapper axial and radial expansion, fuel clad axial and radial expansion);
- (d) Specific electromagnetic pump models.

The CATHARE code has been used in the frame of a previous CRP on the natural circulation test performed during the PHENIX end-of-life experiments [7], [8].

5.1.2. EBRDYN (IGCAR)

EBRDYN is a one dimensional (1-D) lumped parameter systems analysis code with models for core, upper plenum, Z-Pipe, IHX, cold pool, primary sodium pump and grid plate. The code can predict transient core power and the natural circulation phenomena in the circuit. The methodologies adopted in the formulation of the code are similar to those adopted in DYANA-P [9] and DHDYN [10] codes which are being used for the design of Indian Fast Breeder Reactors. The codes are validated against experiments carried out in the FBTR and PHENIX reactors.

5.1.3. FRENETIC (Politecnico di Torino)

The FRENETIC (fast reactor NEutronics/Thermal hydraulICS) code is under development at Politecnico di Torino for the purpose of the simulation of coupled neutronic/thermal hydraulic transients in liquid metal cooled fast reactor cores arranged in closed, hexagonal assemblies [11]. The neutronic module of the code solves the multigroup neutron diffusion equations with delayed neutron precursors according to a nodal discretization method in space and multiple discretization methods in time [12]. The thermal hydraulic module of the code solves

the time-dependent mass, momentum and energy conservation laws for the fuel and the coolant in each subassembly using the finite element method [11]. The neutronic and the thermal hydraulic solutions are coupled through the exchange of power and temperature distributions between the two modules.

5.1.4. MARS-LMR (KAERI)

MARS-LMR is a liquid metal cooled reactor (LMR) version of the MARS (Multidimensional Analysis for Reactor Safety) code, which has been developed by KAERI for multidimensional and multipurpose realistic thermal hydraulic systems analysis of light water reactor transients [13]. The modelling methodology in MARS-LMR is exactly the same as in MARS. The plant can be modelled with various hydraulic and heat structure components, such as pipes, pumps, valves, and so on, provided in MARS-LMR. However, in order to model a LMR, LMR related features were added in MARS-LMR. Sodium properties were embedded using a soft sphere model, which is based on Monte Carlo calculation for particles interacting with pair potentials [14]. And liquid metal heat transfer models for fuel bundle, various heat exchangers, and pressure drop model for fuel bundle were appropriately added [14]. The neutron physics in MARS-LMR is basically a point-kinetics model. In addition, to consider reactivity feedback by structure expansion, a fuel axial expansion, core radial expansion, and control rod drive line/reactor vessel (CRDL/RV) expansion reactivity feedback models were individually added to MARS-LMR ([15], [16], [17]).

5.1.5. NETFLOW++ (U. of Fukui)

The one dimensional system analysis code NETFLOW++ ([18], [19]) can calculate single-phase flow of several kinds of liquid metals and water, as well as two-phase flow of water. One dimensional flow with zero compressibility is assumed in the case of single-phase flow. NETFLOW++ is capable of simulating several special objects, such as shell-and-tube heat exchangers, air cooler with finned heat transfer tubes, steam generators and pumps. Pump characteristics are expressed as a Q-H curve, and the pressure head is approximated as a function of quadratic volumetric flow rate. In the pump characteristics evaluation for steady state and transients such as pump startup and coastdown, the kinetic equation with pump efficiency is solved. Various valves are also available, as well as singular pressure drops. The models in the code have been developed in order to simulate characteristics specific to liquid metal cooled fast reactors, e.g. a model of inter-subassembly heat transfer for natural circulation conditions. The code has been validated with data from the sodium cooled reactors “Joyo” and “Monju” ([20]), and in the IAEA benchmark analysis of the PHENIX natural circulation test ([7], [21], [22]).

5.1.6. RELAP5-3D (ENEA, N.I.N.E., U. of Fukui)

The RELAP5 series of codes was originally developed by the Idaho National Energy Laboratory/Idaho National Energy and Environmental Laboratory, now part of the Idaho National Laboratory. RELAP5-3D[©] ([23], [24], [25], [26]) uses a transient, two-fluid model for flow of a two-phase vapour/gas-liquid mixture that can contain non-condensable components in the vapour/gas phase and/or a soluble component in the liquid phase. RELAP5-3D[©] has fully integrated, multidimensional thermal hydraulic and kinetic modelling capability.

5.1.7. SAS4A/SASSYS-1 (Argonne, CIAE, TerraPower)

SAS4A/SASSYS-1 [5] is a software simulation tool used to perform deterministic analysis of anticipated events as well as design basis and beyond design basis accidents for advanced nuclear reactors. Core models in SAS4A/SASSYS-1 are composed of one or more single pin channels and optional sub-channels; a single pin channel represents the average pin in a subassembly or group of subassemblies. Heat transport system models in SAS4A/SASSYS-1 are represented by a series of zero-dimensional compressible volumes connected by one dimensional flow segments.

5.1.8. SAC-CFR (NCEPU)

The System Analysis Code for China fast reactor (SAC-CFR) ([27], [28]) was developed for fast reactors to predict the plant response during operational and accidental transients. The main components in the primary loop, intermediate loop and tertiary loop are modelled to calculate the response of neutron kinetics, thermal hydraulic, plant control and the protection system. The response includes temperatures and mass flow rates in the core and loop, fuel temperature, pump performance, heat exchanger performance, etc. The SAC-CFR code is suited for different kinds of transients ranging from normal operational conditions to upset conditions caused by such disturbances as loss of flow and loss of heat sink.

5.1.9. SIMMER (KIT)

The SIMMER-III code is a two dimensional (2-D), SIMMER-IV a three-dimensional (3-D), multi-velocity-field, multi-phase, multi-component, Eulerian, fluid dynamics code system coupled with a structure model for fuel pins, hexcans and general structures, plus a space-, angle-, time- and energy-dependent transport theory neutron dynamics model ([29], [30], [31]). An elaborate analytical equation of state (EOS) model closes the fluid dynamics conservation equations. The fluid dynamics portion is interfaced with a structure model through heat and mass transfer at structure surfaces. The neutronics part provides nuclear heat sources based on time-dependent neutron flux distributions consistent with the mass and energy distributions.

The SIMMER codes family was primarily developed for mechanistic analyses of transients and accidents in Liquid Metal Fast Reactors (LMFR) and is used as a reference tool for severe accident simulations.

5.1.10. SOCRAT-BN (IBRAE)

SOCRAT-BN has been developed by IBRAE-RAN in collaboration with JSC OKBM and SRC RF TRINITI for safety analysis of the Liquid Metal Fast Breeder Reactors with sodium coolant. The set of physical models (thermal hydraulics, neutron physics, fission product generation and release from failed fuel pins and fission product transport into the primary side and into the reactor building, core degradation, and melted materials relocation) implemented in the code allows a self-consistent safety analysis for normal steady state conditions and transient conditions, including severe accidents. The SOCRAT-BN code has been validated against various experimental data, including separate effects tests [32] and integral tests (BN-600 [33], BOR-60, PHENIX [34]). Currently, the code is used for BN-1200 safety assessment.

5.1.11. SPECTRA (NRG)

SPECTRA [35] is a thermal hydraulic systems code developed at NRG, designed for thermal hydraulic analyses of nuclear power plants. The main applicability includes light water reactors (LWRs), High Temperature Reactors (HTRs), and Liquid Metal Fast Reactors (LMFRs). The code can be used for thermal accident scenarios involving loss of coolant accidents (LOCAs), operational transients and other accident scenarios in nuclear power plants. Models include multidimensional two-phase flow, non-equilibrium thermo-dynamics, transient heat conduction in solid structures, and a general heat and mass transfer package with built-in models for steam/water/non-condensable gases, including natural and forced convection, condensation and boiling. For liquid metal reactor applications, the fluid properties and heat transfer correlations are defined by the user. A point reactor kinetics model is available, with an isotope transformation model to compute concentrations of important isotopes (for example Xe-135, etc.). The radioactive particle transport package deals with fission product radioactive chains, release of fission products, aerosol transport, deposition and resuspension.

5.1.12. Super-COPD (JAEA)

This code is a one dimensional plant dynamics analysis code for Sodium Fast Reactors (SFRs), which was originally developed by JAEA for simulating whole plant and in-core thermal hydraulics. This code has been validated by many sodium test facilities in Oarai and the operation/test data of Joyo and Monju.

No open literature documentation is available for this code.

5.1.13. THACS (XJTU)

The 1-D systems analysis code THACS (Transient Thermal Hydraulic Code for Analysis of Sodium cooled fast reactor) has been developed by Xi'an Jiaotong University [36], [37]. The code can calculate single-phase and two-phase flows of sodium. One dimensional flow with non-compressibility is assumed in the single-phase flows of sodium. For the two-phase calculation, the multi-bubble model is used in the core module for sodium. A compressible water model is applied on the water side of steam generators. THACS uses an object-oriented structure permitting the representation of any kind of hydraulic circuit, from the analytical experimental facilities to the whole reactor power plant. The code capabilities are listed as below:

- (a) Multiple channel core thermal hydraulic analysis;
- (b) Point-kinetic resolution covering decay heat and reactivity feedback models, including fuel Doppler, fuel and coolant density variations, core radial expansion, control rod driveline expansion and coolant voiding;
- (c) Models of metallic fuel and MOX fuel thermo-physical properties;
- (d) Primary and intermediate loops of reactor coolant systems models, such as pipes, intermediate heat exchangers, centrifugal pumps, hot pools and cold pools, pipe-nets, air-dump heat exchangers, steam generators, inter-wrapper flow and reactor vessel auxiliary cooling systems.

The first version of THACS was published on 25, June 2014.

5.1.14. TRACE (KINS, NRG, PSI)

The TRACE (TRAC-RELAP Advanced Computational Engine) code [38] is the latest in a series of best estimate system codes developed by the US Nuclear Regulatory Commission (NRC) for analysing steady state and transient thermohydraulic-neutronic behaviour in light water reactors [39], as well as in advanced reactor systems cooled by helium, sodium or lead-bismuth eutectic [40]. It can also model phenomena occurring in experimental facilities designed to simulate transients in-reactor systems. Models used include multidimensional two-phase flow (single-phase flow for non-water fluids), non-equilibrium thermodynamics, generalized heat transfer, reflooding, level tracking and reactor kinetics, using either the point-kinetics model or the PARCS 3D [41] reactor kinetics solver integrated into TRACE.

5.2. NEUTRONICS CODES

5.2.1. DIF3D (Argonne)

DIF3D [42] solves one-, two-, and three-dimensional problems for neutron flux by applying either finite difference diffusion (FDD) theory or variational nodal P_n transport theory (VARIATN) solvers. The code is used to calculate the core k_{eff} and the power distribution, as well as to evaluate the core k_{eff} after radial expansion and axial expansion.

5.2.2. ERANOS (KIT, U. Fukui)

The ERANOS code [43] was developed at CEA (France) and validated within the European Collaboration on Fast Reactors in the 1980s with the aim of providing a suitable basis for reliable neutronics calculations of current and advanced nuclear reactors, with specific attention to fast neutron spectrum cores. The code is able to perform the overall neutronics analysis of 3-D, 2-D, and 1-D geometrical models from the multigroup neutron cross-section generation to the computation of direct and adjoint neutron flux distributions by solving the transport or diffusion equation. Several embedded functions allow performing burnup simulations, evaluation of the kinetics parameters, space-time kinetics and perturbation and sensitivity studies. The self-shielded neutron cross-sections are processed by means of the European Cell Code (ECCO) ([44], [45]) and several reference neutron data libraries, i.e. JEFF or ENDF/B, may be employed.

5.2.3. MC²-3 (Argonne)

MC²-3 [46] is a multigroup cross-section generation code for fast reactor analysis. It is used to process neutron and photon cross-sections and to generate multigroup neutron and photon cross-sections. For photon power calculations, MC²-3 was also used to generate the matrix for transforming neutron flux to photon source, as well as the neutron and photon KERMA factors.

5.2.4. MCNP6 (ENEA)

MCNP6TM is a general purpose, continuous energy, generalized-geometry, time-dependent Monte Carlo radiation-transport code designed to track many particle types over broad ranges of energies [47]. The code's main capability is to calculate k_{eff} eigenvalues for fissile systems. It is also able to perform material burnup and delayed particle production calculations. Pointwise cross-section data are used. For neutrons, all reactions given in a particular cross-section evaluation (such as ENDF/B-VII) are accounted for. Thermal neutrons are described

by both the free gas and $S(\alpha,\beta)$ models. A flexible tally structure allows calculation of important parameters such as neutron flux distribution and fluences.

5.2.5. NJOY (U. Fukui)

NJOY [48] is a nuclear data processing system that generates neutron cross-sections from ENDF formatted evaluated nuclear data.

5.2.6. PARTISN (KIT)

The PARTISN (PARAllel, TIme-dependent SN) code [49] is the successor to the DANTSYS code package [50]. PARTISN solves the time-dependent transport equation by using the SN method for 1-D, 2-D (RZ, XY, and R- θ), and 3-D (XYZ, R-Z- θ) geometries. In the past, the DANTSYS code was implemented as a transport solver in the SIMMER-III (2-D) and SIMMER-IV (3-D) multi-physics code systems (see Section 5.1.9). Since the original DANTSYS version solves steady state problems only, the code was extended at KIT [51] for simulating time-dependent problems while being implemented in SIMMER.

5.2.7. PHISICS (ENEA)

PHISICS [52] is an advanced neutronic simulation code. The internal neutron solver discretization scheme is based on the second-order PN equation with the hybrid finite element method also known as the Variational Nodal Method. The maximum angular flux expansion order is 33. Several node geometries such as Cartesian, hexagonal, unstructured triangular and so on are available. The number of energy groups is limited only by the hardware performance, and coupling with RELAP5-3D has just been implemented. The code is designed with the mind-set to maximize accuracy for a given availability of computational resources to provide a state of the art simulation capability to reactor designers.

5.2.8. SCALE6.1 (ENEA)

The Standardized Computer Analysis for Licensing Evaluation (SCALE) code system [53] developed at Oak Ridge National Laboratory provides a comprehensive, verified and validated, user-friendly toolset for criticality safety, reactor physics, spent fuel characterization, radiation shielding and sensitivity and uncertainty analysis. Since 1976, regulators, licensees and research institutions around the world have used SCALE for safety analysis and design. SCALE 6.1 provides improved reliability and introduces a number of enhanced features in a robust yet user-friendly package that are intended to improve safety and efficiency throughout the nuclear community.

5.2.9. SERPENT (Politecnico di Torino, PSI)

Serpent ([54], [55]) is a continuous energy Monte Carlo (MC) neutron transport code being developed for reactor physics applications, including criticality calculations, burnup and decay analyses and generation of few-group homogenized cross-sections for deterministic full core simulators. Serpent uses continuous energy ACE-formatted cross-section libraries. Typically, Serpent outperforms general purpose MC codes due to the use of the Woodcock delta-tracking in a combination with a typical surface-to-surface ray-tracing in a neutron tracking routine [56] and the use of the unionized energy grid for all pointwise reaction cross sections [57].

5.2.10. TRAIN (KIT)

The TRAIN code is part of the C₄P-TRAIN code and data system package developed at KIT [58]. C₄P [59] is used at KIT/IKET to produce problem-oriented neutron cross-section libraries in the CCCC format (ISOTXS and BRKOXS), which are needed in particular for the SIMMER code. The problem-oriented libraries are produced from fine group “master” libraries generated from evaluated nuclear data files by codes like NJOY [48]. TRAIN is a code that - in combination with neutron transport solvers - can be used for reactor physics calculations with C₄P libraries and helps to benchmark these libraries.

5.2.11. VARI3D and PERSENT (Argonne)

VARI3D and PERSENT [60] are perturbation theory codes used for perturbation and sensitivity analysis. VARI3D is based on the neutron flux solution from the diffusion solver of DIF3D [42], while PERSENT is based on the neutron flux solution from the variational nodal solver of DIF3D.

5.3. OTHER TYPES OF CODES

5.3.1. ANSYS CFX (ENEA, NRG, U. of Fukui)

ANSYS CFX [61] is a computational fluid dynamics code used for detailed three-dimensional analyses of fluid flow and (conjugate) heat transfer in the fluid and solid structures in both steady state and transient. The code employs a coupled technique that simultaneously solves all the transport equations in the whole domain through a false time-step algorithm. The linearized system of equations is reconditioned in order to reduce all the eigenvalues to the same order of magnitude. The multi-grid approach reduces the low frequency error, converting it to a high frequency error at the finest grid level; this results in a great acceleration of convergence.

5.3.2. ASFRE (JAEA)

This code is a subchannel analysis code for SFRs and was also originally developed by JAEA for simulating thermal hydraulics of wire-wrapped fuel pin bundles. This code has also been validated by many sodium test facilities in Oarai.

No open literature documentation is available for this code.

5.3.3. COBRA4i (TerraPower, U. of Fukui)

The COBRA4i subchannel methodology [62] decomposes a geometry (such as a rod bundle) into discrete subchannels and then solves the coupled mass, momentum and energy conservation equations to obtain the temperature and flow in each subchannel. Flow redistribution between subchannels is treated via the transverse momentum equation, while radial fluid conduction, azimuthal rod heat conduction, and forced mixing are treated using correlations [63]. Transient analysis capability and use of the transverse momentum equation set the code apart from the other available subchannel codes (e.g., SuperEnergy2). Forced mixing phenomena are treated in two ways: wire wrap sweeping and turbulent mixing. Heat transfer correlations specific to the coolant (sodium) are used to obtain cladding and fuel temperatures. The COBRA-4i code can be used for the analysis of water cooled reactor, liquid metal cooled reactor and gas cooled reactors. For liquid metal cooled fast reactors, the COBRA-4i code has been validated for the core and heat exchangers ([64], [65]).

5.3.4. STAR-CD (IGCAR)

STAR-CD [66] is a commercial computational fluid dynamics code which solves the governing differential equations of flow physics by numerical means on a computational mesh. It has the capability of solving steady, transient, laminar, turbulent, compressible, and incompressible flow phenomena along with heat transfer (convection, conduction and radiation) even in a porous medium. It has a built-in pre-processor and post-processor known as PROSTAR. It has a basic mesh generation capability. Complex meshes can be imported from any standard mesh generating tools. User-defined programme modules can be added to the code to modify the material properties as well as pressure drop and heat transfer characteristics dynamically during a transient. The code has been validated extensively against benchmark data.

5.3.5. Thermo-Calc (Kyushu university)

Thermo-Calc [67] is a commercial software package that can calculate thermodynamic states and equilibrium phase diagrams of multi-component systems based on the CALPHAD (CALCulation of PHase Diagrams) approach [68]. The Thermo-Calc code includes a thermodynamic database of binary and ternary alloys relevant to actinide elements (see, for example, [69]). Thermodynamic properties of solid U-Pu-Zr alloy, such as specific heat, solidus and liquidus temperatures and heat of fusion, were evaluated using this code.

6. GENERAL DESCRIPTION OF CRP ANALYSIS APPROACH

CRP participant analyses were performed in two phases over the four years of the CRP. During the first phase, participants had no access to the recorded data from either transient. Once all phase 1 calculations were completed, participants received experimental data from both transients to begin phase 2.

6.1. PHASE 1

Phase 1 began with the first research coordination meeting (RCM), held in June 2012. At this meeting, the participants received the benchmark specifications that had been prepared by Argonne for both SHRT-17 and SHRT-45R. This meeting provided an opportunity for Argonne to explain the benchmark specifications in detail to the other participants and to address questions and requests for clarification concerning the specifications. Each participant described their planned approach to the analyses.

There were several analysis options in phase 1 for participants to choose from:

- (a) Basic systems analysis of SHRT-17;
- (b) Additional detailed analysis of instrumented subassemblies XX09 and XX10 for SHRT-17;
- (c) Basic systems analysis of SHRT-45R;
- (d) Additional detailed analysis of instrumented subassemblies XX09 and XX10 for SHRT-45R;
- (e) Neutronics analysis of SHRT-45R.

Each participant could choose to perform some or all of these options. Participants who did not perform a neutronics analysis for SHRT-45R were provided by Argonne with reactivity feedback data (see Section 7.19 for more details).

The initial analysis work, which constituted phase 1 of the CRP, was performed as a blind analysis; that is, the participants did not have access to the recorded EBR-II data. Phase 1 lasted until all blind results were submitted in February 2014. Preliminary phase 1 results were discussed by the participants at the second RCM, held in November 2013, with Argonne showing comparisons against the plant data but not yet providing the data tables to the participants. At the second RCM, a number of participants asked that the deadline for blind results be extended to early 2014, and so phase 1 did not end until February 2014.

During the early part of phase 1, it was agreed that Argonne should set-up a project data archive accessible to all participants in order to facilitate group access to CRP information. This archive has grown to include the benchmark specifications, all meeting reports, meeting presentation materials from all participants, simulation results from all participants, and the recorded data for both transients.

To facilitate organization of the results from all 19 benchmark participants, Argonne created a set of spreadsheet templates for participants to use to submit their simulation results. Using these templates made it straightforward for Argonne to generate plots for each required result parameter comparing all participant results against each other and against the recorded data. These templates are also entered into the project data archive.

6.2. PHASE 2

Once all blind results had been submitted in February 2014, Argonne released tables containing the recorded data to the participants through the project data archive, thus beginning phase 2 of the CRP. Participants could then do a detailed evaluation of the comparisons between their simulation results and the data and determine where improvements were needed in their models.

Initial phase 2 results were reported at the third RCM in March 2013. Final results were required to be submitted to Argonne at the end of December 2015 and were reviewed at the fourth and final RCM in April 2016.

At the second RCM, one of the participants (N.IN.E.) suggested that the participants should try to perform a results qualification for the final phase 2 results using the Fast Fourier Transform Based Method. This was something of an experiment in that this type of analysis is not typically part of a CRP. The qualification process required considerable effort on the part of N.IN.E. and Argonne to extract the necessary geometric information about EBR-II and also required each organization to provide more extensive modelling and results information than was expected for the original benchmark project. Participation by each organization was therefore optional, but most organizations agreed to participate in this additional exercise. See Section 9 for a detailed reporting on the outcome of the qualification process.

7. MODELS AND RESULTS

In Section 7, each participant summarizes the models they developed and the simulation results they achieved during both phases of the CRP. Modelling choices are described, including correlations used for friction and heat transfer. These descriptions are supplemented by two annexes to the report: Appendix I, which gives a comprehensive picture of the correlations used by all participants, and Appendix II, which presents several tables that display the various modelling choices made by the participants and the analyses that were performed.

7.1. CHINA INSTITUTE OF ATOMIC ENERGY (CHINA)

7.1.1. Geometry/discretization

In order to model the core performance during the SHRT-17 test, the core was divided into 12 channels, which are listed in TABLE 4. For the SHRT-45R test, the core was divided into 13 channels, which are listed in TABLE 5. The channels are divided based on the type of subassemblies, modelling requirements and the power and flow of the subassemblies. For each channel, the subassembly is divided into zones axially, and each zone is divided into segments axially to calculate the heat transfer.

TABLE 4. CORE CHANNELS FOR SHRT-17 TEST

Channel	Subassembly Type	Number of SAs
1	hot driver (from HFD)	1
2	highest power driver	1
3	driver	31
4	partial driver	10
5	high flux driver	17
6	instrumental SA: XX09	1
7	instrumental SA: XX10	1
8	control rod and safety rod	17
9	reflector, 6–7 rows	34
10	experimental SA	13
11	reflector, 8–16 rows	155
12	blanket, 11–16 rows	354

TABLE 5. CORE CHANNELS FOR SHRT-45R TEST

Channel	Subassembly Type	Number of SAs
1	hot driver	1
2	inner core driver(MARK-II A)	17
3	inner core driver(MARK-II AI)	16
4	external core driver(MARK-II A)	15
5	external core driver(MARK-II AI)	25
6	partial driver(MARK-II A)	12
7	control rod and safety rod	10
8	Steel& experimental	8
9	reflector(power < 2kW)	36
10	reflector(power > 2kW)	165
11	blanket	330
12	instrument(xx09)	1
13	instrument(xx10)	1

7.1.2. Nuclear and thermo-physical data/correlations

CIAE used the neutronics data supplied by Argonne and the SAS4A/SASSYS-1 thermo-physical data correlations.

7.1.3. Thermal hydraulics methods and models

7.1.3.1. Code(s) used

The code used was SAS4A/SASSYS-1, version 3.0. SAS4A/SASSYS-1 is designed to perform deterministic analysis of severe accidents in liquid metal cooled reactors (LMRs). Detailed, mechanistic models of steady state and transient thermal, hydraulic, neutronic and mechanical phenomena are employed to describe the response of the reactor core and its coolant, fuel elements and structural members to accident conditions caused by loss of coolant flow, loss of heat rejection or reactivity insertion.

7.1.3.2. Basic method

In space, each SAS4A/SASSYS-1 channel represents one or more subassemblies with either a single pin model or a multiple pin model. Many channels are employed for a whole core representation. Heat transfer in each pin is modelled with a two dimensional (r/z) heat conduction equation. Single-phase coolant thermal hydraulics is simulated with a unique, one dimensional (axial) liquid metal flow model. Reactivity feedbacks from fuel heating (axial expansion and Doppler), coolant temperature changes and fuel and cladding temperature changes are tracked with first-order perturbation theory. Reactivity effects from reactor structural temperature changes yielding radial core expansion are modelled. Changes in-reactor power level are computed with point-kinetics.

7.1.3.3. Model

For SHRT-17, the average inlet temperature, average outlet temperature, core outlet pressure and steady state coolant flow rate per pin were used in each channel as the core boundary conditions. For SHRT-45R, the reactivity feedbacks for Doppler, axial expansion, radial expansion and coolant density were calculated and point-kinetics was used.

The basic SAS4A/SASSYS-1 modelling options provide for only a single inlet plenum, and so the high pressure and low pressure inlet plena were not modelled separately. Instead, the normalized driving pressure was used as a primary circuit boundary condition for the reactor core.

7.1.4. Blind results

7.1.4.1. SHRT-17

The calculated peak fuel, cladding and coolant temperatures during the SHRT-17 test are illustrated in FIG. 32. The highest fuel, cladding and coolant temperatures are around 900K and appear at around 53s. The sodium saturation temperature is around 1088K, so there is more than a 100K margin to boiling for the coolant. The solidus temperature of the U-5Fs alloy is more than 1200K, which means there is ample safety margin for the fuel during this transient. The simulation results demonstrate well the inherent safety characteristics of the EBR-II reactor during the protected loss of flow transient.

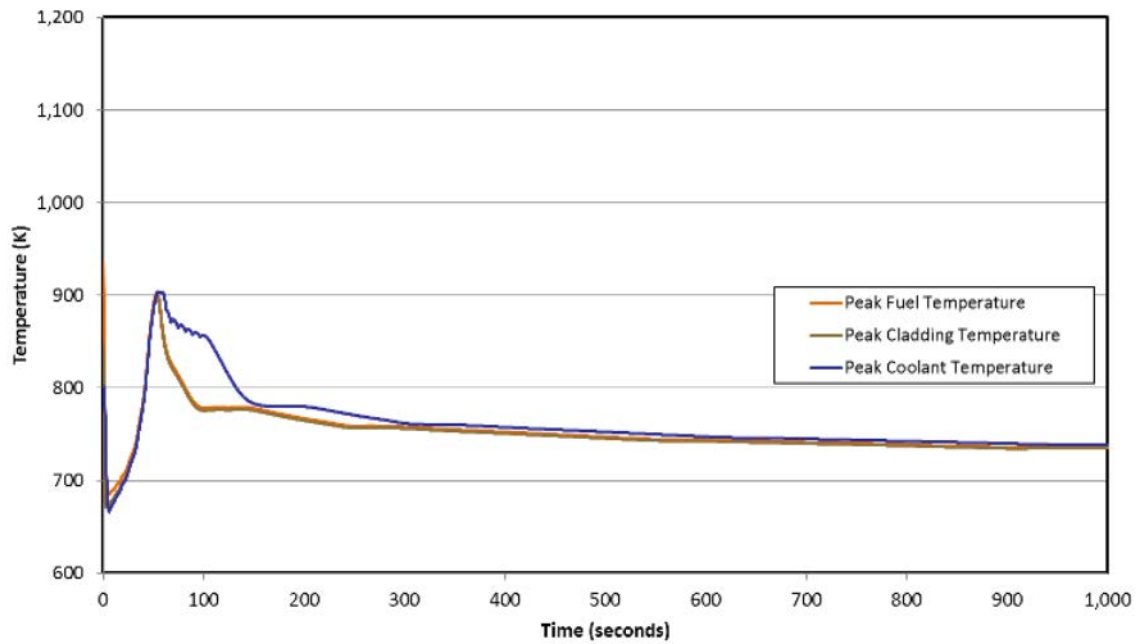


FIG. 32. Peak in-core temperatures during SHRT-17, phase 1.

In order to measure a detailed temperature distribution at different elevations and in subchannels of subassemblies, instrumented subassemblies with thermocouples were placed in the core during the SHRT-17 test. Simulation results for temperatures at different elevations in XX09 are illustrated in FIG. 33. Subchannel modelling was not used, so no radial temperature variation was calculated.

7.1.4.2. SHRT-45R

CIAE did not generate any blind results for SHRT-45R.

7.1.5. Final results, data comparisons

7.1.5.1. SHRT-17

The calculated peak fuel, cladding and coolant temperatures during the SHRT-17 test are illustrated in FIG. 34. The highest fuel, cladding and coolant temperatures are around 822K and the highest temperatures appear at around 70s. The sodium saturation temperature is around 1088K, so there is more than a 100K margin to boiling for the coolant. The solidus temperature of the U-5Fs alloy is more than 1200K, which means there is ample safety margin for the fuel during this transient. The simulation results demonstrate well the inherent safety characteristics of the EBR-II reactor during this protected loss of flow transient.

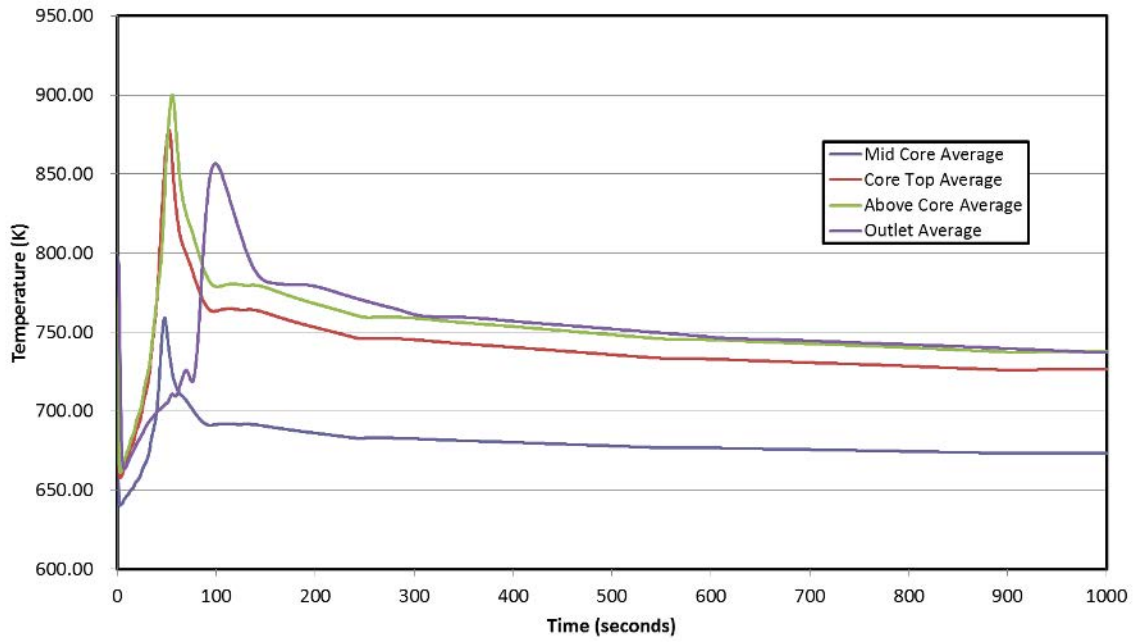


FIG. 33. XX09 temperatures during SHRT-17, phase 1.

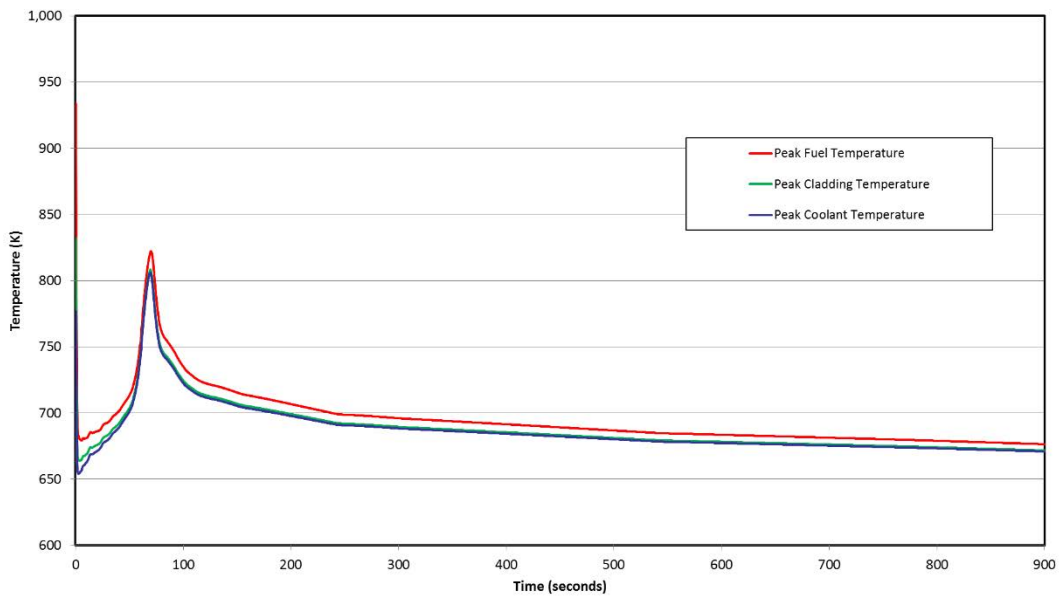


FIG. 34. Peak in-core temperatures during SHRT-17, phase 2.

The calculated core inlet and outlet temperatures during the transient are illustrated in FIG. 35. The experimental data are shown by the dashed lines, and the calculation results are plotted using solid lines. Both experimental and calculated inlet temperatures of the core remain almost invariant and fall on top of each other, while the outlet temperature of the core changes with the transient. The highest outlet temperature occurs at around 100s, and the highest outlet temperature is about 780K. From FIG. 35, it can be seen that the calculated outlet temperature has the general same trend as the experimental data but predicts a much higher peak temperature and faster decline than the experimental data.

Simulation results of temperatures at different elevations in XX09 are illustrated in FIG. 36. The experimental data are plotted using dashed lines, and the calculation results are plotted using solid lines, as indicated in the figure. Only radially averaged temperature results are available, since subchannel modelling was not used. From FIG. 36, it can be seen that the calculation results follow curves similar in shape data to the experimental data but overshoot the actual temperatures.

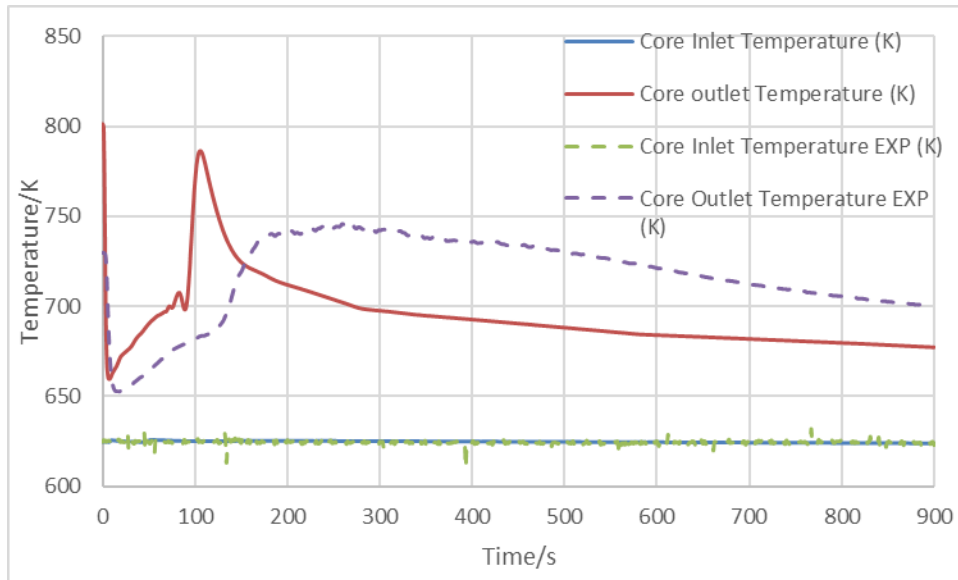


FIG. 35. Core inlet and outlet temperature during SHRT-17, phase 2.

Simulation results of temperatures at different elevations in XX10 are illustrated in FIG. 37. Again, the experimental data are plotted using dashed lines, and the calculation results are plotted using solid lines. From FIG. 37, it is clear that the calculation results do not match the experimental data very well, and this is a problem that remains unsolved.

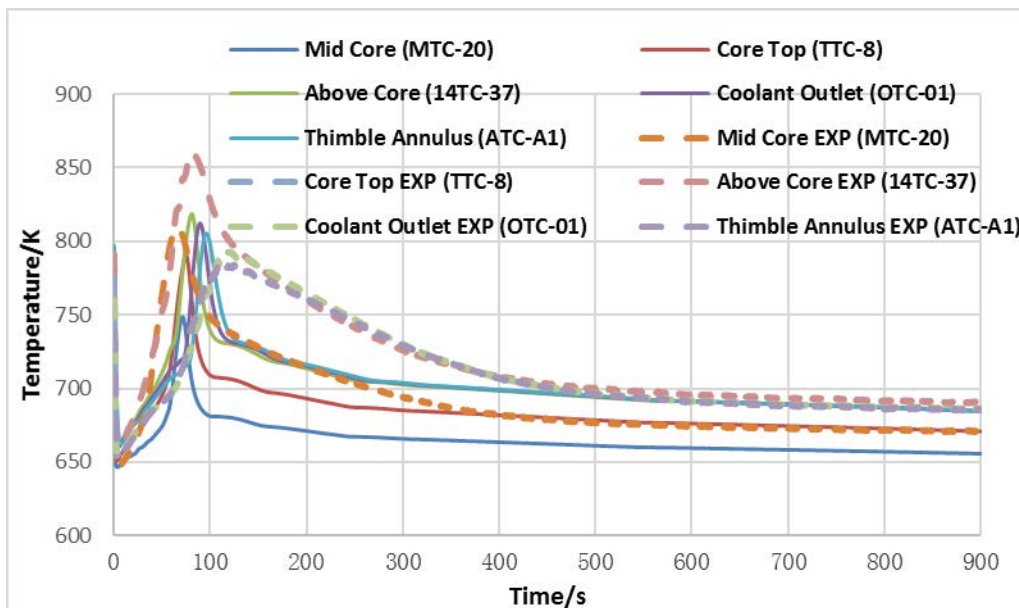


FIG. 36. XX09 temperatures during SHRT-17, phase 2.

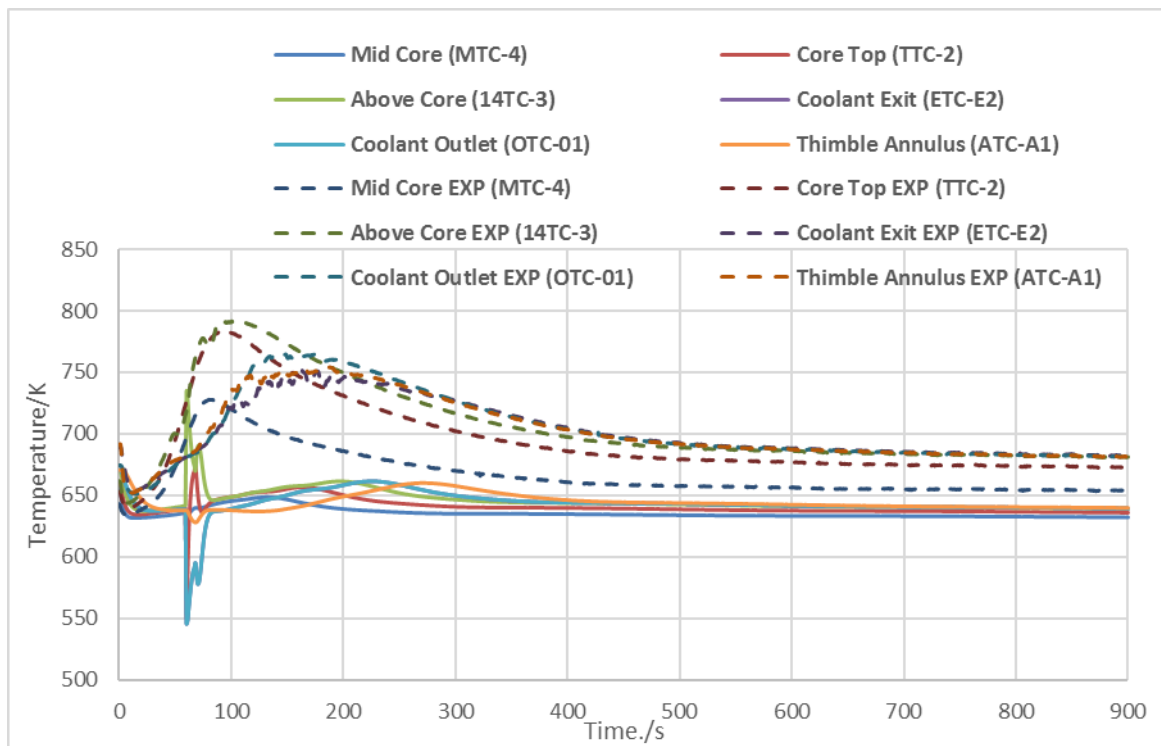


FIG. 37. XX10 temperatures during SHRT-17, phase 2.

7.1.5.2. SHRT-45R

The calculated peak fuel, cladding and coolant temperatures during the SHRT-45R test are illustrated in FIG. 38. The highest fuel, cladding and coolant temperatures are around 1050K, and the highest temperatures appear at around 60s. Sodium saturation temperature is around 1200K, so there is more than 100K margin to boiling. The solidus temperature of the U-5Fs alloy is more than 1200K, which means there is significant safety margin for the fuel during this transient. The simulation results demonstrate well the inherent safety characteristics of the EBR-II reactor during an unprotected loss of flow transient.

The calculated core total power, fission power and decay power are illustrated in FIG. 39. The experimental data for fission power are shown by the dashed line, and the simulation results are plotted with solid lines. As can be seen in FIG. 39, after the station blackout occurs, the power of the reactor decreases quickly and eventually converges to a low power level. The calculated fission power compares very well to the recorded fission power.

The calculated and recorded core outlet temperatures during the transient are illustrated in FIG. 40. The outlet temperature of the core changes with the transient. The highest outlet temperature occurs at around 60s, and the highest predicted outlet temperature is about 980K. From FIG. 40, it can be seen that the calculated results have the same overall trend as the experimental data but overpredict the outlet temperature, especially near the temperature peak.

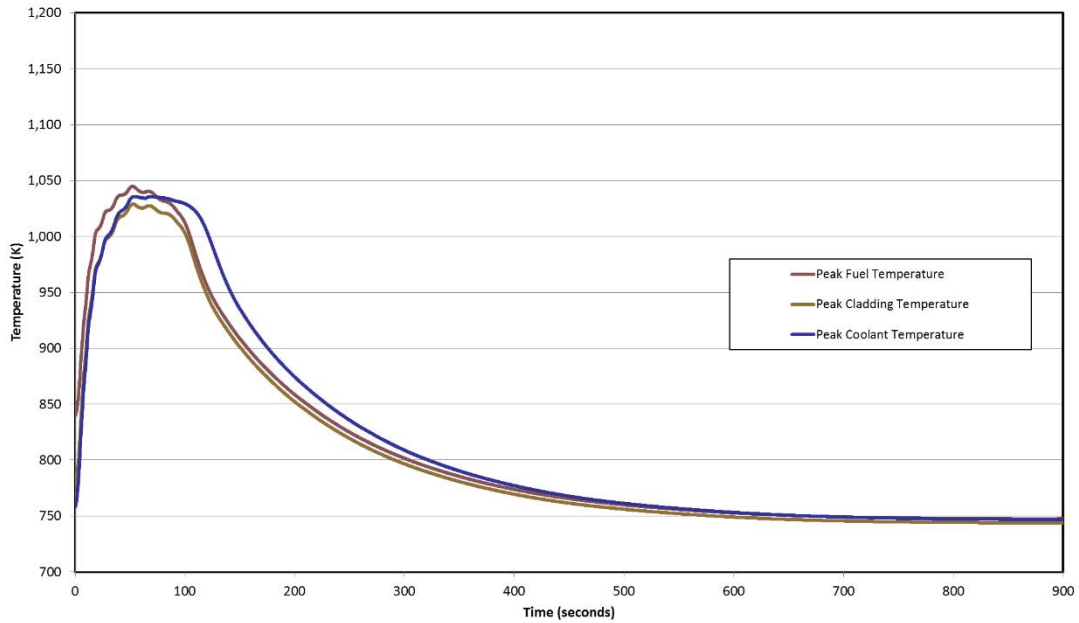


FIG. 38. Peak in-core temperatures during SHRT-45R, phase 2.

The reactivity changes during the transient are illustrated in FIG. 41. Only the Doppler reactivity, axial expansion reactivity, radial expansion reactivity and coolant density reactivity were considered. From FIG. 41, it is clear that the largest reactivity is the sodium void reactivity.

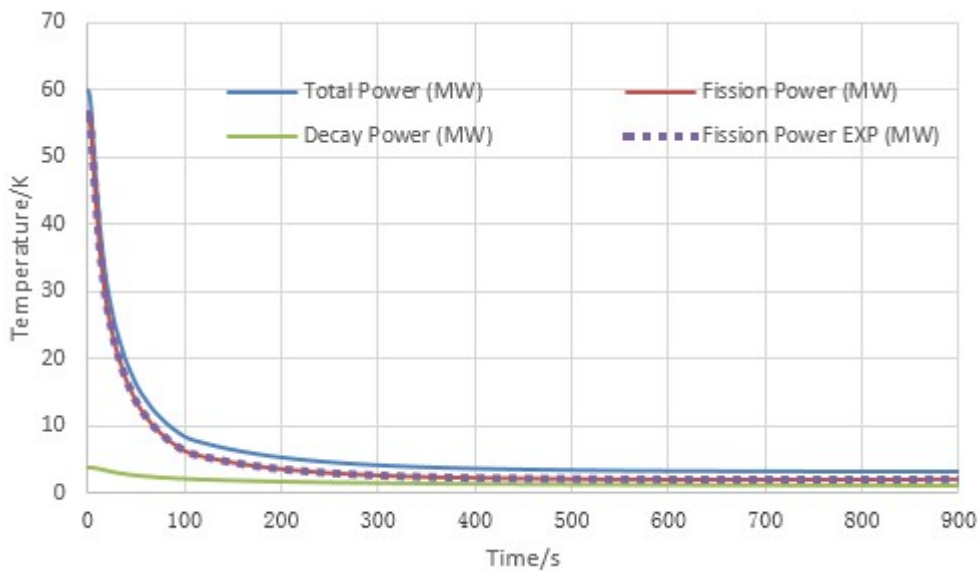


FIG. 39. Power during SHRT-45R test, phase 2.

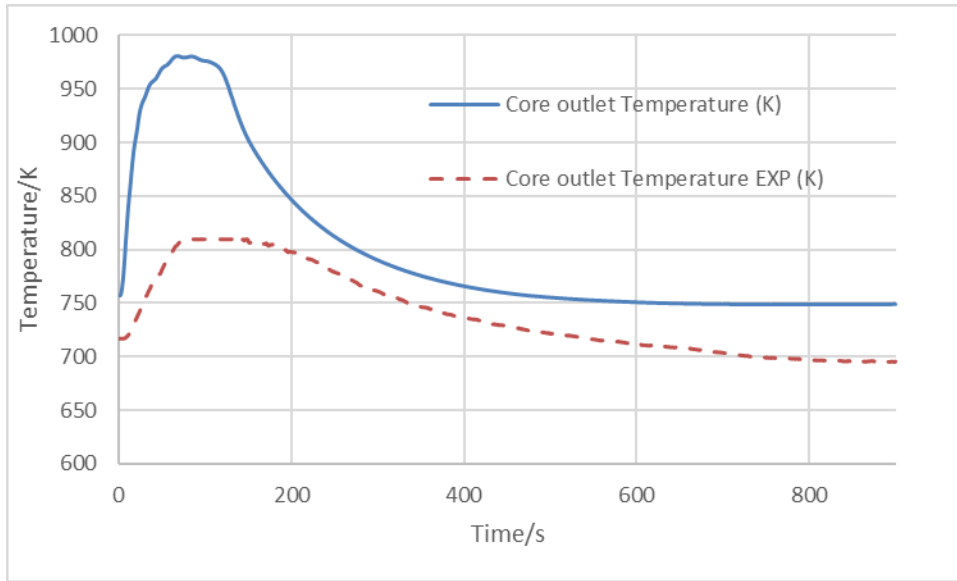


FIG. 40. Core outlet temperature during SHRT-45R test, phase 2.

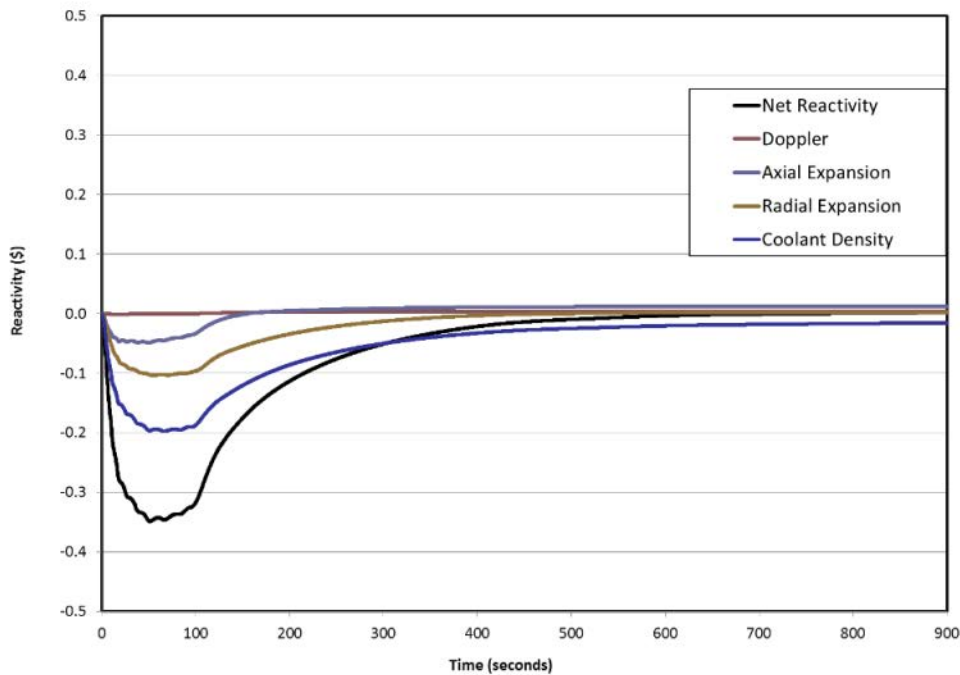


FIG. 41. Reactivity during SHRT-45R test, phase 2.

Simulation results of average temperatures at different elevations in XX09 are illustrated in FIG. 42. It can be seen that the calculation results have the same general trend as the experimental data, with the peak temperature at each elevation close to the experimental data. However the calculated temperatures decrease more quickly than do the recorded data.

Simulation results of average temperatures at different elevations in XX10 are illustrated in FIG. 43. As for XX09, the plots show that the calculation results follow shapes similar to the

experimental data, but in this case, the temperatures at each elevation throughout the transient are significantly lower than the experimental data. The reason for this discrepancy has not yet been identified.

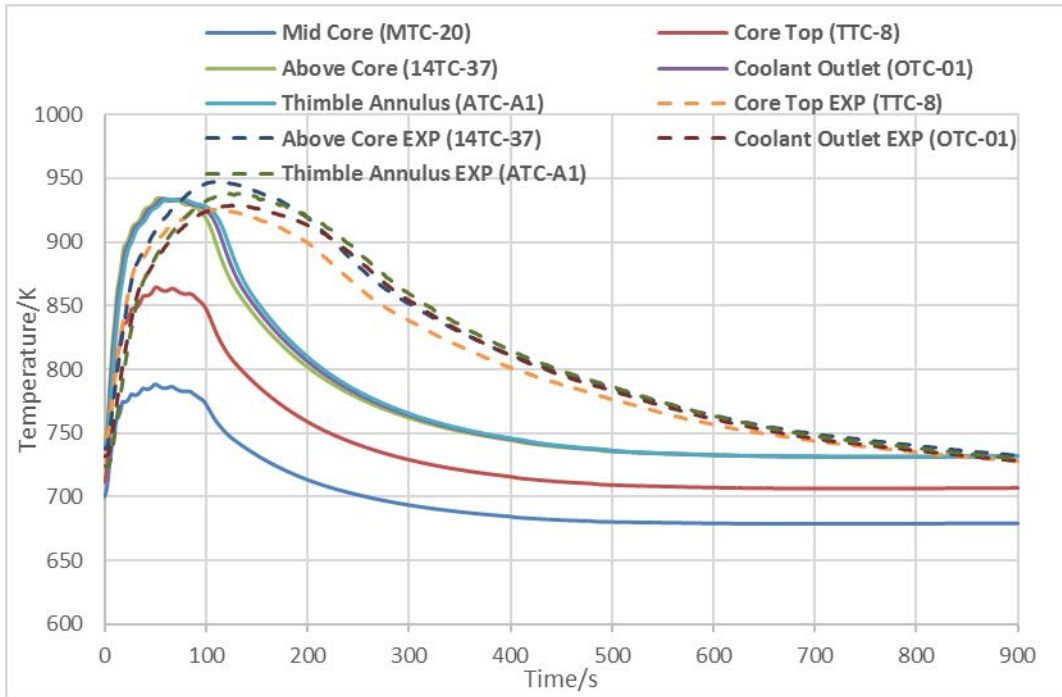


FIG. 42. SHRT-45R temperatures at different elevations in XX09, phase 2.

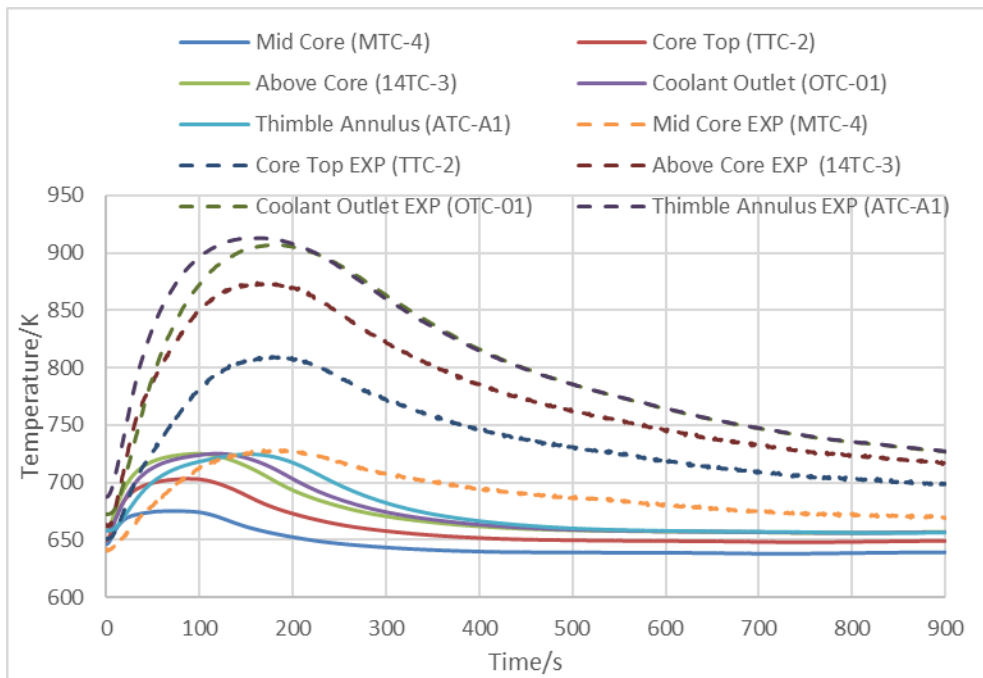


FIG. 43. SHRT-45R temperatures at different elevations in XX10, phase 2.

7.1.5.3. Model improvements

For the final Phase 2 model of SHRT-17, the channel partition and the geometry model were changed appreciably from the Phase 1 model. Also, for each channel, the axial segments partitioning, flow path area and structure and reflector data were modified appreciably. These modifications made little difference to the results. The greatest change was in simulating a natural circulation flowrate of about 3%, determined by experience and the experiment results. Applying this flowrate produced core temperature results that confirmed the core model.

7.2. NORTH CHINA ELECTRIC POWER UNIVERSITY (CHINA)

7.2.1. Geometry/discretization

The main components in this simulation include the reactor core, IHX, sodium pool and pump. The boundary conditions for the secondary side of the IHX are the coolant inlet temperature and the mass flow rate.

All rows of the core subassemblies were divided into 9 channels, representing the driver fuel, stainless steel reflector, control rods and blanket regions. Each channel was divided into 26 axial slices with 4 radial nodes in the fuel and 1 node each in the gap, cladding, coolant and structure. Each channel had a separate power fraction and flow fraction distribution. All channels were treated using similar thermal hydraulic models. Coolant flow in each channel was parallel to the channel axis, without cross-flow between adjacent channels. At the same time, axial heat conduction in the coolant and fuel was neglected.

The nodalization of the intermediate heat exchanger (IHX) is shown in FIG. 44. All the heat transfer tubes were simplified to one representative tube. There are two basic assumptions: 1) ideal mixing of coolant at the inlet and outlet and 2) fully developed convective heat transfer. There were four kinds of radial nodes: secondary coolant, tube, primary coolant and shell wall. The nodes in the coolant and structure were placed in a staggered manner.

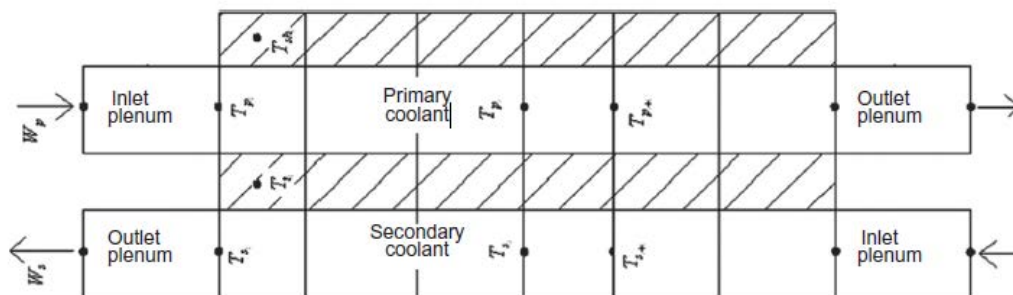


FIG. 44. Nodal diagram for IHX.

7.2.2. Nuclear and thermo-physical data/correlations

Total fission power was calculated based on a neutron point-kinetics model containing six groups of delayed neutrons. The time-dependent portion of the decay heat contribution was handled by a tabular look-up of data supplied in the input file. Thus, paired points of time vs. decay heat fraction were supplied by the user.

Contributions to reactivity feedback effects consisted of the Doppler effect, sodium density, fuel axial expansion and structural expansion bowing. All reactivity feedbacks were calculated based on one control volume for each axial channel.

The basic correlations and laws to calculate the thermo-physical properties, friction factor and heat transfer coefficients are described below. Thermal properties such as thermal conductivity, heat capacity, enthalpy, density, and viscosity for sodium are given in [28].

Friction factors were assumed to be a function of Reynolds number and roughness. Friction factor for laminar flow was calculated as $f=64/Re$. For turbulent flow, the friction factor was determined by the Moody diagram.

The heat transfer coefficient for liquid sodium flow through tube bundles was determined by modifying the Schad correlation [70].

For sodium flow through the piping, the heat transfer coefficient was determined by the Graber-Rieger correlation ([71], [72], [73], [74]).

7.2.3. Thermal hydraulics methods and models

7.2.3.1. Code(s) used

For the SAC-CFR code, the primary options and assumptions used for the EBR-II analysis included:

- (a) Liquid sodium was regarded as an incompressible fluid;
- (b) The assumptions for the IHX model were mentioned in the last section;
- (c) Fractional power and flow deposited in each channel were specified through input and did not change during the transient simulation;
- (d) The radial node mesh in the fuel pin used equal radius increments;
- (e) A three-dimensional sodium pool model was adopted;
- (f) The pressure drop was specified through input. After the steady state initialization, a loss coefficient was calculated. Then the loss coefficient remained constant during the transient simulation.

7.2.3.2. Basic method

The SAC-CFR code is divided into three major subroutine categories: read subroutine, steady state calculation and transient calculation. The basic call relationship among the subroutines is shown in FIG. 45.

Since the thermal properties are independent of pressure, the energy equation and momentum equations for the sodium coolant were decoupled to simplify the calculation. The overall solution logic for the transient simulation is as follows:

- (a) HYDDRV—primary and intermediate loop hydraulic calculation to calculate the mass flow rate in the loop;
- (b) POWDRV—fission power generation calculation, including the reactivity feedback;
- (c) COLDRV—coolant heat transfer calculation in the core;
- (d) FUELDRV—calculation of heat transfer in the fuel, including the heat transfer through the cladding;

- (e) TLPDRV—loop energy calculation for primary and intermediate loops, including the IHX;
- (f) PCSPPS—plant control system and protection system calculation.

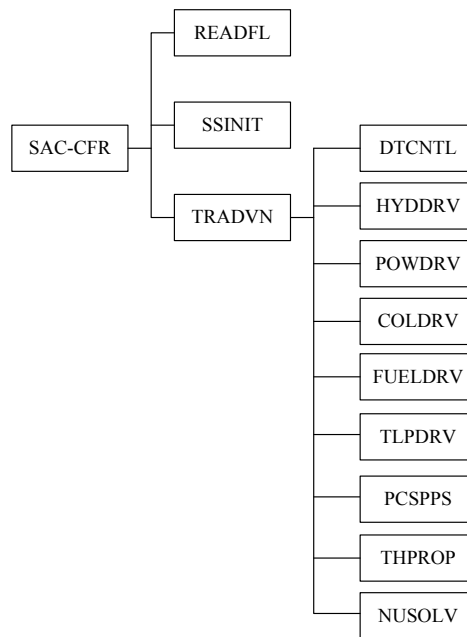


FIG. 45. Call relationship between SAC-CFR subroutines.

In addition, a three-dimensional sodium pool model was used. The simplifications made to the pool model can be summarized as:

- (a) The pool was modelled to 360° circumferentially using a cylindrical coordinate system. The intermediate heat exchanger and pumps occupied one or more control volumes according to their actual size;
- (b) The fuel handling structure was neglected;
- (c) The openings on the primary side of the IHX were inlet boundaries for the pool model, with the rest of the IHX treated as a solid structure;
- (d) The solid structures of the IHX and pumps were modelled with the porous medium method.

7.2.3.3. Model

EBR-II is modelled through the input file. The input file consisted of five parts: main vessel model, primary and intermediate loop model, property data, steady state initialization data and transient input. After reading the geometry data and steady state initialization data, the plant balance state was determined by steady state initialization. Then the transient simulation was started according to the trigger point or boundary conditions specified in the transient input file.

A neutron point-kinetics model was used to calculate the fission power. A single channel model was employed to simulate the thermal hydraulic response in the core. Flow and heat transfer in pipes and the heat exchanger were assumed to be one dimensional. The sodium pool was analyzed with a three-dimensional model.

7.2.4. Blind results

NCEPU did not produce any blind results.

7.2.5. Final results, data comparisons

7.2.5.1. SHRT-17

Peak temperature simulation results for the fuel, cladding, and coolant in the core are plotted in FIG. 46. The peak temperatures increase due to the mismatch between the power and flow in the initial stage, then decrease gradually. The predicted core inlet temperature vs. the measured value is shown in FIG. 47.

The coolant temperatures at the IHX primary inlet and intermediate outlet are shown in FIG. 48. The predicted inlet temperature on the primary side of the IHX agrees well with the measured data. The predicted outlet value at the intermediate outlet differs due to differences between the actual decay power and the decay heat model that was used. The predicted mass flow rate through primary pump 2 vs. the measured value is plotted in FIG. 49.

FIG. 50 and FIG. 51 show the mass flow rate and coolant temperature in the instrumented driver fuel subassembly XX09. The predicted values and measured values agree basically.

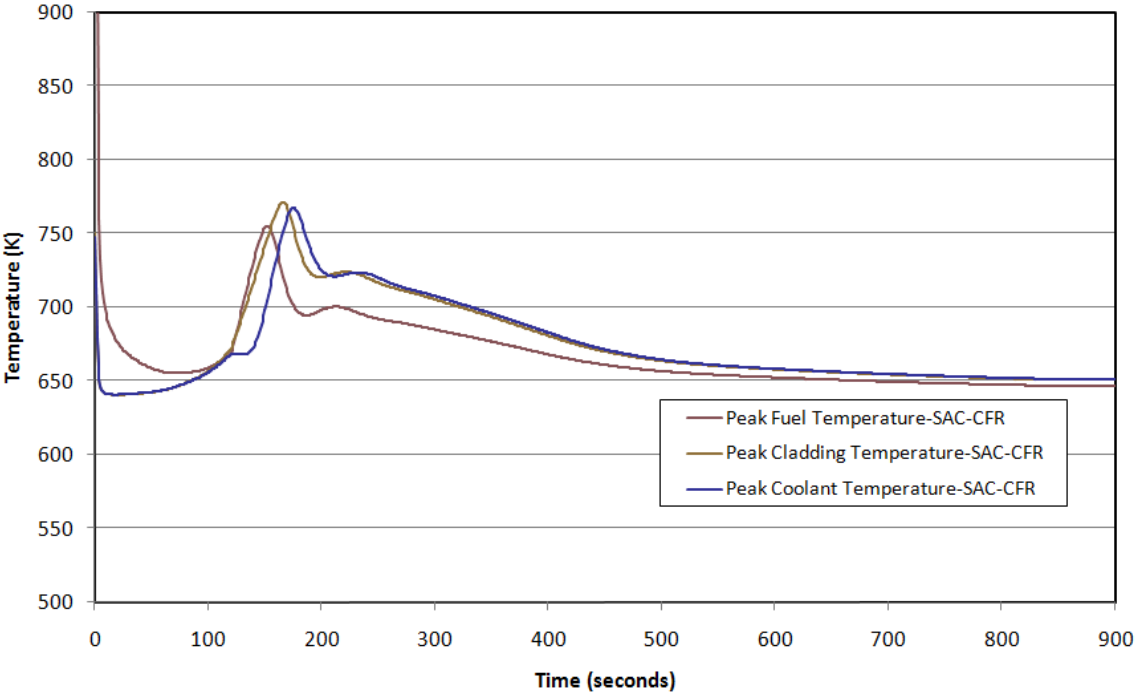


FIG. 46. Peak temperatures in the core, SHRT-17.

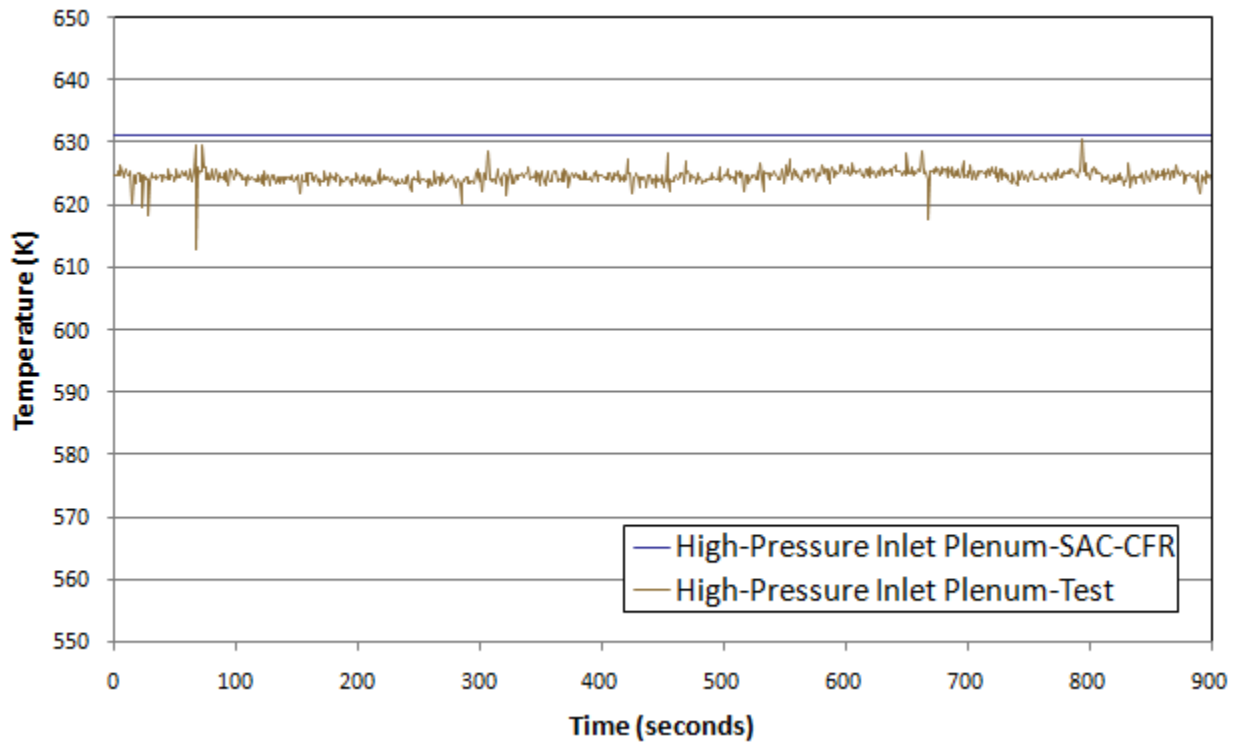


FIG. 47. Core inlet temperature, SHRT-17.

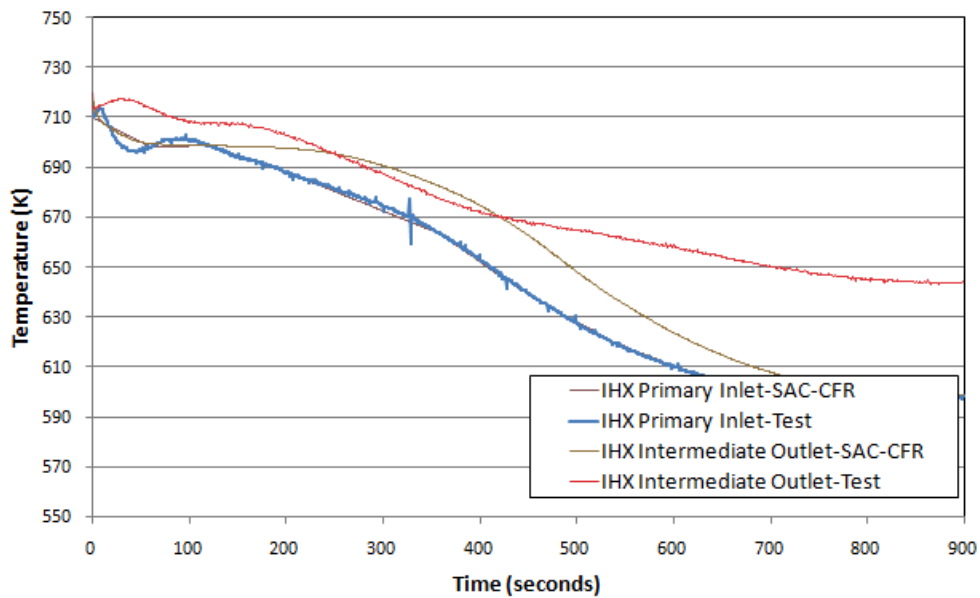


FIG. 48. Coolant temperatures at IHX inlet and outlet, SHRT-17.

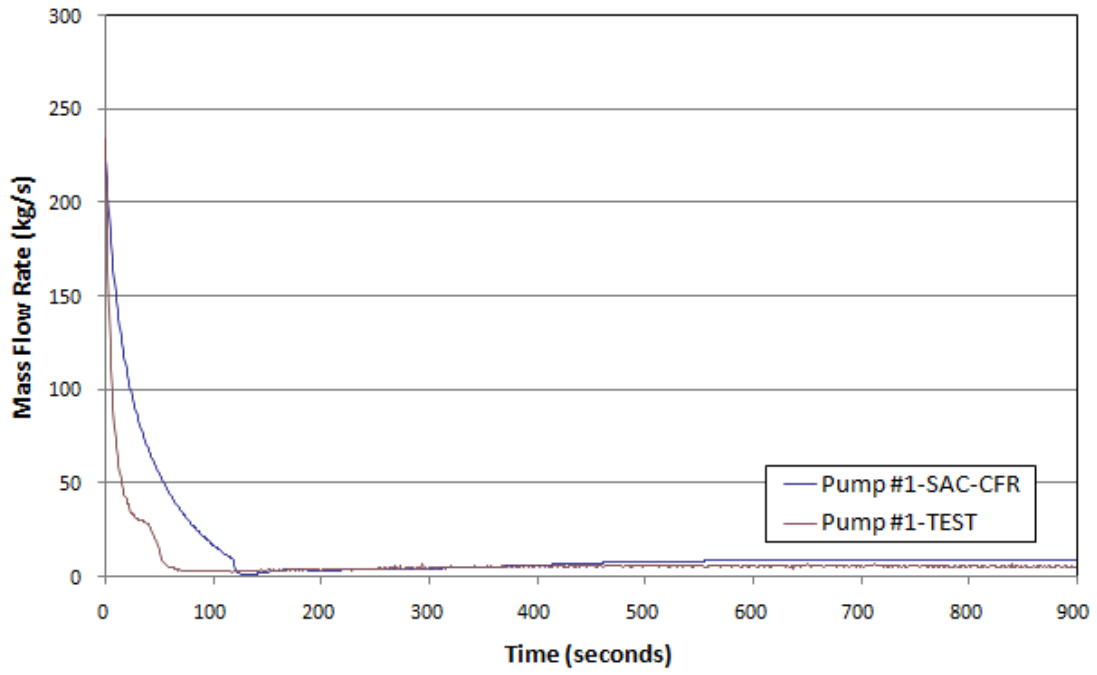


FIG. 49. Primary pump mass flow rates, SHRT-17.

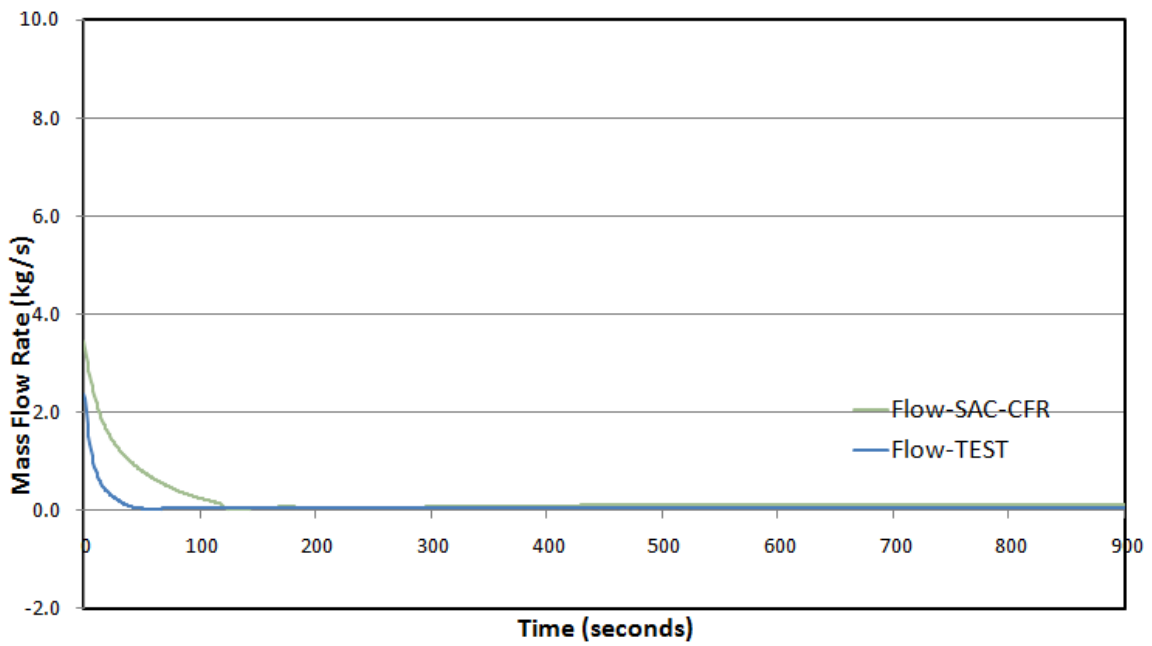


FIG. 50. Mass flow rate in XX09, SHRT-17.

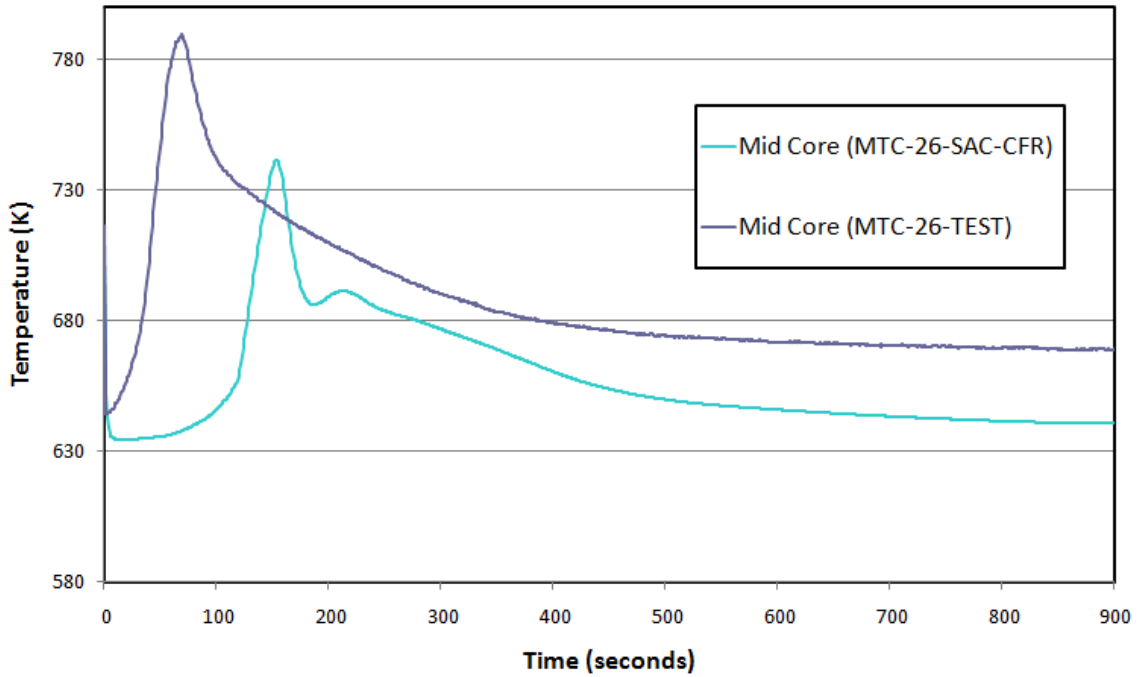


FIG. 51. Coolant temperature at XX09 mid-core, SHRT-17.

7.2.5.2. SHRT-45R

FIG. 52 shows the fission power level predicted and measured values. The predicted power decreases rapidly due to the negative reactivity feedback associated with increased reactor temperature. The measured power is lower than predicted, due to more negative feedback in EBR-II than was predicted by SAC-CFR.

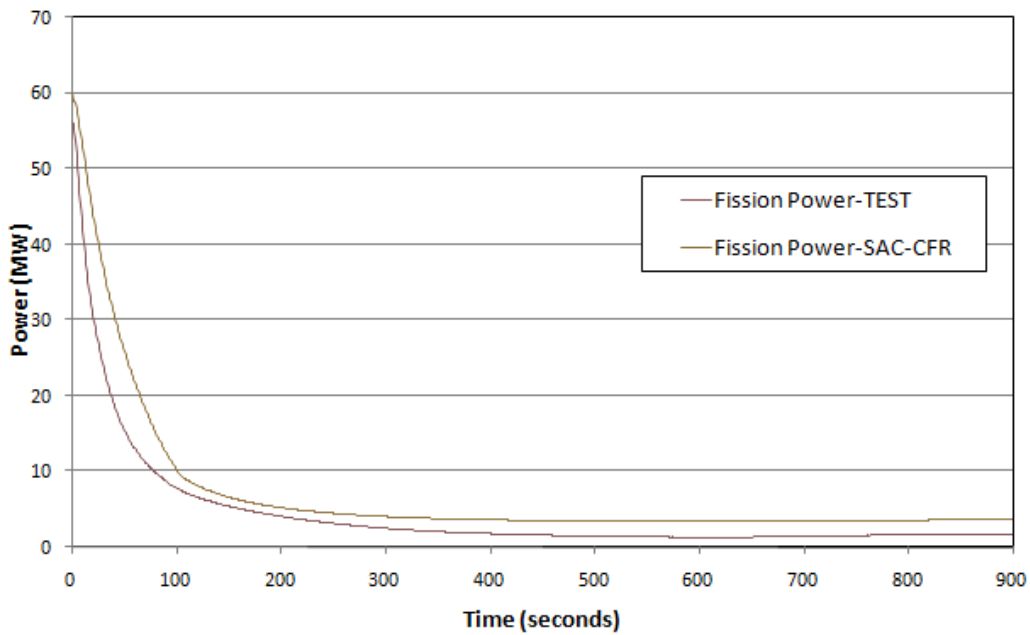


FIG. 52. Fission power, SHRT-45R.

FIG. 53 shows the peak temperatures of the fuel, cladding and coolant in the reactor core.

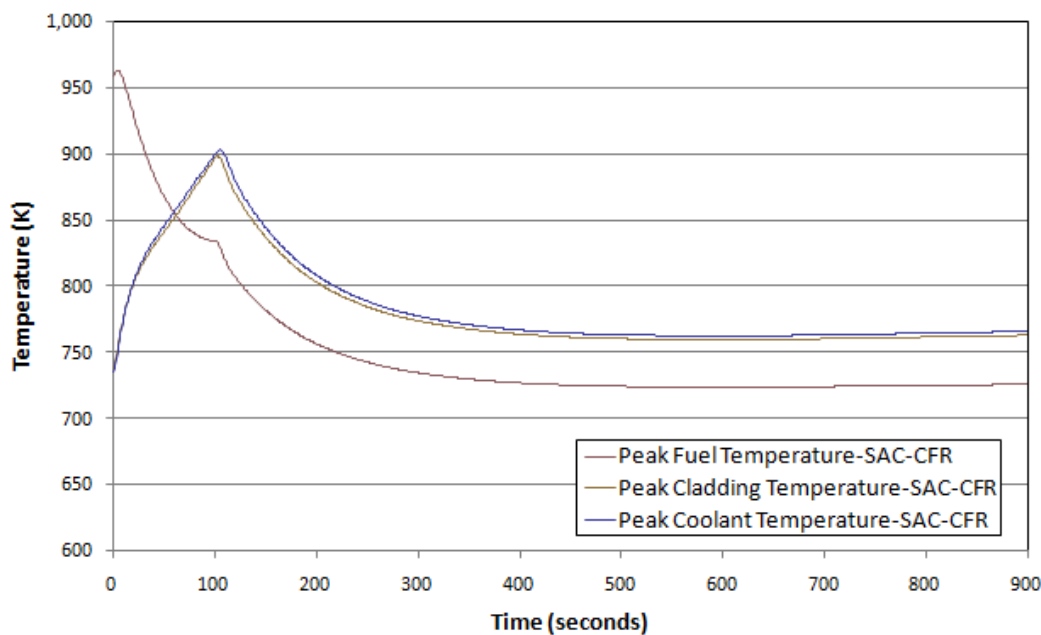


FIG. 53. Peak temperatures in the core, SHRT-45R.

FIG. 54 and FIG. 55 show the change in net reactivity and in various reactivity feedbacks over time. The net reactivity became negative due to rising of the core temperature, which led to a decrease in-reactor power, which eventually resulted in a decrease in the core temperature. When the core temperatures returned towards their initial values, the excess reactivity returned to zero. Radial expansion reactivity feedback plays an important role in all the reactivity feedback contributions.

FIG. 56 shows the Z-Pipe inlet temperature response and IHX primary inlet and secondary outlet temperature responses. FIG. 57 shows the primary pump 2 mass flow rate with time.

Coolant temperatures in the XX09 subassembly are shown in FIG. 58 and FIG. 59. The predicted and measured values agree well during the initial stage of the transient. The difference in the later stage is caused by the difference between the actual decay power and that used by SAC-CFR. The decay power in SAC-CFR is higher than the actual decay power.

A three-dimensional sodium pool model using a porous medium model was developed to predict the thermal hydraulic response of the cold pool, and the flow fields at longitudinal sections and horizontal cross-sections were obtained.

Flow patterns at a longitudinal section of different azimuths within the cold pool are shown in FIG. 60 and FIG. 61. These figures show the same azimuths for both components. The influence on the flow field due to the solid structure of the IHX, pump and DHX can be seen from the longitudinal flow patterns.

The horizontal flow fields shown in FIG. 62 and FIG. 63 are at different elevations. One is at the outlet boundary hon the primary side of the IHX, and the other is at the outlet boundary of the primary pumps. It can be seen that the flow fields at different elevations are basically symmetrical, for the key components are mirror-symmetrically arranged in the pool. In addition, it can be seen from the flow pattern that the solid structure of the IHX, pump and

DHX were successfully simulated with the porous medium model. The good agreement between the computational flow field and the geometry of the pool shows the effectiveness of the porous medium model.

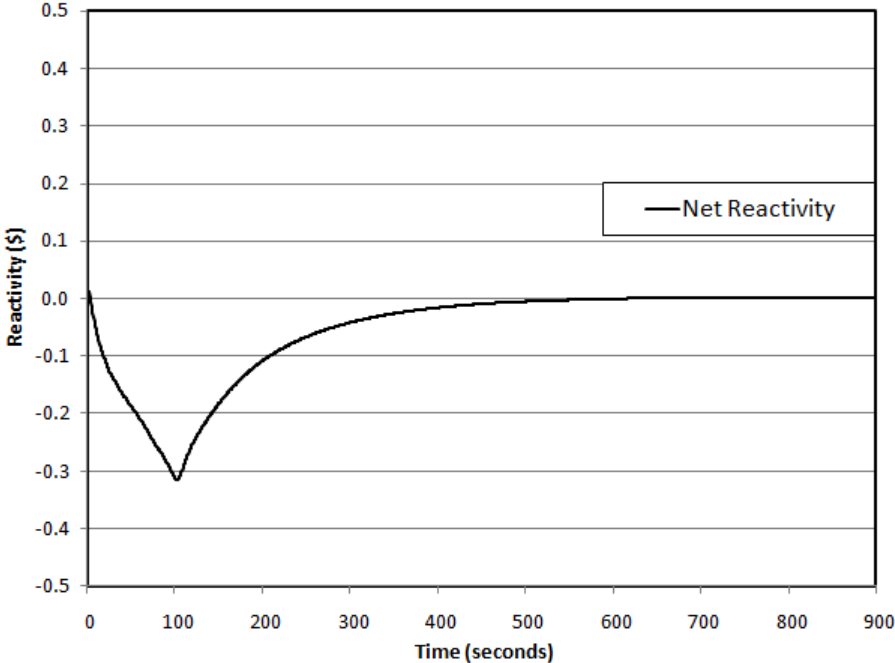


FIG. 54. Net reactivity, SHRT-45R.

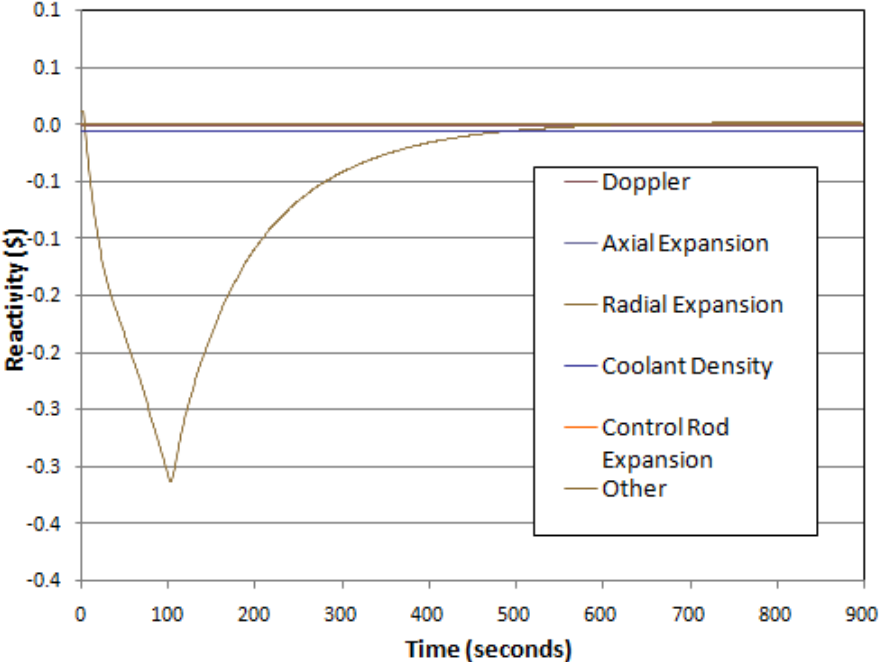


FIG. 55. Reactivity feedback, SHRT-45R.

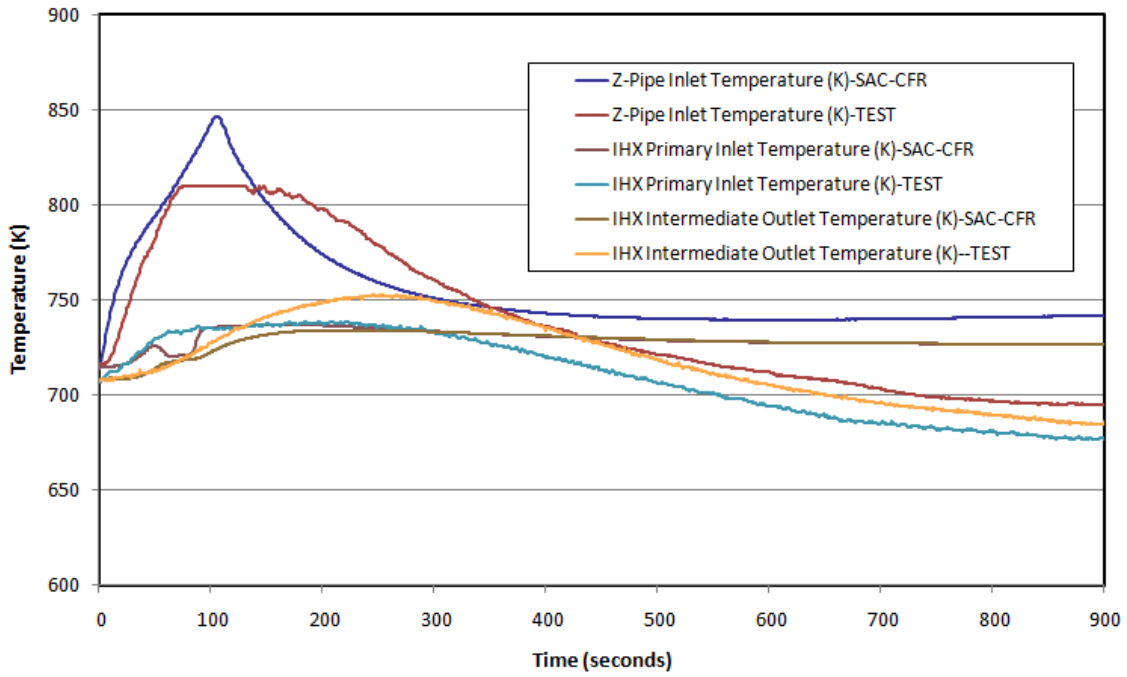


FIG. 56. Coolant temperatures at Z-Pipe inlet and IHX, SHRT-45R.

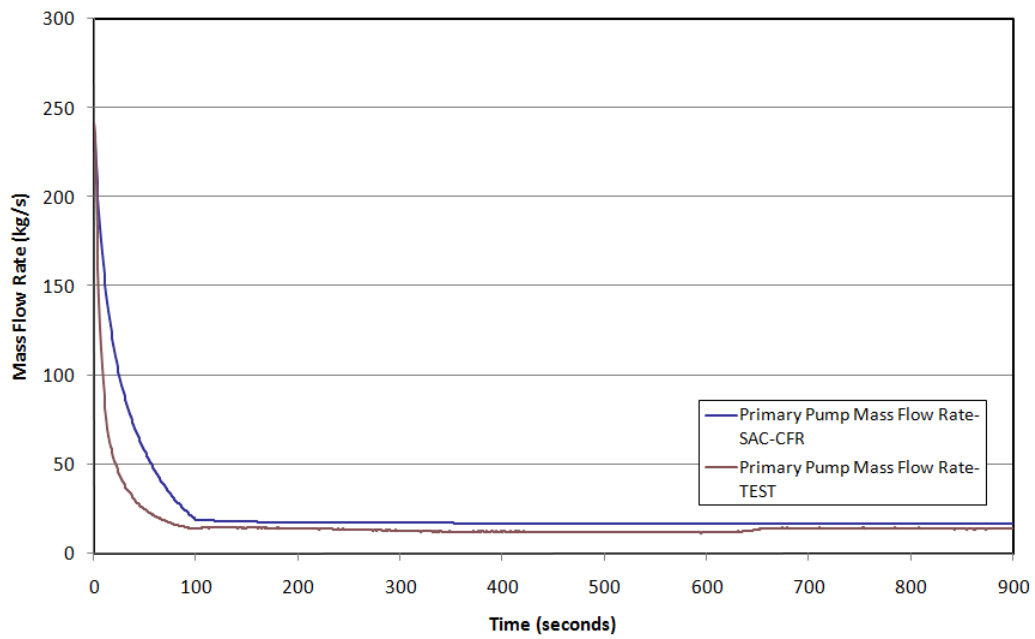


FIG. 57. Pump mass flow rates, SHRT-45R.

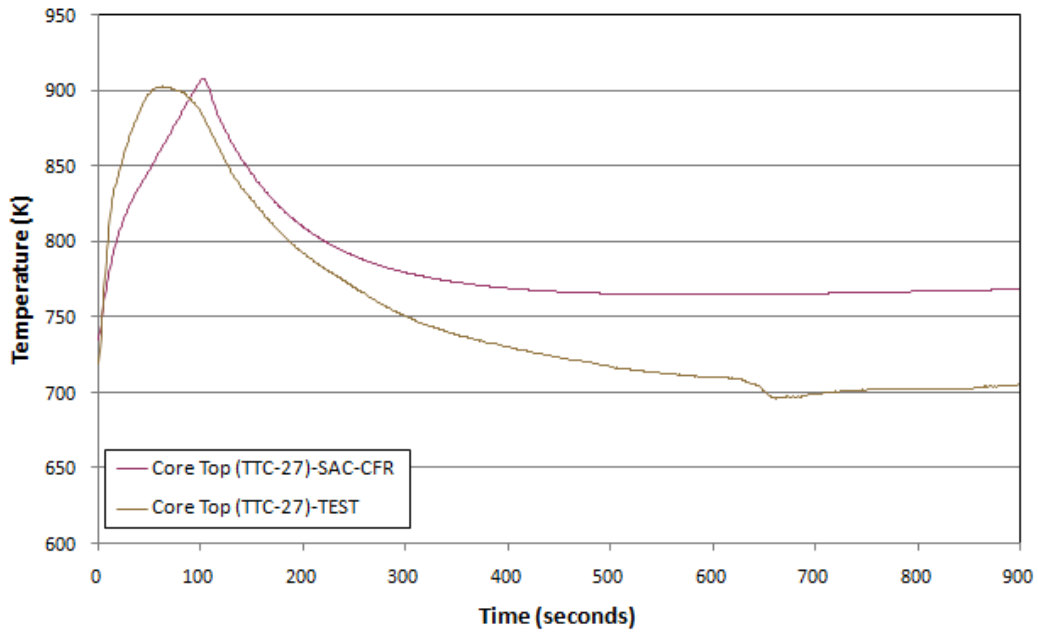


FIG. 58. Coolant temperature at XX09 core top, SHRT-45R.

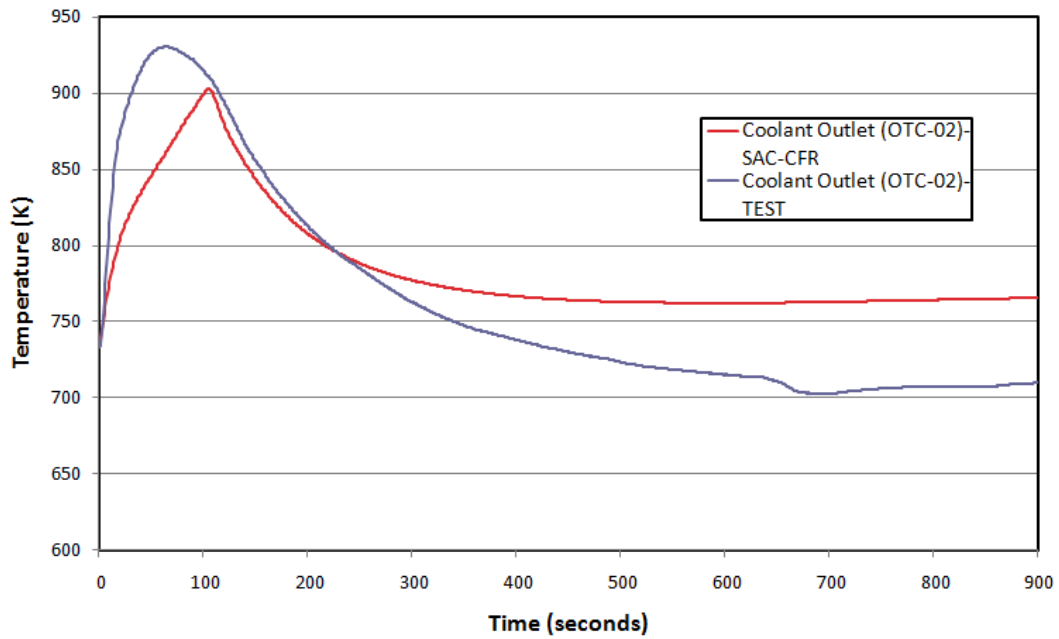


FIG. 59. Coolant temperature at the XX09 outlet, SHRT-45R.

7.2.5.3. Model improvements

Radial expansion reactivity feedbacks were included in the analysis of SHRT-45R.

7.2.6. Neutronics methods and models

NCEPU did not perform a neutronics analysis.

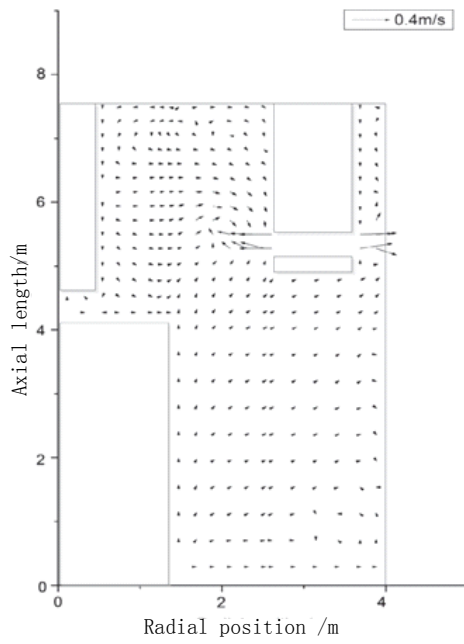


FIG. 60. Flow pattern at a longitudinal section at the azimuth of the IHX, SHRT-45R.

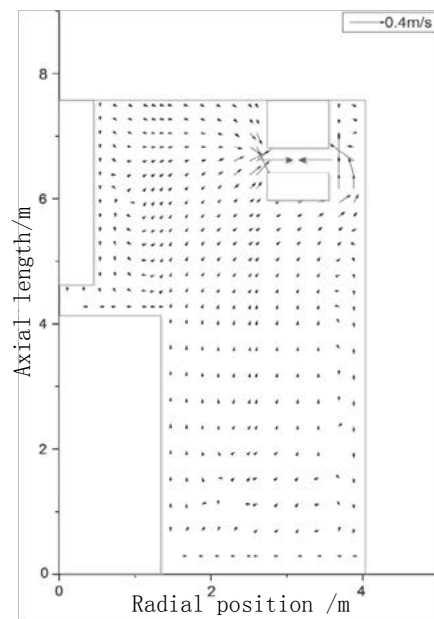


FIG. 61. Flow pattern at a longitudinal section at the azimuth of the primary pumps, SHRT-45R.

7.2.7. Neutronics results

NCEPU did not perform a neutronics analysis.

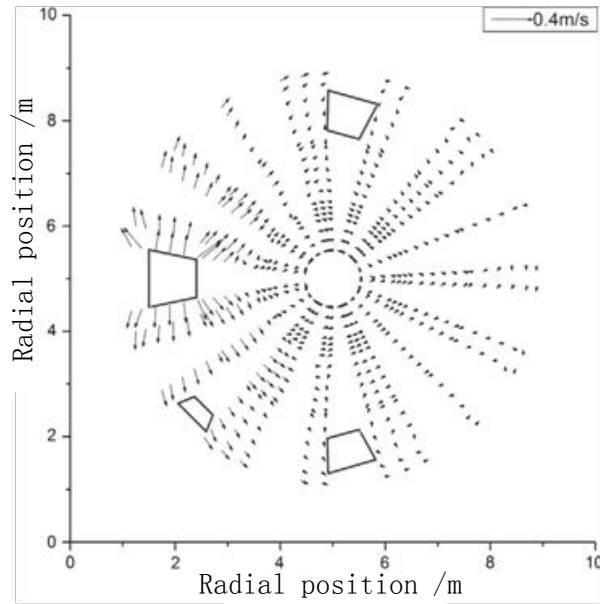


FIG. 62. Flow pattern at a horizontal cross-section of the IHX primary outlet, SHRT-45R.

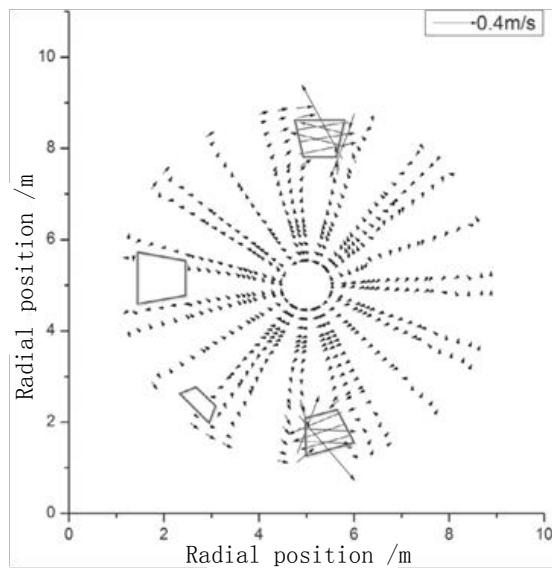


FIG. 63. Flow pattern at a horizontal cross-section of the primary pump inlets, SHRT-45R.

7.3. XI'AN JIAOTONG UNIVERSITY (CHINA)

7.3.1. Geometry/discretization

The THACS code model of the EBR-II plant is shown in FIG. 64. The nodalization used to model driver subassemblies is diagrammed in FIG. 65.

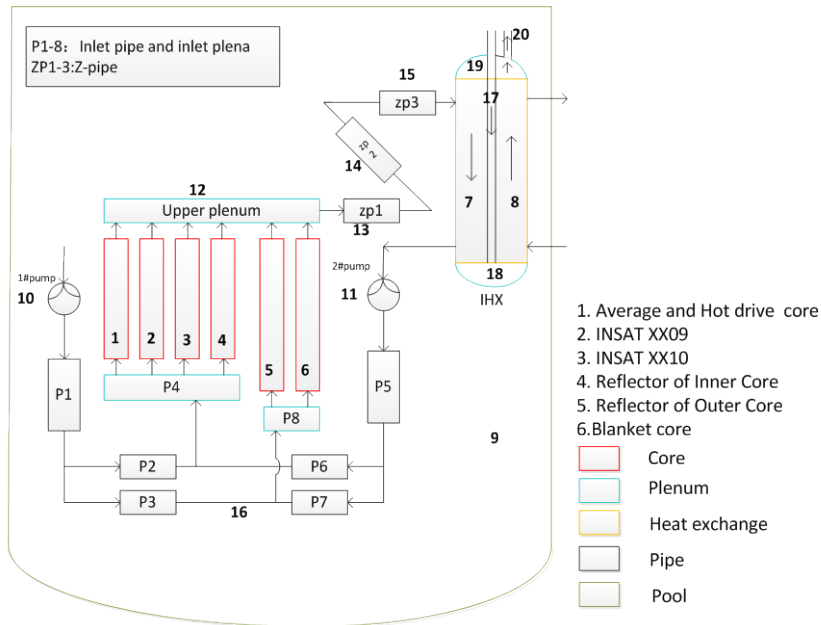


FIG. 64. XJTU nodalization scheme for the EBR-II system.

The core subassemblies were divided by type into 6 different channels, Each channel was then divided into several axial regions based on functional structure. As seen in FIG. 65, the core was divided into five regions, including the subassembly wrapper, sodium, cladding, gas in the fuel pin plenum, and fuel. Every axial region was further divided into several control volumes in both axial and radial directions. Three pipes were used to simulate the Z-Pipe, and every pipe was divided into several volumes. The IHX was simulated with a tube model. The primary side, intermediate side and the tube wall were each divided into 50 volumes in the axial direction. The inlet pipes and inlet plena were simulated with the pipe-net model, which will be described below.

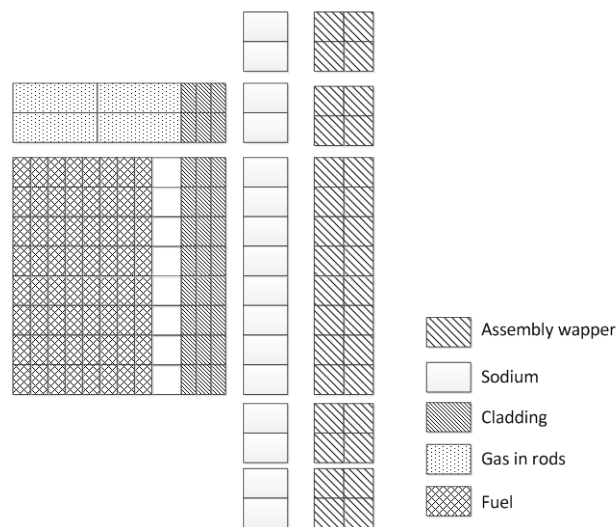


FIG. 65. XJTU nodalization for driver subassembly.

7.3.2. Nuclear and thermo-physical data/correlations

Models for calculating thermodynamic and transport properties of sodium liquid and vapour were developed based on work by Fink and Leibowitz [75]. Thermo-physical properties of steel and B₄C were based on the models from the SSC-K code [76]. The thermal and thermodynamic properties of the metal fuel slugs were provided by Argonne and are unique to the EBR-II U-5Fs fuel.

For flow in a pipe, the correlation for calculating the frictional coefficient of laminar flow used was

$$f = 64 / \text{Re}$$

and for turbulent flow in a rough pipe, the empirical Blasius formula [77] was selected.

The laminar heat transfer coefficient in a pipe was calculated using the correlation from Mikityuk [72],

$$\text{Nu} = 4.36, \quad \text{Re} \leq 3000,$$

and for the turbulent region

$$\text{Nu} = 4.82 + 0.0185 \text{Pe}^{0.827}, \quad \text{Re} > 3000.$$

For single-phase flow and heat transfer in fuel bundles with wire spacers, many correlations are available in the THACS code to calculate the heat transfer coefficient and the flow frictional factor. For the simulation of EBR-II, the flow frictional factor was calculated with the Engel-Markley-Bishop correlation [78], shown below:

$$f = \frac{32}{\sqrt{H}} \frac{(P/D)^{1.5}}{\text{Re}} (1-\psi)^{1/2} + \frac{0.48}{\text{Re}^{0.25}} \psi^{1/2},$$

where H is the wire pitch. This correlation can be used only for $P/D < 1.3$, $H < 0.3$.

$$\psi = \begin{cases} 0, & \text{Re} \leq 400 \\ \frac{\text{Re} - 400}{4600}, & 400 < \text{Re} < 5000. \\ 1, & \text{Re} \geq 5000 \end{cases}$$

The Nusselt number was calculated with the FFTF correlation [79]. When $1.05 < P/D \leq 1.15$, the correlation is

$$\text{Nu} = 4.496 \left[-16.15 + 24.96 \left(\frac{P}{D} \right) - 8.55 \left(\frac{P}{D} \right)^2 \right], \quad \text{Pe} \leq 150,$$

$$\text{Nu} = \left[-16.15 + 24.96 \left(\frac{P}{D} \right) - 8.55 \left(\frac{P}{D} \right)^2 \right] \text{Pe}^{0.3}, \quad 150 \leq \text{Pe} \leq 1000.$$

When $1.15 < P/D \leq 1.30$, the correlation is

$$Nu = 4.0 + 0.16 \left(\frac{P}{D} \right)^{0.5} + 0.33 \left(\frac{P}{D} \right)^{3.8} \left(\frac{Pe}{100} \right)^{0.86}, \quad 10 \leq Pe \leq 5000,$$

where P is the pitch of the bundles and D is the diameter of the rods.

7.3.3. Thermal hydraulics methods and models

7.3.3.1. Code(s) used

For the EBR-II simulation, THACS-V1.0 with some new modules was selected. The core model, pipe and plenum model, IHX model, pipe-net model, pool model and inter-wrapper model were used. The pipe-net model, or pipe network, is the model for the piping that runs from the pump outlets to the EBR-II inlet plenum. A user-defined pump model was employed and the centrifugal pump characteristics were provided by Argonne.

7.3.3.2. Basic method

The numerical method used was the Gear method, in which the equations of variables must be transformed into ordinary differential equations with a finite integral transform,

$$y' = f(t, y, y')$$

The components connection mode for the EBR-II system was implemented as follows. The sodium pool provided the pressures to the IHX outlet and the pump inlet. The mass flow rates of the core channels were calculated using the pressure drop between the core inlet and outlet, which was provided by the pressures at the Z-Pipe inlet and pipe-net outlet. The Z-Pipe inlet pressure was calculated from the mass flow provided by the core channels and the outlet pressure provided by the IHX inlet. The pipe-net outlet pressure was calculated from the mass flow rates provided by the core channels and the inlet pressure provided by the pump outlet. The pool mass was calculated using the mass flow rates from the pump and the IHX. As described above, all the processes are strongly coupled, and the steady state solutions were obtained as a null transient from the transient calculation with the given boundary conditions.

7.3.3.3. Model

Core model: For the core neutronics model, the point-kinetics equations with six groups of delayed neutrons were employed to solve for the core fission power. Four main reactivity feedbacks caused by the Doppler effect, change of coolant density, axial expansion of the fuel rods, and radial expansion of the core were considered. After reactor shutdown, the core power consisted of two parts: the core decay power and the fission power. Four types of fission products were considered.

For the other solid structures such as the fuel, cladding and stagnant sodium in the core, a two dimensional model was used. In the fuel region, there are four types of structures, namely, fuel pellet, cladding, gap and coolant in the radial direction. The fuel pellet and the cladding were discretized into several control volumes. Since the gap of the EBR-II driver fuel was filled with stagnant sodium, only the sodium conductivity mode was considered.

The structure types in the axial direction for all subassemblies were different from those in the radial direction. The average channel was divided into five regions: two bottom shield

regions, one fuel region, one gas plenum region and one upper shield region. There are also five basic core materials – fuel, steel, sodium, control rod and gas – that are available in the THACS core model, and every material model contains several different options for users.

IHX model: The IHX was a tube and shell design with single-wall straight tubes and was operated in the counterflow mode. A lumped parameter model was adopted for simulation of the heat transfer. The IHX was divided into four parts on the intermediate side: the downcomer, the inlet plenum, the tube bundle and the outlet plenum. Heat transfer was considered between the downcomer and the primary side and between the plenum and the cold pool.

Pipe and plenum model: depending on the boundary conditions, there are three different calculation modes in the THACS pipe and plenum model.

If the inlet pressure and inlet flowrate are given, the momentum equation is

$$P_i = P_{i-1} - \Delta P_i - \frac{L_{Pi}}{A_{Pi}} \frac{dW_{Pi}}{dt}.$$

If the inlet pressure and the outlet pressure are known, the momentum equation is

$$\frac{dW_{Pi}}{dt} = \frac{P_{in} - P_{out} - \sum_{i=1}^N \Delta P_i}{L_{Pi} / A_{Pi}}.$$

If the inlet flowrate and the outlet pressure are provided, the momentum equation is

$$P_i = P_{i+1} + \Delta P_i + \frac{L_{Pi}}{A_{Pi}} \frac{dW_{Pi}}{dt}.$$

The Z-Pipe was immersed in the cold pool and was a double-walled structure, and the annular region between the two pipe walls was filled with stagnant sodium. Because of the high temperature at the reactor outlet, the heat transfer and heat capacity of the Z-Pipe walls were included in the THACS model.

Pipe-net model: in LMRs, it always happens that one pipe branches off to more pipes, or several pipes merge into one pipe. The pipe network model was developed in THACS to make the flow distribution calculation work more accurate and easier. The intersection point is calculated as a node, and the liquid flow into the node is equal to the flow out of the node. The same is true for the liquid enthalpy. In EBR-II two primary pumps took suction from the primary sodium tank and provided sodium to the reactor inlet piping, and both sets of inlet piping provided sodium to the high pressure and low pressure inlet plenum, as shown in FIG. 64.

Pool model: in the phase 1 blind calculation, the pool was simulated with a perfect mixing model, and there was only one temperature value representing the entire volume. In phase 2, the pool was simulated with a three-layer model, and the boundaries in the three-layer model were at the pump entries and the IHX exit.

Inter-wrapper model: to accurately and quickly simulate the heat transfer between subassemblies and the cooling capacity of the inter-wrapper fluid, a 2-D inter-wrapper model

was developed in THACS. The inter-wrapper gaps were divided into several layers based on the layout of subassemblies, as shown in FIG. 66. The governing equations of the inter-wrapper fluid in every layer were derived from the Navier-Stokes equations as shown below.

mass continuity equation:

$$A_i \frac{\partial}{\partial t} \rho_i + \frac{\partial}{\partial z} m_i + \sum_{j \in i} w_{ij} = 0$$

energy conservation equation:

$$A_i \frac{\partial \langle \rho h \rangle_i}{\partial t} + \frac{\partial m_i h_i}{\partial z} + \sum_{j \in i} h^* w_{ij} = \bar{q}_i - \sum_{j \in i} \frac{S_{ij}}{l_{ij}} K (T_i - T_j)$$

axial momentum conservation equation:

$$\frac{\partial m_i}{\partial t} + \frac{\partial m_i u_i}{\partial z} + A_i \frac{\partial p_i}{\partial z} = -g \rho_i A_i - \sum_{j \in i} u_i^* w_{ij} - \frac{1}{2} \left(\frac{f_i}{D_i} + \frac{K_s}{\Delta z} \right) \frac{m_i^2}{A_i \rho_i}$$

transverse momentum conservation equation:

$$\frac{\partial w_{ij}}{\partial t} + \frac{\partial (v_{ij} w_{ij})}{\partial x} = \frac{S_{ij}}{l_{ij}} (p_i - p_j) - \sum_{j \in i} m_j^* v_{ij} - \frac{1}{2} \left(\frac{f_j}{D_j} + \frac{K_G}{\Delta x} \right) \frac{|w_{ij}| w_{ij}}{S_{ij} l_{ij} \rho^*}$$

The above four equations comprise the governing equations of the inter-wrapper fluid. In the transverse momentum conservation equation, the pressure drops included frictional and resistance pressure drops. The heat transfer was calculated on the basis of the heat conduction of the wrapper wall and the heat convection of the liquid sodium. The above equations were discretized with a staggered grid and the discretized equations solved in a segregated way with the Semi-Implicit Method for Pressure-Linked Equations algorithm.

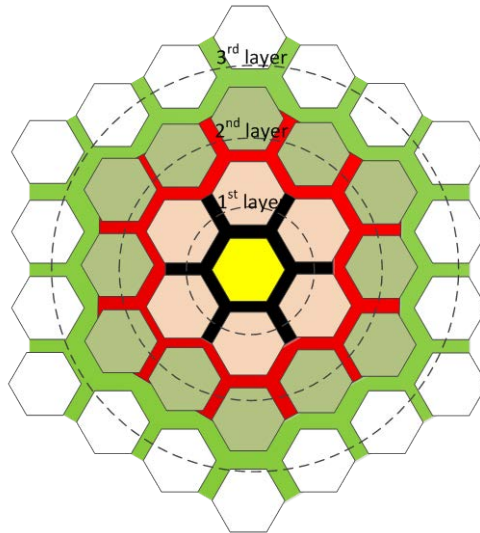


FIG. 66. Diagram of the layers of the inter-wrapper fluid.

7.3.4. Blind results

7.3.4.1. SHRT-17

The blind results for SHRT-17, before the measured data were released, are shown in FIG. 67 through FIG. 69. The small plots in the top right corner of the figures display the low range mass flow rates. From FIG. 68 it can be seen that the peak temperatures in XX09 decrease following establishment of natural circulation. The calculated results of the IHX primary inlet temperature and intermediate outlet temperature are higher than the experiment data. The mass flow rates of pump #2 and the flow in XX09 were in good agreement with the experiment data. The XX09 peak temperature is about 50 K above the experiment data, and the XX10 temperature has a large discrepancy with the experiment data. Reverse flow occurred in XX10.

7.3.4.2. SHRT-45R

The blind results for SHRT-45R are shown in FIG. 70 through FIG. 72. From FIG. 71, it can be seen that the XX09 peak temperatures agree better with the experiment data than was the case for SHRT-17, and the discrepancy becomes bigger as natural circulation is established. The XX10 temperatures in SHRT-45R are again much lower than the experiment data. The mass flow calculated values for pump #2 and in XX09 are higher than the experimental results. In addition, the calculated IHX primary inlet temperature and IHX intermediate outlet temperature are much higher than the recorded data.

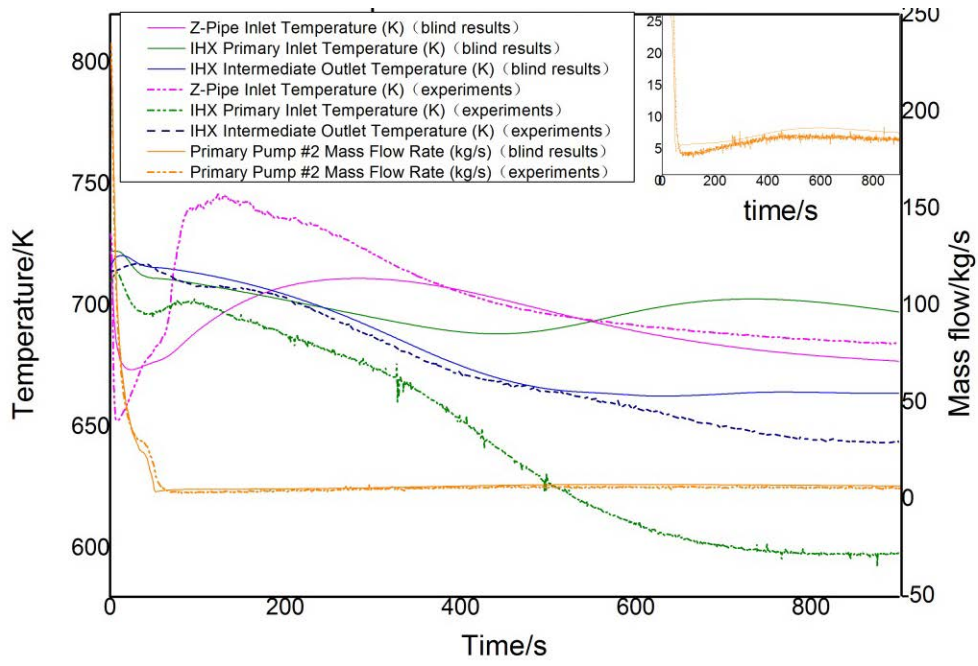


FIG. 67. Comparison of blind results and experiment data for SHRT-17.

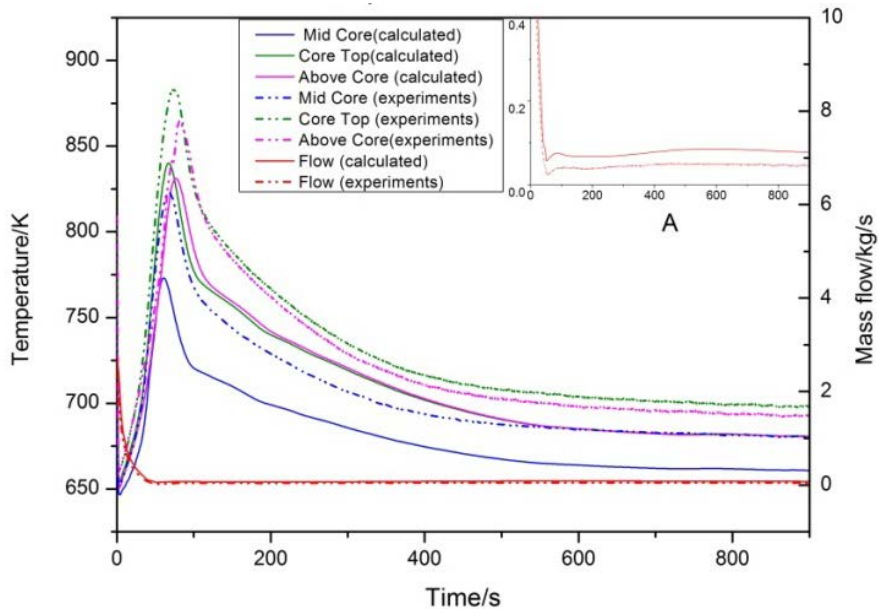


FIG. 68. Comparison of blind results and experiment data in XX09 for SHRT-17.

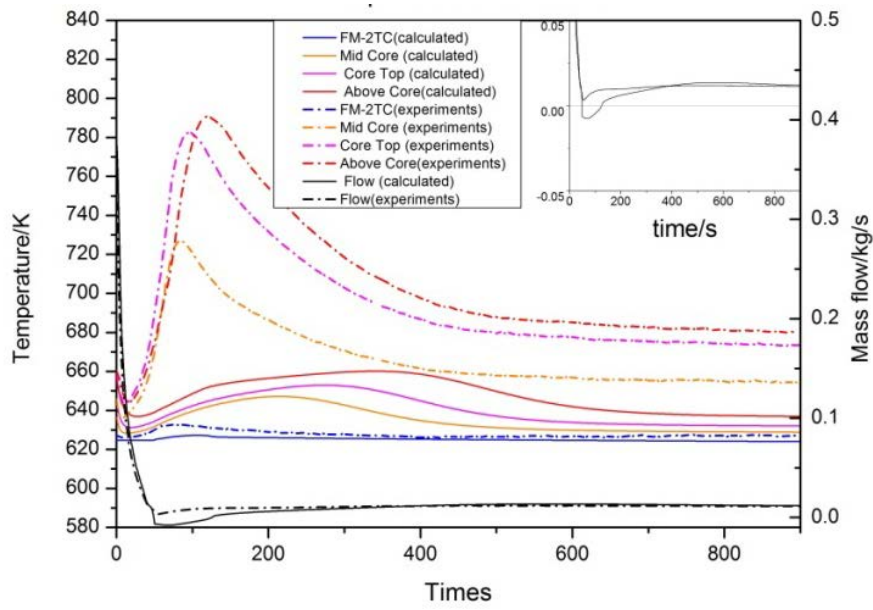


FIG. 69. Comparison of blind results and experimental data in XX10 for SHRT-17.

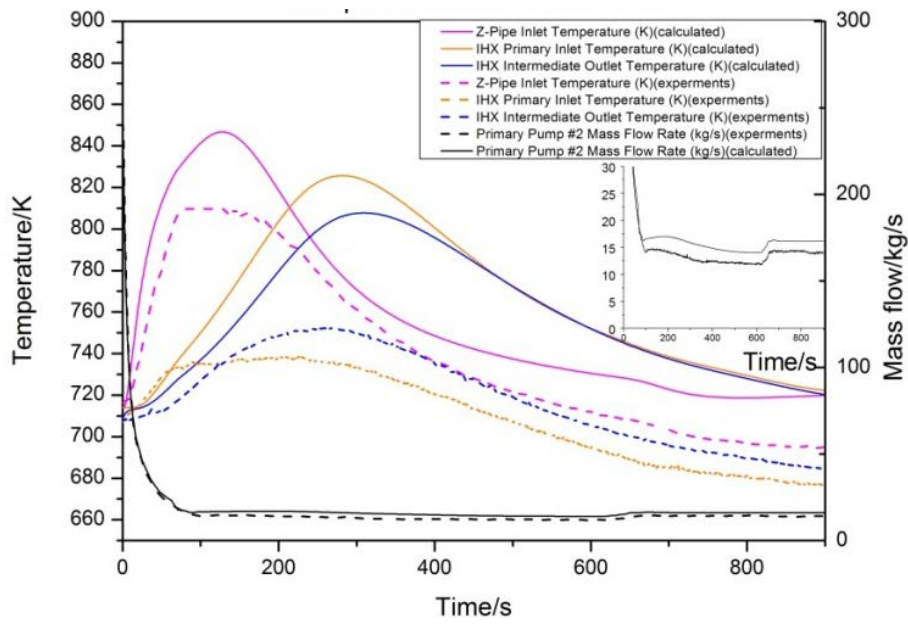


FIG. 70. Comparison of blind results and experimental data for SHRT-45R.

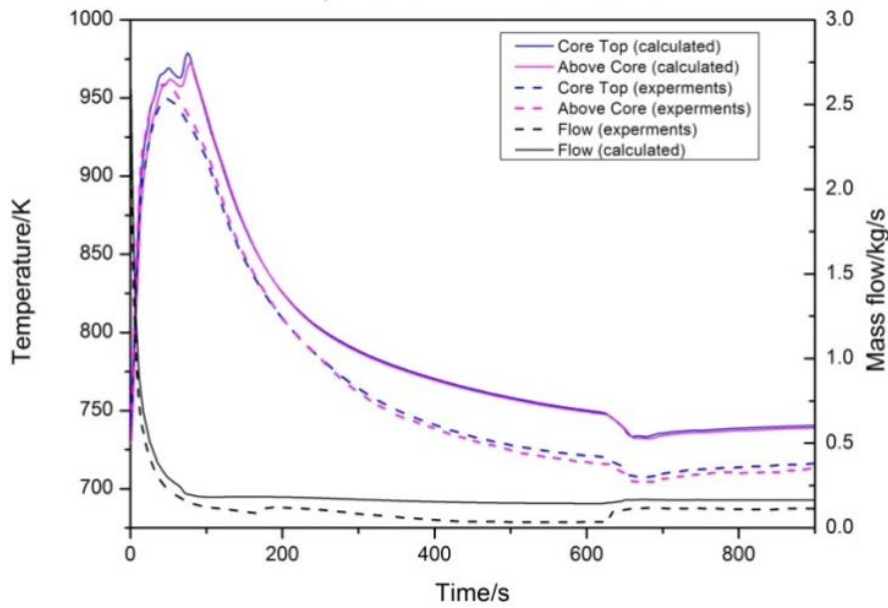


FIG. 71. Comparison of blind results and experimental data in XX09 for SHRT-45R.

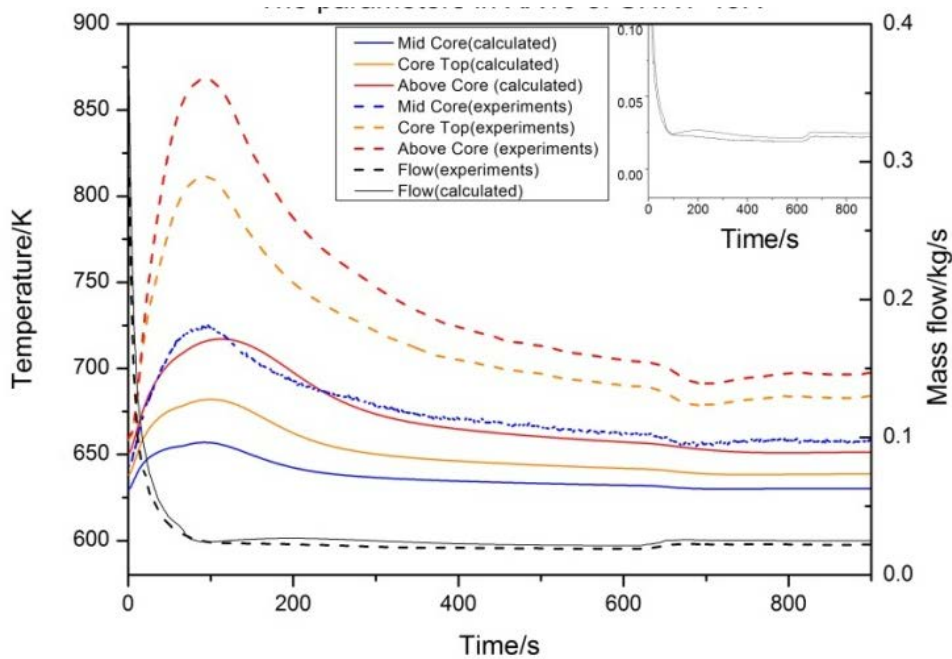


FIG. 72. Comparison of blind results and experimental data in XX10 for SHRT-45R.

7.3.5. Final results, data comparisons

Based on the blind benchmark analyses of SHRT-17 and SHRT-45R, three aspects needed to improve. First, the simulated temperature of the IHX was so much higher than the recorded data. According to the analyses of temperatures of the Z-Pipe and IHX, the problem does not result from the predicted temperature of the core but may be the heat loss in the Z-Pipe. Therefore, a heat transfer model for the Z-Pipe was added. Second, the simulated mass flow during natural circulation was higher than the recorded data, which might have been caused by neglecting thermal stratification of the cold pool. Therefore, a three-layer pool model was

added. Third, the calculated temperatures of XX10 were much lower than the experiment data. XX10 was a non-fueled subassembly surrounded by driver subassemblies. Sodium has the property of high thermal conductivity. The heat transfer between XX10 and the surrounding subassemblies may raise the temperature in XX10. Hence, the inter-wrapper model was used.

With the improved models and the more comprehensive knowledge of EBR-II, the final CRP results are in better agreement with the experiment data.

7.3.5.1. SHRT-17

FIG. 73 displays comparison of final results and experiment data for SHRT-17. For SHRT-17, it was discovered that no Z-Pipe inlet temperature was recorded, and the data shown are actually an average of several subassembly outlet temperatures. The mass flow of pump #2 was more reasonable than the Phase 1 result.

Comparing FIG. 68 and FIG. 74, it can be seen that the predicted temperatures in XX09 are closer to the experiment data with the above modification.

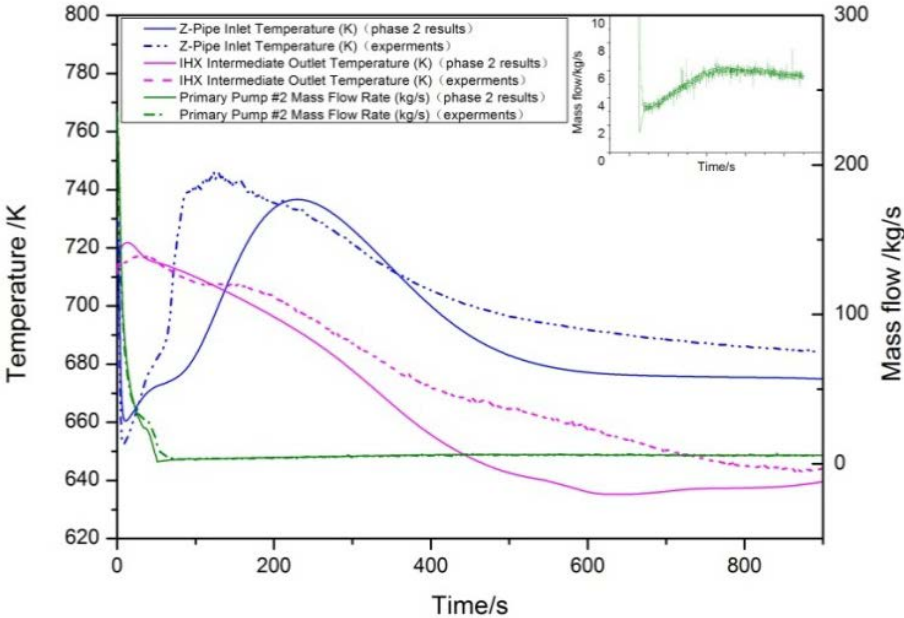


FIG. 73. Comparison of final results and experimental data for SHRT-17.

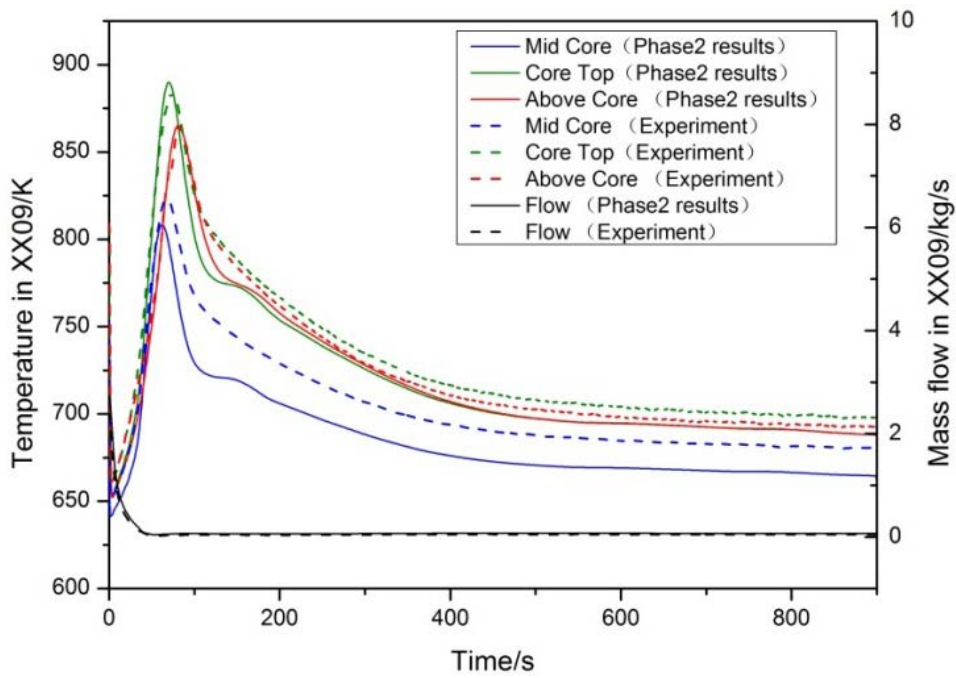


FIG. 74. Comparison of final results and experimental data in XX09 for SHRT-17.

After the addition of the inter-wrapper model, the temperature of XX10 increased and agreed well with the experiment data, as can be seen by comparing FIG. 69 and FIG. 75. The reverse flow in XX10 also disappeared.

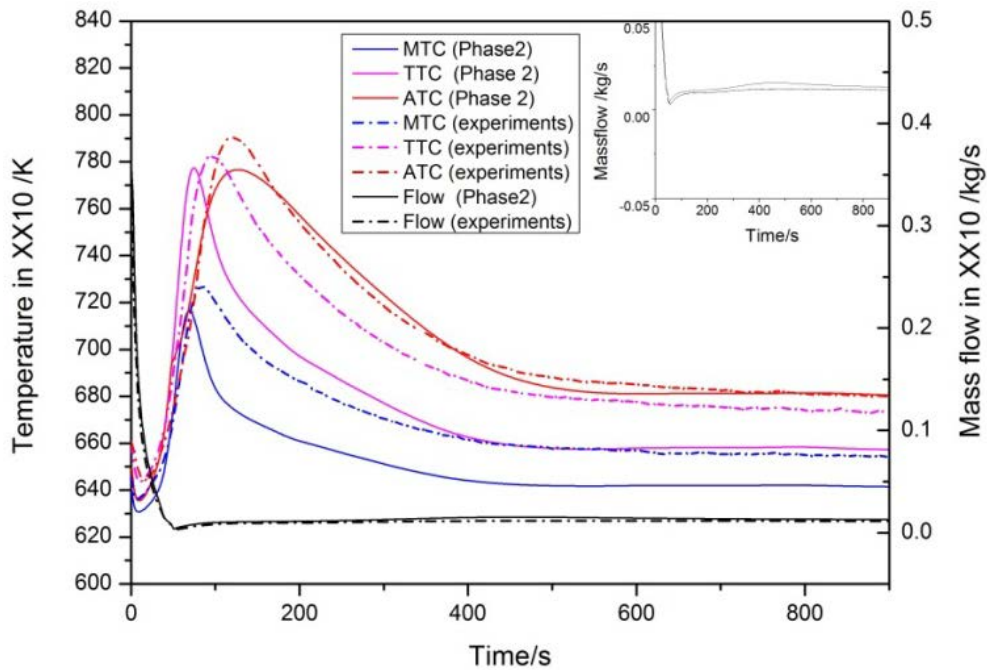


FIG. 75. Comparison of final results and experimental data in XX10 for SHRT-17.

7.3.5.2. SHRT-45R

In FIG. 76, the simulated IHX primary inlet temperature and IHX intermediate outlet temperature are closer to the data in phase 2 than were the phase 1 results. The mass flow rate of pump #2 was a better fit to the data than was the phase 1 result.

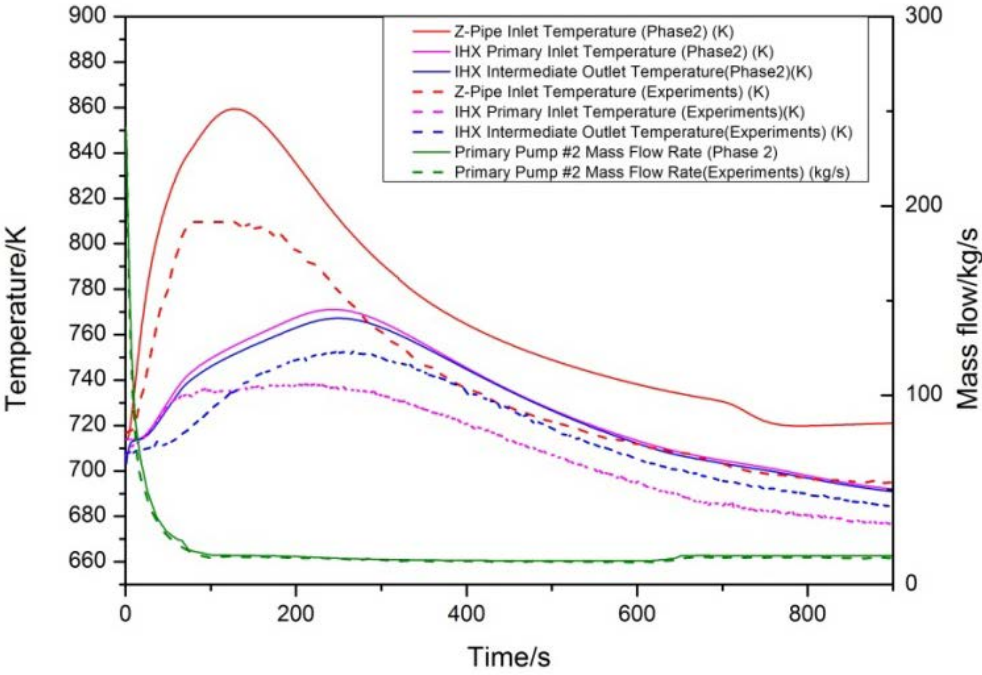


FIG. 76. Comparison of final results and experimental data for SHRT-45R.

Comparing FIG. 71 and FIG. 77, it can be seen that the peak temperature in XX09 decreased but the temperature late in the transient was higher than the experiment data, possibly caused by overestimation of the power.

Looking at FIG. 72 and FIG. 78, the phase temperature of XX10 increased and agreed well with the experiment data, which proves the significance of heat transfer through the inter-wrapper sodium.

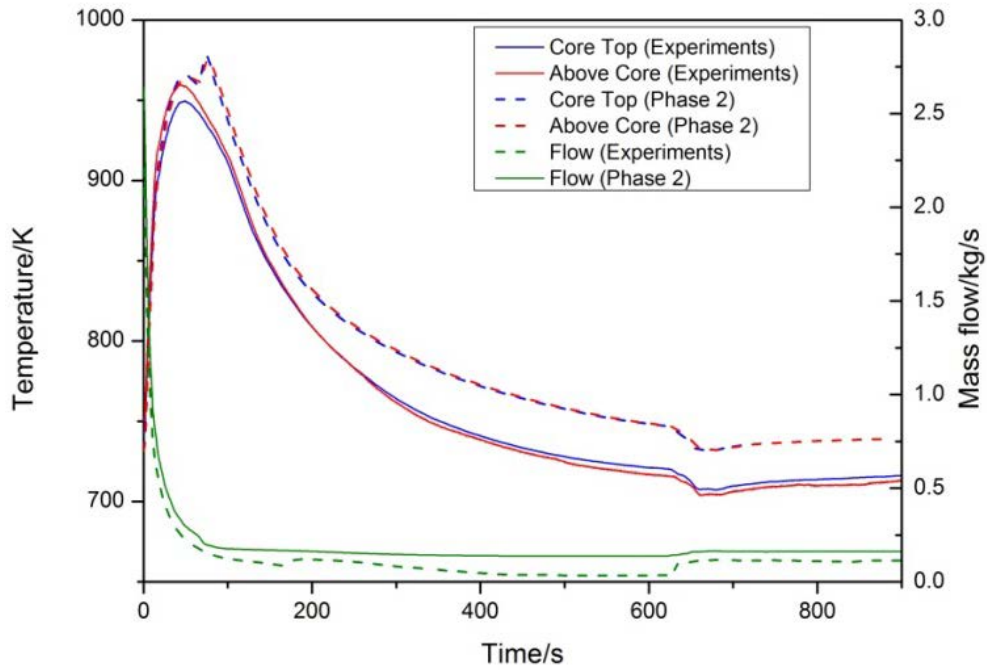


FIG. 77. Comparison of final results and experimental data for XX09 for SHRT-45R.

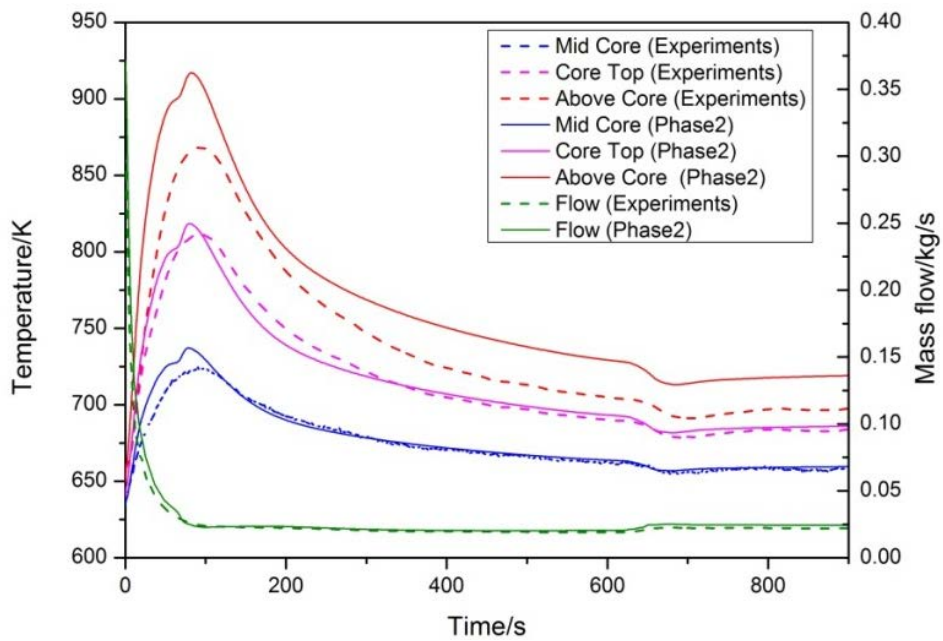


FIG. 78. Comparison of final results and experimental data in XX10 for SHRT-45R.

7.3.5.3. Model improvements

As a result of analyses of the phase 1 results, the three-layer model of the sodium pool, heat transfer between the Z-Pipe and the cold pool, and the inter-wrapper flow model were added.

A comparison between the simulation results with the three-layer pool model and with the perfect mixing model are presented in FIG. 79 for SHRT-17 and in FIG. 80 for SHRT-45R. In both cases, the results using the three-layer model agree with the measured data significantly better than did the results using the perfect mixing model. The three-layer model allowed inclusion of component heat transfer that could cause stratification of the cold pool.

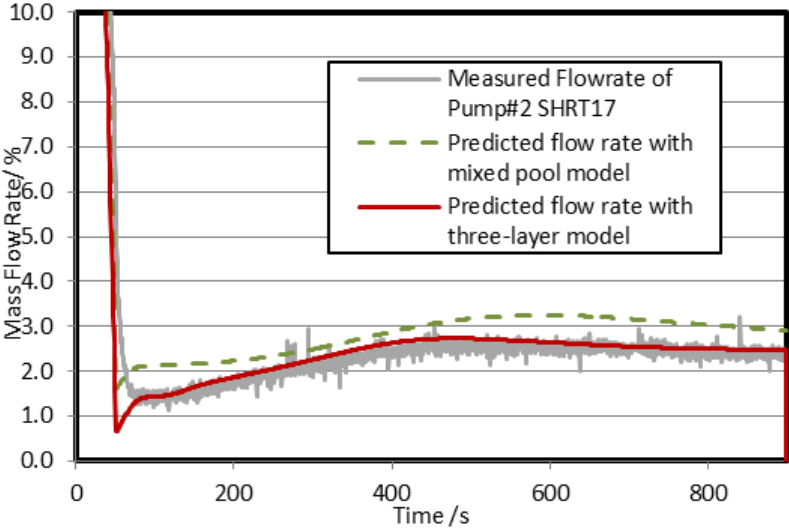


FIG. 79. Comparison between the perfect mixing model and the three-layer model for the cold pool during SHRT-17.

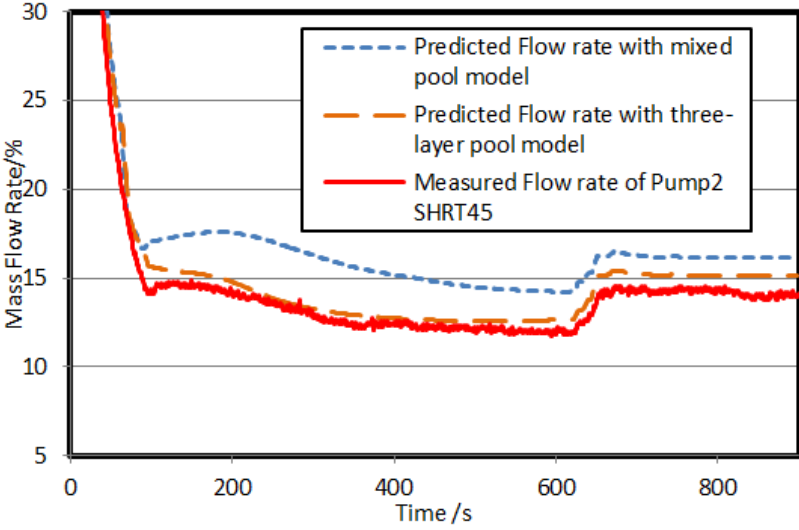


FIG. 80. Comparison between the perfect mixing model and the three-layer model for the cold pool during SHRT-45R.

Since the heat transfer from surrounding subassemblies affects the temperature distribution of XX10 significantly, the inter-wrapper flow model was developed. Comparing FIG. 75 and FIG. 78 clearly shows that, for XX10, heat transfer between subassemblies is significant.

7.4. IRSN (FRANCE)

7.4.1. Geometry/discretization

The CATHARE nodalization of the EBR-II primary circuit is shown in FIG. 81. The modelling of the intermediate circuit is limited to the heat exchangers (IHX), with experimental data as boundary conditions for secondary sodium flow rate and inlet temperature.

The primary circuit is described by a set of:

- (a) 0-D modules (VOLUME) for the tank, the inlet plena and the upper plenum;
- (b) 1-D modules (Axial) for the core, the inlet piping and the Z-Pipe.

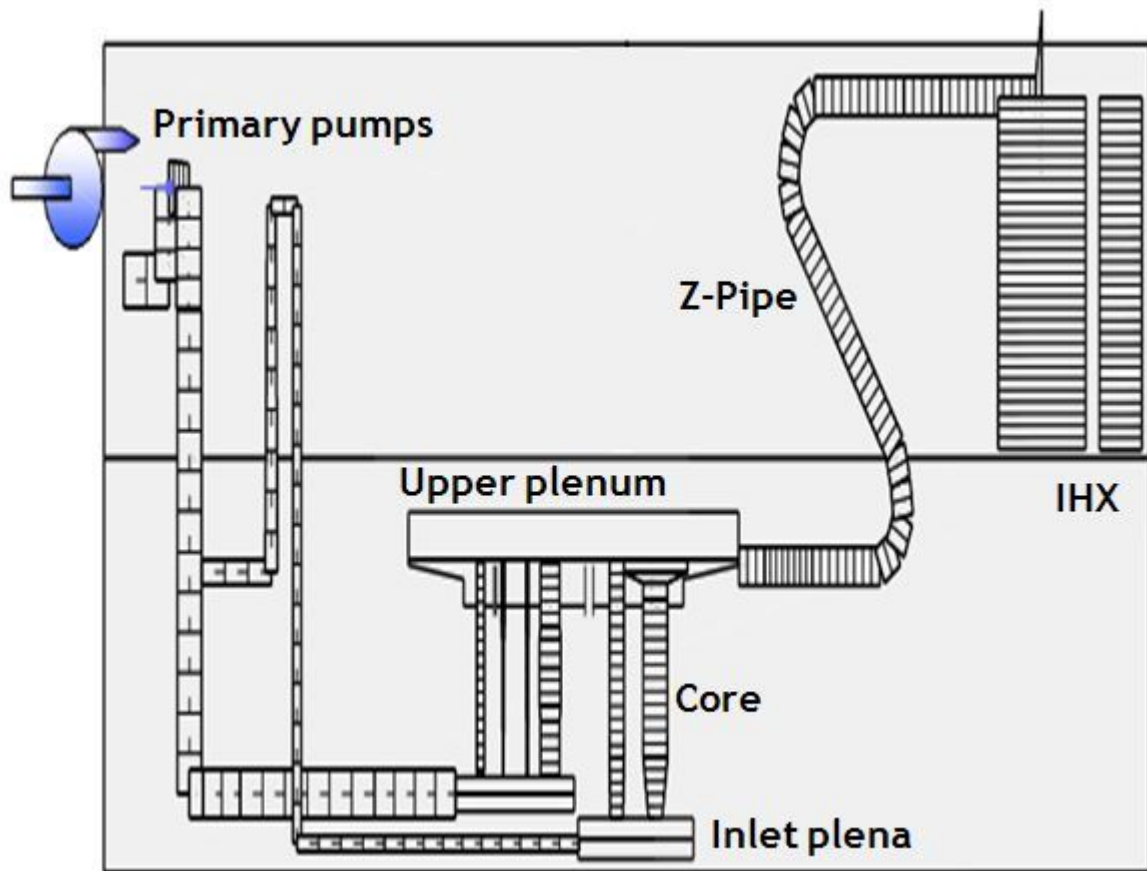


FIG. 81. CATHARE nodalization of the EBR-II primary circuit.

7.4.2. Thermal hydraulics methods and models

7.4.2.1. Code(s) used

The CATHARE system code (version V2.5_3) was used to simulate the SHRT-17 and SHRT-45R tests (see the brief description in Section 5.1.1).

7.4.2.2. Model

The main features and assumptions of the CATHARE model are given below:

- (a) Tank
 - Single volume (thermal stratification not taken into account);
 - Free level (argon cover);
 - Heat losses neglected (short term transient).
- (b) Primary pumps
 - Two primary pumps with associated piping modelled individually;
 - Characteristics described by homologous curves (head and torque by octant), with assumptions for the low flow rate regime, as primary pumps are not totally defined in the benchmark specifications.
- (c) Inlet plena
 - Single volume (perfect mixing).
- (d) Core
 - 4 channels for the high pressure zone (fissile subassemblies, blanket subassemblies, XX09 and XX10 instrumented subassemblies);
 - 2 channels for the low pressure zone (blanket subassemblies, reflector subassemblies);
 - Singular pressure drop coefficients at channels inlet tuned to match the steady state core mass flow rate distribution for run 129-C;
 - Specific friction law used for wire-wrapped fuel pins (Pontier's correlation [80]);
 - Thimble flow region for XX09 and XX10 subassemblies not modelled;
 - Heat exchange between subassemblies not modelled.
- (e) Upper plenum
 - Single volume (perfect mixing);
 - Horizontal and vertical baffles not taken into account.
- (f) Z-pipe
 - Double-wall structure modelled;
 - Stagnant sodium between the inner and outer piping;
 - Heat transfer from the Z-Pipe to the tank taken into account and tuned with the help of a heat exchange coefficient (use of a heat transfer correlation for liquid metal in natural convection from the literature as a first approach).
- (g) Auxiliary electromagnetic pump
 - Specific CATHARE pump model (flow rate proportional to voltage);
 - Only used for the SHRT-45R test.
- (h) IHX
 - Two counter-current pipes;
 - Inlet boundary conditions imposed at the secondary side (experimental data).

The experimental power evolution is directly used as a boundary condition for the SHRT-17 test. The radial power distribution given in the benchmark specifications for run 129-C was used. A uniform axial power distribution is assumed (no information in the benchmark specifications). A point-kinetics model is used for the SHRT-45R test. The reactivity feedback coefficients used (Doppler, radial fuel expansion, axial fuel expansion, axial cladding expansion, radial core expansion) are based on the information provided in the benchmark specifications.

Leakage flows throughout the primary circuit (3.2% of the primary flow rate in steady state according to the benchmark specifications) are neglected.

7.4.3. Blind results

7.4.3.1. SHRT-17

The key parameter for this test is the natural circulation mass flow rate after the trip of the primary pumps. The mass flow rate has been measured for primary pump #2 (no data available for primary pump #1) and the instrumented subassemblies. The predicted values are higher than the measurements for the blind calculation. With CATHARE, the total core flow rate drops from 460 kg/s to 13 kg/s within 65 s after the primary pumps trip (6.5 kg/s for the primary pump #2 as compared to the measured value of 2.96 kg/s, and 8.9×10^{-2} kg/s for the XX09 subassembly as compared to the measured value of 2.3×10^{-2} kg/s). Then, with the development of natural circulation, the core flow rate increases slowly up to 17 kg/s (8.5 kg/s for the primary pump #2 as compared to the measured value of 5.7 kg/s, and 9.7×10^{-2} kg/s for the XX09 subassembly as compared to the measured value of 4.5×10^{-2} kg/s).

This result leads to a significant underestimation of the sodium temperature in the core. The temperature decrease caused by the reactor scram and the temperature increase occurring immediately after is reproduced by CATHARE, but with smaller amplitudes. The peak sodium temperature at the core top for the XX09 subassembly (between 850 and 890°C according to the thermocouples location) is underestimated by 100°C approximately.

The first temperature measurement available downstream of the core is located at the Z-Pipe inlet. The temperature decrease and increase are both largely underestimated (by 30–40°C). Conversely, the IHX primary inlet temperature is overestimated by 60°C. The temperature decrease during the second part of the transient is not as sharp with CATHARE.

The inlet plena temperatures, almost constant during the whole transient (900 s), are well predicted by CATHARE. The slight decrease of the low pressure inlet plenum temperature during the last part of the transient is not reproduced, though.

XX09 and XX10 instrumented subassemblies were modelled by specific channels, but the 1-D modelling (single pin model) restricted the code-to-data comparisons. Other participants used subchannel or computational fluid dynamics (CFD) models to calculate the detailed radial temperature distribution in the subassembly.

7.4.3.2. SHRT-45R

The SHRT-45R test was calculated, but it was decided to mainly focus on the SHRT-17 test as a first step. The power evolution is not a boundary condition for this transient: the reactivity feedback effects need to be calculated. Nevertheless, it was a good opportunity to test the CATHARE point-kinetics model and the electromagnetic pump model (the auxiliary pump was on for this test). The results obtained are consistent overall, with similar trends as those observed for the SHRT-17 test. An in-depth analysis still needs to be conducted.

7.4.4. Final results, data comparisons

7.4.4.1. SHRT-17

Modelling improvements for the final calculations are listed in the next paragraph. Comparisons of final results against temperature and flow rate measurements show significant improvements. With CATHARE, the total core flow rate drops from 460 kg/s to 6.2 kg/s within 55 s after the primary pumps trip (4 kg/s for primary pump #2 as compared to the measured

value of 2.96 kg/s, and 4.96×10^{-2} kg/s for the XX09 subassembly as compared to the measured value of 2.3×10^{-2} kg/s). Then, with the development of natural circulation, the core flow rate increases slowly up to 10.5 kg/s (5.4 kg/s for primary pump #2 as compared to the measured value of 5.7 kg/s, and 6.2×10^{-2} kg/s for the XX09 subassembly as compared to the measured value of 4.5×10^{-2} kg/s).

The peak sodium temperature at the core top for the XX09 subassembly is better predicted as well (878°C with CATHARE as compared to the measured values of 8508–90°C).

However, large discrepancies remain between the measured and calculated temperatures at the Z-Pipe inlet and IHX inlet. It could be explained by different reasons:

- (a) A perfect mixing model seems to be inadequate for the upper plenum: horizontal and vertical baffles may have a significant impact on flow paths;
- (b) According to Argonne, the thermocouple reading at the Z-Pipe inlet was not recorded correctly: the measurement seems actually to be a combination of outlet temperature measurements from several subassemblies;
- (c) Thermal stratification may occur during the establishment of natural circulation. As a consequence, the sensor might not give a mean value;
- (d) Heat losses from the Z-Pipe affect the temperature at the IHX inlet, but sensitivity calculations seem to indicate that it cannot explain the large discrepancies observed.

7.4.4.2. SHRT-45R

Model improvements made for the SHRT-17 test were taken into account for the SHRT-45R test and led to better results. No specific sensitivity calculations (except for the auxiliary electromagnetic pump) were performed to further improve these results.

7.4.4.3. Model improvements

Model improvements for the final calculations are listed below:

Inlet piping

A single set of inlet piping (from primary pumps to inlet plena), with one equivalent primary pump (weight of 2) was used for the blind calculations. As the pump speed differs slightly between the two primary pumps, the inlet piping mass flow rates could not be well predicted with this simplified model. Two sets of inlet piping, with independent primary pumps, were used for the final calculations. A dissymmetrical behaviour and flow inversions are now observed in the inlet piping during the natural convection onset.

Singular pressure drop coefficients at low flow rates

Constant singular pressure drop coefficients were used for the blind calculations. They were tuned to match the nominal flow rate and the core flow rate distribution. No information was available in the benchmark specifications concerning singular pressure drop at low flow rate (for the core and primary pumps). As singular pressure drop coefficients increase at low flow rates [81], a sensitivity calculation was performed with higher values (multiplied by 10) for low flow rates. Better mass flow rate results are found with this modification. This sensitivity calculation also showed, as expected, the strong influence of the core mass flow rate on the core temperatures. Particular attention should be paid to the values used, though. A fine-tuning may hide modelling weaknesses or errors.

Auxiliary electromagnetic pump (SHRT-45R)

Only two voltage values (step) were used for the blind calculations. The accurate voltage evolution from the benchmark specifications was taken into account for the final calculations. Better mass flow rate results are found particularly at the time when the EM pump voltage increases (around 600 s).

Other modelling issues need to be investigated, in particular:

- (a) Leakage paths throughout the primary circuit;
- (b) Axial power distribution;
- (c) Heat exchange between subassemblies;
- (d) Heat transfer between the Z-Pipe and the cold pool.

7.4.5. Conclusions

The objective of this benchmark exercise was to assess the CATHARE capability in simulating the thermal hydraulics behaviour of the EBR-II reactor under natural circulation conditions. The analysis conducted mainly focused on the SHRT-17 test (experimental power evolution used as a boundary condition and auxiliary electromagnetic pump off).

The main conclusions are summarized below:

- (a) A good agreement was obtained in steady state;
- (b) Trends of mass flow rate and sodium temperature in the core are well predicted during establishment of natural circulation with appropriate singular pressure drop coefficients. Precise information concerning primary pump characteristics and singular pressure drops in subassemblies for the low flow rate regime is necessary, as fine-tuning may hide modelling weaknesses or errors;
- (c) The 1-D modelling (with single pin model) for instrumented subassemblies restricted the code-to-data comparisons;
- (d) Large discrepancies between calculated and measured temperatures are observed at the Z-Pipe inlet and the IHX inlet:
 - (i) The comparison is quite limited by the lack of reliability and relevance of the measurements: the thermocouple reading at the Z-Pipe inlet was not recorded correctly according to Argonne, and the thermocouple at the IHX inlet may not give an average value due to thermal stratification in the Z-Pipe during establishment of natural circulation;
 - (ii) Modelling issues related to mixing and thermal stratification for the upper plenum and the Z-Pipe cannot be address with a 0-D/1-D modelling.
- (e) Some modelling assumptions (axial power distribution, leakage flows throughout the primary circuit) still need to be investigated by additional sensitivity calculations.

This benchmark exercise has focused on establishment of natural convection (experimental data limited to 900 s). It would be interesting to pursue this assessment work for long term behaviour.

7.5. KIT (GERMANY)/KYUSHU UNIVERSITY (JAPAN)

7.5.1. Geometry/discretization

All the reactor components were taken into account for creating the 2-D R-Z SIMMER-III v.3E [30] model. Unavoidable approximations were introduced for modelling the reactor outlet ‘Z-Pipe’ and the sodium inlet pipes. In FIG. 82 the SIMMER-III r-z model for SHRT-17 (full tank model) is shown. Values for select model parameters are compared against the benchmark specification values in TABLE 6. As indicated in TABLE 6, the chosen axial meshes reasonably represent the relative positions of the components.

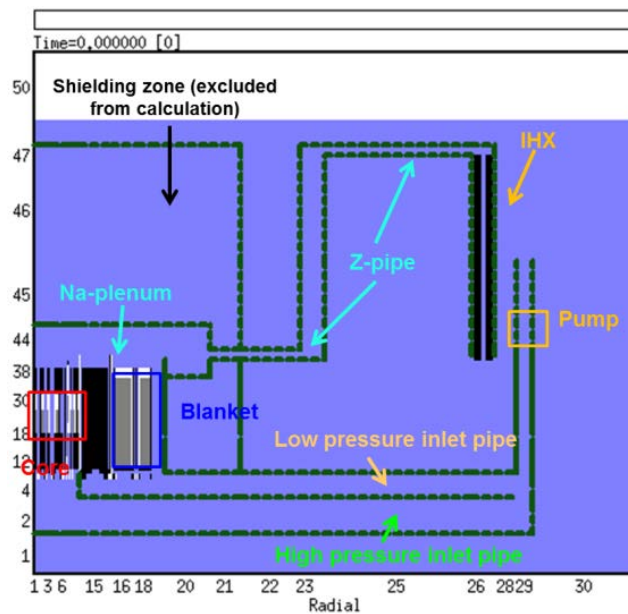


FIG. 82. SIMMER-III EBR-II r-z model (SHRT-17).

TABLE 6. SIMMER-III SHRT-17 R-Z MODEL PARAMETERS

Components	Reference (m.)	SIMMER-III Model (m.)
Total height	7.988	7.988
External radius	3.962	3.962
Sodium free surface level	6.941	6.941
Upper plenum upper boundary (z_{sup})	3.816	3.816
Upper plenum radial boundary (r_{ext})	1.1555	1.1555
Upper plenum lower boundary (z_{inf})	2.975	2.999
Radial position, IHX centre	2.95	2.95
Radial position, pump centre	3.251	3.22
Z-Pipe at upper plenum exit	3.57	3.421

The zones outside of the core were modelled in the same way for the two tests. However, in order to take into account the different core layout and control rod axial positions for the two tests, the core zone was modelled using one discretization for SHRT-17 (18 radial mesh cells) and a different one for SHRT-45R (34 radial mesh cells). In total, the SHTR-17 model

consists of 30 radial and 50 axial fluid-dynamic mesh cells. The SHRT-45R model has, instead, 49 radial and 52 axial fluid-dynamic mesh cells. In order to assess the ring-wise model, the subassemblies (SAs) were grouped according to their location and to their type. TABLE 7 shows some examples for some special SA types.

TABLE 7. DISTANCE FROM THE CORE CENTRE OF SAFETY ROD, HW-CR, XX10, AND XX09

SA type	HEX-Z model	Distance from the centre (m)	
		R-Z SIMMER model SHRT-17	R-Z SIMMER model SHRT-45R
Safety Rod	0.118	0.116	0.116
XX09	0.204	0.215	0.192
HW-CR	0.224	0.225	0.221
XX10	0.236	0.235	0.197

7.5.2. Nuclear and thermo-physical data/correlations

For the EBR-II benchmark, the standard SIMMER-III version was modified by Kyushu University (KU) in order to take into account the thermodynamic properties for the U-5%Fs (Fissium) alloy.

In the SIMMER codes, the thermodynamic properties of reactor core materials in solid, liquid and vapour phases are calculated by using an analytical equation of state (EOS) model ([82], [83], [84]) expressed as polynomial fits for temperature (T) and specific volume (v) as a function of specific internal energy (e). For the EBR-II transients, only solid properties of metal fuel were considered, introducing six fitting coefficients for temperature and six for the specific volume in order to take into account the two solid-solid phase transitions. A comparison with the data provided in the benchmark specifications (Section 4) was performed, as indicated in FIG. 83. Good agreement was obtained also for thermal conductivity.

From the neutronics point of view, SIMMER-III is a deterministic code with separated cell and flux calculations [85]. In each cell the self-shielded macroscopic cross-sections are calculated inside the code from a set of infinite diluted cross-sections and self-shielding factors tabulated as a function of temperature and updated at every timestep of the reactivity calculation [86]. Neutron flux calculations are performed through a SN transport code (TWO-DANT or PARTISN-based) using a diffusion synthetic acceleration scheme [50].

For SHRT-17, only the fluid dynamics modules of SIMMER were applied, and its neutronics module was deactivated. The reasons for choosing this option are: 1) no details on fuel compositions for SHRT-17, and 2) the lack of a gamma heating model in the neutronics model of SIMMER. The power was provided externally as input data and was adjusted to match the power given in the benchmark specifications (see FIG. 84).

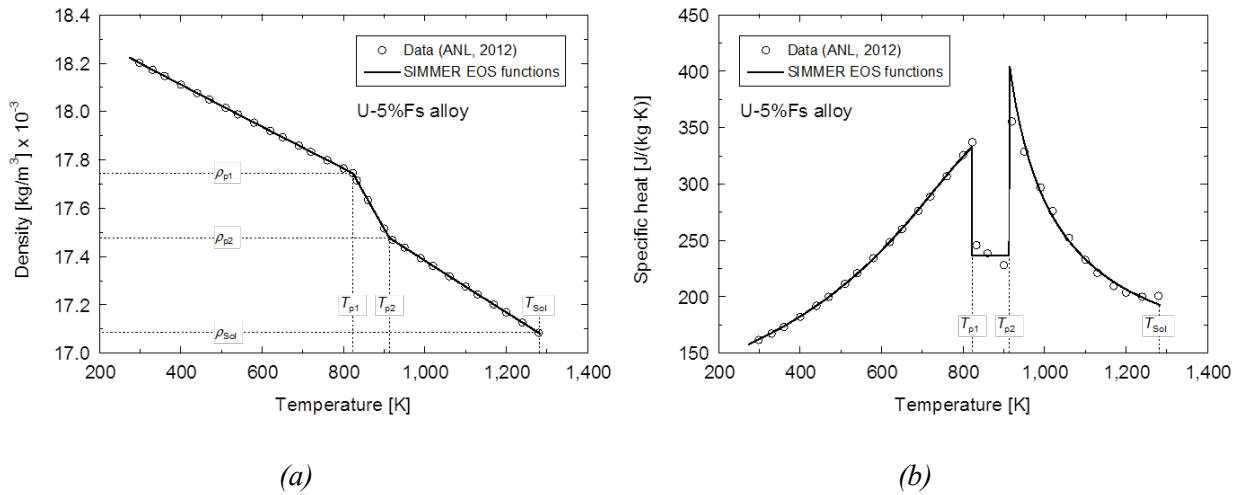


FIG. 83. Comparison of SIMMER EOS analytical model and input data: (a) density-temperature correlation; (b) specific heat-temperature correlation.

For SHRT-45R, coupled neutronics and thermal hydraulics calculations were carried out [87]. Both the TWODANT module of SIMMER [50] and the new KIT development [88] based on the PARTISN code were employed. For the transient calculations, cases were run with a S_8 approximation and 11 energy groups [89] assuming the transport approximation for the treatment of the anisotropy of neutron scattering. A finer (compared to the thermal hydraulic mesh) neutronics mesh was applied for the overall core zone (including blankets). In total, 118 radial and 138 axial neutronics mesh cells were considered. The SIMMER code does not need to use pre-calculated reactivity feedback coefficients. In addition to feedbacks related to fuel, coolant, steel and control material density variations and Doppler effect, core thermal expansion effects were also recently introduced at KIT ([90], [91], [92]). The standard SIMMER version was used for the blind SHRT-45R calculation, while the extended version was used for the final results.

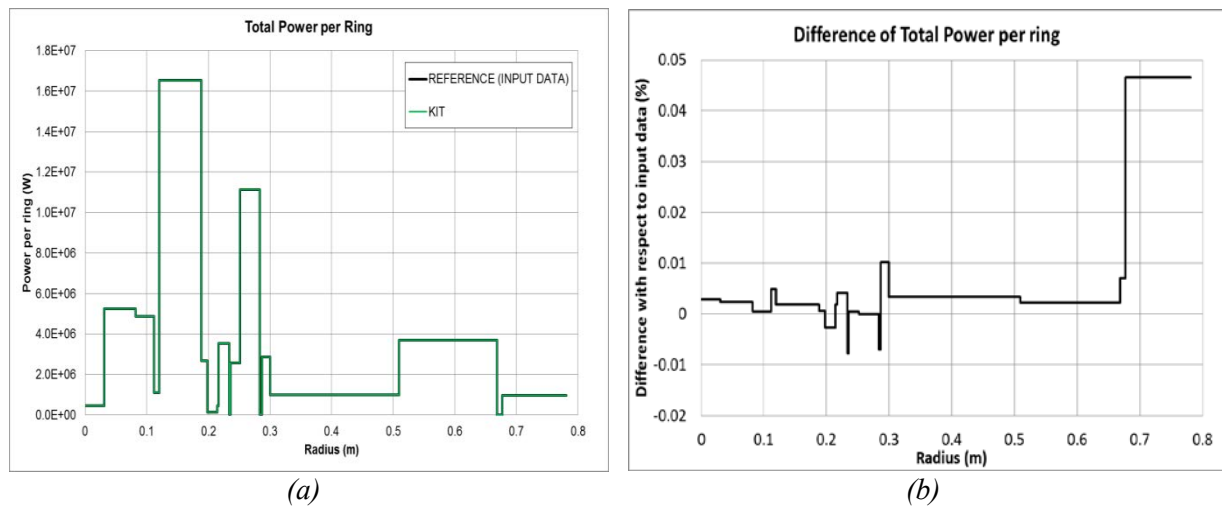


FIG. 84. SHRT-17: comparison of the power per ring between input data and SIMMER results (steady state).

7.5.3. Thermal hydraulics methods and models

7.5.3.1. Code(s) used

For the transient calculations, the SIMMER-III code was used. For SHRT-17, oriented to investigate mainly the effectiveness of natural circulation, only the fluid dynamics modules of SIMMER were applied and its neutronics module was deactivated. For SHRT-45R, coupled neutronics and thermal hydraulics calculations were carried out.

7.5.3.2. Basic method

In the SIMMER code, five basic sodium fast reactor (SFR) core materials – fuel, steel, sodium, control and fission gas – in different physical states can be modelled. The multi-velocity-field formulation and the fluid convection solution algorithm are based on a time-factorization approach. The constitutive models describe intra-cell transfer of mass, momentum and energy at the fluid interfaces. The code includes modelling for convection of interfacial areas based on Ishii's ideas ([31], [93]). The calculations of intra-cell heat and mass transfer include a multiple flow regime treatment and interfacial areas with source terms, momentum exchange functions for each flow regime, inter-cell heat transfer due to conduction, melting and freezing, structure break-up, vapourization and condensation. SIMMER is an Eulerian mesh fluid dynamics code coupled with a structure model for fuel pins, hexcans and general structures, and a space-, angle, time- and energy-dependent transport theory neutron dynamics model.

In the standard SIMMER-III version, there is no intermediate heat exchanger (IHX) model, since it was not relevant in the simulation of loop-type reactors (important in Japan). An alternative approach was therefore developed for modelling the EBR-II plant in which the IHX was modelled as a heat sink by assigning an infinitely high density (modifying the steel EOS) of structure in the IHX region. This model is characterized by an extremely high structure heat capacity and by the IHX coolant outlet temperature being equal to the IHX structure temperature. The secondary loop is assumed to run at 100% mass flow rate.

Heat Transfer Coefficients (HTCs) are necessary to calculate heat and mass transfer between energy components and can therefore play an important role in predicting the evolution of an accident sequence. All components in a SIMMER calculation are divided into the following fields: a) structure, b) liquid and c) vapour. HTC are relevant only for describing heat flux for energy components in the liquid and vapour fields.

Each of the 8 fluid and 3 structure components transfers heat to every other component: $(8+3-1) \times (8) = 80$. Thus heat transfer occurs to and across up to 80 binary interfaces (under transient conditions). In the EBR-II model, 44 HTCs were used to compute heat and mass transfer in each mesh cell. The topology of the energy components is crucial for calculating HTCs. The same flow regimes defined in the Interfacial-area (IFA) model were used to define HTCs. The available heat transfer paths in SIMMER are shown in FIG. 85. The SIMMER HTC models are based on quasi-steady state Nusselt number correlations determined in well-defined topologies under the following fixed conditions:

- (a) Well-defined geometry;
- (b) Constant temperature or constant heat flux;
- (c) Developed flow;
- (d) Single-phase/multi-phase flow (small number of components);
- (e) Discontinuous components (i.e. fluid particles) treated as spheres;
- (f) Undisturbed flow or pressure fields;
- (g) Limited range of tested fluids.

For ill-defined topologies with more than one continuous component, the HTC's are interpolated between the well-defined topologies.

For the EBR-II simulations, one of the three available methods for calculating the gap conductance of the pin in SIMMER was selected. The method selected was that of using an input constant value of the gap conductance. A parametric study was carried out to investigate this effect (see Section 8.1.1.1).

In SIMMER the pump pressure is added into the momentum equation. After having defined a position, the pump head is provided as a function of time in tabular form. Between two successive time points linear interpolation is performed.

The overall mass flow rate at steady state is determined by the pressure loss by friction in the core and by a set of local pressure losses (determined by orifice coefficients provided as input to the SIMMER code). In the EBR-II model, orifice coefficients were defined at the SA inlet and were chosen so as to obtain agreement between the mass flow rate per ring and the input data provided (e.g. see FIG. 86 below for SHRT-17). The orifice coefficient is defined by EQ. 7:

$$\Delta p = -C_{ORF} \times \bar{\rho}_q \times |v_q|^2, \quad (7)$$

where Δp is the pressure drop across the orifice, C_{ORF} is the orifice coefficient, ρ_q is the macroscopic density of the liquid components in the velocity field q , and v_q is the velocity of field q at the orifice. In the SIMMER code, up to 8 velocity fields are allowed, but for the EBR-II simulation, it was assumed 3 fields would be sufficient.

Energy Component	Energy component which is being interacted with:									Fuel Pin Structure			Left Structure			Right Structure			Mass Transfer paths:	
	Gas/ Vapor G	Liquid Fuel L1	Liquid Steel L2	Liquid Sodium L3	Fuel Particle L4	Steel Particle L5	Control Particle L6	Fuel Chunk L7	K1	K2	K3	K1	K2	K3	K1	K2	K3	M/F	V/C	
Gas/ Vapor G		HGLM(1) I1 {1}	V/C HGLM(2) I2 {2}	V/C HGLM(3) I3 {3}	V/C HGLM(4) I4 {3}	V/C HGLM(5) I5 {3}	V/C HGLM(6) I6 {3}	V/C HGLM(7) I7 {3}	HGS I29 {3}	HGS I37 {3}	HGS I45 {3}	-	-	-	-	-	-	-	27	
Liquid Fuel L1	V/C HLMG(1) I1 {1}		V/C HRT(1) I8 {-}	V/C HRT(2) I9 {-}	M/F HRT(3) I10 {1}	M/F HRT(4) I11 {1}	M/F HRT(5) -	M/F HRT(6) I13 {1}	M/F HRS(1) I30 {1}	M/F HRS(8) I38 {1}	M/F HRS(10) I46 {1}	6	1	-	-	-	-	-	-	
Liquid Steel L2	V/C HLMG(2) I2 {1}	V/C HRT(7) I8 {1}		V/C HRT(8) I14 {-}	M/F HRT(9) -	M/F HRT(10) I16 {1}	M/F HRT(11) -	M/F HRT(12) -	M/F HRS(2) I31 {1}	M/F HRS(9) I39 {1}	M/F HRS(11) I47 {1}	4	2	-	-	-	-	-	-	
Liquid Sodium L3	V/C HLMG(3) I3 {1}	V/C HRT(13) I9 {1}	V/C HRT(14) I14 {1}		M/F HRT(15) -	M/F HRT(16) -	M/F HRT(17) -	M/F HRT(18) -	M/F HRS(3) -	M/F HRS(3) -	M/F HRS(3) -	-	-	-	-	-	-	-	3	
Fuel Particle L4	V/C HPT(1) -	M/F HPT(1) I10 {1}	M/F HPT(1) -	M/F HPT(1) -		M/F HPT(1) -	M/F HPT(1) -	M/F HPT(1) -	M/F HRS(4) -	M/F HRS(4) -	M/F HRS(4) -	1	-	-	-	-	-	-	-	
Steel Particle L5	V/C HPT(2) -	M/F HPT(2) I11 {1}	M/F HPT(2) I16 {1}	M/F HPT(2) -	M/F HPT(2) -		M/F HPT(2) -	M/F HPT(2) -	M/F HRS(5) -	M/F HRS(5) -	M/F HRS(5) -	2	-	-	-	-	-	-	-	
Control Particle L6	V/C HPT(3) -	M/F HPT(3) -	M/F HPT(3) -	M/F HPT(3) -	M/F HPT(3) -	M/F HPT(3) -		M/F HPT(3) -	M/F HRS(6) -	M/F HRS(6) -	M/F HRS(6) -	-	-	-	-	-	-	-	-	
Fuel Chunk L7	V/C HPT(4) -	M/F HPT(4) I13 {1}	M/F HPT(4) -	M/F HPT(4) -	M/F HPT(4) -	M/F HPT(4) -	M/F HPT(4) -		M/F HRS(7) -	M/F HRS(7) -	M/F HRS(7) -	1	-	-	-	-	-	-	-	
Fuel Pin Structure K1	V/C I29 {-}	M/F I30 {1}	M/F I31 {1}	M/F -	M/F -	M/F -	M/F -	M/F -	M/F -	M/F -	M/F -	2	-	-	-	-	-	-	-	
Left Structure K2	V/C I37 {-}	M/F I38 {2}	M/F I39 {1}	M/F -	M/F -	M/F -	M/F -	M/F -	M/F -	M/F -	M/F -	3	-	-	-	-	-	-	-	
Right Structure K3	V/C I45 {-}	M/F I46 {2}	M/F I47 {1}	M/F -	M/F -	M/F -	M/F -	M/F -	M/F -	M/F -	M/F -	3	-	-	-	-	-	-	-	
Total no. paths =																		22	33	

FIG. 85. Available heat transfer paths in SIMMER.

7.5.4. Blind results

7.5.4.1. SHRT-17

A set of SA orifice coefficients was developed that would result in good agreement between the mass flow rate at steady state obtained by the SIMMER calculation and the values provided as input for the benchmark. The ring-wise comparison is shown in FIG. 86.

The mass flow rate and the power during the transient were simulated in SIMMER on the basis of the benchmark description. A single “equivalent” pump was considered. This approach leads to some approximations in the overall mass flow rate. The peak fuel, cladding and coolant temperatures are shown in FIG. 87(a). Inlet coolant temperatures at the Z-Pipe and at the IHX are shown in FIG. 87(b). SA averaged temperatures for XX09 and XX10 were also calculated.

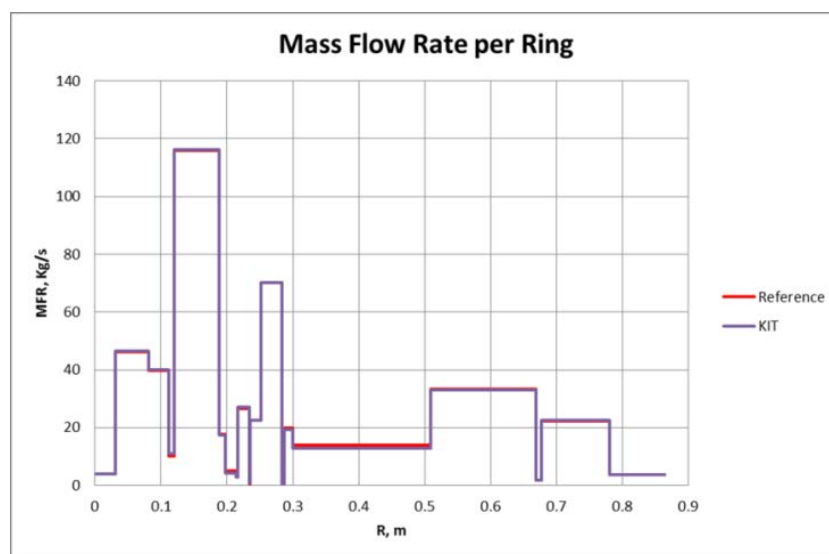


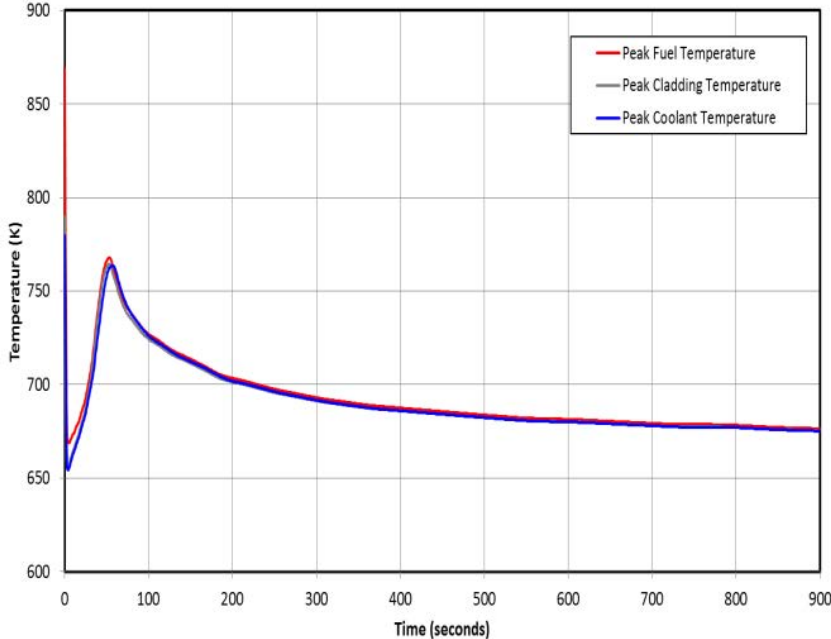
FIG. 86. SHRT-17: comparison of the mass flow rate per ring between input data and SIMMER results (steady state).

7.5.4.2. SHRT-45R

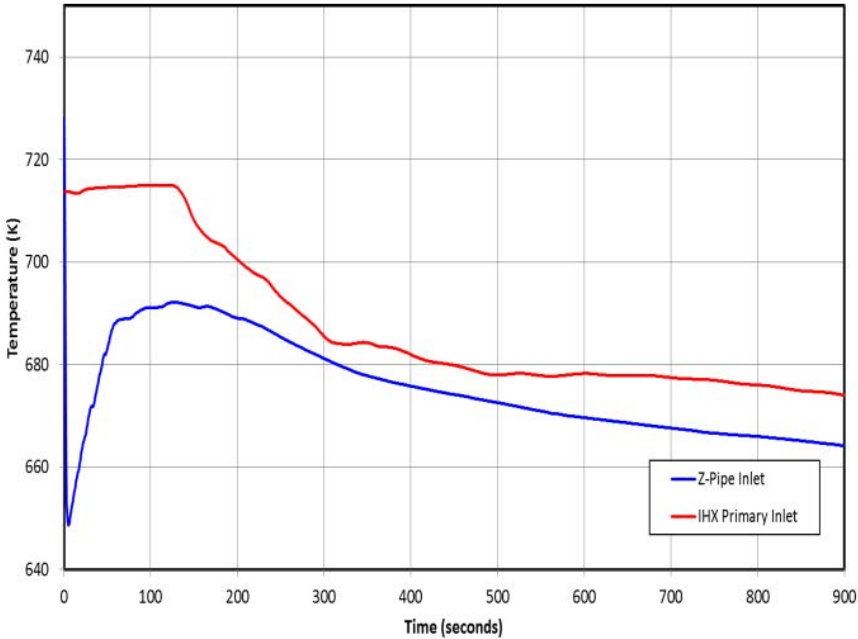
The standard SIMMER version (coupled neutronics/thermal hydraulic calculations) was adopted. With this version, the reactivity feedbacks due to the core thermal expansion were not taken into account. In addition the contribution to the mass flow rate coming from the electromagnetic pump operated on battery power was not included in the study. A set of SA orifice coefficients was set-up in order to achieve good agreement between the mass flow rate at steady state obtained by the SIMMER calculation and the values provided as input to the benchmark. The power distribution was calculated on the basis of the flux calculation in SIMMER. Comparison against the input data is shown in FIG. 88. Concerning the power distribution, large discrepancies (ca. 607–0%) are observed for dummy and reflector SA due to the missing gamma heating contribution in SIMMER.

The mass flow rate during the transient was simulated in SIMMER on the basis of the benchmark description. A single “equivalent” pump was considered also for SHRT-45R, leading to some approximations in the overall mass flow rate. Modelling modifications to improve the mass flow rates were considered in view of the final results. In FIG. 89, the peak

fuel, cladding and coolant temperatures, as well as the coolant temperature at the inlet to the Z-Pipe and to the IHX, are shown. SA averaged temperatures for XX09 and XX10 were also calculated.



(a)



(b)

FIG. 87. SHRT-17 KIT/KU blind results: (a) peak fuel, cladding, and coolant temperatures; (b) coolant temperature at the inlet to the Z-Pipe and to the IHX.

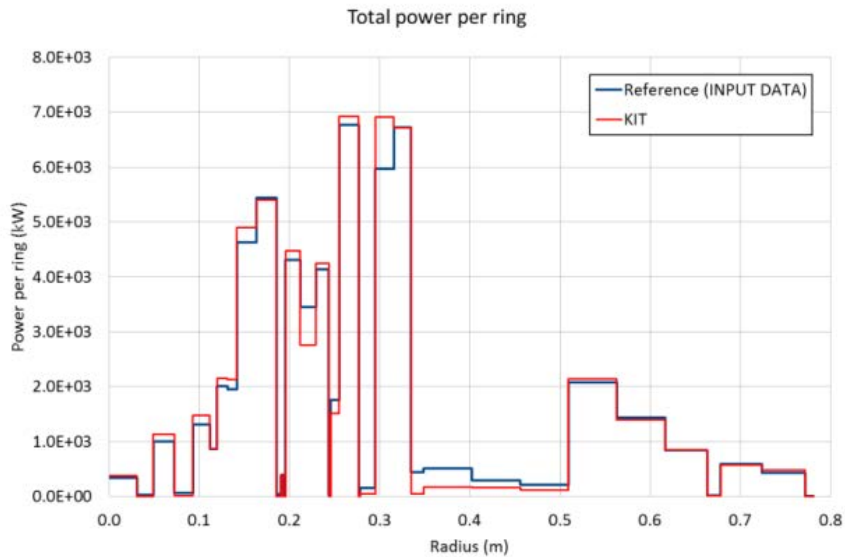


FIG. 88. SHRT-45R: comparison of the input data and SIMMER results (steady state) for power per ring.

7.5.5. Final results, data comparisons

7.5.5.1. SHRT-17

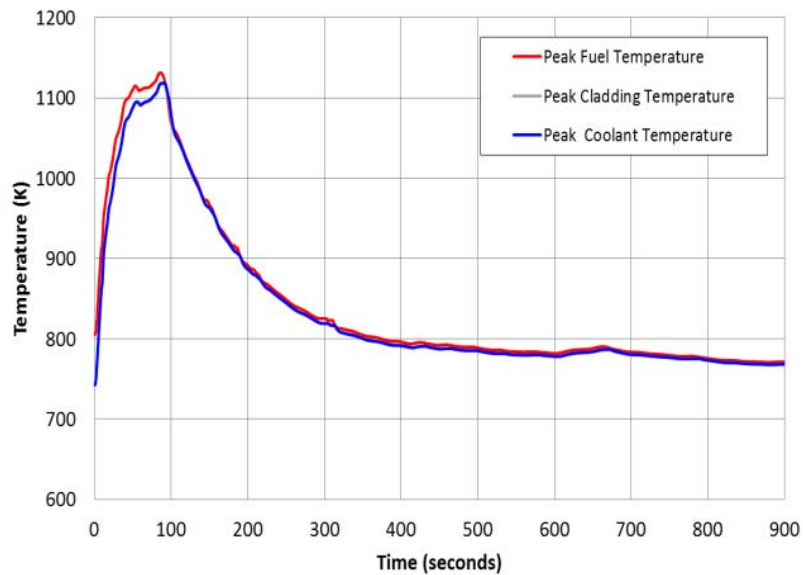
As discussed in detail below in Section 7.5.5.3, the main model improvements considered for SHRT-17 were:

- (a) Total mass flow rate improvement: a slight tuning was performed in order to improve flow rate prediction early in the transient and overcome the limitation caused by modelling the primary pumps as a single “equivalent” pump. Natural circulation later in the transient was improved by changing the position/location of the IHX (simplified model in SIMMER);
- (b) Radial heat transfer from the neighbouring SAs to XX10 was accounted for by introducing modifications in the SIMMER model.

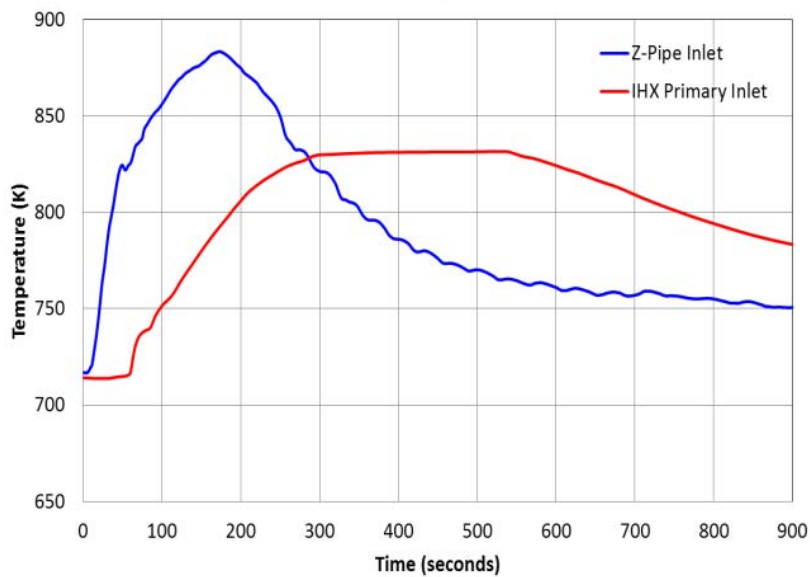
With these modifications, better agreement with the experimental data was obtained, as shown below. The improvement in the mass flow rate is described in Section 7.5.5.3.

In FIG. 90(a), comparison against experimental data for the core outlet temperature is shown. FIG. 90(b) shows the peak fuel temperature behaviour (improvement between blind and final results).

The behaviour of the coolant temperature at different axial positions in the XX09 SA is shown in FIG. 91: (a) at the upper flowmeter location; (b) at mid-core; (c) at core top; and (d) above core.



(a)



(b)

FIG. 89. SHRT-45R KIT/KU blind results: (a) peak fuel, cladding, and coolant temperatures; (b) coolant temperature at the inlet to the Z-Pipe and to the IHX.

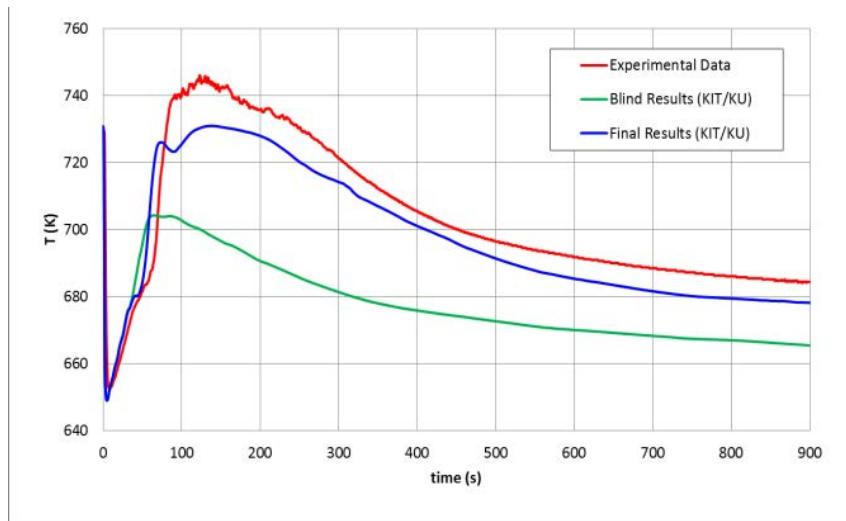
The behaviour of the coolant temperature at different axial positions in the XX10 SA is shown in FIG. 92: (a) at upper flowmeter location; (b) at mid-core; (c) at core top; and (d) above core.

7.5.5.2. SHRT-45R

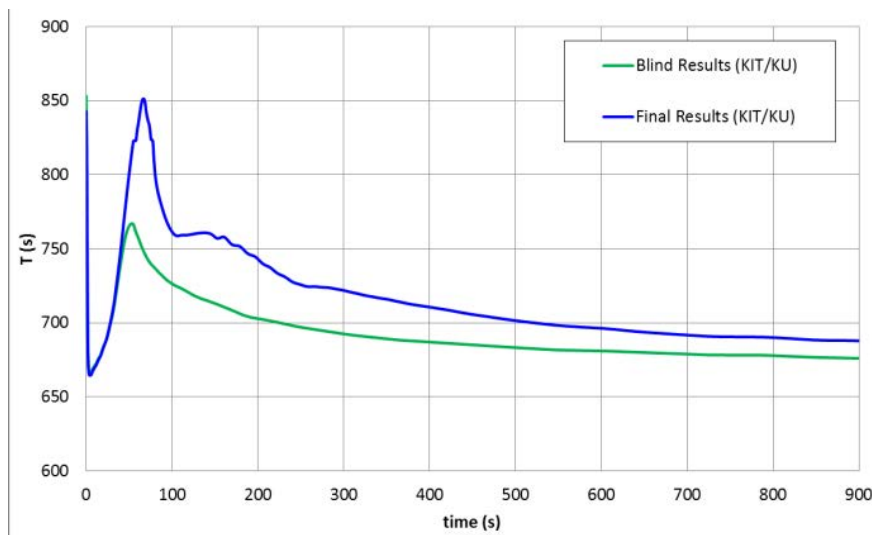
As discussed in detail in Section 7.5.5.3, the main model improvements considered for SHRT-45R were:

- (a) Total mass flow rate improvement by taking into account the mass flow rate due to the electromagnetic pump operated on battery power;

- (b) Taking into account the core thermal expansion reactivity feedbacks by using the recently extended SIMMER version from KIT ([90], [91], [92]);
- (c) Radial heat transfer from the neighbouring subassemblies to XX10 was accounted for by introducing modifications into the SIMMER model.



(a)



(b)

FIG. 90. SHRT-17 KIT/KU final results: (a) core outlet temperature, (b) peak in-core fuel temperature.

With these modifications, better agreement with the experimental data was obtained, as discussed below. The final results were obtained by considering core thermal expansion reactivity feedbacks using clad-driven and conic mode (see the discussion of SHRT-45R in Section 7.5.5.3 for more details).

The net reactivity (that includes contributions from material density variation, Doppler and core thermal expansion) and the fission power behaviour are shown, respectively, in FIG. 93(a) and FIG. 93(b). Because of the negative expansion feedback, the net reactivity is lower compared to the blind results. This improvement allows better agreement with the measurements early in the transient for the fission power. This mode of accurate reactivity and power modelling led to a considerable improvement in the Z-Pipe inlet temperature

behaviour (see FIG. 94(a)). An improvement in the mass flow rate later in the transient (due to the modelling of the EM pump) is also achieved, as shown in FIG. 94(b).

The behaviour of coolant temperature at different axial positions in the XX09 SA is shown in FIG. 95: (a) at core top; (b) above core; and (c) at the core outlet. Better agreement with experimental results is achieved.

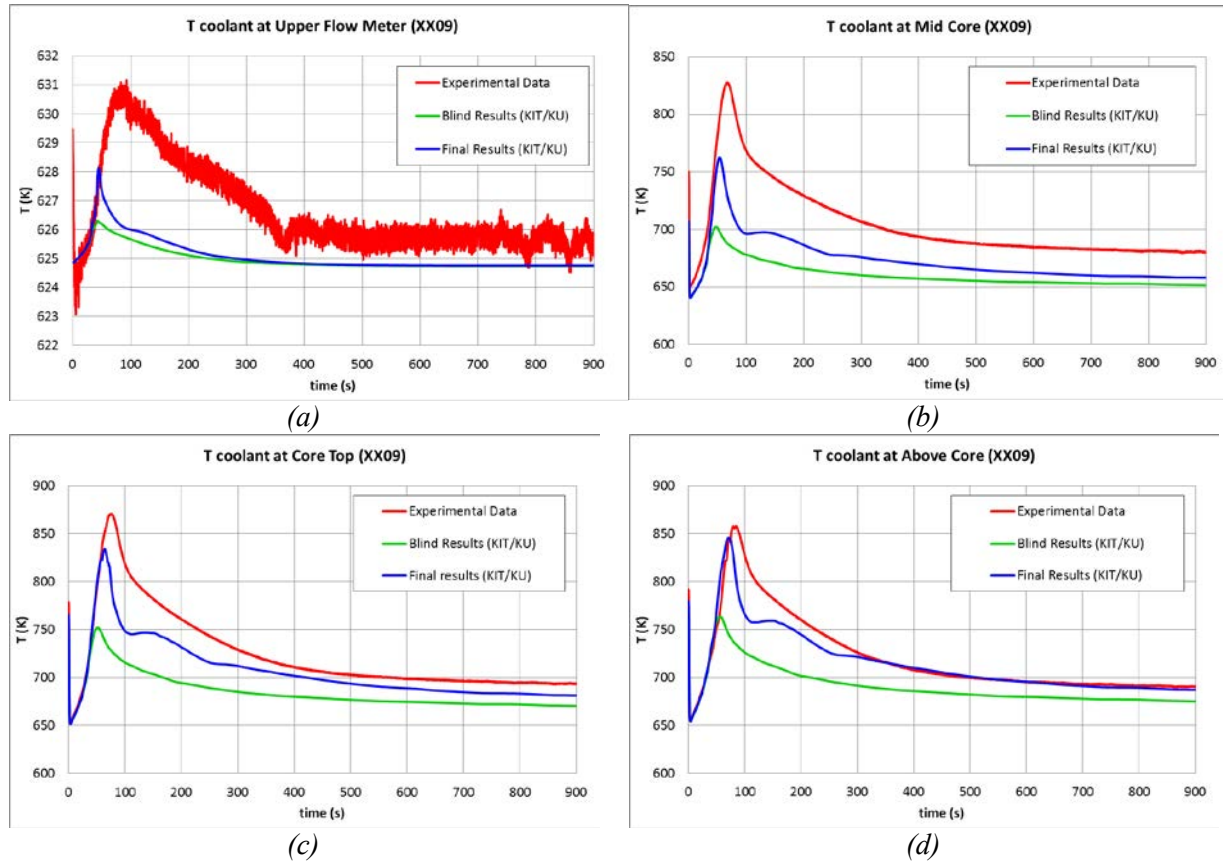


FIG. 91. SHRT-17 KIT/KU final results for XX09 temperatures: (a) at upper flowmeter location, (b) at mid-core, (c) at core top, (d) above core.

As for SHRT-17, allowing radial heat transfer into XX10 improved the axial temperature profile, as shown in FIG. 96.

7.5.5.3. Model improvements

For SHRT-17, several model improvements were introduced between the 2nd and 3rd RCM, with the aim of obtaining a better transient flow rate (including long term natural circulation). As indicated in Section 7.5.3, in the SIMMER model a simplified heat exchanger (IHX) acting as an infinite heat sink was implemented, as well as a single “equivalent” pump for simulating the two primary pumps.

Therefore, in order to improve the mass flow rate, two main modifications were introduced:

- (1) The input pump head was modified early in the transient to take into account the slightly different behaviour of the two primary pumps;
- (2) In addition, the IHX definition/location in SIMMER was slightly modified. In the case of the blind calculation results (Section 7.5.4.1) the thermal centre of the IHX was

higher than expected and therefore a natural circulation that was too “efficient” was established. The thermal IHX centre was lowered as shown in FIG. 97.

By considering these two modifications a better mass flow rate prediction was obtained, as shown in FIG. 97.

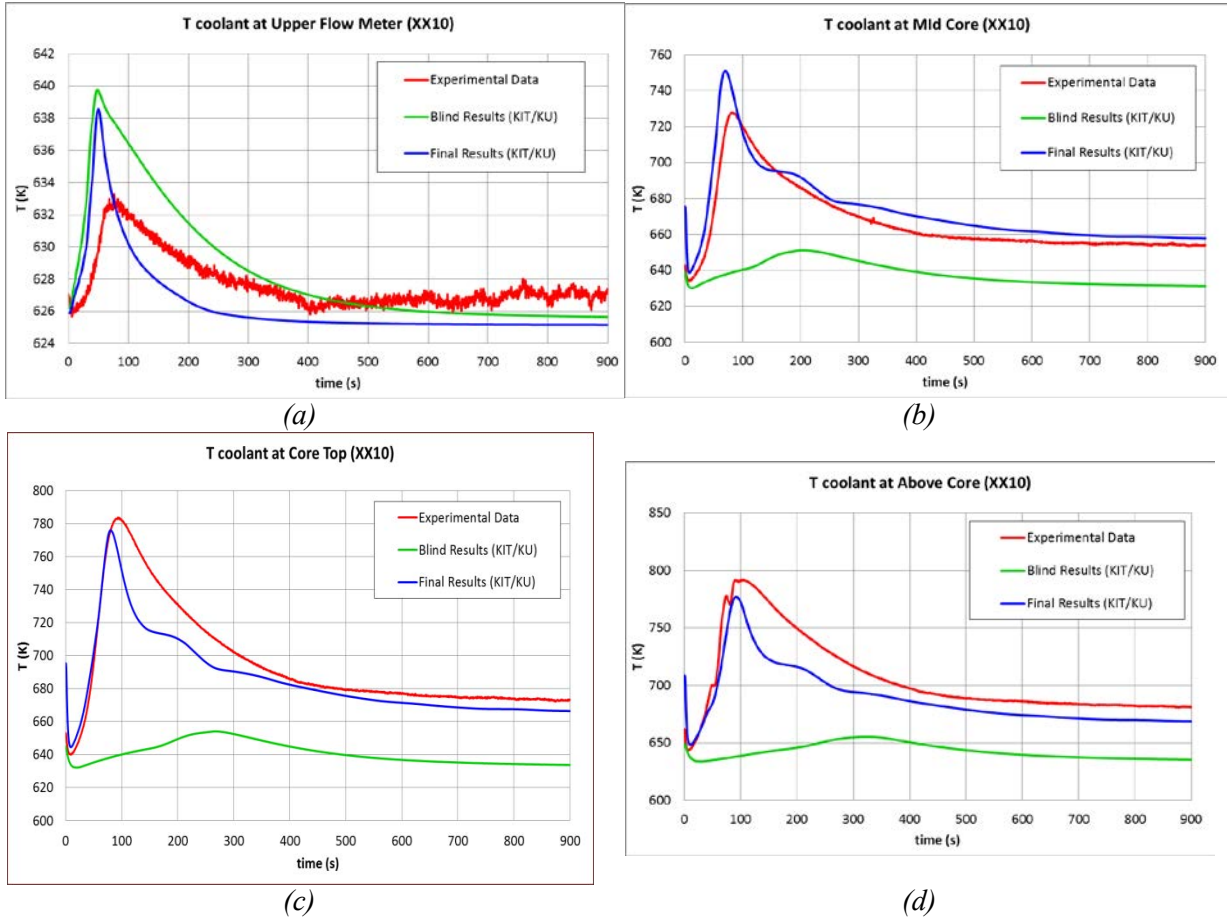
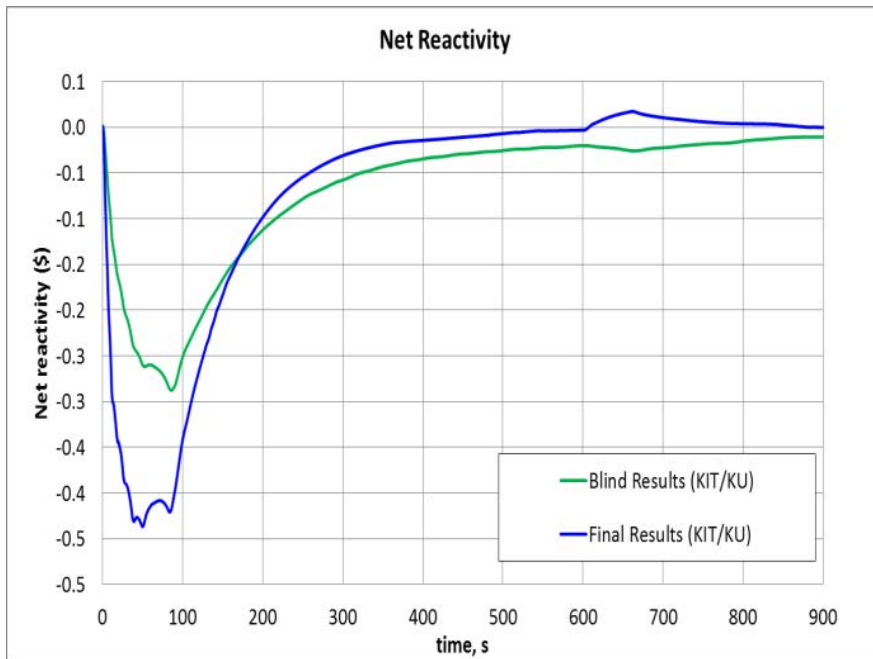
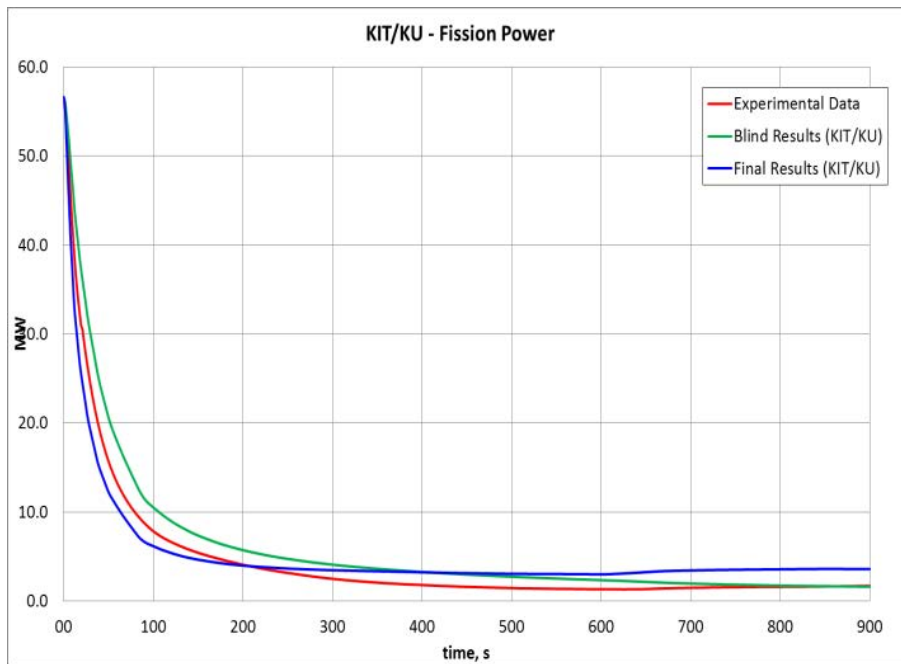


FIG. 92. SHRT-17 KIT/KU final results for XX10 temperatures: (a) at upper flowmeter location, (b) at mid-core, (c) at core top, (d) above core.

Further improvements are related to XX10. In order to take into account the radial heat conduction effect, two rings of sodium, representative of the inter-wrapper zone, were modelled around the XX10 SA (FIG. 98), keeping the rest of the model unchanged. With this refinement, much better agreement with the XX10 experimental data was achieved.

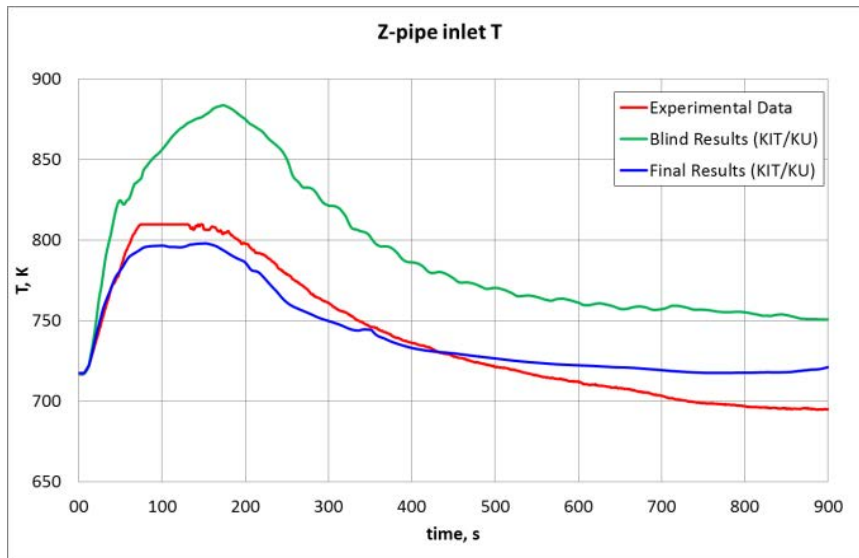


(a)

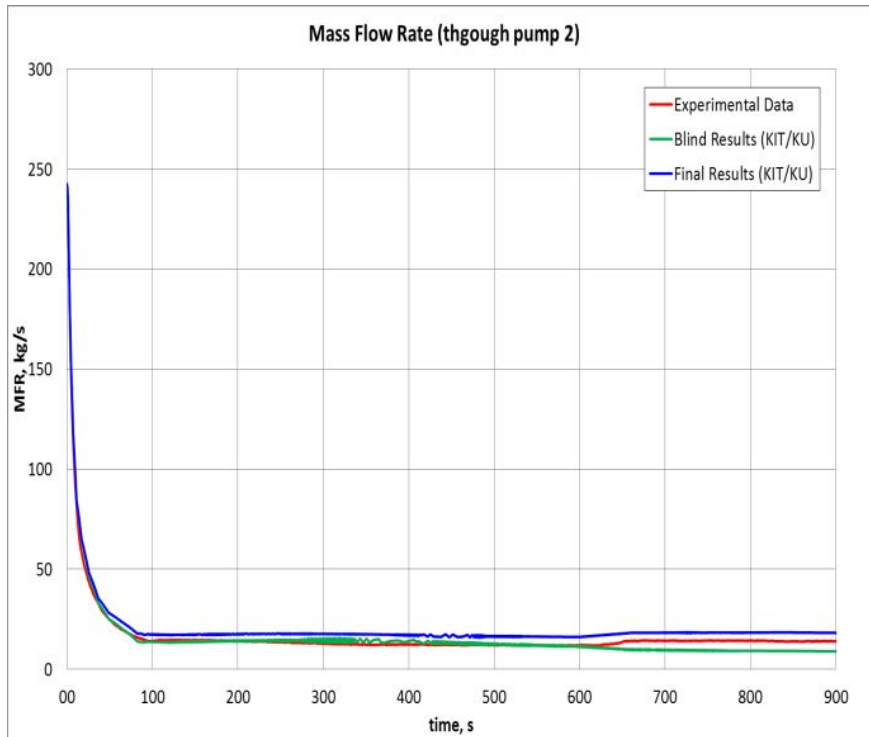


(b)

FIG. 93. SHRT-45R KIT/KU results: (a) net reactivity (contribution from material density variation, Doppler, and core thermal expansion); (b) fission power.

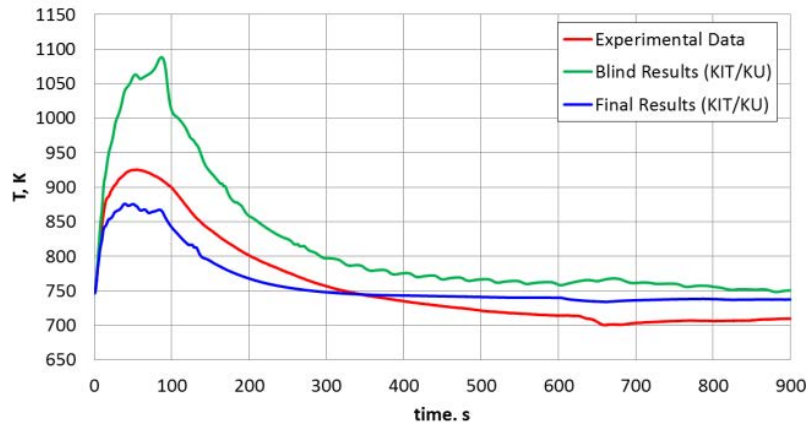


(a)

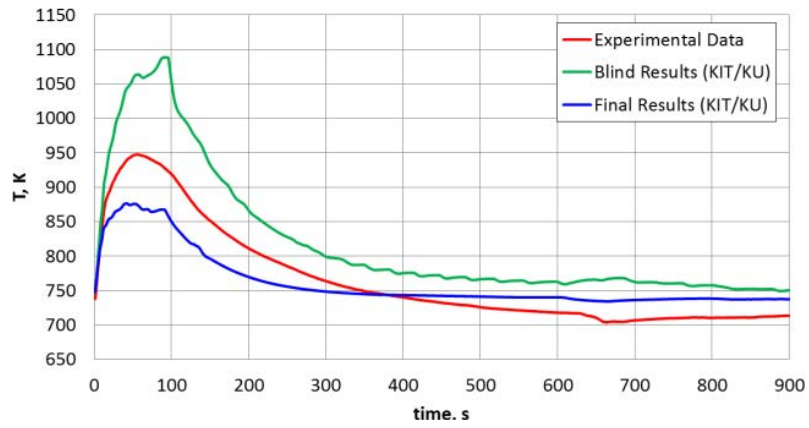


(b)

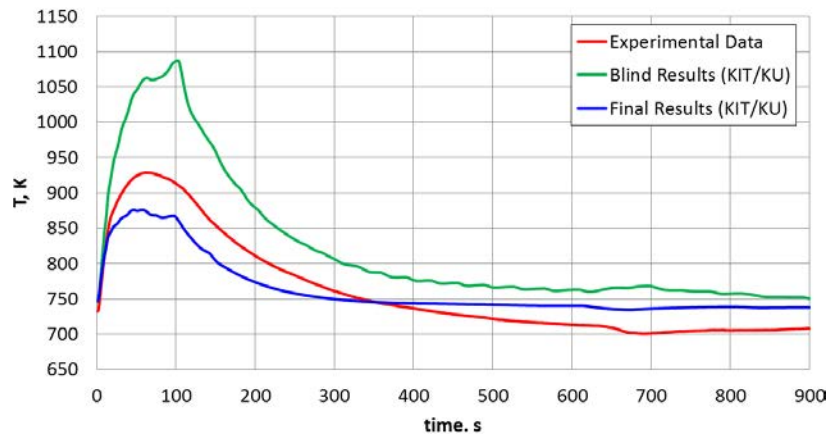
FIG. 94. SHRT-45R KIT/KU results: (a) Z-Pipe inlet temperature, (b) mass flow rate through pump 2.



(a)



(b)



(c)

FIG. 95. SHRT-45R KIT/KU results for XX09: (a) at core top, (b) above core, (c) at core outlet.

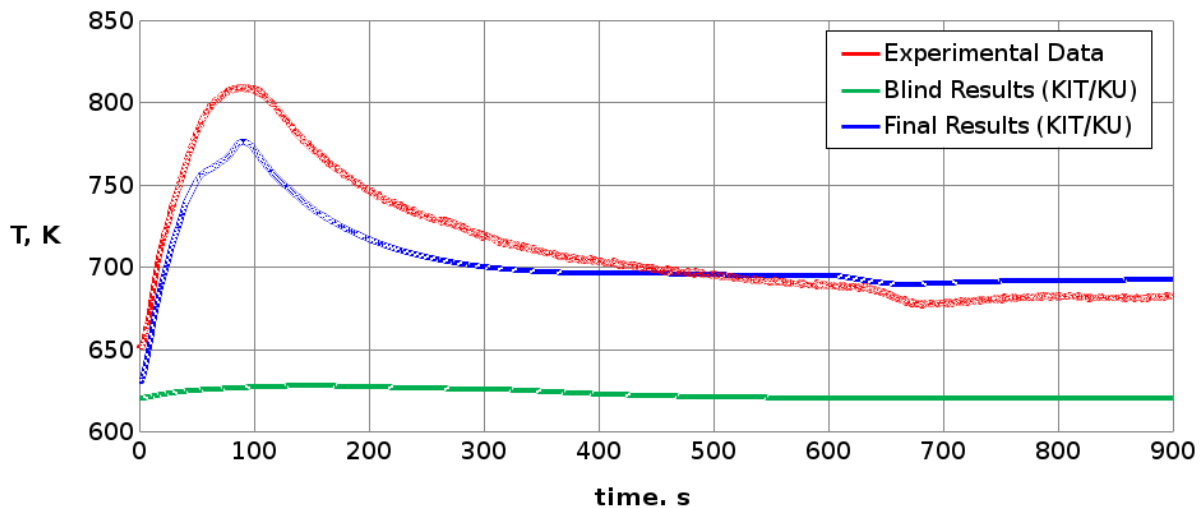


FIG. 96. SHRT-45R KIT/KU results for XX10: coolant temperature behaviour at core top.

Also for SHRT-45R, several model improvements were implemented in order to obtain the final results. The main modifications introduced were:

- (a) Including the modelling of mass flow rate due to the electromagnetic pump operated on battery power (neglected during the blind calculation);
- (b) Taking into account the core thermal expansion reactivity feedbacks by using the recently extended SIMMER version from KIT ([90], [91], [92]);
- (c) Allowing radial heat transfer from neighbouring subassemblies to XX10.

With new fast reactor designs (e.g. low void cores [94]), a delicate balance among reactivity effects exists, and accurate simulation of the accident initiation phase becomes hence more important. Therefore, codes like SIMMER need to be updated to take into account important feedbacks such as the core thermal expansion reactivity feedbacks from the very beginning. In this KIT-extended SIMMER version, a methodology has been implemented that allows taking into account the effects of core thermal expansion reactivity feedbacks within the constraints of the SIMMER code (Eulerian fluid-dynamic space-time kinetics code, i.e. with fixed mesh and spatial kinetics). Modelling of thermal expansion feedback is implemented in the code by the following steps:

- (a) Expanded dimensions (based on time-dependent temperature distribution) are computed independently for each cell at every timestep;
- (b) Application of the “equivalence principle” [92] allows keeping the original radial dimensions by conserving the “expansion” reactivity;
- (c) Application of a factor to determine the reactivity due to modifications of axial dimensions via suitable changes of densities.

In the methodology, both cylindrical (only grid plate expands) and conic (both grid and constraints planes expand) modes are considered for the radial expansion. Axial expansion considers fuel- or clad-driven modes (depending on the burnup level, namely depending on the state of the gap closure).

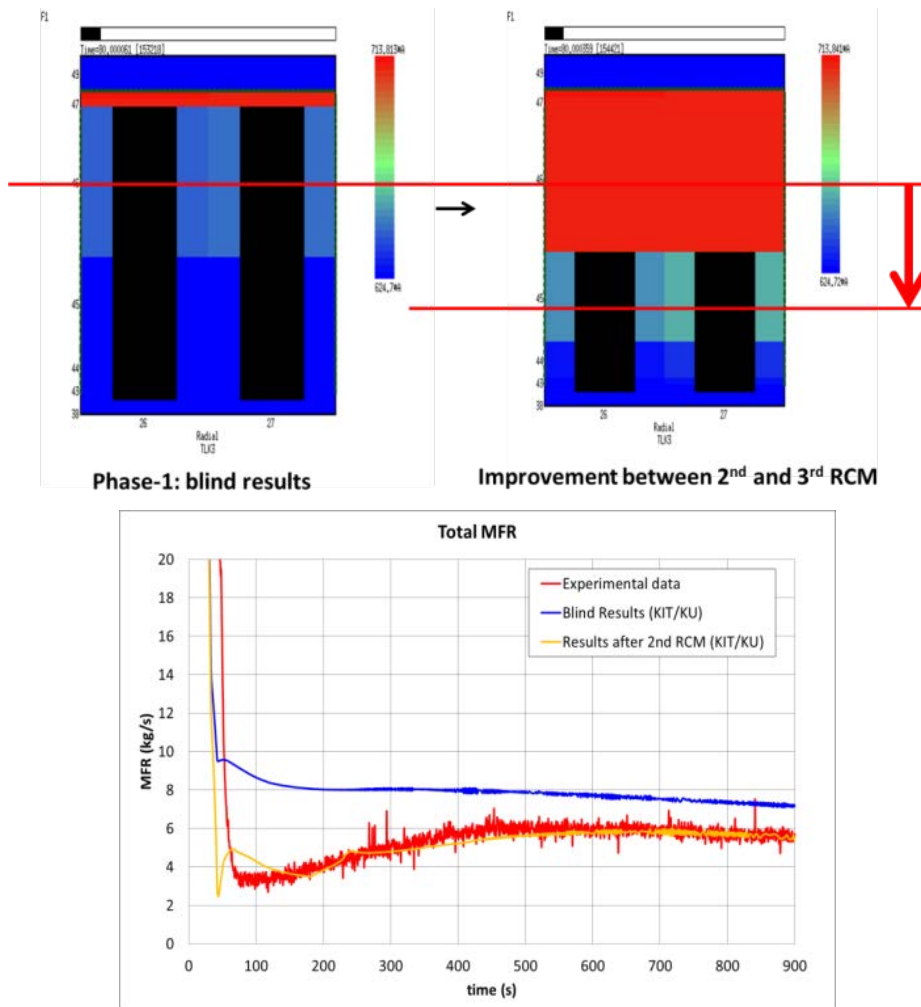


FIG. 97. SHRT-17: SIMMER mode modification (IHX position) after phase 1: effect on IHX thermal centre (red line).

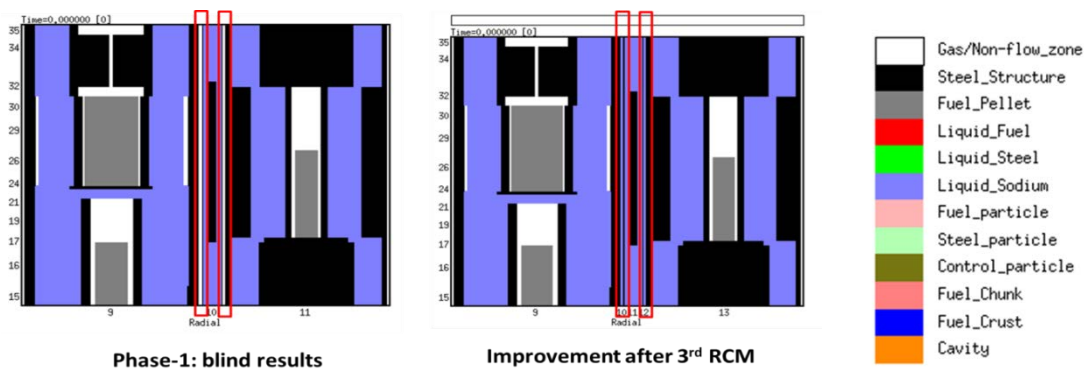


FIG. 98. SHRT-17: Improvement on the XX10 model after 3rd RCM: "explicit" modelling of inter-wrapper sodium.

7.5.6. Neutronics methods and models

7.5.6.1. Code(s) used

In order to take into account the asymmetric core configuration of SHRT-45R, a 3-D HEX-Z model for the ERANOS code was prepared. The ERANOS model has also been assessed for

establishing a neutronics reference for transient simulations carried out with the SIMMER-III code [87].

7.5.6.2. Neutron and photon cross-sections

In the benchmark, more than 1000 isotopic compositions were provided (considering three axial zones for each SA, including blankets) by Argonne after having extracted detailed fuel compositions at the beginning of run 138B [95]. However, in view of the anticipated comparison with the SIMMER code, for which a limited number of isotopic compositions is usually considered, it was decided to limit the number of different burnable zones in the ERANOS model as well. Therefore, only six average compositions, representative of the six burnable zones, were determined by axial (weighting factors proportional to the fission product densities) and radial (weighting factors proportional to the power per SA provided) averaging. For each burnable zone, 33-group self-shielded cross-sections were computed by using the European Cell Code (ECCO) [44] while using actual heterogeneous SA geometry descriptions in a plane and a JEFF3.1-based 1968-group ECCO nuclear data library [96]. For the non-burnable zones (reflectors, dummy, etc.), effective cross-sections were obtained similarly, but considering SAs as homogeneous media. One example for a driver SA is shown in FIG. 99; different homogeneous/heterogeneous treatments for different axial zones were used.

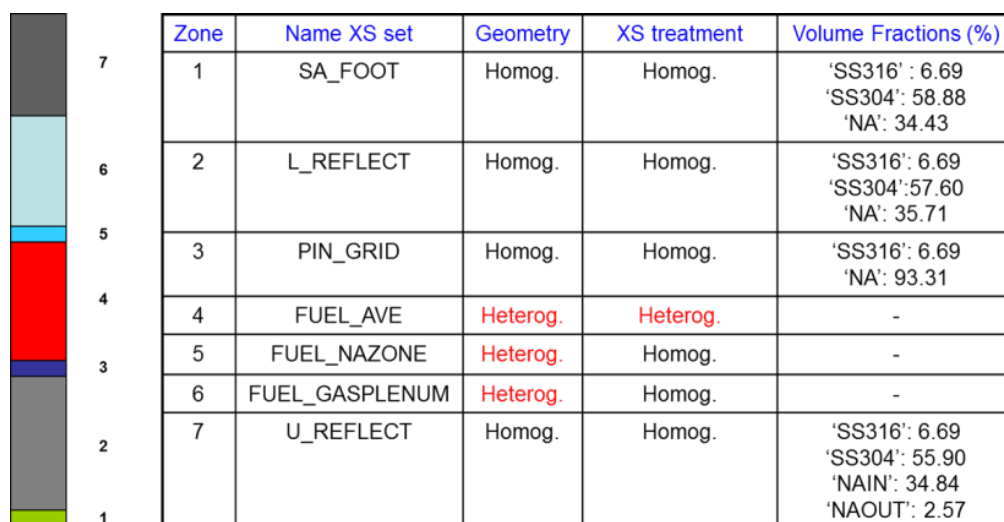


FIG. 99. Cross-section (XS) treatment for the axial zones considered in the driver SA.

In order to further simplify the model, an averaged axial structure for the driver SAs was assumed. The averaged dimensions were calculated by weighting over the number of SAs for each type: 55 SAs for MARK-II AI and 31 SAs for MARK-IIA, respectively. The values adopted in the ERANOS model are: 1) fuel slug height after swelling: 36.65 cm, 2) sodium level above fuel: 1.577 cm, 3) gas plenum height: 22.04 cm and 4) upper reflector: 36.38 cm. For simplicity, the sodium level zone for the safety rods and HW-CR were neglected (both are MARK-IIA type, and the sodium level above the fuel slug is very small, $h=0.1165$ cm).

The whole model includes 721 SAs grouped in 9 different types, represented by 43 effective cross-section sets, 16 hexagonal rings and 30 axial nodes [97].

7.5.6.3. Calculation of power and k_{eff}

The reference calculation route for the KIT results applied the ERANOS 2.2 code [43], 3-D HEX-Z geometry, heterogeneous cross-section treatment for the burnable zones (not expanded conditions). The VARIANT solver (SP3 approximation) was used. Parametric studies (heterogeneous/homogeneous models for generation of multigroup cross-sections, diffusion/transport approximations for neutron transport, etc.) were performed [97]. More details are presented in Section 8.1.

7.5.6.4. Calculation of reactivity feedback

The reactivity feedback coefficients were determined following the definitions provided in the benchmark.

7.5.7. Neutronics results

The core multiplication factor (k_{eff}) and the effective delayed neutron fraction (β_{eff}) are shown in TABLE 8, where comparison with the data provided by Argonne is shown [95]. The effective delayed neutron fraction is in good agreement also with the data available in the literature [98].

TABLE 8. COMPARISON OF k_{EFF} AND β_{EFF} FOR EBR-II BENCHMARK

	Cases	k_{eff}	β_{eff}
Data Provided	VARIANT	0.9885	7.05E-03
KIT	ERANOS 2.2	0.9876	-
	ERANOS 2.2 (not expanded)	0.9997	6.91E-03

The reactivity coefficients (axial and radial expansion, sodium density, and Doppler reactivity feedback coefficients) are shown in TABLE 9. A comparison with data provided by Argonne is shown as well [95]. Differences may also be related to the different thermal expansion coefficients used to convert pcm to pcm/K. The KIT results used the SIMMER-III code correlation between density and temperature for saturated liquid sodium [83]:

$$\rho_l \left[\frac{kg}{m^3} \right] = 1011.8 - 0.22054T - 1.9226 \times 10^{-5} T^2 + 5.6371 \times 10^{-9} T^3, \quad (8)$$

$$T < 1644.26 \text{ K.}$$

TABLE 9. COMPARISON OF REACTIVITY FEEDBACK COEFFICIENTS FOR EBR-II BENCHMARK

	Cases	Reactivity feedback coefficient (pcm/K)			
		Axial Expansion	Radial Expansion	Sodium Void	Doppler
Data Provided	VARIANT	-0.65	-1.67	-1.49	-0.05
KIT	VARIANT	-0.68	-2.42	-2.15	-0.04

The largest difference is observed for the sodium density reactivity coefficient (10% sodium density variation) and can be explained by the different methods used to calculate the coefficient. The KIT value was obtained by considering a density variation of 10% for the sodium density (only the zone internal to the wrapper tubes) for the system (including blankets).

k_{eff} as a function of control rod insertion was also provided. The general shape of the curves agrees well with the results obtained by the other participants [95].

The power distribution per SA was also evaluated at KIT. The final results obtained by KIT include the contribution of photon heating calculated by means of the ERANOS code. The embedded KERMA_CORRECTION module [43] was used with the 33-energy group KERMA file available with the ERANOS 2.2 distribution. A comparison, with and without this KERMA correction, is shown in FIG. 100. The difference between final and preliminary KIT results is of the order of 1 – 2% for driver SAs and of 80% for dummy and 20 – 30 % for reflector SAs, in which the contribution from photons is dominant. The final results show a better agreement with the other participants' results [95].

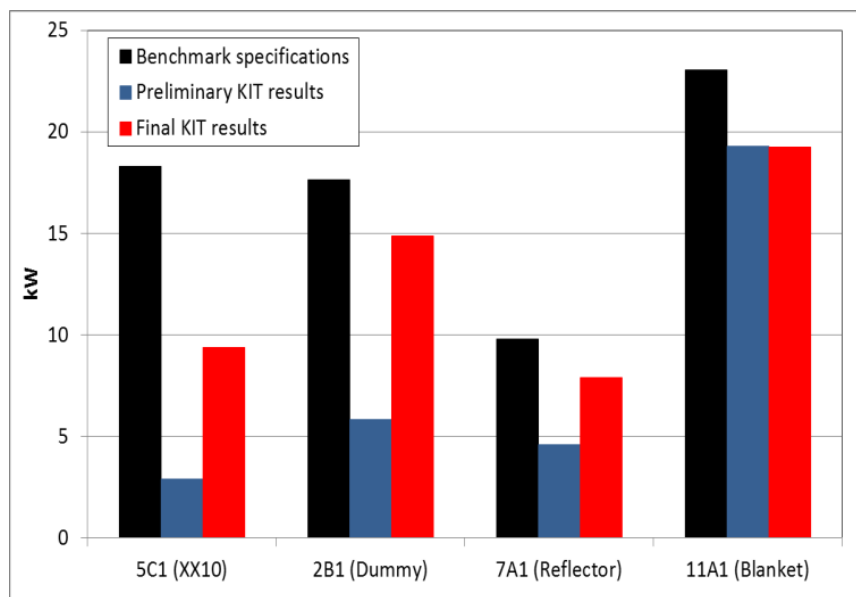


FIG. 100. Power for special SAs.

The decay heat evolution over 900s was analyzed as well. The irradiation history was simulated by means of the TRAIN code [58] and by means of the ORIGEN 2.2 code [99]. The results are in good agreement with those of the other participants [95].

7.6. INDIRA GANDHI CENTRE FOR ATOMIC RESEARCH (INDIA)

7.6.1. Geometry/discretization

The nodalization of the EBR-II primary heat transport system in the EBRDYN code is shown in FIG. 101. The upper plenum, high pressure and low pressure inlet plena, and cold pool are modelled as perfect mixing volumes. The core subassemblies receiving sodium from the high pressure plenum have been grouped into 9 radial zones. The first two zones represent fuel subassemblies, the third zone represents inner blanket subassemblies. The fourth and fifth zones represent the control rods and safety rods, respectively. The sixth and seventh zones represent special instrumented subassemblies XX09 and XX10, respectively. The eighth and ninth zones represent the rest of the subassemblies receiving sodium from the high pressure plenum. The tenth zone represents outer blanket/reflector subassemblies which receive

sodium from the low pressure inlet plenum. One representative subassembly from each zone has been modelled with 20 axial nodes and 4 radial nodes.

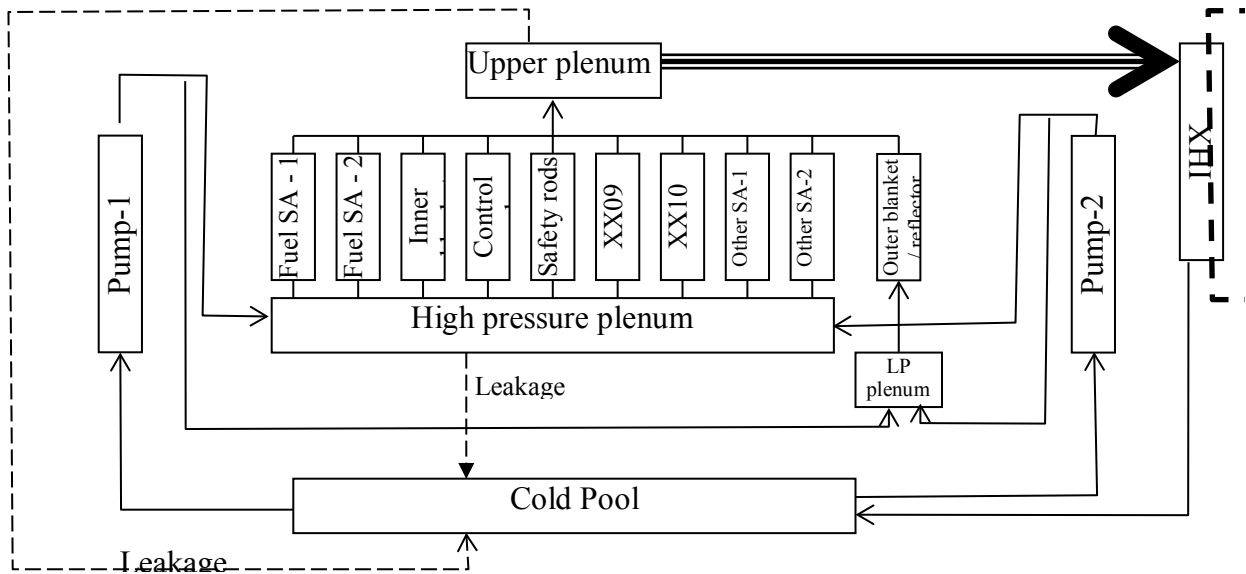


FIG. 101. EBRDYN modelling for EBR-II.

The Z-Pipe is modelled with four nodes in the radial direction representing hot sodium, the inner pipe, stagnant sodium and the outer pipe, respectively. Along the length, the pipe is modelled with 30 nodes. The IHX is modelled with 40 nodes along the length and two nodes in the radial direction, which represent primary and secondary sodium. Each primary sodium pump has been modelled with one node. The high pressure piping connecting the pump and the high pressure plenum of the core has been modelled with two nodes. The low pressure piping connecting the pump and the low pressure inlet plenum of the core has been modelled with a single node.

7.6.2. Nuclear and thermo-physical data/correlations

The correlations used for evaluating properties of sodium as a function of temperature (T , °C) are:

- (a) Density ' ρ ' (kg/m^3) = $949 - 0.223T - 1.75 \times 10^{-5} T^2$;
- (b) Specific heat ' C_p ' (kJ/kg-K) = $(1436.74 - 0.58049T + 4.6229 \times 10^{-4} T^2) \times 10^{-3}$;
- (c) Thermal conductivity ' k ' (W/m-K) = $90.6038 - 0.048523T$;
- (d) Dynamic viscosity ' μ ' (N-s/m^2) = $(B)^{1/3} A e^{[B * C / (T + 273.15)]}$.

where $A = 1.2162 \times 10^{-5}$, $B = 949 - 0.223T - 1.75 \times 10^{-5} T^2$, and $C = 0.6976$.

For modelling the Z-Pipe, the heat transfer and friction factor correlations used are:

- (a) $Nu = 5.0 + 0.025 Pe^{0.8}$ (laminar flow regime)
- (b) $\frac{1}{\sqrt{f}} = -2 \log_{10} \left(\frac{\varepsilon}{3.7 D_h} + \frac{2.51}{Re \sqrt{f}} \right)$ (turbulent flow regime)

The heat transfer correlations used in the IHX modelling are:

- (a) Shell side $Nu = 6 + 0.006 Pe$ [100];
- (b) Tube side $Nu = 4.82 + 0.0185 Pe^{0.827}$ [101]

The heat transfer correlations used for modelling thimble flow in subassemblies are:

- (a) Laminar flow regime:
 - (i) $Nu = 4.36$ for subassembly wrapper inner surface;
 - (ii) $Nu = 8.26$ for subassembly wrapper outer surface.
- (b) Turbulent flow regime:
 - (i) $Nu = 5 + 0.0185 Pe^{0.827}$ for both inner and outer surfaces.

The pressure drop coefficient for thimble flow is calculated as:

- $f = 96/Re$, $Re \leq 10000$ (laminar flow regime)
- $1/(f^{0.5}) = 2.0 \log(Re(f^{0.5}/2.51))$, $Re > 10000$ [102]

7.6.3. Thermal hydraulics methods and models

7.6.3.1. Code(s) used

For the purpose of simulating the EBR-II SHRT-17 test, a one dimensional plant dynamics code EBRDYN was developed and used. For CFD studies, the general purpose CFD code Star-CD was used.

7.6.3.2. Basic method

The general assumptions made in deriving the mathematical models of the various reactor and heat transport components to reduce the complexities are: (i) liquid sodium was assumed to be incompressible, (ii) flow of sodium was treated as one dimensional through the pipelines, fuel rod bundles, heat exchanger tubes etc., (iii) in all the places where mixing and recirculating flow patterns exist, a perfect mixing assumption was made for the thermal model, and the incoming kinetic energy due to the flow was assumed to be fully converted into static pressure head for hydraulic calculations, and (iv) axial conduction heat transfer in coolant pipe material, heat exchanger tubes, fuel pins and cladding walls was neglected with respect to the radial conduction. With these assumptions, the basic governing equations were discretized and a set of simultaneous equations were formed and then solved.

7.6.3.3. Model

For steady state calculations, the primary pump flow, pump speed, primary flow through various subassemblies, reactor inlet temperature, normalized power distribution in the subassembly, and secondary sodium flow and inlet temperature of the IHX were inputs. For transient calculations, the core decay power, primary pump speed and the IHX secondary sodium flow and inlet temperature were the boundary conditions. The transient calculations were grouped as (i) core thermal power, (ii) fuel pin to sodium coolant heat transfer, (iii) inlet and outlet plena and cold pool temperature, (iv) IHX heat transfer and (v) primary sodium hydraulics calculations. The important models are described below.

Core: For the purpose of thermal and hydraulic analysis, one representative subassembly from each zone was modelled. The subassembly was divided into 20 axial zones – 1 zone for the lower shield part, 2 zones for the bottom part of the pin, 10 zones for the active fuel length, 2 zones for the top part of the pin, and 5 zones for the upper shield portion. In each axial zone, the thermal capacities of all the fuel, steel and sodium were separately lumped together, and four heat exchanging nodes were formed, each described by a mean temperature. Two nodes were allotted for fuel pellets and one each for steel and sodium (FIG. 102). Then through the application of an energy balance for each of the axial zones, four coupled ordinary differential equations in time were obtained. Solving them simultaneously in a sequential manner from the bottom to top of the subassembly gave the axial distribution of the sodium, clad and fuel temperatures under steady state and transient conditions. The decay power generated in the core was distributed among the subassemblies based on the steady state power distribution.

Sodium Plena: The upper plenum, lower plenum and cold pool were modelled as perfect mixing volumes. For the upper plenum, the flows and sodium outlet temperatures from the core zones were the inputs and the mixed mean temperature was the output, which is the inlet temperature for the Z-Pipe.

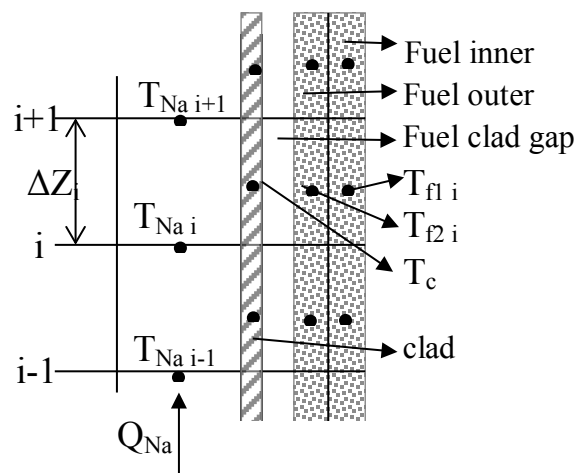


FIG. 102. Fuel pin model.

Z-Pipe: The Z-Pipe was modelled as a double-walled sodium-carrying pipe immersed in the cold pool, with stagnant sodium in the annular gap. In each part, the primary sodium, inner pipe, stagnant sodium and outer pipe were represented by four nodes, respectively (FIG. 103). The heat transfer from the outer surface was accounted for. The Z-Pipe sodium outlet temperature and flow rate formed the inputs for the IHX calculations.

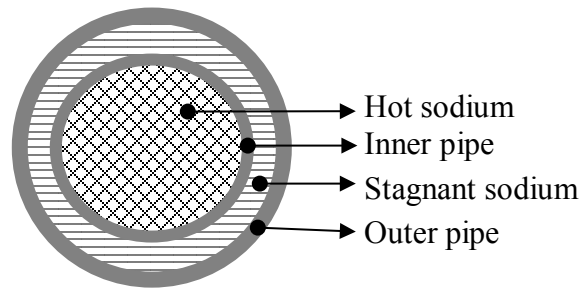


FIG. 103. Z-Pipe model.

IHX: This model evaluated the steady state and transient temperature profiles of the IHX primary and secondary sodium sides, with flows and inlet temperatures as input. A two-zone radial lumped one dimensional model with a single temperature for the primary sodium and secondary sodium was used (FIG. 104). The shell was assumed to be at primary sodium temperature. The thermal capacity of the shell material was lumped with that of the primary sodium. The thermal capacity of the tube material was lumped with the primary sodium and secondary sodium and evenly divided between the two. These assumptions led to a set of two coupled hyperbolic partial differential equations. For the numerical solution of these basic equations, the active length of the heat transfer region was divided into 40 regions. Then the equations were integrated with respect to length over these regions, and a set of ordinary differential equations in time was obtained. These equations were discretized using a nodal heat balance scheme incorporating the weighted mean temperature in the heat transfer term. The IHX primary outlet temperature and flow were the inputs for the cold pool calculations.

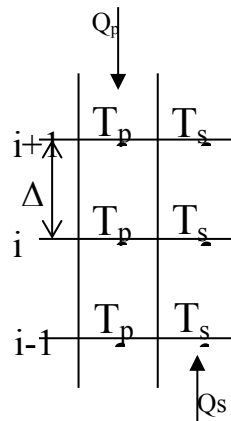


FIG. 104. IHX model.

Core Hydraulics: All the subassembly zones were treated as parallel channels. The pressure drop coefficient for each subassembly was calculated based on the pressure drop across the core and the flow through the subassembly. The modelling was carried out taking care of any possible reverse flows in some of the subassemblies.

7.6.4. Blind results

7.6.4.1. SHRT-17

The reactor power was taken as 57.3 MW(th) (including initial decay heat power of 3.36 MW). The core power was distributed among all subassemblies according to the normalized benchmark data. The speeds of pumps 1 and 2 were taken as 799 rpm and 765 rpm, respectively. The intermediate sodium loop mass flow rate was taken as 312 kg/s, with the IHX secondary inlet temperature as 574K (301°C). The pump flows were obtained as 249 and 211 kg/s, respectively. The core inlet and outlet temperatures were obtained as 624K (351°C) and 722K (449°C) respectively. The IHX primary inlet and secondary outlet temperatures were obtained as 722K and 637K (364°C) respectively.

The transient analysis was carried out with boundary conditions given in the benchmark specification. FIG. 105 shows that the core inlet temperature is almost constant, with a reduction of only 2K in 900 s. FIG. 106 shows the primary sodium pump flows. It can be seen that the pump 1 flow reduces faster than the pump 2 flow and becomes equal to the pump 2 flow when both pumps have completely coastdown. FIG. 107 shows the evolutions of peak clad and coolant temperatures. It can be seen that the peak clad and coolant temperatures go to a maximum of 783K and 727K at 58 s and 80 s, respectively. FIG. 108 shows the evolution of the Z-Pipe inlet, IHX primary inlet and IHX secondary outlet temperatures. It can be seen that the core outlet temperature goes to a maximum of 722K and comes down to 640K in 900 s. The IHX inlet temperature closely follows the core outlet temperature. The IHX outlet temperature goes to a maximum of 693K in 15 s and cools down to 620K in 900 s.

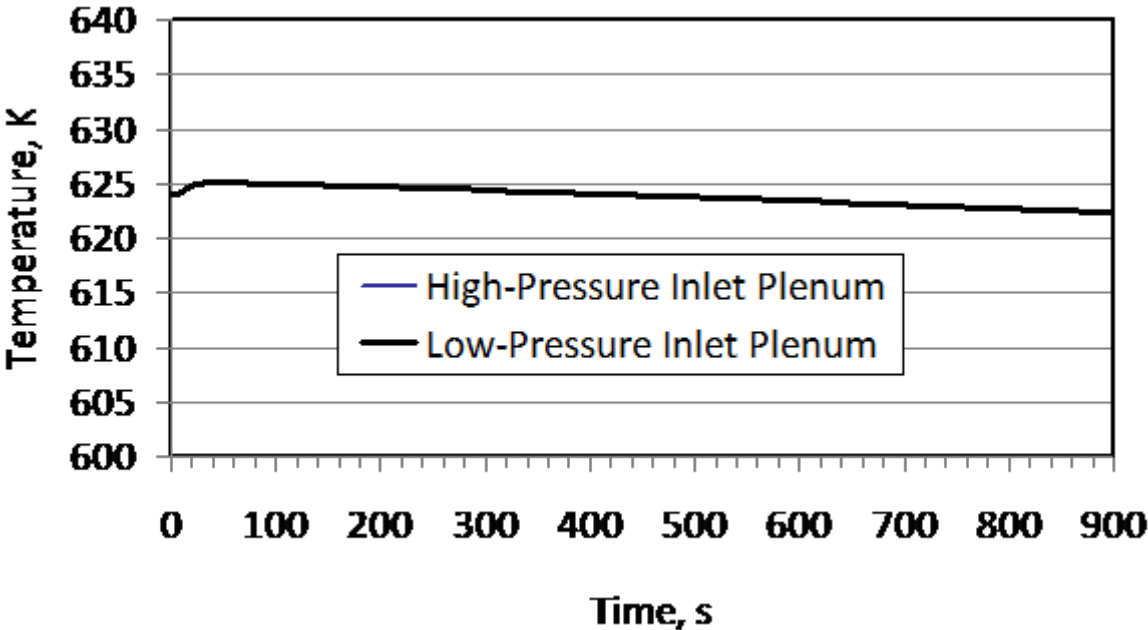


FIG. 105. SHRT-17 core inlet temperature, blind results.

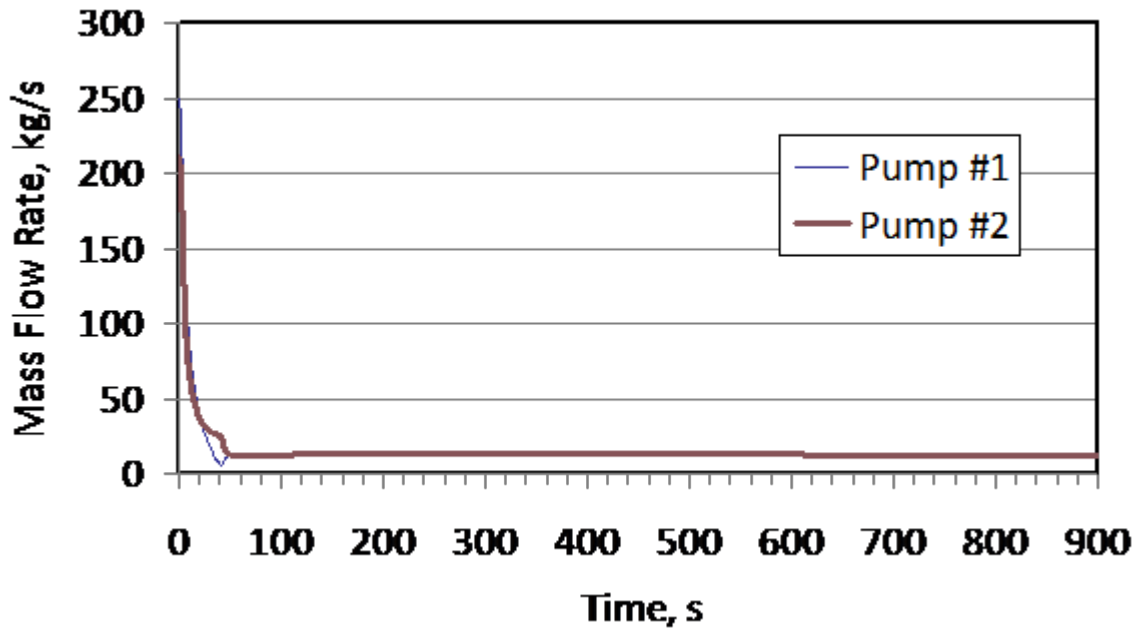


FIG. 106. SHRT-17 primary pump flow rate, blind results.

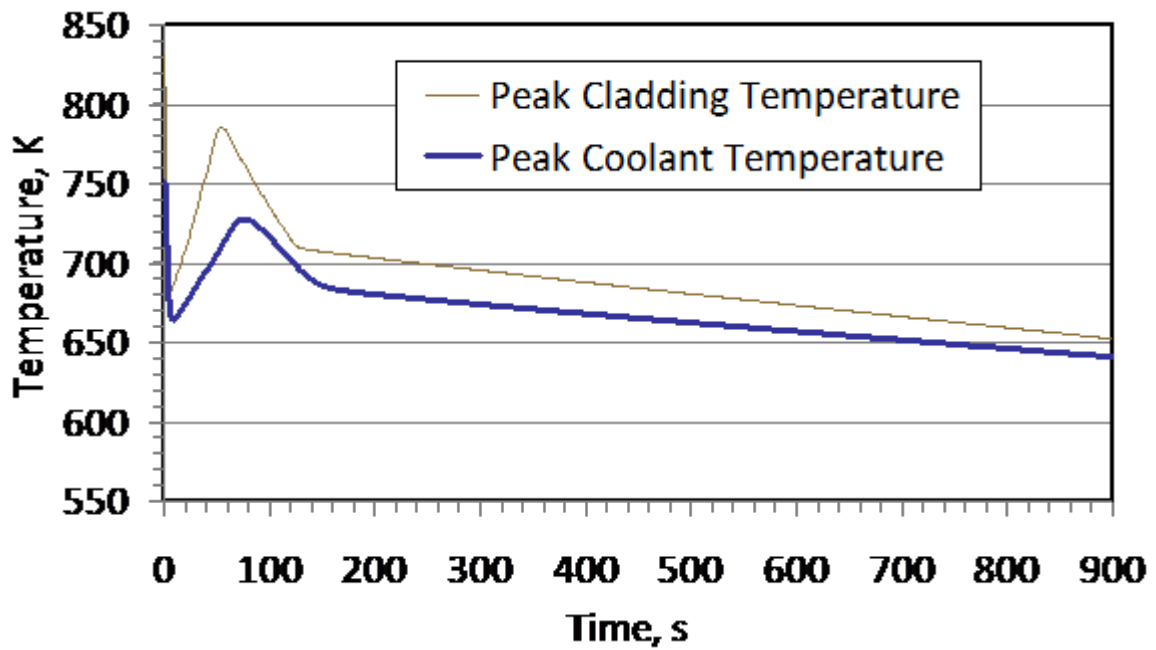


FIG. 107. SHRT-17 peak in-core temperatures, blind results.

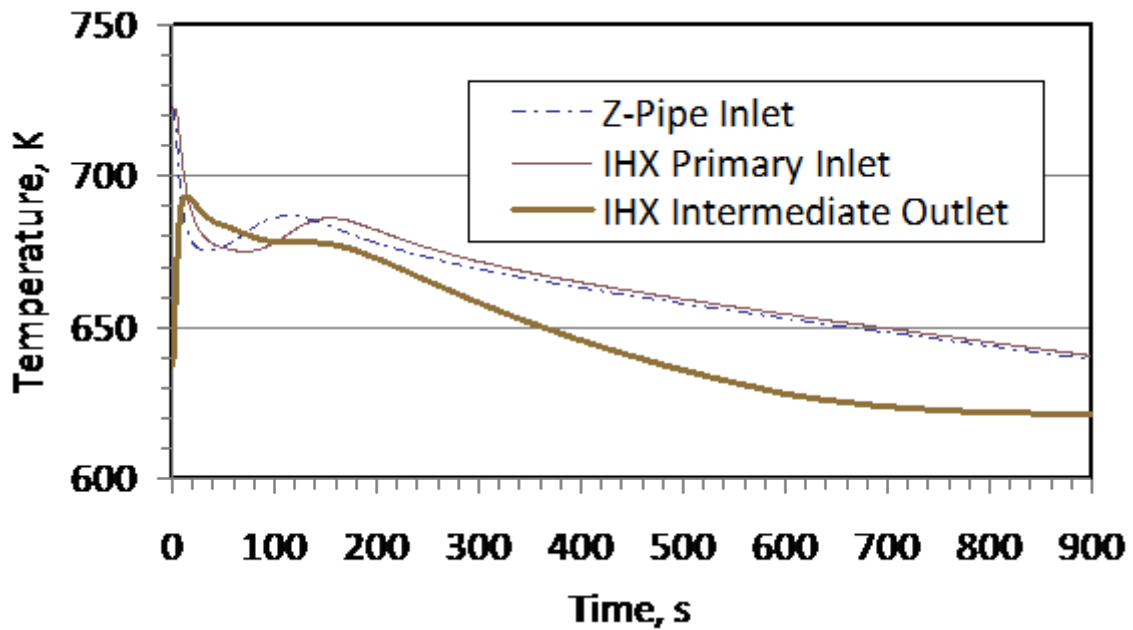


FIG. 108. SHRT-17 Z-Pipe and IHX temperatures, blind results.

7.6.4.2. SHRT-45R

IGCAR did not perform an analysis of SHRT-45R.

7.6.5. Final results, data comparisons

7.6.5.1. SHRT-17

The calculations were refined by improving the modelling. The subassemblies were re-grouped and the subassemblies giving the maximum temperatures were identified correctly. The steady state flow rates of pump 1 and pump 2 were corrected to 276 kg/s and 224 kg/s, respectively. The leakage flows from the high pressure inlet plenum and upper plenum were accounted for. The Z-Pipe was modelled in greater detail, taking into account the heat losses from the pipe to the cold pool. The XX09 subassembly was modelled, along with the thimble flow. From the steady state analysis, the core inlet and outlet temperatures were obtained as 624.3K (351.3°C) and 715.4K (442.4°C), respectively. The IHX primary inlet and outlet temperatures were obtained as 710.9K (437.9°C) and 627.9K (354.9°C), respectively. The IHX secondary sodium outlet temperature was obtained as 706K (433°C).

FIG. 109 shows the evolution of pump 1 and pump 2 flows. It can be seen that the pump 1 flow reverses for a short duration around 40 s. FIG. 110 shows the evolution of the core inlet temperature. The core inlet temperature initially increases from 624.3K to 624.8K at 23 s and reduces gradually to 622.8K by 900 s. FIG. 111 shows that the peak clad and coolant temperatures go to a maximum of 890K at 59 s. The peak fuel temperature goes to a maximum of 911K at 55 s. FIG. 112, FIG. 113, and FIG. 114 show the evolution of the Z-Pipe inlet, IHX primary inlet and IHX secondary outlet temperatures, respectively. It can be seen that the Z-Pipe inlet temperature goes to a minimum of 659K at 20 s, goes to a maximum of 746K (108 s), and comes down to 670K in 900 s. The IHX inlet temperature closely follows the core outlet temperature. The IHX outlet temperature goes to a maximum of 693K at 15 s and cools down to 620K by 900 s. It can be seen that all the temperatures are predicted

reasonably well except the IHX primary inlet temperature. The reason for this is not understood. Also the measured IHX secondary outlet temperature remained constant during the initial 100 s, whereas the predicted temperature decreases to about 660K and comes back to 720K within 120 s. This deviation from prediction also could not be explained.

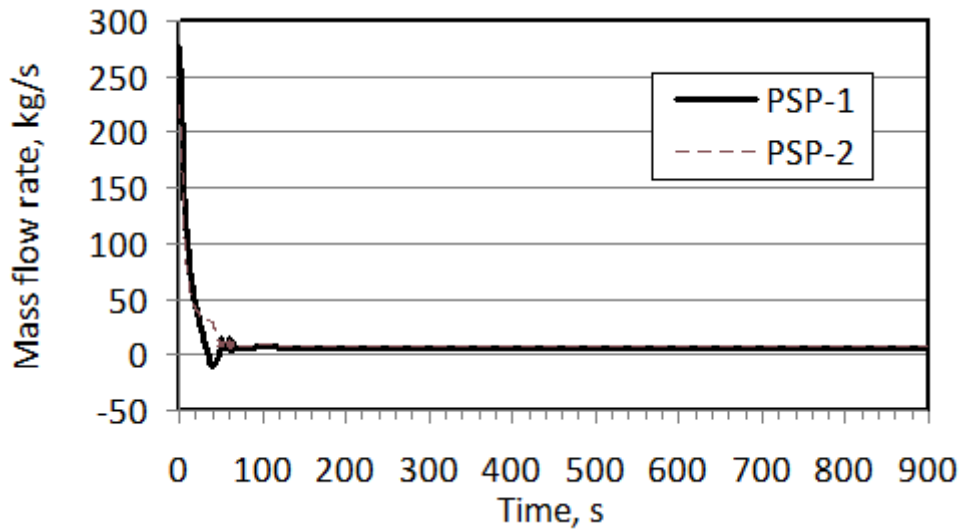


FIG. 109. SHTR-17 primary sodium pump flow, final results.

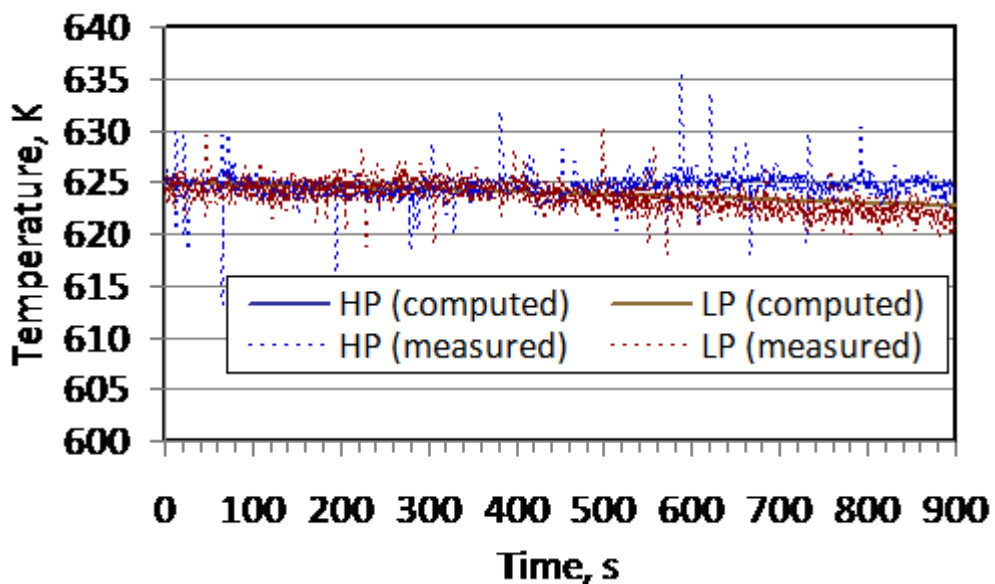


FIG. 110. SHTR-17 core inlet temperatures, final results.

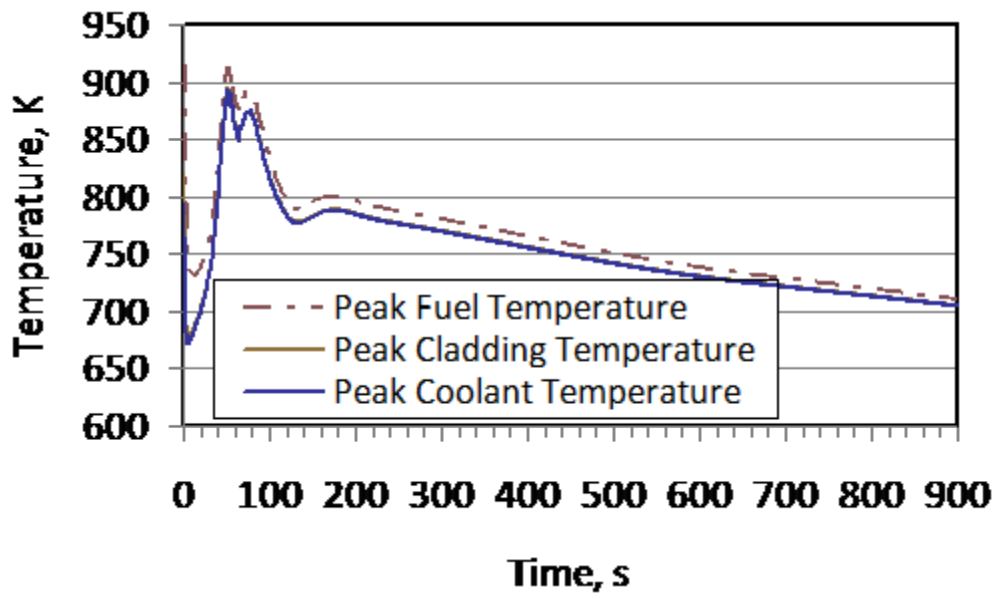


FIG. 111. SHRT-17 peak in-core temperatures, final results.

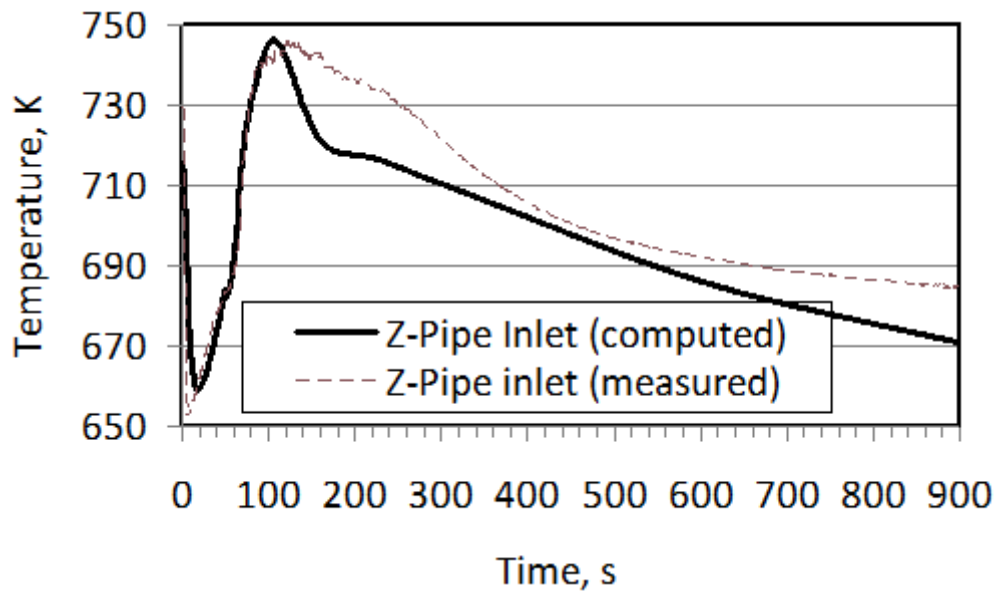


FIG. 112. SHRT-17 Z-Pipe inlet temperature, final results.

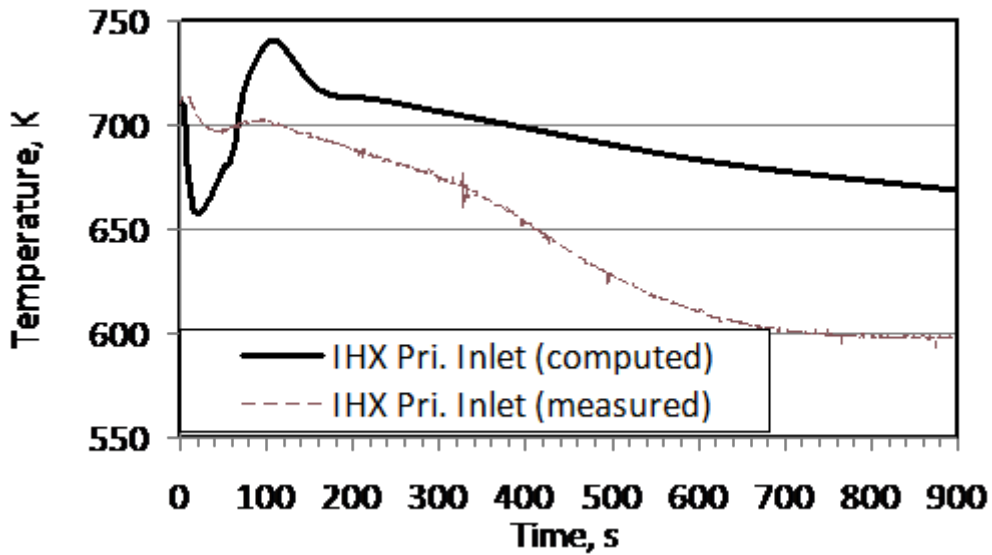


FIG. 113. SHRT-17 IHX primary inlet temperature, final results.

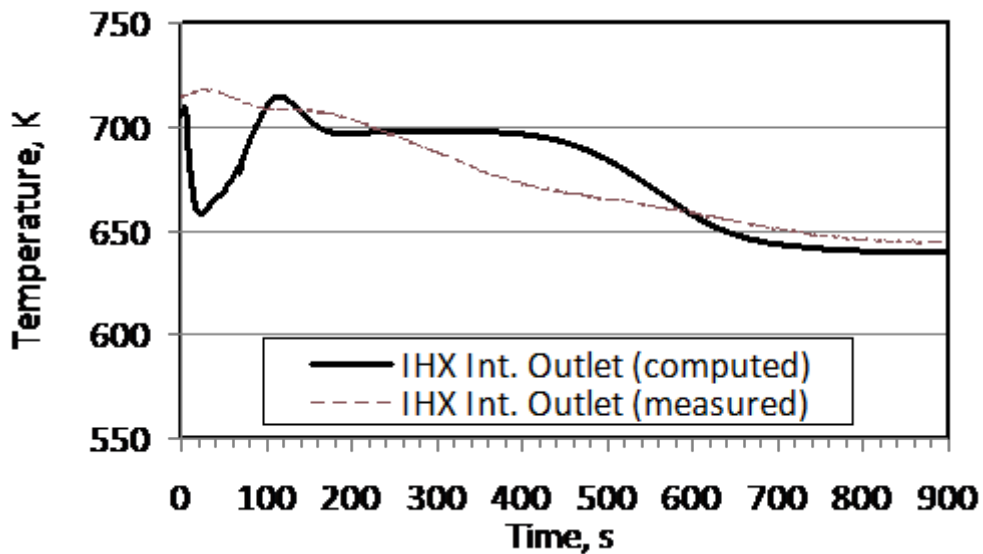
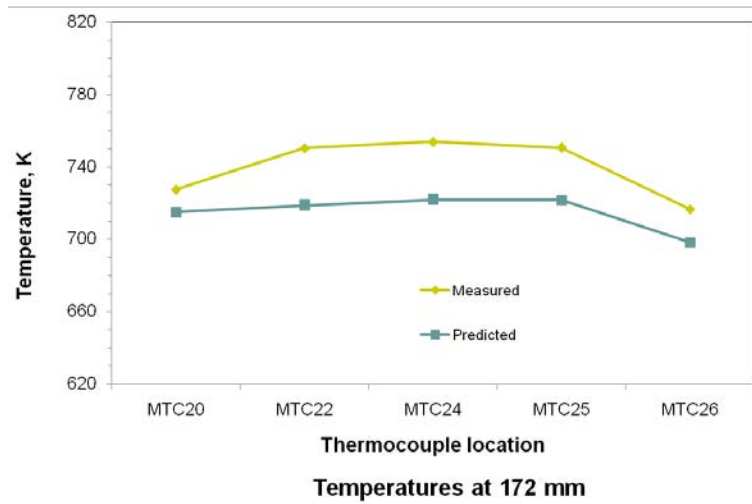


FIG. 114. SHRT-17 IHX intermediate outlet temperature, final results.

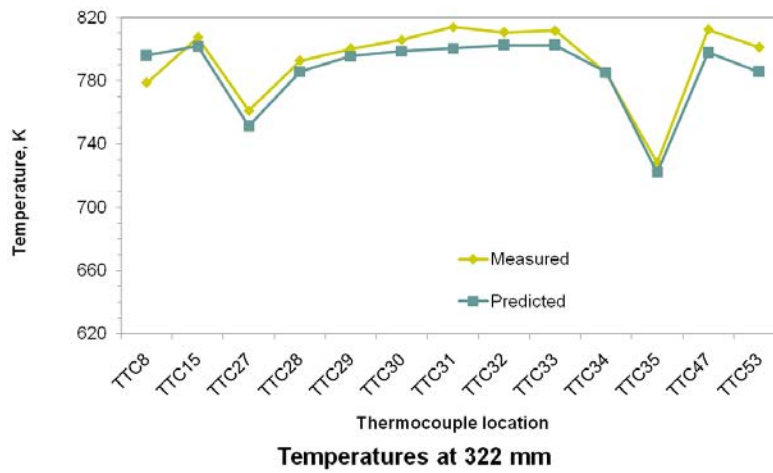
The XX09 subassembly was analyzed with a 3-D mesh using the CFD code Star-CD. The 61-pin bundle, along with the spacer wire, was modelled with 0.8 million mesh cells. The predicted steady state temperatures at various elevations are shown in FIG. 115. It can be seen that the results compare well with the measurements.

7.6.5.2. SHRT-45R

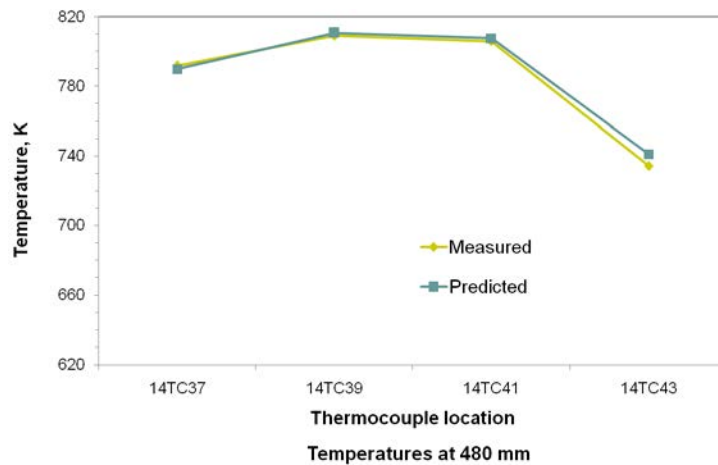
IGCAR did not analyze the SHRT-45R transient.



(a)



(b)



(c)

FIG. 115. Comparison of SHRT-17 predicted and measured temperatures in XX09 at elevations of (a) 172 mm, (b) 322 mm and (c) 480 mm.

7.6.5.3. Model improvements

Model improvements were covered in Section 7.6.5.1.

7.7. ENEA (ITALY)

7.7.1. Geometry/discretization

The RELAP5-3D[®] nodalization (FIG. 116 and FIG. 117) modelled the primary loop and the IHX of EBR-II, using a sliced approach. The pool region was modelled with a 3-D component (i.e., MULTID) consisting of 19 axial nodes, 2 radial rings and 8 azimuthal sectors. The number of azimuthal meshes was chosen on the basis of the geometrical position of the pumps, reactor inlet and outlet pipes, and the IHX. The axial mesh nodes of the pool region and of the other components (reactor region, pipes, and IHX) are equal in length or integral multiples of the smallest node. Each component in the pool was located as in the real 3-D geometry. The pumps were modelled with a PUMP component. The homologous curves were implemented using the characteristic curves provided for the pump. The high and low pressure flow lines, Z-Pipe, and IHX primary and secondary sides were modelled with 1-D components (i.e., PIPE and BRANCH components). A 3-D component (MULTID) represented the reactor vessel: lower plenum, upper plenum and core bypass.

The radial discretization was chosen by grouping the rings according to the EBR-II core regions. The azimuthal subdivision was made to represent the real position of the inlet and outlet of the pipes and the symmetry of the core. It was thermally coupled with the fuel subassembly through the wrappers and the pool system through the neutronic shield. The reactor core was divided into two main parts: 1) the subassemblies of the central core and the expanded core regions, the first 7 rows, modelled one by one, according to the geometrical specifications; and 2) the outer blanket region modelled with 24 equivalent PIPE components, with the reflector and blanket subassemblies grouped separately, according to the azimuthal configuration. The model of each subassembly in the core regions is rather detailed to represent all the relevant geometric characteristics and positions. Fuel subassembly orifices were set-up based on mass flow rate data and overall dynamic pressure drops in the nominal steady state.

CFD was used to model the XX09 instrumented fuel subassembly (FIG. 118). It was geometrically built on the nominal sizing of the pin, the wire and the wrappers dimensions. A collapsed model was adopted for wires and pins simulation, avoiding the contact point issue involved in heat transfer phenomena. The model has 11.5 million nodes and 47.8 million elements, which represents a compromise between number of nodes and accuracy for transient analysis. The computational domain includes: 1) the fuel pins (red); 2) the cladding (grey); 3) the sodium region (light blue); 4) the solid structure of the hexagonal wrapper (yellow); 5) the sodium in the thimble region (blue); 6) the solid structure of the hexagonal wrapper (orange); and 7) the bypass fluid region (purple) shared with the other subassemblies of the core, simulated as a thin fluid region with symmetric boundary conditions on its external surfaces. Unstructured tetrahedral mesh elements were employed for all bodies of the model except for the fuel, where the elements were semi-structured. The working fluid is sodium, using RELAP5-3D[®] physical properties. The buoyancy effect in the subchannels was neglected because the influence of this phenomenon on the final results is negligible for a dimensionless analysis ($R_{itr} \ll 1$).

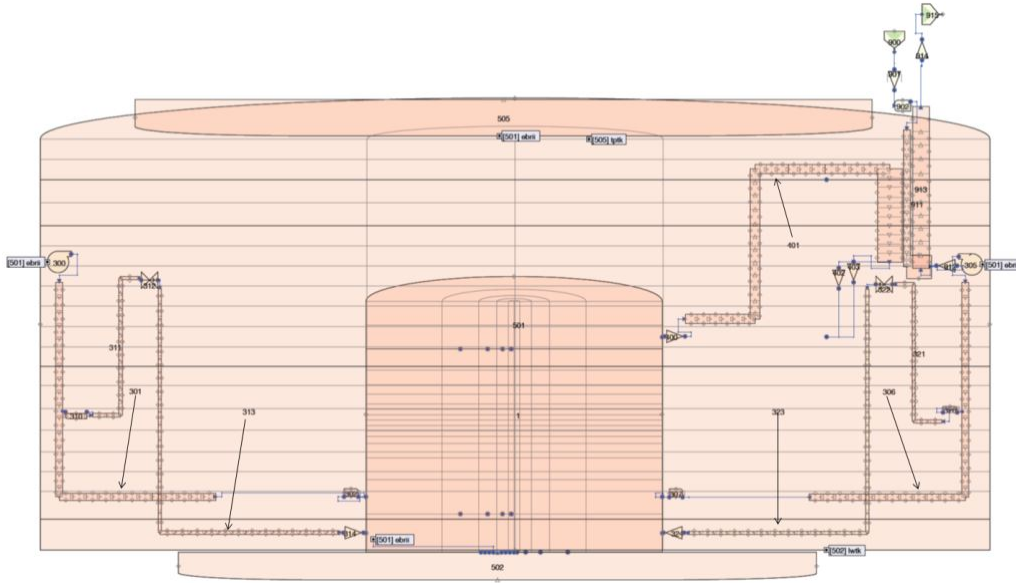


FIG. 116. Overall RELAP5-3D[®] EBR-II nodalization.

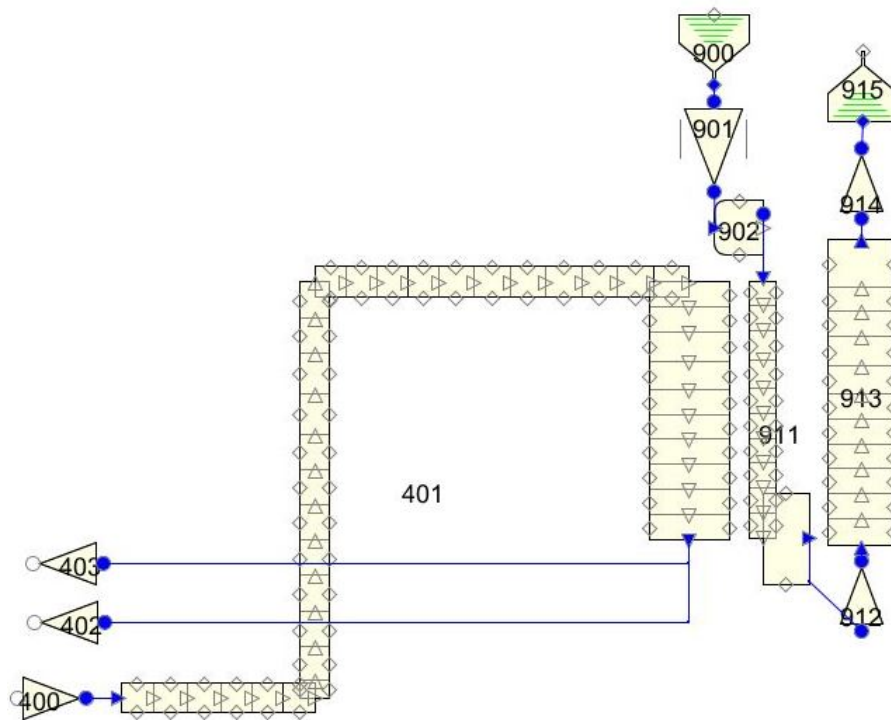


FIG. 117. RELAP5-3D[®] EBR-II nodalization for Z-Pipe and IHX primary and secondary sides.

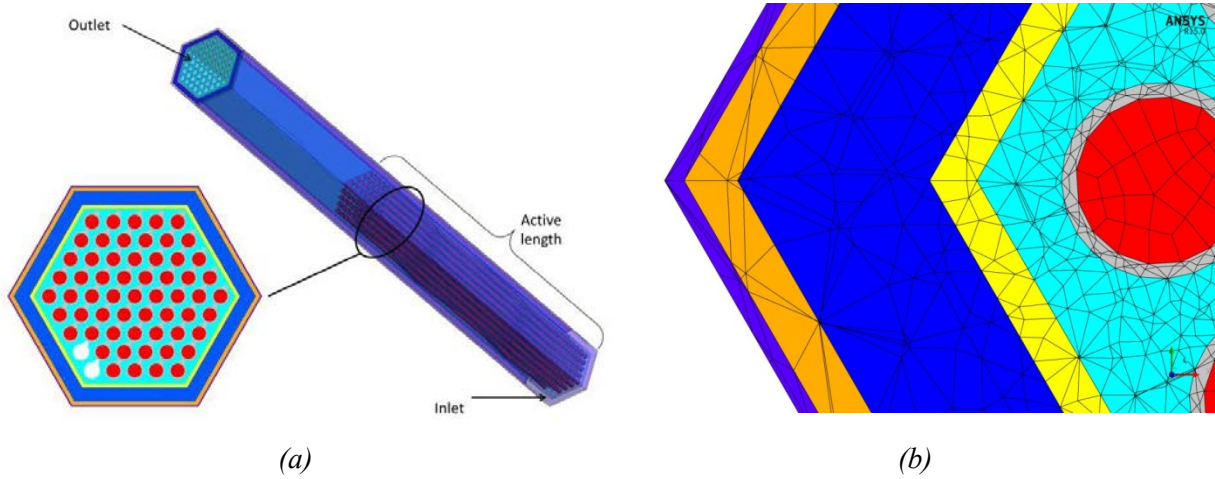


FIG. 118. CFD model of XX09: (a) overall sketch, (b) detailed view of the computational mesh.

7.7.2. Nuclear and thermo-physical data/correlations

Pressure drop in the rod bundle was evaluated using Cheng and Todreas correlations [103] for laminar, turbulent and transition flows (the transition zone in RELAP5 is $2200 < Re < 3000$).

$$f_L = \frac{C_{fL}}{Re} \quad Re < Re_L$$

$$f_T = \frac{C_{fT}}{Re^{0.18}} \quad Re > Re_T$$

$$f = f_L(1 - \varphi)^{\frac{1}{3}} + f_T\varphi^{\frac{1}{3}} \quad Re_L < Re < Re_T$$

where

$$C_{fL} = \left[-974.6 + 1612 \frac{p}{d} - 598.5 \left(\frac{p}{d} \right)^2 \right] \left(\frac{h_w}{d + d_w} \right)^{0.06 - 0.085 \frac{p}{d}}$$

$$C_{fT} = \left[0.8063 - 0.9022 \log_{10} \left(\frac{h_w}{d + d_w} \right) + 0.3526 \left[\log_{10} \left(\frac{h_w}{d + d_w} \right) \right]^2 \right] \left(\frac{p}{d} \right)^{9.7} \left(\frac{h_w}{d + d_w} \right)^{1.78 - 2 \frac{p}{d}}$$

$$\varphi = \frac{\log_{10} Re - 1.7 \frac{p}{d} - 0.78}{2.2 - \frac{p}{d}}$$

d is the rod diameter, d_w the wire diameter, and h_w the axial length of the wire wrap.

The heat transfer correlation for non-bundles ([26], [104]) used by RELAP5-3D[®] is:

$$Nu = 5.0 + 0.025Pe^{0.8}$$

where Pe is the Peclet number. This correlation is applicable for fully developed flow of liquid metal in a tube with constant temperature.

The heat transfer correlation for bundles is the Westinghouse correlation:

$$Nu = 4.0 + 0.33 \left(\frac{p}{D}\right)^{3.8} \left(\frac{Pe}{100}\right)^{0.86} + 0.16 \left(\frac{p}{D}\right)^5$$

where p is the rod pitch and D the rod diameter. The correlation is developed for a range of pitch-to-diameter ratio from 1.1 to 1.4 and Pe from 10 to 5000 [26].

7.7.3. Thermal hydraulics methods and models

7.7.3.1. Code(s) used

The codes used included the RELAP5-3D[®] ([24], [25], [26]) system analysis code and the ANSYS CFX 15.0 [61] CFD code.

7.7.3.2. Basic method

The RELAP5-3D[®] code is based on a nonhomogeneous and non-equilibrium model for a two-phase system that is solved by a semi-implicit numerical scheme with staggered grid and upwind discretization of the convective terms. It is based on a two-fluid model for two-phase flow with a flow regime based modelling of interfacial transport processes for mass, momentum and energy.

The ANSYS CFX 15.0 code employs a coupled technique which simultaneously solves all the transport equations in the whole domain through a false time-step algorithm. The linearized system of equations is reconditioned in order to reduce all the eigenvalues to the same order of magnitude. The multi-grid approach reduces the low frequency error, converting it to a high frequency error at the finest grid level; this results in a great acceleration of convergence.

The SST (Shear Stress Transport) $k-\omega$ model by Menter is extensively used in this context. It is formulated to solve the viscous sub-layer explicitly, and requires several computational grid points inside the sub-layer. The model applies the $k-\omega$ model close to the wall and the $k-\varepsilon$ model (in a $k-\omega$ formulation) in the core region, with a blending function in between. It was originally designed to provide accurate predictions of flow separation under adverse pressure gradients, but it has since been applied to a large variety of turbulent flows and is now the default and most commonly used model in CFX-15 and other CFD codes.

The SST model adopts the eddy diffusivity approach for momentum transport. Regarding heat transfer, the $k-\omega$ family turbulence model adopted in this context uses, coherently with the classical turbulence theory, the well-known analogy between turbulent transport of momentum and energy, i.e. a Reynolds analogy re-proposed at a turbulence level; for the turbulent thermal diffusivity Γ_t :

$$\Gamma_t = \frac{\mu_t}{Pr_t}$$

where Pr_t is the turbulent Prandtl number, which is of the order of 1 for liquid metals. It has been kept constant and fixed to 1.0 for sodium in this case.

7.7.4. Blind results

7.7.4.1. SHRT-17

RELAP5-3D[®] blind results for SHRT-17 [105] (steady state and transient) were carried out on the basis of the initial and boundary conditions delivered to the benchmark participants.

Steady state conditions were achieved, with minor differences with respect to the test specifications (TABLE 10). The results of the main parameters present a qualitative agreement with the experimental data, especially from 0 to 70 s. The main differences are observed at low flows, when the primary pumps have coasted down. In particular, the calculated mass flow rates show an overestimation with respect to the experimental trends (FIG. 119). This causes an underestimation of coolant and cladding temperatures in the instrumented subassemblies (FIG. 120 and FIG. 121). This can be explained by the uncertainty in setting the orifice coefficients at the inlet of the fuel subassemblies (not provided in the specifications) and with the unknown behaviour of the rotor of the pumps, once stopped (i.e. locked or free rotors). Differences are also observed in the upper plenum coolant temperatures (FIG. 122), because of the occurrence of stratification.

TABLE 10. EBR-II, RELAP5-3D[®]: STEADY STATE COMPARISON

#	Parameter	Unit	Exp	Blind Calc	Open Calc
1	Core Driver thermal power	MW(th)	52.28	52.28	52.28
2	Core Blanket thermal power	MW(th)	5.02	5.02	5.02
3	Core inlet temperature	K	624.15	625.6	625.9
4	Core outlet temperature	K	--	730.3	720.9
5	IHX SS inlet coolant temperature	K	574.2	574.2	574.2
6	MCP1 mass flow rate	kg/s	233.5	231.2	233.8
7	MCP2 mass flow rate	kg/s	233.2	230.9	233.8
8	Core Driver mass flow rate	kg/s	387.0	384.6	389.9
9	Core Blanket mass flow rate	kg/s	65.2	66.0	65.9
10	IHX SS mass flow rate	kg/s	311.4	311.4	311.4
11	Primary pressure @ MCP out	kPa	441.2	452.5	473.0
12	Primary pressure @ Upper Plenum	kPa	213.9	217.1	210.6

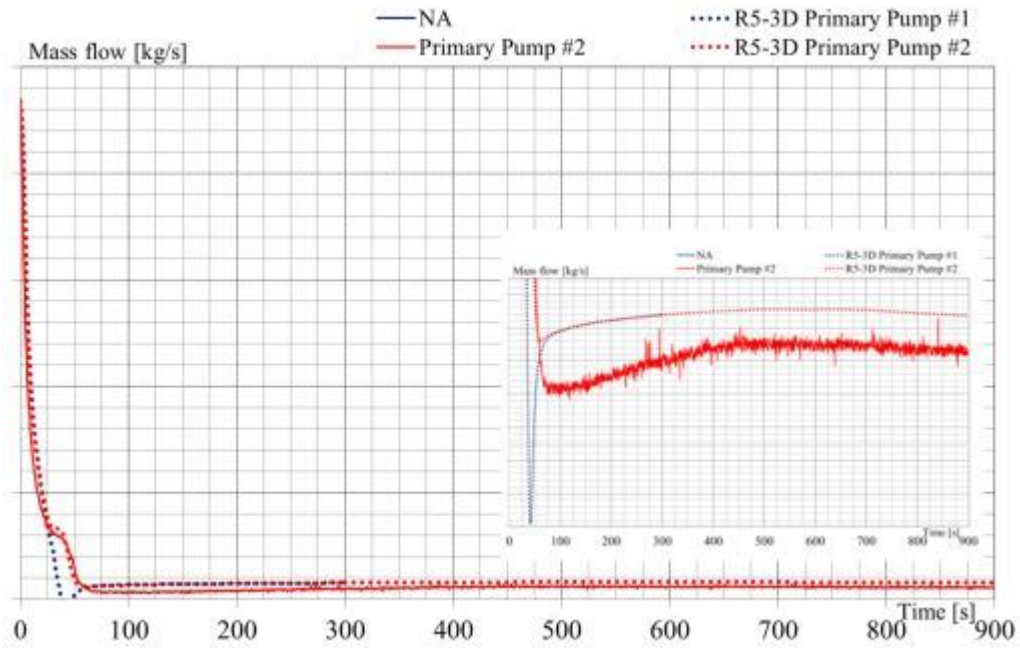


FIG. 119. Primary pumps mass flow rate, blind results.

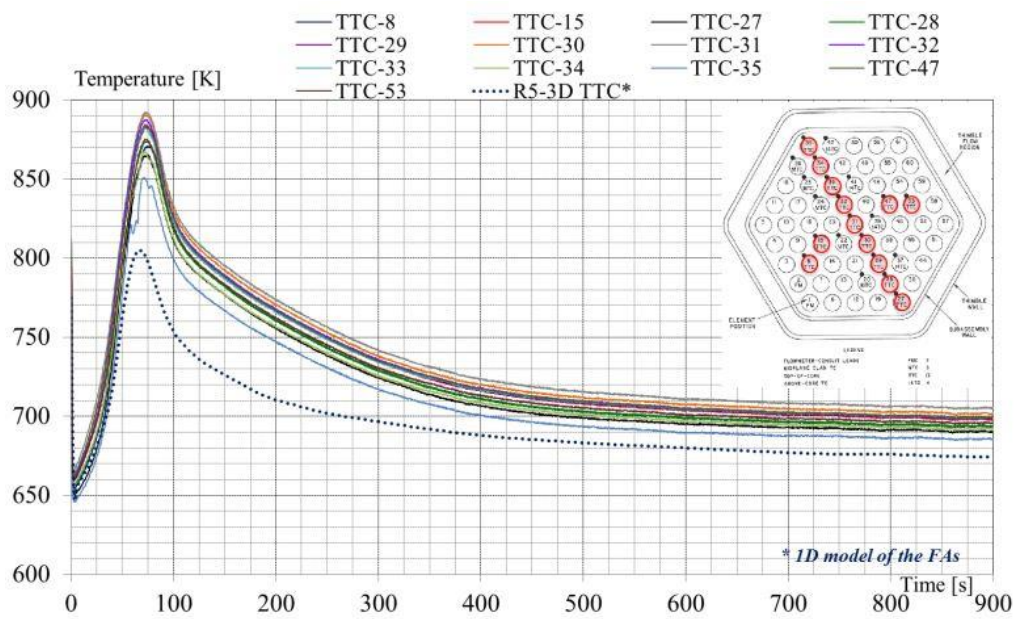


FIG. 120. XX09 top of core temperatures, blind results.

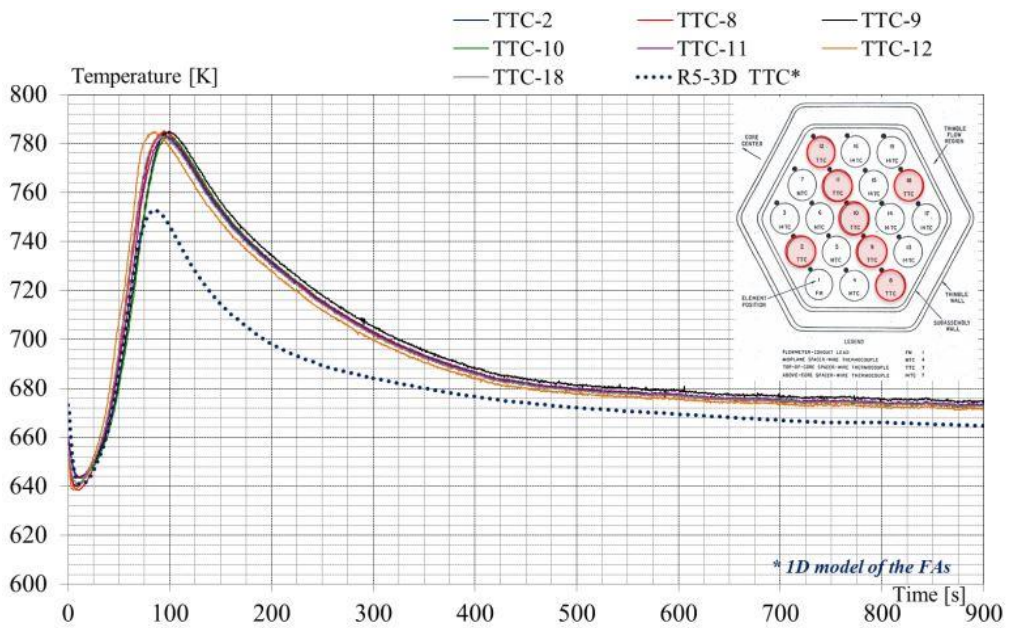


FIG. 121. XX10 top of core temperatures, blind results.

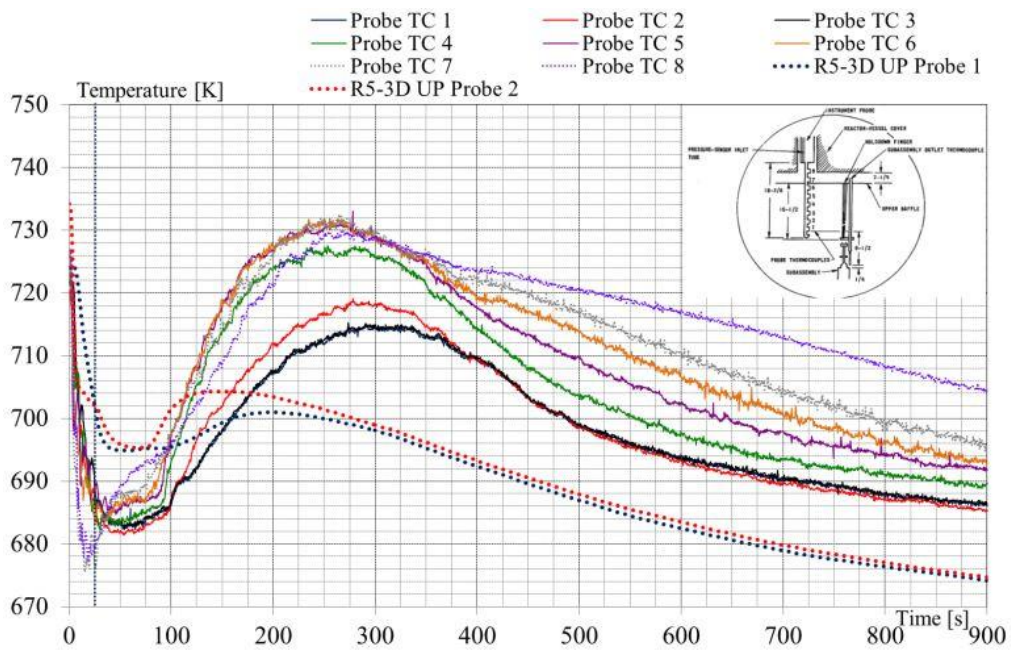


FIG. 122. Upper plenum temperature, blind results.

7.7.4.2. SHRT-45R

ENEA did not analyze the SHRT-45R transient.

7.7.5. Final CRP results and comparisons with the experimental data

7.7.5.1. SHRT-17

The steady state results are compared against the experimental data in TABLE 10: a few minor deviations are observed [105]. Three phases are identified in the transient: the first phase corresponds to the effective core cooling during pump coastdown; the second is characterized by the primary system energy increment and temperature rise; in the third phase, buoyancy forces are effective in removing energy, and natural circulation stabilizes. The main parameter trends are satisfactory during the first phase: the convective heat transfer between the core structures and the coolant was correctly calculated by the code. During phase 2, enhancements are related to the proper calculation of pressure drops in the subassembly inlet orifices (properly set using the experimental data) and in the wire-wrapped fuel bundles (i.e. Cheng and Todreas correlations).

The timing and rates of coolant and cladding temperature increases in the core were qualitatively and quantitatively well predicted in the final results. The results show an excellent simulation of the mass flow rates measured in the high and low pressure lines (FIG. 123), as well as of the mass flow rates in the available instrumented subassemblies XX09 and XX10. Experimental cladding and coolant temperatures were simulated with satisfactory accuracy, in particular when the safety-relevant parameters are considered (FIG. 124 and FIG. 125). Nevertheless, some quantitative differences are observed. In the upper plenum (FIG. 126) of the reactor zone, the measured temperature trends are connected with the coolant thermal mixing and stratification phenomena, which cannot be accurately predicted by the RELAP5-3D[®] code. These phenomena are influenced by the nodalization scheme, and thus sensitivity analyses were performed.

The results of the simulation predicted correctly the third phase: coolant temperature at the core outlet, and thermal structures in the core zone were cooled down as natural circulation was stabilized. Improved quantitative accuracy is observed in the final results, thanks to a better simulation of natural circulation flow.

ANSYS CFX v15.0 was used to perform a detailed CFD steady state and transient simulation of the XX09 subassembly. The simulation was limited to the first 100s of the test. The boundary conditions adopted are from the benchmark specifications and from the RELAP5-3D[®] simulation results (i.e. single-way coupling). Post-processing temperature distributions show good agreement with the experimental values (FIG. 127). Some differences still remain for the radial temperature profiles, due to asymmetric thermal behaviour of the neighbouring fuel subassemblies (challenging for the simulation) influencing the bypass flow temperature. The CFD model was based on a symmetric boundary condition on the external surfaces of the bypass region. This implies that asymmetric effects from the neighbouring fuel subassemblies were neglected.

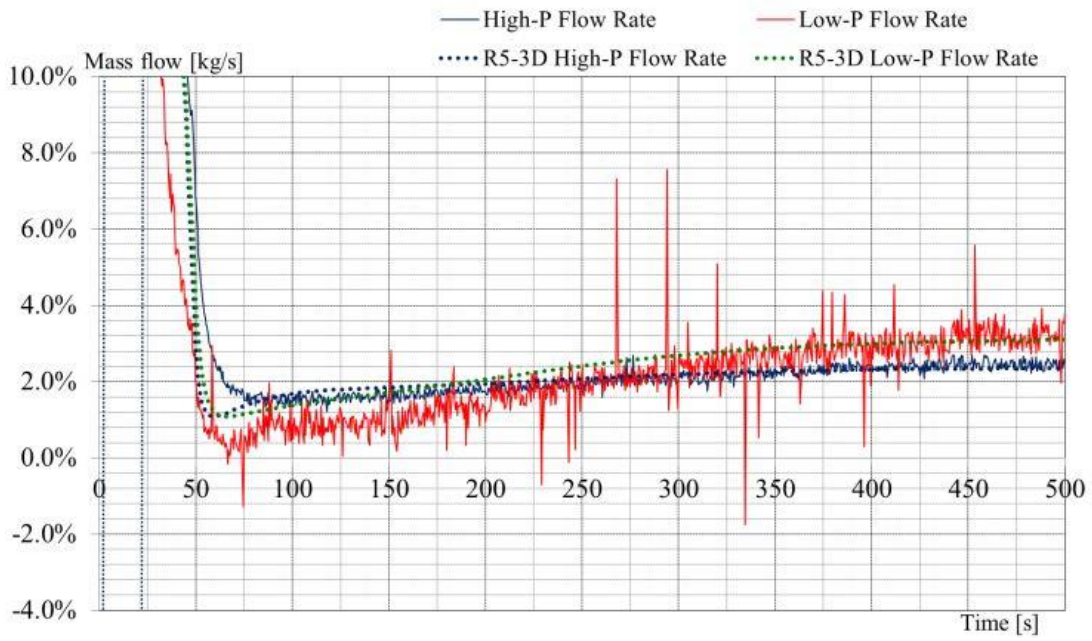


FIG. 123. High- and low pressure mass flow rates, final results.

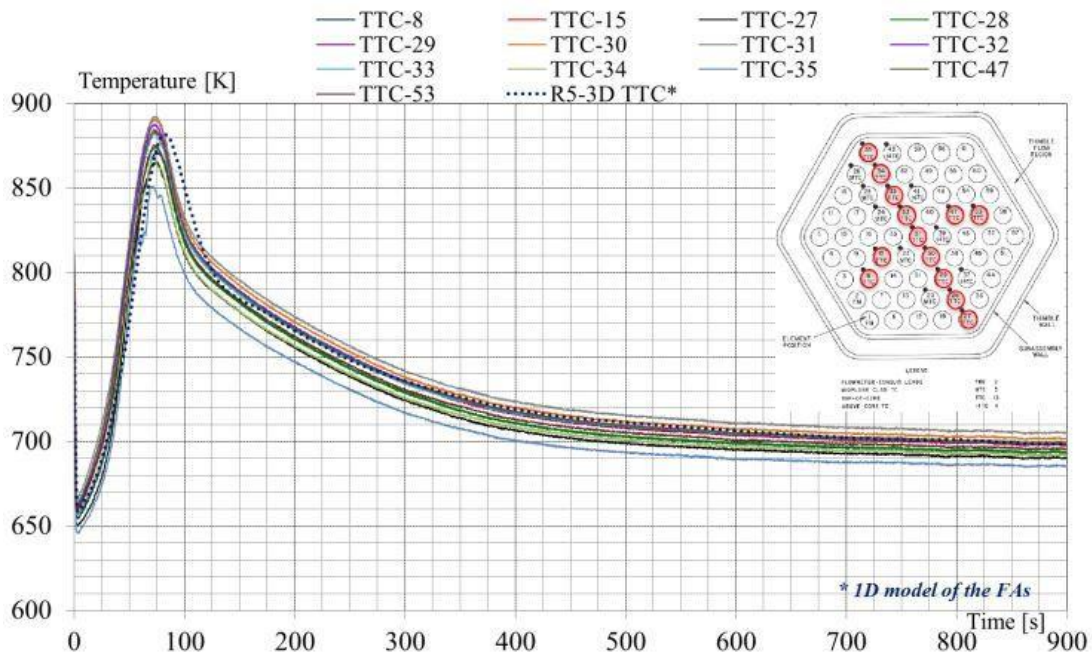


FIG. 124. XX09 cladding temperatures at top of active core, final results.

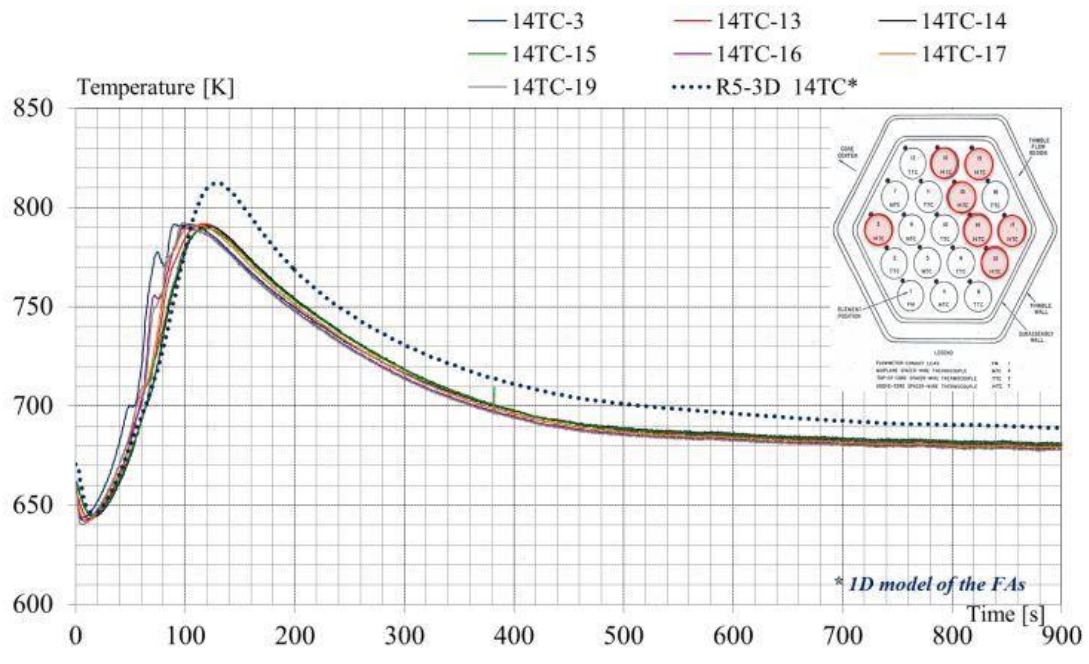


FIG. 125. XX10 cladding temperatures at top of fuel bundle, final results.

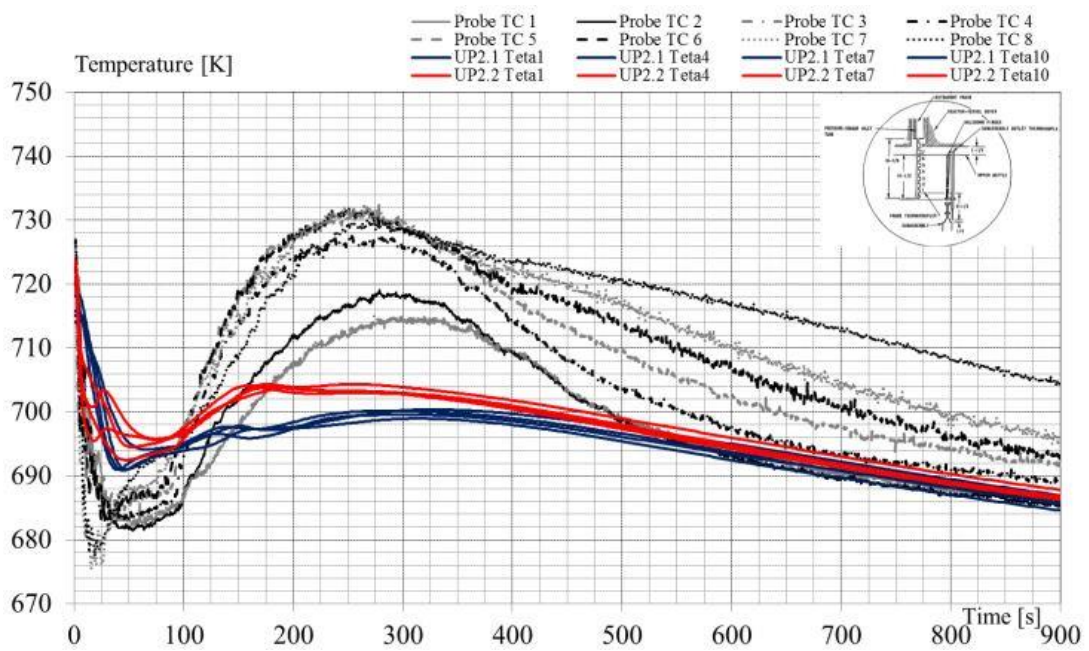


FIG. 126. Upper plenum coolant temperatures, final results.

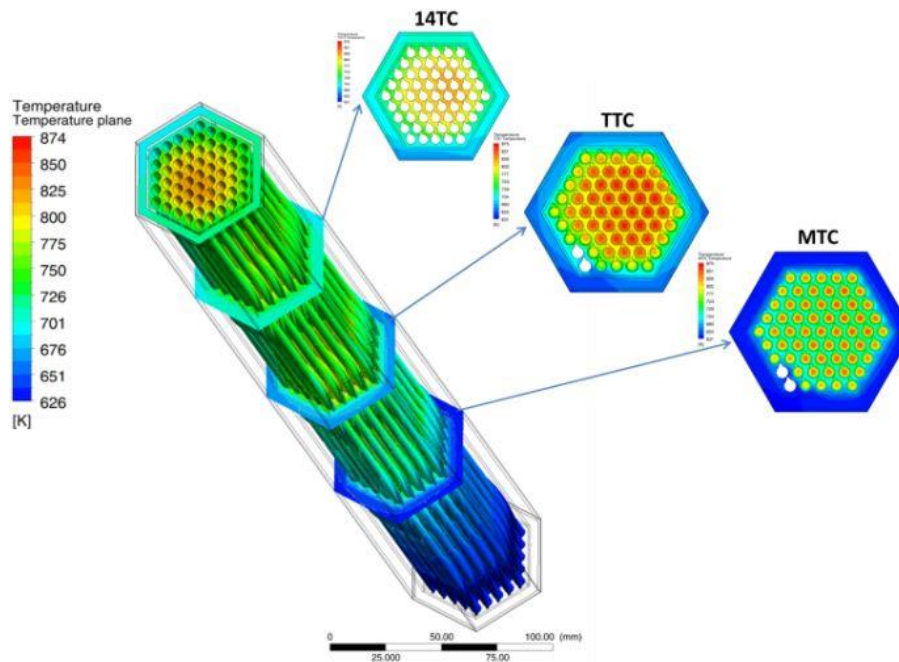


FIG. 127. CFX steady state results for XX09 temperatures.

CFD results for the mid-core plane MTC in the transient simulation present good agreement with experimental results (FIG. 128), with a peak in the clad temperature of about 810 K at 65 s. There is a shift in time of 3–4 s on the maximum clad temperature prediction. Cladding temperatures at the top of the core plane (TTC) were in agreement with experimental results for $t < 45$ s. From 45 on, the maximum clad temperature was overestimated and showed a delay of about 10–15 s. In the mixing region, 14TC, the agreement with experimental data was good up to 70 s. After, there was an overestimation of the peak (60 K) and a delay (5 s).

7.7.5.2. Model improvements

The final simulation of test SHRT-17 was carried out with a few modifications, as hereafter specified:

- (a) The pressure drops at the subassembly orifices were set-up consistent with the experimental results of the test. Dependence of energy loss coefficients on the Reynolds number was taken into account to improve the prediction of the mass flow rate in the subassembly;
- (b) A “free rotor” was assumed in the blind calculation, whereas “locked rotor” conditions were imposed in the final calculation;
- (c) The Cheng and Todreas correlations were implemented to model friction losses in the wire-wrapped fuel bundle region;
- (d) The orientation of the core with respect to the high and low pressure line connections was corrected to be consistent with the real configuration, thanks to updated information delivered by the benchmark coordinators;
- (e) Correct sodium table proprieties were used: the “default” table was used in the blind calculation, whereas the “tpfna2” table was used in the final calculations (as suggested in the user manual).

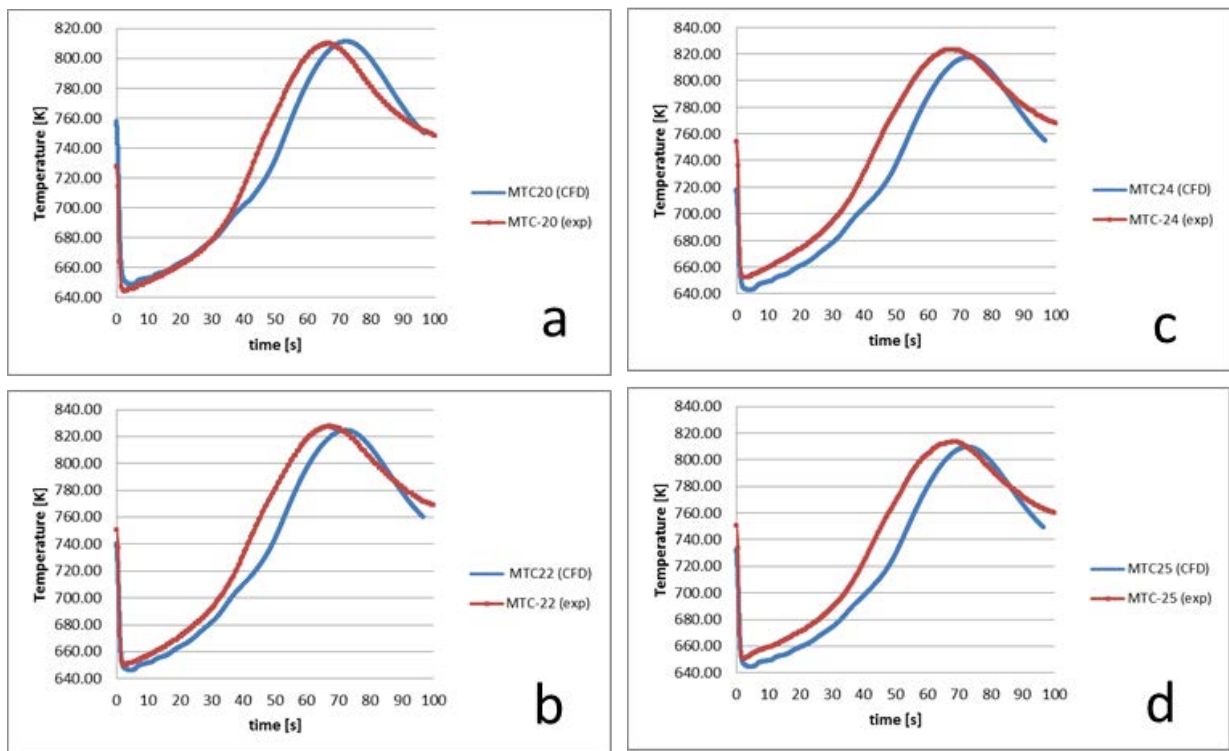


FIG. 128. CFX XX09 cladding temperatures at the middle of the fuel bundle.

7.7.6. Neutronics methods and models

7.7.6.1. Code(s) used

- (a) MCNP6;
- (b) SCALE 6.1.2 release;
- (c) PHISICS, version under development (alpha testing).

7.7.6.2. Neutron and photon cross-sections

The reference tool chosen to calculate the EBR-II cross-sections was SCALE6.1.2. The 238-group cross-section library based on ENDF/B-VII was selected. The CENTRM module was used for the self-shielding calculations. CENTRM calculates problem-dependent, group-averaged cross-sections, using as weight the flux calculated by solving the 1-D Boltzmann transport equation with a continuous energy cross-section library. For the present work, a 33-energy group structure, used also by the ERANOS code, was used for the few-groups homogenization.

Since EBR-II has a heterogeneous core structure, many different 2-D SCALE models were used to calculate the final cross-section library. The “B1” critical spectrum search option was used after the transport calculations to generate the homogenized constants. The 97 core subassemblies were modelled using 75 collapsed compositions. Three layers were used for taking into account the axial burnup and temperature variations. As shown in FIG. 129, several SCALE models were developed for each composition.

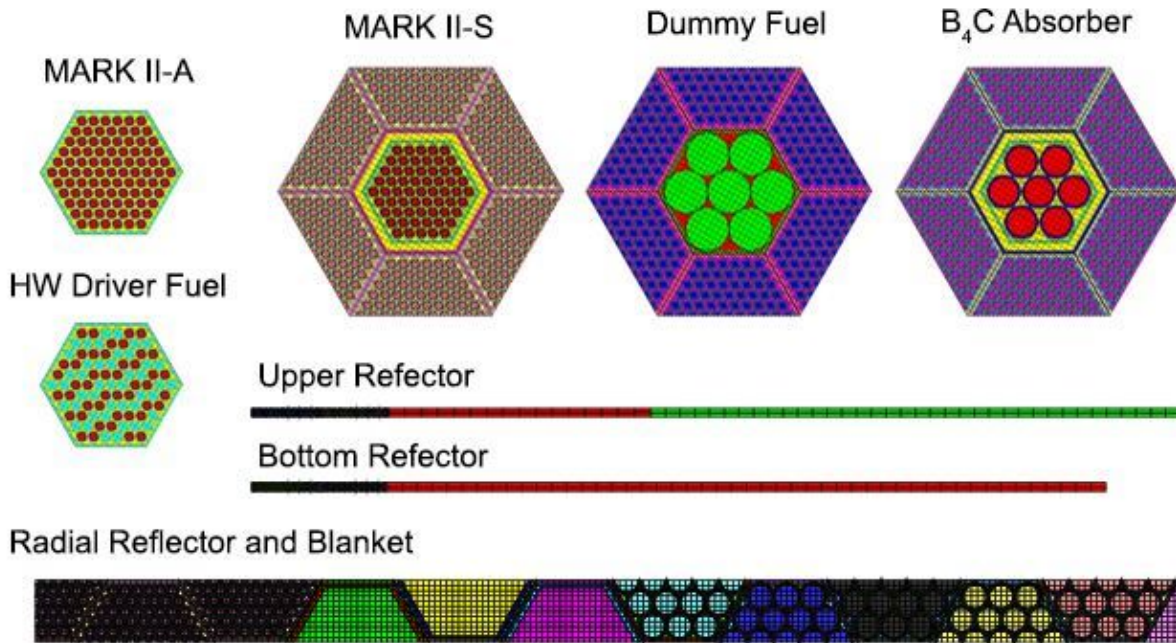


FIG. 129. SCALE models for lattice calculations.

The MARK-IIA and half-worth driver fuel models consisted of a single subassembly with reflective boundary conditions. The MARK-IIS subassembly and all the non-fissile subassemblies, however, were calculated using a super-cell model composed of seven subassemblies. The central subassembly was collapsed, the remaining six (driver subassembly with an average fuel composition) were used to generate a neutron flux with a spectrum as similar as possible to the real one. The radial reflector and the blanket subassembly constants were calculated using a mini-core model composed of parts of the core itself, of the radial reflector and of the blanket. Top and bottom reflectors were calculated using two simple models composed of a section of three subassemblies (almost half core) followed by the homogenized reflector materials. Two homogenized materials were used, the first to take into account the plenum zone of the fuel pins and the second all the components above the fuel pins (upper shield sodium, etc.).

7.7.6.3. Calculation of power and k_{eff}

The 33-group cross-section library (75 cross-sections for the active fuel materials and 23 for non-fissile material) was implemented in the 3-D neutron kinetic (NK) PHISICS model to perform three-dimensional core calculations. Fifteen rings of subassemblies plus the central subassembly were used, totaling 721 radial nodes. Axially, 32 mesh cells were used with a variable length from 2 to 6 cm to take into account the extreme heterogeneity of the reactor. The full model was composed of 24 072 neutronic nodes. Calculations were performed using the P1-diffusion approximation. In FIG. 130 the PHISICS full 3-D NK model (left), and the inner core model (right) are shown. No gamma transport was taken into account.

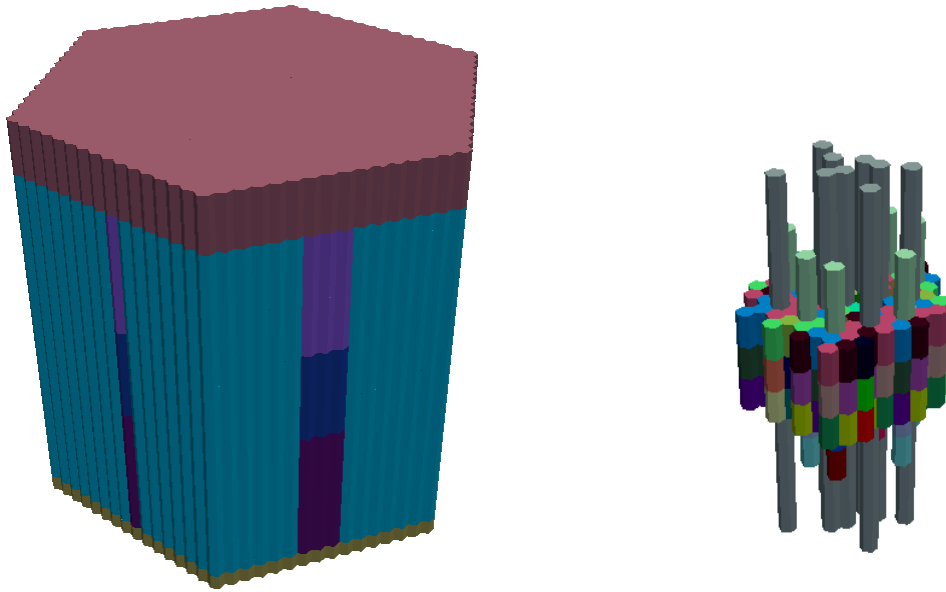


FIG. 130. PHISICS EBR-II 3-D-NK model, full (left) and central core (right).

Monte Carlo static 3-D NK calculations were performed. The purpose of this activity was to obtain a detailed reference solution by evaluating neutronic parameters such as k_{eff} , reactivity coefficients, power and flux distributions. These data were used for validating the multigroup cross-section libraries and the PHISICS code deterministic model. The tool chosen for the static neutronic analysis was the Monte Carlo neutron transport code MCNP6. The EBR-II core is a very heterogeneous system, requiring simulation of the different hexagonal subassemblies composing the core (61 subassemblies), the inner blanket (66 subassemblies) and the outer blanket (510 subassemblies), the control and safety subassemblies, etc. MCNP6 made it possible to perform a neutron transport simulation without introducing significant geometry simplifications. Detailed subassembly modelling was performed, up to the pin-level. A detailed view of the driver and of the core periphery (interface with the stainless steel reflector) is shown in FIG. 131. The lower and upper parts of the core were also modelled in detail, in order to take into account realistic axial neutron leakage effects. H-shaped cylindrical plugs and sodium volumes are shown in FIG. 132.

Material temperatures and core dimensions of the MCNP model are for hot full power conditions (HFP) (MCNP6 HFP conditions in TABLE 11). The same dimensions and material densities were used to build the corresponding deterministic PHISICS model (PHISICS HFP conditions in TABLE 11). In addition, in order to understand the influence of the material expansion from a cold zero power condition, another deterministic model was developed, considering the non-thermally expanded geometry (PHISICS CZP dimensions in TABLE 11).

7.7.6.4. Calculation of reactivity feedback

The reactivity feedbacks were calculated using both the MCNP6 and the two PHISICS models, by perturbing the input parameters according to the specifications. The number of mesh cells in the deterministic models was preserved, changing only the mesh height. It should be noted that the temperature difference used for scaling some of the reactivity coefficients was calculated by:

- (a) deriving the equivalent temperature difference from the RELAP5-3D[®] sodium thermodynamic tables, when calculating the coolant density coefficient;
- (b) using a temperature difference corresponding to 10% (axial) and 1% (radial) expansion of the fuel, when calculating the expansion coefficients.

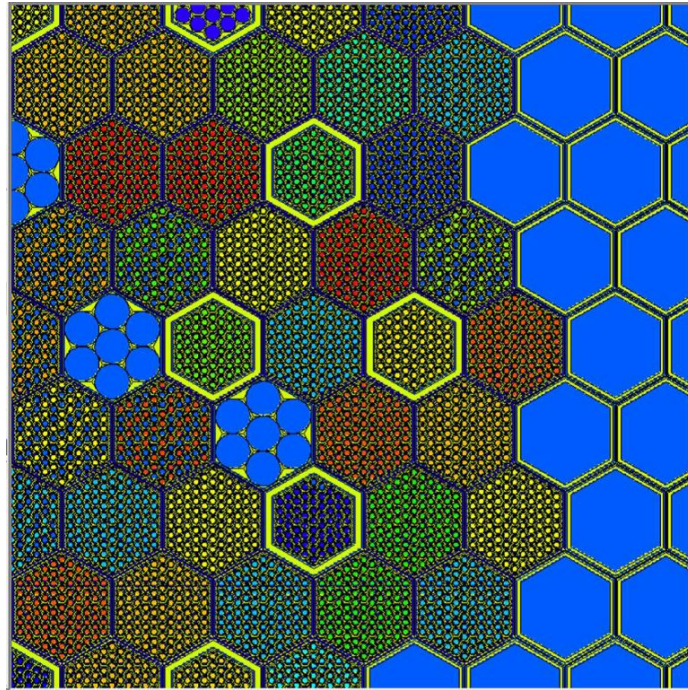


FIG. 131. Detail of core modelling – driver/SS reflector interface.

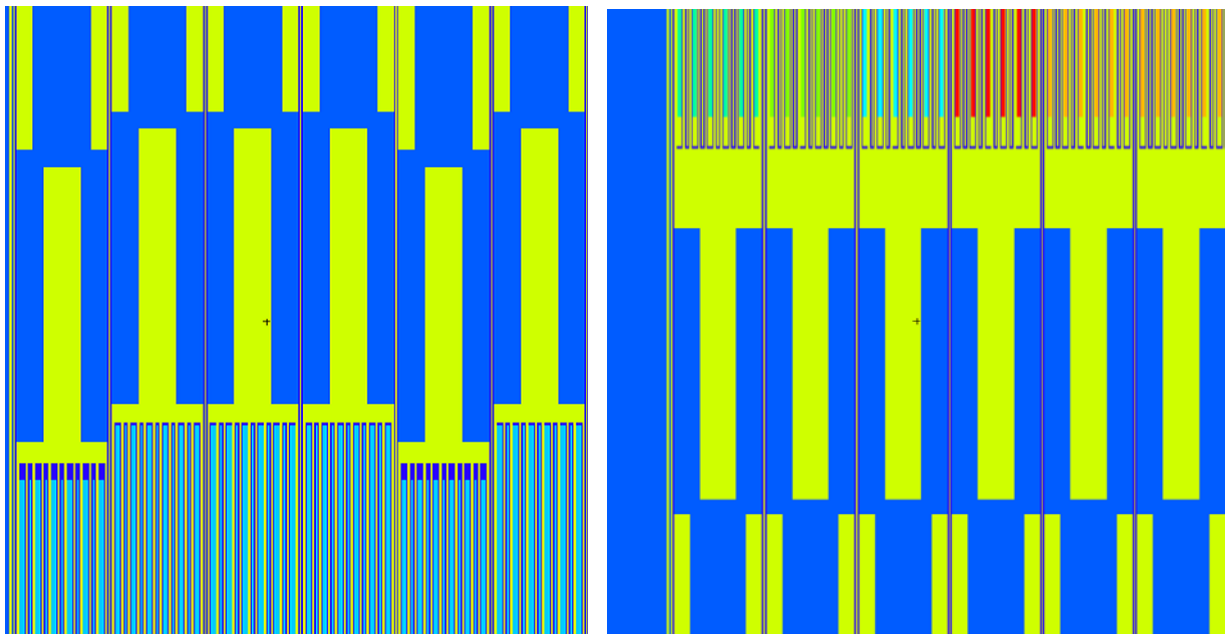


FIG. 132. Top and bottom reflector modelling – subassembly steel plugs.

TABLE 11. PHISICS, MCNP NEUTRON KINETIC RESULTS

Parameter	MCNP6	PHISICS	PHISICS
	HFP conditions	HFP conditions	CZP dimensions
k_{eff}	0.99667±0.00007	1.00004	1.00612
β_{eff}	0.00685±0.00010	0.00694	0.00692
Doppler (pcm/K)	-0.060±0.020	-0.069	-0.069
Sodium density (pcm/K)	-1.813±0.041	-2.355	-1.608
Axial expansion (pcm/K)	-0.514±0.003	-0.444	-0.576
Radial expansion (pcm/K)	-1.605±0.027	-2.263	-1.726

7.7.7. Neutronics results

In TABLE 11 the NK calculation results are reported. Comparison between the MCNP6 and PHISICS models at hot full power conditions shows acceptable agreement. The difference between the two values of k_{eff} is 337 pcm, a reasonable difference considering that the MCNP6 model is geometrically very detailed and uses continuous energy cross-sections, while the PHISICS model is a nodal model and uses a 33 broad group cross-section library. The β_{eff} values and the Doppler coefficient of the deterministic model are into the uncertainty range of the MCNP6 results. By contrast, the deterministic model overestimates the sodium density and radial expansion coefficients. The difference between Monte Carlo and PHISICS for the perturbed cases used for the calculations of these coefficients is of the same magnitude as the difference obtained for the hot full power criticality calculations (around 300 pcm). Conversely, the axial expansion coefficient is slightly underestimated.

The results obtained using the deterministic model with cold zero power dimensions give back very different results. The core from a near critical configuration became almost prompt critical and the sodium density and radial expansion coefficients showed a decrease of about 40%. The axial expansion coefficient slightly increased. The radial power shape and the relative error with respect to the reference solution in the specification are given in FIG. 133. The average absolute error was about 6%, but in some subassemblies, e.g. in the half-worth driver subassemblies, the error reached about 25%. This large discrepancy could be associated with a poor approximation for the boundary conditions (reflective boundary conditions) used when performing lattice calculations. This approximation is not valid when the driver subassemblies are bordering several non-fuel subassemblies (e.g., in the central zone of the core).

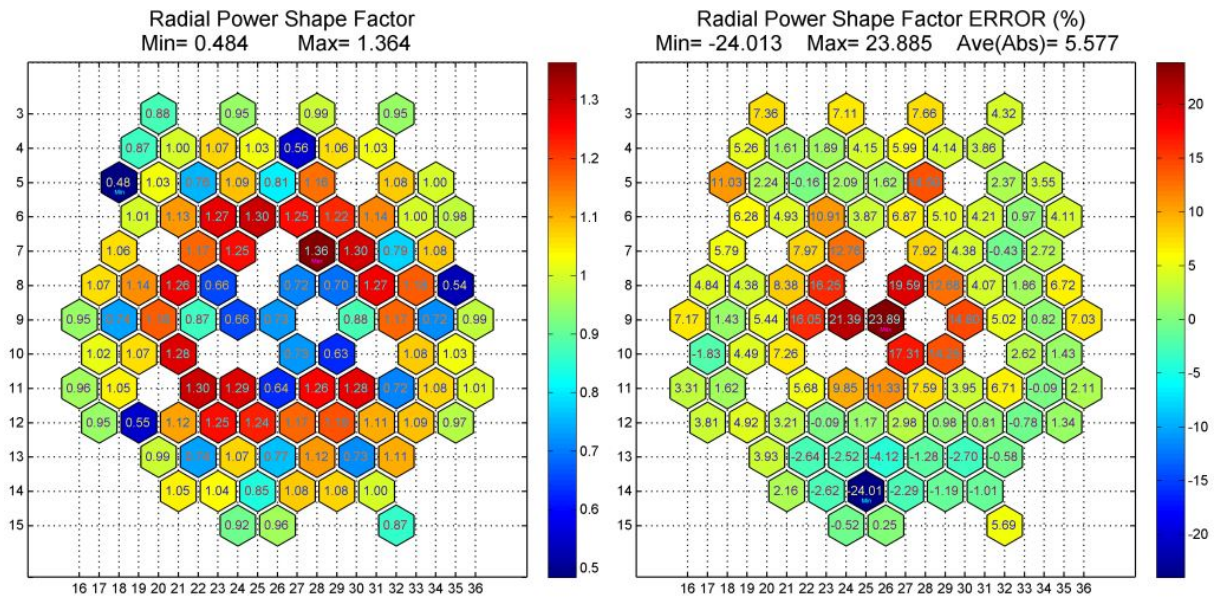


FIG. 133. PHISICS HFP DIM model radial power shape factor and relative error.

7.8. NUCLEAR AND INDUSTRIAL ENGINEERING (ITALY)

The EBR-II benchmark specifications and designs were used to develop the thermal hydraulic model of the reactor. The RELAP5-3D system thermal hydraulic code was used for preparing the nodalization.

7.8.1. Geometry/discretization

A detailed nodalization reproducing each geometrical zone of the reactor was developed. Basically, the model can be divided into two parts: the core, which consists of the central core, inner blanket and outer blanket regions, and the coolant system, which includes the pool and the remaining part of the primary sodium circuit (i.e. high and low pressure piping, pumps, inlet plena, upper plenum, Z-Pipe, IHX and the secondary side).

The whole core region consists of 96 channels, representing all 10 types of subassemblies used in the reactor, and two bypasses. The core was divided into 16 rows, according to the real geometry of the EBR-II core. The first 6 rows that represent the central core region were modelled individually (1 subassembly per channel) with 81 channels, except for the safety/control rods, which were combined into one channel. Rows 7 to 16 consist of reflector or blanket subassemblies, and they were modelled with one channel per type of subassembly in each row. Each channel is made up of 36 thermal hydraulic volumes, where the active part of the reactor core has 24 volumes. From both the hydraulic and the thermal point of view, the core is divided into two zones: the central core region simulating the driver subassemblies and the external core region representing the reflector and blanket subassemblies. The heat structures for each subassembly in the central core region consist of:

- 1 heat structure component used to simulate the active part of the fuel pins;
- 1 heat structure component used to model the non-active part of the fuel pins and the steel rods (if present);
- 1 heat structure component used to model the gas plenum;

- (d) 6 heat structure components to represent each edge of the subassembly walls.

The pin power profile imposed on the active heat structures was assumed to be flat and constant along the entire active length. In the second phase of the benchmark, an axial power profile was also assumed below and above the active part of the fuel, to take into account gamma heating. The heat structures in the inner and outer blanket regions were modelled with two heat structure components for each row, one to simulate the internal rods and the other one to represent the subassembly walls.

The pool was initially modelled with three parallel pipes connected above and below with two branch components and with all the nodes connected radially to simulate the mixing of sodium among them. In the second phase of the benchmark the three pipes were replaced with a cylindrical multidimensional component having 2 radial meshes, the internal one coinciding with the reactor vessel cover; 3 azimuthal meshes, thermally linked to the pumps or the IHX; and 72 axial meshes, to preserve the sliced approach adopted in the nodalization. The region of the 3-D pool occupied by the reactor vessel cover was blocked.

The pumps were modelled with a PUMP component, with the homologous curves implemented based on the specifications provided for the benchmark. The high and low pressure piping was modelled by one dimensional components (i.e. PIPE and BRANCH), as were the inlet plena, which were modelled using two sets of BRANCH components: one set for the high pressure plenum that feeds the central and expanded core regions (the first 7 rows), and the other set for the low pressure inlet plenum that feeds the outer blanket region.

Also the upper plenum and the Z-Pipe were modelled by one dimensional components: 6 BRANCH components simulated the upper plenum in a fictitious 3-D model and a PIPE component modelled the Z-Pipe, connected by two single junctions to the upper plenum and to the IHX.

The intermediate side of the EBR-II reactor was represented with the IHX, modelled as a counter-current flow-type heat exchanger. Both the primary side and the secondary side of the IHX were modelled by one dimensional components (i.e. PIPE and BRANCH). The boundary conditions of the secondary system were set according to the reactor design using TMDPVOL and TMDPJUN components.

7.8.2. Nuclear and thermo-physical data/correlations

From the hydraulic part of the model the standard RELAP5-3D thermodynamic properties of sodium were used. The thermal properties of the heat structures were derived from the benchmark specifications. No specific correlation was developed for the simulation.

7.8.3. Thermal hydraulics methods and models

7.8.3.1. Code(s) used

The EBR-II nodalization was developed using the RELAP5-3D V4.1.3 system thermal hydraulic code.

7.8.3.2. Basic method

The following general rules, among others, were adopted during the development of the RELAP5-3D nodalization of EBR-II:

- (a) The ratio between the volumes of two adjacent nodes shall be between 0.5 and 2;
- (b) The ratio between the lengths of two adjacent nodes shall be between 0.5 and 2;
- (c) To use a standard set of code options;
- (d) To use more than nine mesh points for simulating the heat structures of the fuel bundles;
- (e) To adopt the “slice technique” approach in order to improve the capability of the code and of the nodalization to simulate phases of transients involving natural circulation phenomena.

Regarding the last item, given the fact that the density of liquid sodium is much higher than water, a sliced approach was necessary for avoiding any kind of oscillations in the code calculation and unrealistic pressure differences among parallel flow paths. The sliced approach is a nodalization technique consisting of dividing the hardware in parallel slices in order to have the centres of each node in parallel pipes at the same elevation position. This is a good practice to better reproduce phenomena connected with natural circulation, where small gravitational head differences play a significant role.

7.8.3.3. *Model*

As default, the following RELAP5-3D models were adopted for the nodalization of EBR-II:

- (a) The non-equilibrium (unequal temperature) calculation was used;
- (b) The non-homogeneous (two-velocity momentum equations) option was activated;
- (c) Use of momentum flux in both the ‘to volume’ and the ‘from volume’;
- (d) The vertical stratification model was used for the volume;
- (e) The choking model was adopted (if a choked flow condition is predicted by the code);
- (f) The wall friction effects were computed along the x-, y- and z- coordinates of the volume.

7.8.4. **Blind results**

7.8.4.1. *SHRT-17*

After achieving acceptable steady state conditions, the blind transient calculation was performed. Starting from full power and flow, both the primary loop and intermediate loop coolant pumps were simultaneously tripped and the reactor was scrammed to simulate a protected loss of flow accident. In addition, the primary system auxiliary coolant pump, that normally had an emergency battery power supply, was turned off. The reactor core power and the intermediate side boundary conditions were imposed according to the benchmark specification.

At this stage of the benchmark, the EBR-II primary pumps were modelled identically (as can be seen from FIG. 134). During the MCPs coastdown (up to about 10 s) the cladding and the outlet coolant temperature decreased in both instrumented subassemblies (see FIG. 135 for XX09 and FIG. 136 for XX10) due to the sharp decrease in the nuclear fission power. During the transition from forced to natural circulation (between about 10 and 100 s), the imbalance between the total core power and the energy removed from the primary coolant caused a rapid increase in the cladding temperatures and a somewhat less rapid increase in the coolant

temperatures. Note that in instrumented subassembly XX10 the cladding temperatures increased in two distinct steps (see FIG. 136). As can be seen in FIG. 137, the calculated mass flow rate in subassembly XX10 became negative for about 130 seconds. Since the power generated in this subassembly is quite low compared to the others, the temperature increase is due mainly to the decrease of the mass flow rate and occurred in parallel with the flow reversal (i.e. when the mass flow rate became negative and vice versa). When natural circulation was fully established (after about 100 s) the total core power was efficiently removed in all subassemblies and the coolant and cladding temperatures decreased.

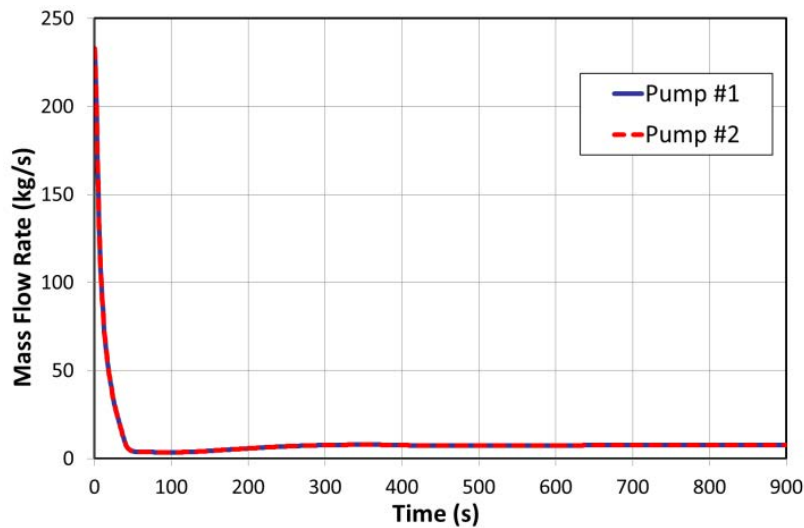


FIG. 134. SHRT-17 primary pump mass flow rates, blind results.

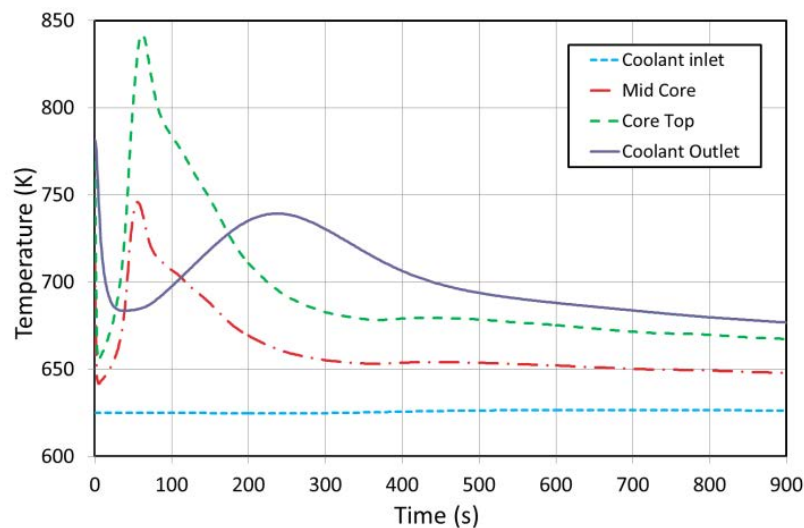


FIG. 135. SHRT-17 coolant and cladding temperatures of XX09, blind results.

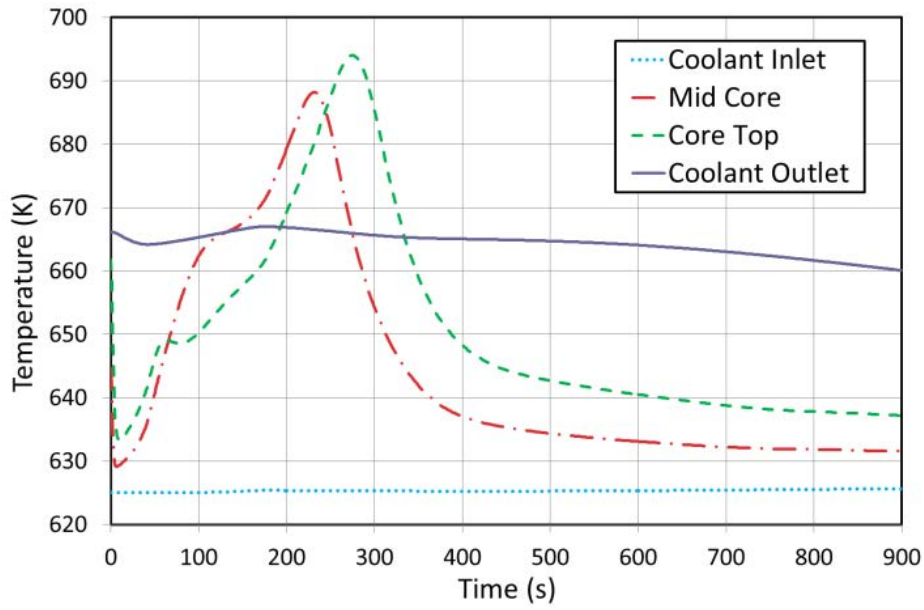


FIG. 136. SHRT-17 coolant and cladding temperatures of XX10, blind results.

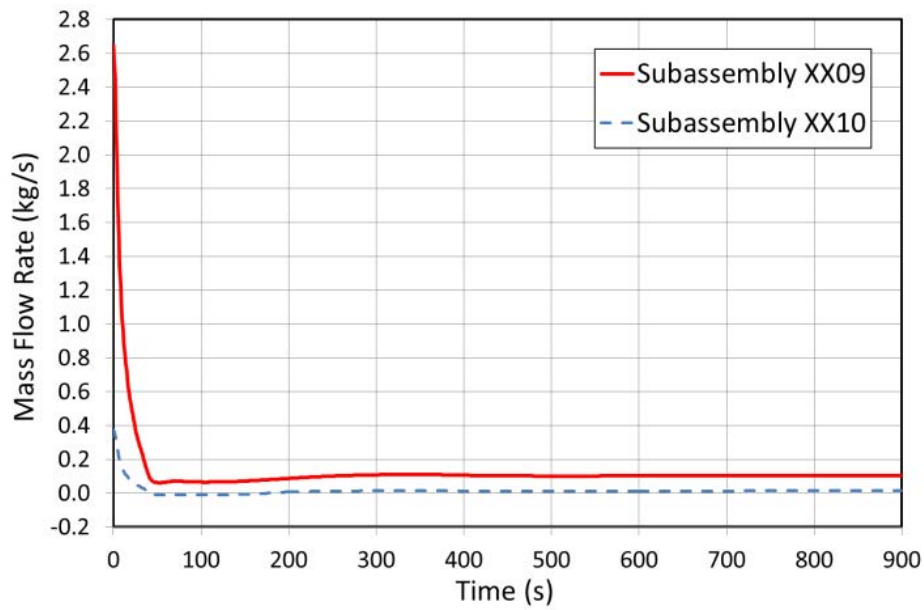


FIG. 137. SHRT-17 mass flow rates in XX09 and XX10, blind results.

7.8.4.2. SHRT-45R

N.IN.E. did not perform an analysis of SHRT-45R.

7.8.5. Final results, data comparisons

7.8.5.1. SHRT-17

The final results of the RELAP5-3D simulation of SHRT-17 are reported below. Among the various improvements developed for the final simulation, discussed in more detail in Section 7.8.5.2, the most significant concerns are:

- (a) *The mass flow rate:* the primary pumps were modelled as separate pumps, with the pump speeds updated according to the input specifications, and the energy loss coefficients in the subassemblies were improved, taking into account their dependence on the Reynolds number;
- (b) *The axial power distribution:* a power source was added below and above the active part of the fuel, to take into account gamma heating. This will be discussed in more detail in Section 8.3, where sensitivity analyses are covered.

Following the primary and intermediate pump trips and the reactor scram, the calculated mass flow rates decreased rapidly and the coolant and cladding temperatures started to increase. During the pump coastdown, the calculated mass flow rate in instrumented subassembly XX09 remained a little bit higher than the experimental data (see FIG. 138). This affected the coolant and cladding temperatures in the whole subassembly. Indeed, both the coolant temperatures below (FIG. 139) and above (FIG. 140) the active part of the rods and the cladding temperatures at the middle and at the top of the core (FIG. 141) were slightly lower than the experimental data. These small differences became negligible in the latter portion of the transient because the mass flow rate reached the correct value. It should be noted that the flowmeter temperatures, where the gamma heating occurred, were predicted well qualitatively by the code simulation.

Conversely, in instrumented subassembly XX10, the mass flow rate during the pump coastdown (FIG. 142) reached a slightly lower value compared to the experimental data, followed by a faster increase before it stabilized at the correct value. The effect of this flow prediction can be seen especially in FIG. 143, where the cladding temperatures at the middle and at the top of the core are shown. In both curves, the temperatures reached slightly higher peak values, followed by a bit faster decrease before reaching the correct value during the last half of the transient.

Regarding the coolant temperatures outside the active part of the core, since the power to flow ratio of subassembly XX10 is lower compared to the remaining subassemblies, the gamma heating and the heat conduction with the adjacent subassemblies play an important role in the temperature trends. Below the core, the predicted coolant temperature (see FIG. 144) remained a little bit lower than the experimental data during the pump coastdown because the gamma heating was not modelled well in the heat structure (in this case, a certain percentage of the subassembly power was used to model gamma heating, based on the analysis of instrumented subassembly XX09, see Section 8.3). At the subassembly outlet and in the guide thimble annulus (see FIG. 145) the coolant temperature decreased early compared to the experimental data after the pump coastdown because the gamma heating, and therefore also the heat conduction from the adjacent subassemblies, was slightly underestimated. However, during the latter half of the transient, the coolant and cladding temperatures were predicted well by the code.

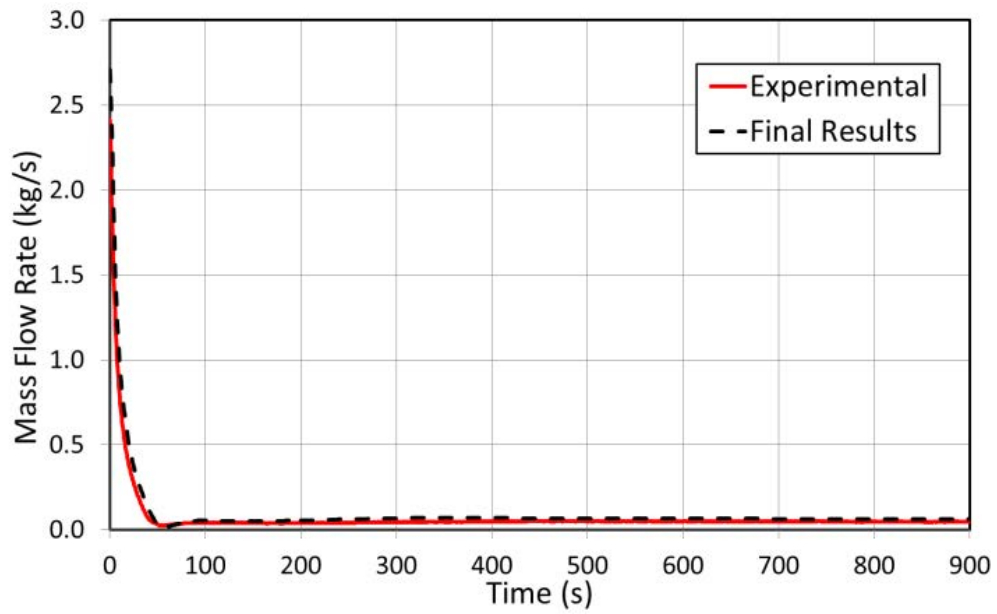


FIG. 138. SHRT-17 XX09 mass flow rate, final results.

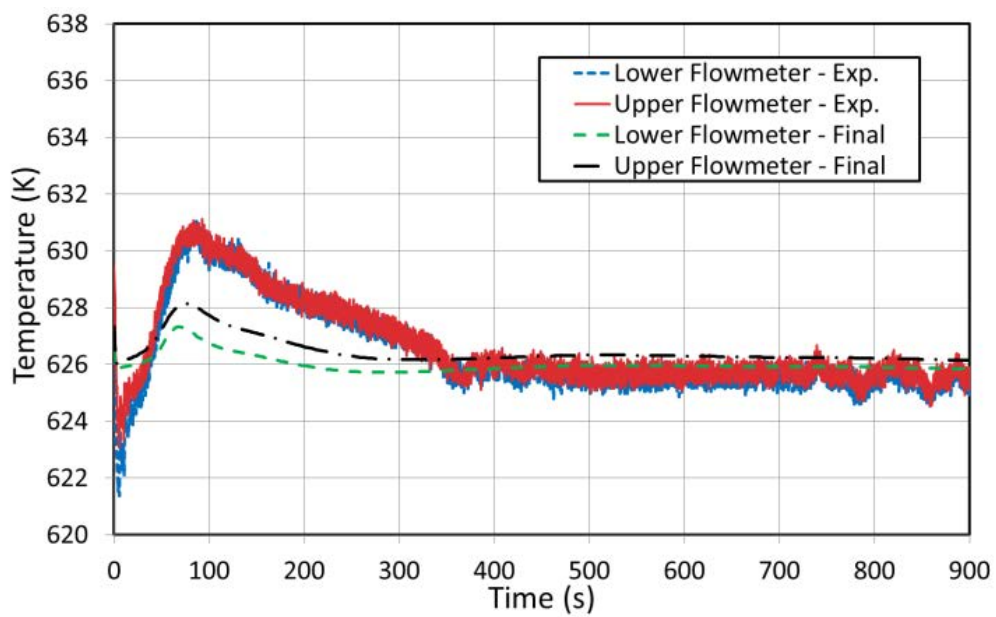


FIG. 139. SHRT-17 XX09 flowmeter temperatures, final results.

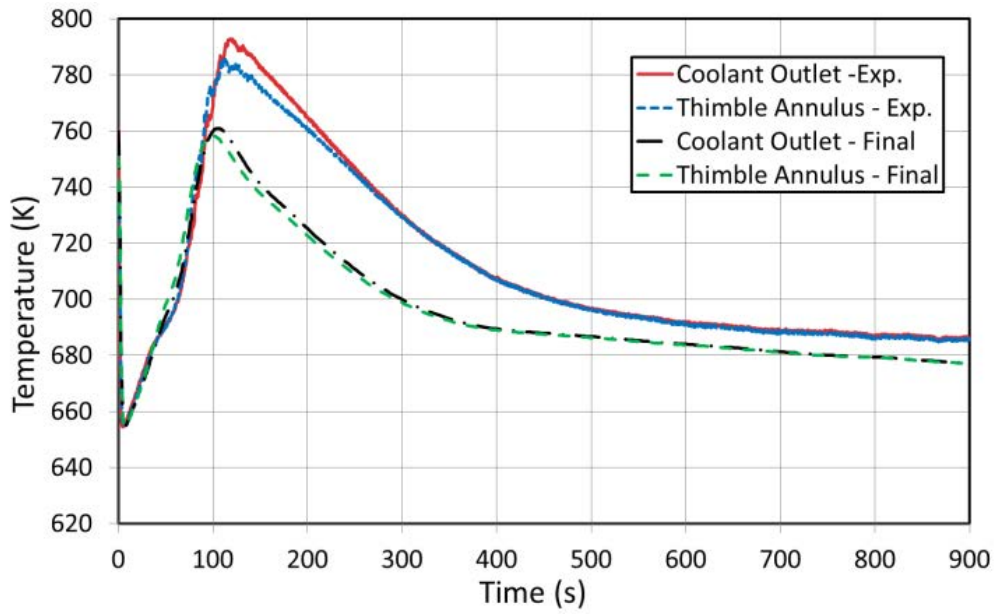


FIG. 140. SHRT-17 XX09 coolant temperatures, final results.

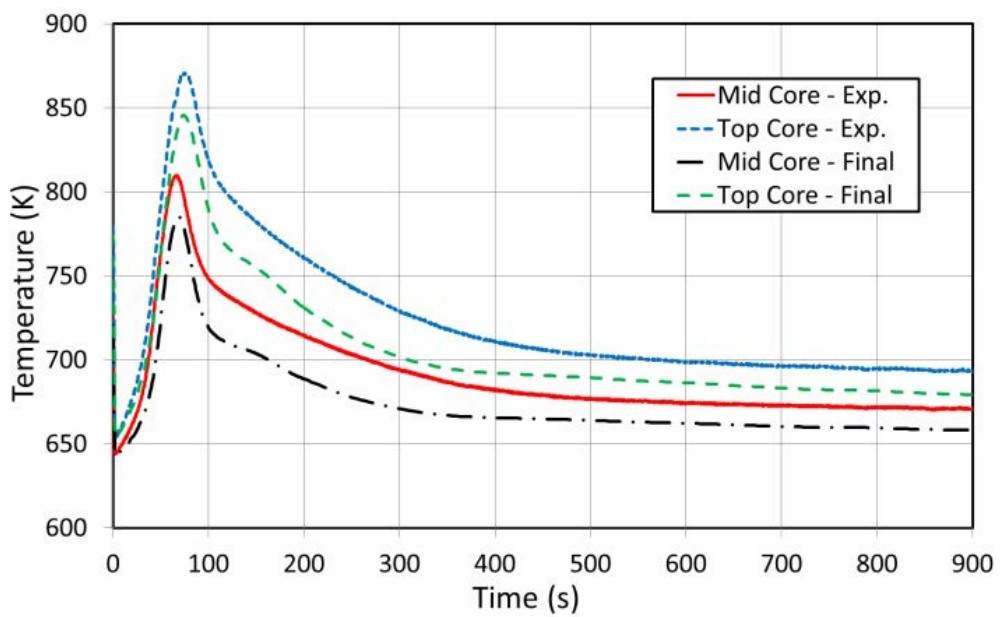


FIG. 141. SHRT-17 XX09 cladding temperatures, final results.

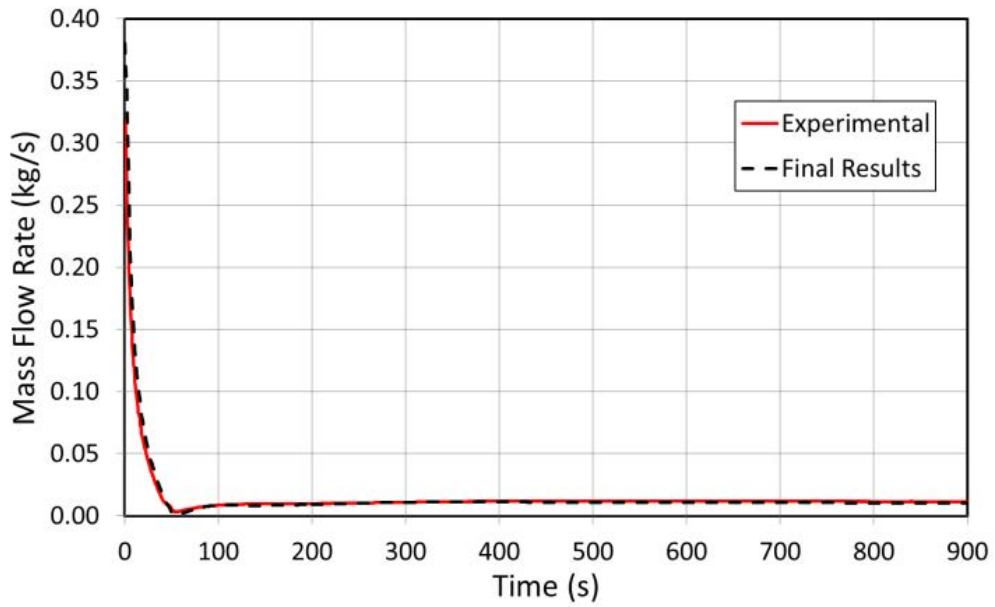


FIG. 142. SHRT-17 XX10 mass flow rate, final results.

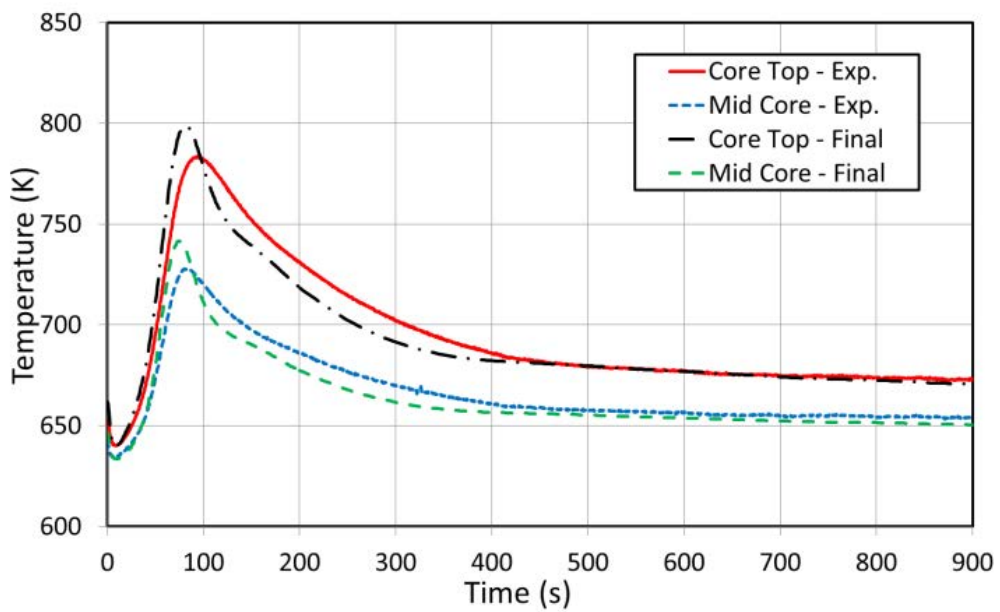


FIG. 143. SHRT-17 XX10 cladding temperatures, final results.

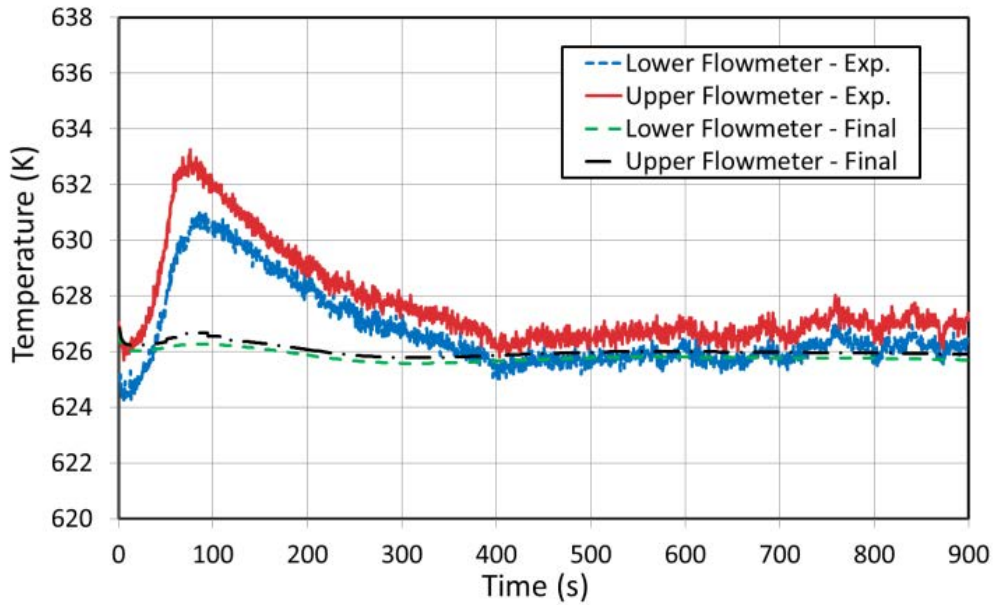


FIG. 144. SHRT-17 XX10 flowmeter temperatures, final results.

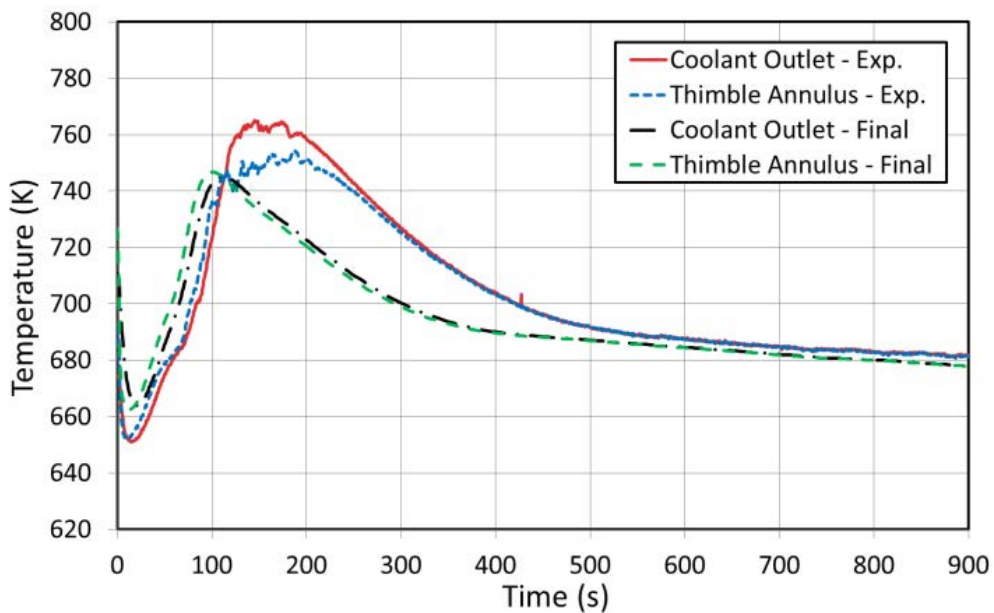


FIG. 145. SHRT-17 XX10 coolant temperatures, final results.

7.8.5.2. Model improvements

As mentioned before, several improvements were implemented in the RELAP5-3D model during the benchmark. Initially, the reactor core was modelled with 25 channels total, collapsing 16 rows into 9 rows. The first 7 rows were modelled using one PIPE component for each type of subassembly located in each row. The remaining part of the core was split into two regions, one region formed by merging rows 8 through 11, and the other region

formed by merging rows 12 through 16, always keeping the different types of subassemblies separated. Also, the heat structures inside the core were simulated following the same approach adopted for the hydraulic part, using three different heat structures for each channel: one modelling the active part of the core, one representing the gas plenum, if any, and the last one simulating the hexagonal tube and other non-active heat structures (i.e. upper and lower shield, stainless steel rods, guide thimble) if present.

In the last version of the RELAP5-3D model, the whole core consisted of 96 channels that represent all 10 types of subassemblies used in the reactor, plus two bypasses. The first 6 rows were modelled separately (1 channel per subassembly) with 81 channels, except for the safety/control rods, which were combined into one channel. Rows 7 through 16 were modelled with one channel per type of subassembly in each row. In addition, for the two instrumented subassemblies (XX09 and XX10), each guide thimble flow region was modelled with a PIPE component. Also the number of heat structures was increased within the hydraulic channels, especially in the core central region. In particular, the subassembly walls were modelled with 6 heat structure components to represent each edge of the hexagonal tube and thermally connect with the adjacent subassemblies.

Regarding the power distribution, the initial power was updated to the value recorded for SHRT-17 (equal to 57.29 MW instead of 59.97 MW of run 129 C). The pin power profile was kept flat and constant along the active length, but an axial power profile was implemented below and above the active part of the fuel, to take into account gamma heating.

Another significant improvement is related to the cold pool. The three parallel pipe components were replaced with a cylindrical multidimensional component having 2 radial mesh cells, the internal one coinciding with the reactor vessel cover; 3 azimuthal mesh cells, thermally linked to the pumps or the IHX; and 72 axial mesh cells, to preserve the sliced approach adopted in the nodalization. The region of the 3-D pool occupied by the reactor vessel cover was blocked.

The velocity of pump #2, initially set equal to that of pump #1, was modified to match the benchmark specifications. Also the energy loss coefficients were modified to improve the prediction of the mass flow rate in the subassemblies, taking into account their dependence on the Reynolds number.

The heat structure of the Z-Pipe was modified by adding a double layer of stainless steel with stagnant sodium that filled the annular region. Also, the IHX was changed by refining the heat structure simulating the tube bundle and modifying the intermediate side in order to have both the inlet and the outlet of the intermediate side pipes at the top of the IHX.

Finally, the leakage flow paths were also modified to be consistent with the benchmark specifications. Initially, they were all collapsed and located in the inlet plena. In the final model, the leakage paths were placed in the correct locations throughout the primary sodium circuit, including the three clearance flow paths through the core.

7.8.6. Neutronics methods and models

N.IN.E. did not participate in the neutronics benchmark.

7.9. POLITECNICO DI TORINO (ITALY)

In general, the analyses of Politecnico di Torino focused on the modelling of the coupled neutronics/thermal hydraulics of the core of the reactor rather than the study of the entire system. The assessment of the behaviour of the core of the reactor during the transient was performed with the FRENETIC code [11], and the phenomena which occur outside of the core were represented by an appropriately defined set of thermal hydraulic boundary conditions. The manner in which these boundary conditions were constructed in the present analyses differed between the SHRT-17 transient and the SHRT-45R transient. Additional data requirements, from the point of view of the neutronics, and therefore relevant to the SHRT-45R transient, include a set of temperature dependent macroscopic cross-sections which describe the materials present in the reactor. The approaches to modelling the neutronic and the thermal hydraulic aspects of each of the SHRT-17 and the SHRT-45R transients are described and the results are discussed below.

7.9.1. Geometry/discretization

In both SHRT-17 and SHRT-45R, the part of the system which was modelled in the analysis is the core of the reactor. In SHRT-17, only the inner seven rings (comprised of the 127 subassemblies of the driver core) were modelled, while in SHRT-45R, all 637 subassemblies were modelled. In the axial direction, the portion of the reactor which was modelled for the thermal hydraulics analyses is limited to the region occupied by the fuel pins, as indicated in FIG. 146. The radial mesh on which the solution was computed within the pins varies approximately between 0.015 cm and 0.10 cm, depending on the dimensions of the pin itself. The axial mesh is uniform with a characteristic dimension of approximately 0.51 cm.

In SHRT-45R, the part of the reactor modelled in the neutronics analyses comprised all 637 subassemblies of the reactor core and the axial domain extended from the bottom of the lower shield to the top of the upper shield. The spatial mesh employed in the nodal analysis corresponds to one hexagonal node per subassembly in the xy -plane and an axial mesh such that each hexagonal prism is approximately 10.0 cm to 13.5 cm in height. The discretization of the energy domain is discussed in Section 7.9.6, together with the generation of the group constants. The method of temporal integration applied to the time-dependent few-group nodal balance equations is the point-kinetic method, for which the reactivity is updated every 5×10^{-3} s; this is also the timestep used to integrate the thermal hydraulics equations, as well as the timestep according to which the neutronic and the thermal hydraulic solutions are coupled.

7.9.2. Nuclear and thermo-physical data/correlations

For the analysis of both the SHRT-17 and the SHRT-45R transients, the following thermo-physical properties were implemented in the FRENETIC code for the different materials:

- (a) Sodium: the Argonne thermo-physical properties were used [75];
- (b) Stainless steel: the RELAP5-3D[®] thermo-physical properties [23] were implemented as tables, with linear interpolation among selected points;
- (c) Fuel (U-5Fs alloy): the Argonne thermo-physical properties were used [106].

Concerning the friction factor in the fuel rod bundle, the recipe described in Chapter 9 of [107] ('Single-Phase Fluid Mechanics') for the pressure drop in rod bundles was adopted.

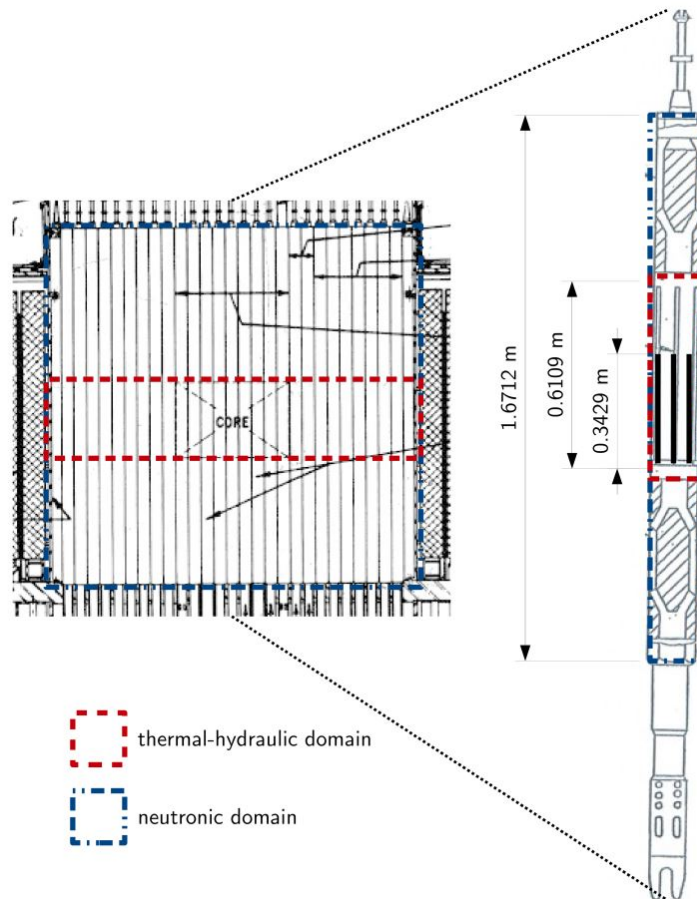


FIG. 146. Axial domain of EBR-II modelled in the analysis.

Finally, the convective heat transfer coefficient for sodium was evaluated in these simulations by two different correlations:

- (a) the Westinghouse correlation reported in Chapter 10 of [107] ('Single-Phase Heat Transfer') for the heat transfer in turbulent flow of metallic fluids in rod bundles was adopted for the pin-sodium heat transfer coefficient;
- (b) the Seban-Shimazaki formula [8], developed for hexagonal boxes, for turbulent fully developed flows at constant wall temperatures,

$$Nu_i = 5 + 0.025 \cdot Pe_i^{0.8}$$

where Nu is the Nusselt number and Pe the Peclet number, was adopted for the heat transfer coefficient between the sodium and the subassembly wall.

In the assessment of SHRT-45R, the elementary nuclear data used to construct the group constants for the prompt and the delayed neutrons was obtained from the JEFF-3.1.1 library ([108], [109]). The specific procedure according to which the temperature dependent set of group constants was generated is described in Section 7.9.6.

7.9.3. Thermal hydraulics methods and models

7.9.3.1. Code(s) used

The transient analyses of the reactor core were performed with the FRENETIC code [11], recently developed at Politecnico di Torino. In the case of SHRT-17, the thermal hydraulic boundary conditions (BCs) are the output of an analysis performed with the RELAP5-3D[®] [23] code by ENEA in the framework of this international benchmark.

7.9.3.2. *Basic method*

The FRENETIC code was applied here to the detailed analysis of the core only. No system analysis was performed. For this reason, proper thermal hydraulic BCs were needed at the inlet and outlet of the fuel pin region of the core.

In particular, for this type of analysis three BCs are needed, and the following combination of inlet and outlet BCs was adopted for each hydraulic channel:

- (a) inlet mass flow rate;
- (b) inlet temperature;
- (c) outlet pressure.

For both the blind phase and the final phase of the SHRT-17 analysis, all these BCs were provided by the RELAP5-3D[®] simulation performed by ENEA, as stated above. In the radial direction, for the SHRT-17 tests analysis an adiabatic BC was assumed by FRENETIC between the seventh ring and the rest of the core, i.e. the reflector and blanket region.

For SHRT-45R, the set of thermal hydraulic boundary conditions was created through implementation of the available data describing the nominal operating conditions and the experimental measurements. The spatial distribution of the inlet mass flow rates under stationary conditions was obtained from the computations made by Argonne during the planning phase of the test using the EBRFLOW code, the results of which are provided in the benchmark specifications. Data for the flow rate in the thimbles of the relevant channels were derived by setting the thimble-to-total ratio of the mass flow rates to match the experimental values of the two instrumented channels. Inlet coolant temperatures for both the inner channel and the thimble were set equal to the temperature of the coolant in the inlet plenum, which is available as an experimentally measured quantity. During the transient analysis, the relative spatial distribution of the inlet mass flow rates was kept constant while the total flow rate was scaled according to an amplitude factor coming from the measured data of the second of the two primary pumps.

7.9.3.3. *Model*

The thermal hydraulic module adopted for the analysis of both transients solves the time-dependent mass, momentum and energy conservation laws for the coolant in each subassembly.

With the inclusion of appropriate heat transfer correlations, as well as relationships for the relevant thermo-physical properties of the materials, the conservation equations of this set were solved simultaneously in one dimensional form along the channel axis for a given channel by the finite element method in space and the theta method in time. As a result, a single, average value of the coolant temperature and coolant velocity and pressure was computed at each axial node of each channel.

For the fuel, two different models were adopted in the blind analysis of the SHRT-17 transient and for the phase 2 analysis:

- (1) A purely axial heat conduction model, in which the heat conduction equation was solved along each subassembly axis at each timestep. As for the coolant, a single, average temperature value was computed for each subassembly at each axial element;
- (2) A radial heat conduction equation, implemented for phase 2, was solved for the pin at each axial node. A single equation was solved at each axial element, thus computing a single radial temperature distribution representative of the average pin over the subassembly cross-section.

The individual one dimensional channels were then thermally coupled to their adjacent neighbours in the two dimensional horizontal plane, resulting in a three-dimensional, full core model. During the transient, the inter-channel coupling was explicit with respect to time.

Thermal coupling between neighbouring channels was implemented at each axial element as a heat transfer across a series of thermal resistances, which include the pure conductive resistance of the stainless steel subassembly wall, the pure conductive resistance of the sodium in the gap (that, in view of the small mass flow area, is considered stagnant in the model, for simplicity) and the convective heat transfer resistance due to the convective heat transfer between the sodium in the subassembly and the subassembly wall.

7.9.4. Blind results

7.9.4.1. SHRT-17

In view of the need for BCs in the FRENETIC code, and due to the lack of experimental data for one of the two pumps during the SHRT-17 test, the mass flow rate BCs from the RELAP5-3D[®] simulations were treated parametrically during both phase 1 and phase 2. Therefore, while for XX09 and XX10 the measured mass flow rate was adopted as a BC, the measurements of the temperature evolution in XX09 and XX10 are compared below with the results computed by FRENETIC adopting as BC for the rest of the subassemblies the distribution of the mass flow rate computed by RELAP5-3D[®], either as is or reduced by the instantaneous value of the ratio (measured)/(computed by RELAP) for the total mass flow rate in pump#2.

The measured temperature evolution at the end of the heated zone (the green colored band covers the range between minimum and maximum measured temperature on the subassembly cross-section) is compared with the FRENETIC simulation in FIG. 147 (the average between computed pin surface temperature and sodium temperature is shown for consistency). The two sets of computational results for each instrumented subassembly correspond to two different distributions of the coolant inlet mass flow rate across the core cross-section, with the red curves corresponding to the mass flow rate computed by RELAP5-3D[®] and the blue curves corresponding to rescaling of the RELAP5-3D[®] mass flow rate by the measured data.

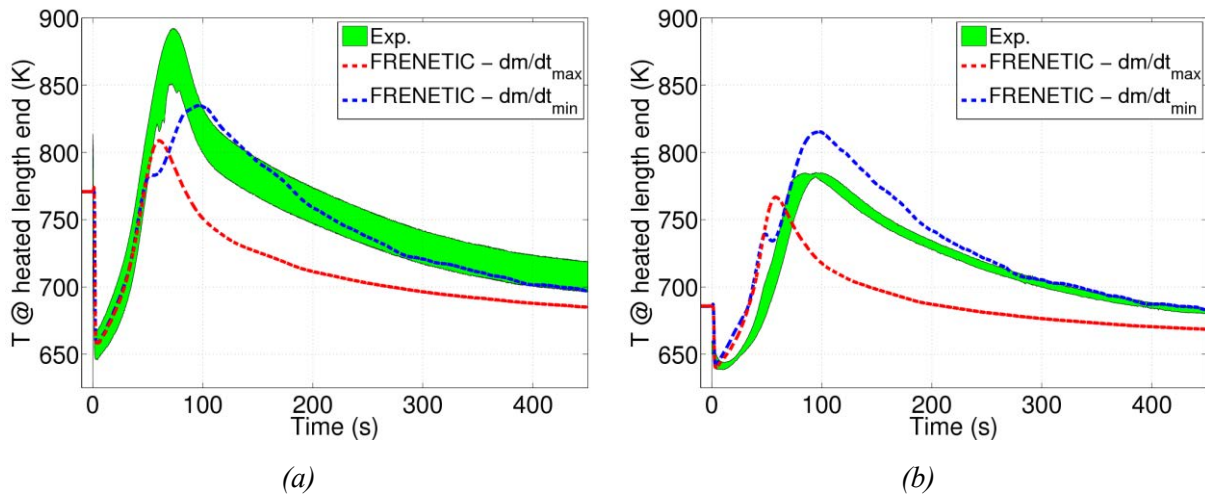


FIG. 147. SHRT-17 computed vs. measured temperature evolution at the end of the heated zone, blind results: (a) XX09, (b) XX10.

It is seen that the qualitative behaviour of the measured temperature is reasonably reproduced by the simulation. While the initial temperature increase is similar for both mass flow rate distributions, the later evolution is rather different in the two cases and presents features directly related to the strong variation of the ratio (measured)/(computed by RELAP) mass flow. It is to be noted that the measured temperature decrease is nicely bracketed by the two simulations.

7.9.4.2. SHRT-45R

SHRT-45R was not analyzed during the blind phase by Politecnico di Torino.

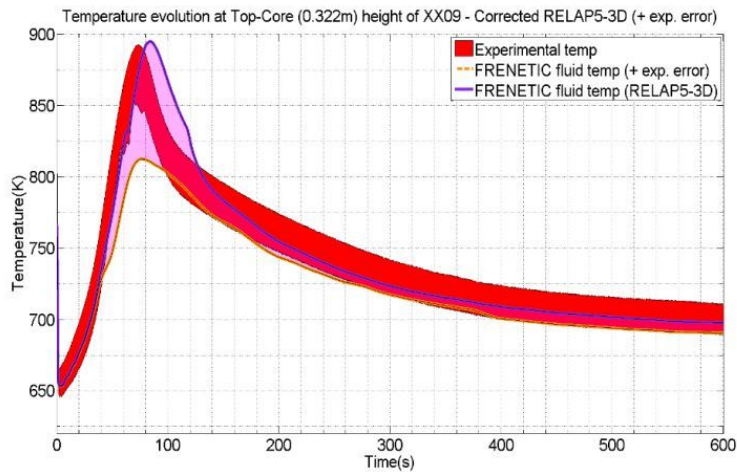
7.9.5. Final results, data comparisons

7.9.5.1. SHRT-17

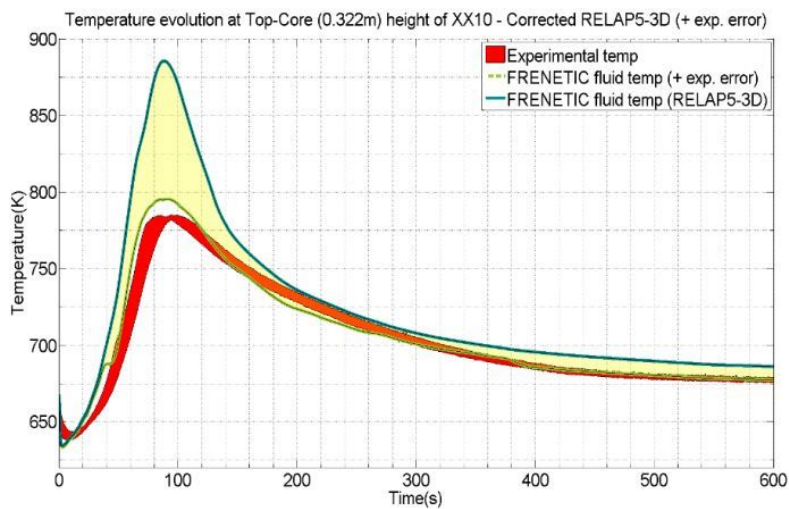
The RELAP5-3D[®] simulation was recomputed in phase 2 of the international benchmark, knowing the experimental pump data and improving the model for the subassembly inlet orifices. These new flow rates were used as FRENETIC BCs (referred to as “RELAP” in the figures below), without any rescaling factor, in order to try to better describe the SHRT-17 transient. The new data have resulted in a significant improvement in the simulation transient behaviour, especially of the instrumented XX09 subassembly.

In view of the important role of the mass flow rate BCs, a parametric analysis was performed as was done for the blind phase (see above). A second set of BCs was then generated, referred to as “RELAP+exp.err” in the figures.

The results show how the XX10 temperature curve is closely followed by the rescaled set of mass flow rates. The XX09 temperatures, on the other hand, are closely represented by the RELAP5-3D[®] flow rates, and the results from the two treatments of the mass flow rate BCs bracket the measured data. In all cases, the second part of the transient is well reproduced by the code results, see FIG. 148.



(a)



(b)

FIG. 148. SHRT-17 temperature evolution at Top-Core height (0.322 m.) in (a) the XX09 and (b) the XX10 instrumented subassemblies, with the different sets of mass flow rate BCs – final results.

Steady state results in FIG. 149 show an analogous behaviour, showing a very good agreement between the computed and experimental axial temperature distributions in both the XX09 and XX10 subassemblies.

7.9.5.2. SHRT-45R

The temporal evolution of the total power, both experimental and computed, is shown in FIG. 150, along with the accompanying temporal evolution of the computed net reactivity. At steady state, the disagreement between the measured and the computed values for the fission power is due to neglecting decay heat; this is confirmed by the fact that the relative error between the two values is +6.8 %. By neglecting decay heat, the model predicts that more heat is deposited early in the transient than with respect to the real situation, thereby leading to stronger feedback effects that decrease the power level at a rate faster than in reality, which, in part, compensates for the initial discrepancy. Thereafter, the computed power is in relatively good agreement with the experimentally measured value for times up to approximately 100 s and then begins to deviate. This behaviour may be explained by the absence of a model in the FRENETIC code for some relevant feedback effects (for example,

thermal expansion of the core structures). Another contributing factor regards neglecting the decay heat, as the presence of a source of thermal energy which decays more slowly in time would contribute to increased temperatures, hence amplified thermal feedback effects.

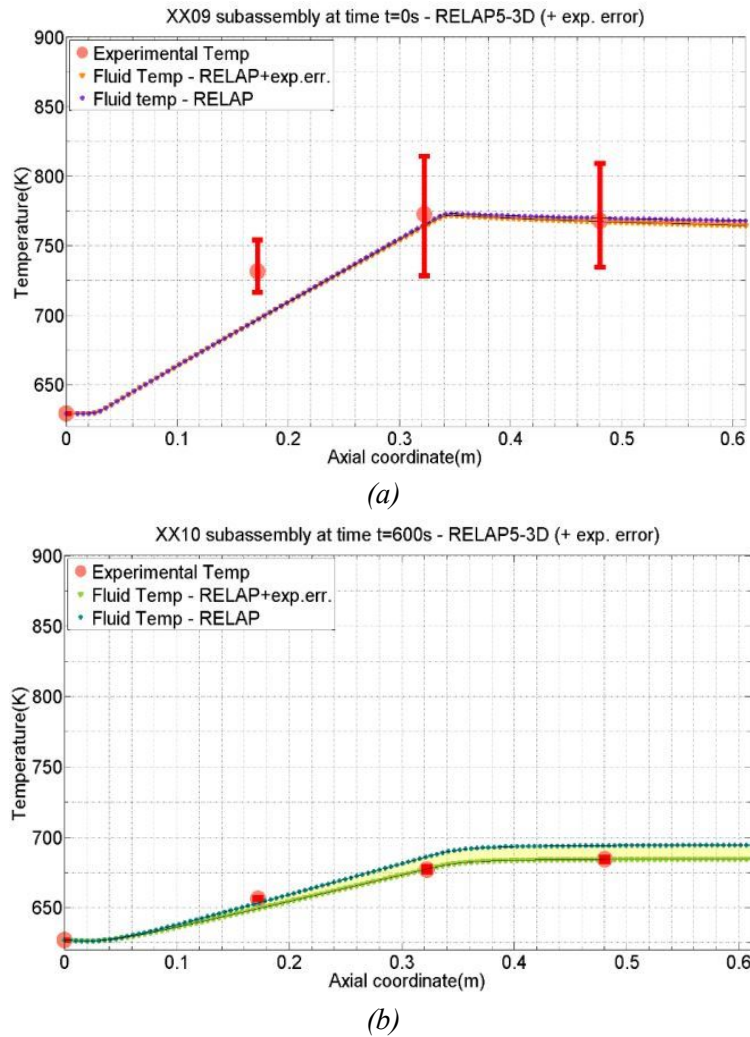


FIG. 149. SHRT-17 steady state axial temperature distribution before the start of the transient in (a) XX09 and (b) XX10 with the different sets of mass flow rate BCs, final results.

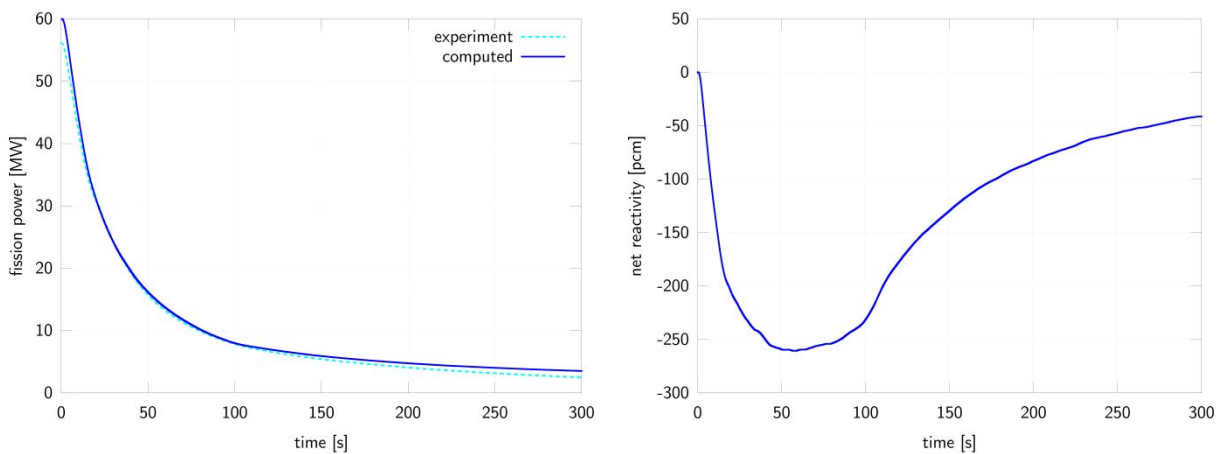


FIG. 150. SHRT-45R temporal evolution of the total power (left) and the net reactivity (right).

The temporal evolution of the computed coolant temperature at selected axial locations of the instrumented subassemblies is shown in FIG. 151 and FIG. 152, together with the experimentally measured values, which are depicted as a band spanning the minimum and the maximum temperatures measured by the thermocouples in the subassembly at the specified axial location. In the XX09 instrumented subassembly, for both of the available thermocouples, the computed result remains within the experimental band for the first 25 s, underestimating the peak value, which is measured at around 50 s. At times thereafter, the computed result follows a trend similar to the measurement, although underestimating it by about 25 K-50 K. In the XX10 instrumented subassembly, the observed behaviour differs along the axis. At the mid-core thermocouple, the computed result follows the trend of the experimental measurement but underestimates it by approximately 25 K. At the top-core and above core thermocouples, the computed peak value is overestimated, more so as the axial position increases. After approximately 125 s, the experimental measurement is reproduced with an error within ± 10 K.

7.9.5.3. *Model improvements*

The thermal hydraulic model improvements following the blind phase can be summarized as:

- (a) Implementation of the radial thermal conduction model of the pins, substituting for the previous axial model. For the sake of simplicity and to still allow fast and reliable transient evaluations of liquid metal cooled fast breeder reactors (LMFBRs), which is the main goal of the FRENETIC code, the new model had to drop axial conduction in favor of the radial conduction model. This is not a major concern, since the contribution of axial heat conduction with respect to the other heat transfer mechanisms is negligible (for the same reason, the most well-known nuclear codes such as RELAP5-3D[®] and CATHARE[®] do not include this feature as well). The new model approximates space derivatives with a 1-D linear Finite Element approach. An adiabatic BC is prescribed at the fuel centerline, thanks to the symmetry of the problem, while the Robin BC, which relates the surface temperature of the pin to the heat exchanged with the liquid sodium flowing inside the hexagonal subassembly, is applied at the outer radius of the pin. The radial problem is solved once for each axial node for each subassembly at every timestep. The surface temperature is then used explicitly in the subsequent timestep in the equation for the temperature of the coolant. With this model, the geometrical radial distribution of the temperature inside the fuel pin is no longer forced to be parabolic but can assume a shape more representative of the state of the reactor, following the real transient evolution of the temperature profile in the pins;
- (b) Implementation of the coolant flow in the thimble of the so-called “box-in-the-box” hexagonal subassemblies, where the external hexagonal wrapper contains a second, smaller hexagonal wrapper in which the pins are located. The clearance between the two wrappers is cooled by a sodium flow which was neglected in the blind phase (the sodium there being considered stagnant and accounted for only as an additional thermal conduction resistance in the model for the thermal coupling between neighbouring subassemblies), while it is modelled as a separate hydraulic channel in the final simulation. This allowed improvement of the cooling model;
- (c) Improvement of the model for the subassembly inlet orifices in the RELAP5-3D[®] simulation, recomputed in phase 2 of the international benchmark programme, also using the recorded pump data.

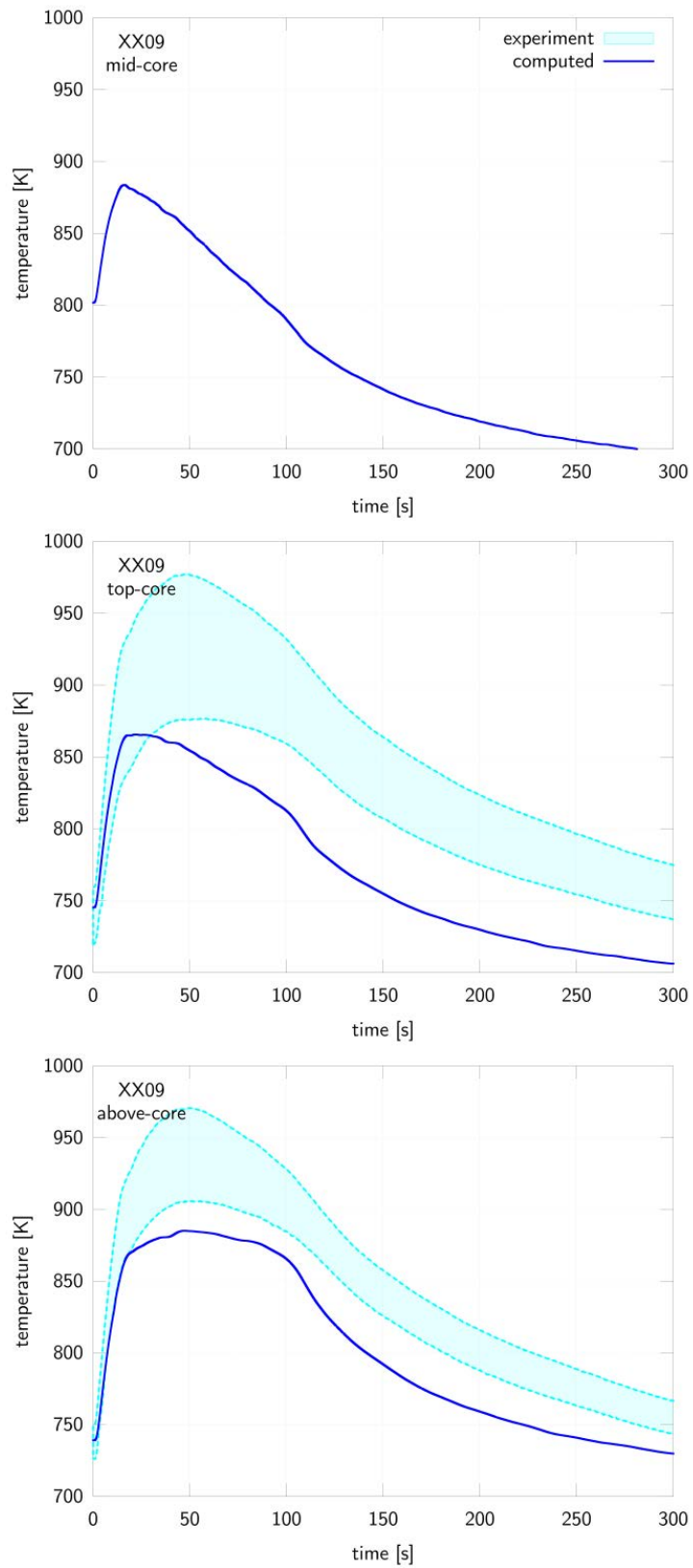


FIG. 151. Temporal evolution of the coolant temperature at multiple axial positions in XX09, SHRT-45R.

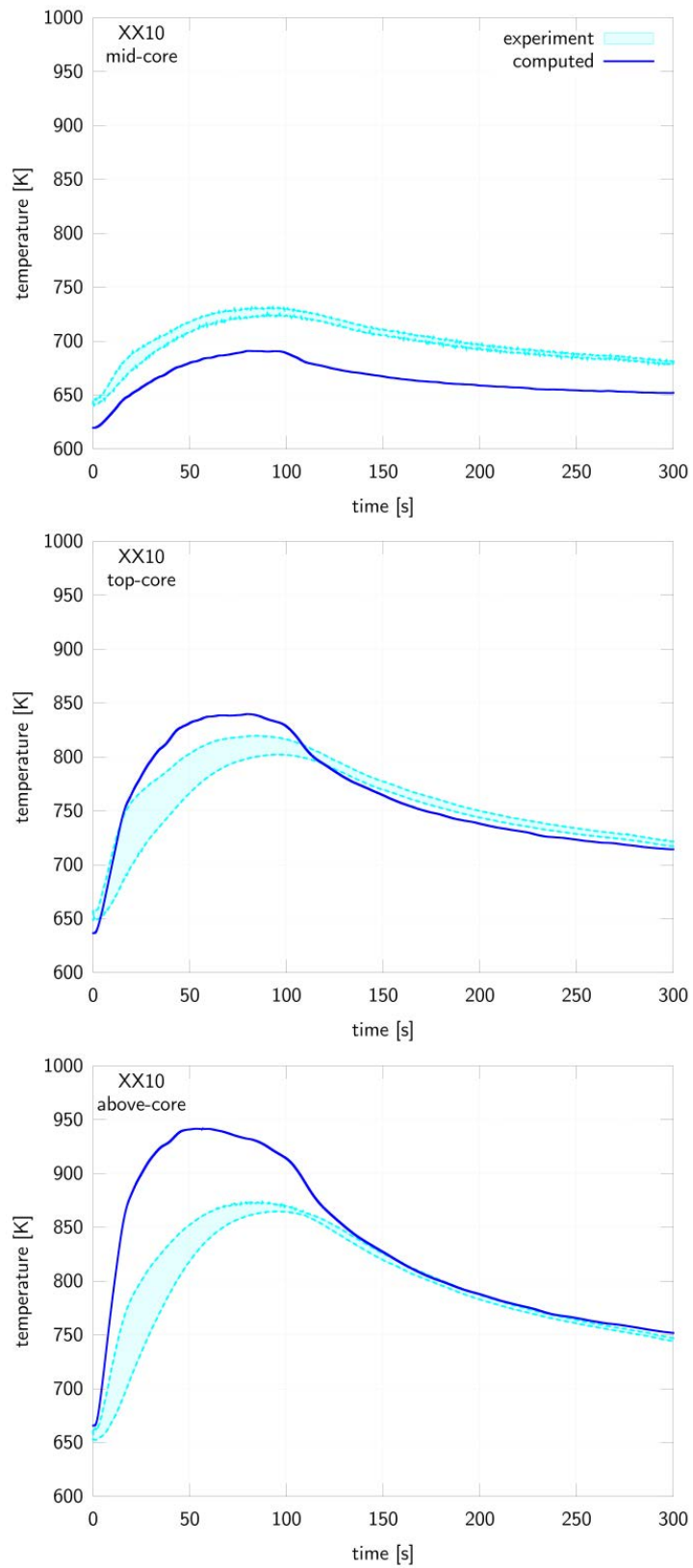


FIG. 152. Temporal evolution of the coolant temperature at multiple axial positions in XX10, SHRT-45R.

7.9.6. Neutronics methods and models

7.9.6.1. Code(s) used

The multigroup neutron cross-sections were computed with the Serpent Monte Carlo code [55]. The steady state and transient analyses of the reactor core were performed with the FRENETIC code.

7.9.6.2. Neutron and photon cross-sections

The multigroup neutron cross-sections were computed by the following procedure. Based upon the geometrical specifications and the isotopic compositions of the relevant materials, an equivalent axial-symmetric cylindrical model of the reactor was defined, consisting of six radial regions and up to five axial regions of homogeneous materials; the regions were defined in order to group subassemblies of similar geometry and composition. A steady state neutronic analysis of the cylindrical model of the reactor was then performed using the Serpent Monte Carlo code and the JEFF-3.1.1 cross-section library. As a result of this analysis, the multigroup cross-sections were generated on the six-group energy structure defined in TABLE 12, while the standard eight families of delayed neutron precursors were used to generate the delayed neutron data.

TABLE 12. ENERGY STRUCTURE ADOPTED FOR THE FEW-GROUP CROSS-SECTIONS FOR EBR-II

Group, g	Upper energy, E_{g-1} [MeV]	Lower energy, E_g [MeV]
1	–	4.0e-01
2	4.0e-01	6.0e-02
3	6.0e-02	1.0e-02
4	1.0e-02	1.5e-03
5	1.5e-03	2.5e-04
6	2.5e-04	0.0e+00

In order to obtain a library of macroscopic cross-sections which depend on the temperature, the previously described process was repeatedly applied to the system with the same materials evaluated at different temperatures. In particular, the temperatures of the materials which comprise the fuel and the temperatures of the materials which comprise the coolant were independently varied (at temperatures of 400 K, 750 K and 1000 K), while each was maintained spatially uniform throughout the reactor. This process of varying the temperatures accounts for thermal feedback due to the Doppler effect as well as the coolant density effects, but it does not account for the geometric deformation and the corresponding density effects of the structural materials.

Having obtained the macroscopic cross-sections from the Monte Carlo model, the nodal model was then defined. The hexagonal geometry of the subassemblies constituting the reactor core were defined, with each subassembly homogenous and assigned the material of the cylindrical zone to which it belonged in the cylindrical model. Axially, the mesh was imposed so as to allow the same homogeneous regions between the two models. In returning to the hexagonal configuration from the axial-symmetric cylindrical configuration, some material substitutions were made in order to account for local heterogeneity; after all substitutions were complete, the global set of macroscopic cross-sections was then adjusted by applying a set of correction factors. The correction factors were applied individually to

each macroscopic cross-section of each energy group of each homogeneous material, in order that the reaction rate density in the region in which a substitution was made would be preserved.

Photon cross-sections were not generated, as photon heating was not modelled in the analysis.

7.9.6.3. *Calculation of power and k_{eff}*

The distribution of the power in steady state conditions and the corresponding effective neutronic parameters (the effective multiplication eigenvalue, the effective delayed neutron fraction and the effective neutron lifetime) resulted from a coupled neutronic/thermal hydraulic analysis performed with the FRENETIC code. The multigroup neutron diffusion equations were solved with a coarse mesh nodal method; the energy group structure is shown in TABLE 12 and the spatial mesh corresponds to one hexagonal node per subassembly in the xy -plane and an axial mesh such that each hexagonal prism is approximately 10.0 cm to 13.5 cm in height. All recoverable energy was assumed to be generated and to be deposited instantaneously at the point of fission.

The effective delayed neutron fraction and the effective neutron lifetime were computed by their corresponding integral definitions, appropriately adapted for use in the context of a nodal discretization method.

7.9.6.4. *Calculation of reactivity feedback*

The net reactivity at any point in time during the transient was determined through the integral definition of the dynamic reactivity, which is given by the ratio of the adjoint-weighted perturbation of the operators applied to the instantaneous neutron flux and the instantaneous importance for neutron fission. As in the case of the effective delayed neutron fraction and the effective neutron lifetime, this expression was appropriately defined for use with the nodal discretization method.

Hence, the overall reactivity feedback effects were accounted for by the temperature dependence of the macroscopic cross-sections. Only the reactivity feedback effects which were modelled during the generation of the library of temperature dependent macroscopic cross-sections were then present in the total feedback reactivity. The repartition of the feedback reactivity due to the various individual phenomena was not computed, as it is unnecessary for the present approach to the modelling of the transient.

7.9.7. **Neutronics results**

At steady state, the computed value of the effective multiplication eigenvalue is 0.97619. The computed value of the effective delayed neutron fraction is 728 pcm, redistributed among the eight families of delayed neutron precursors, as shown in TABLE 13. The effective neutron lifetime is determined to be $2.795 \cdot 10^{-7}$ s.

The steady state distribution of the axially-integrated subassembly power is reported in FIG. 153. Those subassemblies for which zero power is reported are due to the assumption that the only source energy production is that due to fission events; that is, the neutron kerma term and the photon kerma term are neglected, the latter of which is due to the lack of a photon transport model in the FRENETIC code. Since the total power of the system is imposed, the error due to not modelling this particular aspect of the physics is propagated to all the other

subassemblies of the reactor: compared to the true situation, more power comes to be generated in those subassemblies containing fissile material.

TABLE 13. COMPUTED VALUES OF THE EFFECTIVE DELAYED NEUTRON PRECURSOR FRACTIONS BY FAMILY

Delayed neutron precursor family, i	Decay constant, λ_i [s^{-1}]	Effective delayed neutron fraction, $\beta_{eff,i}$ [pcm]
1	0.012467	22
2	0.028292	106
3	0.042524	67
4	0.133042	140
5	0.292467	226
6	0.666488	77
7	1.634780	67
8	3.554600	24

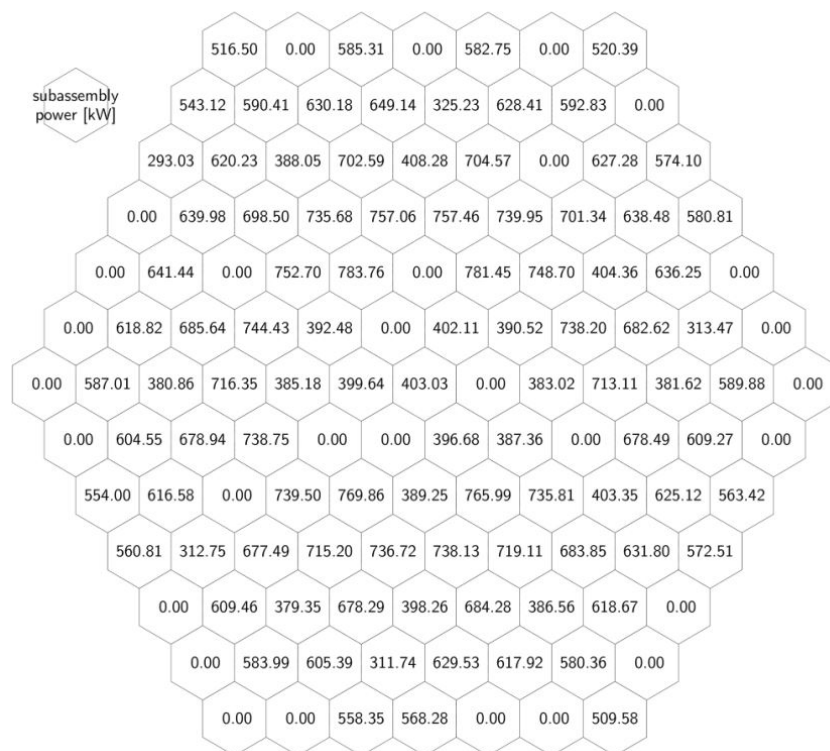


FIG. 153. Axially-integrated subassembly power of the inner seven rings of the EBR-II core at steady state conditions.

7.10. JAPAN ATOMIC ENERGY AGENCY (JAPAN)

7.10.1. Geometry/discretization

The EBR-II reactor had a tank-type vessel. Components in a primary circuit such as the core, intermediate heat exchanger (IHX) and pumps were immersed in a cold pool, as shown in FIG. 154(a). The core is divided into two regions. The fuel assemblies in the inner and the

outer regions are connected to the high pressure and the low pressure lower plena, respectively. The core upper plenum is connected through Z-shaped piping to the IHX. Throttle valves control the flow distribution of coolant flow to the high pressure and the low pressure plena. The instrumented subassemblies shown in FIG. 154(b) are installed in the inner core.

For the numerical analysis, the thermal hydraulics in the primary circuit was modelled by component, and then the component models were interconnected with each other to simulate whole plant dynamics. The core thermal hydraulics was modelled by fuel subassembly to simulate whole core dynamics, and each instrumented subassembly was modelled by a subchannel that is surrounded by fuel pins or a wrapper wall to simulate temperature distributions in a subassembly.

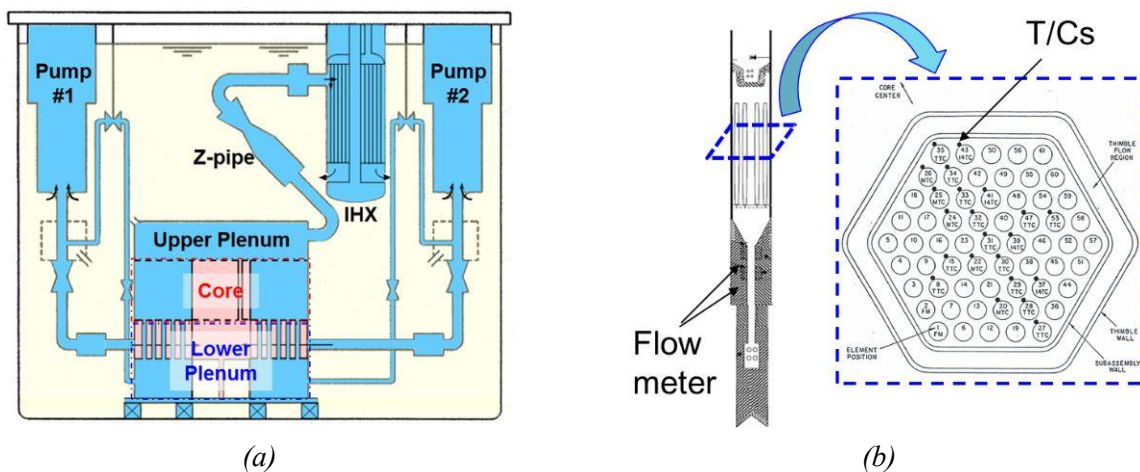


FIG. 154. Sketch of EBR-II: (a) primary loop, (b) XX09.

7.10.2. Nuclear and thermo-physical data/correlations

The correlations used in the analysis are listed in TABLE 14.

TABLE 14. LIST OF CORRELATIONS USED IN JAEA ANALYSIS

Friction Factor	
Fuel Pin Bundle	Cheng & Todreas [110]
Inter-Wrapper Tube	Parallel Plate Correlations
IHX Tube Bundle	Pipe Flow Correlations
Heat Transfer Coefficient	
Fuel Pin Bundle	Lyon [111]
Wrapper Tube	Parallel Plate Correlations
IHX Tube Bundle	Mikityuk [72]
Z-Pipe	Seban & Shimazaki [112]

7.10.3. Thermal-hydraulics methods and models

7.10.3.1. Code(s) used

Whole plant and in-core thermal hydraulics were simulated by using a plant dynamics analysis code Super-COPD developed by JAEA. Thermal hydraulics in the instrumented subassemblies XX09 and XX10 were simulated by using the subchannel analysis code ASFRE developed by JAEA.

7.10.3.2. Basic method

Simulations were performed using the two-step procedure shown in FIG. 155. In the first step, whole plant and in-core thermal hydraulics were simulated by using Super-COPD. Thermal hydraulics in the primary heat transport system of EBR-II were described with a flow network model, and thermal hydraulics in the core were described with all fuel subassemblies as individual flow channels of 27 types in order to consider characteristic thermal hydraulic phenomena under natural circulation conditions: core flow redistribution, radial inter-subassembly heat transfer and inter-wrapper gap flow. In the second step, thermal hydraulics in the instrumented subassemblies XX09 and XX10 were simulated by using ASFRE with the boundary conditions of subassembly flow rate and heat flux at the subassembly wrapper tube set to the values obtained in the first step of the analysis.

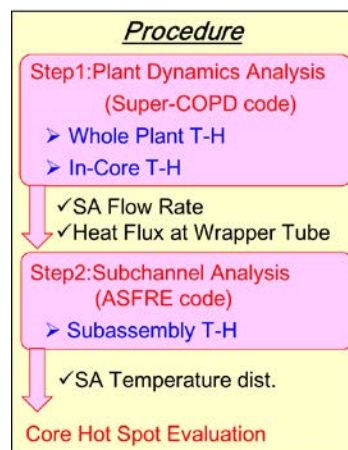


FIG. 155. Two-step procedure of thermal hydraulics analysis for SHRT-17.

7.10.3.3. Model

The model for the primary heat transport system (PHTS) is illustrated in FIG. 156. The two loops of the PHTS were represented independently as one dimensional flow network models. The EBR-II pump model implemented in the NATDEMO system simulation code was used for estimation of pump head or pressure loss. As shown in FIG. 157, the core upper plenum was described with two mixing volumes for the final simulation model; one volume is the region above the core which is surrounded by a baffle plate and another volume is the outer surrounding region. The other plena were modelled with single mixing volumes; cold pool, high pressure and low pressure plena, and the inlet and outlet plena of the IHX.

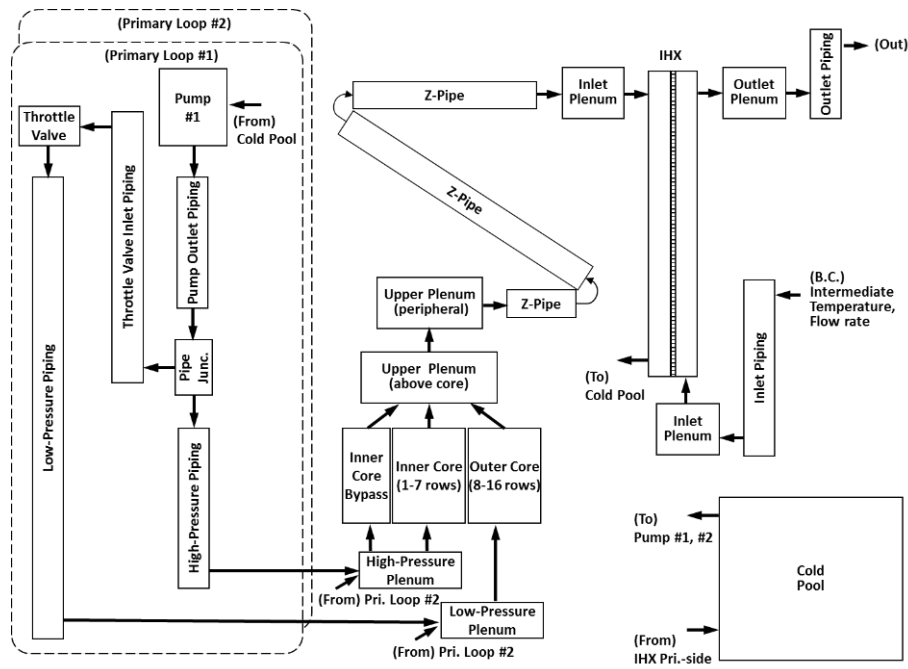


FIG. 156. Flow network model for primary heat transport system.

The model for the whole core is illustrated in FIG. 158(a). All subassemblies in the core were modelled with the 27 types of flow channels listed in TABLE 15, so the core flow redistribution phenomena due to buoyancy under natural circulation conditions could be simulated. In order to estimate the subassembly-to-subassembly heat transfer, the temperature distribution in a subassembly was described with the seven temperature regions shown in FIG. 158(b). Sodium flow paths between subassembly wrapper tubes were described with the three-dimensional flow network shown in FIG. 158(c) to consider the inter-wrapper gap flow effect on the core temperature distribution.

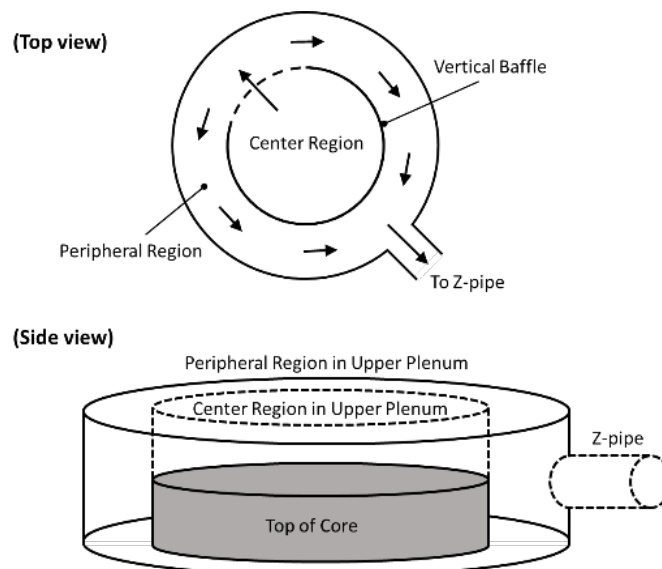


FIG. 157. Two mixing volume model for core upper plenum of EBR-II.

Models for instrumented subassemblies XX09 and XX10 are illustrated in FIG. 159. The coolant flow area in a subassembly was divided into sub-channels. The pressure drop in each subchannel was described by Chang and Todreas's correlation as well as the plant dynamics analysis code. The heat transfer coefficient of the fuel pin bundle was described by Kazimi and Carelli's correlation [79].

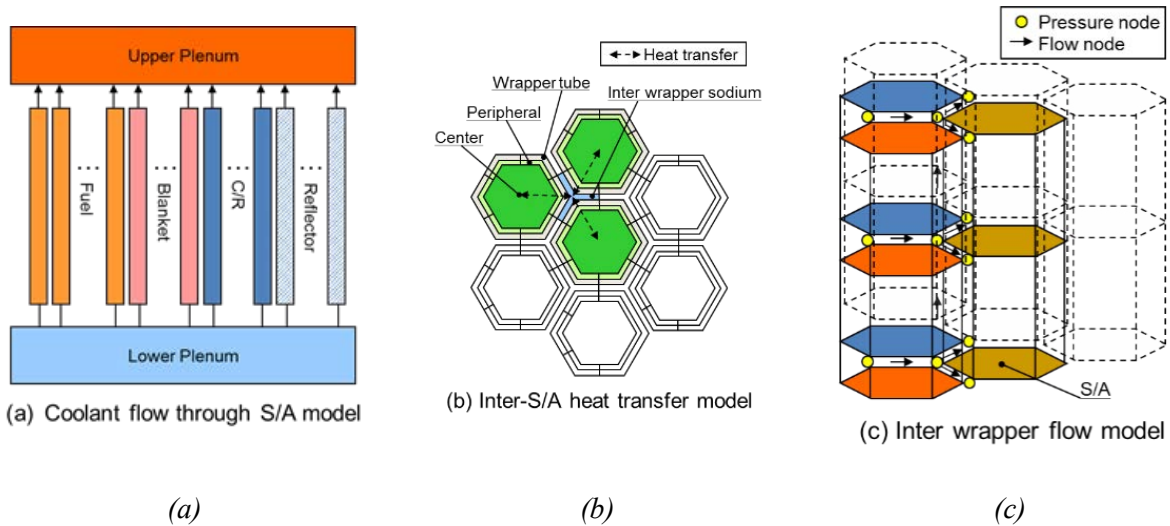


FIG. 158. Thermal hydraulics models for the core.

7.10.4. Blind results

7.10.4.1. SHRT-17

The blind calculation was performed using the specified conditions of this benchmark simulation. The main results of this calculation in the heat transport system, which are the IHX intermediate outlet temperature and the flow rates of pumps #1 and #2, are shown in FIG. 160(a) and FIG. 160(b), respectively. The heat balance in the initial steady state did not agree well with the experimental results. This discrepancy was speculated to be caused mainly by inaccuracies in the calculated pump head, the pressure loss of the primary loop, and heat transfer in the IHX. The upper plenum was modelled with a single mixing volume in this blind calculation, while the actual plenum is divided by a partial vertical plate with many flow holes. This modelling affected the coolant temperature of the Z-Pipe and the IHX primary inlet in the transient state.

The temperatures in the centre and the peripheral subchannel at the core top of XX09 are shown in FIG. 161(a). These temperatures are lower than the measured ones because the calculated flow rate of XX09 was larger than the measured one, as shown in FIG. 161(b). As the pressure loss coefficients of XX09 were estimated the same way as were those for the AI MARK-II driver subassemblies, the pressure loss was correctly set in this model. The subassembly-to-subassembly heat transfer may not be calculated accurately because of the approximation of only five kinds of subassemblies.

7.10.4.2. SHRT-45R

JAEA did not perform an analysis of SHRT-45R.

TABLE 15. LIST OF FLOW CHANNEL TYPES IN-CORE MODEL

Core Region	No.	Subassembly Type	# of SA	# of Pins
Inner	1	Driver	32	91
	2	High Flow Driver	18	91
	3	Partial Driver	10	91
	4	High-Worth CR	8	61
	5	Safety Rod	2	61
	6	Steel 7-pin	5	7
	7	Inner Reflector	34	1
	8	XX09 Instrumented	1	61
	9	XX10 Instrumented	1	19
	10	Steel 61-pin	1	61
	11	Steel 19-pin	1	19
	12	Neutron Source	1	7
	13	X319 Experimental	1	1
	14	X320 Experimental	1	1
	15	X328 Experimental	1	7
	16	X390 Experimental	1	91
	17	X393 Experimental	1	91
	18	X399 Experimental	1	91
	19	X400 Experimental	1	91
	20	X401 Experimental	1	91
	21	X402 Experimental	1	91
	22	X406 Experimental	1	91
	23	X407 Experimental	1	91
	24	X408 Experimental	1	91
	25	X409 Experimental	1	91
Outer	26	Outer Reflector	156	1
	27	Outer Blanket	354	19
Total number of SA			637	

7.10.5. Final results, data comparisons

7.10.5.1. SHRT-17

First, the fission power used in the simulation was slightly modified to be in accordance with the initial steady state of the benchmark problem, because there was a difference between the initial total power (sum of fission and decay heat) and the initial heat removal from the primary circuit through the IHX. Second, the pump head, throttle valve opening and pressure loss at the core entrance nozzle were adjusted so that initial flow rates and pressure differences were equal to the initial conditions of the benchmark problem. Finally, the heat transfer area of the IHX was adjusted to make an initial condition for the intermediate outlet temperature of the IHX. These modifications are summarized in TABLE 16 and were consistent with the range of the data uncertainties. The system analysis result for the steady

state was in good agreement with the benchmark problem, as shown in TABLE 17. The above settings were used in the final transient analysis.

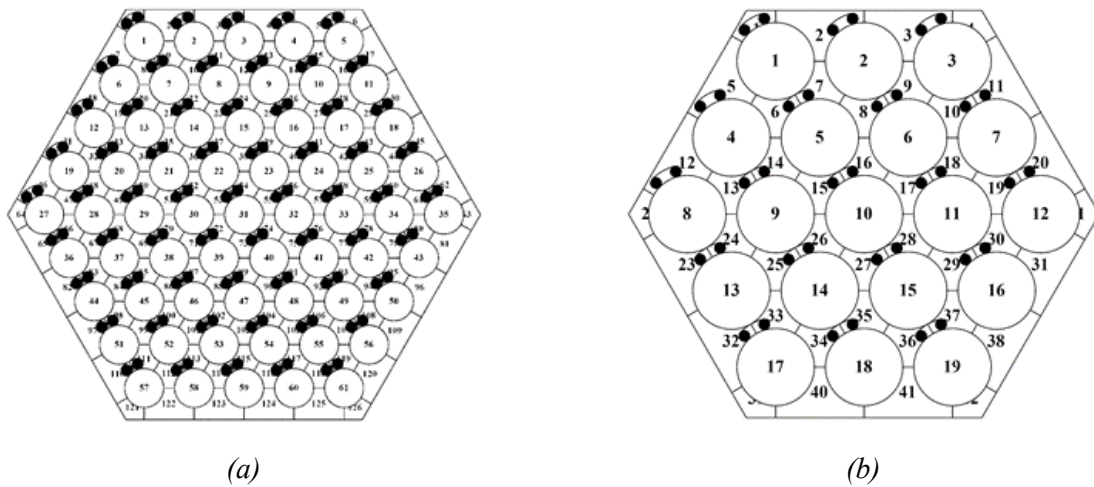


FIG. 159. Subchannel model for instrumented subassemblies (a) XX09, (b) XX10.

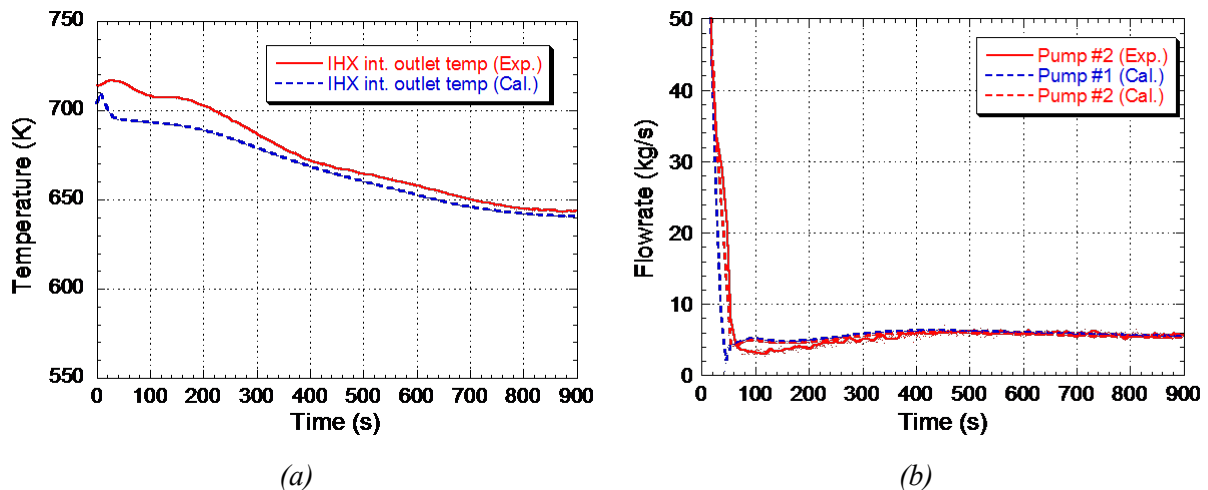


FIG. 160. SHRT-17 blind results: (a) IHX intermediate outlet temperature, (b) mass flow rates for pumps #1 and #2.

The measured and the simulated primary flow rates through pump #2 are shown in FIG. 162. The measured flow rate coasted down in the initial 50 sec and then recovered by buoyancy to 2 - 3 per cent of the rated flow rate. On the whole, the simulated flow rate increased slightly earlier than the measurement but after 250 sec was in good agreement with the measurement. As can be seen in FIG. 162(a) during the initial 50 sec, the simulation predicted that pump #1 stopped earlier than pump #2, so reverse flow must have occurred in the pump #1 circuit. Although the pump #1 predicted flow rate could not be compared directly with recorded data, a response appearing in the pump #2 flow rate as a small rise at about 40 sec could be traced in the simulation. The simulated heat removal via the IHX from the primary side to the intermediate side followed a similar curve to the measured intermediate side outlet temperature, as shown in FIG. 163.

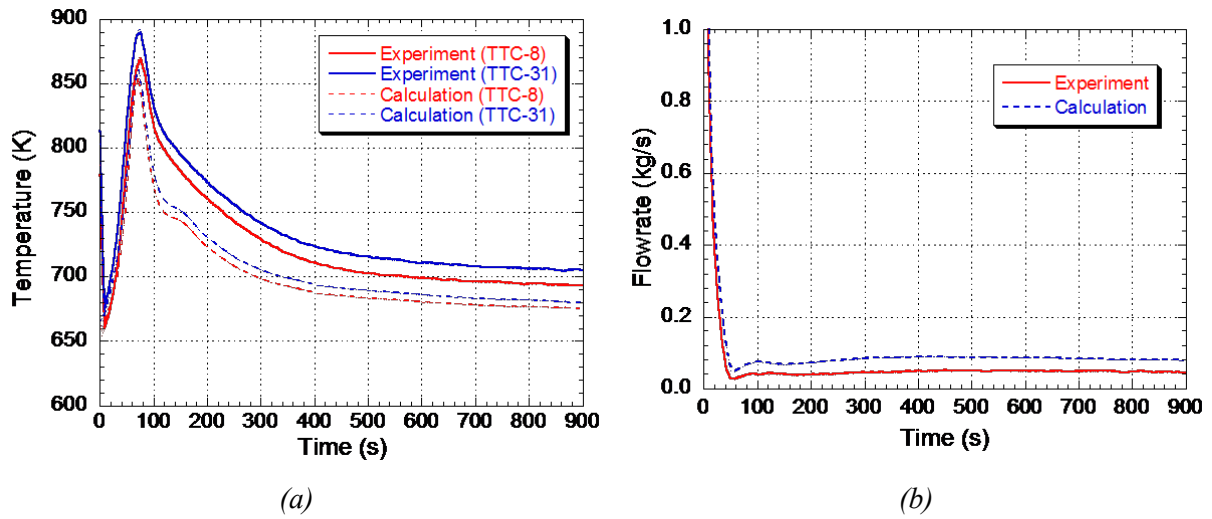


FIG. 161. SHRT-17 blind results: (a) core top temperature of XX09, (b) IHX intermediate outlet temperature

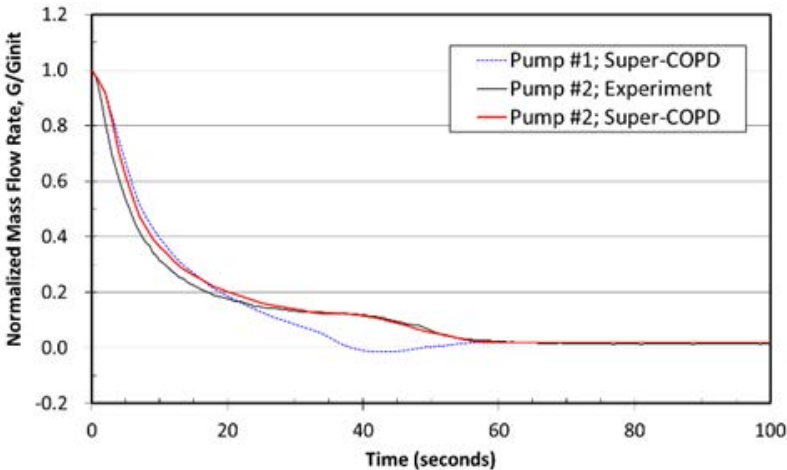
TABLE 16. PARAMETER SETTINGS

Parameter	Setting
Fission power	-2.3%
Pump head characteristics eq. of #1	-3.4%
Pump head characteristics eq. of #2	+5.0%
Valve opening of throttle #1	Adjusted
Valve opening of throttle #2	Adjusted
Pressure loss of core entrance nozzle	Adjusted
Heat transfer area of IHX	Adjusted

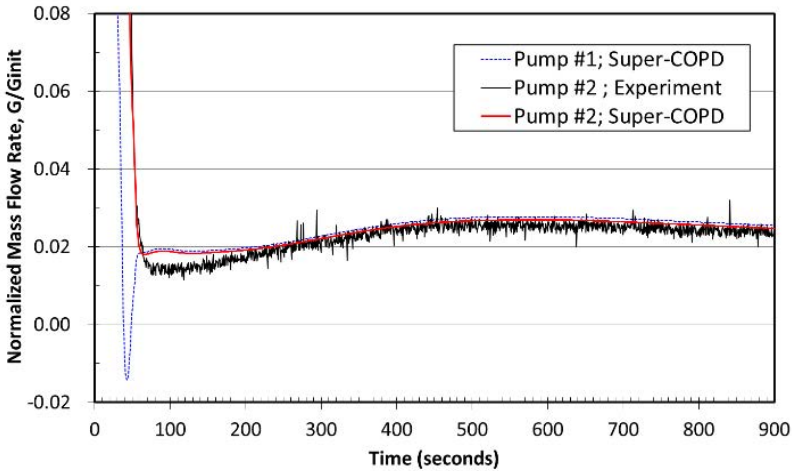
TABLE 17. STEADY STATE FOR THE SYSTEM ANALYSIS

Location	Ref.	Cal.
Initial Power (MW)	57.3	56.0
Sodium Mass Flow Rate (kg/s)	-	-
Reactor Core	456.9	459.9
Inner Core	386.6	392.5
Bypass	3.8	3.8
Outer Core	65.3	63.6
Pump #1	234.0	235.4
Pump #2	233.6	235.0
Sodium Temperature (K)	-	-
IHX Primary side Outlet	628.5	623.8
IHX Intermediate side Outlet	714.2	712.7
Pressure Diff. from Core Outlet (kPa)	-	-
Discharge of Pump #1	251.9	256.9
Discharge of Pump #2	245.0	250.0

Supplemental data for 21 subassembly outlet temperatures were provided by Argonne in Phase 2 of the CRP. These data are useful for understanding the flow rate redistribution in the core and the radial heat transfer between subassemblies. Four simulated subassembly outlet temperatures were compared with the measurements in FIG. 164. The overall response of temperature at each subassembly outlet was in good agreement with the measurements. However, after 50 sec the simulation slightly overpredicted the 2nd and the 4th row drivers and underpredicted the 6th row driver, compared with the experimental results. Also, there was a phase lag at the peak point of the 2nd and the 4th row drivers.



(a)



(b)

FIG. 162. Primary flow rates of pumps #1 and #2: (a) near-term trend, (b) long term trend.

Two reasons why the over-/under-predictions occurred can be considered. One is thermal diffusion at the core outlet in the core upper plenum due to the mixing of sodium. The measured temperatures at the 2nd row driver and those at the 6th row driver could have been decreased and increased, respectively, by mixing. Another one is a lack of accuracy in the volume estimation of the upper shield region in a subassembly, which is located above the fuel pin bundle. This may have caused the over/underprediction and the phase lag of the outlet

temperature. In fact, the upper shield region was described as the same as the fuel bundle region in this model. Future work should reduce the volume estimation error of the upper shield region in a subassembly as much as possible. It should, however, be noted that the core analytical model can simulate realistically the flow rate redistribution in the core and the radial heat transfer between subassemblies.

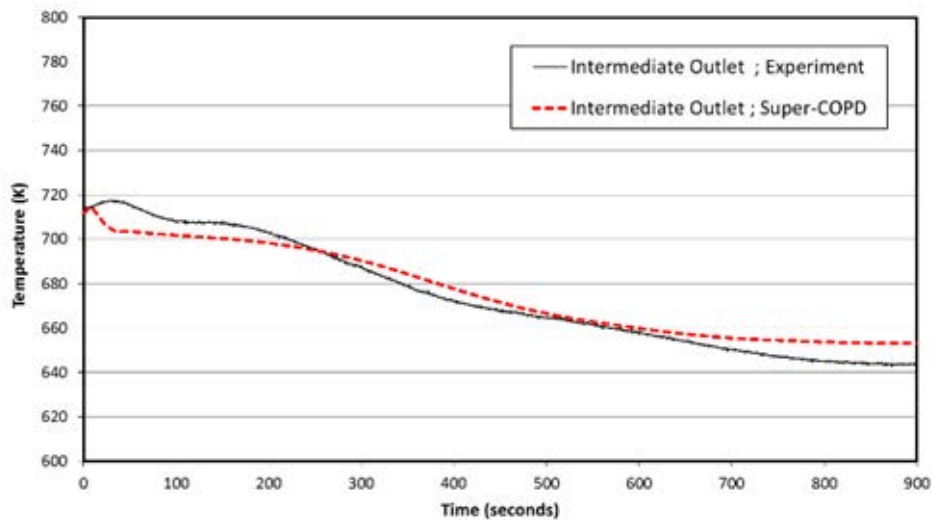


FIG. 163. IHX intermediate side outlet temperature.

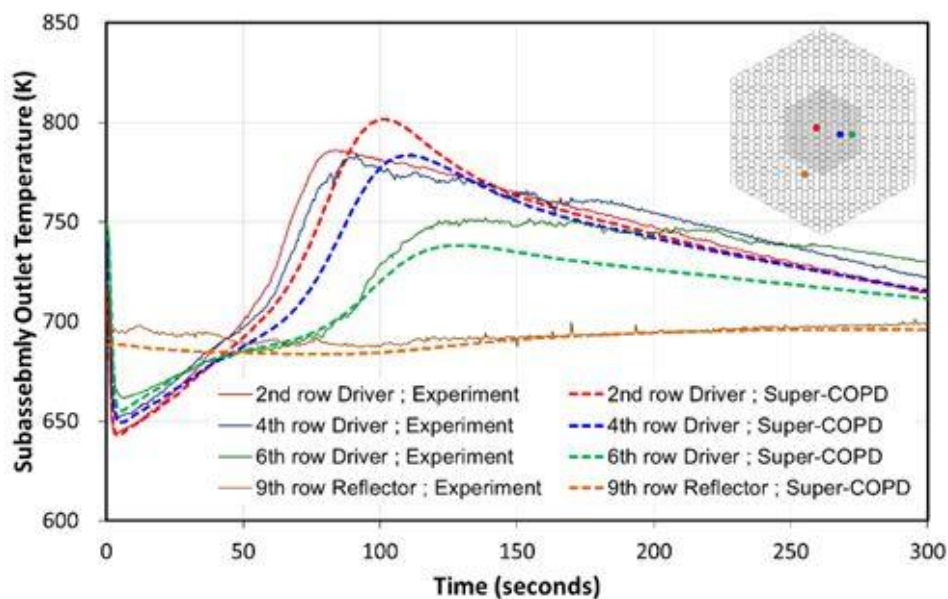


FIG. 164. Subassembly outlet temperatures.

The subassembly flow rates were directly measured in instrumented subassemblies XX09 and XX10, which have flowmeters at the entrance of each subassembly. As can be seen in FIG. 165, the simulated flow rate of XX10 is in good agreement with the measurement. There is, however, a discrepancy in XX09 at low flow rates by a factor of 1.5. A plausible explanation is that the flowmeter offset setting has a wider uncertainty at low flows. The simulated XX09 flow rate may fall within this uncertainty range.

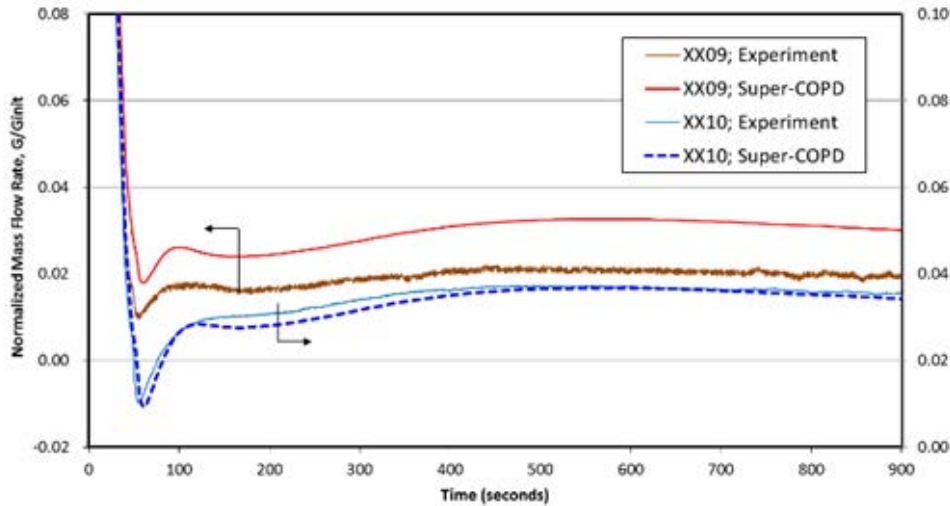


FIG. 165. Flow rates through XX09 and XX10.

Axial and radial sodium temperature distributions were recorded in instrumented subassemblies XX09 and XX10. Subchannel analyses for XX09 and XX10 were carried out by setting the boundary conditions of the core inlet temperature, the flow rate of the subassembly and the heat flux across the wrapper tube at the values obtained by the system analysis results. FIG. 166 shows the sodium temperatures near the centre of the subassembly for XX09 and XX10 in the middle (MTC) and on the top (TTC) of the active core. In both cases, as can be seen, the numerical model tends to give predictions that are parallel to the measured temperatures. The simulated peak temperatures at the top of the core in XX09 and XX10 were underestimated by only 16 K and 9 K, respectively. From FIG. 167 it can be seen that the simulated radial temperature distribution in XX09 has a parabolic shape initially at steady state and eventually flattens when natural circulation is established, similar to the behaviour of the measurements, while XX10 has a flat radial temperature shape throughout the transient because it is made of steel and has a low power density.

The simulation results of the EBR-II SHRT-17 test demonstrated the feasibility of prediction of core hot spot temperature under natural circulation decay heat removal operations in SFRs.

7.10.5.2. Model improvements

The thermal stratification in the upper plenum may be related to the recovery of primary flow after the flow coastdown. In this study, therefore, the upper plenum model was modified from the single perfect mixing volume used in the blind simulation to two mixing volumes. Comparison of the primary flow rates obtained using the single mixing volume model versus the two mixing volumes is shown in FIG. 168. The two mixing volume result seems to be slightly better than the single mixing volume result. In future work, the 3-D analysis for the upper plenum will be coupled to the current 1-D analysis to investigate the effect of thermal stratification in the upper plenum on the primary flow.

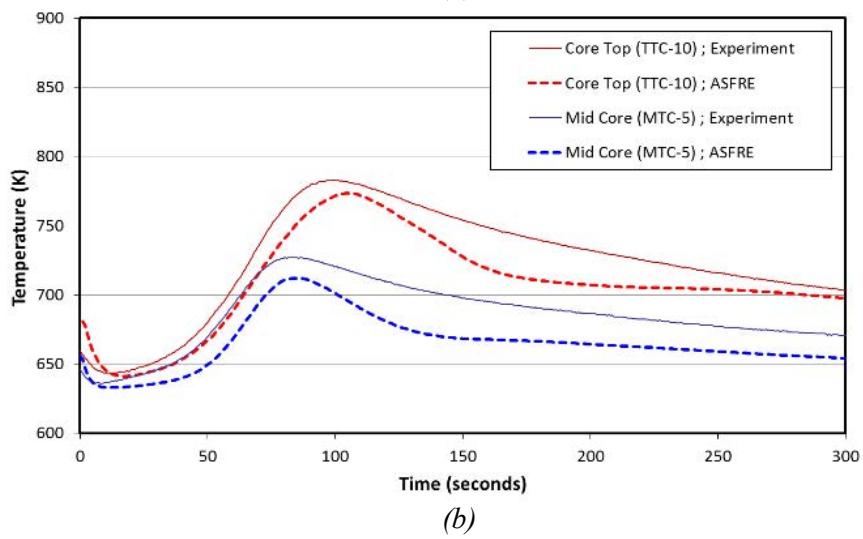
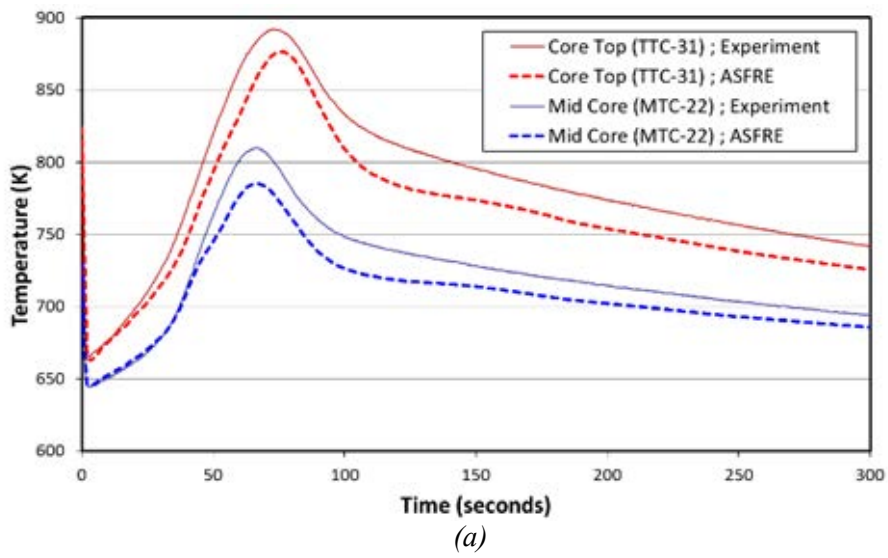


FIG. 166. Sodium temperatures near the centre of the subassembly at the top and middle of the core: (a) XX09, (b) XX10.

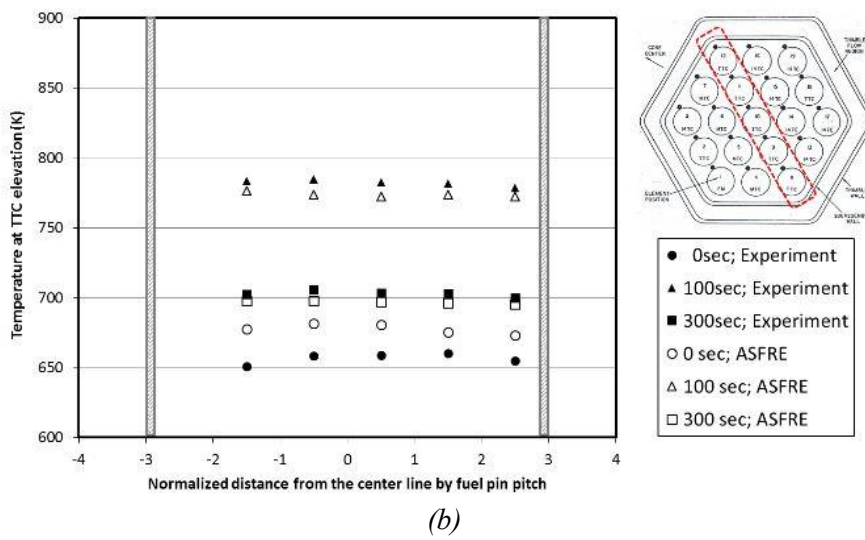
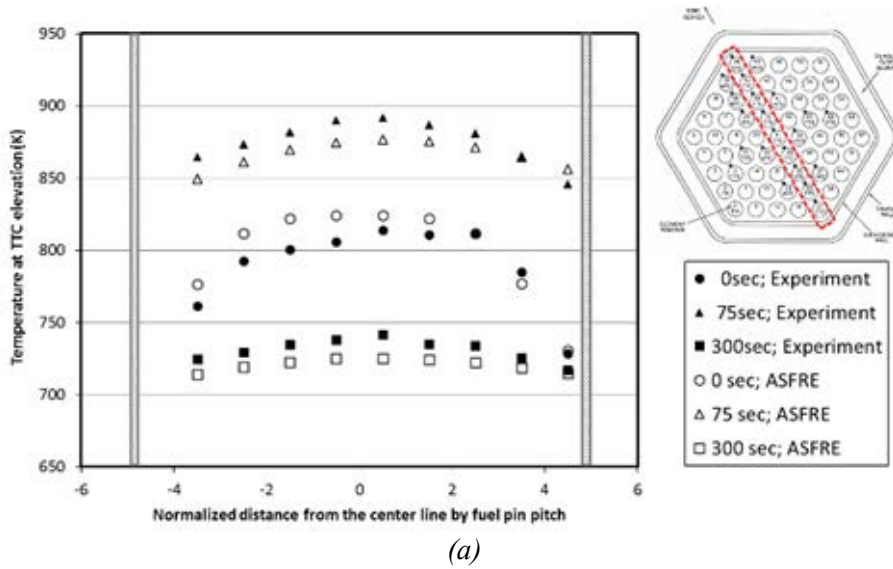


FIG. 167. Horizontal sodium temperature distributions at steady state, at the peak of the flowrate (at 75 s), and under natural circulation conditions: (a) XX09, (b) XX10.

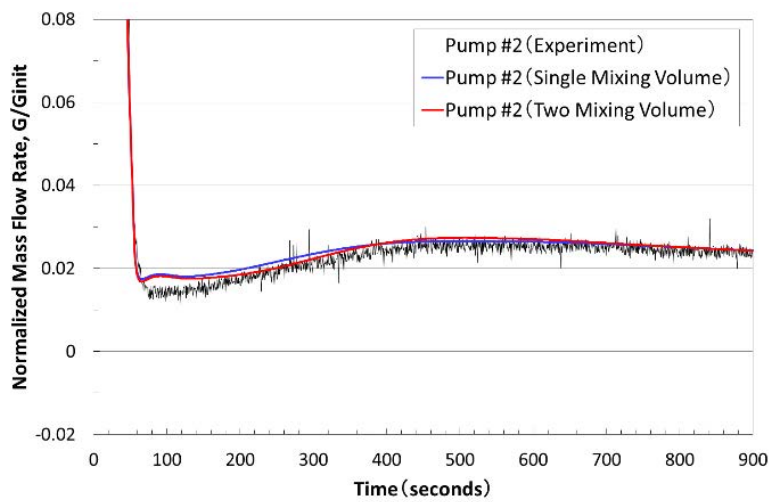


FIG. 168. Comparison of primary flow rates obtained by using single and two mixing volume models for the upper plenum.

7.11. UNIVERSITY OF FUKUI (JAPAN)

7.11.1. Geometry/discretization

A simplified calculation model is shown in FIG. 169. The tank containing liquid sodium is modelled as a large diameter pipe with an equivalent inventory as the primary tank. Most pipes in the calculation model are divided into several nodes. A number enclosed by a circle is called a 'main joint' and a number with a bracket is called a 'main link'. The main link is a flow path with volume like a pipe, which connects two joints and can be divided into several sub-links with sub-joints, depicted with small circles. Since the relative elevations for the main joints and sub-joints, indicated with small italic numbers in the figure, are input to the code, the elevations of the heat transport system are correct.

Many kinds of subassemblies are loaded in the reactor (XX09 and XX10 instrumented channels, 47 driver fuel, 13 half-driver fuel, 23 high flow driver fuel, 10 control rods, 164 reflectors, 366 blanket fuel, etc.). The core configuration is slightly different between the SHRT-17 and SHRT-45R tests. Since natural circulation conditions should be calculated in the benchmark, the heat transfer between the fuel subassemblies is not negligible. In order to calculate accurately the inter-subassembly (SA) heat transfer, the loading pattern of the fuel assemblies should be explicitly available. Since the NETFLOW++ code can model only 10 kinds of core channels, all subassemblies are grouped for the calculation. In total, 88 fuel subassemblies, 7 steel subassemblies, 165 reflectors and 366 blanket subassemblies are taken into account in the calculation. The inter-SA heat transfer is calculated taking into account the arrangement of the 10 core channels. Channels (Link-1 to Link-8) from the high pressure plenum to the upper plenum are divided into 6 sub-links. The outer reflector and blanket are divided into 4 sub-links. The first part is the entrance nozzle. Second is beneath the reactor core, third is the fuel SA. The fuel part is meshed precisely with 19 nodes. Other parts have only one node. The piping is meshed as follows: Z-Pipe (Link-11 in FIG. 169) with 6 sub-links, Link-12 and Link-13 with 4 sub-links, Link-14 and Link-15 with 3 sub-links, Link-16 and Link-17 with 6 sub-links. The IHX heat transfer tubes and shell side are divided into 20 nodes.

7.11.2. Nuclear and thermo-physical data/correlations

In the SHRT-45R test, the reactor was not scrammed while the coolant pumps are coasting down. Only natural reactivity feedback effects were available to shut down the neutron chain reaction. Therefore it is important to calculate the reactivity feedback effects with sufficient accuracy. In the NETFLOW++ code the fission power is calculated with the well-known point-kinetics equations. Thus, the relevant neutronic parameters are the effective delayed neutron fraction and decay constant for each of the precursor families, the neutron lifetime and the overall reactivity of the core, including feedbacks. The one-point-kinetics parameters are calculated by the ERANOS v2.0 code. TABLE 18 and TABLE 19 show the parameters which are given to the code. In terms of the reactivity coefficient of control rods, the value is not calculated because the initial position is not clear.

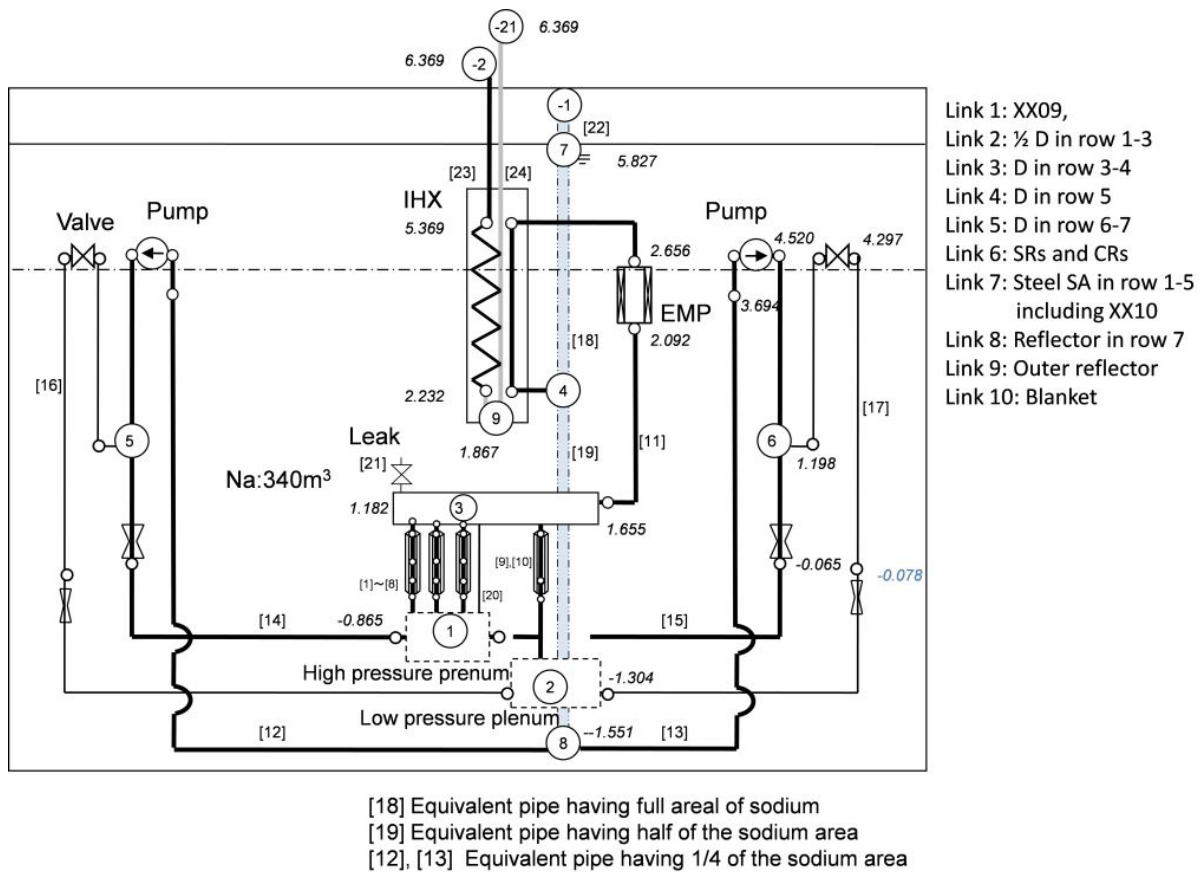


FIG. 169. Calculation model of EBR-II for the NETFLOW++ code.

7.11.3. Thermal hydraulics methods and models

7.11.3.1. Code(s) used

The NETFLOW++ code was used to calculate the plant thermal hydraulics in general. NETFLOW++ is a 1-D systems analysis code. For instrumented assemblies XX09 and XX10, the COBRA-4i code was used to calculate temperature profiles during the test. For these analyses, the calculated results from the NETFLOW++ code, i.e., inlet flow rate and temperature for individual tests, are used as boundary conditions.

TABLE 18. DELAYED NEUTRON DATA

Delayed neutron group	Fraction (-)	Decay constant (1/s)
β_1	2.183285×10^{-4}	1.246870×10^{-2}
β_2	1.458326×10^{-3}	3.062465×10^{-2}
β_3	1.334071×10^{-3}	1.130473×10^{-1}
β_4	2.695671×10^{-3}	3.056735×10^{-1}
β_5	8.615698×10^{-4}	1.171473×10^0
β_6	3.063377×10^{-4}	3.129448×10^0
β_{eff}	6.874304×10^{-3}	-
Neutron lifetime: 3.876173×10^{-7} sec		

TABLE 19. REACTIVITY FEEDBACK COEFFICIENTS USING JENDL-4.0

Item	pcm/K (=10 ⁻⁵ /K)
Doppler	-0.024
Axial expansion	-0.84
Radial expansion	-2.10
Sodium density core only	-0.71
Sodium density all	-1.90
Control rod expansion	0.0

7.11.3.2. Basic method

Since the data of primary pump speed is given in the working material, a pump trip transient of SHRT-17 was calculated in advance. After confirmation that the rotational speed of the main pump was properly calculated, the SHRT-17 transient was calculated using the given power transient curve. In this calculation, basic constants of the models were tuned. The NETFLOW++ code calculates neutronic power using one-point-kinetics with 6 delayed neutron groups. Therefore, data relevant to the one-point-kinetics model was calculated using the ERANOS v2.0 code. The characteristic data were given to the NETFLOW++ code, and the SHRT-45R transient was calculated. The following is the calculation model incorporated in the NETFLOW++ code.

The reactor power was calculated by a subroutine in the NETFLOW++ code using the following procedure. The initial thermal power is given to the code based on the reactor operation. The steady state calculation is conducted with the time marching method. Then, the one-point neutron characteristics data is given to the code to calculate the initial reactivity. In the calculation, the fractions of powers by fission and decay heat were given to the code, e.g., $f_f=0.94$ and $f_d=0.06$. The number of neutrons and the density of the precursor during the transient were calculated by the following EQS. (1)-(4). Each equation is discretized assuming a prompt jump and a central difference.

$$\frac{dn}{dt} = \frac{\rho - \beta_{eff}}{\Lambda} n + \sum_{i=1}^6 \lambda_i C_i + S \quad (9)$$

$$\frac{dC_i}{dt} = \frac{\beta_i}{\Lambda} n - \lambda_i C_i, \quad i=1,2,\dots,6 \quad (10)$$

$$C_i^{k+1} = \frac{(1 - 0.5\lambda_i\Delta t)C_i^k}{(1 + 0.5\lambda_i\Delta t)} + \frac{\beta_i\Delta t}{2\Lambda} \frac{(n^{k+1} + n^k)}{(1 + 0.5\lambda_i\Delta t)} \quad (11)$$

$$\left(\beta_{eff} - \rho^{k+1} - \frac{\Delta t}{2} \sum_{i=1}^6 \frac{\lambda_i \beta_i}{(1 + 0.5\lambda_i\Delta t)} \right) n^{k+1} = \Lambda \sum_{i=1}^6 \lambda_i \left\{ \frac{(1 - 0.5\lambda_i\Delta t)C_i^k}{(1 + 0.5\lambda_i\Delta t)} + \frac{\beta_i\Delta t}{2\Lambda} \frac{n^k}{(1 + 0.5\lambda_i\Delta t)} \right\} + \Lambda S^{k+1} \quad (12)$$

The number densities of the neutrons and the six precursor families were solved without solving any simultaneous differential equations. The transient calculation was conducted in

order to find the timing of the reactor power to decrease. The fission power and the decay heat power were calculated simultaneously with EQ. (5) and EQ. (6):

$$P^{k+1} = P_o (f_f \times n^{k+1} + f_d) \quad (13)$$

$$f_d = 0.005a \{t^{-b} - (t+t_s)^{-b}\}, \quad (14)$$

with

$$\begin{aligned} a= 12.05, b=0.0639 & \quad 0.1 < t < 10, \\ a= 15.31, b=0.1807 & \quad 10 < t < 150, \\ a= 27.43, b=0.2962 & \quad 150 < t < 8 \times 10^8. \end{aligned}$$

The decay power in SHRT-45R was calculated with EQ. (6), using constants verified by Garland [113].

7.11.3.3. Model

Regarding the pressure loss calculation for the driver fuel subassemblies with wire spacers, Cheng & Todreas [110] proposed a correlation, and this correlation was modified by Chen *et al.* [114]. Since this correlation is not incorporated into the NETFLOW++ code to take into account the wire spacer effect, a local loss coefficient was used. The pipe friction factor was calculated by an approximated correlation of Moody's chart, taking into account 10^{-5} m roughness on the surface. As for the heat loss from the piping of EBR-II, a heat transfer coefficient of approximately 8 W/(m²-K) was assumed. It is mentioned in the benchmark document that there is a sodium leakage in the primary flow path. The flow rate of 3.4 kg/s through the upper plenum suggested in the benchmark document was assumed in the present calculation. However, it was confirmed through a sensitivity analysis that this leakage had negligible effect on the peak temperature. The other major leakages mentioned in the document occur at adapters of core subassemblies, control and safety subassemblies and expanded core subassemblies. A leakage of 9.9 kg/s in total was considered, using a bypass flow passage. The pump momentum equation was solved in the code to obtain the proper flow rate and pressure. The data required for the model are values of pump discharge pressure, volumetric flow rate and rotation speed under the rated condition. Other than these, data about moment of inertia, shaft power, pump friction torque and characteristic curves like Q-H, torque and efficiency were given to the code. In case of an electromagnetic pump, a special pump model which gives discharge pressure at a volume of interest without solving the momentum equation was used. In terms of metal fuel properties, density, specific heat and thermal conductivity were given by correlations in the working material. Since the gap between the fuel and the cladding is filled with sodium, the gap conductance was calculated by the thermal conductivity of liquid sodium and the gap width. The properties of other materials, such as sodium and stainless steel, were taken directly from correlations included in the NETFLOW++ code. The inter-SA heat transfer should be taken into account in order to obtain an accurate coolant temperature during the transient because the transient is natural circulation. The model of the inter-SA heat transfer of the NETFLOW++ code was verified with measured data at the experimental fast reactor "Joyo" [20]. The heat transfer was calculated after the 10 core channels were defined, and neighbouring channels were designated by a matrix based on the core configuration of EBR-II.

Regarding boundary conditions of the calculation for SHRT-45R, the reactor power, inlet flow rate and temperature of the IHX on the secondary heat transport system were used based on the given data.

7.11.4. Blind results

7.11.4.1. SHRT-17

A blind analysis for the SHRT-17 test was conducted at first referring to the open literature. Since the peak temperature of the reactor outlet is sensitive to the pump coastdown characteristics, values of the pump friction torque and inertia were investigated.

Although the value of 0.0286 is mentioned in the working material, it was clarified that characteristics between the two pumps were slightly different in order to reproduce the coastdown curve in the working material. FIG. 170 through FIG. 173 depict evolutions of primary pump flow rates, IHX primary and intermediate temperatures, Z-Pipe inlet temperature, temperatures in lower plena and sodium temperatures in instrumented subassemblies.

7.11.4.2. SHRT-45R

FIG. 174 through FIG. 177 illustrate the calculated results of the plant parameters and the reactor power by fission and decay heat. A blind analysis for the SHRT-45R test was conducted on the basis of the calculation experience of the SHRT-17 test. One-point neutron kinetics data were given to the code to calculate the reactor power.

7.11.5. Final results, data comparisons

7.11.5.1. SHRT-17

After the data measured at EBR-II were opened, it was possible to recognize the improvements to the input data that would result in a better simulation of the transient. They are leak flow rate from the reactor vessel, heat loss from the Z-Pipe, and heat loss from the inlet piping to the plena. Flow rate evolution in pump #2 had been calculated correctly. When the scale is magnified, it can be seen that the code overpredicts slightly the measured result. However, the temperature at the inlet of the IHX primary was not predicted correctly. Therefore, the heat transfer rate from the Z-Pipe to the cold pool was changed significantly. When this temperature is accurately predicted, other plant parameters were affected significantly and in a different direction. Heat losses from the piping connected to the lower plena were set to simulate the temperatures in the lower plena. Plant parameters calculated by NETFLOW++ were almost the same as the result in the blind benchmark. In FIG. 178 through FIG. 181, comparisons between calculated final results and measured data for SHRT-17 are presented.

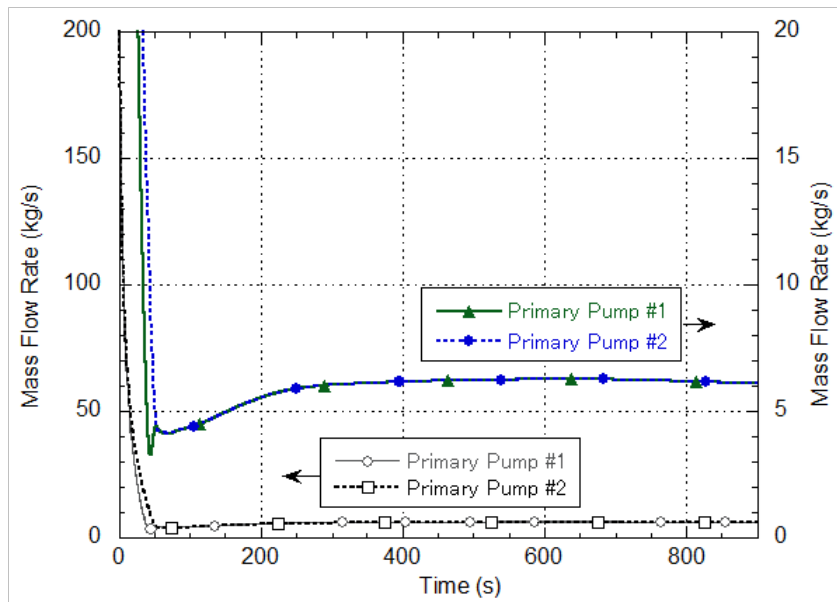


FIG. 170. SHRT-17 primary pump flow rates, blind results.

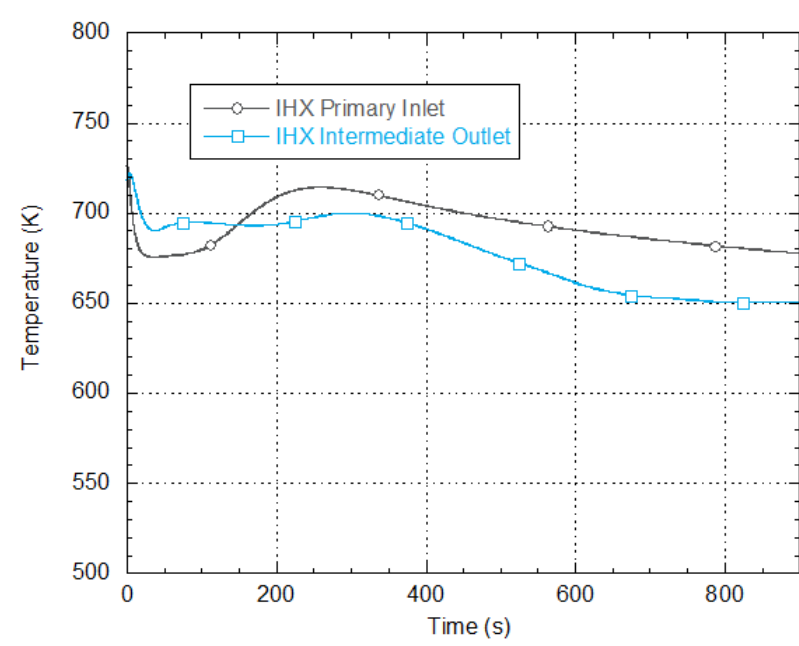


FIG. 171. SHRT-17 IHX temperatures, blind results.

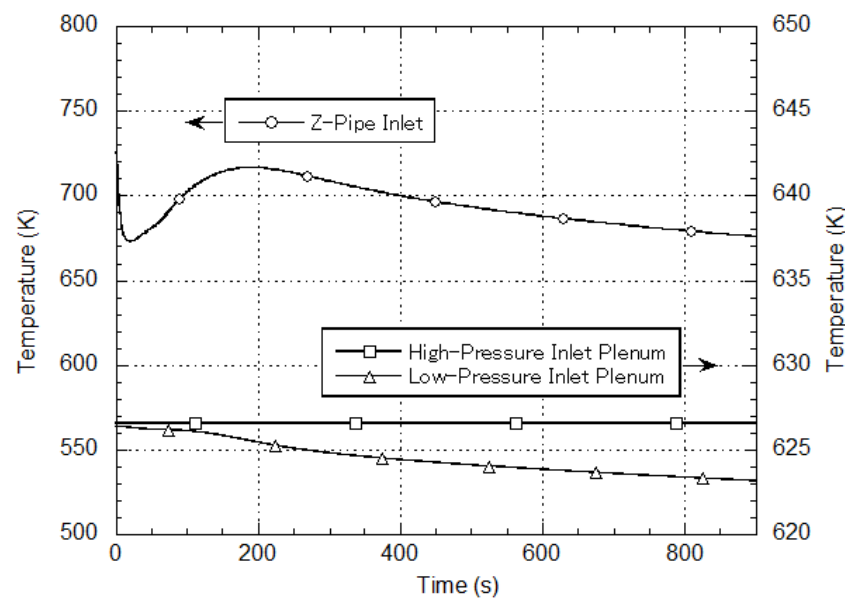


FIG. 172. SHRT-17 Z-Pipe and inlet plenum temperatures, blind results.

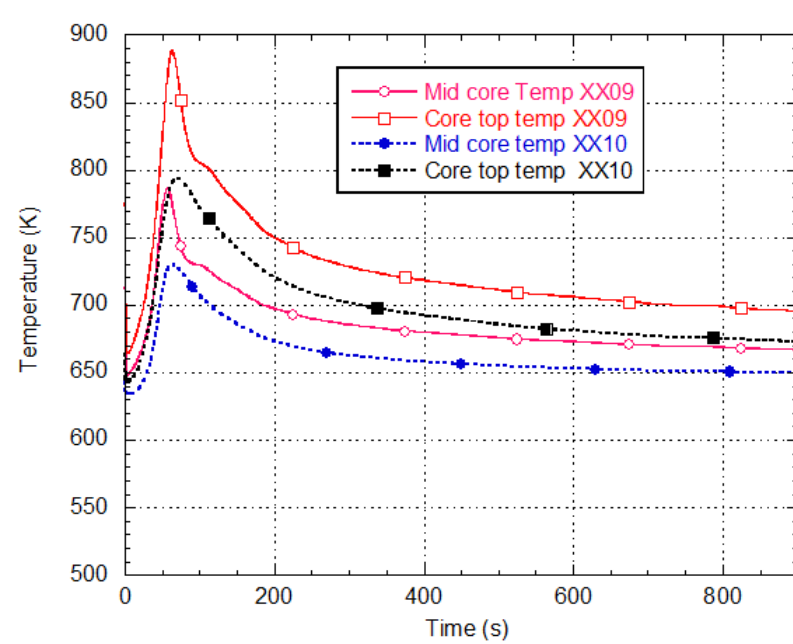


FIG. 173. SHRT-17 instrumented subassembly temperatures, blind results.

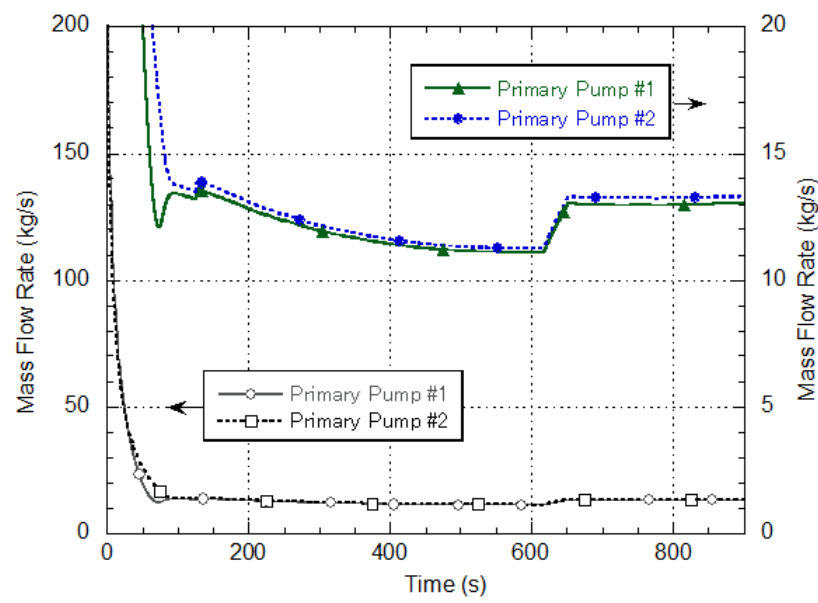


FIG. 174. SHRT-45R primary pump flow rates, blind results.

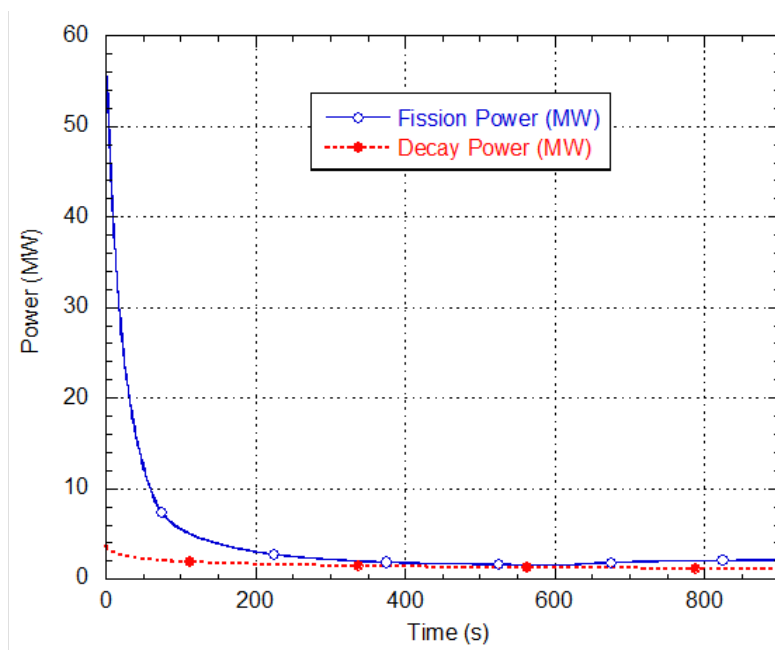


FIG. 175. SHRT-45R reactor power, blind results.

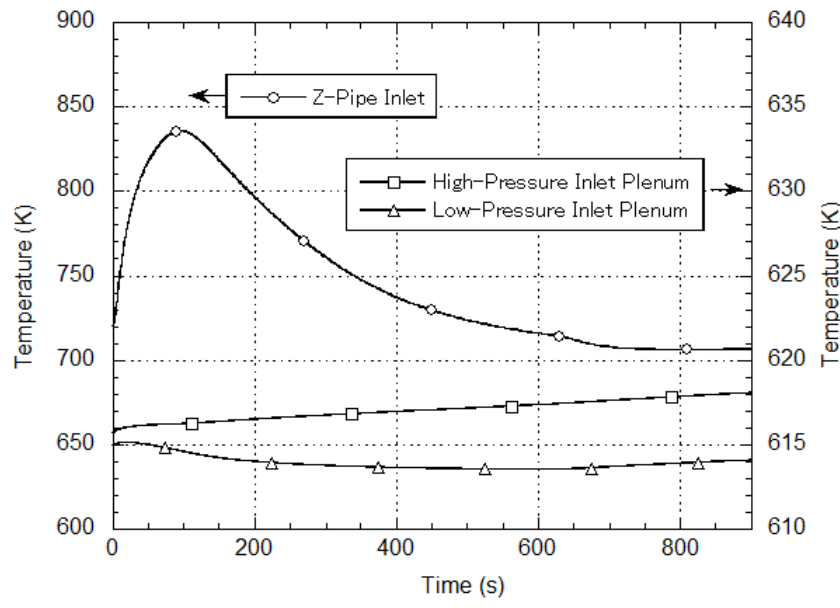


FIG. 176. SHRT-45R Z-Pipe and inlet plenum temperatures, blind results.

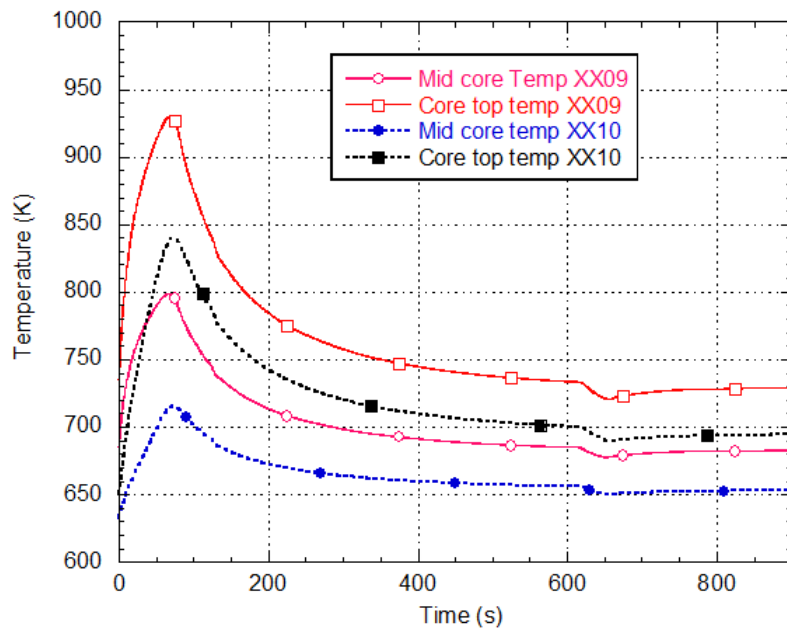


FIG. 177. SHRT-45R instrumented subassembly temperatures, blind results.

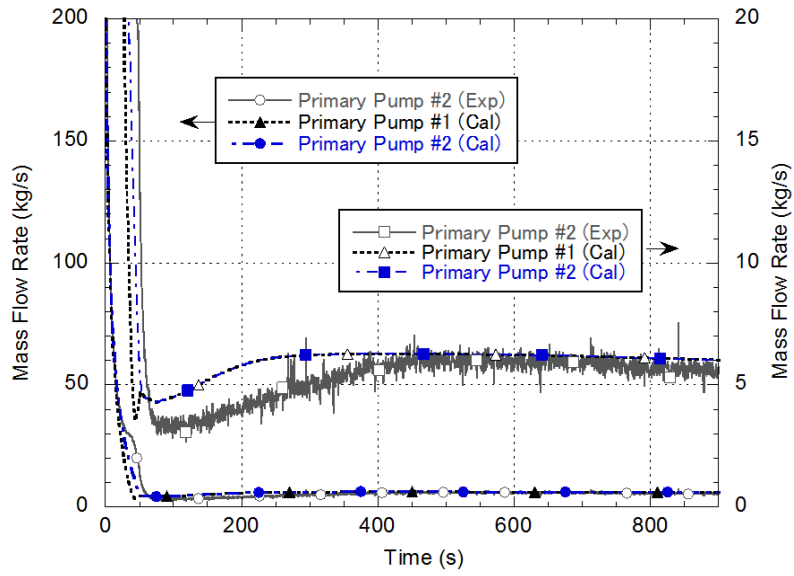


FIG. 178. SHRT-17 comparison of final NETFLOW++ results and plant data for primary pump mass flow rates.

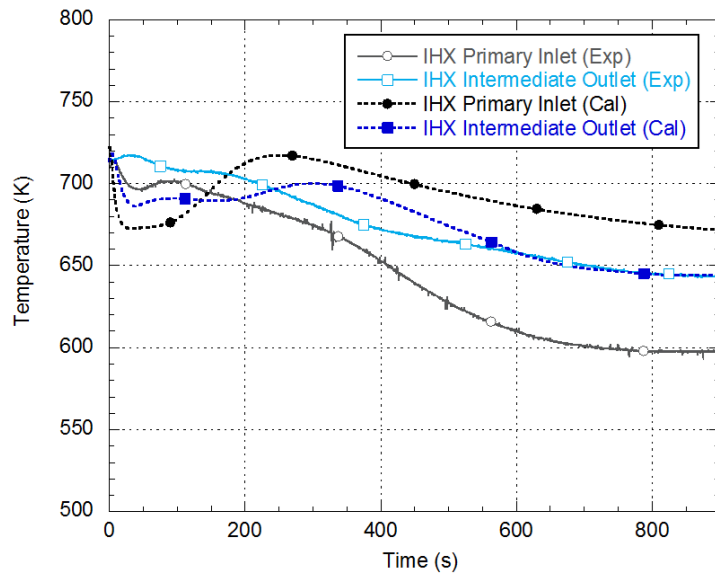


FIG. 179. SHRT-17 comparison of final NETFLOW++ results and plant data for IHX temperatures.

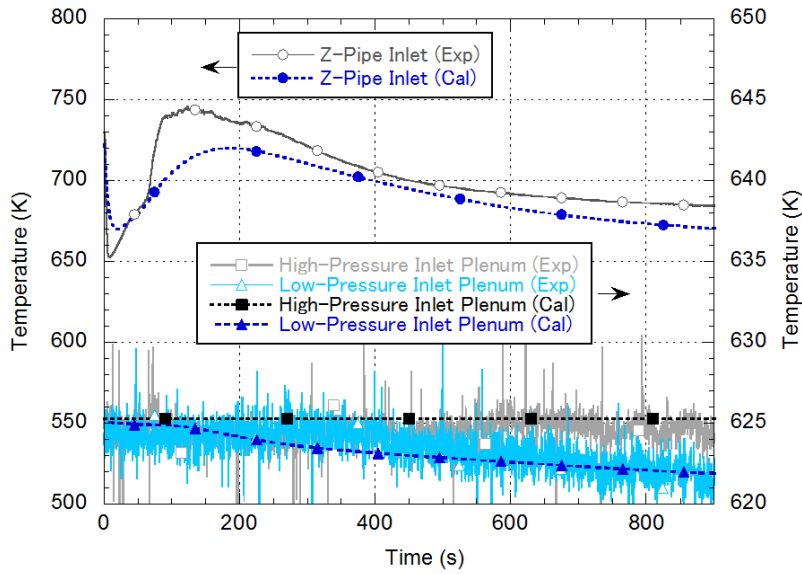


FIG. 180. SHRT-17 comparison of final NETFLOW++ results and plant data for Z-Pipe and inlet plenum temperatures.

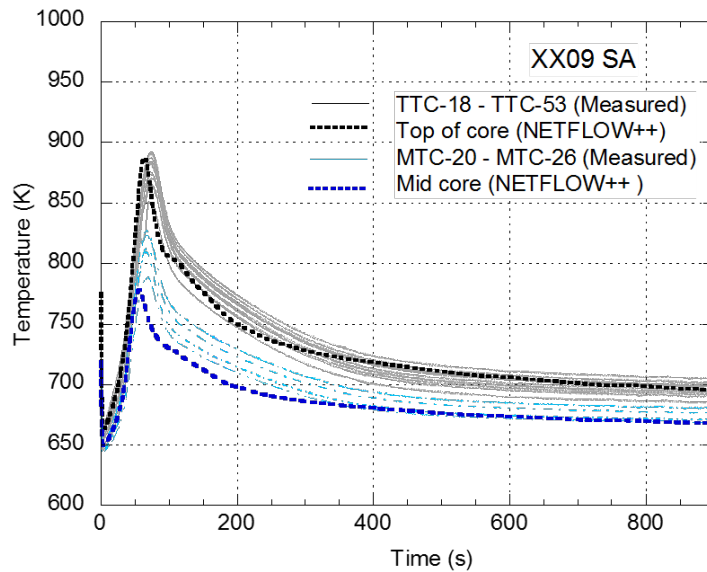


FIG. 181. SHRT-17 comparison of final NETFLOW++ results and plant data for XX09 temperatures.

For calculation of temperatures in instrumented channel XX09, inlet flow rate and temperature calculated by the NETFLOW++ code were transferred to the COBRA-IV-I code. In the present calculation, the fuel meat was neglected. Therefore, the peak temperature was underpredicted, as shown in FIG. 182. By contrast, the NETFLOW++ result is in the midst of the measured temperature band. In terms of the initial conditions, the code simulates the radial temperature profile caused by the wire spacers. In addition to the effect of the wire spacers, the power tilt effect on the temperature distribution was taken into account, since the neutron flux has a gradient from the centre of the core to the peripheral region. Therefore, the power gradient caused by the initial power distribution of the reactor was assumed to have a power

tilt in the XX09 SA. Both COBRA-IV-I calculation results at steady state are illustrated in FIG. 182.

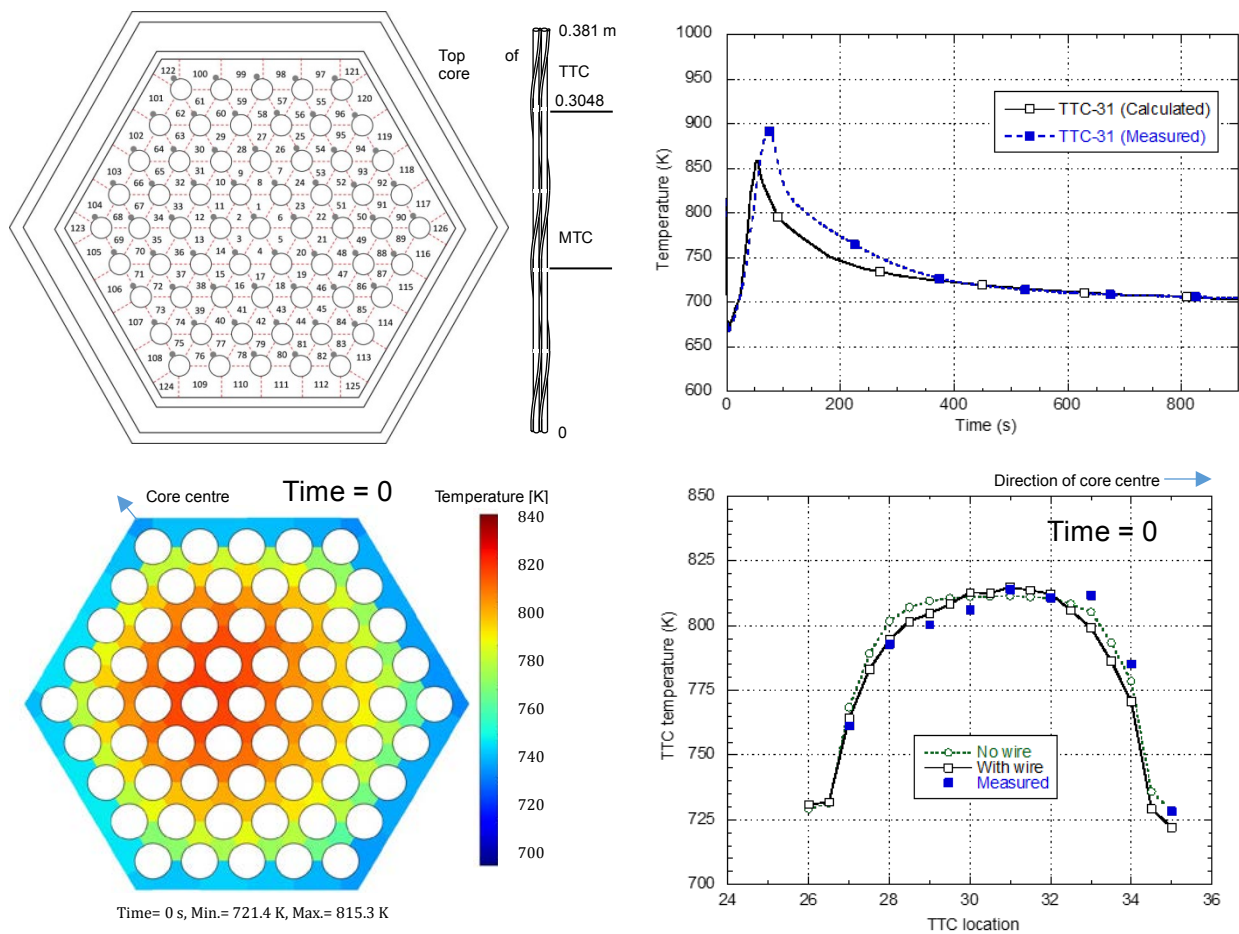


FIG. 182. Comparison of the peak temperature in XX09 SA of SHRT-17 between measurement and calculation by the COBRA-IV-I code.

7.11.5.2. SHRT-45R

In the SHRT-45R benchmark, the reactivity feedback is reviewed. The comparison between measured and calculated results is illustrated in FIG. 183. Flow rate evolution with the EM pump was correctly reproduced by the code. The Z-Pipe inlet temperature was slightly overpredicted. The calculated temperature at the top of the XX09 SA matches the measured temperature well except in the tail region, at the end of the transient. The calculated temperature at the XX10 subassembly mid-core is in good agreement with the measured result. However, the temperature at the top of XX10 was overpredicted. This is because the power in the steel SA is overpredicted by the code.

Temperatures in the XX09 SA calculated using COBRA-IV-I are depicted in FIG. 184. In this case, the power tilt was not taken into account because of the deployment situation around the XX09 SA. The initial radial fuel temperature profile in the SA was calculated almost correctly except for the peripheral region on the core centre side. Good agreement was obtained for the peak temperature. A difference between the SHRT-17 and SHRT-45 test is sharpness of the power transient. In the case of SHRT-45R, the power transient rate is slightly milder than for SHRT-17. Therefore, it is estimated that the heat capacity and heat conduction have only a

small effect on the temperature transient. Radial temperature profiles during the transient were calculated properly.

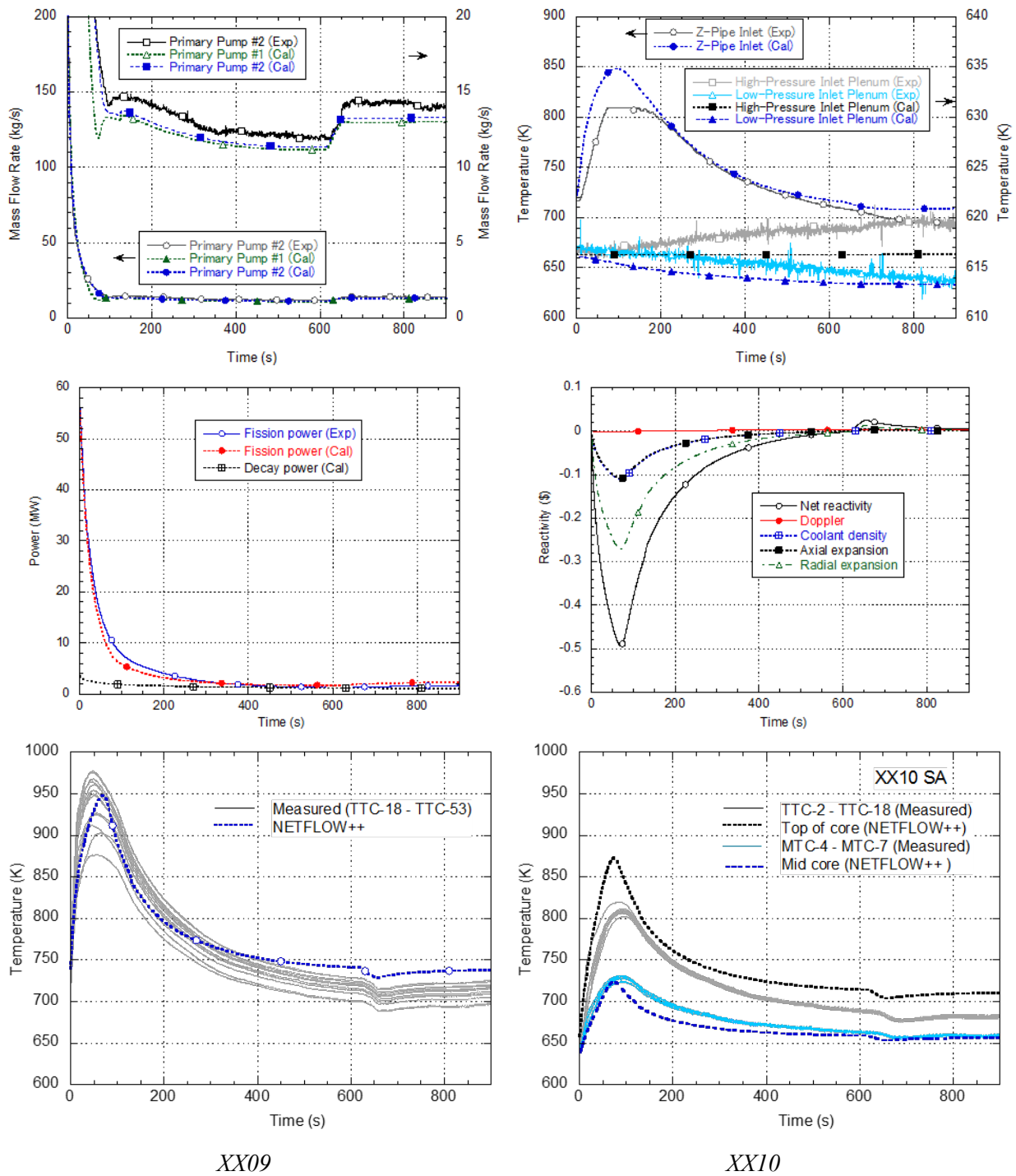


FIG. 183. Comparison of plant parameters during the SHRT-45R test between measurement and calculation by the NETFLOW++ code.

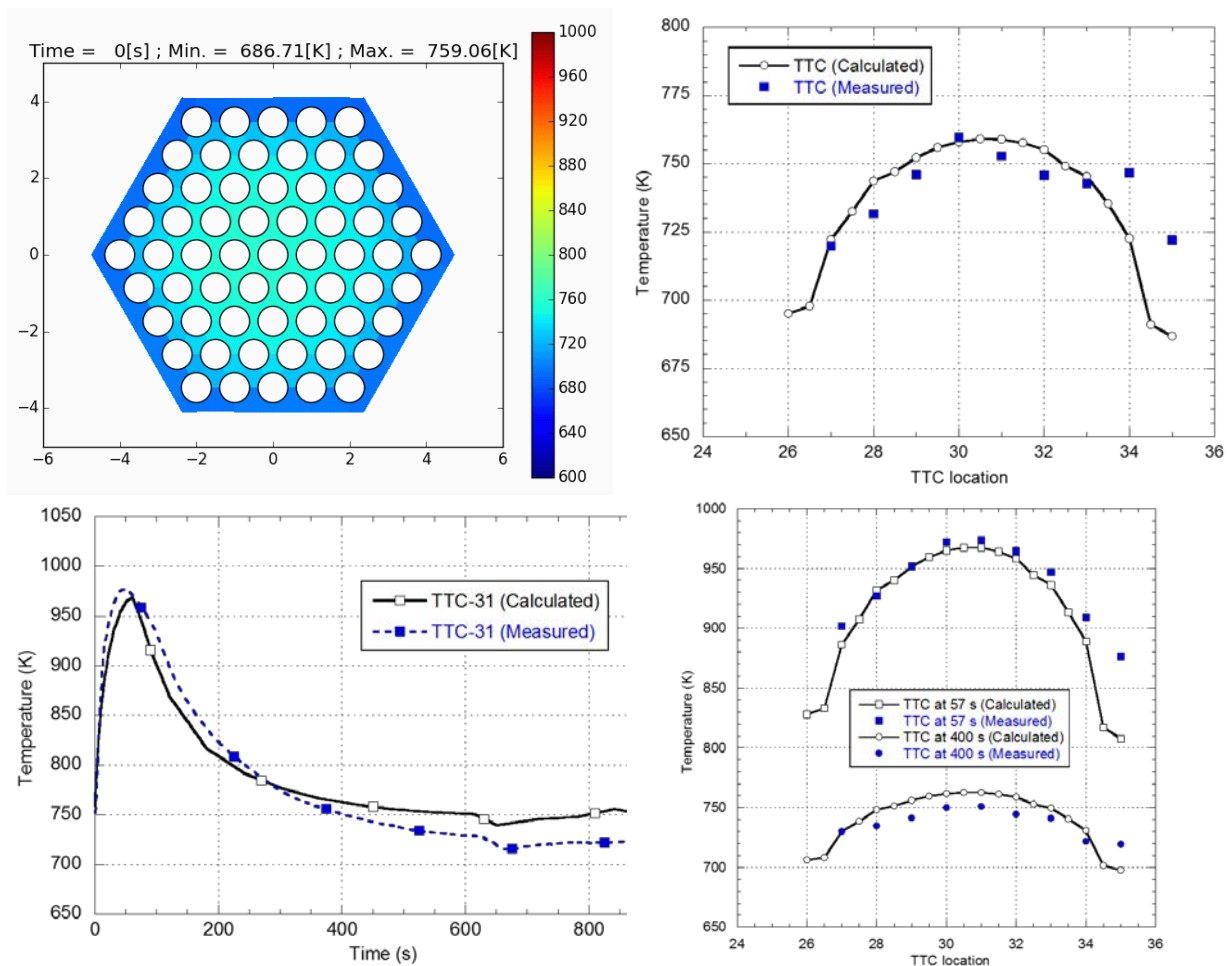


FIG. 184. Comparison of the peak temperature in XX09 SA of SHRT-45R test between measurement and calculation by the COBRA-IV-I code.

7.11.5.3. Model improvements

A discharge line from the reactor tank to the cold pool was added after the blind calculation in order to check the effect of the leakage on the plant behaviour. It was clarified that the effect was negligible. Local loss coefficients were adjusted in order to reproduce the measured data. Heat transfer coefficients from the inlet piping of the lower plena to the cold pool were adjusted based on the CFD result.

7.11.6. Neutronics methods and models

7.11.6.1. Code(s) used

The ERANOS v2.0 code system was used. To accommodate the benchmark specification, some modifications were made. The modifications are discussed below.

7.11.6.2. Neutron and photon cross-sections

Three sets of neutron cross-sections were prepared, based on JENDL-4.0, JEFF-3.1.2 and ENDF/B-VII.1. The standard energy structures of ERANOS were used, i.e. 1968 energy groups for the “major” isotopes (actinides and some important scattering isotopes) and 33 energy groups for all other isotopes. Cross-sections for pseudo-fission products and the

special “fissium” material were prepared in accordance with the specifications from Argonne. Standard photon cross-sections, included in ERANOS v2.0, were used in combination with standard KERMA factors and KERMA corrections.

7.11.6.3. Calculation of power and k_{eff}

Cell calculations were performed with the ECCO cell code for 12 “representative” mixtures: for each SA type (full-worth fuel SA, half-worth fuel SA, control SA, reflector SA) and for each of the three axial levels described in the benchmark. The microscopic cross-sections were used in combination with the individual mixture compositions to make macroscopic cross-sections. Full core calculations were done in 33 groups with transport theory (TGV-VARIANT module) for k_{eff} , while the power profile was calculated with 3-D diffusion theory. The calculated power profile was then corrected for gamma heating, using a 2-D RZ transport calculation for the transport of gamma rays and KERMA cross-sections to determine the power deposition due to gamma interaction. The results of this approach were not completely satisfactory.

7.11.6.4. Calculation of reactivity feedback

For feedback calculations the core materials were grouped into “non-fluids” (fuel and cladding) and “fluids”. Upon a change of temperature, all material densities were recalculated and a complete set of cross-sections was made. Feedback due to control rod expansion was treated in a limited way due to a lack of information about the control rod drives. The sodium void effect was calculated in two stages: (1) voiding the core only, and (2) voiding in all regions. The Doppler effect was calculated by increasing the temperature of the fuel in the core only. Since the fuel is highly enriched, the Doppler effect is small. The rationale for this choice was that during transients, only the temperature of the fuel in the core will change instantaneously. Any other model will implicitly overestimate the true impact of the Doppler effect.

7.11.7. Neutronics results

In TABLE 20 are given the major results for the neutronics benchmark. Where available, the uncertainty due to cross-section covariances has been included (see also Section 8.5.2). It is clear that geometrical feedback is very important for EBR-II. In comparison, the Doppler effect is negligible.

TABLE 20. RESULTS OF THE NEUTRONICS BENCHMARK

Parameter	JENDL-4.0	JEFF-3.1.2	ENDF/B-VII.1
k_{eff}	0.992280061	0.985027581	0.984920862
<i>Uncertainty [%]</i>	0.44	2.1	2.1
β_{eff} [pcm]	691	702	708
Feedback parameters [pcm/K]			
Axial expansion	-0.84	-0.85	-0.85
Radial expansion	-2.10	-2.14	-2.15
Axial and radial expansion	-2.94	-3.00	-3.02
Sodium density (core only)	-0.71	-0.73	-0.70
Sodium density (all)	-1.90	-2.02	-1.89
<i>Uncertainty [%]</i>	1.71	3.75	4.07
Doppler	-0.024	-0.023	-0.024
<i>Uncertainty [%]</i>	5.81	5.44	5.34
Control rod expansion	-0.8	-0.8	-0.79

FIG. 185 presents an example of the calculated power distribution for JENDL-4.0 (results for other data are similar). There are large errors (up to 66%), especially in non-fuel subassemblies. Partly fueled SAs also have large errors. This indicates a problem with the treatment of the energy deposition in stainless steel due to gamma heating. The standard methods of ERANOS v2.0 were used for this analysis but it seems that there remains an inconsistency. Finally, it should be mentioned that the benchmark values were calculated with the EBR-II core management software of the time, and uncertainties in the power distribution are not specified in the benchmark documents.

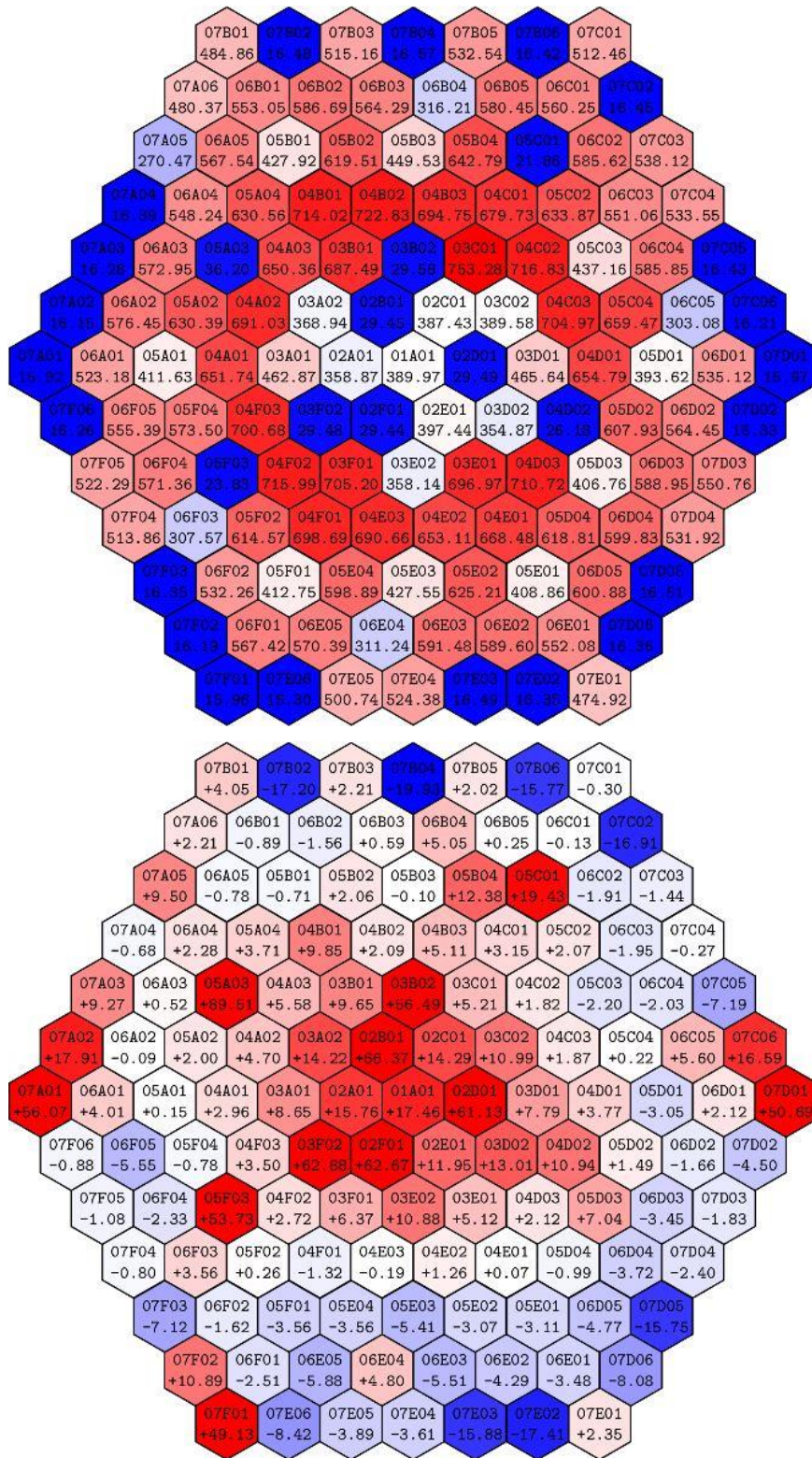


FIG. 185. Top: power distribution from ERANOS. Bottom: error to benchmark values in per cent.

7.12. KOREA ATOMIC ENERGY RESEARCH INSTITUTE (REPUBLIC OF KOREA)

7.12.1. Geometry/discretization

FIG. 186 shows the nodalization of EBR-II for MARS-LMR. The inlet and outlet conditions on the tube side of the intermediate heat exchanger (IHx) were modelled as boundary

conditions. The IHX was modelled with components no. 780 and 520 on the tube and shell sides, respectively. The Z-Pipe connecting the IHX shell side inlet and the core upper plenum outlet was modelled with component no. 460. The sodium cold pool was modelled with 6 volumes of component no. 300. Each volume elevation was defined to match the locations of the connecting component. For example, the pump inlets are connected to the junction between the 1st and 2nd volumes of the pool, and the IHX shell outlet is connected to the junction between the 3rd and 4th volumes of the pool. The core is modelled with 10 subassembly groups as summarized in TABLE 21. The two primary pumps were individually modelled with components no. 305 and 335. The high and low pressure inlet plena were modelled separately with components no. 370 and 380, respectively.

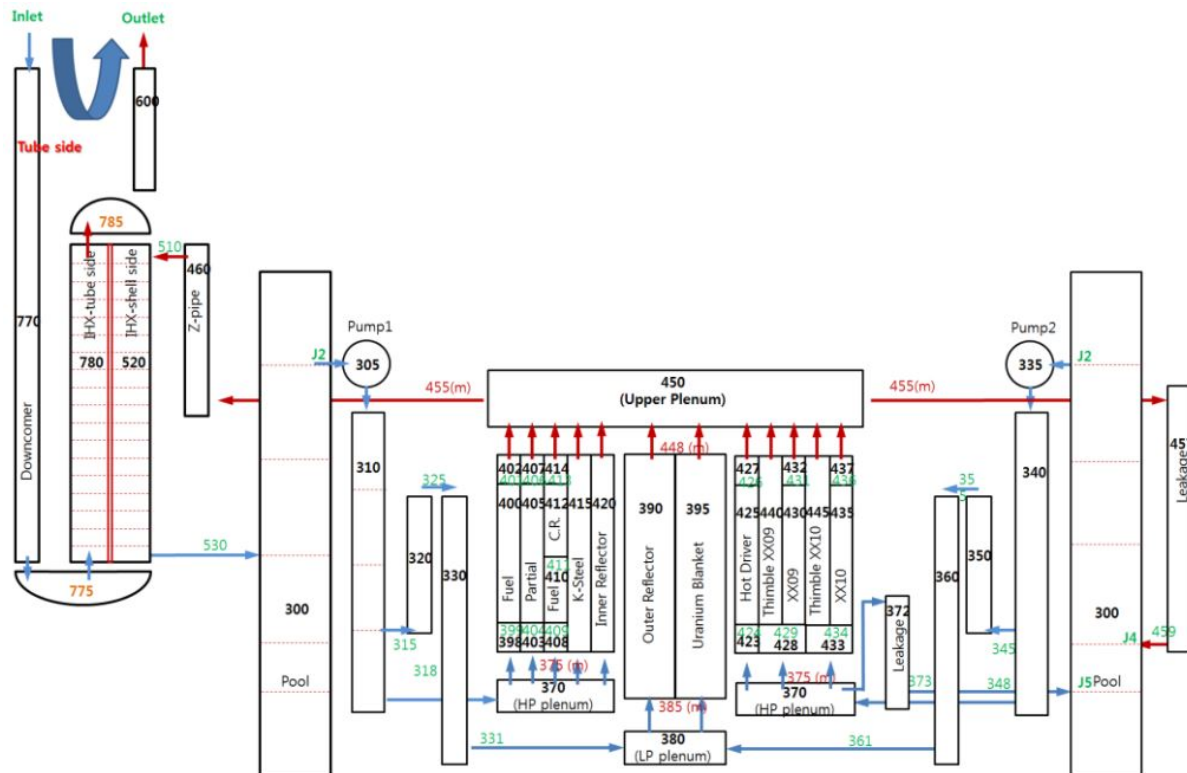


FIG. 186. Nodalization of EBR-II in MARS-LMR analysis.

7.12.2. Nuclear and thermo-physical data/correlations

The heat transfer and pressure drop models in specific components are summarized in TABLE 22. The frictional pressure drops in all components were evaluated with the Darcy friction factor, based on the defined hydraulic diameter in the component. The neutron analysis in MARS-LMR is based on point-kinetics. Reactivity feedbacks were evaluated using a separate model that was called for the SHRT-45R analysis. Doppler, sodium density, fuel axial, core radial, and control rod driveline/reactor vessel (CRDL/RV) expansion reactivities in MARS-LMR were applied. Doppler, sodium density and fuel axial expansion reactivities were modelled based on the core subassembly groups. The core radial expansion reactivity was modelled with the assumption of uniform radial expansion. The CRDL/RV expansion reactivity was modelled assuming linear expansion in each structure and control rod. The decay heat model of ANS94 was used for SHRT-45R.

TABLE 21. CHANNEL GROUPS IN THE CORE

Group No.	Subassembly Type	Total No. of Subassemblies
1	Fuel driver	62
2	Partial driver	10
3	Control and Safety rod	10
4	K-steel	7
5	Inner reflector	35
6	Outer reflector	156
7	Uranium Blanket	354
8	Hottest driver	1
9	XX09	1
10	XX10	1

TABLE 22. HEAT TRANSFER AND PRESSURE DROP CORRELATIONS IN MARS-LMR

Models	Correlation	Component
Heat transfer in the fuel pin bundle	Modified Schad [79]	Subassembly
Pressure drop in the fuel pin bundle	Cheng and Todreas [110]	Subassembly
Heat transfer in the downcomer	Aoki [115]	IHX tube
Heat transfer in the tube bundle	Graber and Rieger [71]	IHX shell

7.12.3. Thermal-hydraulics methods and models

7.12.3.1. Code(s) used

MARS-LMR is a safety analysis code which has been developed for the Prototype Gen-IV sodium cooled reactor (PGSFR) in Korea. MARS-LMR is a LMR version of the MARS code, as described in Section 5.1.4.

7.12.3.2. Basic method

MARS-LMR is a system code developed for sodium cooled fast reactor transient analyses. The code is a liquid metal reactor version of MARS, which was developed for light water reactor transient analyses. The code basically solves a two-phase system using a semi-implicit numerical scheme. The basic governing equations are two mass conservation equations, two momentum equations and two energy equations for liquid and vapour, plus a non-condensable mass equation. The primary dependent variables are pressure, phase specific energies, vapour volume fraction, phase velocities and non-condensable quality. The code has various models, including hydrodynamic and heat structure models, trip and control systems and a point-kinetics model for a water system analysis. The sodium properties routines, liquid metal heat transfer correlations and wire-wrapped core pressure drop models were added to create MARS-LMR.

Heat structures provided in MARS-LMR permit calculation of the heat transferred across solid boundaries of hydrodynamic volumes. The modelling capabilities of heat structures are general and include fuel pins or plates with nuclear or electrical heating, heat transfer across steam generator tubes, and heat transfer pipe and vessel walls. Heat structures are assumed to be represented by one dimensional heat conduction in rectangular, cylindrical or spherical

geometry. Surface multipliers are used to convert the unit surface of the one dimensional calculation to the actual surface of the heat structure.

The point reactor kinetics model can be used to compute power behaviour in a nuclear reactor. The power is computed using the space-independent or point-kinetics approximation, which assumes that power can be separated into space and time functions. This approximation is adequate for cases in which the space distribution remains nearly constant. The point reactor kinetics model computes both the immediate fission power and the power from decay of fission products. The user can select decay power models based on the American Nuclear Society (ANS) proposed standard. Various reactivities are separately defined in the net reactivity equation.

7.12.3.3. *Model*

The pipe, branch, valve and pump models provided in the hydrodynamic model were used to model the EBR-II plant, along with related input parameters. Heat transfer components, such as core fuel pins, the intermediate heat exchanger and various internal structures in the cold pool, were modelled with heat structures, along with related input parameters. As described in Sec. 7.12.2, the appropriate heat transfer correlations were applied to each component. The power distribution was implemented using the appropriate heat source fraction in each subassembly group, which was modelled with a heat structure for the fuel pins. The core flow distribution in the steady state was treated with a minor loss coefficient in each inlet junction of the subassembly group, which was modelled with a pipe in the hydrodynamic model.

For the SHRT-45R analysis, the reactivity feedback models, including Doppler, sodium density, fuel axial, core radial, and control rod drive line/reactor vessel (CRDL/RV) expansion were applied. The Doppler reactivities were calculated with fuel temperatures in the grouped subassemblies, which were modelled with heat structures. The sodium density reactivities were calculated with sodium temperatures in the grouped subassemblies, which were modelled with pipes in the hydrodynamic model. The fuel axial expansion reactivities were evaluated with fuel strains, which were calculated with fuel and clad temperatures and their thermal expansion coefficients in the heat structures. The core radial expansion reactivities were calculated with strains of the grid plate and above core load pads, which were modelled with heat structures in the core. Lastly, the CRDL/RV expansion reactivities were calculated with strains in the CRDL and RV, which were modelled with heat structures.

7.12.4. **Blind results**

7.12.4.1. *SHRT-17*

The simulation overestimated the core flow during natural circulation, as shown in FIG. 187(a). Therefore, the Z-Pipe inlet temperature was underestimated, as shown in FIG. 187(b). The natural circulation flow in XX09 was also overestimated due to the higher core flow rate (FIG. 187(c)). Axial coolant temperatures in XX09 were slightly underestimated, as shown in e(d). The transient flow in XX10 during the transition from forced flow to natural circulation was significantly underestimated (FIG. 187(a)). However, the calculated coolant temperatures in XX10 were considerably lower than the experimental results, as shown in FIG. 187(f). In addition, there was a flow reversal predicted between about 50 and 100 seconds. Although the flow in the natural circulation region for XX10 was predicted well, the coolant temperature was still underestimated. This means that an additional power source from outside of XX10 was not accounted for in the simulation. Overall results indicate that natural circulation flows

were overestimated, thus the coolant temperatures were underestimated. The exception is the transition flow in XX10, which was underestimated.

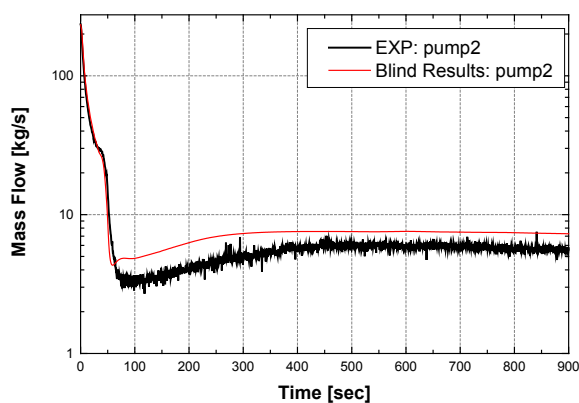
7.12.4.2. SHRT-45R

SHRT-45R was an unprotected event, thus reactor power was controlled by reactivity feedbacks. In other words, calculation of the power and thermal hydraulics is coupled. FIG. 188 shows representative results for the blind phase. The fission power was underestimated (FIG. 188(a)). The pump 2 flow rate was underestimated, especially during the natural circulation regime (FIG. 188(b)). The Z-Pipe inlet temperature, driven by the core outlet temperature, was overestimated, as shown in FIG. 188(c), which means the lower flow rate had a more dominant effect on the core outlet temperature than did the lower power. The flow in XX09 was well predicted except for the flow reduction that occurs between 200 and 600 seconds (FIG. 188(d)). It is difficult to find the reason for this kind of flow reduction during the transient. It might be a measurement error. The flow in XX10 was also underestimated (FIG. 188(e)). However, the coolant temperature in XX10 was significantly underestimated, which is similar to the results for the SHRT-17 calculation (FIG. 188(f)).

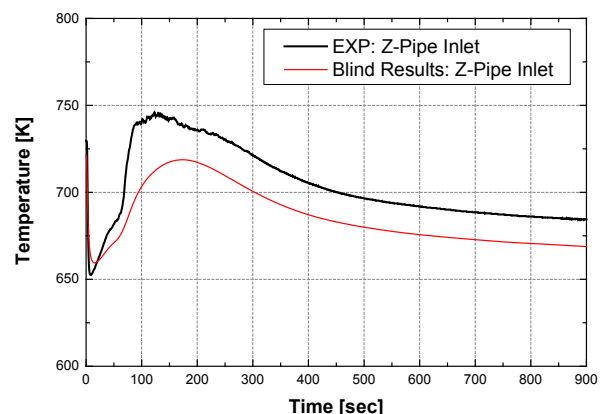
7.12.5. Final results, data comparisons

7.12.5.1. SHRT-17

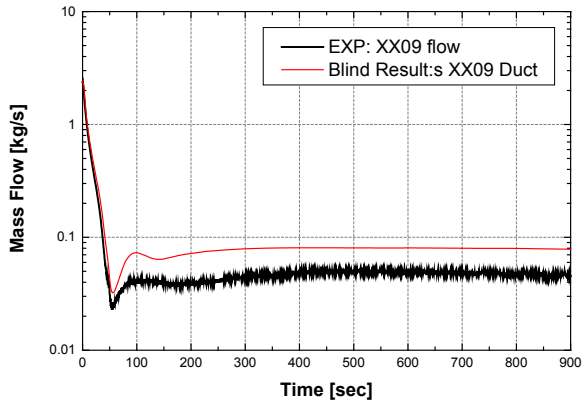
Sensitivity tests for various parameters were conducted. Then, based on the experimental results, some modifications were applied. In addition, errors in the modelling were corrected. The blind test results indicate that the flows were overestimated. Basically, the orifices at the inlet of the core were modelled using a form loss coefficient, K , which is a function of the Reynolds number. However, in the blind test simulation, the form loss coefficient was simplified and modelled as a constant that matched the flow rate and distribution at the initial state. Therefore, to match the natural circulation flow in the core, the form loss coefficient was modified in phase 2 to be a function of Reynolds number using a known natural circulation flow in the latter part of the transient. FIG. 189 shows the final results for the pump flow with the new form loss coefficient model. Since the flow rate was now modelled well, the predicted Z-Pipe inlet temperature was much closer to the experimental result (FIG. 190).



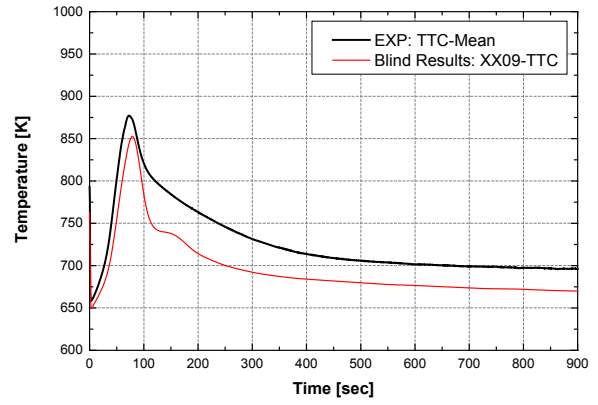
(a) pump #2 flow



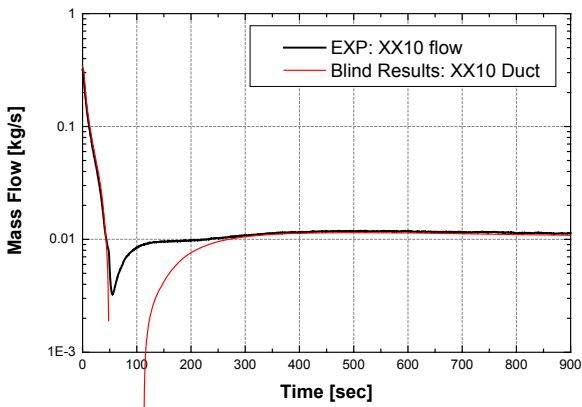
(b) Z-Pipe inlet temperature



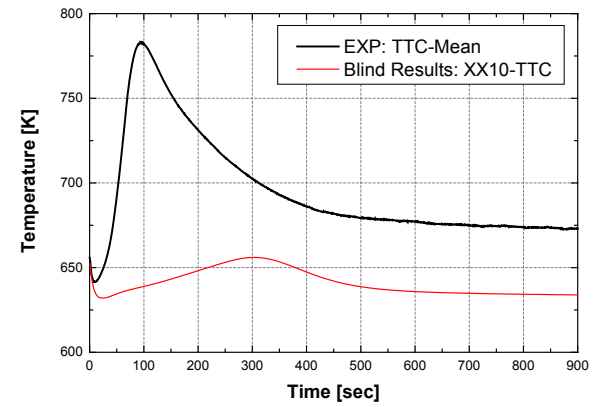
(c) flow in XX09



(d) XX09 top of core temperature

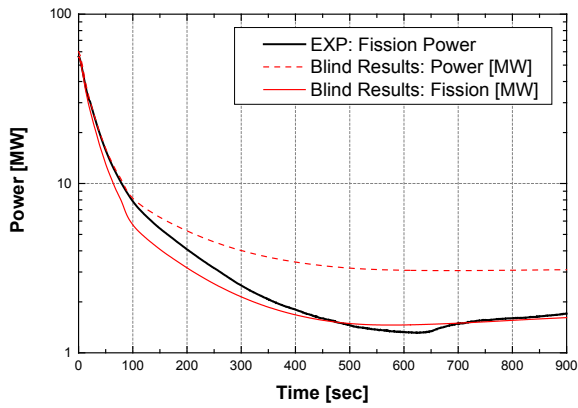


(e) flow in XX10

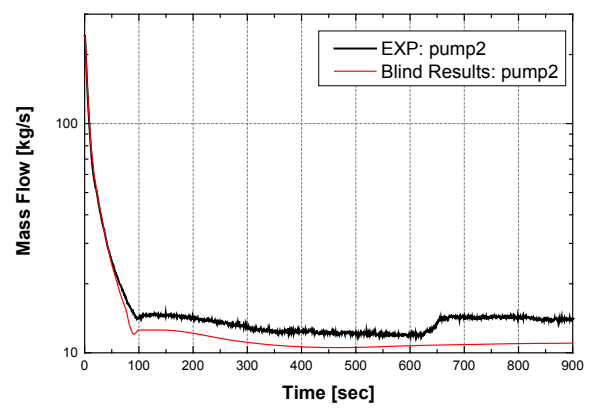


(f) XX10 top of core temperature

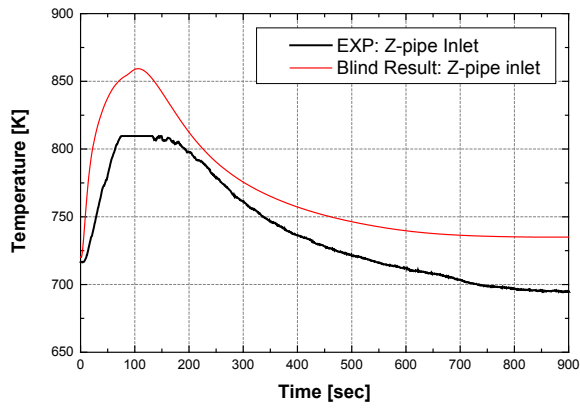
FIG. 187. SHRT-17 blind results



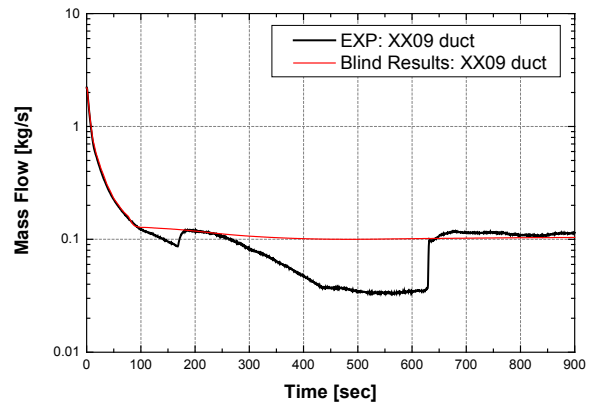
(a) reactor power



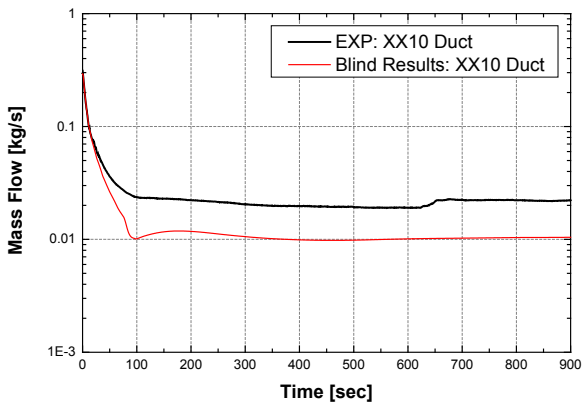
(b) pump 2 flow



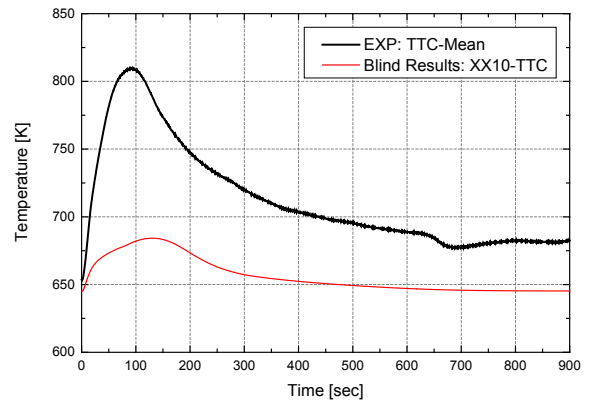
(c) Z-Pipe inlet temperature



(d) flow in XX09



(e) flow in XX10



(f) top of core temperature in XX10

FIG. 188. Blind calculation results for SHRT-45R.

FIG. 191 shows the major results in the XX09 subassembly. The predicted flow rate in XX09 agreed well with the experimental result, especially in the natural circulation region. Because the flow rate during natural circulation was lower and agreed better with the experimental result, the coolant temperature during natural circulation increased and moved closer to the experimental results, as shown in FIG. 191(b) through FIG. 191(f).

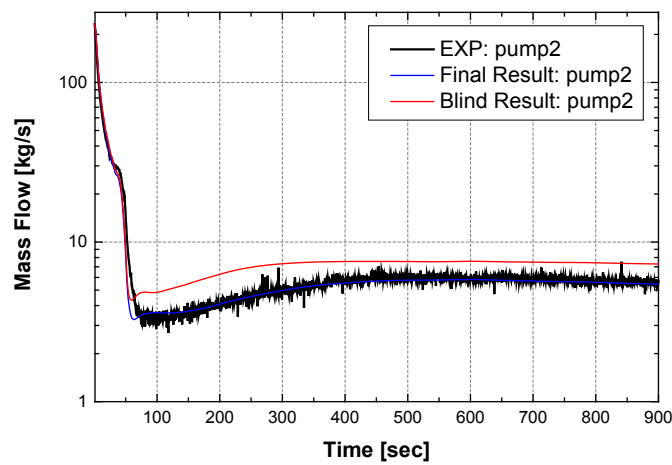


FIG. 189. SHRT-17 pump #2 mass flow rate.

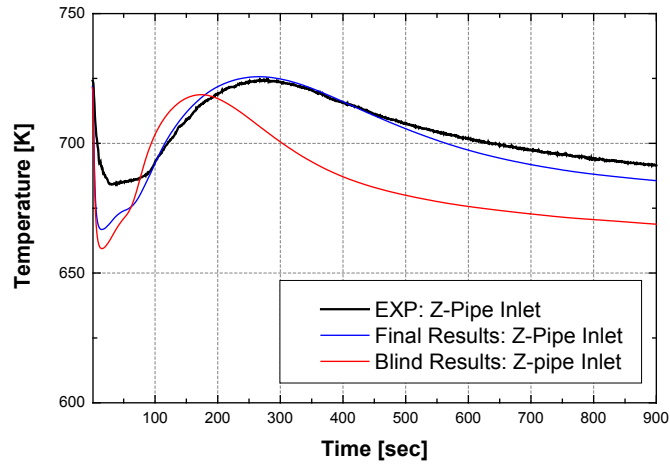
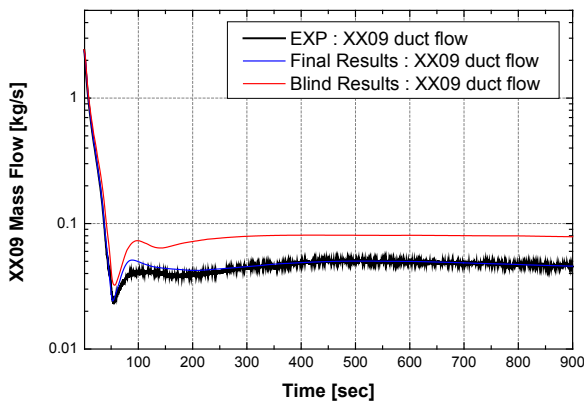
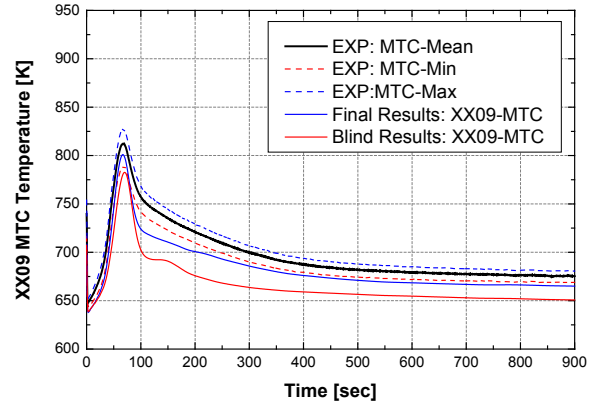


FIG. 190. SHRT-17 Z-Pipe inlet temperature.

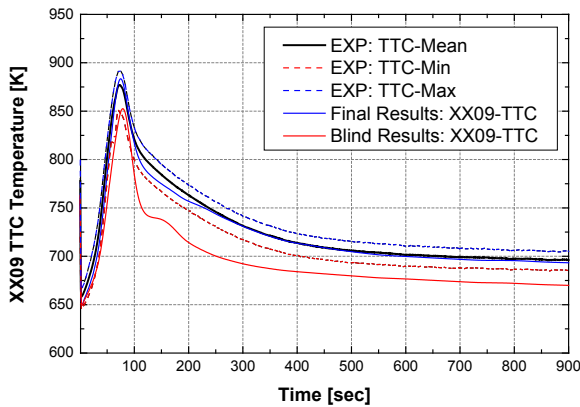
FIG. 192 shows final calculation results for XX10. In the blind test results, the coolant temperatures were significantly underestimated. Because XX10 is a non-fueled subassembly, the primary source of heat is the heat transferred into XX10 from surrounding subassemblies. Therefore, an inter-subassembly heat transfer model was added. As shown in FIG. 192(b) through FIG. 192(f), predicted coolant temperatures agreed well with experimental data. The heat transfer in the duct and the thimble region were adjusted to match the experimental results, based on sensitivity tests (see Section 8.6.1). However, the phase 2 calculated flow in XX10 was underestimated. The form loss coefficient in the subassembly might be better modelled as a function of the Reynolds number to achieve a better prediction.



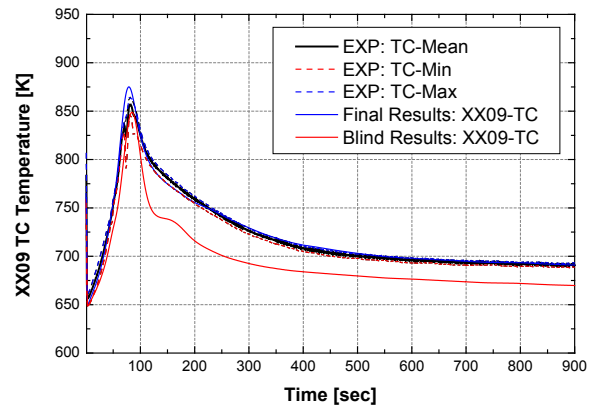
(a) duct flow



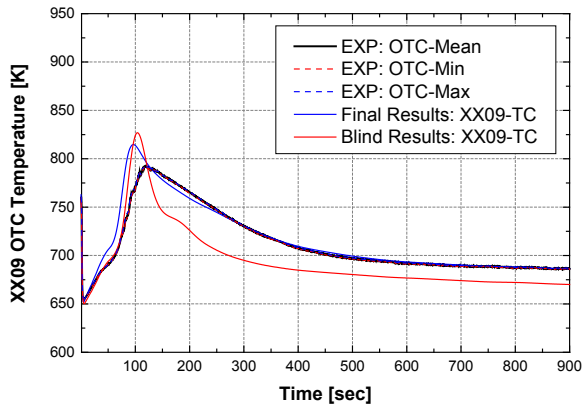
(b) mid-core temperature



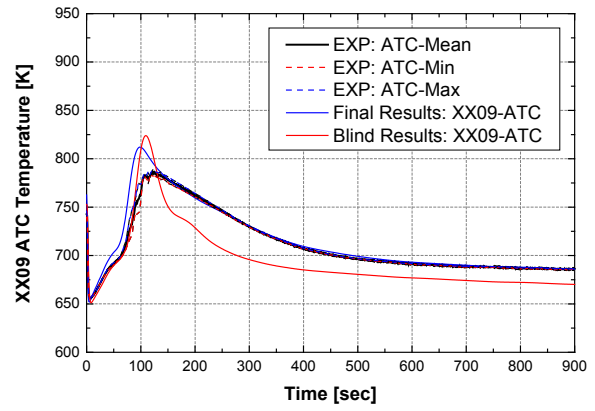
(c) top of core temperature



(d) above core temperature

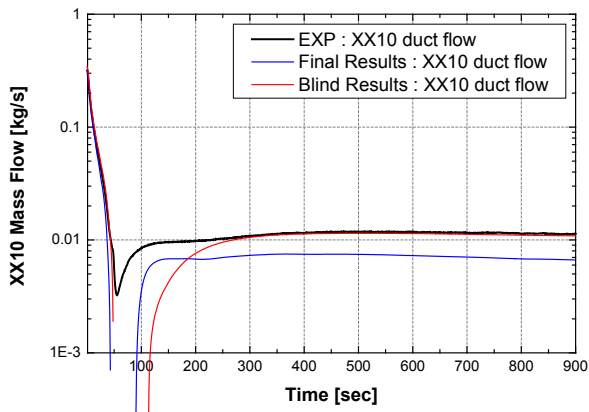


(e) core outlet temperature

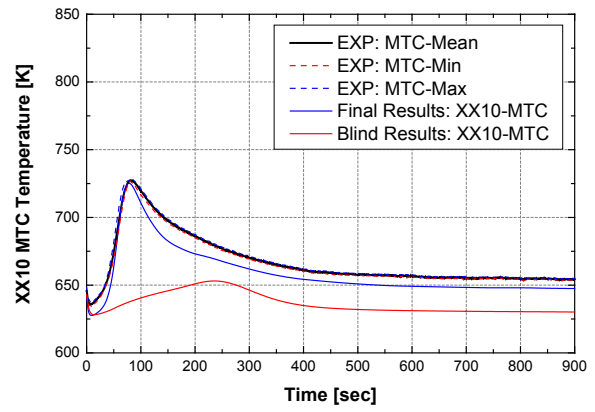


(f) annulus thimble temperature

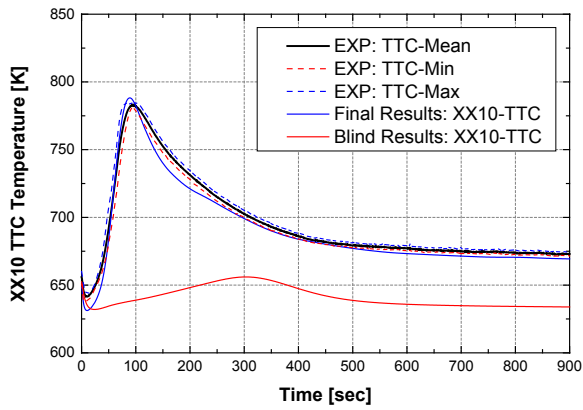
FIG. 191. Final calculation results for XX09 during SHRT-17.



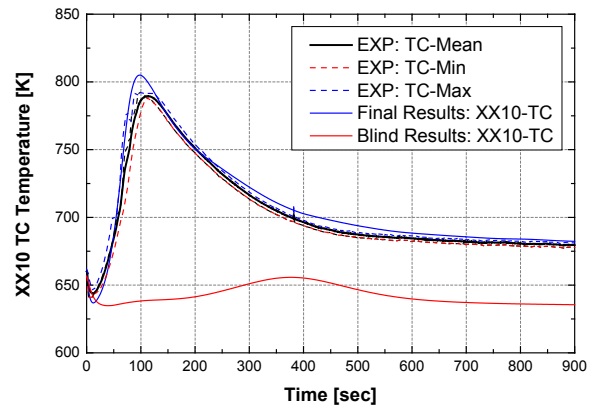
(a) duct flow



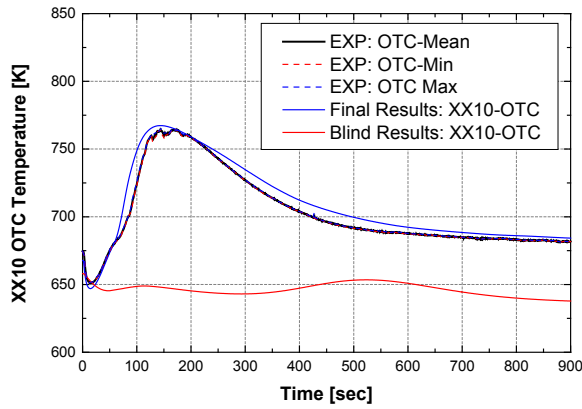
(b) mid-core temperature



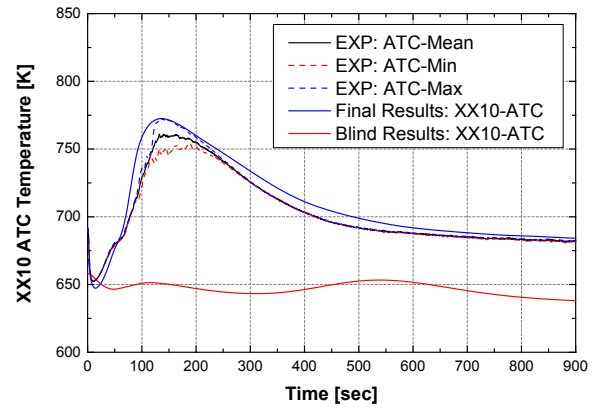
(c) top of core temperature



(d) above core temperature



(e) core outlet temperature



(f) annulus thimble temperature

FIG. 192. Final calculation results for XX10 during SHRT-17.

7.12.5.2. SHRT-45R

SHRT-45R was an unprotected loss of flow test. It is therefore very complicated to improve the modelling based on experimental results due to neutronic/thermal hydraulic coupled behaviour. Sensitivity tests for various parameters were conducted. Then, based on the experimental results, some modifications were applied. In addition, previous errors in the modelling were corrected.

In the blind test results, the reactor power was overestimated due to excessively large negative reactivity feedback during the transient. In order to match the recorded power, the fuel axial expansion reactivity feedback was reduced in phase 2 by 10%. During phase 1, the fuel axial expansion was modelled with fuel volumetric free expansion. However, fuel expansion can be limited by cladding expansion due to contact between fuel and cladding. FIG. 193 shows reactivity feedback results for SHRT-45R. By reducing the net reactivity feedback, the fission power became higher than that calculated during phase 1 and higher than the measured data after about 300 s, as shown in FIG. 194(a).

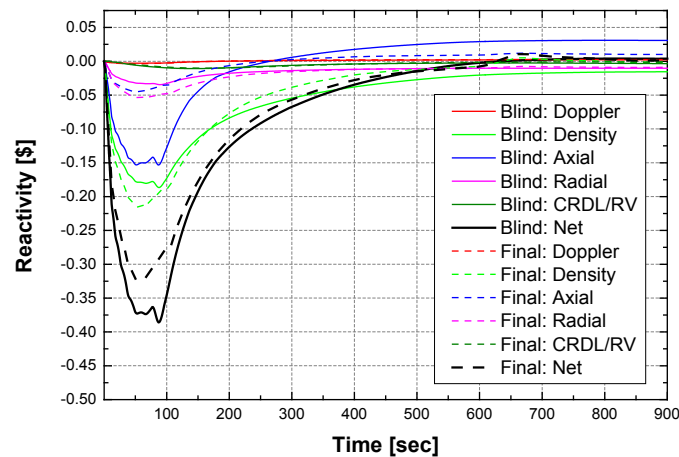


FIG. 193. Reactivity feedback final results for SHRT-45R.

In order to consider the contribution of the auxiliary EM pump in the Z-Pipe, an additional head was added in the primary pump. When the auxiliary EM pump was added, the pump 2 flow increased closer to the experimental results, as shown in FIG. 194(b).

In the final simulation, internal heat structures that were not modelled during phase 1, such as the IHX shroud, Z-Pipe walls, reactor vessel and shield, were added. When all the heat structures were modelled, the IHX shell inlet temperature was reduced and came closer to the experimental results. This trend is also observed in the IHX tube outlet temperature.

FIG. 195 shows coolant flow rate and temperatures in XX09. Comparing with the blind test results, flow in XX09 was not much improved. However, the coolant temperatures increased due to increased reactor power. In the latter part of the transient, the coolant temperatures were higher than the experimental results due to the fact that the calculated reactor power was higher in the second half of the transient than the experimental results, as shown in FIG. 194(a).

FIG. 196 shows coolant flow and temperatures in XX10. The flow increased due to additional head from the auxiliary EM pump. Although the flow increased, the coolant temperatures increased primarily due to the inter-subassembly heat transfer effect. Additional heat was added to XX10 by heat transfer from surrounding subassemblies. This is similar to what was observed for XX10 in SHRT-17.

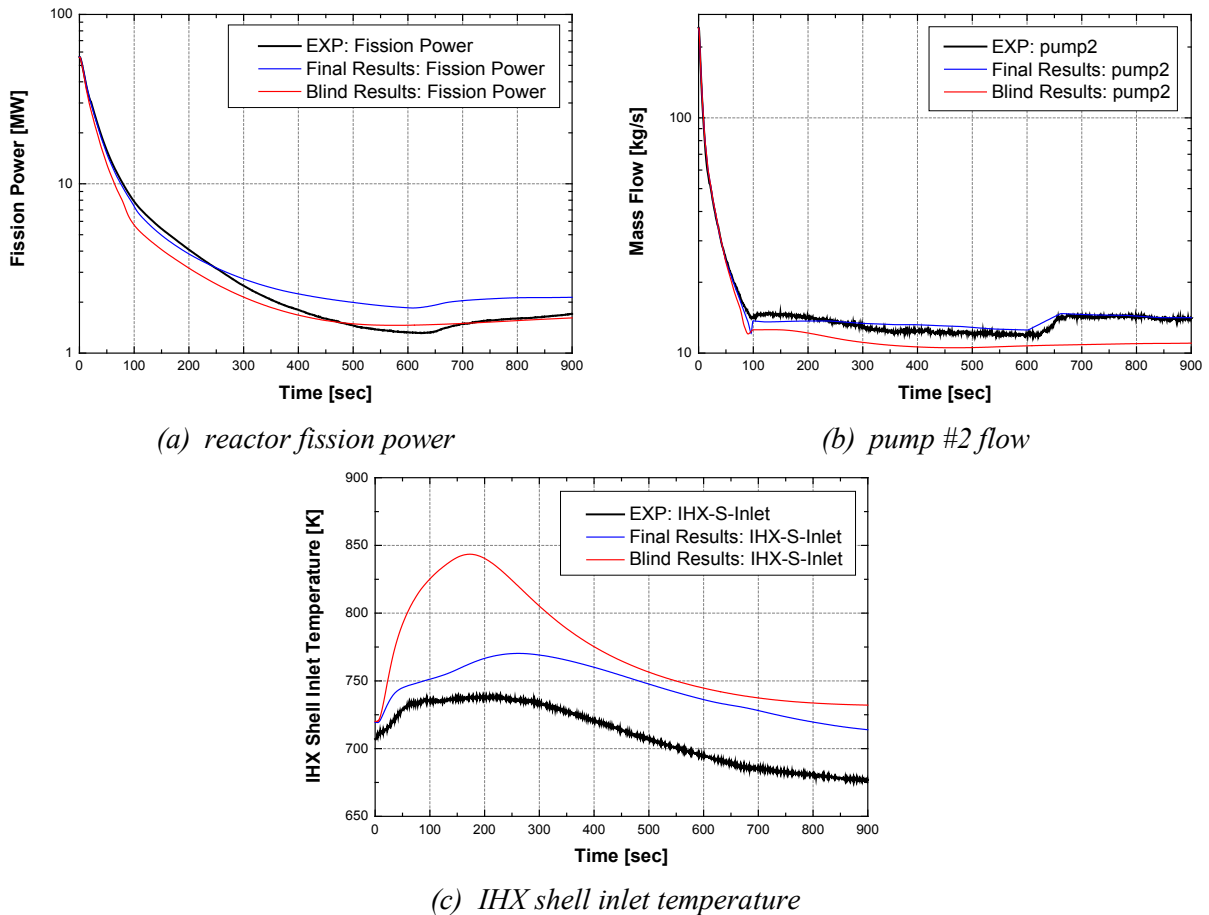


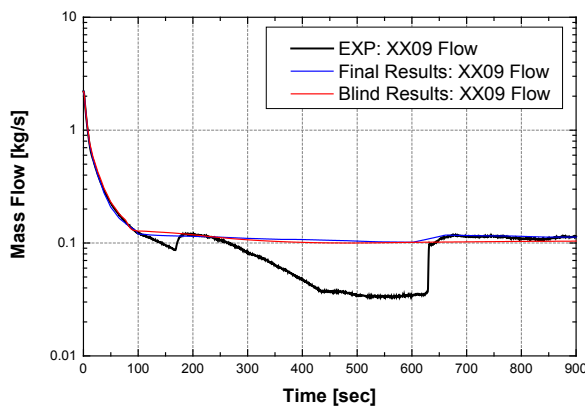
FIG. 194. Final calculation results for SHRT-45R.

7.12.5.3. Model improvements

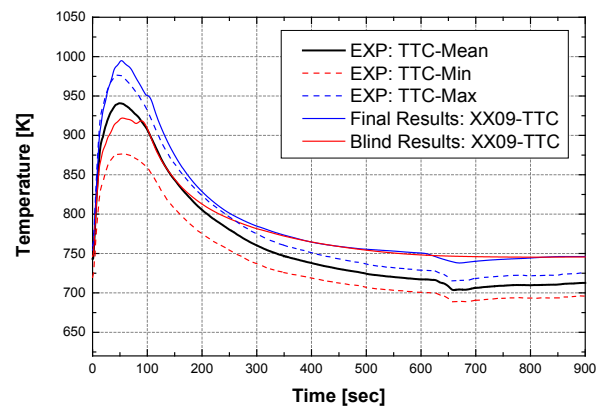
In order to improve the analysis results in MARS-LMR, several parameters were modified using results of a sensitivity test, which is summarized in TABLE 23. Some minor errors in the previous model were also corrected.

In the blind results, flow rates in the core and the XX09 and XX10 subassemblies were overestimated. One possible reason is that the inlet orifice of each subassembly was modelled using a constant minor loss coefficient for the normal operation condition. Generally, when the flow is reduced, a form loss in an orifice should increase. When a modified form loss coefficient that was a function of the Reynolds number was applied, good agreement between prediction and experimental results was achieved.

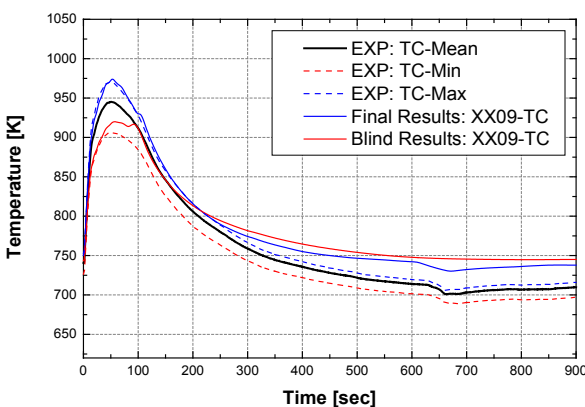
In SHRT-45R, when the auxiliary EM pump was included in the phase 2 simulation, the pump flow increased and moved closer to the experimental results due to the additional head. When the heat transfer between neighbouring subassemblies around XX10 was applied, the coolant temperatures were closer to the experimental results due to heat addition from the surrounding subassemblies. Moreover, the heat transfer between subassemblies was governed by heat transfers through the duct inner wall and the thimble region, which was determined by a sensitivity test.



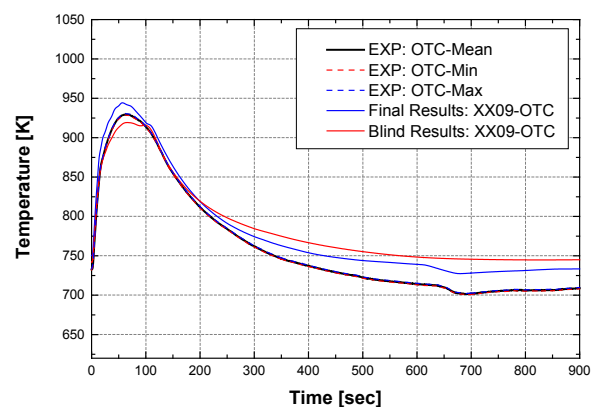
(a) Duct flow



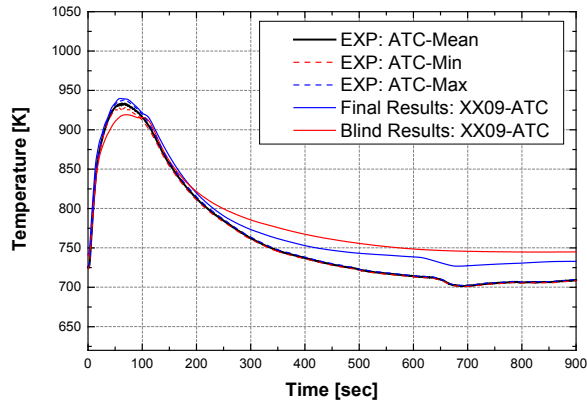
(b) Top of core temperature



(c) above core temperature

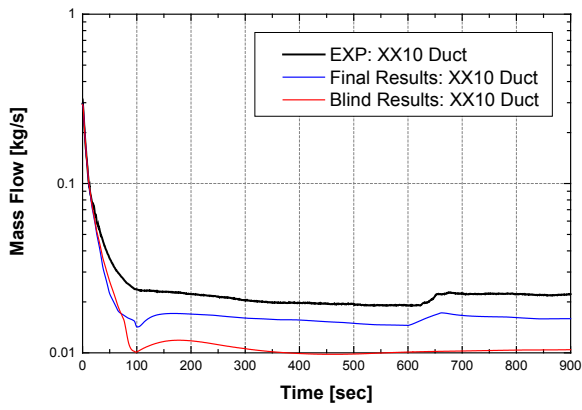


(d) core outlet temperature

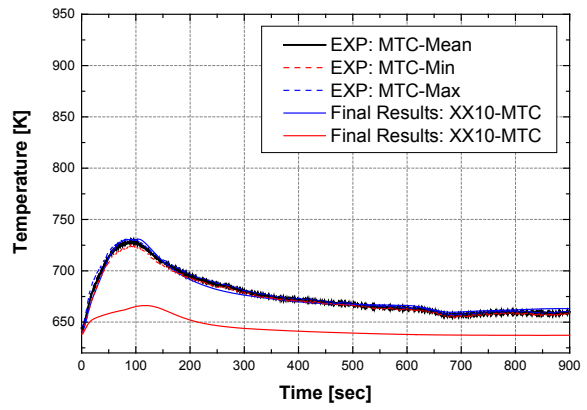


(e) annulus thimble temperature

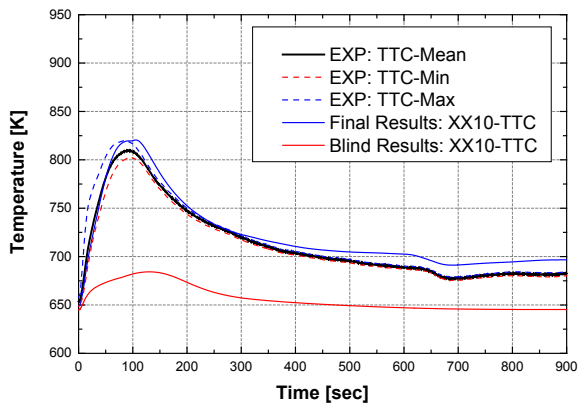
FIG. 195. Final XX09 calculation results for SHRT-45R.



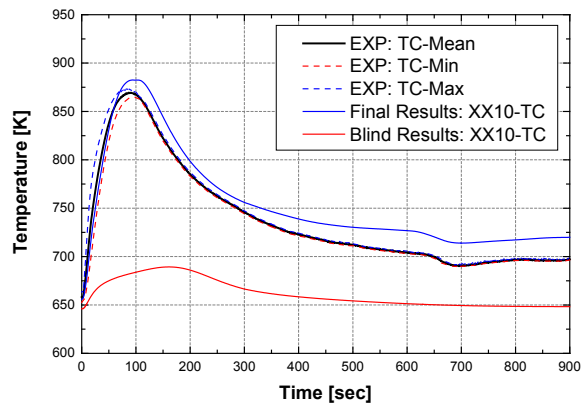
(a) duct flow



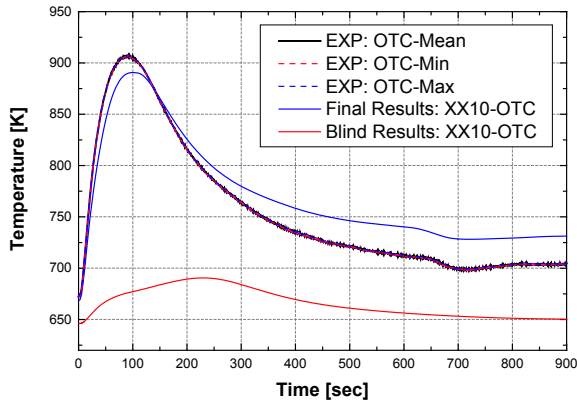
(b) mid-core temperature



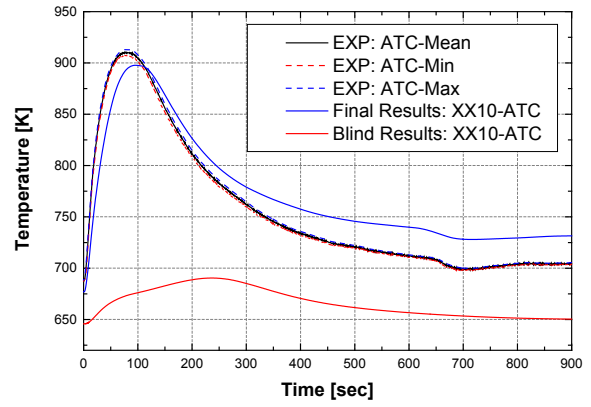
(c) top of core temperature



(d) above core temperature



(e) core outlet temperature



(f) annulus thimble temperature

FIG. 196. Final XX10 calculation results for SHRT-45R.

In SHRT-45R, neutronic and thermal hydraulic effects should be simultaneously considered. In the blind test, the reactor power was underestimated because the negative reactivity feedback was too large. Based on a sensitivity test, the axial expansion reactivity feedback was reduced by 10%, which gave a better power prediction than that in the blind test. But the power was still overpredicted in the latter portion of the transient. Volumetric expansion in the fuel was assumed in the blind test. However, a metallic fuel expands linearly in general. In addition, when the fuel and cladding are in contact, the fuel expansion is governed by the cladding expansion. Therefore, the 10% reduction of the axial fuel expansion was reasonable for the final calculation.

TABLE 23. MODIFIED PARAMETERS IN MARS-LMR ANALYSES

Parameters	Model improvement	Remarks
Core flow	form loss coefficient, k	
Inter-Subassembly Heat Transfer	addition of sodium gap between SAs	Heat transfer modelling between subassemblies in XX09 and XX10
Heat Transfer in thimble region	heat transfer coefficient	
Heat Transfer on the duct inner wall	heat transfer coefficient	
Internal structures	heat structure modelling	IHX, Z-Pipe and reactor shield
Decay heat model	ANS94	weighting factor is applied to match initial fission power (SHRT-45R)
Reactivity feedback	10% reduction in axial expansion	fuel expansion can be limited by clad expansion. (SHRT-45R)
Auxiliary EM pump	additional head	(SHRT-45R)
Measurement location in XX09 and XX10	Axial node locations are corrected	mid-points in the node are changed to end points for the measurement locations
SA duct material	Stainless Steel	material of duct in MARS-LMR was HT9
Fuel property	conductivity	previous fuel conductivity data was wrong

7.12.6. Neutronics methods and models

KAERI did not participate in the neutronics benchmark exercise.

7.13. KOREA INSTITUTE OF NUCLEAR SAFETY (REPUBLIC OF KOREA)

7.13.1. Geometry/discretization

The TRACE code model for the EBR-II system is composed of the reactor tank, primary pumps, high pressure and low pressure piping into the high pressure and low pressure inlet plena, core channels, upper plenum, Z-Pipe and the IHX. Leakage paths are also modelled at the HPP, upper plenum and IHX primary side inlet. An overview of the code model is shown in FIG. 197.

The reactor tank was modelled with 9 axial cells initially; later a 120-cell 3-D vessel component was introduced in which the tank volume was divided into two radial rings, 6 azimuthal sectors and 10 axial levels. Two paths composed of the primary pumps plus the high and low pressure piping were connected between the 3-D vessel component and the high pressure and low pressure inlet plena.

The reactor core was modelled by dividing the core into channels for the outer core subassemblies, inner core driver subassemblies, other inner core subassemblies, the hottest driver, XX09, XX10, thimbles and surrounding drivers for XX09 and XX10, and the core bypass. The outer core channel represented 510 reflector and blanket subassemblies. The inner core subassemblies were modelled with channels representing the hottest driver, XX09, XX10, the XX09 and XX10 thimbles and surrounding drivers, wire-wrapped fuel drivers plus safety and control drivers, and inner core steel and reflector subassemblies.

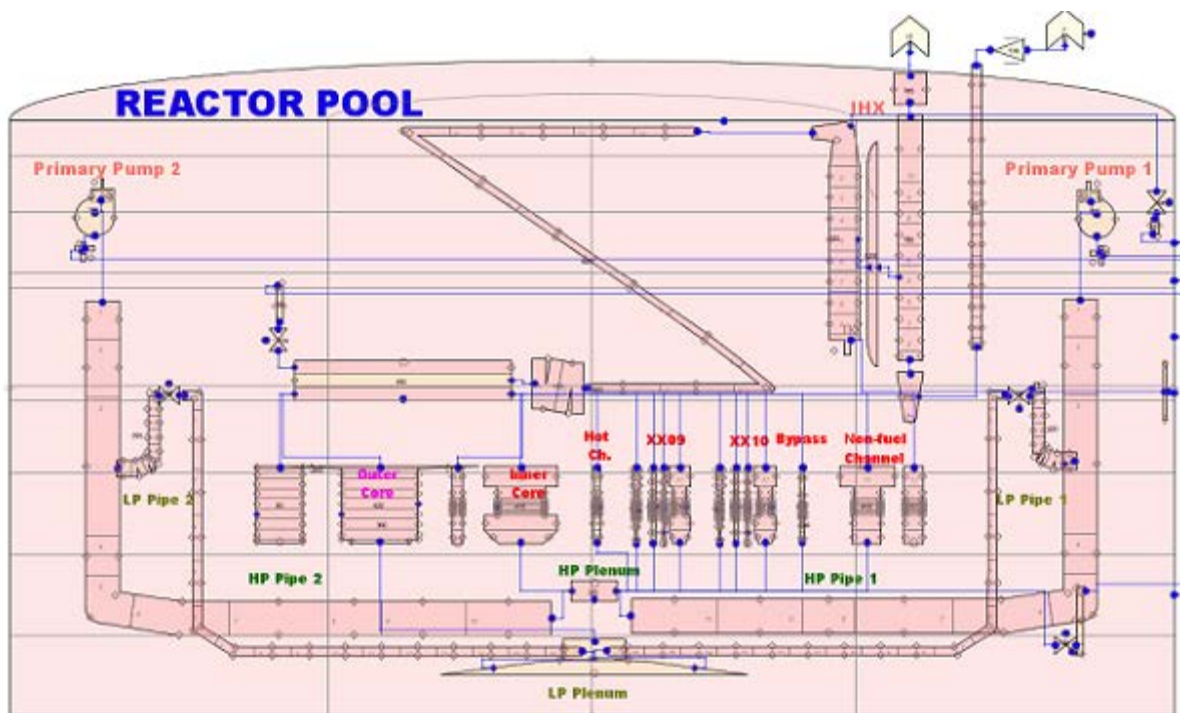


FIG. 197. TRACE code model for EBR-II transient SHRT-17.

All of the core channels, including the core bypass channel, were connected into the upper plenum component, which was also connected on the side to the Z-Pipe component inlet. The Z-Pipe outlet was connected to the inlet of the IHX shell side, with the outlet of the IHX shell connected to the sodium cold pool.

The intermediate loop included the IHX downcomer, the IHX lower dome and the IHX tubes and upper dome. Steady state and transient intermediate sodium pressure and temperature conditions were applied at the IHX intermediate side inlet.

7.13.2. Nuclear and thermo-physical data/correlations

The Churchill friction correlation [116] was used for normal pipe and non-fuel subassemblies.

$$f_w = 8 \left[\left(\frac{8}{Re} \right)^{12} + \frac{1}{(a+b)^{\frac{3}{2}}} \right]^{\frac{1}{12}}$$

where

$$a = \left\{ 2.457 \times \ln \left[\frac{1}{\left(\frac{7}{Re} \right)^{0.9} + 0.27 \left(\frac{\varepsilon}{D_h} \right)} \right] \right\}^{16}$$

$$\text{and } b = \left(\frac{3.753 \times 10^4}{Re} \right)^{16}.$$

For the wire-wrapped fuel subassembly channels, the simplified Cheng and Todreas (CTS) correlation [110] was used.

— Laminar region: $f_L = \frac{C_L}{Re}$

$$C_L = \left[-974.6 + 1621 \left(\frac{P}{D} \right) - 598.5 \left(\frac{P}{D} \right)^2 \right] \times (H/D)^{0.06 - 0.085(P/D)}$$

$$\text{When : } Re < Re_L = 300 \times 10^{1.7(P/D-1)}$$

— Turbulent region: $f_T = \frac{C_T}{Re^{0.18}}$

$$C_T = \left[\begin{array}{l} 0.8063 - 0.9022 \times \text{Log}_{10} \left(\frac{H}{D} \right) + 0.3526 \\ \times \left(\text{Log}_{10} \left(\frac{H}{D} \right) \right)^2 \end{array} \right] \times (P/D)^{0.97} \times (H/D)^{1.78 - 2(P/D)}$$

$$\text{When : } Re > Re_T = 10\,000 \times 10^{0.7(P/D-1)}$$

— Transition region: $f_{tr} = (1 - \varphi)^{1/3} f_L + \varphi^{1/3} f_T$

$$\varphi = \frac{\text{Log}_{10}(Re/Re_L)}{\text{Log}_{10}(Re_T/Re_L)}$$

$$\text{When : } Re_L \leq Re \leq Re_T$$

The sodium heat transfer correlation used for fuel bundles and the IHX was:

$$Nu = 5.0 + 0.025(Pe)^{0.8}$$

7.13.3. Thermal hydraulics methods and models

7.13.3.1. Code(s) used

For the EBR-II benchmark calculations, the modified TRACE5 Patch 3 code was used to simulate the initial and transient conditions. This code version has different sodium properties compared to the original version. In particular, the sodium enthalpy correlation was revised on the basis of [75]. Because the original TRACE code does not include a wire-wrapped fuel bundle pressure drop model, the simplified Cheng and Todreas (CTS) correlation [110] was also implemented in the code for the wire-wrapped fuel subassembly channels.

7.13.3.2. Basic method

The geometric model of the flow paths in the EBR-II system was prepared based on the benchmark specification. The structural material included in the model accounted for the fuel subassemblies, the IHX tubes, the high pressure and low pressure piping into the inlet plena, the Z-Pipe, the reactor shield and the reactor tank shell.

Two primary sodium pumps were modelled using the design parameters and the pump characteristic curves. These two primary pumps supply sodium into the reactor core channels.

The EBR-II SHRT-17 test was implemented in two steps: initial steady state and transient. The criterion for reaching a steady state condition was taken as convergence to within a change of less than 10^{-4} . The transient calculation was started from the steady state condition and applying the transient boundary conditions, including the reactor power history, primary pump speed and intermediate sodium conditions.

7.13.3.3. Model

To simulate the initial core conditions, the proposed initial power and flow data for run 129C, calculated with the EBRFLOW code by Argonne, were normalized for the benchmark test. These normalized powers and flows for each subassembly were categorized into core modelling channels for the steady state sodium flow and power distribution in the core.

Each core channel included the axial region from the elevation of the top of the upper reactor grid plate to the top of the outer hexcan. The CTS correlation was used for the wire-wrapped fuel pin bundle section of each core channel. To adjust the channel flow to the desired value, an inlet K-factor was adjusted for each channel.

The instrumented subassemblies XX09 and XX10 have thimbles. Thimble channel flow was assumed to be 4.82GPM (0.25847kg/s) for the blind calculation. The surrounding six driver channels for XX09 and XX10 were also modelled, to identify the effect of surrounding drivers. Heat transfer between the instrumented subassemblies and surrounding drivers through the gap of the outer hex can was considered in the phase 2 model only. Other driver channels were assumed for the phase 1 calculations to be adiabatic at the outer hex surface. The phase 2 modelling added an averaged gap volume between drivers in each modelling channel, and heat transfer through the driver gap volume was included.

During steady state, most of the core heat is transferred to the intermediate loop through the IHX tubes. Some of the core heat is transferred into the sodium pool through the reactor shield and Z-Pipe wall and the IHX outer shell. Thus an overall system heat balance during steady state is reached.

During the transient analysis, the pump model followed the given pump speed table to simulate the primary pump coastdown. The transient power of each channel was assumed to follow the total power fraction as a function of time.

7.13.4. Blind results

7.13.4.1. SHRT-17

The phase 1 blind calculation was done using information from the test specification and the modified TRACE5 Patch2 code version. In this code version, a wire-wrapped fuel bundle pressure drop model was not available. Therefore, the Reynolds-dependent K input option was used for each wire-wrapped fueled channel, such as the inner core and the instrumented subassembly channels. Each inner core channel was modelled as an averaged wire-wrapped fuel pin.

A simplified model was used in the core channels, the leakage path channel and the sodium tank modelling. Core channels included outer core subassemblies, inner core subassemblies, the peak temperature driver, XX09, XX10, the thimbles of the instrumented subassemblies, and the core bypass channels. The outer surface of these channels was treated as adiabatic. A leakage path was included at the high pressure plenum and at the upper plenum. The gap volume between drivers was not included in the model. The sodium tank was modelled with a 9-cell 1-D pipe component.

The axial power profile was assumed to have a bottom-skewed profile taken from [117]. The radial power profile within the fuel slugs was assumed uniform. The initial thimble flow within the instrumented subassemblies was set to 4.82 gpm (0.2585kg/s).

A steady state condition was achieved that satisfied the 10^{-4} convergence criterion. Results included the flow distribution in the primary loop and the channel power and flow distribution in all core channels.

The transient calculation results for SHRT-17 showed that sodium mass flow from primary pump 1 decreased faster than the flow from pump 2, so flow reversal for pump 1 was estimated to occur between 36 ~ 58 s. Peak coolant, clad and fuel centerline temperatures were calculated at the hot channel, which was selected as the highest initial power to flow driver. Calculated coolant, clad and fuel temperatures were 909 K, 974 K and 977 K, respectively.

The XX09 flow decreased to 0.0174 kg/s at 51 s, then increased slightly up to 0.056 kg/s by 310 s. It then decreased again. The calculated XX09 radially averaged coolant temperatures at the MTC, TTC, TC, OTC and ATC levels are shown in FIG. 198(a). The highest XX09 averaged coolant temperature was 935 K at the TTC location at 83sec. A second coolant temperature peak was estimated at the TC location. The calculated OTC and ATC peak temperatures were 833 K at 133s and were much lower than expected.

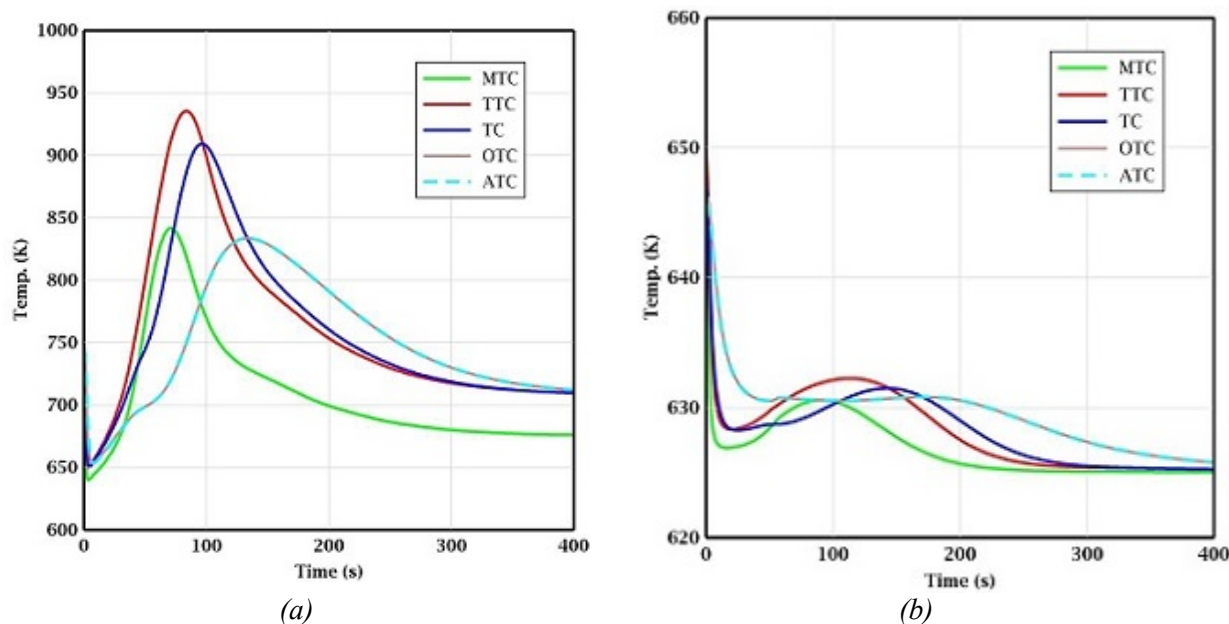


FIG. 198. Estimated temperatures in blind phase for (a) XX09, (b) XX10.

For the case of XX10, the minimum calculated flow was 0.0028 kg/s at 53s. Flow reversal was observed between 52 ~62 sec. Then the XX10 flow slightly increased up to 0.029kg/s at 344 s, then decreased slowly. The calculated XX10 coolant temperatures all dropped quickly below the initial temperature at all measured locations, and the highest coolant temperature was calculated at the TTC location and was 632.7K at 113 s, as shown in FIG. 198(b).

7.13.4.2. SHRT-45R

KINS did not perform a SHRT-45R analysis.

7.13.5. Final results, data comparisons

7.13.5.1. SHRT-17

The final benchmark results for SHRT-17 were calculated using a different TRACE code version. The CTS correlation was incorporated into the modified TRACE5 Patch 3 version to improve modelling efficiency and accuracy of the pressure drop of wire-wrapped fuel bundles. During the final calculations, a 2.5 times higher form loss coefficient in the laminar region of the CTS correlation was used to improve the transient pump flow estimation.

Through examination of the test data, major disagreements with the blind calculation results were identified. The calculated pump 2 mass flow rate was higher than the data by about 1kg/s from 70 s to 400 s, with the measured flow varying between 3 kg/s and 6 kg/s during this period. Readings of the flowmeter thermocouples (FM-1 TC, FM-2 TC) of the instrumented subassemblies showed higher temperatures than the high pressure inlet plenum temperature; otherwise, the calculated flowmeter temperatures showed no difference from the high pressure plenum sodium temperature, since no heat structure was modelled in the inlet nozzle region. The calculated system temperature response showed that the Z-Pipe inlet temperature peak appeared at 120s then gradually decreased. The calculated IHX intermediate outlet temperature was higher than the IHX primary side inlet temperature over most of the transient, and the IHX primary side outlet temperature showed little variation over the time of the transient.

By contrast, the system analysis predictions from the blind calculation showed that the Z-Pipe inlet temperature peak occurred at about 300 s and that this peak temperature was lower than the recorded data. The IHX intermediate outlet temperature and IHX primary inlet temperature were predicted in the phase 1 calculations to have the same value and were similar to the predicted IHX intermediate outlet temperature. The largest disagreement was in the IHX primary outlet temperature prediction, in which the calculated temperature dropped very quickly during the primary pumps coastdown.

According to the observation of the data, the code model was improved during phase 2 in the modelling of the core, IHX, upper plenum, sodium tank and leakage path and in the modelling of the structural material in the IHX, reactor graphite shield and the outer hex can and the gap between subassemblies. The core model was especially refined. The inner core channel model included a fueled driver channel, a non-fuel fuel subassembly channel, and surrounding driver channels for XX09 and XX10.

To improve initial temperature conditions, the data flow and temperature at MTC, TTC, TC, OTC and ATC locations were used to identify the area-averaged temperature at each thermocouple location and to decide on the initial subassembly power, axial power profile, thimble flow and outer hex can heat transfer coefficient. These parameters were identified by a parametric study.

The calculated flows showed good agreement with the data before the end of the pump coastdown and after 400 sec. But during the period in between, the calculated flows for pump 2 and the instrumented subassemblies were still slightly high, as shown in FIG. 199.

Flowmeter temperature responses were simulated with a bottom nozzle heat structure and inclusion of gamma heating. The overall shape of the calculated flowmeter temperatures were similar to the data but still showed an estimation error of around 2 K.

Calculated system temperatures are shown in FIG. 200. The core outlet and IHX intermediate side outlet temperatures showed a reasonable shape. The IHX primary side inlet temperature was overpredicted after 400 s by about 20 K. The IHX primary side outlet temperature was underpredicted by around 20 K.

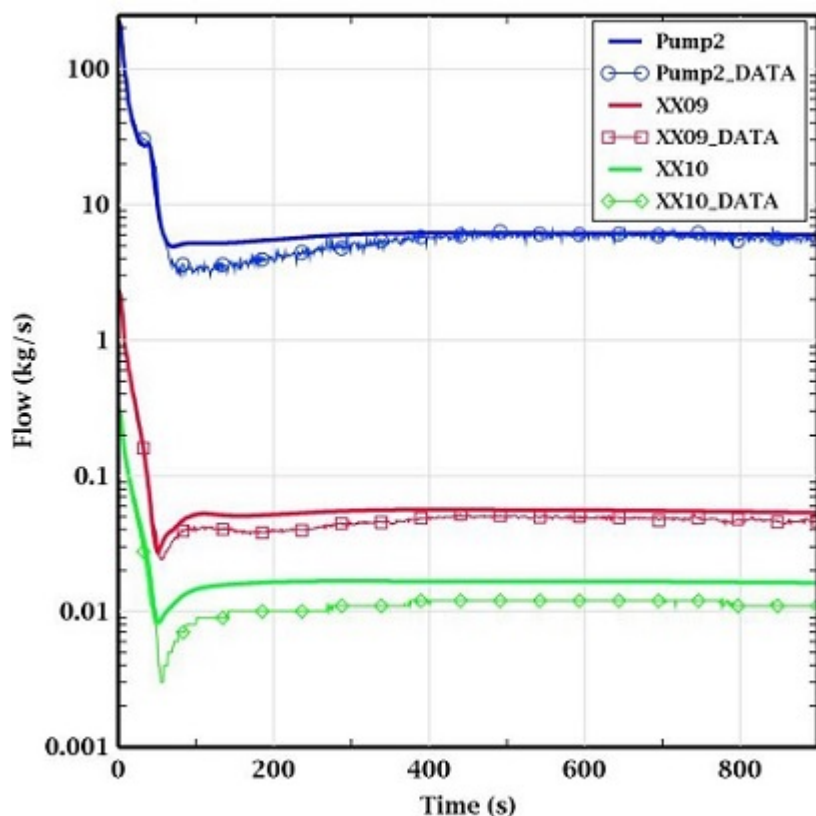


FIG. 199. Final calculated flows for pump #2, XX09 and XX10.

Calculated XX09 temperatures at the MTC, TTC, TC, OTC and ATC locations are compared with the area-averaged data in FIG. 201(a). During the transient calculation, heat transfer from the surrounding subassemblies was neglected for XX09. Each temperature showed good agreement with the data before 100 s, then each temperature was underestimated due to the high XX09 channel flow estimation. For the case of XX10, the calculated temperatures showed good agreement with the data, as shown in FIG. 201(b), only when the surrounding driver heat transfer was reduced and the XX10 transient power history followed the decay power fraction and a flatter axial power profile was used.

7.13.5.2. Model improvements

The simplified model used in the blind phase was improved for phase 2 in the core model and the heat structures for the upper plenum, Z-Pipe and IHX shell. The core outlet temperature estimation was improved by finer nodalization of the upper plenum. Heat structure modelling of the upper plenum and the outer Z-Pipe affected the calculated IHX primary side inlet temperature and intermediate outlet temperature, but the effect of the locations at which system temperatures were calculated was significant on the estimation of system temperatures such as the core outlet vs Z-Pipe inlet temperature and the Z-Pipe outlet temperature vs. the IHX primary inlet temperature.

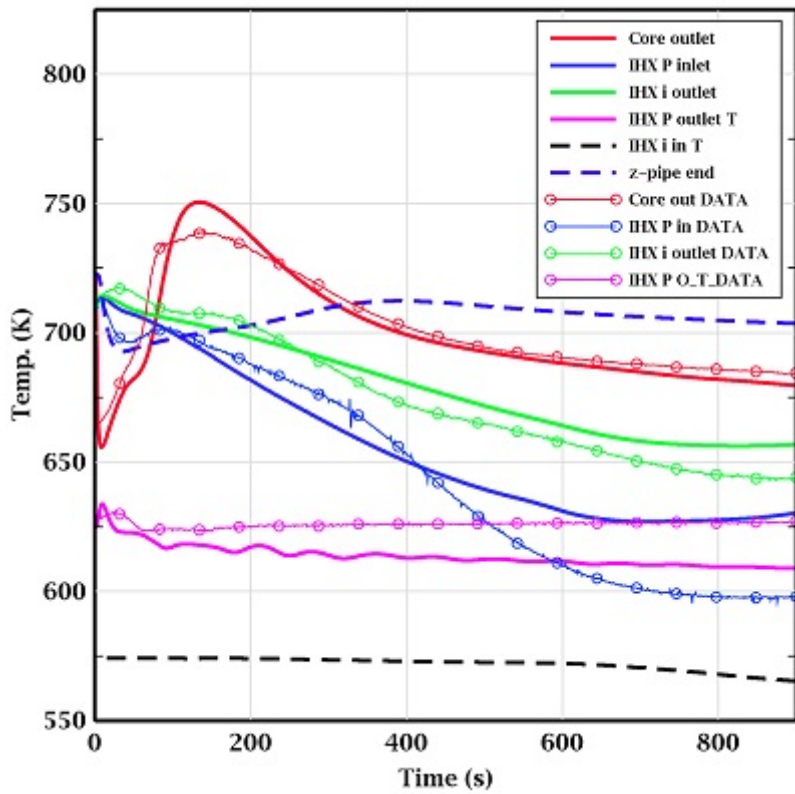


FIG. 200. Final calculated system temperatures.

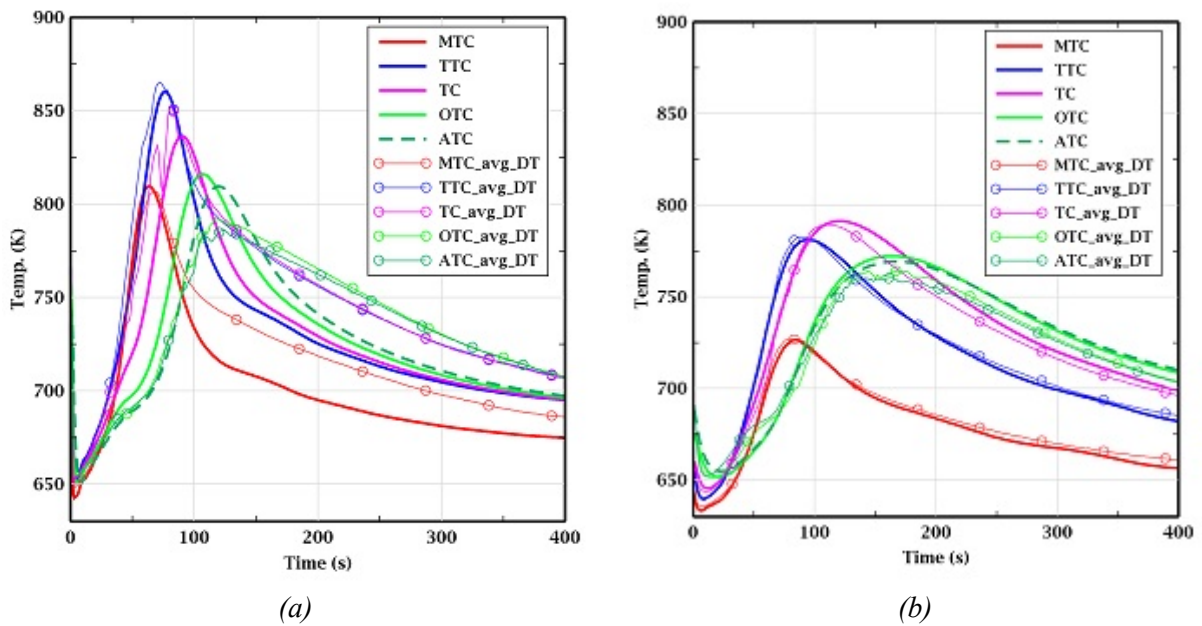


FIG. 201. Final calculated temperatures for (a) XX09, (b) XX10.

For the instrumented subassemblies, the gamma heating effect was modelled at the inlet nozzle to reduce the inlet temperature estimation error. This resulted in reducing the inlet flowmeter temperature estimation error from 8 K to 3 K in the early phase of the transient.

The core model was also improved by considering different pressure drop characteristics between the wire-wrapped fuel bundles and non-wire-wrapped bundles for the inner core subassemblies. Steel and reflector subassemblies were modelled with a separate channel. The subassemblies surrounding XX09 and XX10 were also modelled with separate channels to simulate heat transfer from neighbouring drivers.

When the initial power, flow rate and the deduced axial power profile based on the initial axial temperature data for the instrumented subassemblies and heat transfer from neighbouring drivers were considered in the model, estimations of the radially averaged initial and transient coolant temperatures at each measurement location were improved, as shown in FIG. 202. Especially for XX10, composed of steel elements and surrounded by high power drivers, estimated temperature results were much closer to the measured data when heat transfer from surrounding drivers and a higher transient power history similar to the decay power fraction were used in the calculation.

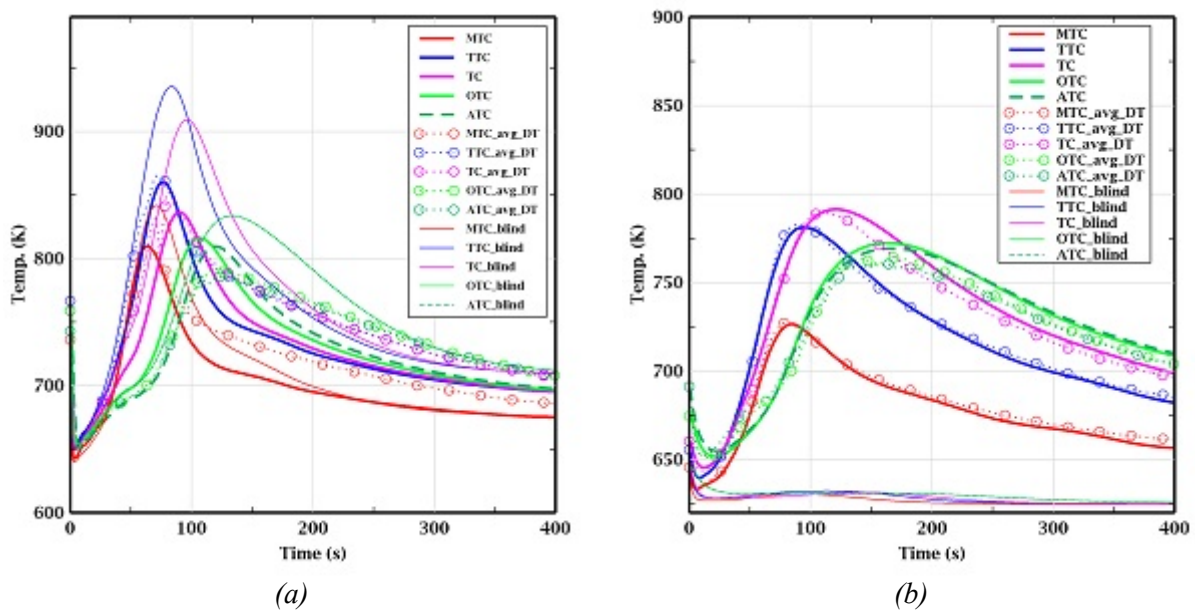


FIG. 202. Comparison of blind phase and final temperature results for (a) XX09, (b) XX10.

7.14. NRG (NETHERLANDS)

7.14.1. Geometry/discretization

The EBR-II reactor and primary loop were modelled using the system thermal hydraulic (STH) code SPECTRA [35] and coupled STH/CFD codes SPECTRA/CFX [61]. The instrumented subassemblies were modelled using the STH codes SPECTRA and TRACE [38].

The system model in SPECTRA includes the primary system and the intermediate heat exchanger. The model consists of 212 Control Volumes, 235 Junctions, 190 1-D Solid Heat Conductors, with from 2 to 10 internal nodes, depending on the thickness of the represented structure. The core is modelled using a separate component for every subassembly type, assuming that, within a type, all subassemblies are identical, with the exception of the hottest subassembly and the instrumented subassemblies XX09, XX10, which are modelled separately. There are 12 subassembly types: the hottest subassemblies, XX09, XX10 and the averaged subassemblies with appropriate multiplicity for the driver subassemblies, the high

flow drivers, the half drivers, the experiments with fuel, the non-fuel experiments, the control subassemblies, the safety subassemblies, the reflector and the blanket subassemblies.

For the analysis of the instrumented subassemblies, XX09 and XX10, a single channel representation was used in SPECTRA, while a subchannel representation of XX10 was used in TRACE. The XX10 subassembly is modelled in TRACE with 48 PIPE components, which all represent a subchannel in either the internal subassembly, or the thimble region. The internal subassembly consists of the following subchannels: 24 PIPEs represent the CENTRAL subchannels; 12 PIPEs represent the edge subchannels; 6 PIPEs represent the corner subchannels. The remaining 6 PIPEs are used to represent the THIMBLE. In addition to the 48 PIPEs, the model consists also of: two lower plena (1 for the thimble, 1 for the subassembly); upper plenum, 102 HEATSTR which represent the steel rods (each facing a different subchannel); 18 HEATSTR which represent the subassembly inner-walls (each facing a different subchannel); 6 HS's representing the thimble walls (including the sodium gap for the neighbouring subassemblies); 924 side-junctions representing cross-flows within the subassembly and thimble.

For phase 2 a coupled SPECTRA/CFX model was used. The geometry that was modelled in CFX is the sodium pool with the walls of the five main components: the IHX, the two pumps, the Z-Pipe and the reactor vessel. In order to obtain a simulation with a feasible computational time for the transient, the discretization was low resolution, containing 392,254 tetrahedral cells.

7.14.2. Nuclear and thermo-physical data/correlations

The following materials were used in the EBR-II model: Stainless Steel 316, 304, U-5Fs fuel. The thermal conductivity of the fuel, as a function of fuel porosity and gas porosity, was obtained from [106].

The porosities were assumed to be 15% and 10% for the gas-filled and the Na-filled porosities, respectively. The thermal conductivity of the fuel, used for the base case and the sensitivity case, is shown in FIG. 203. The difference in the fuel conductivity is about 30%.

The following heat transfer correlations were used:

- (a) Flow inside a pipe - [111], applicability range: $Pr < 0.1$, $10^4 < Re < 5 \times 10^6$:

$$Nu = 5.0 + 0.025 \cdot Pe^{0.8}$$

- (b) Flow outside a single cylinder - [116], applicability range: $Pe > 0.2$ ($Pe = Re \cdot Pr$), applied on the outside surface of the Z-Pipe and the inlet pipes:

$$Nu = 0.3 + 0.62 \cdot Re^{0.5} \cdot Pr^{1/3} \cdot \left[1 + \left(\frac{Re}{282,000} \right)^{5/8} \right]^{4/5} / \left[1 + \left(\frac{0.4}{Pr} \right)^{2/3} \right]^{1/4}$$

- (c) Flow in a tube bundle - [72], applicability range: $30 < Pe < 5000$, $1.1 < P/D < 1.95$, applied in the core subassemblies and IHX:

$$Nu = 0.047 \cdot \{ 1 - \exp[-3.8 \cdot (P/D - 1)] \} \cdot (Pe^{0.77} + 250)$$

- (d) Flow in a tube bundle - [118], applicability range: $Pe < 4000$, $1.3 < P/D < 2$, applied as an alternative correlation for the core and IHX in sensitivity calculations:

$$Nu = 7.55x - \frac{20}{x^{13}} + \frac{0.041}{x^2} \cdot Pe^{(0.56+0.19x)} \quad x = P/D$$

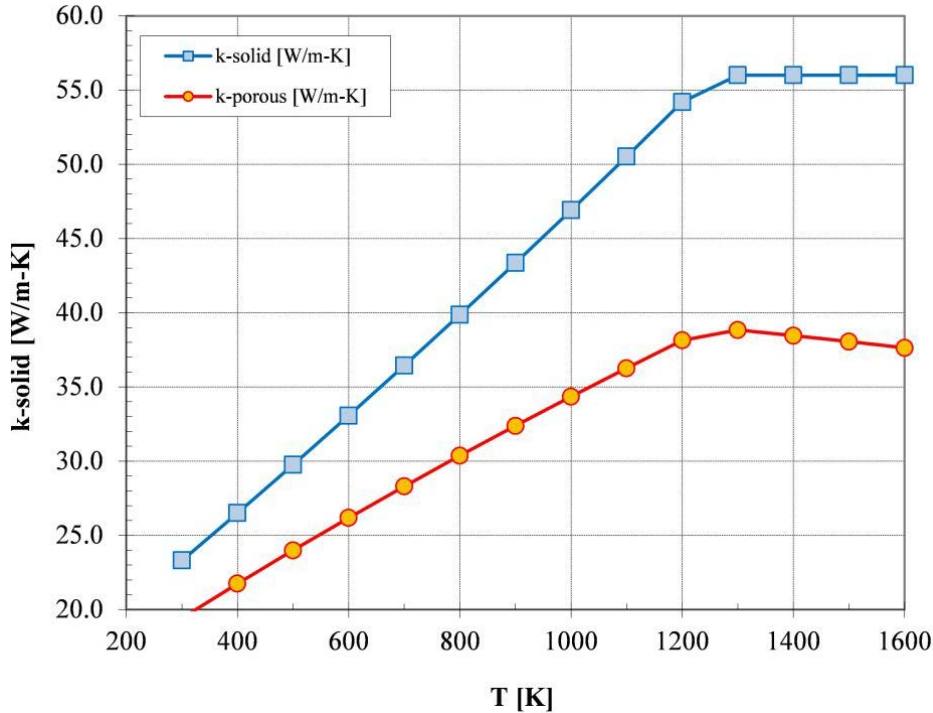


FIG. 203. U-5Fs fuel thermal conductivity.

7.14.3. Thermal hydraulics methods and models

7.14.3.1. Code(s) used

The SPECTRA thermal hydraulic system code was used to model the EBR-II reactor and primary loop. The TRACE thermal hydraulic system code was used to perform an alternate modelling of instrumented subassemblies XX09 and XX10.

ANSYS CFX is a computational fluid dynamics (CFD) software tool that was used to model the EBR-II sodium cold pool. It was coupled to the SPECTRA code.

7.14.3.2. Basic method

NRG participated in the following parts of the EBR-II benchmark exercise: SHRT-17, SHRT-45R, XX09, XX10. The following basic strategy was applied: SHRT-17 and SHRT-45 were modelled with the system code SPECTRA. In phase 2, coupled SPECTRA-CFX was used. The instrumented assemblies, XX09 and XX10, were modelled in SPECTRA and TRACE. NRG did not participate in the neutronics benchmark. All calculations are summarized in TABLE 24.

TABLE 24. CALCULATIONS PERFORMED

	SPECTRA	TRACE	SPECTRA/CFX ^a
SHRT-17	Phase 1 / Phase 2	-	Phase 2
SHRT-45R	Phase 1 / Phase 2	-	Phase 2 ^b
SHRT-17, XX09	Phase 2	-	-
SHRT-45R, XX09	Phase 2	-	-
SHRT-17, XX10	Phase 2	Phase 2	-
SHRT-45R, XX10	Phase 2	-	-

^a Coupled CFX-SPECTRA

^b Not finalized before the data transfer deadline, therefore not in the comparison.

7.14.3.3. Model

A full model of EBR-II was built for the STH code SPECTRA — FIG. 204, based on [106]. In the blind phase, SPECTRA calculations for SHRT-17 and SHRT-45R were performed. In phase 2, the coupled SPECTRA/CFX model was used, where the sodium pool was modelled in CFX, see FIG. 205, and the coupling points were the inlet to the pool from the IHX and the outlet from the pool into the pump inlets.

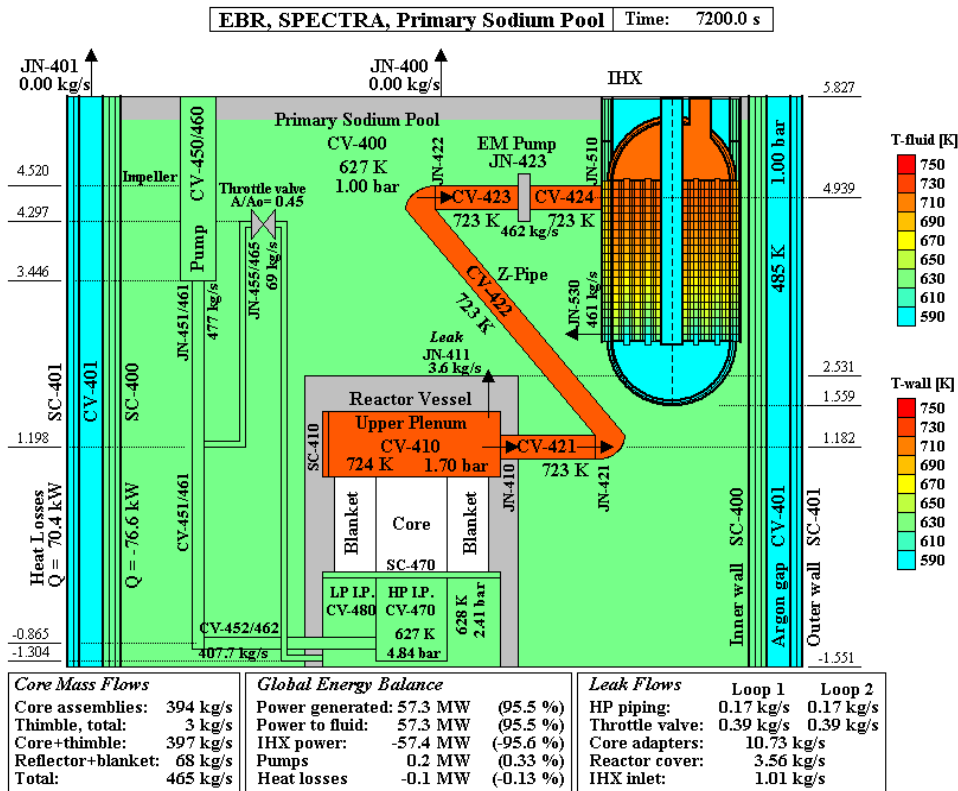


FIG. 204. EBR-II SPECTRA full system model.

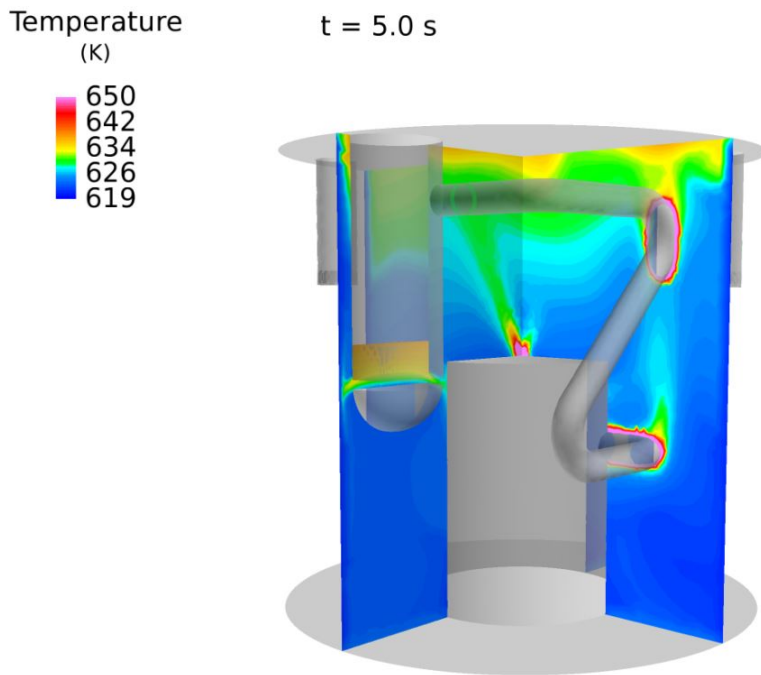


FIG. 205. EBR-II cold pool CFX temperatures at $t=5 \text{ s}$.

The instrumented subassemblies, XX09 and XX10 were modelled in SPECTRA using a single channel representation — FIG. 206. XX10 was modelled in TRACE using the subchannel division — FIG. 207. The subchannel division allows obtaining a better representation of the local temperatures, although the code does not have a cross-flow model.

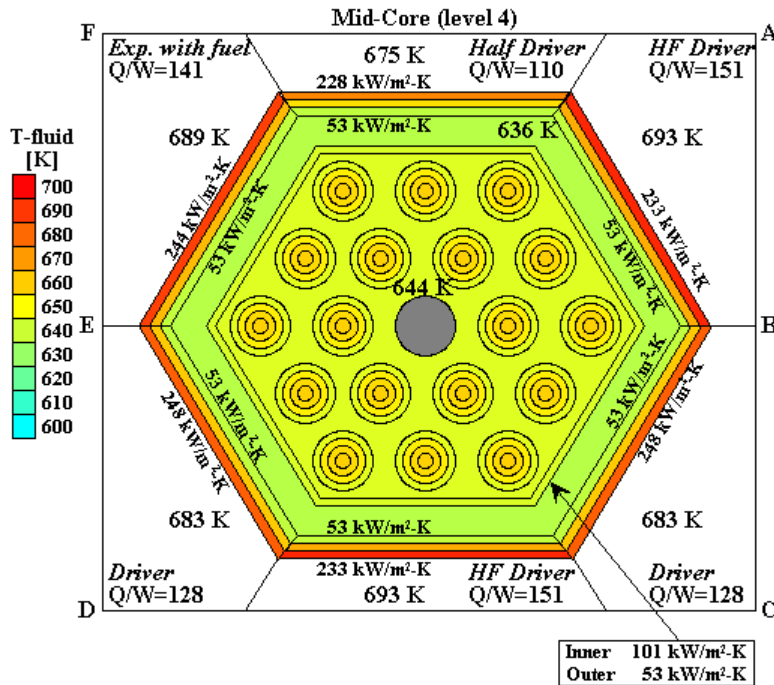


FIG. 206. SPECTRA single channel model of XX10.

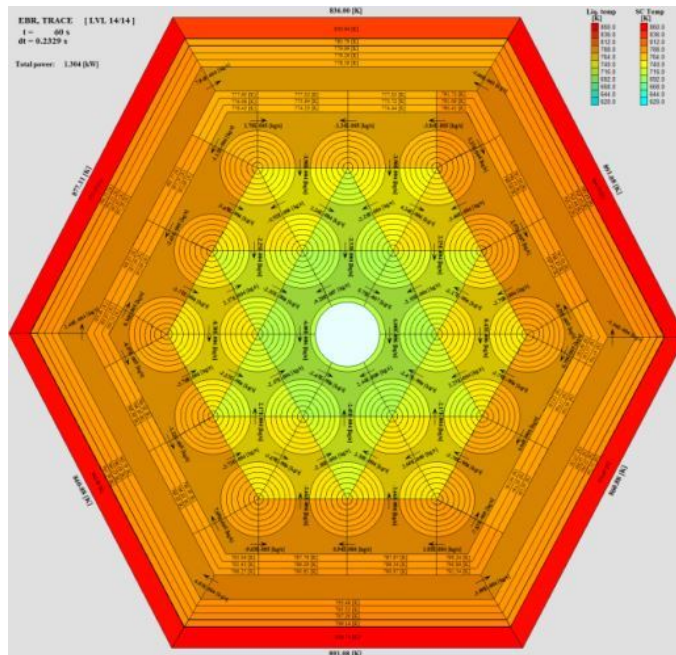


FIG. 207. TRACE subchannel model of XX10.

7.14.4. Blind results

7.14.4.1. SHRT-17

In case of SHRT-17, the measured data include the primary coolant flow rate and temperatures at the core inlet, Z-Pipe inlet, IHX primary side inlet and IHX secondary side outlet, see, for example [119]. The calculated values are compared to the measured values in FIG. 208 and FIG. 209. The natural circulation mass flow is somewhat overpredicted, most likely because the actual flow resistance of the locked pumps is much larger than was assumed in the blind model. This was improved in the final model (see model improvements, Section 7.14.5.3).

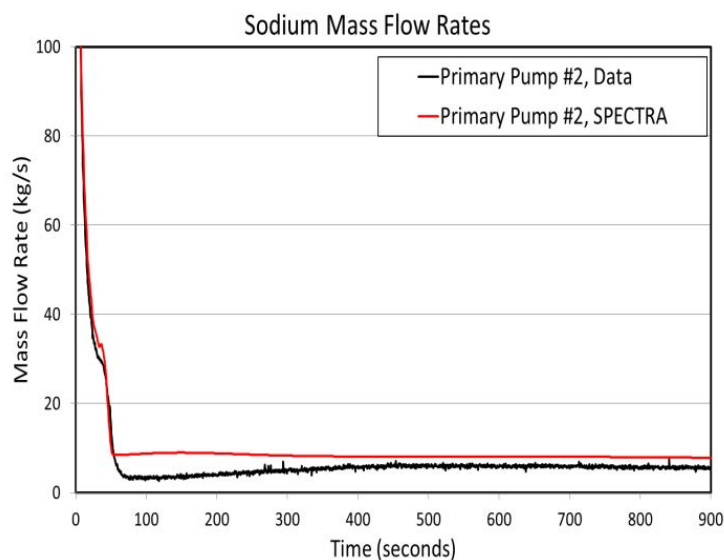


FIG. 208. SHRT-17 pump flow, blind results.

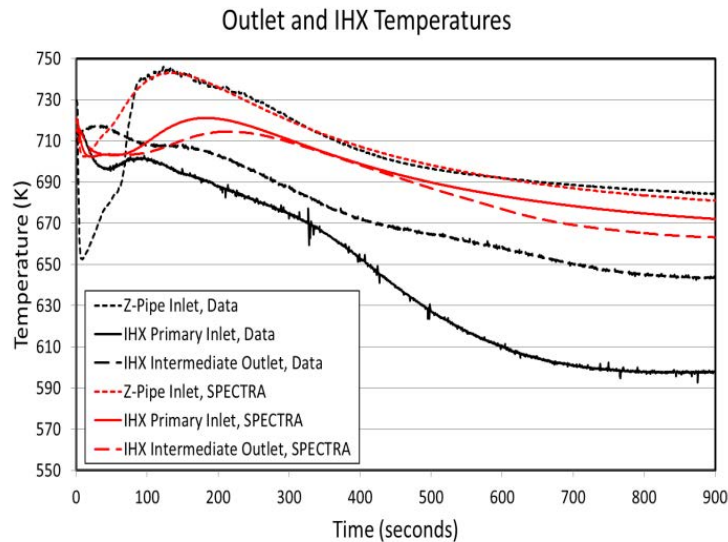


FIG. 209. SHRT-17 coolant temperatures, blind results.

The temperature of the Z-Pipe inlet was in good agreement, except for the initial period. The largest discrepancy was observed in the IHX inlet data. The Z-Pipe average outlet temperature was used as the “IHX inlet temperature” in the blind runs, which was corrected in the final runs.

7.14.4.2. SHRT-45R

In the case of SHRT-45R, the measured data include the fission power, the primary coolant flow rate, temperatures at the core inlet, Z-Pipe inlet, IHX primary side inlet and IHX secondary side outlet. The values obtained in the blind analysis are compared to the measured values in FIG. 210 through FIG. 213. The core fission power was clearly overpredicted, almost by a factor of 2 towards the end of the test — FIG. 210. The natural circulation mass flow is somewhat overpredicted — FIG. 212, similarly as in SHRT-17. The temperatures of the Z-Pipe, IHX inlet and IHX outlet were generally overpredicted — FIG. 213, which is linked to the overprediction of the core fission power.

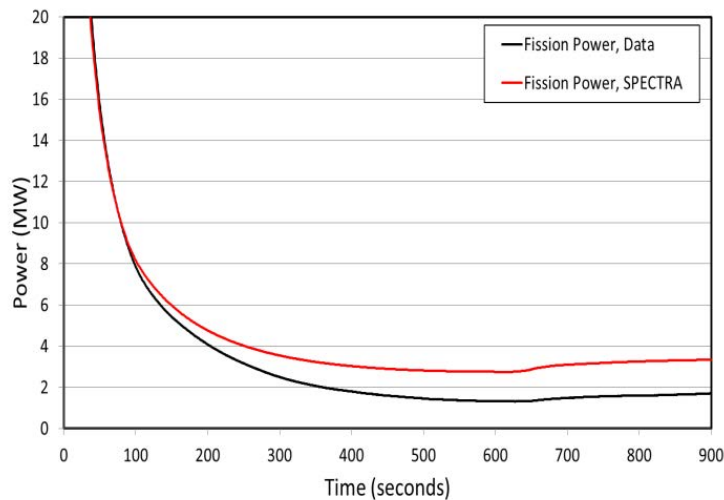


FIG. 210. SHRT-45R fission power, blind results.

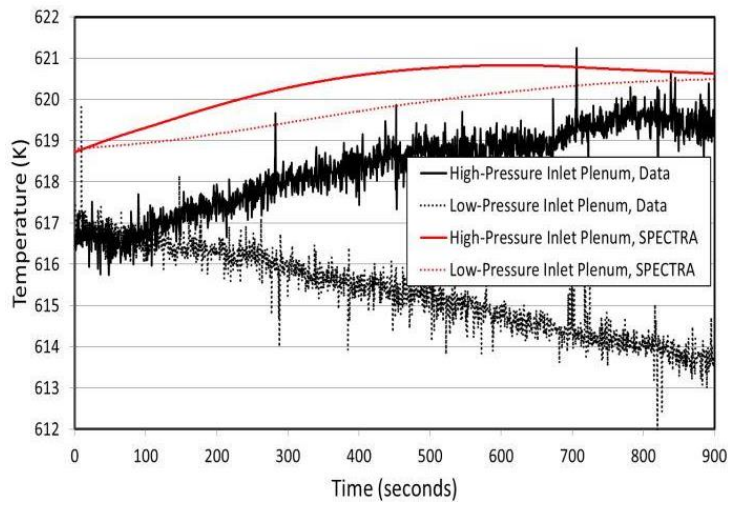


FIG. 211. SHRT-45R core inlet temperatures, blind results.

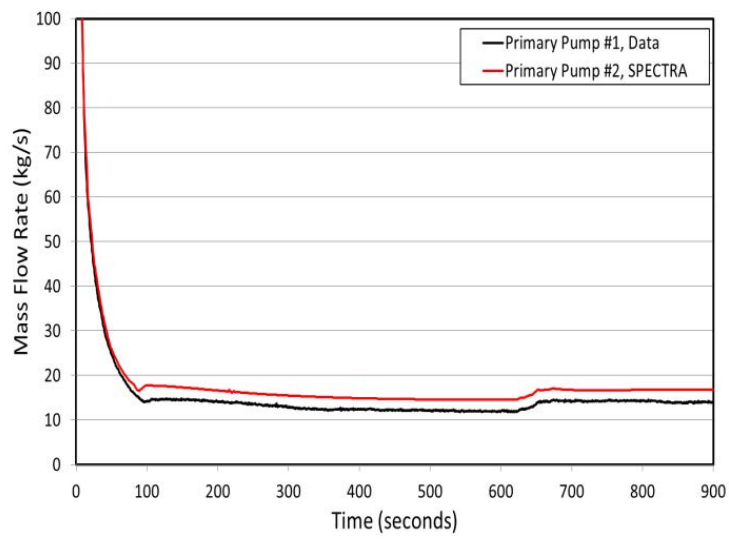


FIG. 212. SHRT-45R mass flow rates, blind results.

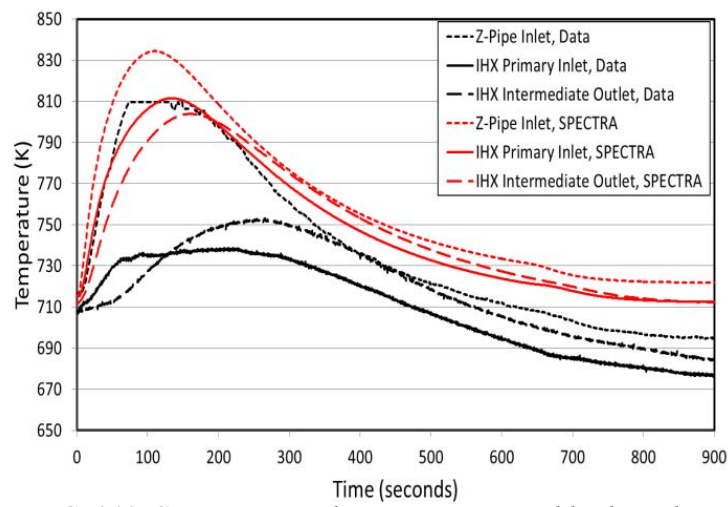


FIG. 213. SHRT-45R coolant temperatures, blind results.

7.14.5. Final results, data comparisons

7.14.5.1. SHRT-17

The final results of the coupled SPECTRA/CFX calculations (interactive coupling with overlapping domains was applied) of SHRT-17 are shown in FIG. 214 and FIG. 215. The natural circulation mass flow agrees quite well with the measured data. The improved agreement is due to applying a larger resistance factor for the locked pumps (see model improvements, Sec. 7.14.5.3). Also the coolant temperatures in the measured locations are in good agreement, owing mainly to selecting different location of the IHX inlet temperature (see model improvements, Section 7.14.5.3). SPECTRA/CFX results compared to the standalone SPECTRA results showed that the main results are quite similar and therefore the advantage of using CFD is, in this particular case, small.

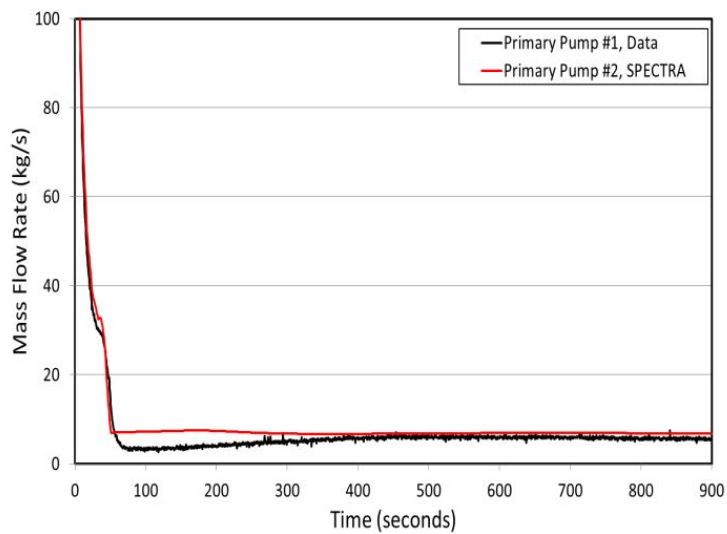


FIG. 214. SHRT-17 pump flow, final results.

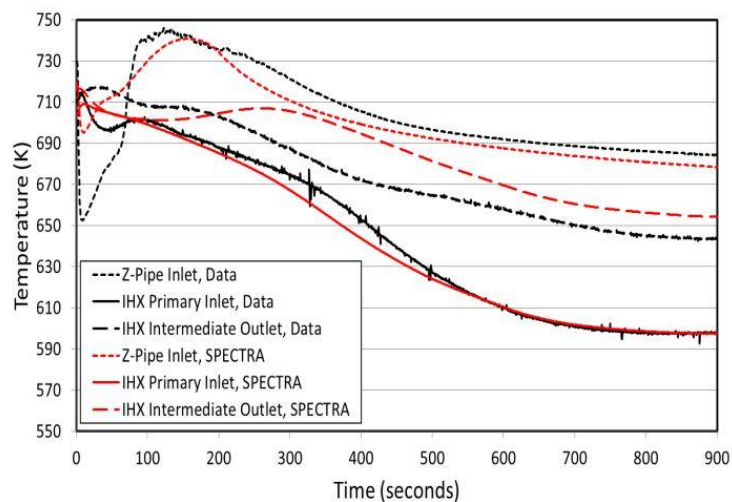


FIG. 215. SHRT-17 Z-Pipe and IHX temperatures, final results.

FIG. 216 and FIG. 217 show the XX10 results obtained with the TRACE code, subchannel model. The TRACE results show bigger channel-to-channel differences than does the measured data, because no cross-flow mixing, induced by spirally shaped wires, was taken into account by the code.

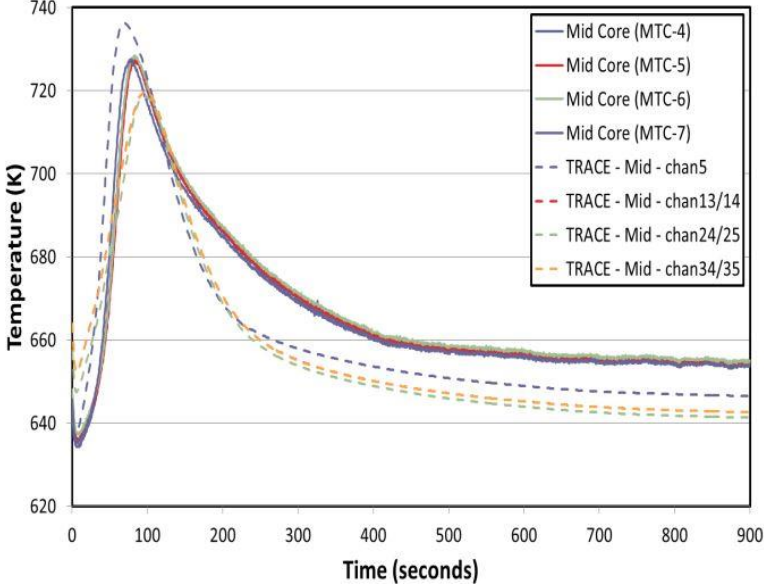


FIG. 216. SHRT-17, XX10 mid-core temperatures, final results.

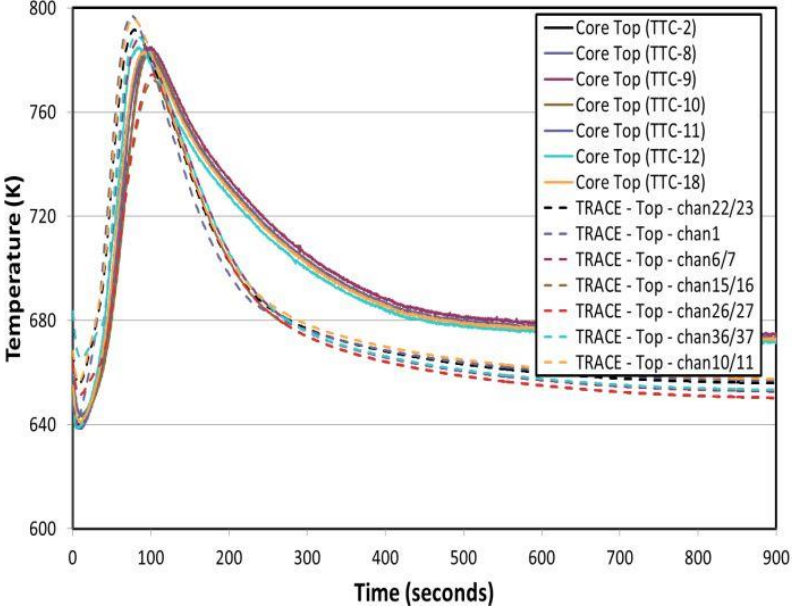


FIG. 217. SHRT-17, XX10 core top temperatures, final results.

7.14.5.2. SHRT-45R

The final results of the SPECTRA calculations of SHRT-45R are shown in FIG. 218 through FIG. 221. The reactor power is in good agreement with the measured values, due to the correction of the radial expansion reactivity effect (see model improvements, Section 7.14.5.3). The core inlet temperatures are in very good agreement with the measured data, mainly due to improved modelling of the heat losses (see model improvements, Section 7.14.5.3). The natural circulation mass flow agrees very well with the measured data. Also the coolant temperatures in the measured locations are in good agreement.

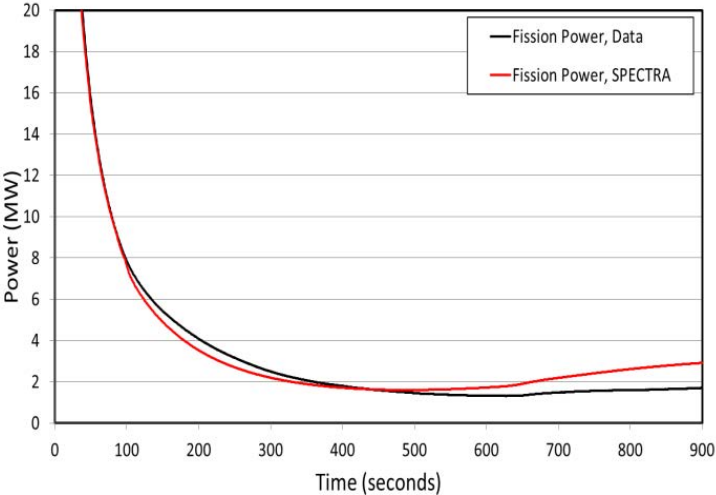


FIG. 218. SHRT-45R fission power, final results.

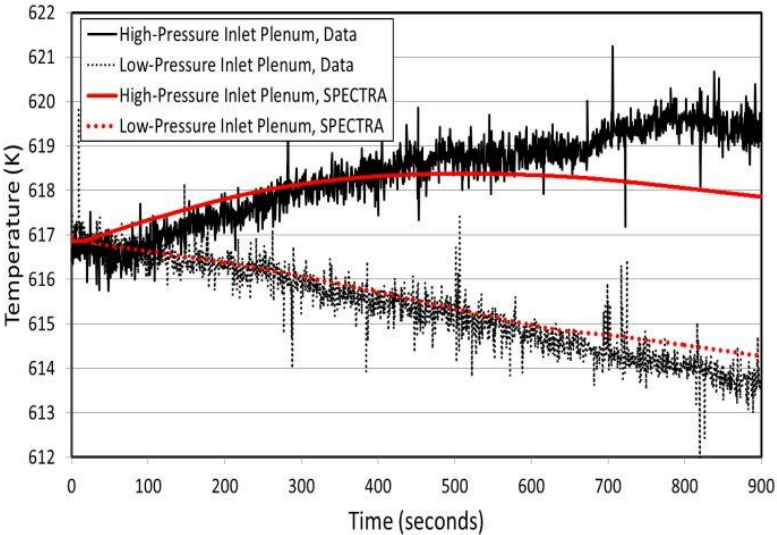


FIG. 219. SHRT-45R core inlet temperatures, final results.

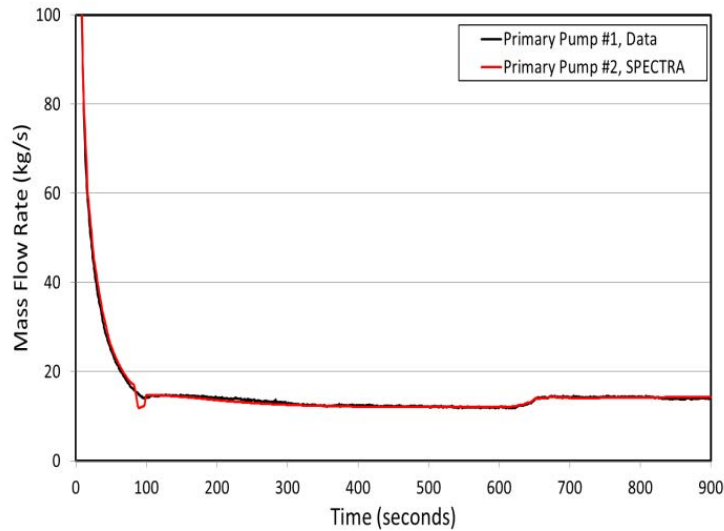


FIG. 220. SHRT-45R pump flow, final results.

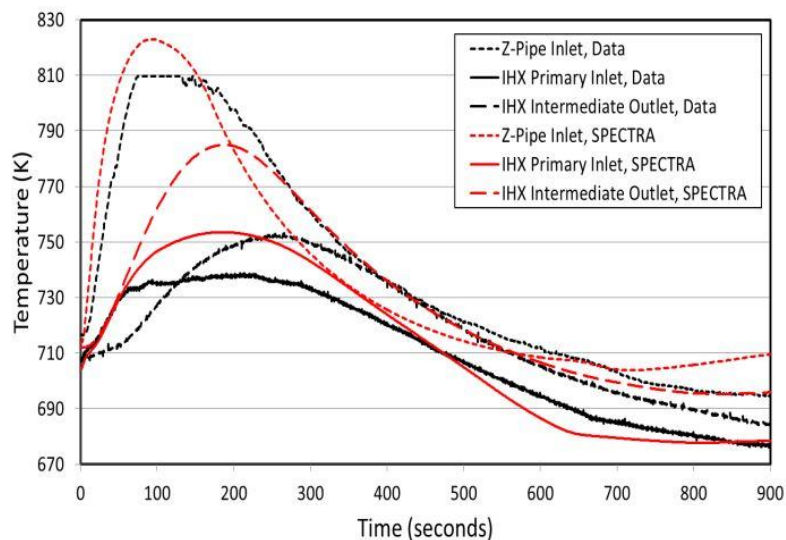


FIG. 221. SHRT-45R Z-Pipe and IHX temperatures, final results.

7.14.5.3. Model improvements

Radial expansion reactivity effect

In the blind calculations a mistake was made in defining the radial expansion reactivity effect. As a consequence, there was almost no effect of radial expansion and the fission power was overestimated — FIG. 210. This mistake was corrected in the final calculations and the power is in better agreement with the data — FIG. 218.

Loss factor for the locked pumps

In the blind calculations the loss factor for the primary pumps was assumed to be constant and equal to $K = 0.1$. The calculated sodium mass flows were somewhat higher than measured — FIG. 212. For the final runs, the loss factor was defined as dependent on the pump speed, with a maximum value for the locked pumps — FIG. 222. The final sodium mass flow through the pump is much closer to the experimental mass flow — FIG. 214, FIG. 220.

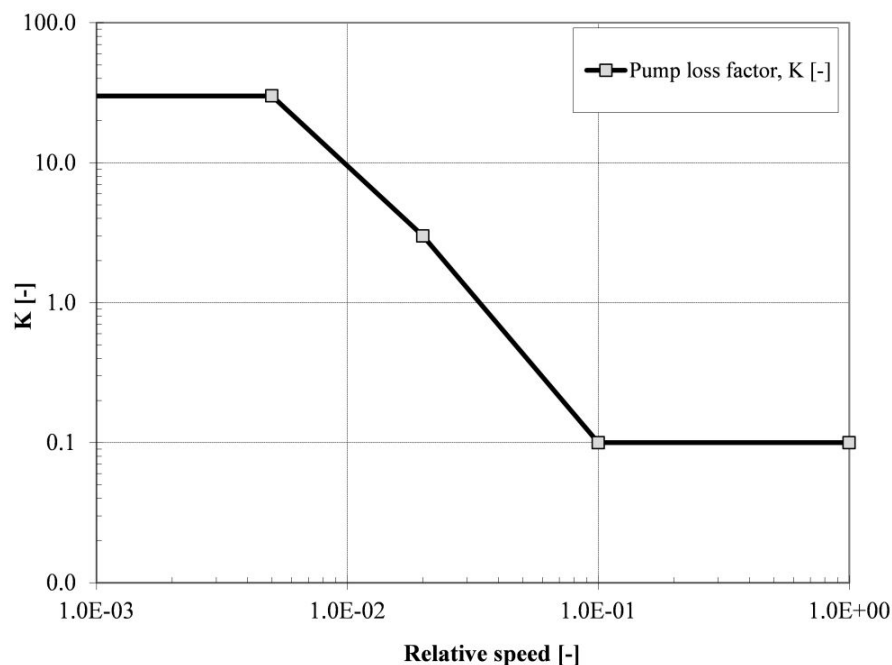


FIG. 222. SHRT-17 primary pump loss factor.

Decay heat - match based on SHRT-17 data

In the blind calculations the default (built-in) group constants were used for decay heat calculations. For the final calculations, the group constants were modified to match the measured data from SHRT-17, as shown in FIG. 223.

Refinement of the upper plenum nodalization

In the blind calculations the upper plenum was represented by a single control volume. For the final runs, the upper plenum nodalization was re-defined, as shown in FIG. 224.

Refinement of the lower plenum nodalization

In the blind calculations no solid structures were modelled within the lower plenum. For the final runs, the structures representing the HP and LP inlet plena internals were added (FIG. 225):

- (a) HP inlet plenum: SC-471 and 472;
- (b) LP inlet plenum: SC-481, 482, 483.

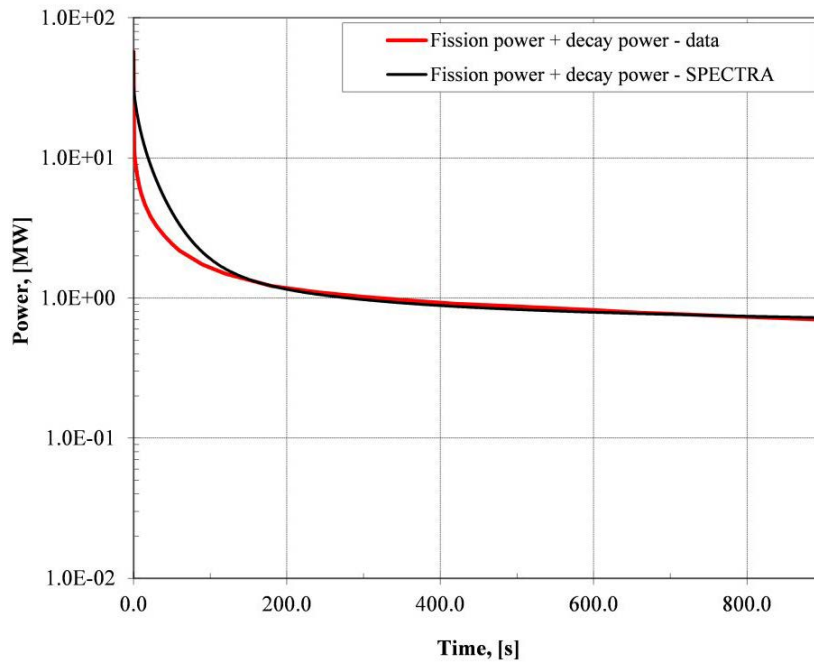


FIG. 223. SHRT-17 fission power and decay power.

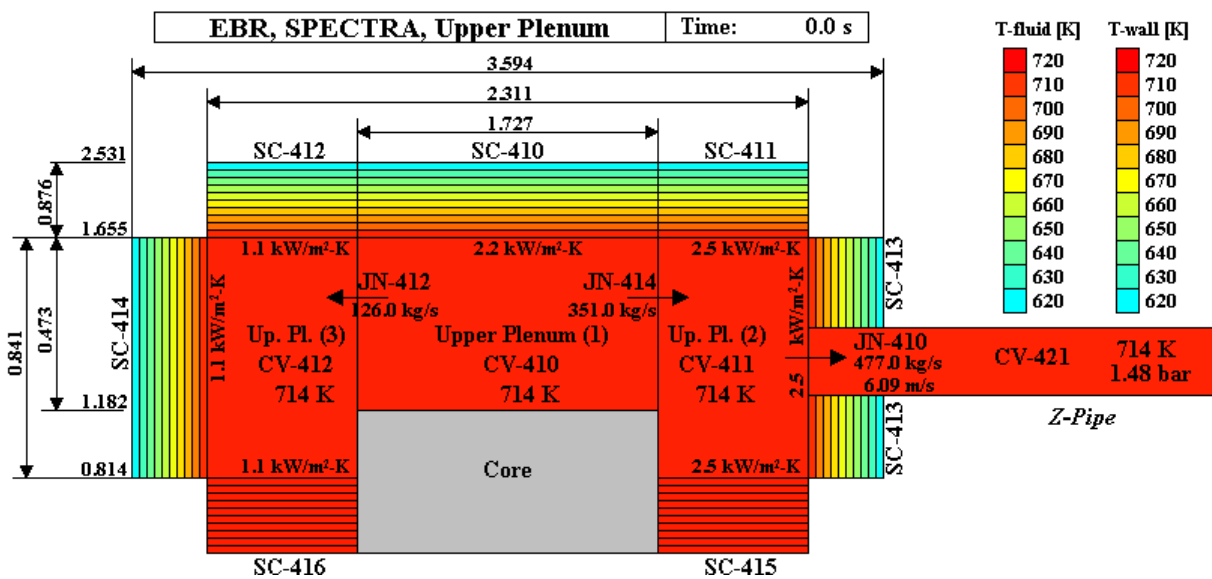


FIG. 224. Upper plenum nodalization in the final model.

IHX inlet temperature

In the blind calculations the Z-Pipe average outlet temperature was used as the “IHX inlet temperature”. For the final runs, the temperature in one of the IHX upper nodes was used.

IHX intermediate outlet temperature definition

In the blind calculations the temperature of the IHX tube exit was used. For the final runs, this was replaced by the temperature in the IHX upper dome, to take into account thermal inertia of the upper dome.

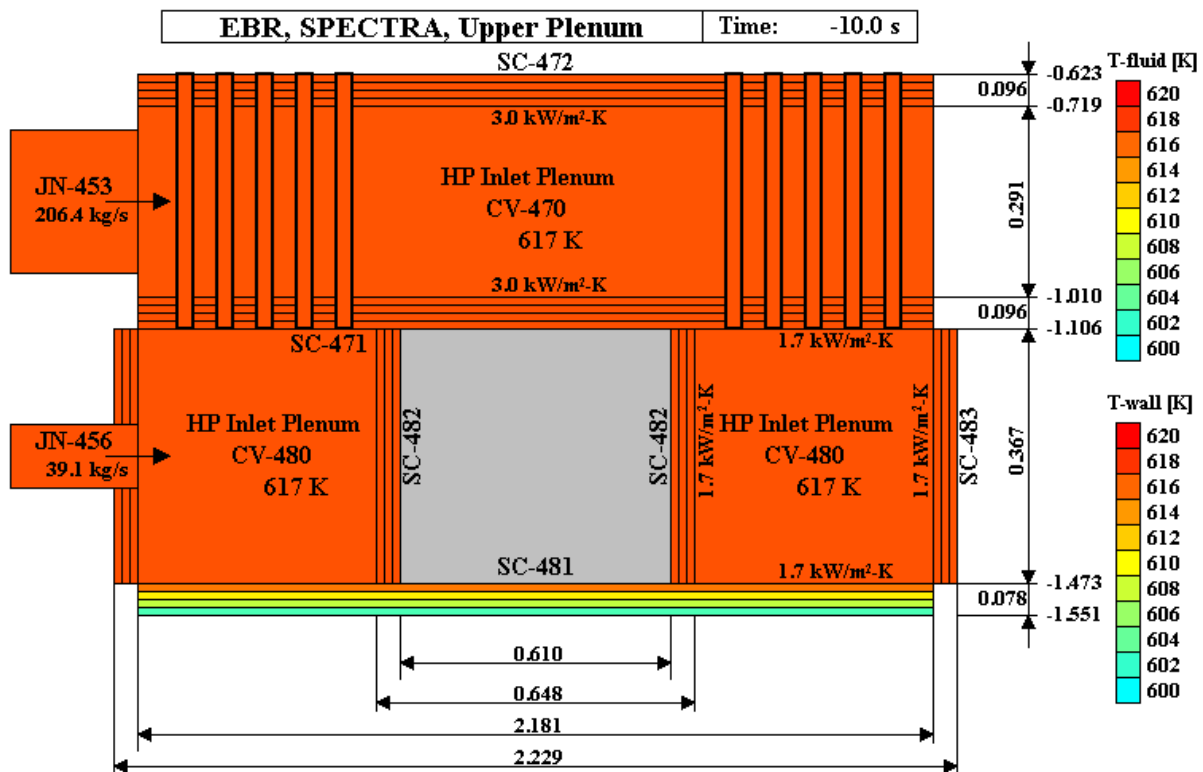


FIG. 225. Lower plenum nodalization in the final model.

Axial power profile

For the blind calculations a flat axial power profile was applied because no data were found. For the final calculations, a cosine power profile was used.

Heat loss from the PSP

In the blind calculations only heat loss through the walls was modelled. In the final run the loss through the floor was added. This made it possible to obtain a more accurate value for the initial temperature of the sodium pool — FIG. 219.

7.14.6. Neutronics methods and models

NRG did not participate in the neutronics benchmark.

7.15. IBRAE-RAN (RUSSIAN FEDERATION)

7.15.1. Geometry/discretization

To perform the calculations for the EBR-II SHRT-17 and SHRT-45R experiments, a nodalization scheme for the SOCRAT-BN code was developed (see FIG. 226). The primary heat transport model consists of the core, inlet and outlet plena, Z-Pipe, intermediate heat exchanger (IHX), primary and auxiliary pumps, reactor tank and reactor inlet piping. The

secondary heat transport model is limited to the IHX tubes, IHX inlet and outlet plena, and the IHX inlet and outlet piping, with corresponding boundary conditions for sodium mass flow rate and temperature (the secondary is not included in FIG. 226).

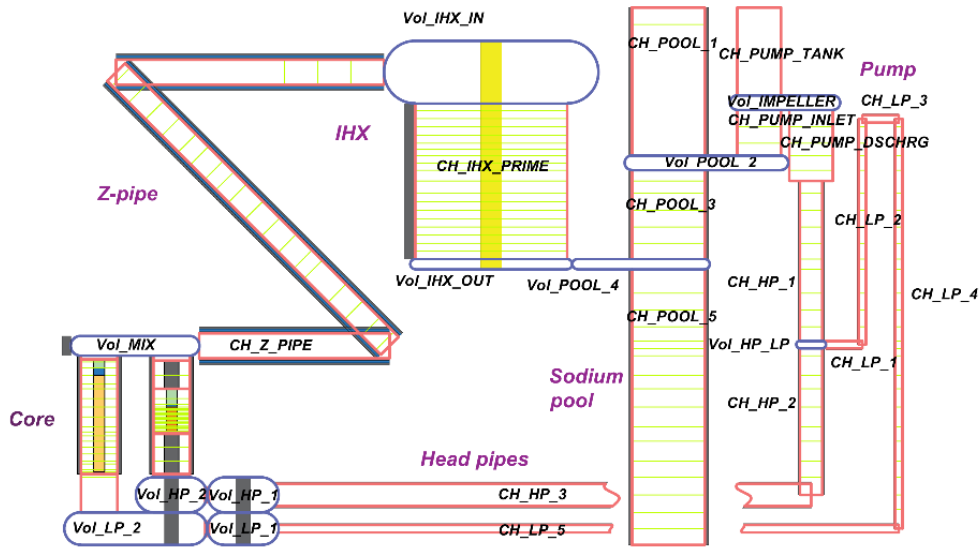


FIG. 226. EBR-II nodalization scheme for SOCRAT-BN.

The only difference between the models for SHRT-17 and SHRT-45R is the core model, due to the fact that each transient was run with a different core loading.

The core model consists of several parallel channels (13 for SHRT-17, 15 for SHRT-45R). Each channel represents one type of subassembly. The types of simulated subassemblies and their multiplicity factors for the model are presented in TABLE 25 below. To evaluate the maximum temperatures for fuel, cladding and sodium, one maximum loaded (maximum ratio of power to mass flow rate) subassembly was simulated for each transient.

TABLE 25. MULTIPLICITY FACTORS FOR SUBASSEMBLIES IN SOCRAT-BN CORE MODEL

Subassembly Type	SHRT-17	SHRT-45R
Driver (MARK-II AI)	32	32
Driver (MARK-II A)	-	14
High Flow Driver (MARK-II AI)	17	12
High Flow Driver (MARK-II A)	-	12
Partial Driver	10	13
Experimental subassemblies (treated as driver subassemblies)	13	4
Steel subassemblies	7	7
High pressure reflector subassemblies	35	20
Low pressure reflector subassemblies	156	179
Blanket subassemblies	354	331
Control rod subassemblies	8	8
Safety rod subassemblies	2	2
XX09	1	1
XX10	1	1
Maximum loaded subassembly	1 (HFD)	1 (MARK-II A Driver)

7.15.2. Nuclear and thermo-physical data/correlations

To solve the system of governing equations, the following thermo-physical data/correlations are implemented in the SOCRAT-BN code:

- (a) Equations of state for liquid and vapour sodium are used according to [75];
- (b) Required thermo-physical properties of construction materials (fuel, cladding, reactor inlet piping steel, neutron shield graphite), for solving the heat transport equations are used in accordance with the benchmark specification and handbooks, and set through the input file;
- (c) Closure relations for liquid sodium heat transfer and friction with the wall, which are described in [33];
- (d) Closure relations for two-phase sodium heat transfer and friction with the wall, which are described in [120];
- (e) Closure relations for interphase sodium interactions, which are described in [120].

It is important to accurately model the heat transfer in a natural convection regime because there is a significant influence on the coolant temperatures in the Z-Pipe and the reactor inlet piping at low flow velocities. In order to estimate the heat losses from the Z-Pipe and reactor inlet piping to the sodium in the cold pool, the following correlation for natural convection heat transfer was used in SOCRAT-BN [121]:

$$Nu = C \left(\frac{Gr Pr^2}{1 + Pr} \right)^n$$

if $Gr = 10^2 \div 10^8$ $C = 0.67; n = 0.25$; if $Gr \geq 10^8$ $C = 0.35; n = 1/3$.

There are several options for assessing the reactor power in a transient:

- (a) Enter power as a function of time through the input file (this option was used for SHRT-17);
- (b) Point-kinetics model (this option was used for SHRT-45R experiment). Reactivity feedback coefficients and delayed neutron data for the SHRT-45R experiment are presented in TABLE 26 and TABLE 27 below.

TABLE 26. REACTIVITY FEEDBACK COEFFICIENTS

Parameter	Reactivity feedback coefficient, pcm/K
Axial expansion	-0.36
Radial expansion	-1.78
Sodium density	-1.7
Fuel Doppler	-0.024
Control rod expansion	0

TABLE 27. DELAYED NEUTRON DATA

Delayed neutron group	Fraction	Decay constant (1/s)
β_1	2.3929×10^{-4}	1.3345×10^{-2}
β_2	1.2372×10^{-3}	3.2658×10^{-2}
β_3	1.1967×10^{-3}	1.2091×10^{-1}
β_4	2.7082×10^{-3}	3.0429×10^{-1}
β_5	1.1734×10^{-3}	8.5587×10^{-1}
β_6	4.9210×10^{-4}	2.8738
β_{eff}	7.04689×10^{-3}	-

Neutron lifetime is 3.46402×10^{-7} s.

7.15.3. Thermal hydraulics methods and models

7.15.3.1. Code(s) used

The SOCRAT-BN code was used to analyse both SHRT-17 and SHRT-45R.

7.15.3.2. Basic method

The basic method of the SOCRAT-BN code provides self-consistent calculations of the parameters, which is important from the safety point of view. The code performs transient calculations, taking into account the parameters of the primary heat transport system, secondary heat transport system, tertiary heat transport system (steam generator side), and decay heat removal system, including sodium-air heat exchangers.

Much effort was put into developing a core model. The model consists of the sodium inside the subassemblies and the heat structures (steel hexcan, fuel pin, cladding etc). To implement intra-subassembly heat transfer, a bypass channel was included in the model. For each type of subassembly, one channel was used. Due to the complicated geometry of the experimental subassemblies (XX09, XX10), these subassemblies were modelled with two hydraulic channels, instead of one. One channel was used for the sodium inside the inner hexcan, the other for sodium between the inner and outer hexcan. This approach successfully simulated the sodium temperature behaviour in the pin region. To provide the necessary pressure drop and mass flow rates through the channels, a local resistance was used.

To perform the simulation for the SHRT-45R transient, a point-kinetic model was used. It was necessary to provide an averaging of the heat structure components inside the core model. For radial and axial expansion effects, the average temperatures of hexcans and pin claddings were used. To take into account the Doppler effect, the average temperature of the fuel in the core region was determined during the simulations. Expansion of control rods was not included in the model.

7.15.3.3. Model

The basic modelling approach of the SOCRAT-BN code consists of representing a reactor (facility) with a set of one dimensional and zero-dimensional elements and two dimensional heat structures. For the EBR-II analyses, for both the primary and secondary heat transport systems, in general, 1-D channel elements were used. Such elements were used for modelling subassemblies, the Z-Pipe, the primary and secondary side of the IHX, the sodium pool and

the reactor inlet piping. 0-D elements were used to represent volumes where the mixing of several flows occurred. For example, the core inlet and outlet plena and the IHX inlet/outlet regions were modelled with 0-D elements. All heat structures employed a two dimensional R-Z approach. Relevant boundary conditions were used for inner and outer surfaces (heat transfer from fuel pins, heat transfer between the two sides of the IHX, and heat transfer between the cold pool and the Z-Pipe).

7.15.4. Blind results

IBRAE-RAN did not join the CRP until phase 2, so no blind results were generated.

7.15.5. Final results, data comparisons

7.15.5.1. SHRT-17

The calculations performed for SHRT-17 were a test of the ability of the SOCRAT-BN models to simulate transients in which natural circulation was established in the primary heat transport system after the reactor scrammed.

Prior to the transient calculation, the EBR-II model was run at nominal steady state conditions. The criterion used to determine when a steady state had been reached was the commonly used requirement that the main calculation parameters do not change more than 1% in 100 s.

FIG. 227 compares the experimental and calculated time dependencies of the sodium temperatures at the IHX primary side inlet and secondary side outlet and the sodium mass flow rates in primary loop 2 (high pressure pipe, low pressure pipe and total). There is good agreement between the measured data and the calculated results. The discrepancies between the measured and predicted results can be explained by some uncertainties in the thermocouple locations in the loop and by the possible stratification of the sodium in the piping, which cannot be tracked with the 1-D hydraulics SOCRAT-BN approach.

Comparisons of calculated sodium temperatures and mass flow rates in experimental subassembly XX09 against the experimental data are presented in FIG. 228. The SOCRAT-BN results for the peak sodium temperatures overpredict the data by about 25 K. Note that at about 100s, the recorded sodium temperature at the middle of the fuel bundle (Core Top TTC) is higher than the recorded temperature at the top (Above Core 14TC). This would seem to indicate that the sodium in the subassembly is almost stagnant. However, the recorded mass flow rate is significantly above zero or near-zero values, which would indicate that significant radial heat loss occurs through the inner hexcan as the sodium travels from the Core Top to the Above Core elevation. The calculated mass flow rate is in good agreement with the experimental data, but the SOCRAT-BN results show no such temperature behaviour. To correctly describe the sodium temperatures, a more detailed model, which will take into account the heat dissipation from the sodium inside the inner hexcan to the sodium between the inner and outer hexcans, is needed

7.15.5.2. SHRT-45R

The aim of the SHRT-45R SOCRAT-BN calculations was to check the consistency between the thermal hydraulics and point-kinetics models. Prior to the transient calculations, steady state conditions were established using the same method as for SHRT-17.

The calculated SOCRAT-BN powers are compared against the recorded fission power in FIG. 229. The calculated values are in a good agreement with experiments; however, it is evident that until 300s, the calculated fission power decreases faster than in the experiment, and, conversely, after 300s, the calculated power exceeds the recorded power. These discrepancies can be explained by the point-kinetics approach, which is used in SOCRAT-BN; apparently, with this approach, it is impossible to catch the spatial effects..

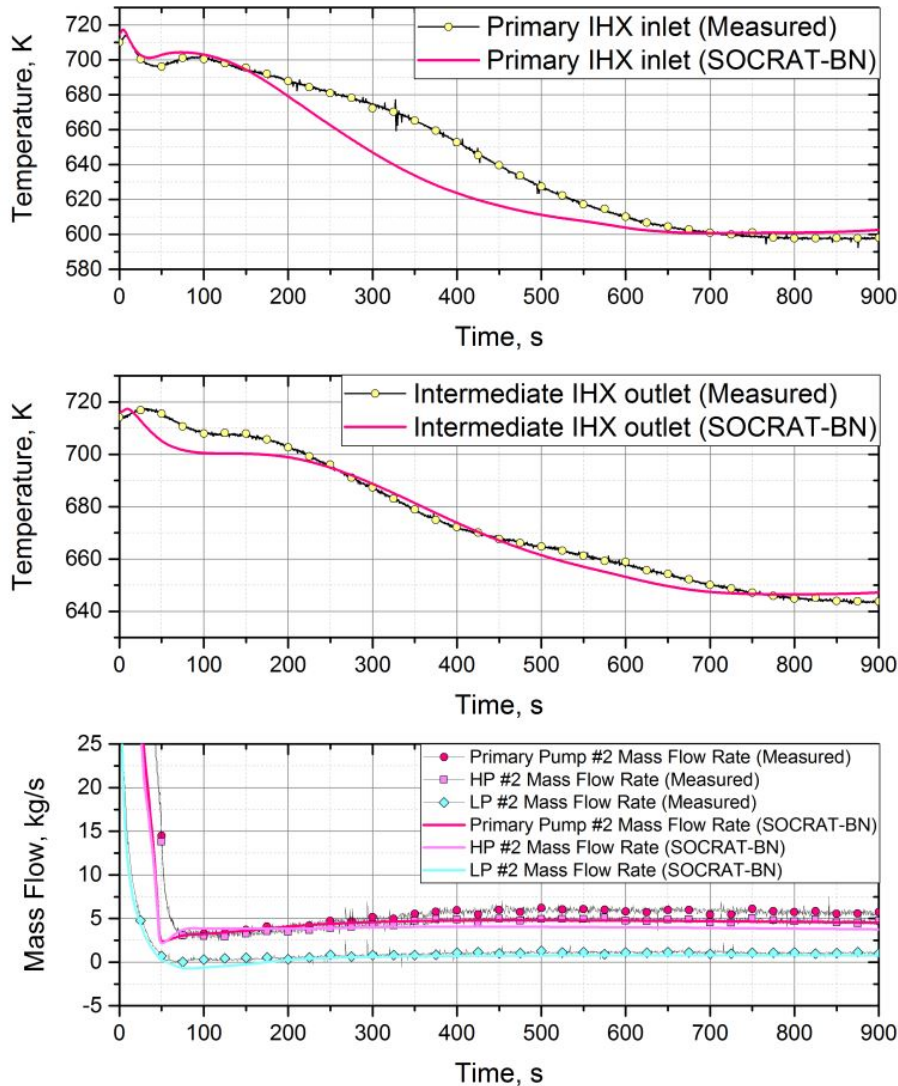


FIG. 227. Comparison of the SHRT-17 experimental and calculated results.

The SOCRAT-BN values for mass flow rates are in good agreement with the measured ones both before and after the auxiliary pump flow increases.

FIG. 229 also compares the XX09 sodium temperatures. Due to the overestimation in the calculated power, there is an overestimation of about 25K in the calculated sodium temperatures, beginning at about 300s.

The sodium temperatures at the Z-Pipe inlet, primary side IHX inlet, and secondary side IHX outlet are depicted in FIG. 230. There is good agreement between the predicted and measured values for the Z-Pipe inlet sodium temperature. However, again, because there is a power overestimation in the calculation, higher calculated values occur in the sodium temperature at

the end of the experiment, with a discrepancy up to 20K. The same errors are in the sodium temperatures at the primary side IHX inlet and secondary side IHX outlet. As for the SHRT-17 experiment, these discrepancies can be explained by the fact that there are some uncertainties in the thermocouple locations and possible sodium stratification in the piping.

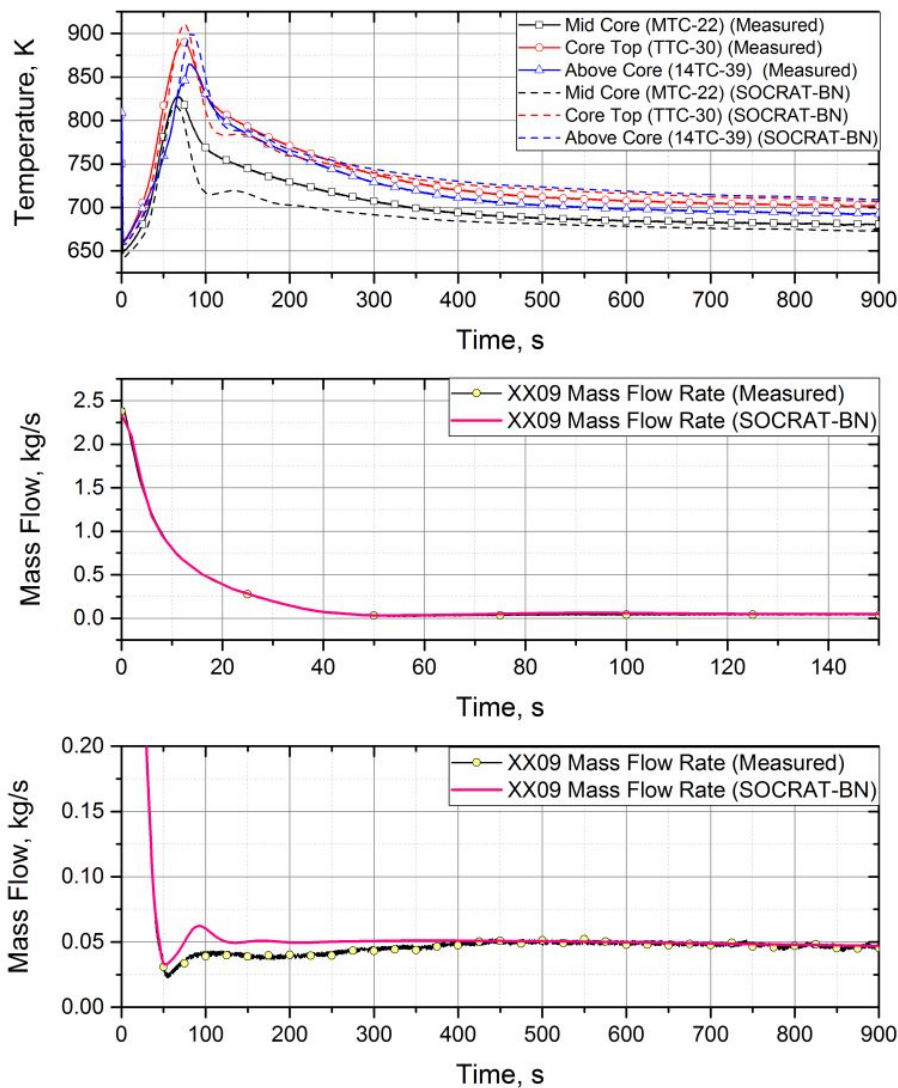


FIG. 228. Comparison of the SHRT-17 experimental and calculated results for XX09.

Overall, the SOCRAT-BN code has demonstrated the ability to produce self-consistent calculations of transients such as unprotected loss of flow scenarios.

7.15.6. Neutronics methods and models

IBRAE-RAN did not participate in the neutronics benchmark.

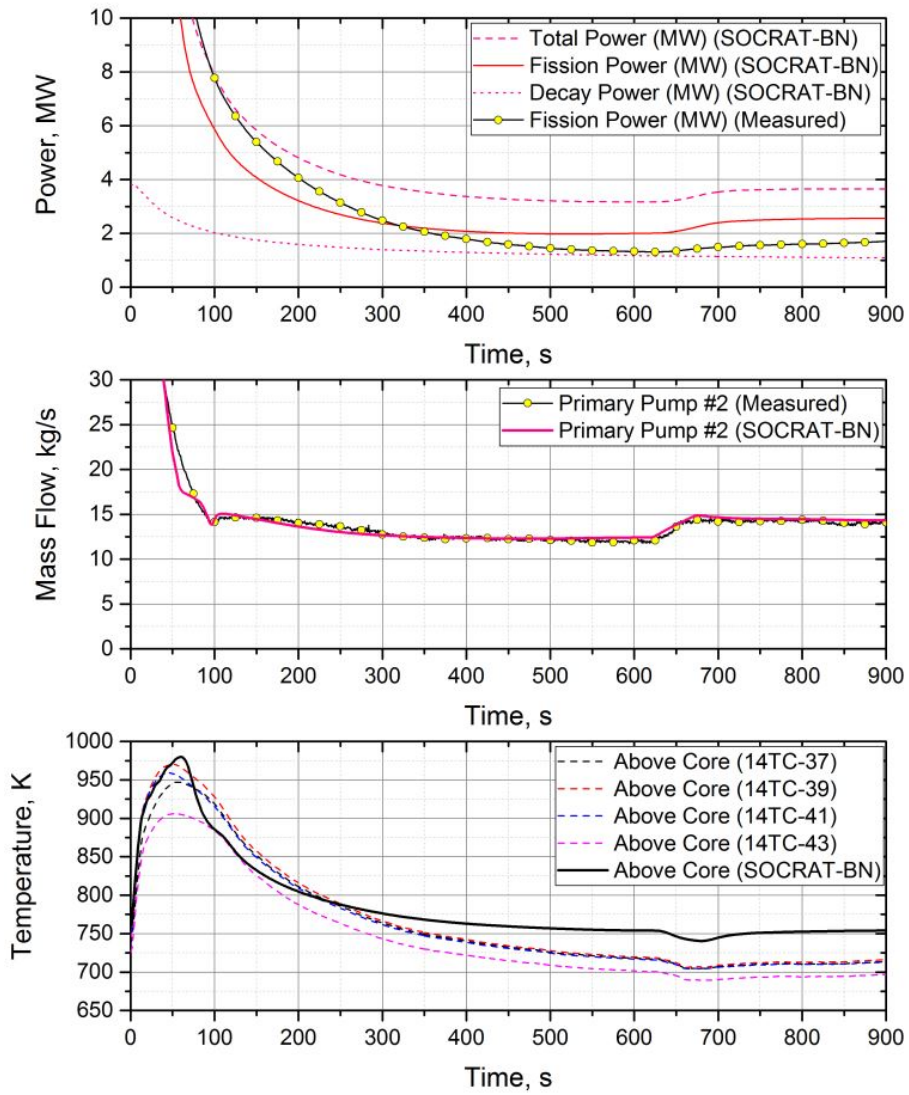


FIG. 229. Comparison of the SHRT-45R experimental and calculated results for power, flow and XX09 temperatures.

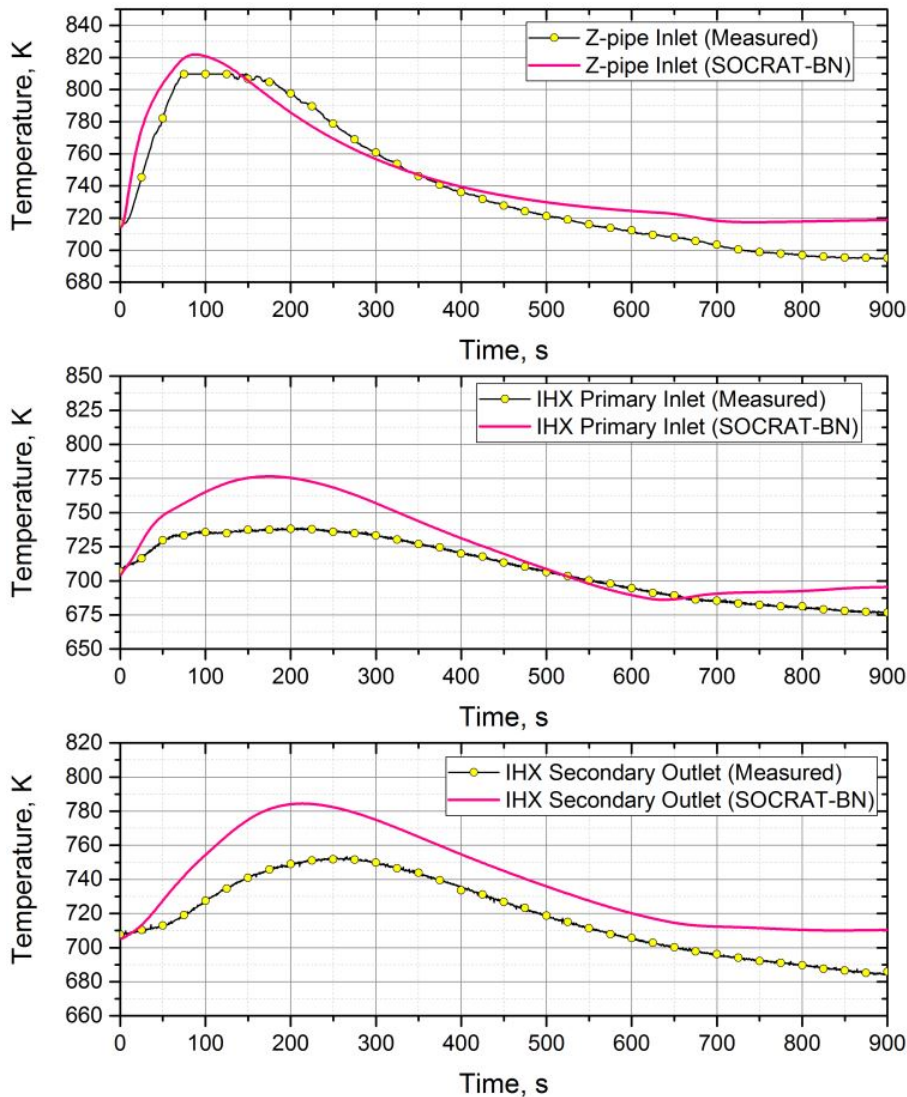


FIG. 230. Comparison of the SHRT-45R experimental and calculated Z-Pipe and IHX sodium temperatures.

7.16. PAUL SCHERRER INSTITUTE (SWITZERLAND)

7.16.1. Geometry/discretization and assumptions

In order to perform a detailed thermal hydraulic analysis of the EBR-II core behaviour during the transients, a full core model was developed with TRACE. Dedicated “PIPE” and attached “HTSTR” (heat structure) components were defined to model 4 channels representing the high power core zone connected to the high pressure inlet plenum (see FIG. 231):

- (a) the peak-power channel representing the hottest fuel SA (with the highest power/flow ratio at normal operating condition);
- (b) the average-power channel representing the other 82 fuel SAs;
- (c) the two channels containing the two experimental subassemblies XX09 and XX10.

and 3 channels representing the low power core zone connected to the low pressure inlet plenum (see FIG. 231):

- (a) the reflector channel representing all reflector assemblies;
- (b) the peak-power blanket channel representing the hottest blanket assembly;
- (c) the average-power blanket channel representing all other blanket assemblies.

Therefore, the EBR-II core, consisting of 637 SAs, was modelled with 7 parallel channels as discussed above. Heat structure components were defined for different channels to allow simulations of the hottest channels to investigate the maximum temperatures that can be achieved and also the average channels to calculate reactivity feedbacks incurred by whole core temperature change during the transients. No dedicated decay heat removal system was simulated, since in the tests considered, the main heat removal path was used.

Primary coolant comes out from the core and enters into the Z-Pipe (subdivided into connected sections with different orientations). Then it heads to the intermediate heat exchanger through the auxiliary pump and the IHX inlet sections. After being discharged from the IHX, the primary coolant enters into the cold pool, in which two primary pumps are located. The outlet of the primary pumps was divided into two branches, high pressure outlet and low pressure outlet. The high pressure outlet was directed to the inlet of the fuel subassemblies, while the low pressure outlet (with a throttle valve installed to release coolant pressure, leading to a lower flowrate) was connected to the inlet of the reflector and blanket subassemblies, which need less cooling. The cold pool section was connected to a “BREAK” component to represent the free coolant surface. The overall structure of the TRACE model can be seen schematically in FIG. 231.

Due to the absence of an EBR-II type metallic fuel pin model in the current version of TRACE, all fuel pins were modelled as linked fuel with a constant gap conductance calculated based on pin geometries provided in the benchmark specifications. Fuel pin expansion was assumed to be driven by the thermal expansion of the metallic fuel column. Since there is no metallic fuel alloy database available in the TRACE code version that was used, major thermophysical parameters for metallic fuel were implemented directly in the TRACE model for the U-5Fs metallic fuel alloy in the fuel pins and the depleted uranium metallic fuel alloy loaded into the blanket pins.

7.16.2. Results for SHRT-17 and SHRT-45R

Before performing transient analyses with TRACE, the main operational parameters at steady state were first compared with the specification or with the measured data.

TABLE 28 shows the specified flowrate distributions for the SHRT-17 operating condition. The coolant flowrate of all channels obtained from the TRACE calculations matches those provided in the specification with less than a 4% deviation. As seen from TABLE 29, the TRACE model was properly adjusted, providing operational parameters with less than 5% discrepancies comparing to the reported experimental data.

7.16.2.1. SHRT-17

For the SHRT-17 transient test, changes of chief operational parameters with time, including core fission power, primary coolant flowrate and temperatures at the core inlet, Z-Pipe inlet, IHX primary side inlet and IHX secondary side outlet, were measured and provided by Argonne during phase 2 of the CRP as reference data for the benchmark. As shown in FIG.

232, no significant difference between the calculated and measured evolution of the primary coolant flowrate was observed, which confirms the primary pump module in TRACE properly modelled the EBR-II primary pumps. As seen from FIG. 233, the evolution of the primary coolant temperature at the Z-Pipe inlet agrees with the measured values with less than 20 K difference. This difference is mainly caused by the 0-D simplified model of the upper plenum.

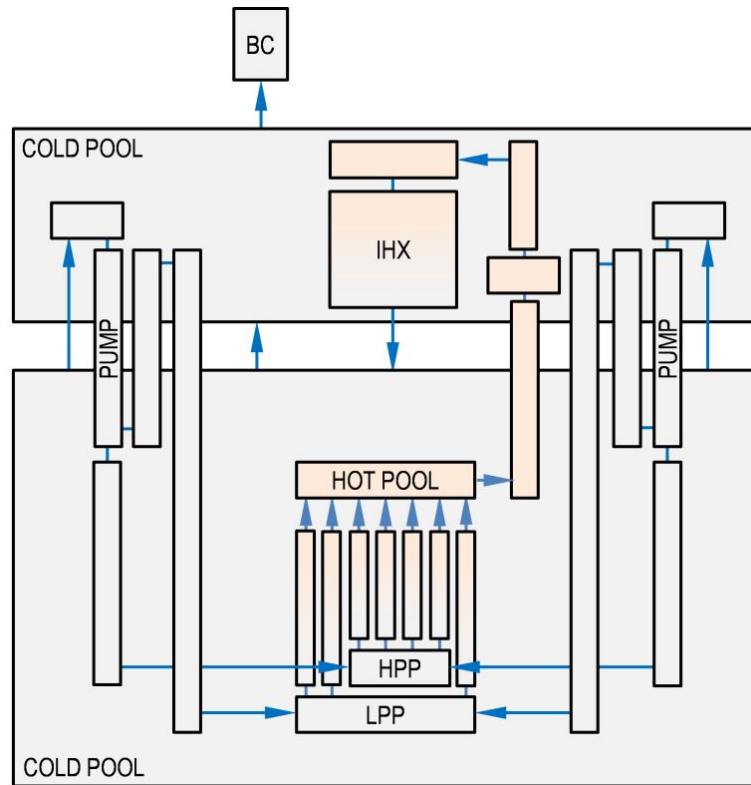


FIG. 231. TRACE nodalization diagram of EBR-II primary system.

TABLE 28. SHRT-17 FLOWRATE (KG/S) IN DIFFERENT CHANNELS CALCULATED BY TRACE AND COMPARED WITH THE BENCHMARK SPECIFICATION

Channel	Specification	TRACE
Peak fuel	3.70	3.76
Average fuel	3.79	3.81
Peak blanket	0.13	0.14
Average blanket (all)	59.49	63.07
Reflector (all)	7.42	7.83
XX09	2.60	2.61
XX10	0.35	0.37

TABLE 29. BOUNDARY CONDITIONS OF THE SHRT-17 TEST AT STEADY STATE

Parameter	Measured	TRACE
High pressure inlet, K	624.7	631.9
Low pressure inlet, K	623.7	631.9
Z-Pipe inlet, K	729.7	732.4
IHX primary inlet, K	719.0	730.5
IHX intermediate inlet, K	574.0	574.0
IHX intermediate outlet, K	714.2	725.6
Primary pump flowrate, kg/s	234.9	224.2
Initial power (prompt/decay), MW	53.93/3.36	53.79/3.66
Primary coolant flow, m ³ /s (700 K)	0.54	0.52
Intermediate flow, m ³ /s (579 K)	0.35	0.34
Core inlet temperature, K	625	630
Pressure at primary pump I/II, MPa	0.30/0.29	0.30/0.30
Pressure at core outlet, MPa	0.04	0.04

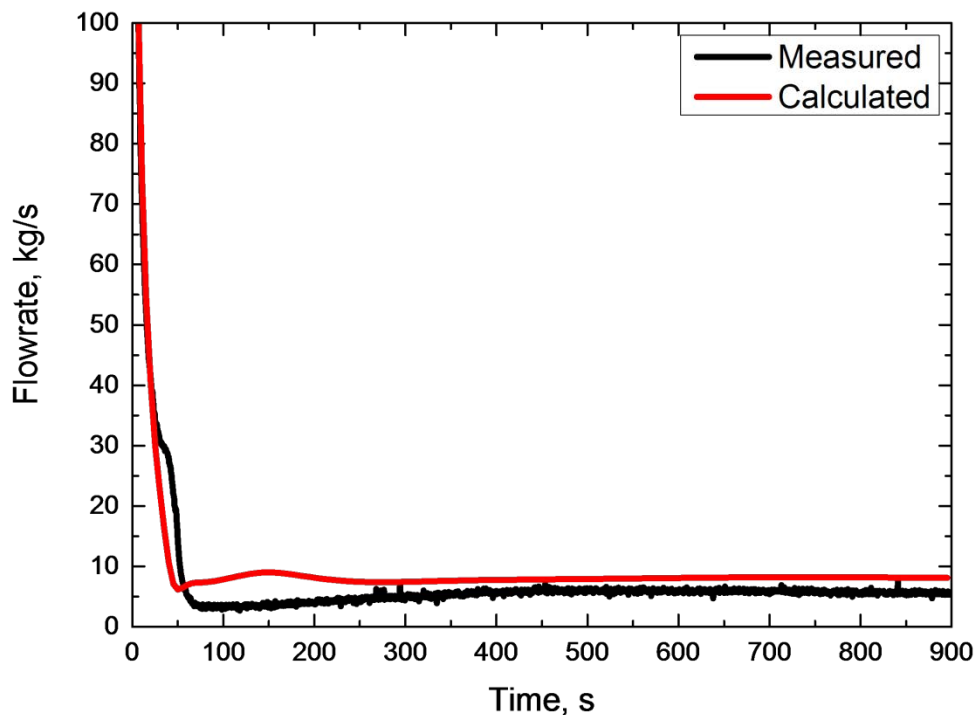


FIG. 232. Primary flowrate during the SHRT-17 transient.

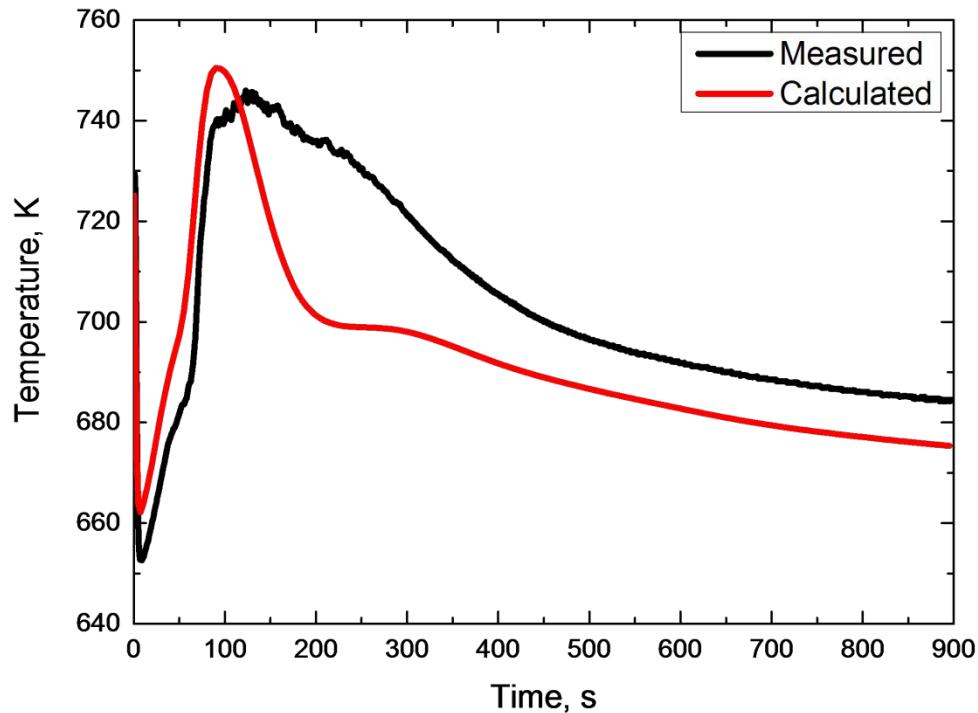


FIG. 233. Coolant temperatures at Z-Pipe inlet during the SHRT-17 transient.

However, as can be noticed from FIG. 234 and FIG. 235, TRACE gave quite different results compared to the measured data for the IHX primary/secondary coolant temperatures. Considering the similarity between the calculated and measured Z-Pipe inlet temperature, it can be concluded that this difference is mainly due to limitations on modelling the components located between the Z-Pipe inlet and the IHX inlet, basically the EM auxiliary pump and the heat exchange between the double layer Z-Pipe wall and the cold pool. The main limitation of the Z-Pipe model in TRACE is the 1-D modelling of the cold pool, which introduces a high uncertainty in evaluation of the Z-Pipe heat losses due to exchange of heat with the cold pool. In the current version of TRACE, there is no proper model to define an electromagnetic pump. Hence, in the TRACE model, a mechanical pump model was used with coolant flow area equal to the Z-Pipe cross-section area. Other operational parameters of this pump were set at the values provided by Argonne. The limitation of this assumption is that the electromagnetic pump provides part of the power of heating up the primary coolant but no inertia, which cannot be simulated by the current pump model. Therefore, it is recommended that future work on these analyses be aimed at improvement of the upper plenum and cold pool modelling, including using the 3-D VESSEL component of TRACE.

7.16.2.2. SHRT-45R

For the SHRT-45R test, transient values of the core fission power and primary coolant flowrate, plus values of the temperatures at the core inlet (both high pressure and low pressure), Z-Pipe inlet, IHX primary side inlet and IHX secondary side outlet were compared with the measured data provided by Argonne in Phase 2 of the CRP, as shown in FIG. 236 through FIG. 239.

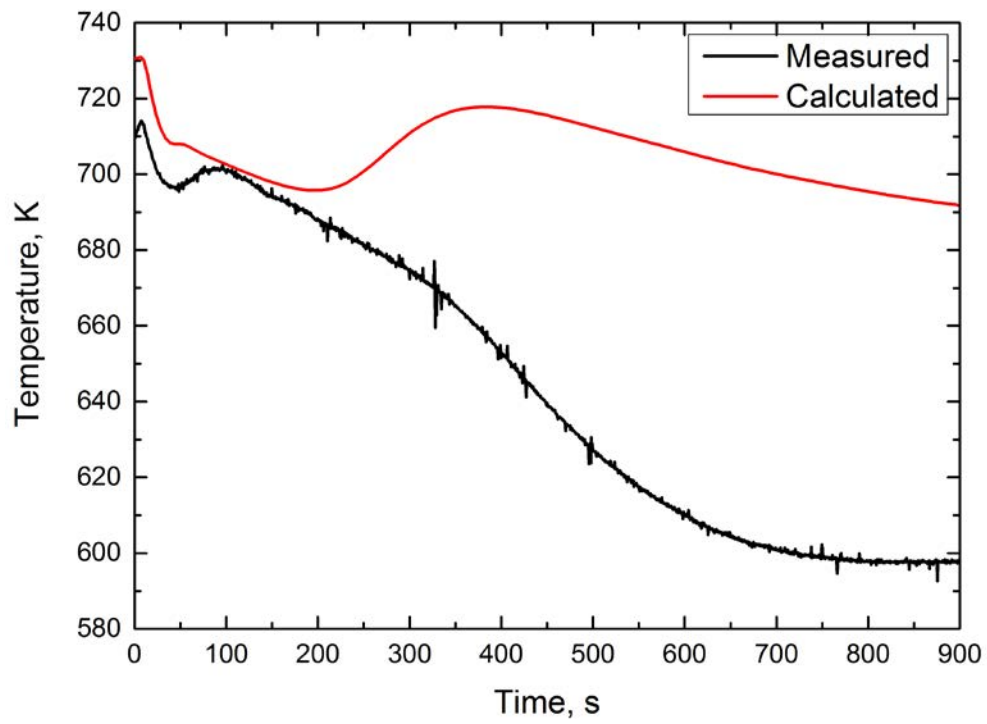


FIG. 234. Coolant temperature at IHX primary side inlet during the SHRT-17 transient.

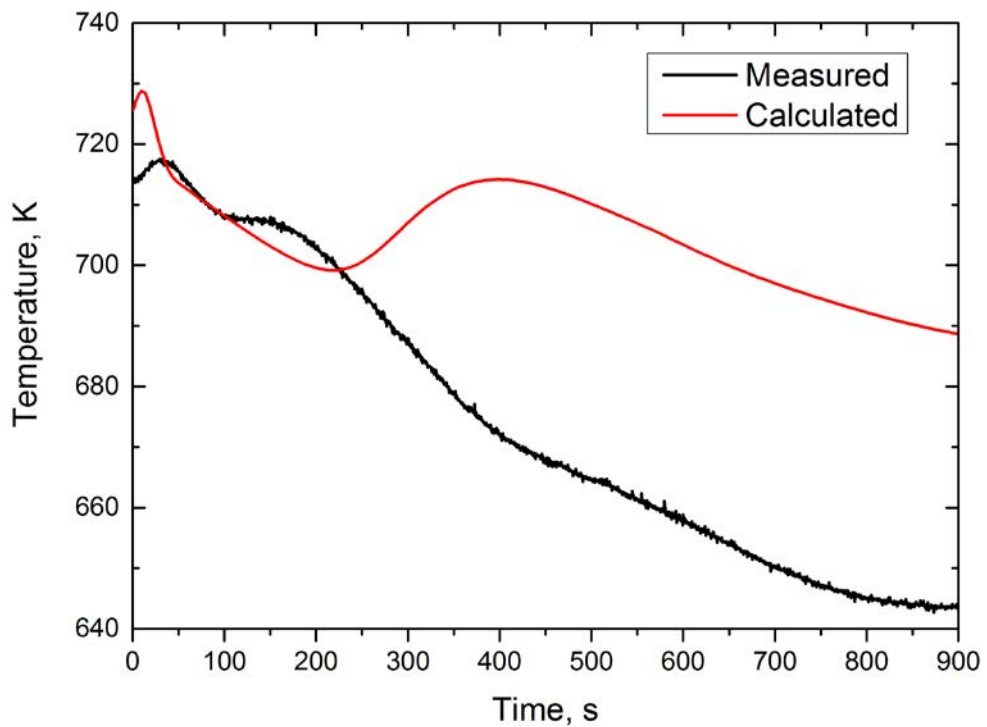


FIG. 235. Coolant temperature at IHX secondary side outlet during the SHRT-17 transient.

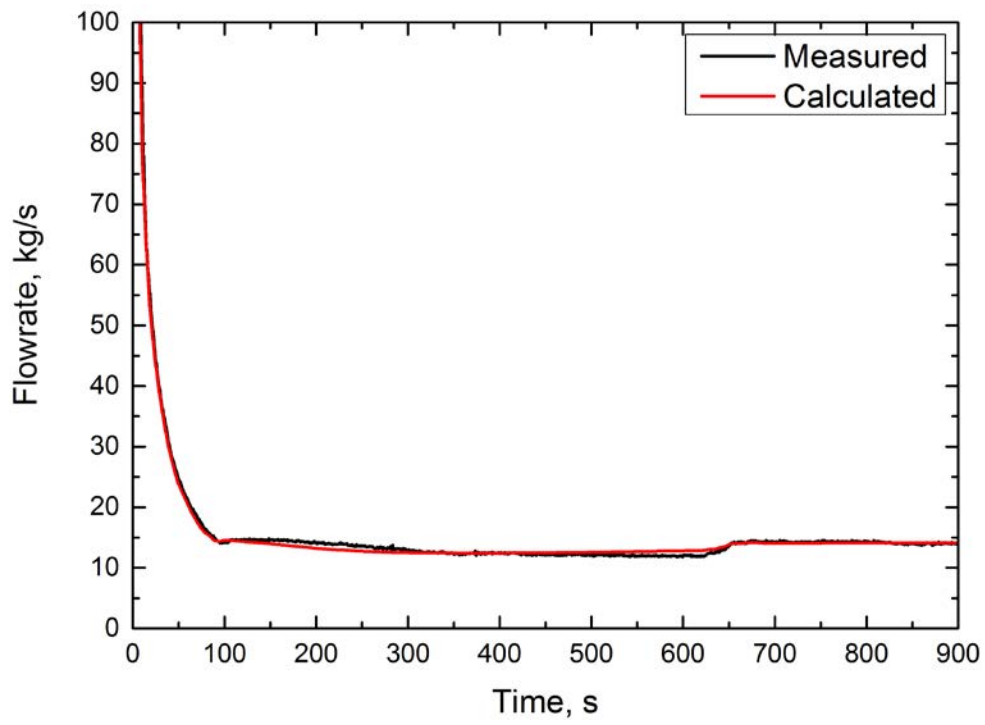


FIG. 236. Primary flowrate during the SHRT-45R transient.

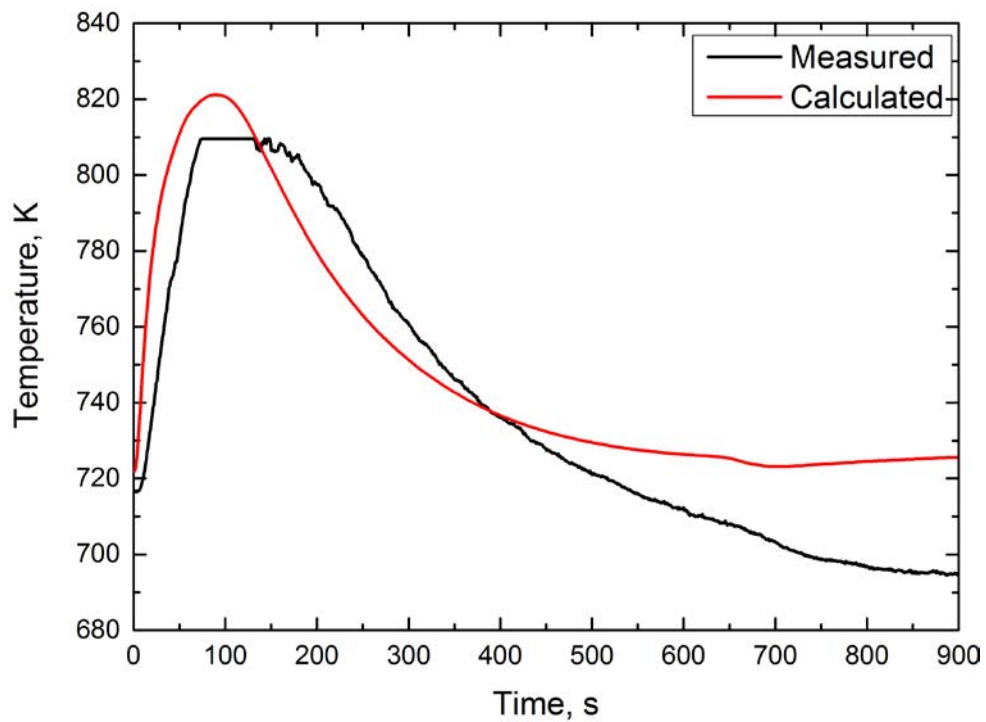


FIG. 237. Coolant temperature at Z-Pipe inlet during the SHRT-45R transient.

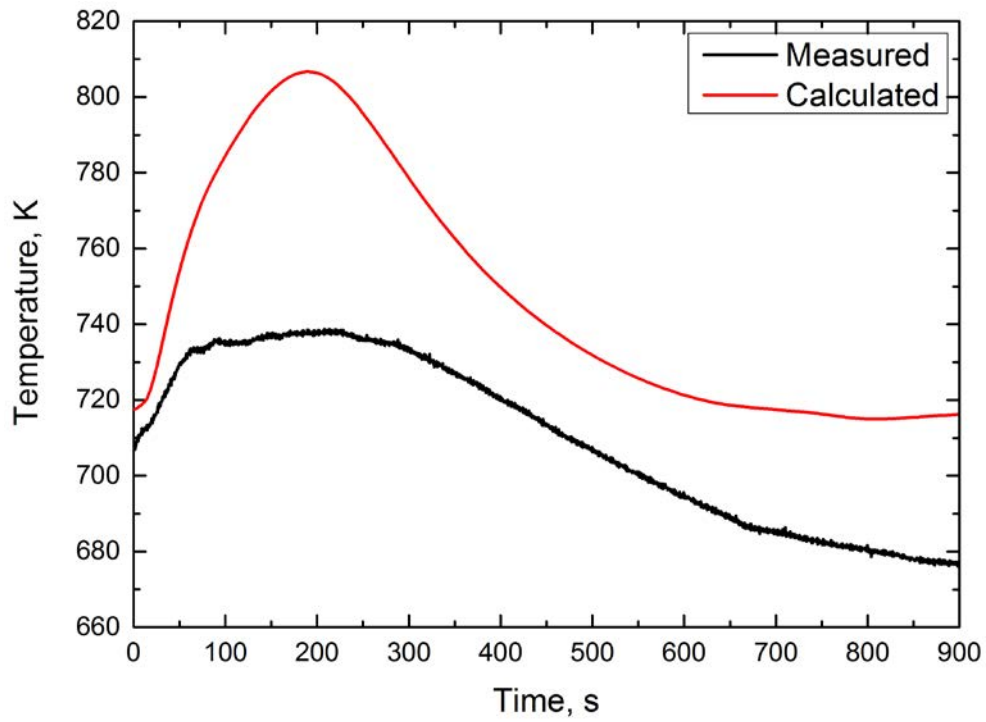


FIG. 238. Coolant temperature at IHX primary side inlet during the SHRT-45R transient.

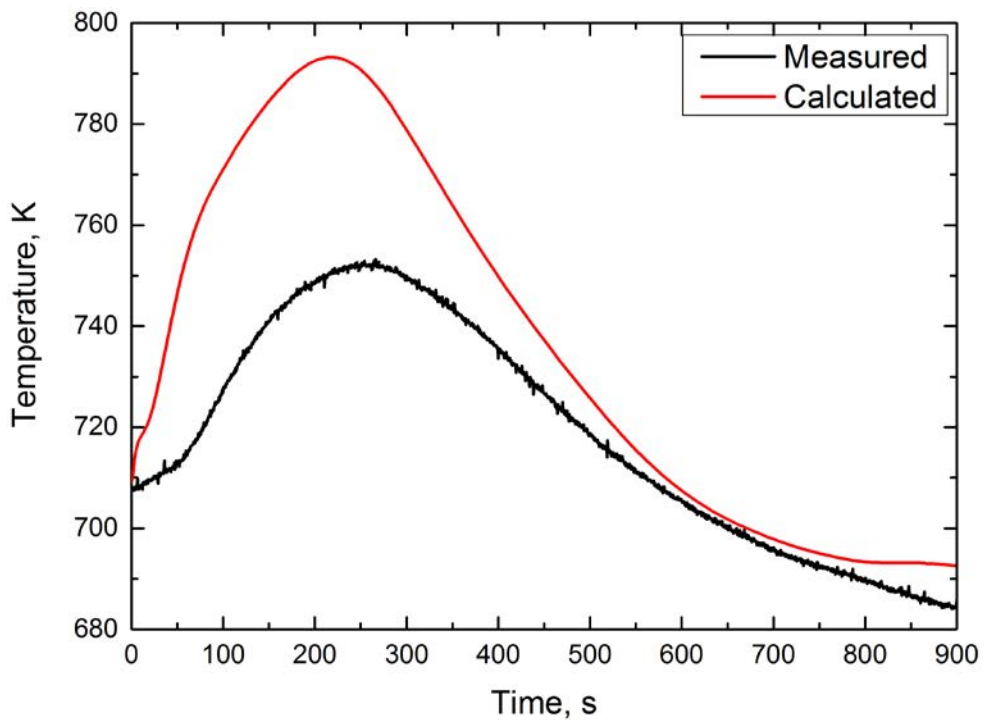


FIG. 239. Coolant temperature at IHX secondary side outlet during the SHRT-45R transient.

As seen in FIG. 236, the difference between the calculated and measured primary coolant flowrate of the SHRT-45R transient is small and is much smaller than that of the SHRT-17 transient (shown in FIG. 232), which confirms that both primary pumps and auxiliary pump

are properly modelled in TRACE. FIG. 237 shows that there is a ~30-s delay in the measured primary coolant temperature at the Z-Pipe inlet compared to the TRACE prediction. This can be explained as due primarily to the simplified (zero-dimensional) model of the upper plenum, as well as by the fact that the bypass flow from the cold pool goes directly into the upper plenum after the primary pump head was totally removed. The obvious differences of coolant temperatures at the IHX primary side inlet and the IHX secondary side outlet, as shown in FIG. 238 and FIG. 239, are also due to simplifications and limitations of the TRACE model, which have already been discussed above for the SHRT-17 transient. This confirms the recommendations made at the end of the SHRT-17 results discussion.

7.16.3. Neutronics model and results

Serpent is a continuous energy Monte Carlo code developed by VTT (Finland). The main features of the code are the Woodcock delta-tracking method used for neutron transport and the unionized energy grid used for the cross-sections tabulation. Version 1.1.16 of Serpent with the JEFF 3.1.1 pointwise nuclear data library using a unionized energy grid was used. The library was included in the code distribution.

The 3-D core geometry (FIG. 240) as specified in the benchmark is described using heterogeneous geometrical representation for the driver fuel, absorber, stainless steel reflector and blanket subassemblies and homogeneous representation for all other regions (FIG. 241). The graphite block surrounding the core was also included in the model (FIG. 242).

No thermal expansion of the core materials was modelled for the reference calculation, and the “cold” geometry as given in the benchmark specification was used. Another major simplification is that the same composition was specified for all blanket subassemblies, and the isotopic compositions of this material were assumed to be an average between the two blanket subassemblies modelled: one located at the innermost ring (11A01) and another located in the outermost ring (16F08).

5000 active and 10 inactive cycles with 50 000 source neutrons per cycle (250 million neutron histories in total) were simulated. The multiplication factor obtained is 1.00070 ± 0.00008 , and the effective fraction of delayed neutrons is 0.00694 ± 0.00124 [95].

The power distribution was calculated by using the code’s built-in detectors and presented in FIG. 243. As seen from this figure, only the fission power was calculated by the code; the models to calculate the transport and the heat generation from gamma rays were not available in the Serpent version used for the calculations. The “strange” increase of the power in the outermost ring of the blanket assemblies could be explained by the influence of the graphite block and increase of the thermal neutron flux at the periphery of the core.

In addition to the reference calculation, five more calculations were done to evaluate the safety-related neutronic parameters by implementing the following small perturbations to the core specification:

- (1) The driver fuel slug height was increased while the fuel density was proportionally decreased to preserve the fuel mass (axial expansion reactivity effect);
- (2) The interassembly gap for all assemblies was increased (radial expansion reactivity effect);
- (3) The sodium density in the whole core was decreased (sodium density reactivity effect);
- (4) The nuclear data for different temperature for all nuclides included in the fuel were changed (Doppler effect);

(5) The control rods position was changed (control rod driveline expansion effect).

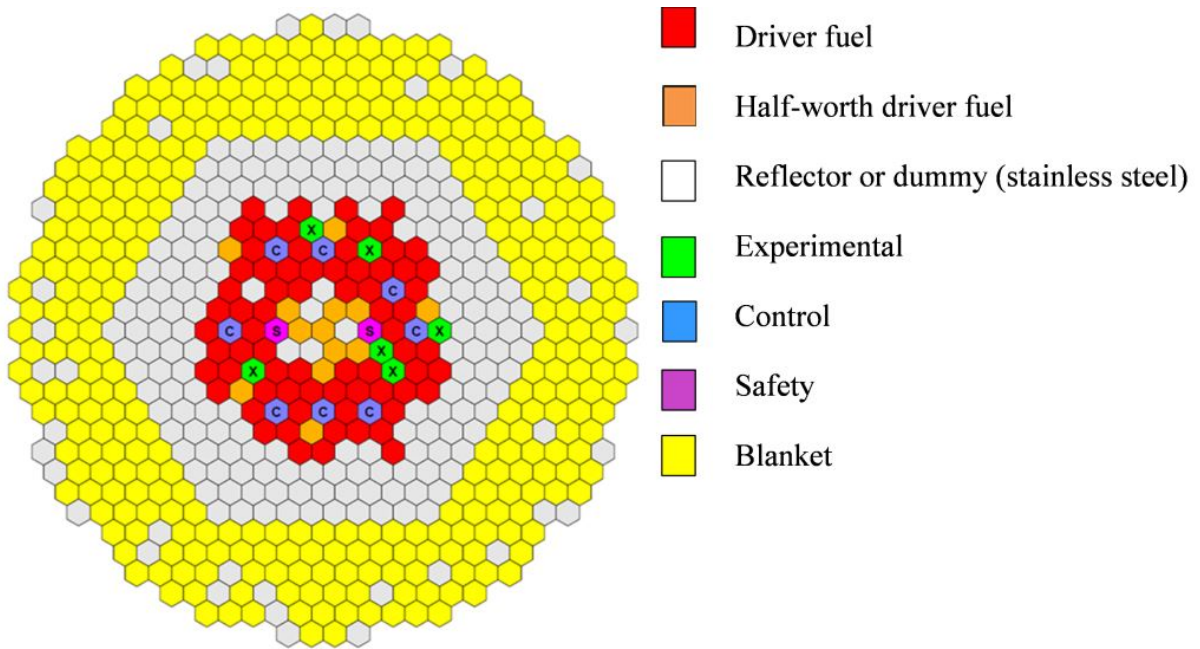


FIG. 240. EBR-II core loading pattern.

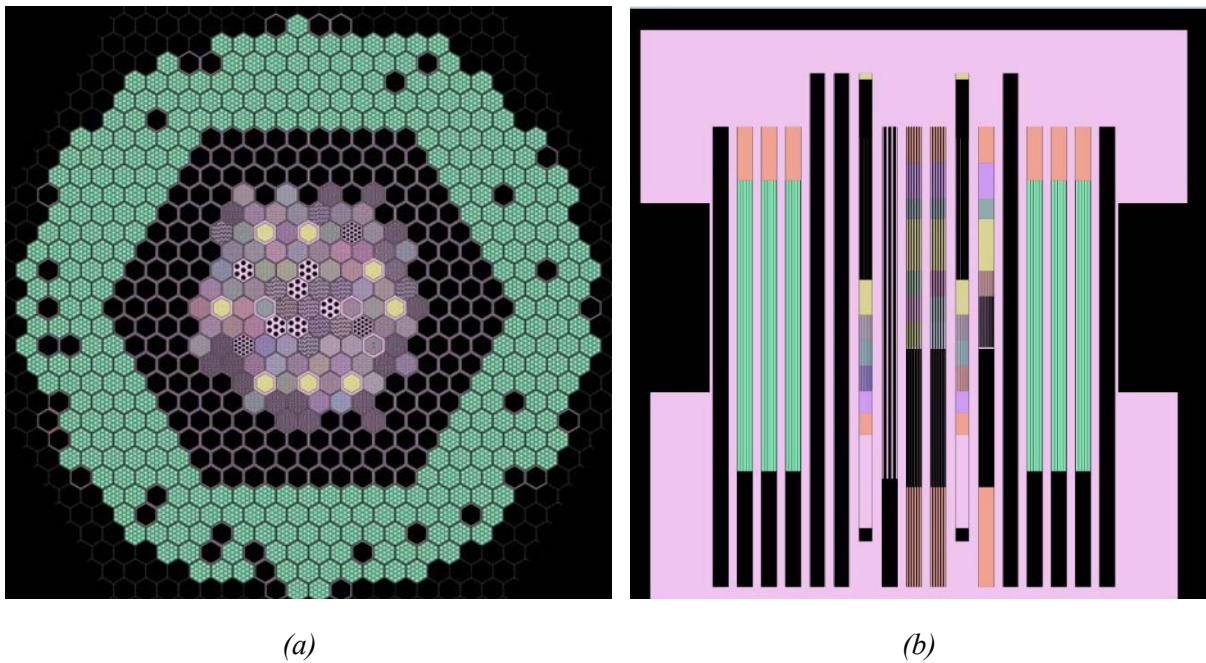


FIG. 241. Serpent model—horizontal cut (a) and vertical cut (b).

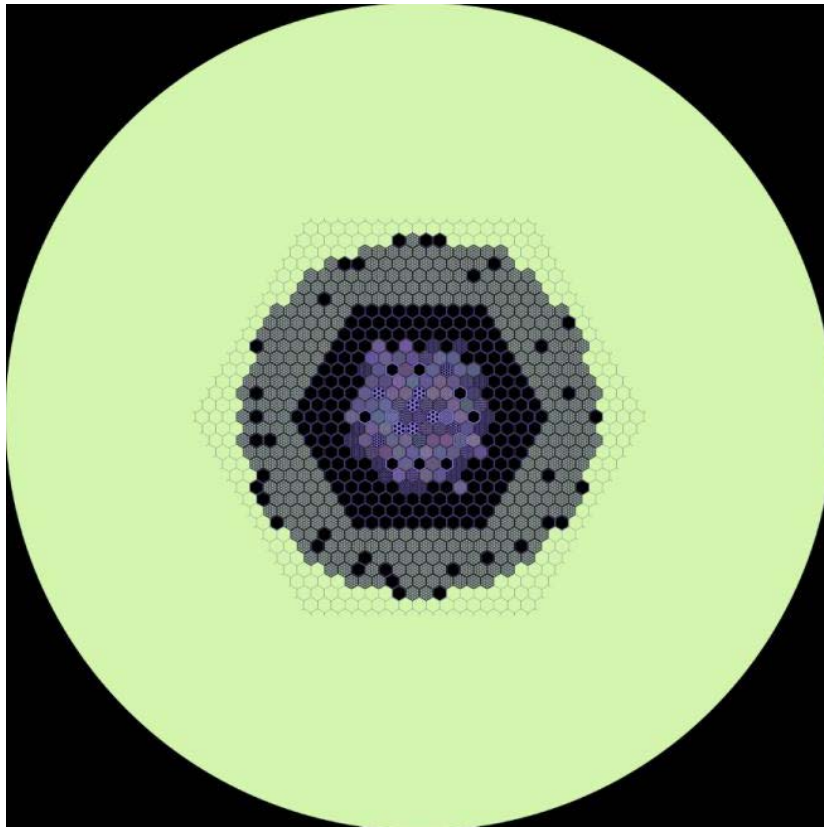


FIG. 242. Full Serpent model—graphite block at the periphery.

The perturbed multiplication factors obtained were used to evaluate the corresponding reactivity effects and reactivity feedback coefficients according to the benchmark specification. The reactivity coefficients obtained are presented in TABLE 30. All reactivity coefficients are negative. Some observations on the results for the reactivity feedback coefficients are as follows:

- (a) The nearly zero Doppler effect could be explained by the fuel composition (high enrichment by U-235 and low content of U-238);
- (b) The control rod driveline expansion is negative because the elongation of the metallic driveline inserts absorber into the core;
- (c) The negative sodium temperature coefficient could be explained by the domination of the neutron leakage component over the spectral component, due to the small dimensions of the core. The thermal expansion of sodium makes the core more transparent for neutrons due to the reduction of the sodium-to-fuel ratio and the corresponding reduction of the scattering rate;
- (d) The negative reactivity effect due to the axial expansion of the driver fuel slug could be explained by the relative insertion of absorber into the core, which could explain the similar magnitudes of the reactivity coefficients of axial fuel expansion and control rod driveline expansion;
- (e) The negative reactivity effect of the radial thermal expansion could be caused by the fact that the increase in the amount of sodium in the intersubassembly gap does not significantly impact the axial neutron leakage but does soften the neutron spectrum and therefore introduces negative reactivity (the spectral component dominates over the leakage component in this case).

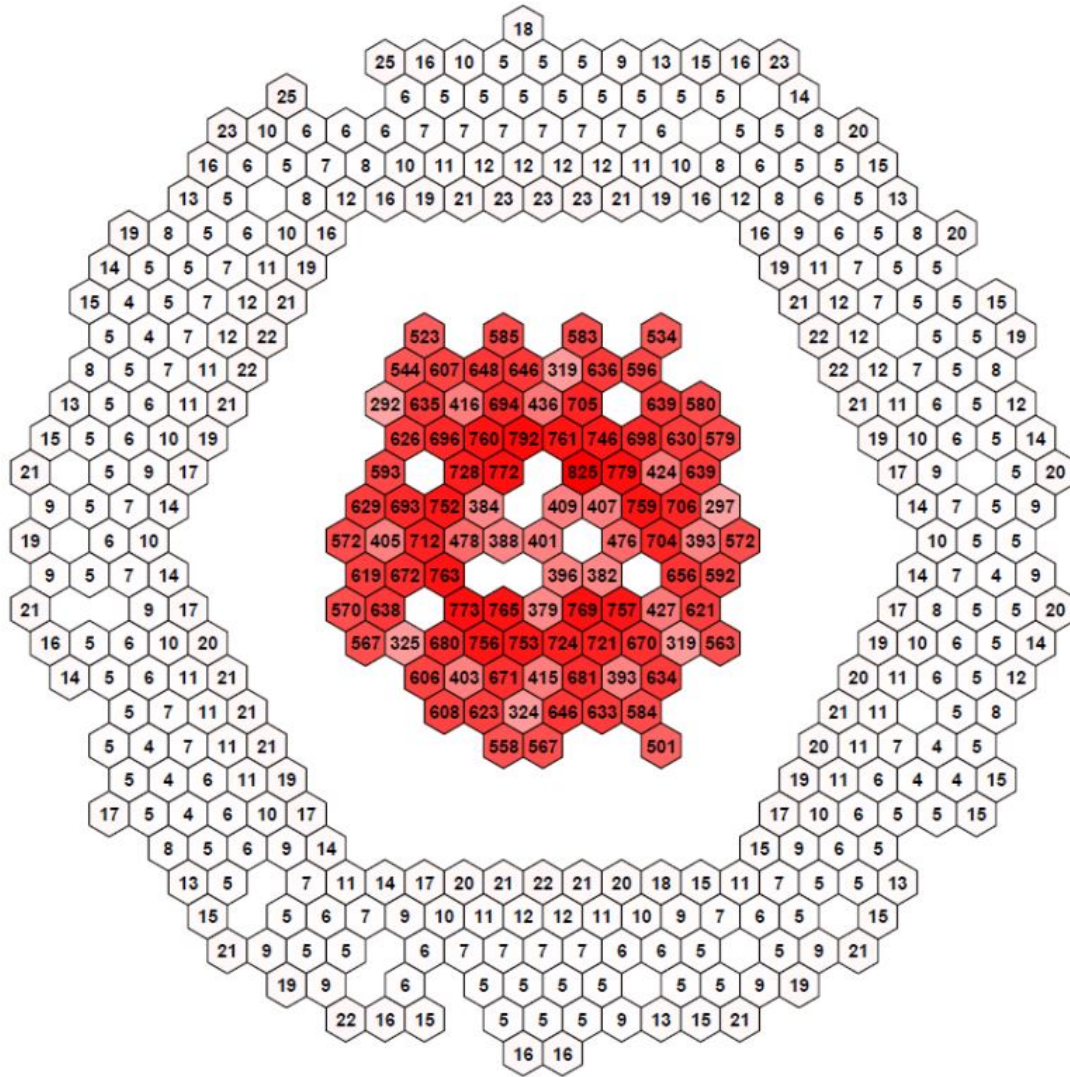


FIG. 243. Results of the Serpent calculations: SA-wise power (W).

TABLE 30. EBR-II NEUTRONIC PARAMETERS CALCULATED BY SERPENT

Parameter	Value
k_{eff}	1.00070 ± 0.00008
β_{eff} , pcm	694 ± 124
Axial expansion, pcm/K	-0.48 ± 0.04
Radial expansion, pcm/K	-1.72 ± 0.03
Sodium temperature, pcm/K	-1.68 ± 0.05
Doppler coefficient, pcm/K	-0.05 ± 0.005
Control rod driveline expansion, pcm/K	-0.45 ± 0.04

For a more detailed discussion of the PSI SHRT-17 and SHRT-45R analysis results, see [119].

7.17. TERRAPOWER (USA)

7.17.1. Geometry/discretization

In SAS4A/SASSYS-1 [5], SAS4A models the core, while SASSYS-1 models the temperatures and sodium flows throughout the primary and intermediate systems. TerraPower's system model representation of the primary and secondary loops (based on interconnecting elements and compressible volumes) is shown graphically in FIG. 244.

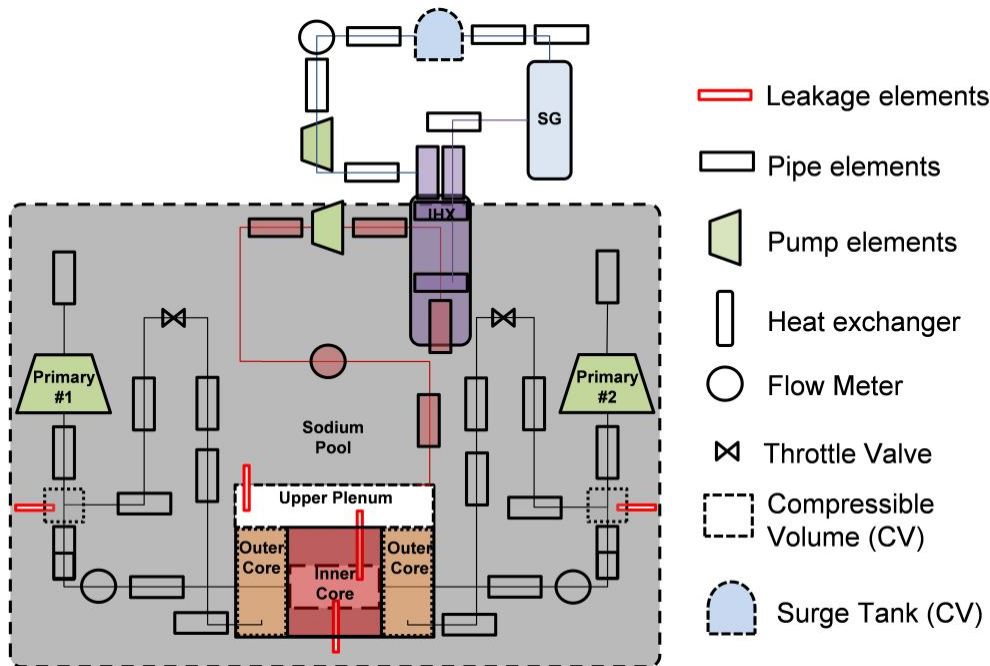


FIG. 244. EBR-II primary system layout (left) and SASSYS-1 representation.

Some key features of the system model are summarized below:

- Mixing in volumes (such as the upper plenum and sodium pool) is treated in 1-D;
- The SASSYS homologous and electromagnetic (EM) pump models were used for the primary and Z-Pipe pumps, respectively;
- Thermal inertia and hydraulic losses of all components are modelled;
- An intermediate loop was created (no benchmark information was provided). Temperatures at the IHX intermediate inlet were adjusted via control of the steam generator (SG) inlet temperature.

The core model (accounting for thermal hydraulic and neutronic phenomena) is coupled to the primary system via the inlet and outlet plena. The core model (discussed in detail in Section 7.17.3.3) is composed of independent channels which are axially discretized, as shown, for example, in FIG. 245.

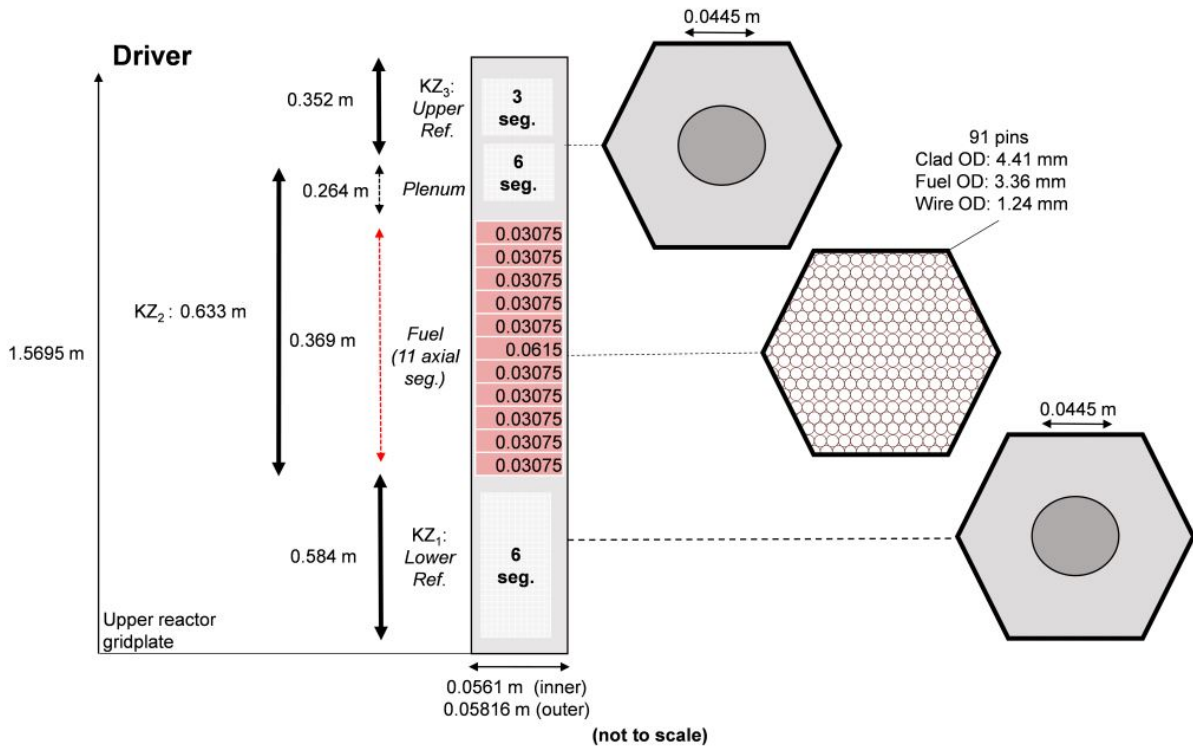


FIG. 245. Geometry and axial nodalization assumed for the driver subassemblies (Channels 1,2,10).

7.17.2. Nuclear and thermo-physical data/correlations

7.17.2.1. Thermophysical data

For the axial, radial and control rod driveline expansions, modelling assumptions and thermophysical properties were required to predict the displacements and reactivity feedback, given the temperature increases that SASSYS calculates. The models [77] used are reviewed as follows:

- (a) Radial expansion depends on the average temperature of structural components at two heights (inlet, top of core), geometry, and structural materials of the core (see TABLE 31);
- (b) Axial expansion depends on the thermomechanical properties of fuel and cladding (see TABLE 32), and assumes a force balance exists between the two. Expansion coefficients are calculated from benchmark density correlations. The fuel and cladding properties are averaged over temperature ranges of 350-700°C and 300-600°C, respectively;
- (c) Control rod driveline (CRDL) expansion depends on the mean outlet temperature of specified channels and thermomechanical properties of the CRDL (see TABLE 33) to calculate its expansion during the transient;

TABLE 31. RADIAL EXPANSION REACTIVITY FEEDBACK INPUT ASSUMPTIONS

Parameter	Value [‡]
Steel expansion coefficient (1/K)	2.1×10^{-5}
Distance from grid plate to core midplane (m)	0.799
Distance from grid plate to top of assembly (m)	1.5695

[‡] No significant change from phase 1 to phase 2.

TABLE 32. AXIAL EXPANSION REACTIVITY FEEDBACK INPUT ASSUMPTIONS

	Fuel (Phase 2 , Phase 1)	Cladding (Phase 2 , Phase 1)
Axial expansion coefficient (1/K)	$(2.73 \times 10^{-5}, 2 \times 10^{-5})$	$(2.1 \times 10^{-5}, 1.4 \times 10^{-5})$
Young's modulus (Y) in GPa	(150 [5], 2.8)	(164, 150)

TABLE 33. PHASE 2 CONTROL ROD DRIVELINE (CRDL) EXPANSION REACTIVITY FEEDBACK INPUT ASSUMPTIONS

Parameter	Value	Comment
Density of CRDL (steel)	7900 (kg/m ³)	
Specific heat of CDRL (steel)	500 (J/kg-K)	
Thermal expansion coefficient (steel)	2.1×10^{-5} 1/K	
k_{Na} (Thermal conductivity of sodium at 500°C)	61.8 (W/m-K)	
Heat transfer coefficient (minimum value assumed) from outlet plenum sodium	5057 (W/m-K)	Subbotin's correlation [122] as Reynolds number $\rightarrow 0$
Mass \times specific heat of the control rod	4.382×10^4 J/K	(Phase 1 was 1.12×10^5 J/K)

7.17.2.2. Correlations

SAS4A/SASSYS-1 determines the sodium heat transfer coefficient (h_c) using a correlation dependent on the Peclet number, shown in EQ. 1),

$$Nu = \frac{h_c D_h}{k_c} = C_1 (Pe)^{C_2} + C_3 \quad (15)$$

The heat transfer coefficient depends on the geometric parameters of the hexagonal pin array (most importantly, P/D, the ratio of pin spacing and pin diameter). Available correlations which reflect this dependence ([79], [72]) and are used in the sensitivity portion of this study are shown in TABLE 34.

TABLE 34. HEAT TRANSFER CORRELATION PARAMETERS

Source	C ₁	C ₂	C ₃
SAS4A/SASSYS-1 example input	0.025	0.8	5
K+C [†] [79]	0.0161	0.86	4.552
Mikityuk [†] [72]	0.0309	0.77	7.71

[†] Calculated using a P/D=1.28.

With regard to pressure drop, SASS4A/SASSYS-1 calculates the friction factors using EQ. 2),

$$f_L = \frac{A_{flam}}{Re}, \text{ for } Re < Re_{lam}, \quad f_T = A_{fr}(Re)^{-B}, \text{ for } Re > Re_{lam} \quad (16)$$

where f_L is the laminar friction factor, f_T is the turbulent friction factor, and Re_{lam} is the Reynolds number for transition to laminar flow. The two pressure drop correlations tested were Blasius (appropriate for non-wire wrap geometries) [77] and Chen-Todreas-Petroski (CTP) [114]. The input parameters for the SAS4A/SASSYS-1-equivalent of the CTP (as calculated using the EBR-II driver assembly geometry) are compared to the Blasius correlation in TABLE 35.

TABLE 35. LAMINAR AND TURBULENT FRICTION FACTOR INPUT PARAMETERS

Source	A_{flam}	Re_{lam}	A_{fr}	B
Blasius (phase 1, phase 2)	64	2400	0.33211	0.25
CTP	91	2400 (although correlation specifies a region from 897-1.57×10 ⁴)	0.174	0.18

7.17.3. Thermal hydraulics methods and models

7.17.3.1. Code(s) used

For calculating system- and subassembly-level temperatures, core reactivity feedback and power, SAS4A/SASSYS-1 (version 5.0) was used. For calculating pin-level temperatures for the XX09 subassembly, the COBRA4i-MIT subchannel code (version 1.5) was used.

7.17.3.2. Basic method

The SAS4A/SASSYS-1 system model (accounting for heat removal, geometry, and flow resistances in the system) provides the inlet boundary conditions of sodium temperature and pressure to the core model. The temperatures in the primary system (including the hot and cold pools) are treated using lumped parameter models, with thermal mixing of volumes treated in 1-D. In the core model, a channel represents the basic and representative unit of fuel, cladding, coolant and structure, characterizing the average of the pins, wires and ducts in the subassembly. A channel is radially symmetric and sodium flow is 1-D (up or down). All properties (e.g., geometry, reactivity feedbacks, initial power, flow, etc.) of all subassemblies grouped into a single channel designation are averaged during the channel definition process. The fuel, cladding and sodium temperatures of the channel have reactivity feedback through Doppler, axial and coolant expansion. Collections of channels affect the reactivity feedbacks of radial and control rod driveline expansion. All reactivity contributions are summed into a point-kinetics model for core fission power. The model for decay heat production of the core depends on the operating power history of the core.

The Massachusetts Institute of Technology (MIT) modifications [123] to the original COBRA4i subchannel code incorporated friction factor, heat transfer and other correlations specifically developed for wire-wrapped rod bundles and liquid metal coolant. Differences in behaviour between water and sodium (such as turbulent mixing) are captured by the implementation of these specific correlations developed from sodium experiments. The MIT modifications allow use of the Cheng and Todreas correlations [114], so the pressure drop in each subchannel can be calculated according to the specific subchannel type (e.g., centre,

edge or corner). Further details on the governing equations and correlations selected in COBRA4i-MIT for this work are available in [122].

7.17.3.3. Model

FIG. 246 shows the phase 2 channel classification scheme. The outer hexagonal rows (8–16) connected to the low pressure (LP) plenum are channels 3, 12, and 13 (blanket, inner reflector, outer reflector, respectively). TABLE 36 reviews the designation and reactivity feedback contributions from each channel.

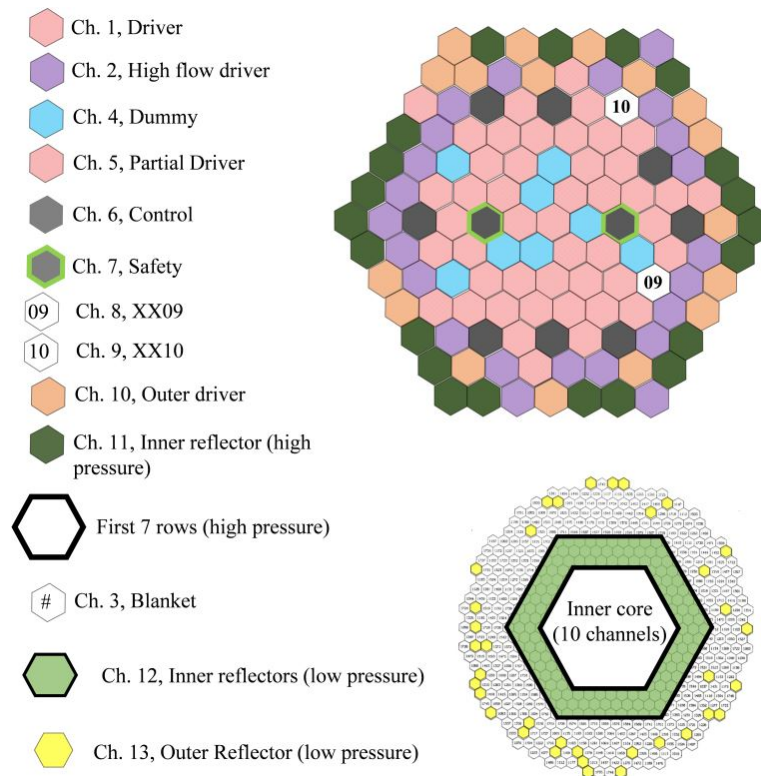


FIG. 246. Channel categorization used in phase 2.

7.17.4. Blind results

7.17.4.1. SHRT-17

TerraPower produced some early blind results for SHRT-17 but did not complete a SHRT-17 analysis.

7.17.4.2. SHRT-45R

The phase 1 results for SHRT-45R were completed with slightly different assumptions than phase 2. A major difference was the channel classification system, as reviewed in FIG. 247. Also, minor modifications were made to the geometry, nodalization, and reactivity feedbacks (see previous discussion).

TABLE 36. OVERVIEW OF CHANNEL CLASSIFICATIONS AND REACTIVITY FEEDBACKS IN PHASE 2

Ch. #	Description	Plenum	# SA	Coolant (Void)	Cladding (Axial)	Fuel (Axial)	Doppler	Radial Exp.
1	Inner driver	HP	33	Yes	Yes	Yes	Yes	Yes
2	High flow driver	HP	23	Yes	Yes	Yes	Yes	Yes
3	Blanket	LP	331	Yes ^b	[X] ^d	[X] ^d	[X] ^d	No
4	Dummy	HP	8	Yes ^b	[X] ^d	- ^a	- ^a	Yes
5	Partial	HP	13	Yes	Yes	Yes	Yes	Yes
6	Control	HP	8	Yes	Yes	Yes	Yes	Yes
7	Safety	HP	2	Yes	Yes	Yes	Yes	Yes
8	XX09	HP	1	Yes	[X] ^d	Yes	Yes	Yes
9	XX10	HP	1	Yes ^b	[X] ^d	[X] ^d		Yes
10	Outer driver	HP	17	Yes	Yes	Yes	Yes	Yes
11	Inner reflector	HP	21	Yes ^b	[X] ^d	- ^a	- ^a	Yes
12	Inner reflector	LP	144	Yes ^b	[X] ^d	- ^a	- ^a	Yes
13	Outer reflector	LP	35	Yes ^b	[X] ^d	- ^a	- ^a	No ^c

^a No contribution from that channel to the reactivity feedback effect.

^b Neglected in phase 1.

^c Included in phase 1.

^d No value provided by benchmark.

- Driver fuel – CH1
- High flow driver fuel – CH2
- Blanket – CH3
- Dummy assembly – CH4
- Partial driver – CH5
- Control rods – CH6
- Safety rods – CH7
- Instrumented XX09 – CH8
- Instrumented XX10 – CH9
- Experimental Assemblies – CH10
- Reflector – CH11, CH12

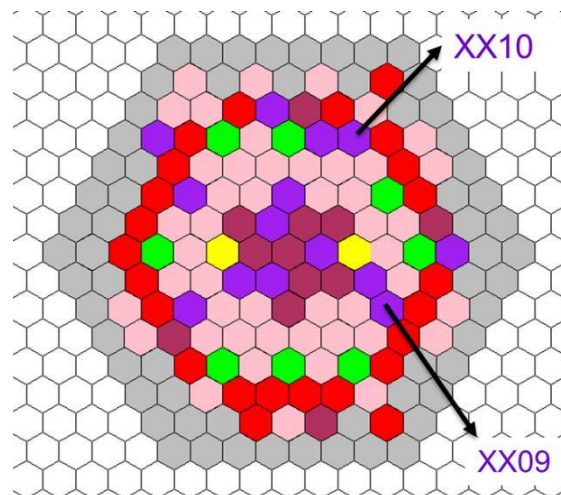


FIG. 247. Channel classifications for phase 1.

The power prediction (fission and decay heat) for phase 1 is shown in FIG. 248, and the net reactivity feedback components affecting power are plotted in FIG. 249.

The fission power was overpredicted during phase 1, especially at longer time scales. The edges apparent in the reactivity feedback curve at the peak (~50 seconds) are most likely due to errors (jumps) in the pump coastdown behaviour. The core outlet temperatures (as measured at the Z-Pipe and IHX inlets) are shown in FIG. 250 and FIG. 251.

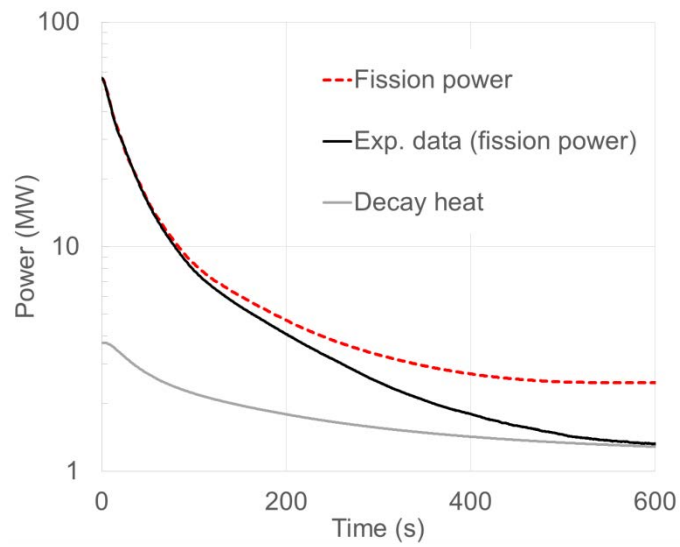


FIG. 248. Semi-log plot of fission power and decay power vs. time for phase 1.

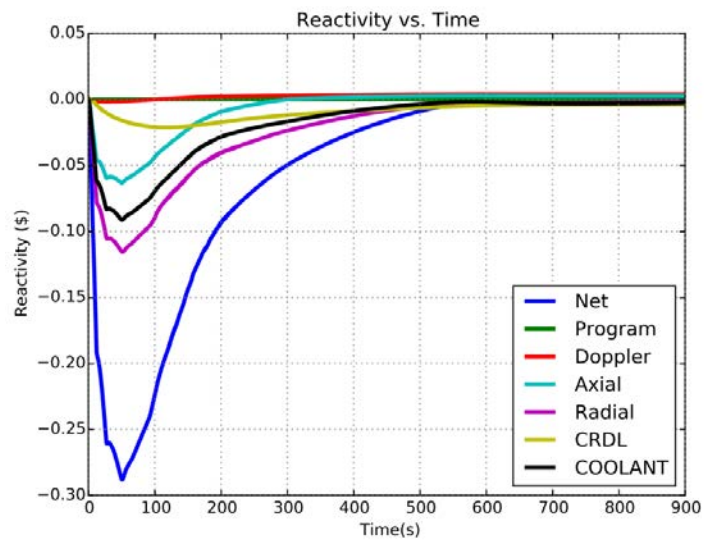


FIG. 249. Reactivity component by type vs. time for phase 1.

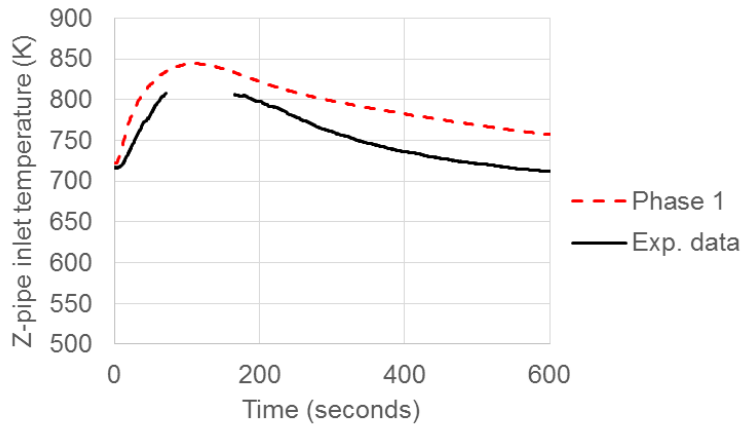


FIG. 250. Z-Pipe inlet temperature vs. time for phase 1.

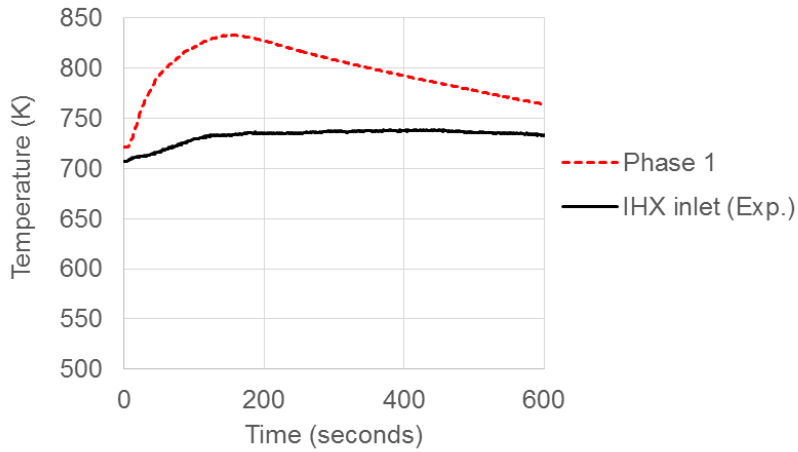


FIG. 251. IHX inlet temperature vs. time for phase 1.

7.17.5. Final results, data comparisons

7.17.5.1. SHRT-45R

Decay heat predictions did not change from phase 1 to phase 2, so the major changes in temperatures and total power are due to differences in flow, reactivity feedback (temperature) and fission power. FIG. 252 compares the % error in predicting fission power and pump flow rate for phase 1 and phase 2.

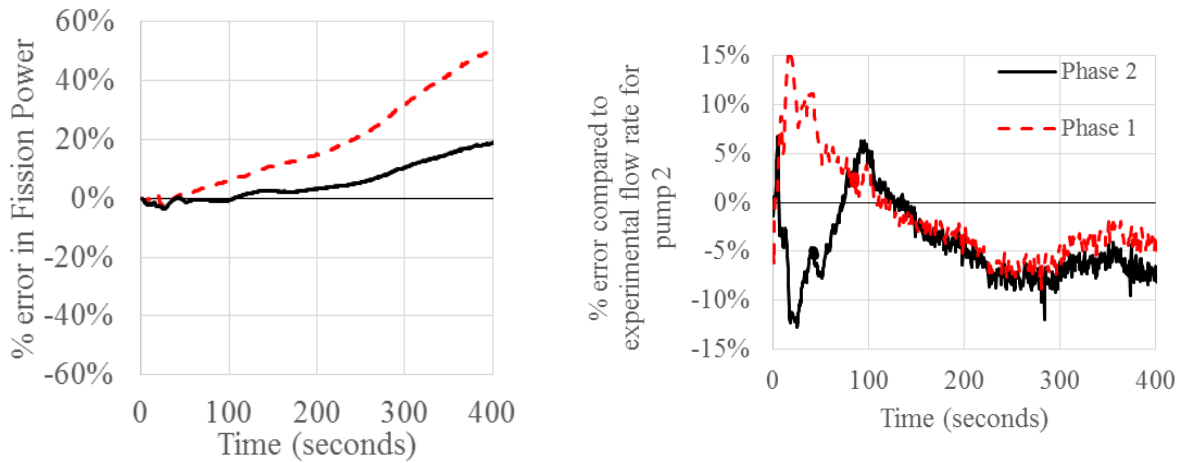


FIG. 252. Error in SHRT-45R fission power and pump 2 flow for phase 1 and phase 2.

In phase 2, accuracy in predicting both power and flow improved to be within $\pm 20\%$ within the first 400 seconds of the transient, where temperatures peak and fall to their initial values. As shown in FIG. 253, the reactivity feedbacks of radial and coolant expansion largely determine the metric of peak cladding temperature (PCT) in the first 50 seconds. Axial expansion feedback is also noticeably different in phase 2 (see further discussion in Section 8.11.3).

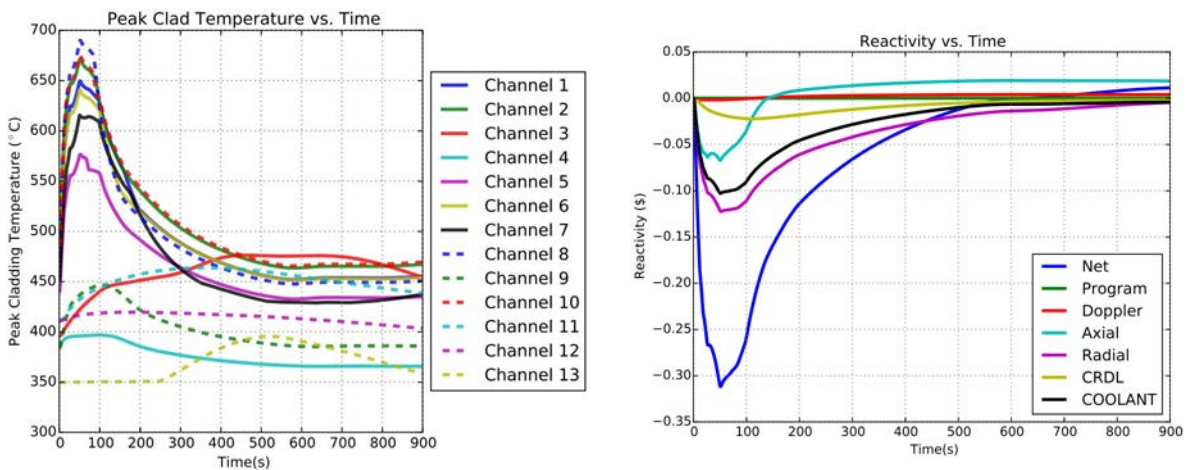


FIG. 253. Channel peak clad temperature and reactivity feedbacks vs. time during SHRT-45R.

In phase 2, the peak cladding temperature occurs in high power driver subassemblies (channel 8), which seems much more realistic than the result from phase 1, which suggested that peak temperatures occurred in the partial driver subassemblies. Core outlet temperatures from phase 1, phase 2 and the experiment are compared in FIG. 254.

The core outlet temperatures (as represented by the IHX inlet and Z-Pipe inlet) are still overpredicted for phase 2. Phase 2 Z-Pipe temperatures peak at slightly higher values than phase 1, due to the pump coastdown in phase 1 providing more flow (cooling) in the period up to 100 seconds. At longer times (> 250 s), the phase 2 outlet temperatures are lower (due to relatively lower power production compared to phase 1) and closer to the experimental data. Since the error in power prediction is quite small (especially in phase 2), there must be other phenomena causing the overprediction of the core outlet temperature. SAS4A/SASSYS-1

results did not show a significant temperature difference between the core outlet and the Z-Pipe inlet, which means that the code is not incorporating any complex mixing, stagnation, and/or significant heat loss phenomena occurring during flow from the outlet plenum to the Z-Pipe inlet. Alternatively, there might be significantly more heat transfer through the reactor vessel head to the cold pool than is being modelled.

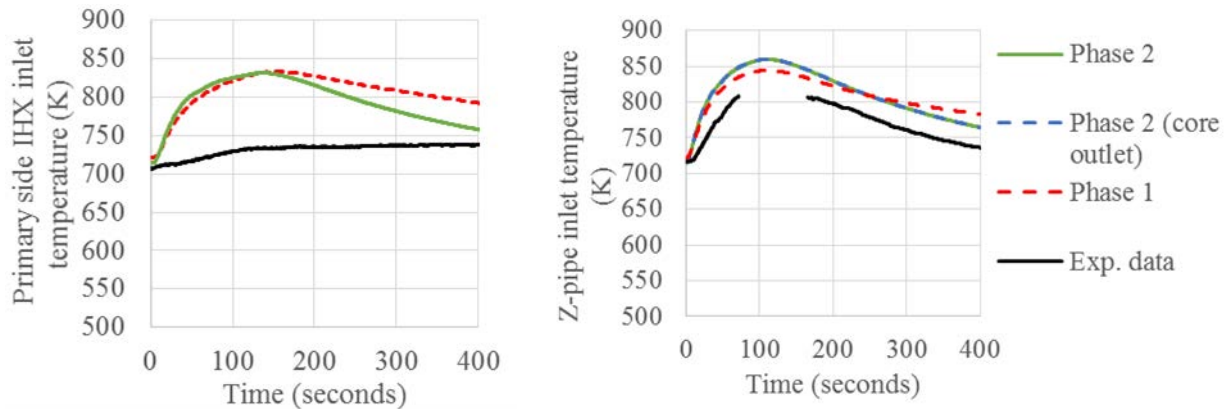


FIG. 254. Primary IHX inlet (left) and Z-Pipe outlet (right) temperatures vs. time, compared with the data.

With regard to the XX09 subassembly data and pin-level temperature modelling, the total assembly power was not measured (only normalized fission power of the core is available from the experiment). Furthermore, the experimental flow rate data is suspicious after a time period of ~180 seconds. This is clearly apparent in FIG. 255, where the experimental temperature trend does not follow the power to flow trend, as it should by heat balance considerations.

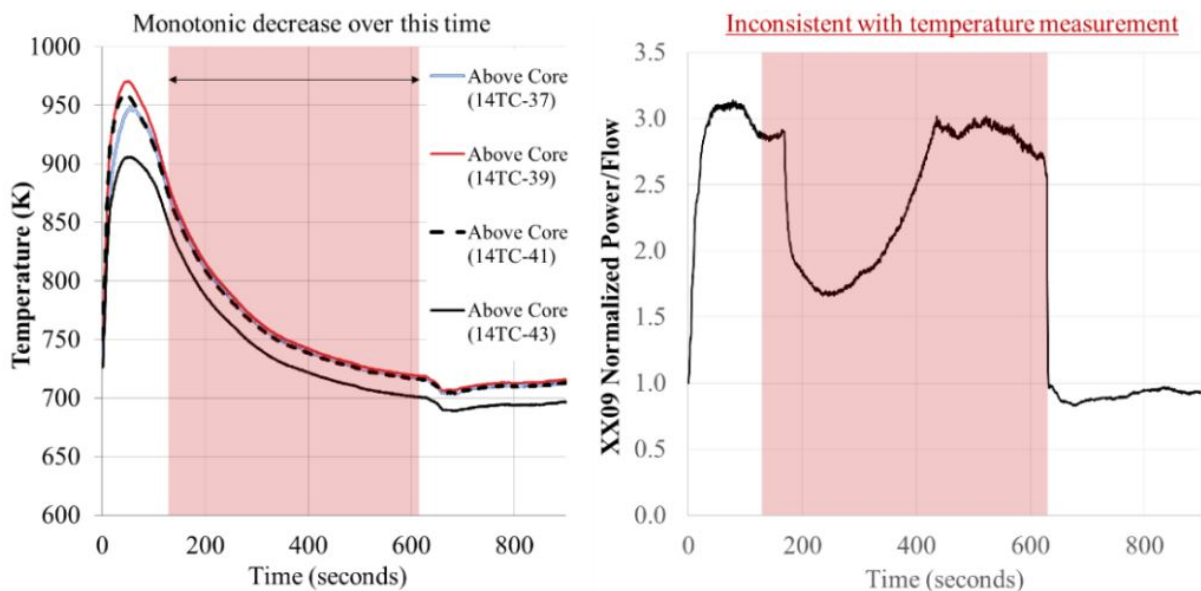


FIG. 255. Above core temperatures and P/F ratio as calculated from XX09 experimental data.

As a result, SAS4A/SASSYS-1 was used to provide both the input flow rate and total power vs. time to COBRA4i-MIT. This means that inaccuracies in the flow prediction (e.g., due to complex flow redistribution phenomena) propagate from SAS4A/SASSYS-1 into the

subchannel code. FIG. 256 compares the assembly outlet thermocouple predictions from phase 1 and phase 2, while FIG. 257 and FIG. 258 show the error of the top of core thermocouple predictions.

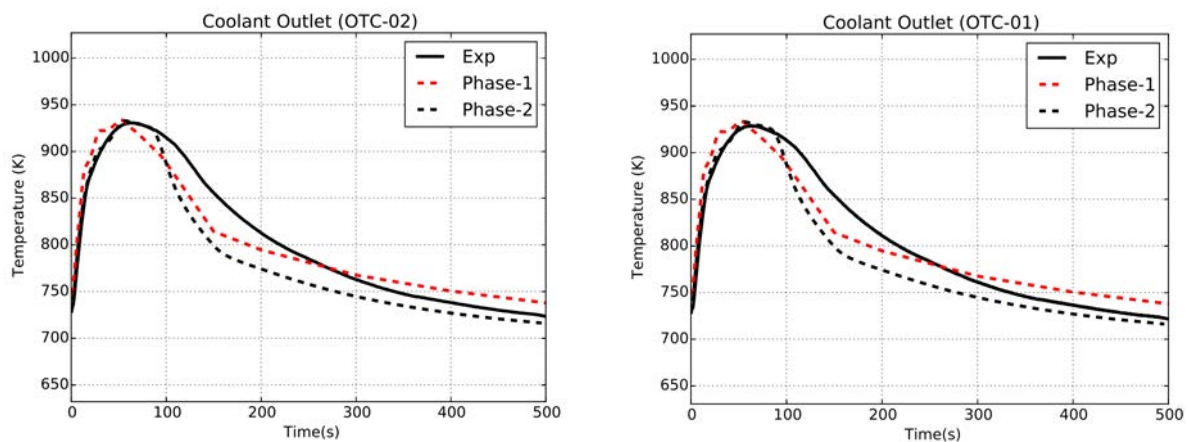


FIG. 256. Comparison of outlet thermocouple data for phase 1 and phase 2.

Overall, the data accuracy for XX09 improved from phase 1 to 2. The two main changes are:

- (1) In phase 1, COBRA4i-MIT was run to 150 seconds, and thereafter it was run as a series of steady state snapshots, at 100 second intervals. In phase 2, COBRA4i-MIT was run in transient mode for the entirety of the transient;
- (2) Phase 2 power was closer to the experiment (relatively lower than phase 1), which explains the relative differences in phase 1 and phase 2 at the longer time scales.

Uncertainties (some of which are unquantified) propagate as boundary conditions into the subchannel analysis. Most importantly, the error in the assumed flow rate of XX09 is at least 5-10%, as extrapolated by the SAS4A/SASSYS-1 error for the pump 2 flow rate. Even if the total core flow rate were measured and available, the flow in a single subassembly does not follow the same coastdown profile, due to flow redistribution effects resulting from differences in orificing and flow regimes (laminar vs. turbulent). Taking these uncertainties into account, the agreement between COBRA4i-MIT and the experimental results is good. Excluding the two outermost thermocouples (which are expected to have the greatest error due to wall effects that are not considered in COBRA4i-MIT), the error for temperature rise of the top of core thermocouples is within $\pm 15\%$ for the two timesteps of interest. At longer times, the error in cumulative flow will accumulate, and this makes it difficult to explain the discrepancies after ~ 200 seconds.

Another potential source of error is that the XX09 subassembly may have had larger decay heat than the rest of the fueled subassemblies in the core, since it was used in previous experiments. This could explain the slight, consistent, underprediction of the temperatures in phase 2. The overprediction at the walls of the subassembly will have to be treated in the future with inter-assembly heat transfer models, and/or sensitivity studies on the conduction shape and turbulent mixing factors that affect the temperature distribution in the subassembly. Overall, this represents the first independent validation of COBRA4i-MIT (i.e., using separate

data that was not used to develop the input correlations) and the first analysis of its transient capabilities.

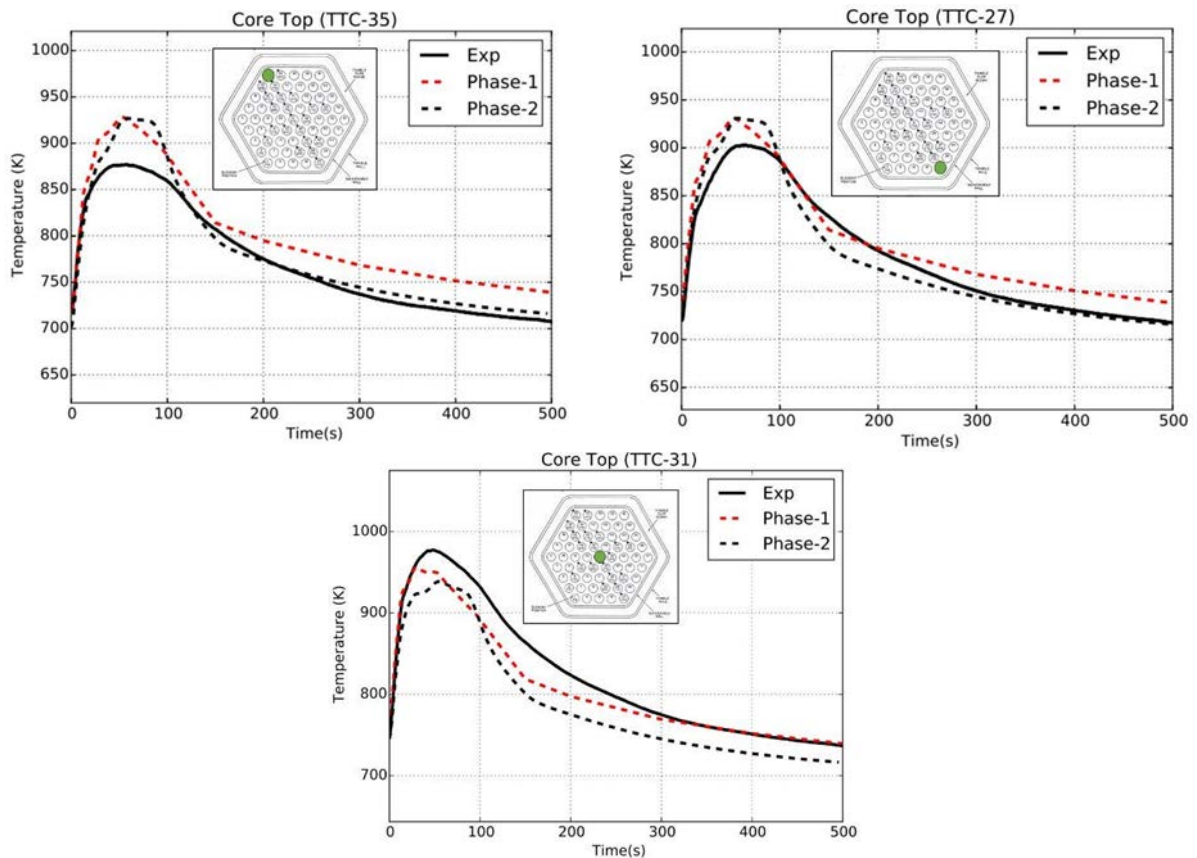


FIG. 257. Comparison of top of core thermocouple data.

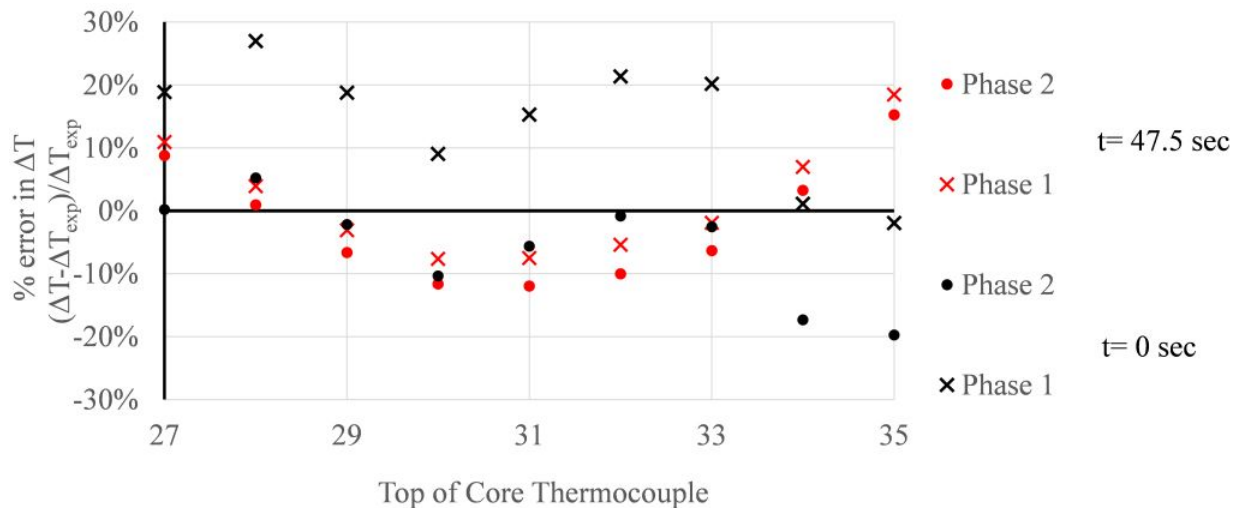


FIG. 258. Comparison of core ΔT error for phase 1 and phase 2.

7.17.5.2. Model improvements

In phase 1, almost 60% of the power in the core was represented by a single channel. Therefore, a channel classification choice that improved reactivity feedback accuracy was the splitting of the driver subassemblies into inner and outer channels (Ch. 1 and Ch. 10). The

motivation for this is that the reactivity feedback characteristics of the inner and outer core display an important axial variation that probably cannot be captured by a simple averaging. The axial variation in coolant feedback is shown in FIG. 259.

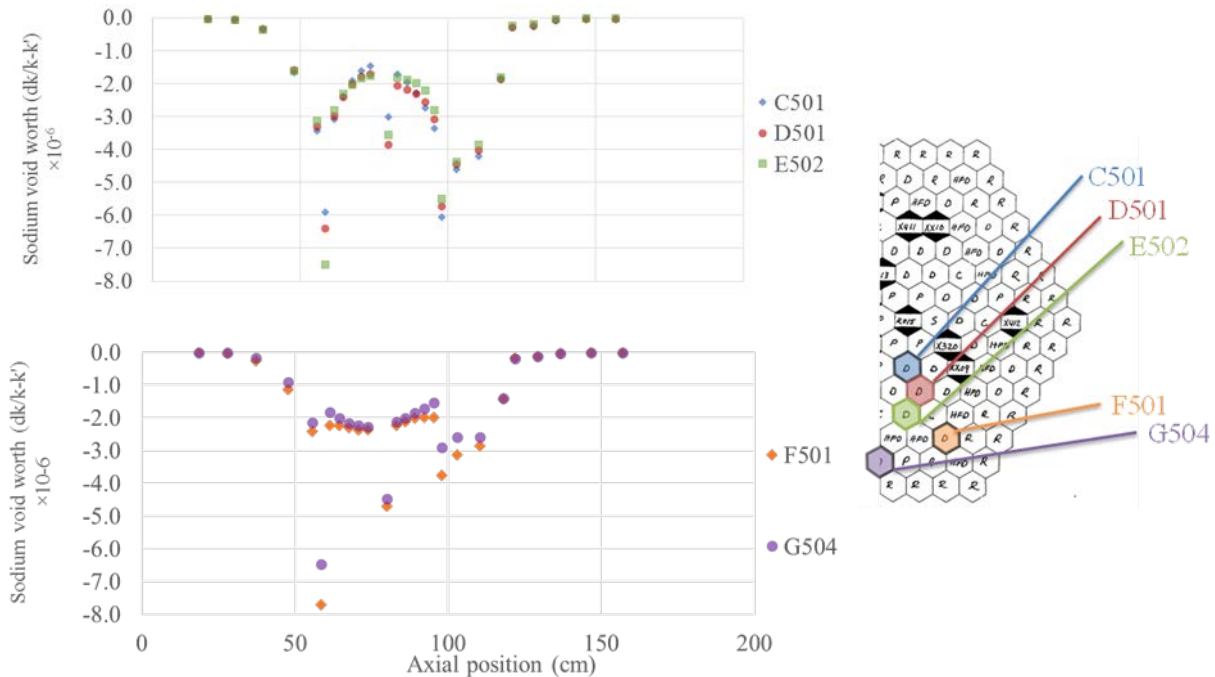


FIG. 259. Axial and radial variation of sodium void worth in the SHRT-45R core loading.

In particular, the concavity of the inner driver feedback does not match the concavity of the outer driver (rows F-G) feedback; therefore, it follows that if all these subassemblies are grouped into a single channel (as was done in phase 1 of the benchmark), the resulting average, axially varying reactivity coefficients modelled in SAS4A will not be entirely accurate. The steel expansion coefficient (which contributes to the negative feedback from axial expansion) displays very similar trends to the sodium expansion coefficient (as a function of space). Furthermore, since the two channels have different flow characteristics (one group of subassemblies must have a smaller orifice/loss coefficient to have more flow), their relative flow will not stay equal during a pump coastdown (see the sensitivity study on hydraulic correlations discussed in Section 8.11.2).

In addition, in phase 1, all 165 reflector subassemblies were represented by a single channel, and the coolant reactivity feedback from these assemblies was neglected. A major change (correction) in the phase 2 core model was to have three channels represent the innermost reflectors (Ch. 11), the low pressure plenum inner reflectors (Ch. 12), and the outermost reflectors in the blanket region (Ch. 13). Reflectors in the high pressure plenum have significant power and coolant reactivity feedback compared to the outer reflectors, and therefore they should be modelled separately from the outer reflectors.

Overall, the corrections in channel classification and inclusion of previously neglected coolant feedback resulted in a significantly more negative sodium void worth and feedback in phase 2. The enhanced negative reactivity brought the fission power predictions much closer to the experimental data.

7.17.6. Neutronics methods and models

TerraPower did not participate in the neutronics benchmark.

7.18. ARGONNE NATIONAL LABORATORY (USA)

7.18.1. Geometry/discretization

Argonne National Laboratory simulated the SHRT-17 and SHRT-45R tests using the sodium fast reactor safety analysis code SAS4A/SASSYS-1. Core models in SAS4A/SASSYS-1 consist of a number of single pin channels and optional sub-channels. A single pin channel represents the average pin in a subassembly, and subassemblies with similar reactor physics and thermal hydraulic characteristics are grouped together. The left side of FIG. 260 illustrates the geometry used in the SAS4A/SASSYS-1 channel thermal hydraulic model. SAS4A/SASSYS-1 models include axial zones to represent the fueled and gas plenum regions as well as up to six upper and lower reflector zones. Each axial zone is also connected to a structure region, which can be used to model components such as the wire wrap or duct walls.

The PRIMAR-4 module in SAS4A/SASSYS-1 simulates the thermal hydraulics of the heat transport systems outside the core. The right side of FIG. 260 illustrates the geometry used in a PRIMAR-4 model. In a PRIMAR-4 model, compressible volumes, or CVs, are zero-dimensional volumes that are used to model larger volumes of coolant such as inlet and outlet plena and pools. Compressible volumes are connected by liquid segments, which are composed of one or more elements. Elements are modelled by one dimensional, incompressible, single-phase flow and can be used to model pipes, valves, heat exchangers, steam generators and more.

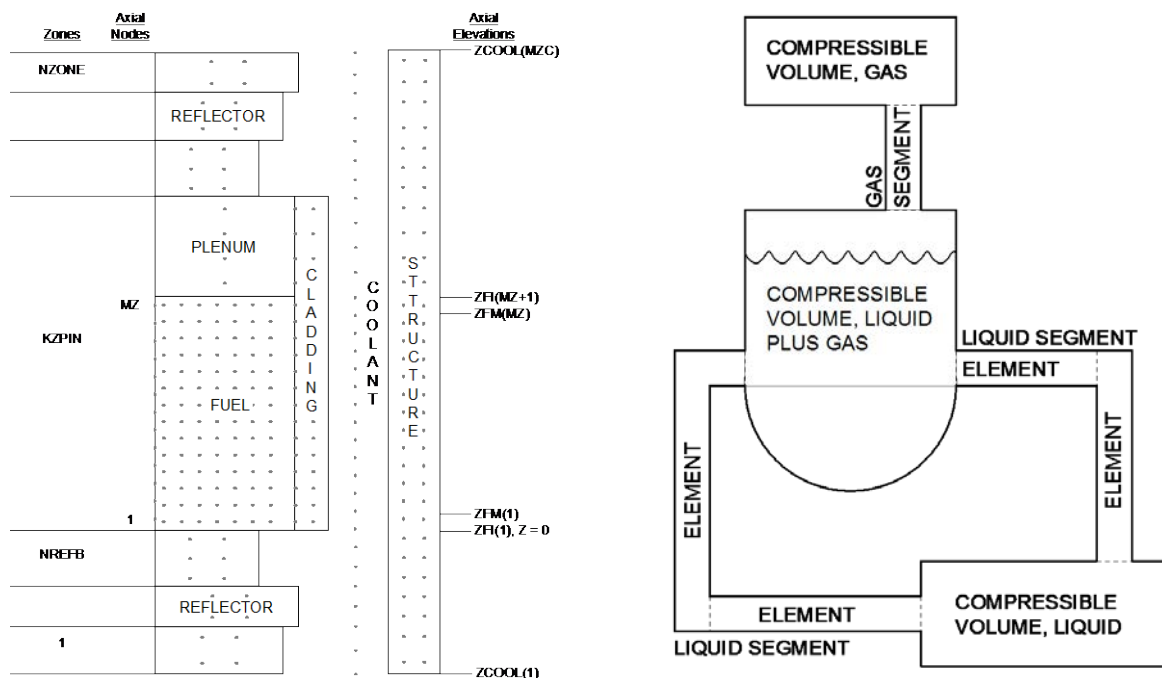


FIG. 260. SAS4A/SASSYS-1 single pin channel geometry (left) and heat transport systems model geometry (right).

7.18.2. Nuclear and thermo-physical data/correlations

The reactor point-kinetics, decay heat, and reactivity feedback models built into SAS4A/SASSYS-1 were used for calculating the power level during the SHRT-45R test. The point-kinetics equations, which assume a time-independent spatial power distribution within the reactor core, were solved using the second-order accurate Kaganove method [124], which was extended by Fuller [125]. To calculate the contributions from decay heat, a model based on the ANS decay heat standard for light water reactors was used [4].

The fuel Doppler effect was calculated assuming a logarithmic dependence on the local absolute fuel temperature ratio. Reactivity feedback effects associated with material density changes, specifically changes in the fuel, cladding and coolant mass distributions within the core, were calculated using first-order perturbation theory. SAS4A/SASSYS-1 also includes a simple one -node model for calculating the change in the control rod insertion depth due to control rod driveline thermal expansion and the subsequent reactivity feedback effect.

Section 4.2 of the benchmark specification provides the thermo-physical properties that were used for the U-5Fs fuel. Thermo-physical properties for the stainless steel 316 cladding were provided in [126]. The default sodium properties in SAS4A/SASSYS-1, which are documented in Chapter 12 of the SAS4A/SASSYS-1 manual, were also used [5].

Within a sodium channel, coolant was treated as incompressible before the onset of voiding. The friction factor for non-voided sodium within a core channel is given by

$$f = \begin{cases} A_{fr}(Re)^{b_{fr}} & \text{for } Re \geq Re_L \\ A_{fL}/Re & \text{for } Re < Re_L \end{cases}$$

where Re is the Reynolds number, and A_{fr} , b_{fr} , and Re_L are user-supplied coefficients. The default values of 0.1875 for A_{fr} and -0.2 for b_{fr} were used, and a value of 76.5 was used for A_{fL} . For turbulent flow within pipes, the Moody friction factor was used:

$$f = C_{1,f} \left[1 + \left(C_{2,f} \frac{\epsilon}{D_h} + \frac{C_{3,f}}{Re} \right)^{C_{4,f}} \right]$$

where D_h is the hydraulic diameter, and $C_{1,f}$, $C_{2,f}$, $C_{3,f}$, and $C_{4,f}$ are 0.0055, 20 000, 1.0×10^6 , and 1/3, respectively. The pipe roughness, ϵ , was assumed to be 1.0×10^{-5} .

The sodium heat transfer coefficient within a coolant channel was calculated as

$$h_c = \frac{k_c}{D_h} \left[C_{1,c} \left(\frac{D_h |w| c_{p,c}}{A_c k_c} \right)^{C_{2,c}} + C_{3,c} \right]$$

where k_c is the coolant thermal conductivity, w is the coolant flow rate, $c_{p,c}$ is the coolant specific heat, A_c is the coolant flow area, and $C_{1,c}$, $C_{2,c}$, and $C_{3,c}$ were assumed to be 0.025, 0.8, and 5.0, respectively.

7.18.3. Thermal hydraulics methods and models

7.18.3.1. Code(s) used

SAS4A/SASSYS-1 was used for simulating the SHRT-17 and SHRT-45R tests (see Section 5.1.7). Reactivity feedback coefficients for the SHRT-45R model were generated using DIF3D, PERSENT, and VARI3D (see Sections 5.2.1 and 5.2.11).

7.18.3.2. *Basic method*

The SHRT-17 and SHRT-45R tests were evaluated using standalone SAS4A/SASSYS-1 simulations. Single pin core channel models were developed for the driver, partial driver, control, dummy, reflector and blanket subassemblies. Each of the 637 subassemblies for the standard SHRT-17 and SHRT-45R models was modelled with one of these six channel types. As there was limited information available for many of the experimental subassemblies, and there were only two safety subassemblies, those subassemblies were also modelled with one of the six channel types.

For the standard analyses of the SHRT-17 and SHRT-45R tests, the core was modelled using only single pin channel models. Additional analyses were performed in which the XX09 and XX10 instrumented subassemblies and their six neighbouring subassemblies were modelled using the SAS4A/SASSYS-1 subchannel model. This model requires significantly longer computation times, so it was activated only for evaluation of the XX09 and XX10 temperatures and flow rates.

During Phase 2 analyses, the reactivity feedback models and power prediction for SHRT-45R were evaluated by enforcing the measured conditions at the inlet of the core. Additional analyses were performed to evaluate the primary heat transport system model by enforcing the measured total power level during the SHRT-45R test. Any modelling refinements introduced as a result of these analyses were applied to the model that was used to generate the final Phase 2 results. Neither the conditions at the core inlet nor the total power level were treated as boundary conditions for the final Phase 2 model.

7.18.3.3. *Model*

FIG. 261 illustrates which channel each of the 637 core subassemblies was modelled with for the SHRT-45R test. This 22-channel model was used for most of the SAS4A/SASSYS-1 analyses. A similar model was created for the SHRT-17 core model. For detailed analyses of the XX09 and XX10 instrumented subassemblies, the fourteen subassemblies modelled with channels 21 and 22 were replaced with a 2448-channel subchannel model.

FIG. 262 illustrates the EBR-II primary heat transport system model. For these analyses, the two inlet plena, upper plenum and cold pool were modelled with zero-dimensional compressible volumes. The cold pool was modelled with two compressible volumes to account for sodium below the pump inlets and IHX outlet that is not well mixed with sodium at the top of the core during these loss of flow tests. Segments 1 and 2 represent the inner core and outer core subassemblies, respectively and Segment 3 represents the core bypass flow. Segment 4 represents the Z-Pipe and IHX. Segments 5-7 represent one of the primary pumps and the core inlet piping that follows it. Segments 8-10 represent the other pump and inlet pipes.

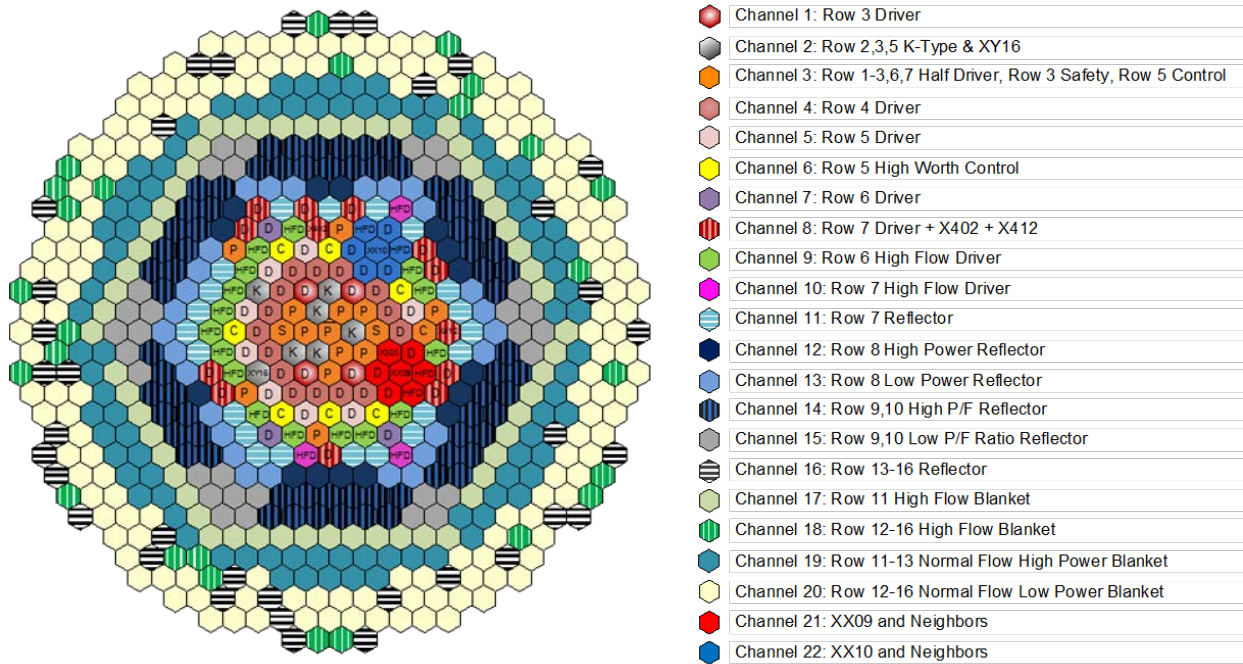


FIG. 261. SHRT-45R core channels.

7.18.4. Blind results

7.18.4.1. SHRT-17

Although Argonne's SHRT-17 simulation during the blind phase of the CRP predicted similar trends as the measured test data, overpredicted flow rates after the beginning of the test led to underpredicted temperatures. The left side of FIG. 263 compares Argonne's predicted flow rates with the flow rates measured in the high and low pressure piping following primary pump #2. The low pressure flow rate prediction agreed very well with the measured data throughout the entire transient. During the first minute of the test while the pump speed was still coasting down, the high pressure flow rate was also well predicted. However, issues that were later identified with the pump locked rotor input parameters led to significantly overpredicted pump #2 high pressure flow rates.

Because the high pressure flow rate represents approximately 85% of the total core flow rate, large discrepancies for the high pressure flow rate had a larger effect on the rest of the simulation than discrepancies for the low pressure flow rate. Accurate predictions of upper plenum, Z-Pipe and IHX temperatures require accurate core flow rate predictions. For the initial SHRT-17 simulations, Argonne's SAS4A/SASSYS-1 model predicted the core outlet temperature well during the beginning of the test. But as the test continued and the flow rates were overpredicted, the core outlet temperature was underpredicted by 20-30K. The right side of FIG. 263 illustrates the predicted and measured core outlet temperature. Accurate flow rate predictions are also important for predicting reactivity feedbacks and transient levels for tests in which the control rods were not scrammed, such as SHRT-45R.

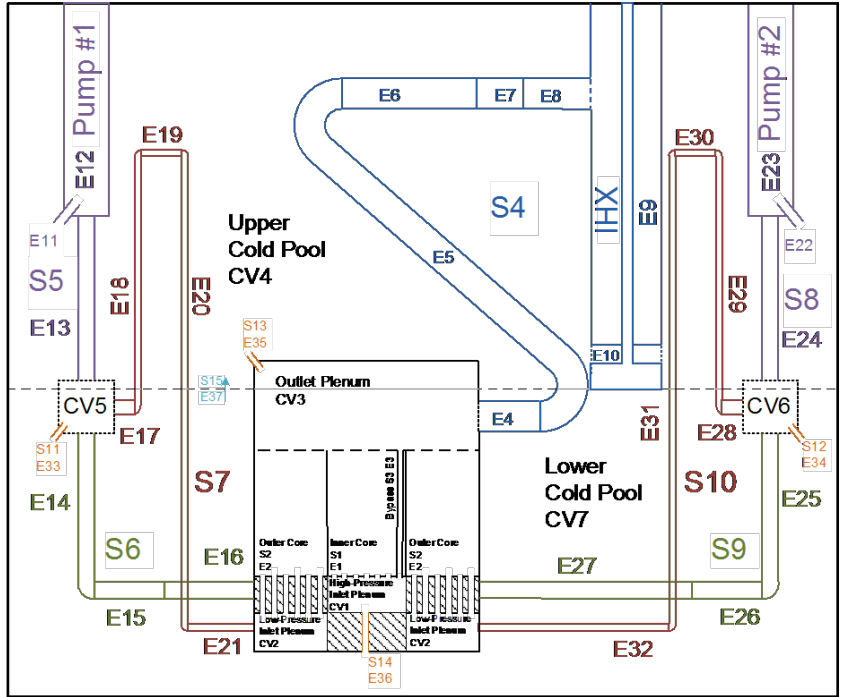


FIG. 262. Primary system model geometry.

7.18.4.2. SHRT-45R

Predictions of the SHRT-45R flow rates through the core inlet piping agreed much better with the measured data for SHRT-45R than for SHRT-17. The left side of FIG. 264 illustrates the measured and predicted flow rates for SHRT-45R. The flow rate predictions were most accurate during the initial flow coastdown and during the second half of the transient. During the middle part of the transient, the model predicted a slightly lower flow rate when the pump coastdown ended. Accurate predictions of the high pressure flow rate are necessary for reactivity feedback calculations and accurate predictions of the power level during the transient.

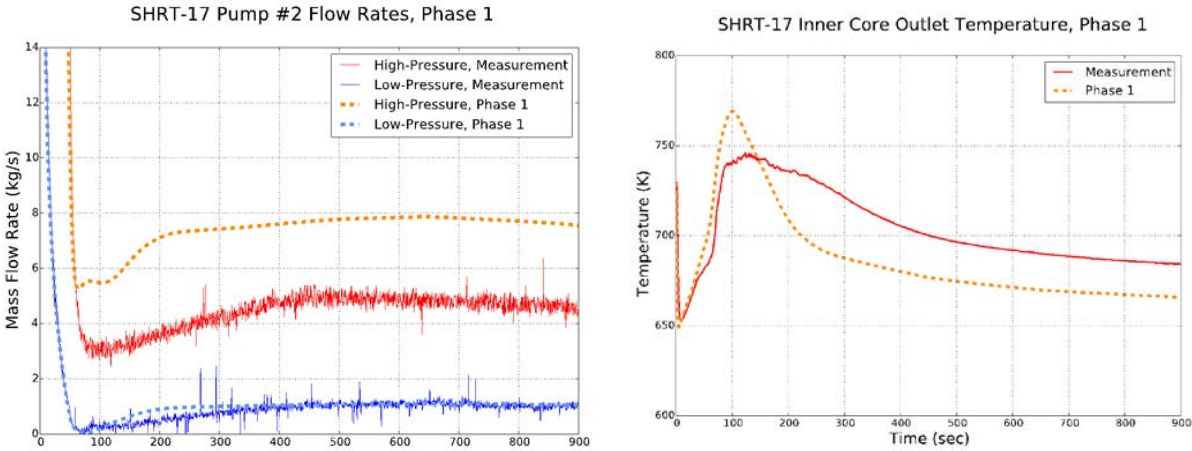


FIG. 263. SHRT-17 Initial Results: Pump #2 Flow Rates (left) and Inner Core Outlet Temperature (right).

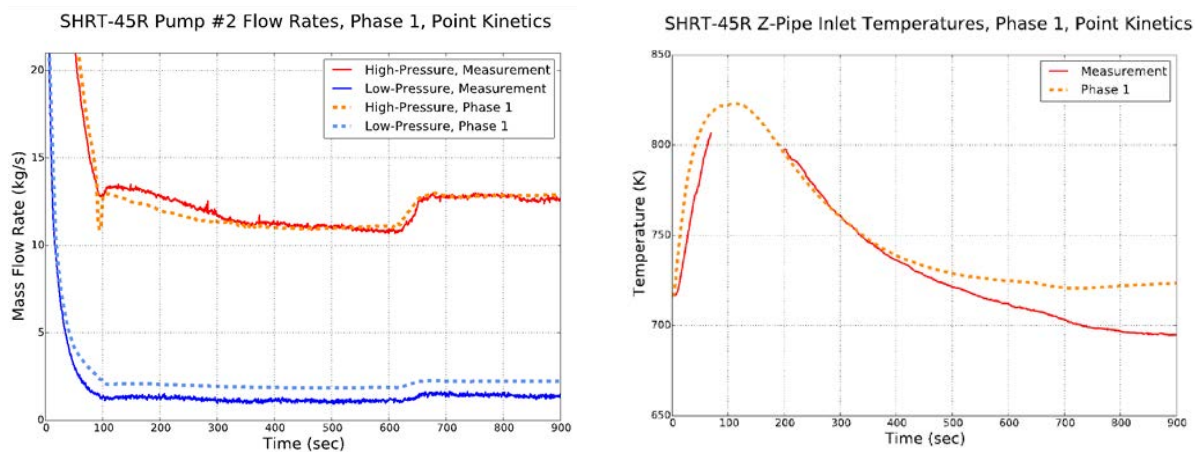


FIG. 264. SHRT-45R Initial Results: Pump #2 Flow Rates (left) and Z-Pipe Inlet Temperature (right).

The low pressure flow rate was overpredicted by approximately 50% but, as discussed in the previous section, this flow rate represents only 15% of the total core flow rate. Furthermore, the low pressure piping feeds the reflector and blanket subassemblies, so discrepancies in the flow rates for those subassemblies do not significantly affect the core power level during the transient.

The predicted Z-Pipe inlet temperature agreed well with the measured data for the first half of the transient. Although the predicted Z-Pipe inlet temperature rose faster than the measured temperature, this is to be expected because the upper plenum was modelled with a zero-dimensional volume. Therefore, thermal stratification and delays as sodium flows around the upper plenum baffle plate were not captured by the SAS4A/SASSYS-1 model.

Total power was predicted reasonably well for SHRT-45R, as shown in FIG. 265. Agreement was better during the first half of the test. During the second half of the test, the power level was very low, around 5%, so small absolute differences led to larger relative differences. This discrepancy during the second half of the test was the reason for the overpredicted Z-Pipe inlet temperature after 400 seconds.

7.18.5. Final results, data comparisons

7.18.5.1. SHRT-17

The largest improvement in the Argonne SHRT-17 results was for the flow rate predictions. Adjustments to the pump locked rotor loss coefficient and locking thresholds led to a more accurate high pressure flow rate prediction. The initial low pressure flow rate prediction showed better agreement with the measured data, but accuracy in the high pressure flow rate is more important to the transient results due to its effect on the temperatures in the fuel subassemblies. The left side of FIG. 266 illustrates Argonne's final SHRT-17 flow rate predictions.

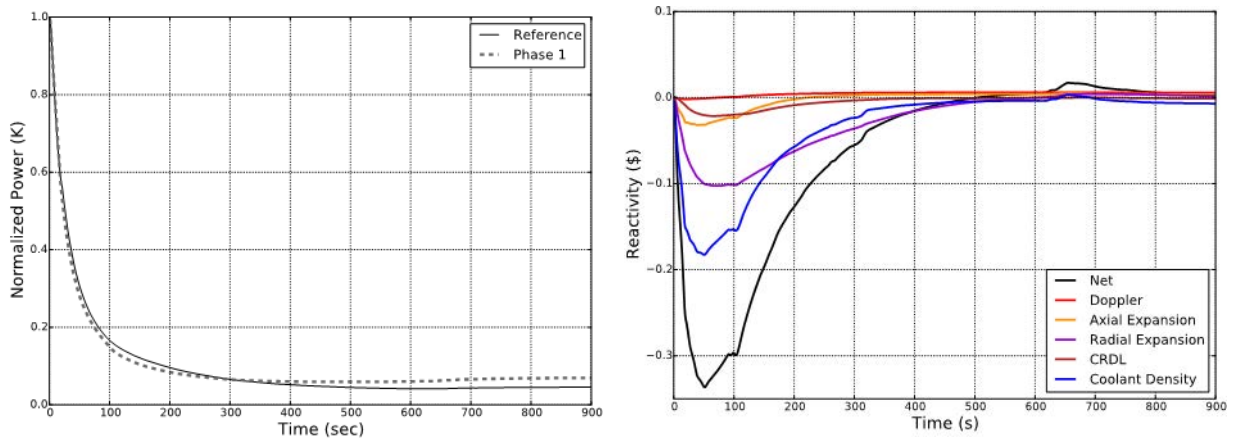


FIG. 265. SHRT-45R initial results: power (left) and reactivity feedbacks (right).

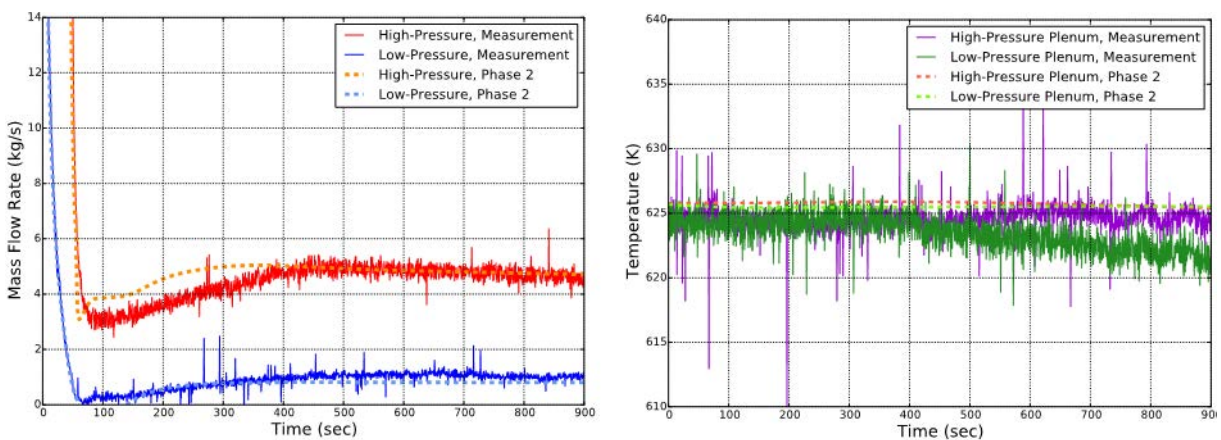


FIG. 266. SHRT-17 final results: pump #2 flow rates (left) and core inlet temperatures (right).

Because the primary vessel is so large, the cold pool temperature does not change much during the fifteen-minute SHRT-17 test, which led to relatively unchanged inlet plenum temperature profiles. The low pressure inlet plenum temperature decreased several degrees during the test, likely due to heating and cooling in the upper and lower parts of the stratified cold pool. SAS4A/SASSYS-1 predicted relatively flat inlet temperatures because of large thermal inertia. The model did not capture the heat transfer between sodium in the inlet pipes and the stratified cold pool, but not capturing this effect did not significantly affect the simulation results. The final core inlet temperature predictions are illustrated in the right side of FIG. 266.

The left side of FIG. 267 illustrates the final SHRT-17 core outlet temperature predictions. The improvements made to the pump model led to more accurate flow rates through the core. Because the flow rates were no longer significantly overpredicted, the core outlet temperature agreed much better with the measured temperature. It should be noted that multiple instruments are believed to have been combined to produce the inner core outlet temperature measurement shown in FIG. 267. The specific measurements could not be identified, but the measurement has similar tendencies to some of the inner core subassembly outlet temperature measurements. Therefore, it was determined that this measurement should be compared against the predicted inner core outlet temperature.

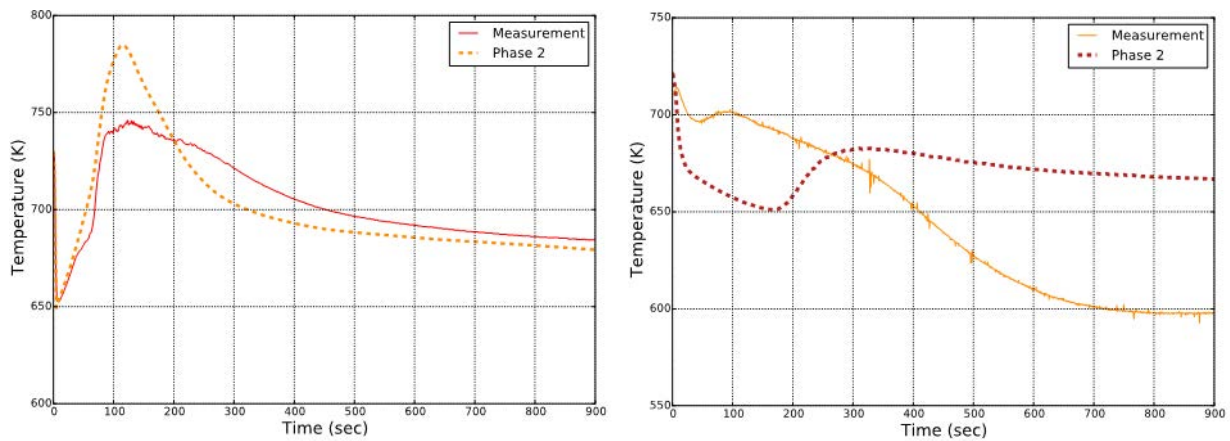


FIG. 267. SHRT-17 final results: inner core outlet temperature (left) and IHX inlet temperature (right).

While the SAS4A/SASSYS-1 core outlet temperature predictions agreed reasonably well with the measured data, one of the harder measurements to predict was the IHX primary side inlet temperature. The right side of FIG. 267 illustrates the IHX inlet temperature. The IHX inlet thermocouple was located near one of the IHX tubes behind multiple impact baffle plates, so it is expected that the thermocouple did not measure the average temperature of sodium leaving the Z-Pipe.

The initial temperature difference between the Z-Pipe and IHX inlet temperatures represents a loss of nearly 5 MW to the cold pool. Based on the IHX temperature measurements, the primary side rejected 53 MW to the intermediate sodium; but the intermediate IHX measurements represent a heat transfer rate of 60 MW. Losses through the primary vessel walls were too small to account for 7 MW, and based on the intermediate side instrument locations, confidence is higher in those measurements. Additional intermediate temperature measurements upstream and downstream from the IHX also suggest a similar heat rejection rate of 60 MW.

To further confirm that the Z-Pipe temperature drop was not as large as the measurements suggest, the overall heat transfer coefficient necessary to reject 5 MW to the cold pool was analyzed. Based on the geometry of the Z-Pipe, a coefficient of $3800 \text{ W/m}^2\text{K}$ would be required. However, the thermal resistance of one stainless steel pipe wall alone limits the heat transfer coefficient to approximately $2900 \text{ W/m}^2\text{K}$. The second pipe wall and stagnant sodium between the pipe walls would further insulate the sodium in the Z-Pipe. It was therefore concluded that the measurement did not reflect the average temperature of sodium entering the IHX.

Following these analyses, it was concluded that the measured IHX inlet temperature did not represent the average temperature of sodium leaving the Z-Pipe. Higher fidelity models would be required to capture the effects in the IHX inlet region. Therefore, the discrepancy between the measured data and the SAS4A/SASSYS-1 predictions is considered acceptable.

Despite small differences between the model predictions and the data measurements, the changes made to the pump model led to a model that accurately represents the behaviour of SHRT-17.

7.18.5.2. SHRT-45R

The left side of FIG. 268 illustrates the final flow rate predictions for SHRT-45R. The slightly higher flow rates predicted by the final model were caused by a lower pump locking threshold, which reduced the flow resistance through the pumps. This threshold is discussed in the following section. The discrepancy for the total power prediction was responsible for the slightly overpredicted flow rates during the second half of the SHRT-45R test. Although the final flow rate predictions did not agree as well with the measured data as with the initial model, the predicted high pressure flow rate agreed very well with the measured data when the measured total power level was treated as a model boundary condition. When power was predicted by the model and not treated as a boundary condition, the overpredicted power during the second half of the test led to lower sodium densities in the hot leg, which caused a higher driving head and overpredicted flow rates.

The measured and predicted low pressure flow rates still disagreed. Because the low pressure flow rate measurement is so low, it is difficult to know if the inaccuracy was in the SAS4A/SASSYS-1 prediction or in the measurement. Either way, this is less of a concern because the low pressure flow rate represents a small fraction of the total flow rate, and the high pressure flow rate is much more important for the reactivity feedback calculations.

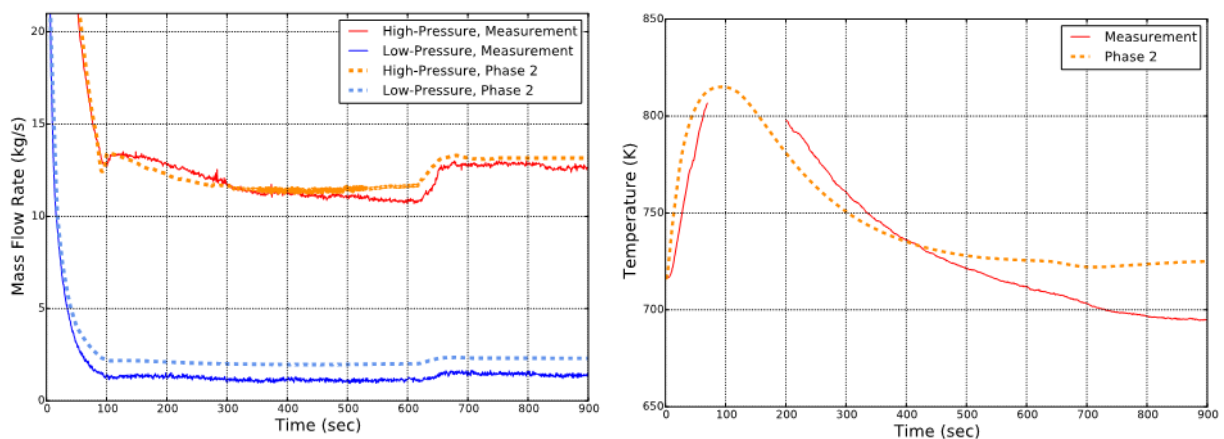


FIG. 268. SHRT-45R final results: pump #2 flow rates (left) and Z-Pipe inlet temperature (right).

Like the SHRT-17 results, the SHRT-45R core inlet temperatures did not change much during the test. The high pressure inlet temperature increased by 5K, while the low pressure inlet temperature decreased by 4K. The SAS4A/SASSYS-1 model did not capture these changes because cold pool thermal stratification was not accounted for and therefore the cold pool did not heat or cool the sodium in the inlet piping. But this difference has a minimal effect on the rest of the result.

The right side of FIG. 268 illustrates the measured and predicted Z-Pipe inlet temperature. Higher phase 2 flow rates led to lower core outlet temperatures and therefore lower temperatures in the Z-Pipe. The Z-Pipe inlet temperature rose faster than the measured data because the upper plenum was modelled as a zero-dimensional volume. There was no delay as hotter sodium entered the volume, flowed through or around the baffle plate, and entered the Z-Pipe. The Z-Pipe inlet temperature was overpredicted in the second half of the test because the power was overpredicted. As with SHRT-17, there was a discrepancy between the SHRT-45R IHX inlet temperature measurement and model prediction. Because the IHX inlet thermocouples were installed inside the IHX along the outer surface of a tube, not at the inlet where higher flow mixing is expected, it is speculated that the thermocouples did not measure the average temperature of sodium leaving the Z-Pipe. The SAS4A/SASSYS-1 model can

provide only the average Z-Pipe outlet temperature, so disagreement between the measurement and the model is expected.

The left side of FIG. 269 compares the predicted total power level with the reference transient power level, which is the sum of the measured fission power and calculated decay heat. Because the reactivity feedback coefficients were not updated after the blind phase of the CRP concluded, the initial and final power predictions were very close to each other. The final power prediction was slightly higher at the end than the reference power level primarily due to the higher predicted core flow rate. While the absolute differences between the SAS4A/SASSYS-1 and measured power levels are small, the relative differences cannot be neglected. SAS4A/SASSYS-1 underpredicted total power by approximately 20% during the first 200 seconds. At the end of the test, SAS4A/SASSYS-1 overpredicted total power by approximately 60%. The right side of FIG. 269 illustrates the reactivity feedback predictions for SHRT-45R.

Separate analyses were performed to understand how sensitive the power prediction is to the reactivity feedback coefficients. These analyses used the measured core inlet temperature and flow rate as boundary conditions. Eliminating the core inlet temperature discrepancy reduced the power difference at the end of the test from 60% to 33%. Another effect that may be responsible for a large portion of the difference is the radial core expansion model. Currently, the simple radial core expansion is used. A simple subassembly bowing model was tested, and this improved the power level agreement early in the test. But a more detailed bowing model may be required to further improve the power prediction.

Although there are still differences in the power level predictions at the end of the test, the SAS4A/SASSYS-1 model captured the behaviour of EBR-II during the SHRT-45R test.

7.18.5.3. *Model improvements*

Argonne's modelling efforts during Phase 2 focused primarily on improving the predicted flow rates for SHRT-17. In order to maintain model consistency for the two tests, any modifications made to the pump model for SHRT-17 were also applied to the SHRT-45R model. The modifications described below led to vastly improved agreement with the SHRT-17 flow rate measurements without significantly affecting the agreement for the SHRT-45R flow rates. A parametric evaluation of the pump locked rotor loss coefficient was performed for SHRT-17. This evaluation led to the observation that an increased pump locked rotor loss coefficient caused the SHRT-17 simulated flow rate to decrease through one pump but increase in the other pump. Pump #1 locked during the initial SHRT-17 simulation, but pump #2 did not lock. In contrast, both pumps locked for the SHRT-45R simulation. Because the flow rates are much lower for SHRT-17 than for SHRT-45R, the pumps should be much more likely to lock during SHRT-17.

The reason pump #2 did not lock for the SHRT-17 simulation was because pump speed is a boundary condition for the benchmark, and the lowest recorded normalized pump speed was 0.00299 at 50 seconds, which is above the assumed locked rotor normalized speed threshold. The other SHRT-17 and SHRT-45R pump speed measurements fell well below the threshold during the transient. With pump #2 not locking, an increased locked rotor resistance in pump #1 resulted in a higher predicted flow through pump #2. Because the measured SHRT-17 flow rates are much lower than the SHRT-45R flow rates, it was concluded that the transient pump #2 speed measurement was inaccurate and both pumps locked for SHRT-17. The pump #2 speed was decreased in the simulation below the locked rotor normalized speed threshold to

enforce this assumption. Once a pump locks during a simulation, the pump speed value no longer matters.

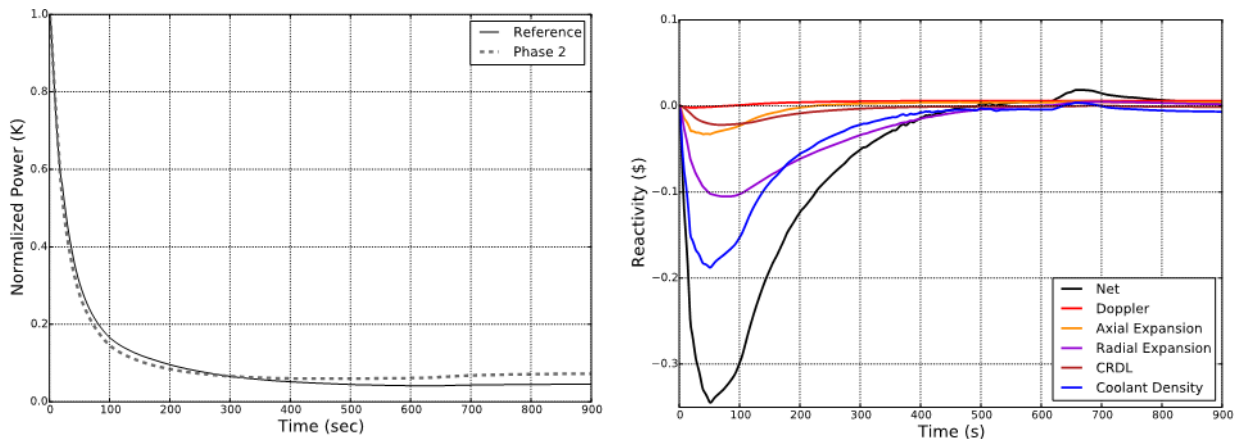


FIG. 269. SHRT-45R Final Results: Power (left) and Reactivity Feedbacks (right).

After concluding that both pumps locked for SHRT-17, the next step was to determine the appropriate flow resistance through a locked pump and also determine the appropriate thresholds for assuming a locked pump. During the initial phase, a locked rotor loss coefficient of 1.0 was assumed, which produced reasonably good agreement for SHRT-45R. A parametric analysis revealed that a loss coefficient of 3.6 was necessary for accurate SHRT-17 flow rate predictions. A loss coefficient of 3.6, however, led to significantly underpredicted SHRT-45R flow rates. It was postulated that the flow rate threshold for locking the pumps that was assumed for the initial phase was too low. Because the transient SHRT-45R flow rates were nearly 2.5 times larger than the transient SHRT-17 flow rates, it was assumed that the pumps locked for SHRT-17, but natural circulation and the auxiliary EM pump head prevented the pumps from locking during SHRT-45R. These changes to the pump model produced significantly better agreement with the SHRT-17 measured flow rates without negatively affecting the good agreement for the SHRT-45R flow rates.

Several other changes to the model were made but none had as significant an impact as the pump model changes. One such change was made to the upper plenum sodium-to-steel heat transfer coefficient, which was increased from 50.5 w/(m²-K) to 700 w/(m²-K) based on a parametric study of Z-Pipe inlet temperatures during SHRT-45R. This parametric analysis was performed with the measured power level enforced as a boundary condition to eliminate the impact of power level discrepancies and produced significantly better agreement with the SHRT-45R Z-Pipe inlet temperature measurement.

7.18.6. Neutronics methods and models

7.18.6.1. Cross-section generation

MC²-3/TWODANT was used to generate neutron and photon cross-sections, the neutron flux to photon source conversion matrix, and the neutron and photon KERMA factors. The cross-section generation followed a 2-step MC²-3 calculation. The first step used a 1041-group neutron cross-section library and performed a 2-dimensional RZ transport calculation by TWODANT to solve the neutron flux spectrum for different regions in EBR-II. In the second step, the flux spectrum obtained from the first step was used to condense the neutron library to 33 groups, and this condensed neutron cross-section set was used in the DIF3D calculation. This 2-step cross-section generation procedure was performed for three different EBR-II

cores: a normal core (no perturbation), a core with the fuel temperature doubled, and a 10% sodium voided core.

7.18.6.2. Calculation of power and k_{eff}

DIF3D was employed to evaluate the power distribution in the EBR-II core. The hexagonal-Z model of DIF3D was employed with both diffusion and P3 angular approximations. The power distribution calculation followed three steps. The first step calculated neutron flux and generated a photon source by the GAMSOR module of DIF3D. The second step used the photon source to evaluate the photon flux distribution. The neutron flux from step 1 and photon flux from step 2 were multiplied by the corresponding KERMA factors in the last step to calculate the power distribution in the EBR-II core.

7.18.6.3. Calculation of reactivity feedback

DIF3D was also employed to evaluate the axial and radial expansion reactivity feedback coefficients, and the control and safety subassembly worth curves. Delayed neutron fraction, Doppler and sodium void reactivity feedback coefficients were evaluated by two perturbation codes, PERSENT (transport theory) and VARI3D (diffusion theory) [60].

7.18.7. Neutronics results

The results are summarized in TABLE 37 for k_{eff} , β_{eff} and reactivity feedback coefficients, in FIG. 270 for control and safety subassembly worth curves, and in FIG. 271 for power distribution. The control and safety subassembly insertions were measured as the distance between the bottom of the fuel region of a regular driver subassembly and that of the control or safety subassembly.

TABLE 37. k_{eff} , β_{eff} , AND REACTIVITY FEEDBACK COEFFICIENTS

Parameters	DIF3D FDD	VARIANT
k_{eff}	0.9670	0.9885
β_{eff} (pcm)	705	705
Axial expansion (pcm/K)	-0.36	-0.65
Radial expansion (pcm/K)	-1.78	-1.67
Sodium density (pcm/K)	-1.70	-1.49
Doppler (pcm/K)	-0.06	-0.06

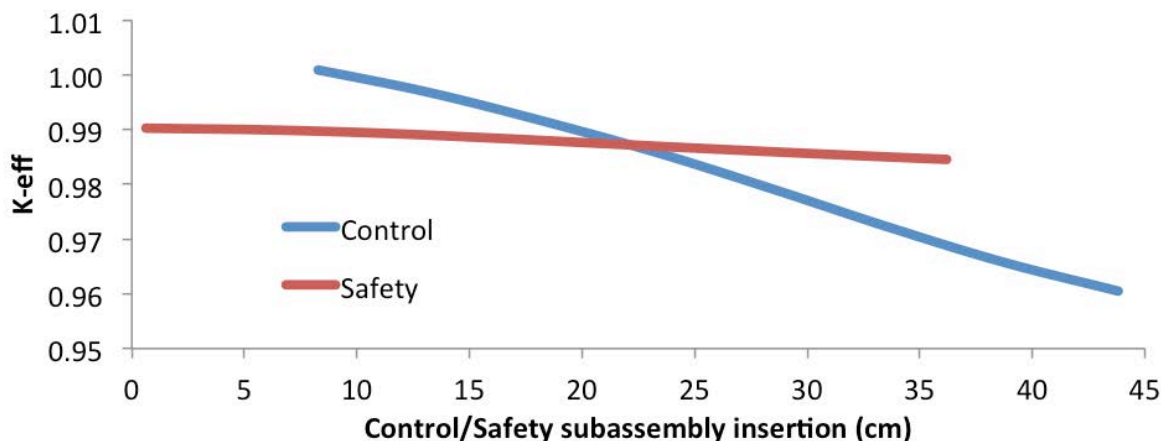


FIG. 270. Control and safety subassembly worth curve.

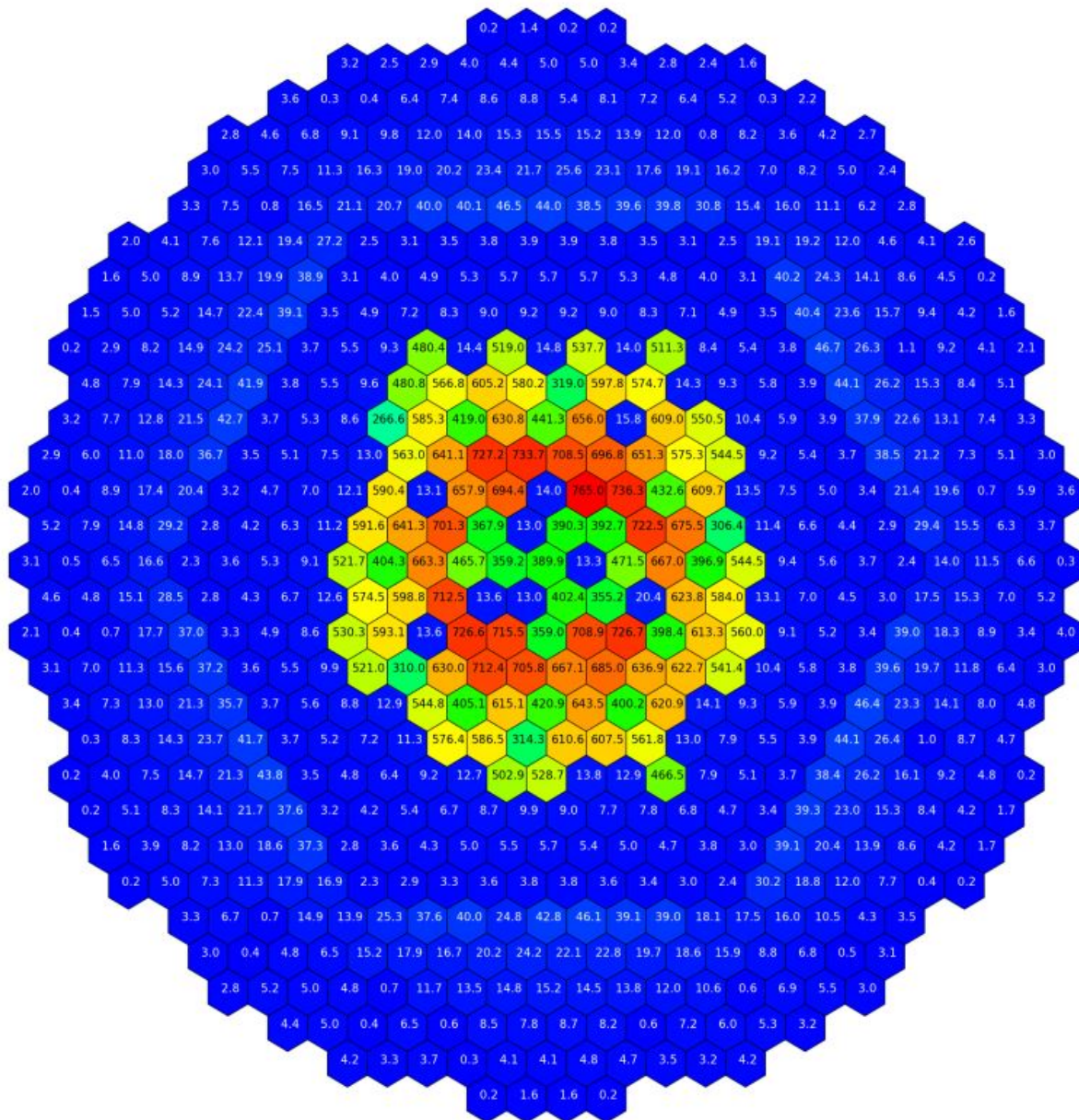


FIG. 271. Power (kW) generation in EBR-II core.

7.19. REACTIVITY FEEDBACK DATA PROVIDED FOR SHRT-45R

Participants who analyzed the SHRT-45R transient had the option of either generating their own neutronics parameters or using parameters provided by Argonne. β_{eff} and λ were provided for six groups of delayed neutrons, as well as values of 3.46402×10^{-7} s. for prompt neutron lifetime and 3.58238×10^{-7} s. for prompt neutron generation time. For each type of subassembly, an axial mesh was defined, and reactivity changes within each axial mesh cell were provided for Doppler, steel density, fuel density, sodium void and voided Doppler. These were summed to give the respective reactivity feedback coefficients.

Radial expansion and axial fuel expansion feedback coefficients that assumed uniform dilation were also provided. The calculation of the radial expansion coefficient assumed a subassembly pitch increase of 1%, accompanied by dividing number densities, except sodium,

in all regions by $(1.01)^2$. For the axial expansion coefficient, the heavy metal density was assumed to decrease by 10%, while the fuel height increased by 10% in the core regions of the driver, half-worth driver, control and safety subassemblies. This resulted in a radial expansion coefficient value of -1019 pcm and an axial fuel expansion coefficient of -2019 pcm.

Finally, k_{eff} values were given for various control rod and safety rod positions, and an axial power profile was provided for all subassemblies.

8. SENSITIVITY AND/OR UNCERTAINTY ANALYSES

8.1. KIT (GERMANY)/KYUSHU UNIVERSITY (JAPAN)

8.1.1. SHRT-17

Several sensitivity and parametric studies were carried out by KIT/KU while performing the SHRT-17 tests. The most significant improvements were selected for the phase 2 final results as described in Section 7.5.5.1 and Section 7.5.5.3.

TABLE 38 shows an overview of the options considered. The options included in the final results were already discussed in Section 7.5.5.3. The other options considered are briefly described here.

TABLE 38. OVERVIEW OF THE MODELLING OPTIONS CONSIDERED FOR SHRT-17

Option number	Options considered	Effect on the results	Adopted for final results
1	Short term mass flow rate tuning	High	yes
2	IHX position	High	yes
3	Different Gap Conductance	Limited	no
4	Axial conduction	Limited	no
5	Modelling reactor shielding	Negligible	no
6	Radial conduction for XX10	High	yes
7	Fuel porosity	Limited	no

8.1.1.1. Variation in gap conductance

In the SIMMER model that was used, a constant value of the gap conductance was input. The reference value used was 718095.42 W/m²/K. As an alternative, a lower value (half of the reference one) was considered.

As indicated in FIG. 272, where the core outlet temperature and the coolant temperature at mid-core for XX09 are shown, the impact on the results of changing the gap conductance is not significant.

8.1.1.2. Axial conduction

In the standard SIMMER version, axial conduction within a ring is not modelled. Options exist in which axial conduction may be activated. Its effects at the XX10 upper flowmeter

position are significant, as indicated in FIG. 273(a). Other quantities are not influenced by the axial conduction (see FIG. 273(b), where the coolant temperature at mid-core for XX09 is shown).

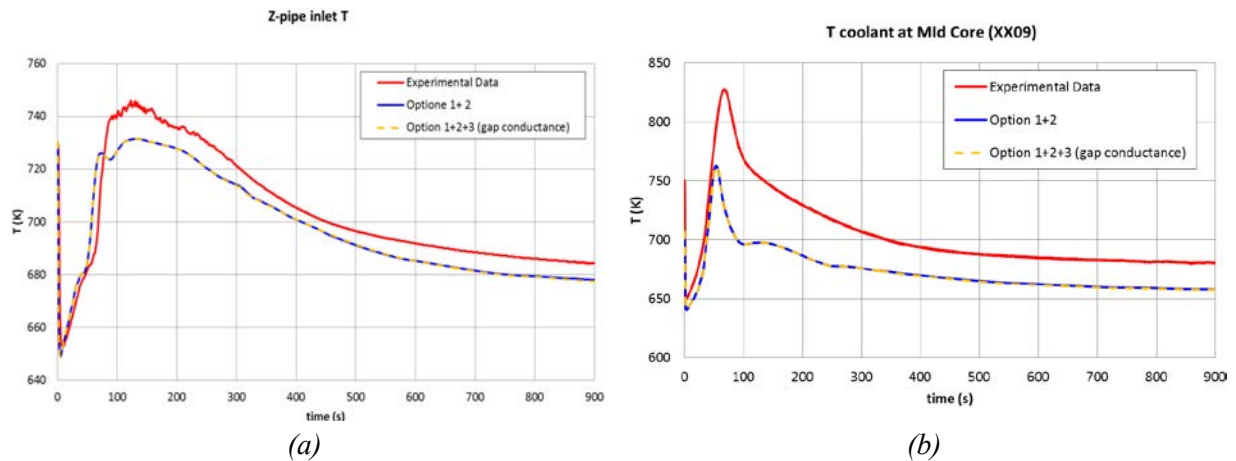


FIG. 272. SHRT-17 – parametric study (gap conductance): (a) core outlet temperature, (b) coolant temperature at mid-core for XX09.

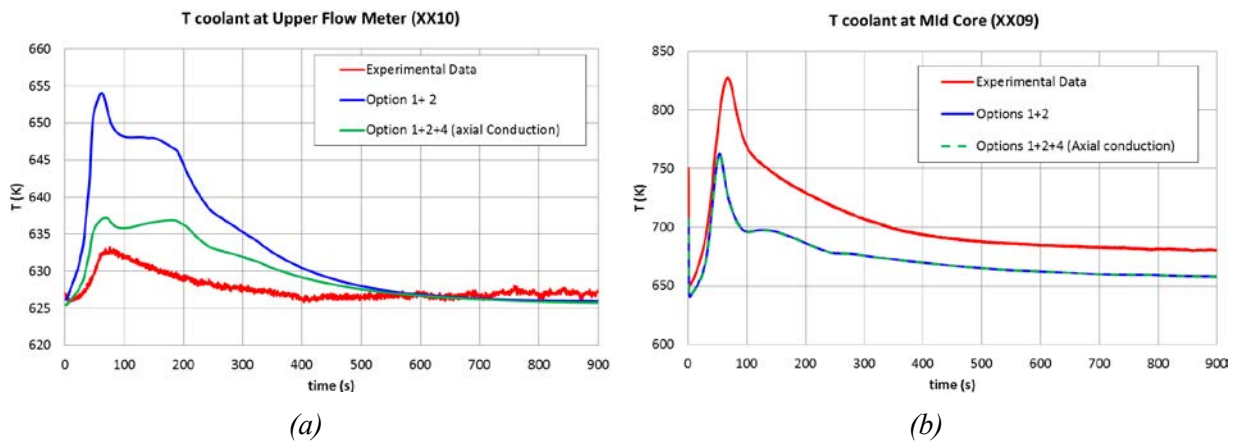


FIG. 273. SHRT-17 – parametric study (axial conduction): (a) coolant temperature at upper flowmeter position (XX10), (b) coolant temperature at mid-core for XX09.

8.1.1.3. Modelling of reactor shielding

The graphite shielding of EBR-II was modelled in SIMMER using a virtual walls delineation, namely it was excluded (isolated) from the calculation region. In order to test the effect, the zone was modelled as a steel zone without virtual walls around (see FIG. 274). The difference between the two modelling options is negligible, as indicated in FIG. 275, where the Z-Pipe inlet temperature is plotted.

8.1.1.4. Fuel porosity

No specific data about fuel porosity were indicated in the benchmark description. Initially, a value of 10% was assumed in the calculation. This value has an impact on the fuel mass (that is currently underestimated). In order to obtain better agreement with the true fuel mass, a

porosity of 1% was assumed. The input was then modified in order to obtain at steady state the same power per ring as in the case with 10% porosity (see FIG. 276).

As indicated in FIG. 277, the impact on the transient results is negligible.

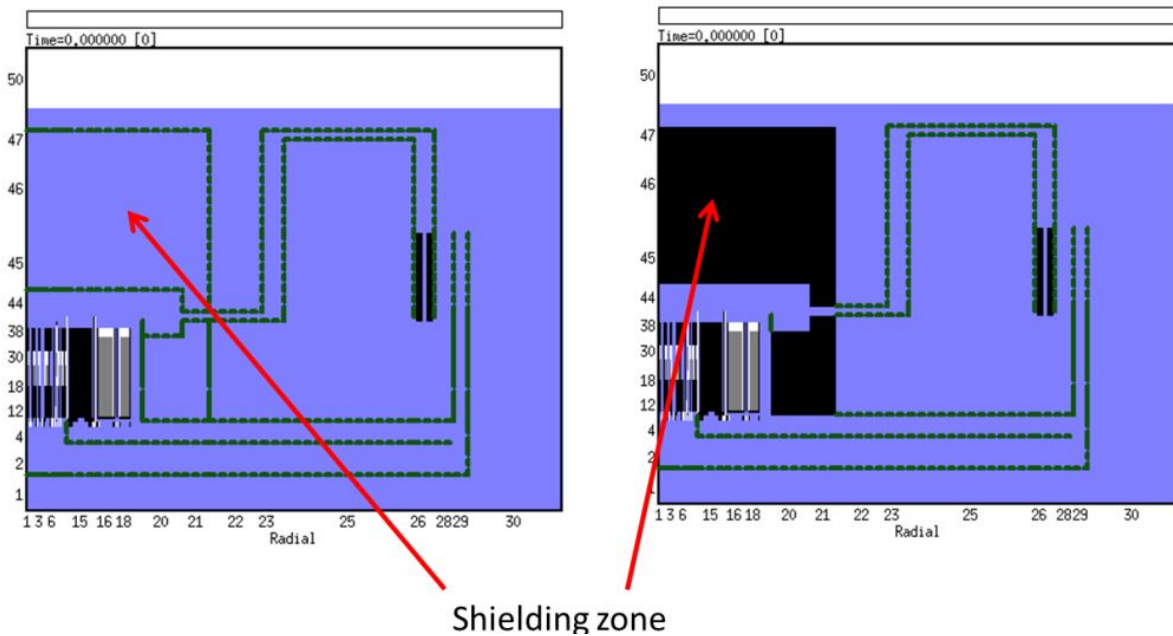


FIG. 274. SHRT-17 – parametric study (shielding modelling): (left) zone among virtual walls modelled by sodium, (right) modelled by steel zone.

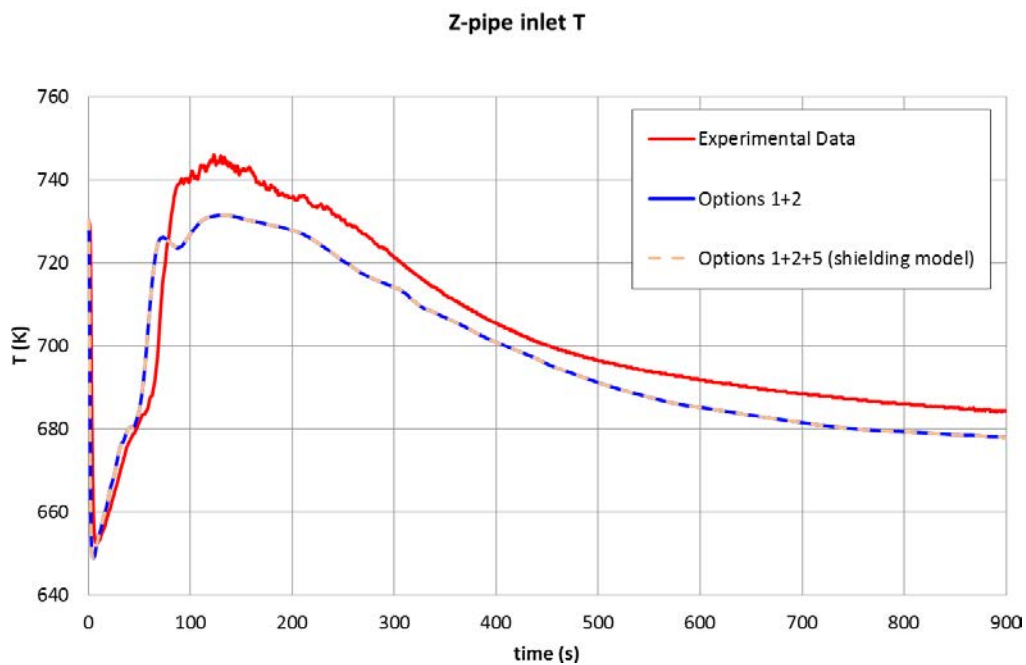


FIG. 275. SHRT-17 – parametric study (shielding modelling): Z-Pipe inlet temperature results.

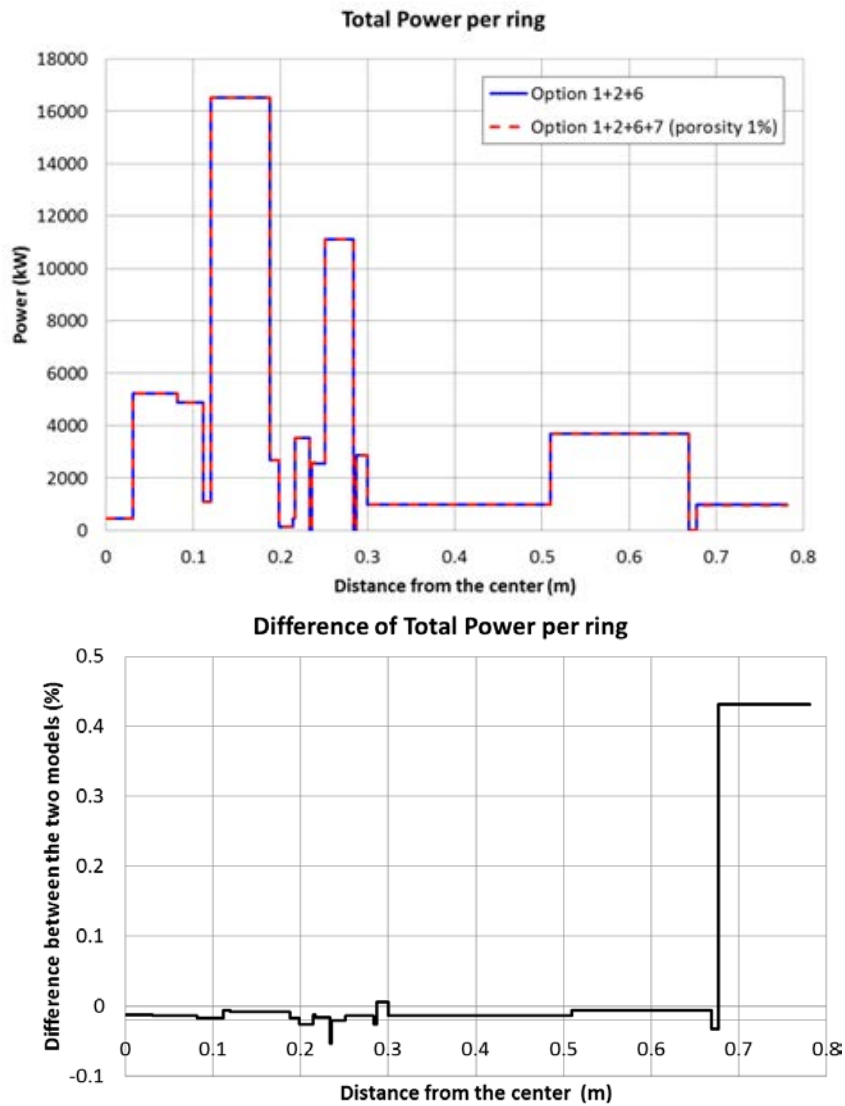
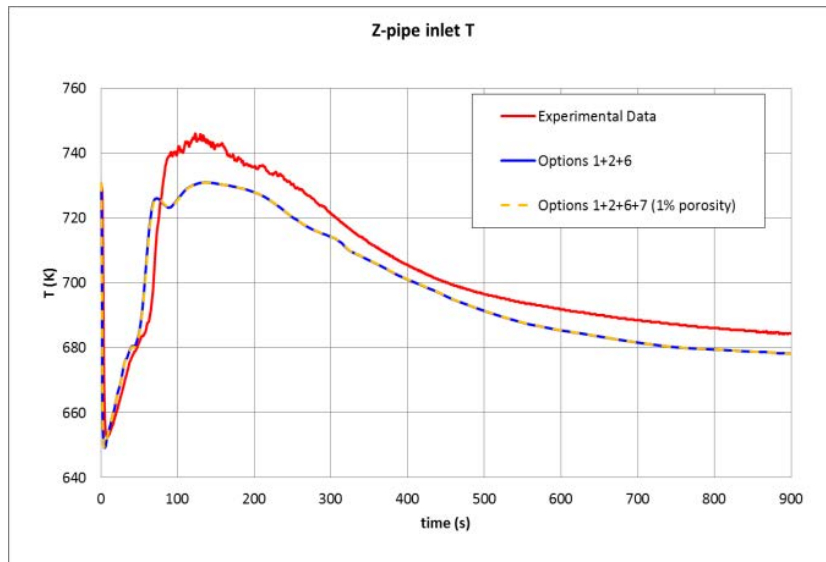


FIG. 276. SHRT-17 – parametric study (fuel porosity): power per ring (steady state).

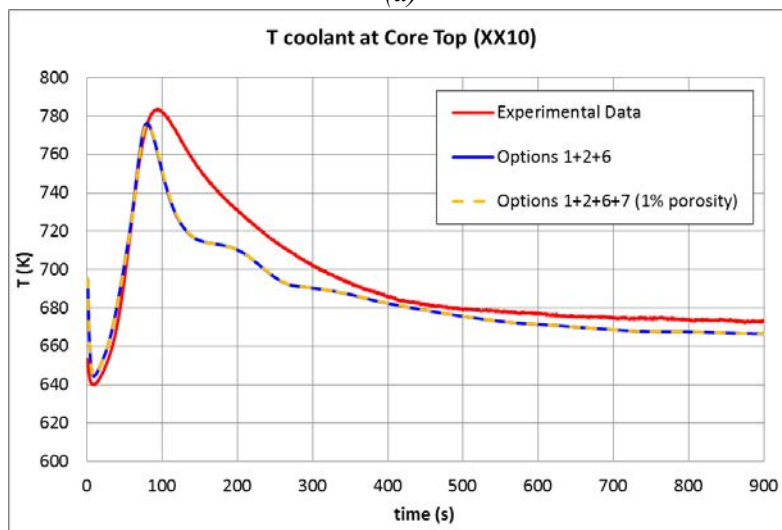
8.1.2. Neutronics benchmark

Several sensitivity and parametric studies were carried out by KIT while performing the neutronics benchmark on SHRT-45R. Several codes (ERANOS 2.2 [43], PARTISN v5.97 [49]) and modelling options (heterogeneous/homogeneous models for generation of multigroup cross-sections, diffusion/transport approximations for neutron transport, etc.) were compared [97]. A short overview is presented here.

A list of the different options considered is shown in TABLE 39. Not all the benchmark results were recalculated for each option. The impact of modelling options on k_{eff} was evaluated as indicated in TABLE 40. Very good agreement was obtained between the results calculated with VARIANT for the two geometries considered (HEX-Z and XYZ). The difference in the computational time (8 times more for the XYZ compared to the HEX-Z) is due to the nodalization adopted for the XYZ cases (each HEX was represented by two rectangular nodes with the same total area as HEX) [97].



(a)



(b)

FIG. 277. SHRT-17 – parametric study (fuel porosity): (a) Z-Pipe coolant inlet temperature, (b) coolant temperature at core top for XX10.

The heterogeneity effect was determined to be about 220 pcm (about 0.3%), and the effect of thermal expansion was of the order of 1200 pcm. The results show that the diffusion approximation significantly underestimated the k_{eff} by ~ 2500 pcm when compared to other transport solvers, as expected, since EBR-II had a small core with a large amount of neutron leakage. A very good agreement between the value obtained with PARTISN (SN=16) and VARIANT (without the simplified spherical harmonics approximation, P3 option) was obtained (the same effective cross-sections were used in the two models) [97].

Some of the reactivity feedback coefficients (axial and radial expansion and sodium void) were also recalculated using the PARTISN code, as shown in TABLE 41. The results are in good agreement with the reference results.

Concerning the sodium density reactivity feedback coefficient, a parametric study was carried out. Several configurations were investigated, as indicated in TABLE 42. Depending on the option considered, the values obtained show a difference of almost 50% (see TABLE 42).

TABLE 39. EBR-II SHRT-45R MODELLING OPTIONS CONSIDERED AT KIT

CASE ID:	Options considered
REF	ERANOS 2.2, VARIANT solver, HEX-Z geometry, SP3 approx., Not Expanded
ERANOS-1	ERANOS 2.2, VARIANT solver, HEX-Z geometry, SP3 approx., Expanded
ERANOS-2	ERANOS 2.2, VARIANT solver, HEX-Z geometry, SP3 approx., Not Expanded, XS homogeneous treatment
ERANOS-3	ERANOS 2.2, VARIANT solver, HEX-Z geometry, P3 approx., Not Expanded
ERANOS-4	ERANOS 2.2, VARIANT solver, HEX-Z geometry, Diffusion approx., Not Expanded
ERANOS-5	ERANOS 2.2, VARIANT solver, XYZ geometry, SP3 approx., Not Expanded
PARTISN-1	PARTISN v5.97, XYZ geometry, Sn=4, Not Expanded
PARTISN-2	PARTISN v5.97, XYZ geometry, Sn=16, Not Expanded

For control rod driveline expansion reactivity coefficients, studies evaluating the diffusion approximation were also performed. The results are underestimated by about 2500 pcm.

The spatial distribution of sodium density was also investigated by using the KIN3D code [127]. The spatial distribution was calculated by using the reference model and by considering the perturbations introduced by two different sets of cross-sections (reference and voided conditions¹). Reactivity effects (total and distribution) were then evaluated by using exact perturbation theory. FIG. 278 shows the spatial distribution for voided conditions (direction - E-). More details are available in [128].

TABLE 40. EBR-II SHRT-45R: IMPACT OF MODELLING OPTIONS ON k_{eff}

Case	Modelling options	k_{eff}	Time (s)	Effect on k_{eff} of Modelling options (pcm)
REF	HEX-Z Cold dimensions	0.99969	409	-
ERANOS-1	HEX-Z Expanded dimensions	0.98761	-	-1224
ERANOS-2	HEX-Z Homogenous XS treatment	0.99751	-	-219
ERANOS-3	HEX-Z P3	1.00198	3305	229
ERANOS-4	HEX-Z Diffusion	0.97482	-	-2552
ERANOS-5	XYZ	0.99960	6380	-9
PARTISN-1	SN-4	1.00375	13 ^a	405
PARTISN-2	SN-16	1.00339	62 ^a	369

^a Calculations run with 16 processors

¹ Void effect calculated as density reduction of the Na inside the wrapper for the active height only (i.e. 36.65 cm) and for drivers + HW-CR + SR.

TABLE 41. EBR-II SHRT-45R: IMPACT OF MODELLING OPTION ON REACTIVITY COEFFICIENTS

Reactivity feedback coefficients	REF (pcm/K)	PARTISN-2 (pcm/K)
Axial expansion reactivity feedback coefficient	-0.68	-0.71
Radial expansion reactivity feedback coefficient	-2.42	-2.41
Sodium density reactivity feedback coefficient	-2.15	-1.98

TABLE 42. SODIUM DENSITY REACTIVITY FEEDBACK COEFFICIENT: KIT PARAMETRIC STUDY

Na density reactivity feedback coefficient (10% Na density variation)	pcm/K
Whole system (SP3)	-2.15
Whole system (Diffusion)	-2.52
Inside Wrapper tube, active height, drivers only	-0.63
Inside Wrapper tube, active height, drivers, HW-CR, SR, XX09	-0.72
Inside Wrapper tube, active height plus above, drivers only	-0.97
Inside Wrapper tube, active height plus above, drivers, HW-CR, SR, XX09	-1.17

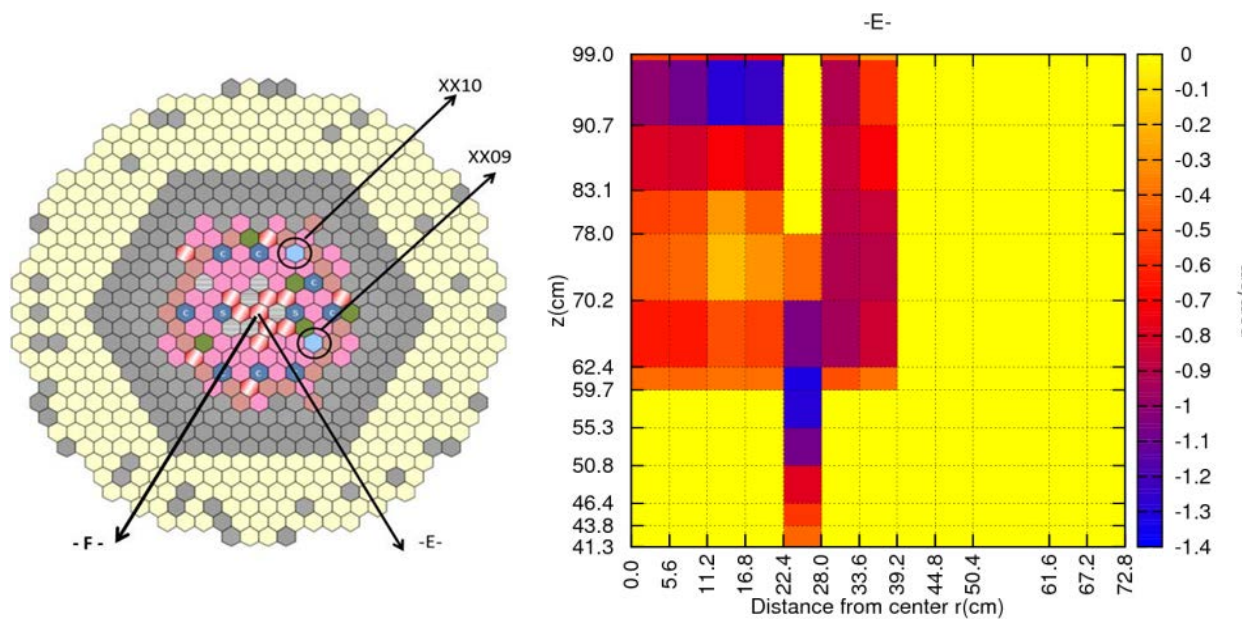


FIG. 278. Spatial distribution of reactivity effects for the sodium voided scenario.

The power distribution per subassembly was also evaluated by using the PARTISN code (PARTISN-2 case). Relative differences in the core between ERANOS and PARTISN were well below 1%. However, at the periphery of the reactor, those differences increased up to 10%. One example is shown in FIG. 279, where the radial distribution (direction -F-) has been compared with the data provided initially in the benchmark by Argonne (Section 4).

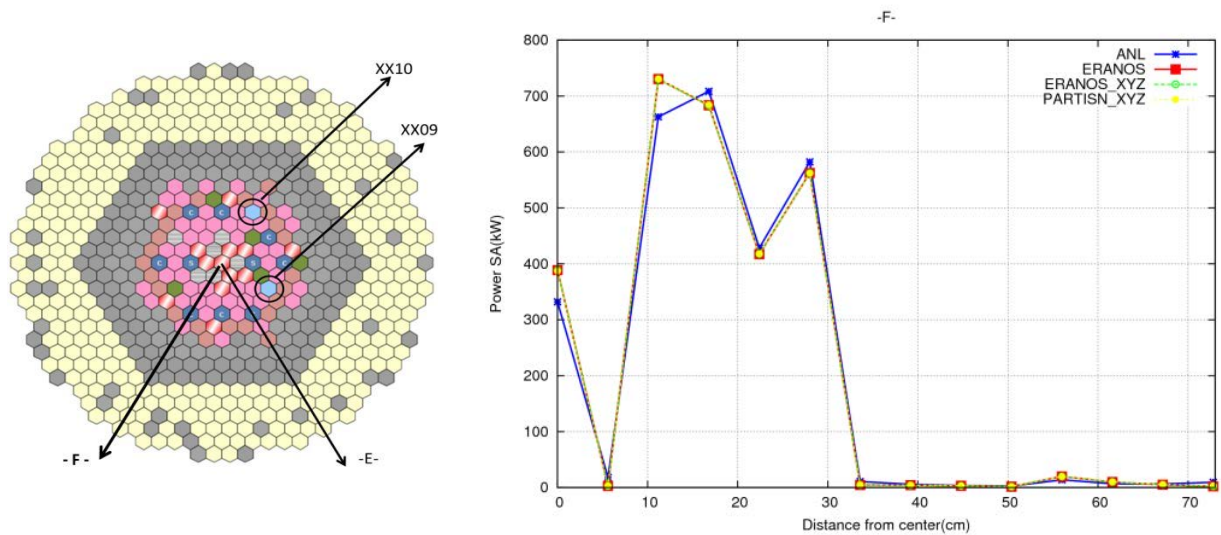


FIG. 279. Radial distribution of the power following direction -F- (ERANOS vs. PARTISN).

8.2. ENEA (ITALY)

Two types of sensitivities are discussed: one activating the axial conduction model implemented in RELAP5-3D[®], the other increasing the axial detail in the reactor upper plenum region to improve the prediction of the thermal stratification.

- (1) The axial conduction model was activated in two runs: S1) axial conduction in the reactor core passive heat structures and S2) conduction in all heat structures modelling the bundles and the thimbles of subassemblies XX09 and XX10. The results are reported in FIG. 280, which highlights, in the case of S2, a large underestimation of cladding temperatures at the top of the active fuel and an overestimation of coolant temperatures in the lower part of the subassemblies. No difference is observed in case S1;
- (2) The number of axial meshes in the upper plenum was doubled (i.e. 4 axial volumes instead of 2). The measured temperature trends are connected with the mixing, induced by the forced circulation during the start of the test (first 10 s). The onset of thermal stratification is in the second portion of the transient, becoming the prevailing process after 100 s from the start of the transient. The coolant thermal mixing and stratification phenomena cannot be accurately predicted by the RELAP5-3D[®] code. They are influenced by the nodalization scheme, and thus by the user's choices. Improved prediction of thermal stratification was achieved by increasing the number of axial meshes in the upper plenum from 2 to 4 and thus improving the granularity of the flow paths in this zone. The results of this sensitivity analysis are reported in FIG. 281, which compares temperatures calculated using 4 axial volumes in the upper plenum against the recorded data from the probe thermocouples in the upper plenum. The locations of the probe thermocouples are indicated in FIG. 282.

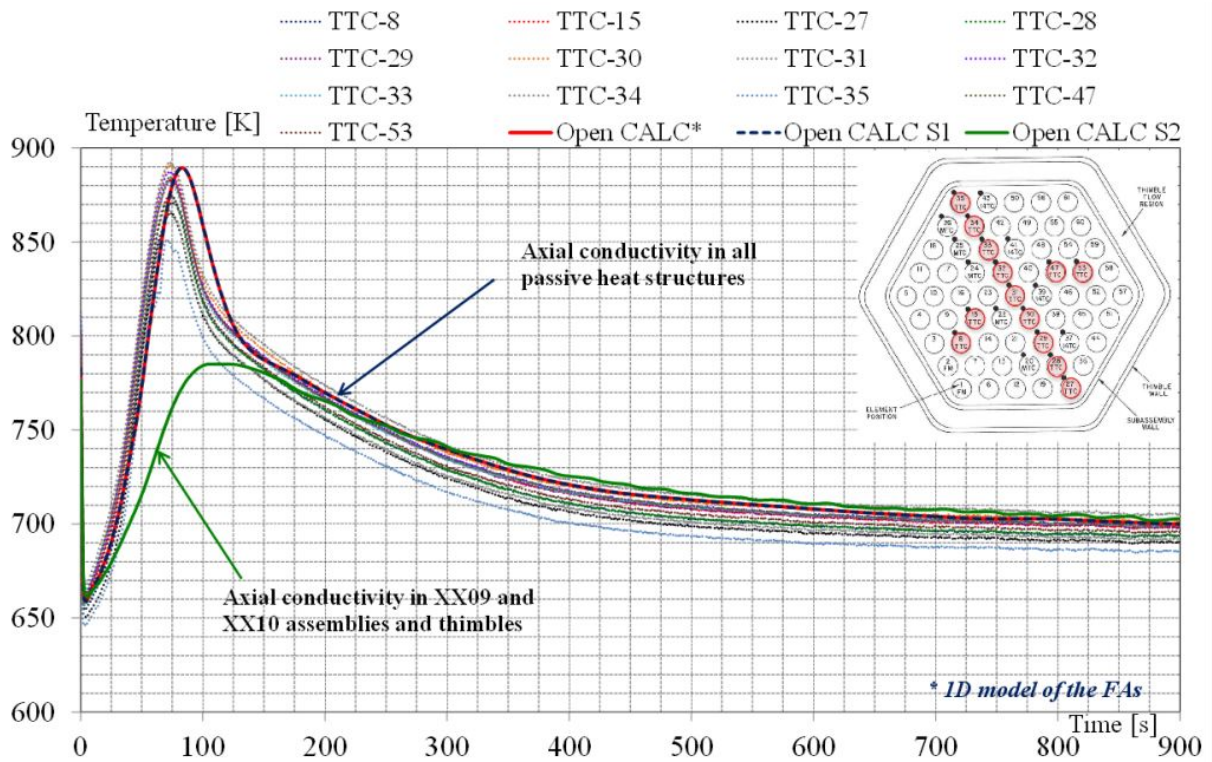


FIG. 280. EBR-II, RELAP5-3D[®] sensitivity analyses on axial conduction model: XX09 temperatures.

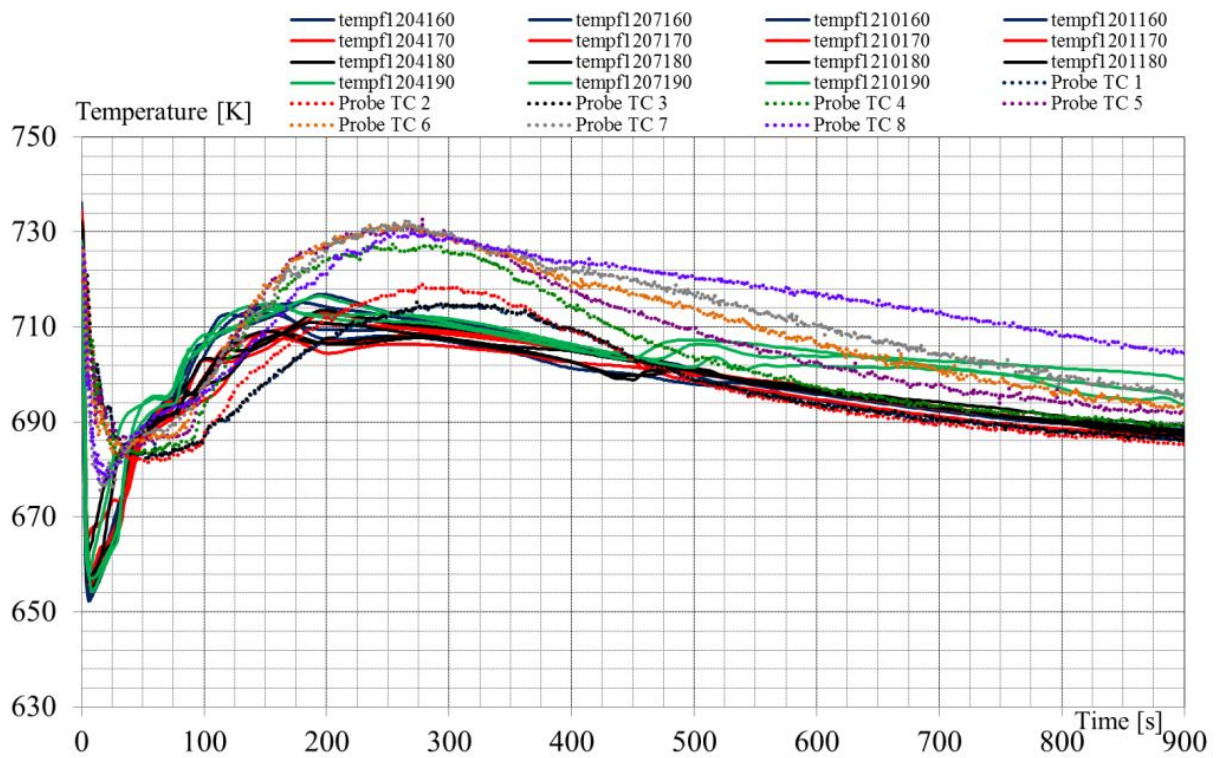


FIG. 281. EBR-II SHRT-17, RELAP5-3D[®] sensitivity analyses on nodalization: upper plenum coolant temperatures.

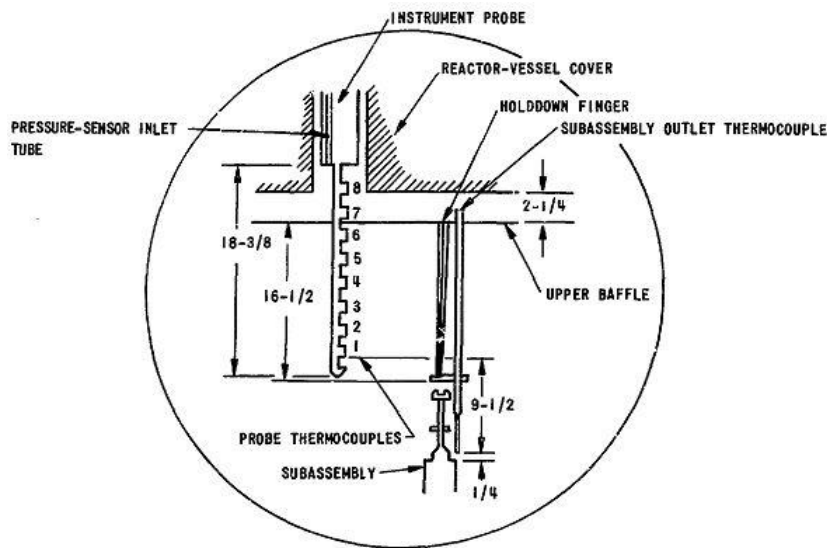


FIG. 282. Locations of probe thermocouples in the EBR-II upper plenum.

8.3. NUCLEAR AND INDUSTRIAL ENGINEERING (ITALY)

During phase 2 of the benchmark, the following sensitivity analysis on gamma heating was performed by NINE, aimed at understanding the experimental behaviour of the coolant temperature at the inlet and outlet of the instrumented subassemblies (in particular, instrumented subassembly XX09).

To perform the sensitivity analysis, a simple model (see FIG. 283) of instrumented subassembly XX09 was developed, taking into account only the subassembly channel and the guide thimble annulus channel, thermally connected with a passive heat structure simulating the subassembly walls. The heat structure simulating the guide thimble wall was isolated. Regarding the active heat structure, in addition to the flat power profile adopted in the early stage of phase 2 of the benchmark (Phase-2A), four different axial power distributions (see FIG. 283) were implemented:

- (1) Power supplied below the active part of the core;
- (2) Power supplied above the active part of the core;
- (3) Power supplied both above and below the active part of the core;
- (4) Axial power distribution as in SHRT-45R.

The axial power distribution below the active part of the core was calculated in order to match the experimental steady state values of the coolant temperature at the lower and upper flowmeter thermocouples. The same axial power profile was then implemented symmetrically above the active part of the core for sensitivity cases 2, 3 and 4.

The boundary and initial conditions regarding the coolant inlet temperature and mass flow rate were implemented through time-dependent volume and time-dependent junction components and were derived from the experimental data. At the subassembly outlet, the

upper plenum pressure was imposed in a time-dependent volume based on the final calculation.

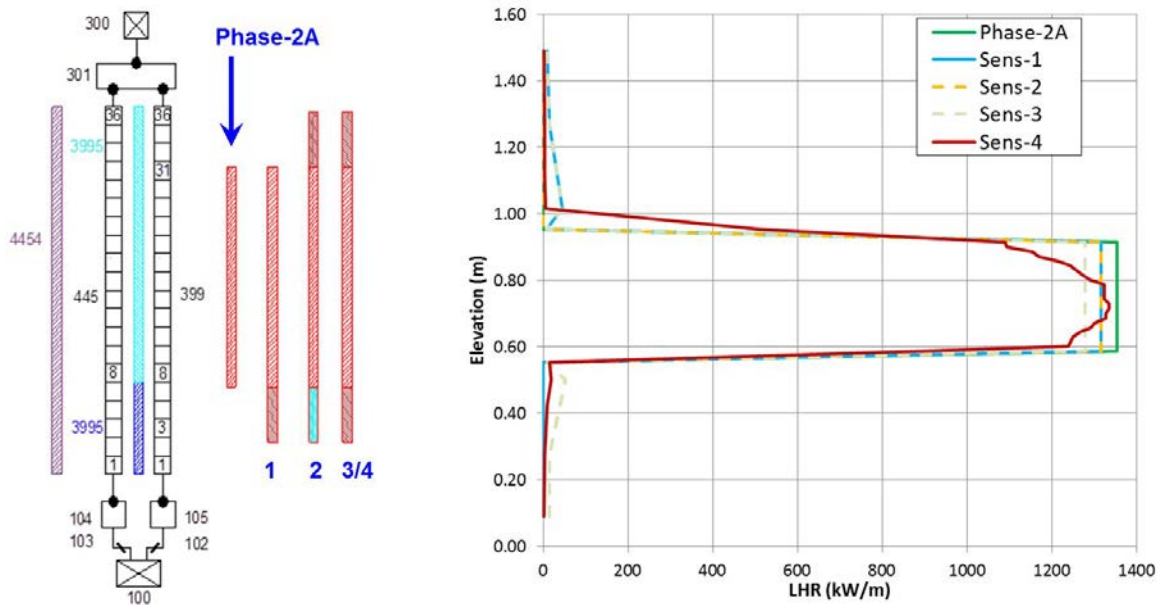


FIG. 283. Model of instrumented subassembly XX09 (left) and axial linear heat rates used in the sensitivity study (right).

In the following figures (FIG. 284 through FIG. 289) the coolant and cladding temperatures at various elevations of XX09 are shown for each sensitivity case and compared with the experimental data.

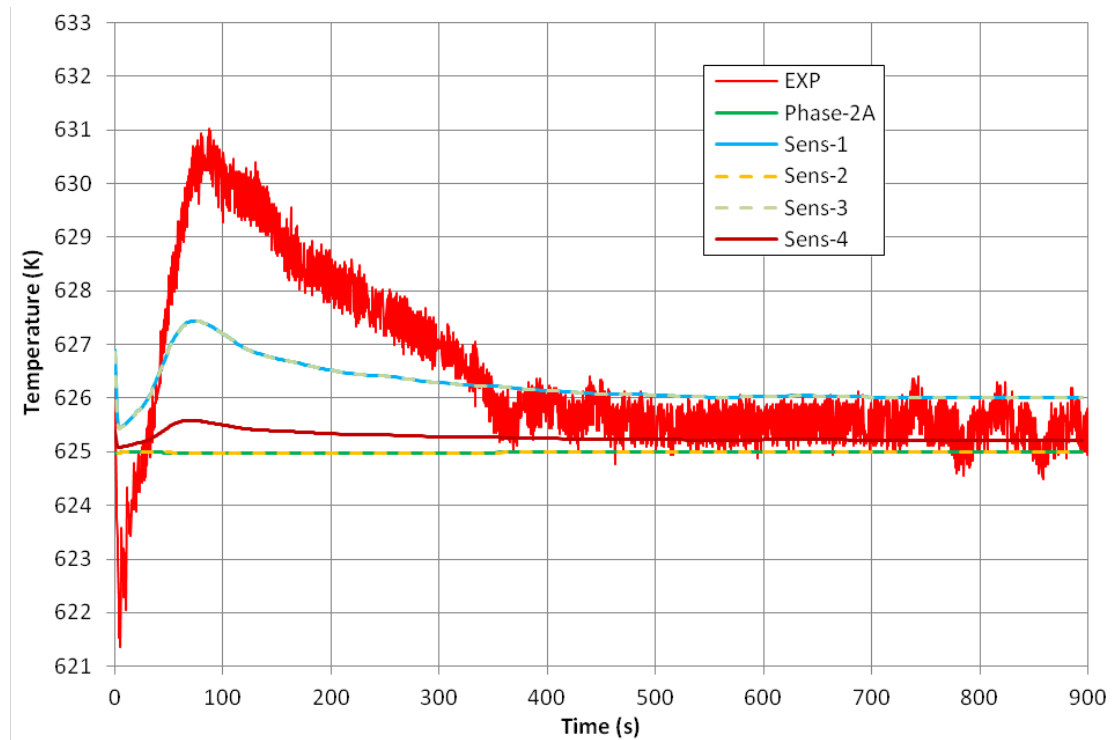


FIG. 284. XX09 lower flowmeter temperature.

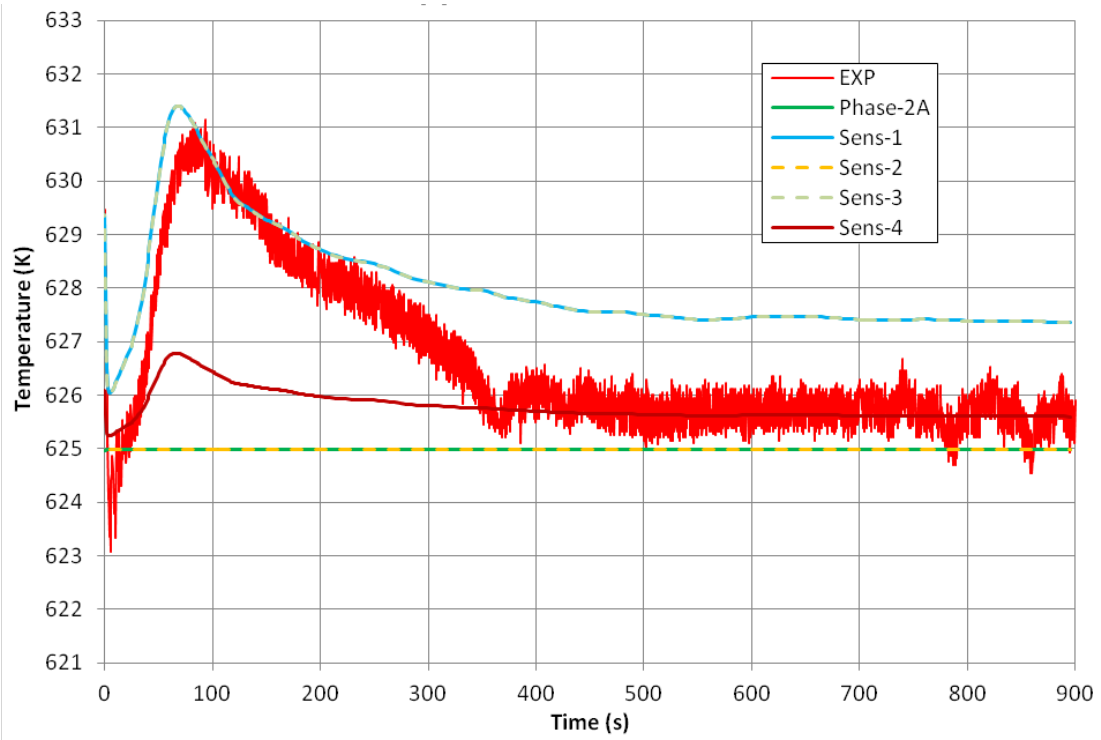


FIG. 285. XX09 upper flowmeter temperature.

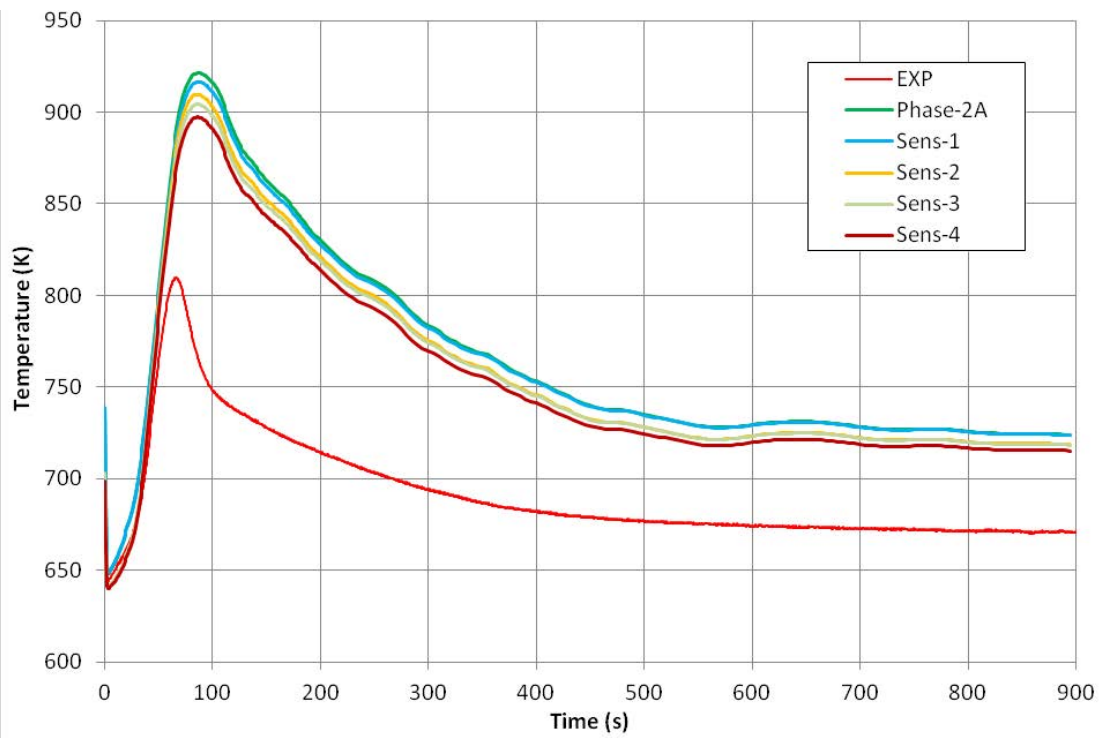


FIG. 286. XX09 mid-core temperature.

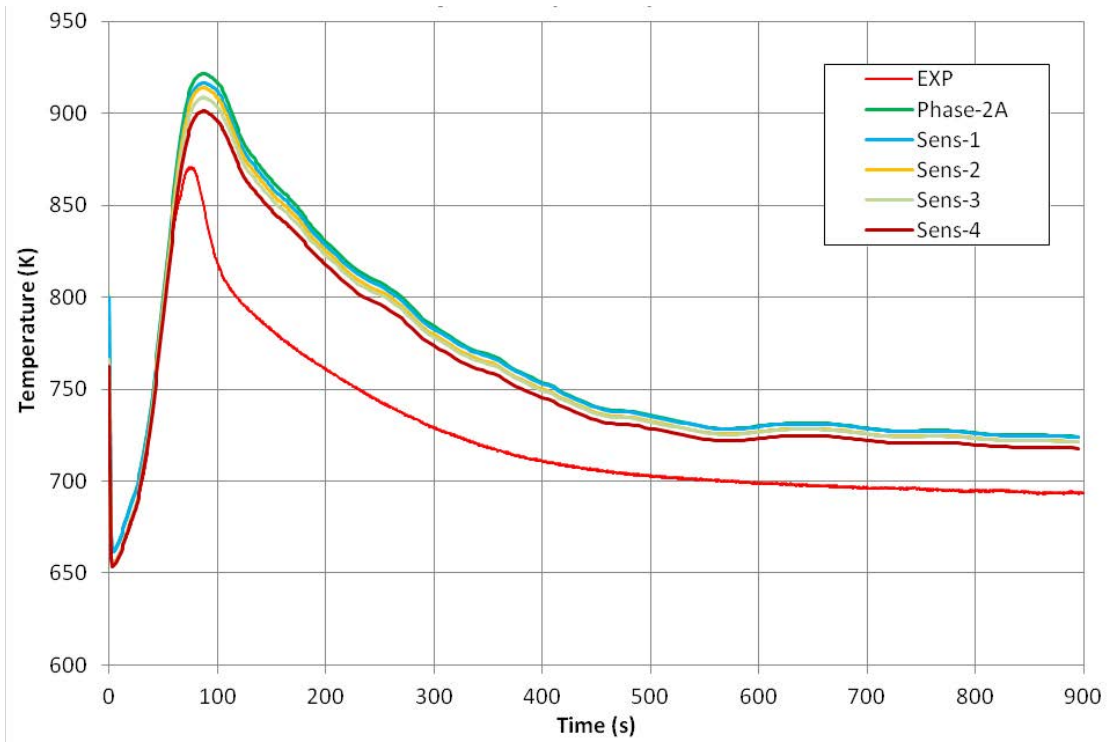


FIG. 287. XX09 top of core temperature.

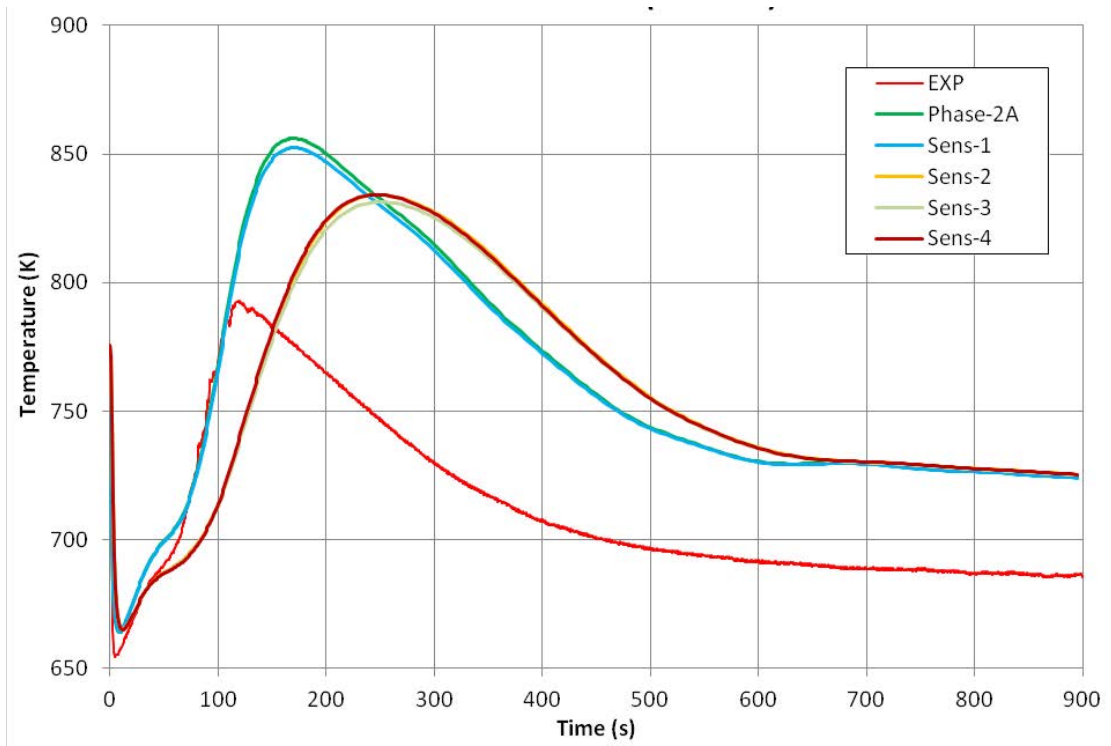


FIG. 288. XX09 coolant outlet temperature.

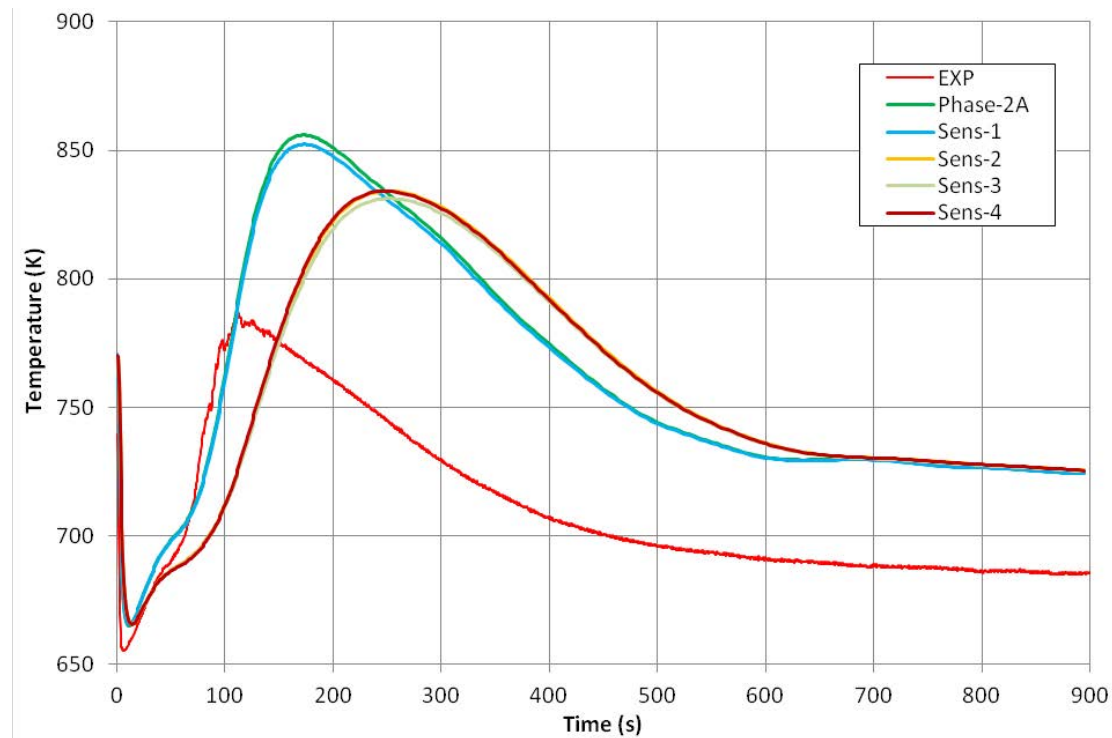


FIG. 289. XX09 thimble annulus temperature.

It can be noted that power supplied below the active part of the core (sensitivity cases 1, 3 and 4) positively affects the temperature trends at the lower and upper flowmeter thermocouples (see FIG. 284 and FIG. 285, respectively). For the cladding temperatures (FIG. 286 and FIG. 287) the shape of the temperature increase after the pump coastdown is well predicted by all the sensitivity cases, although the peak value is overestimated (especially at the middle of the core, see FIG. 286). This is due to the fact that the outer boundary condition of the heat structure simulating the guide thimble walls is isolated. Conversely, supplying power above the active part of the core (sensitivity cases #2, 3 and 4) results in only a minor effect on the temperature trends. In particular, in the coolant outlet and in the thimble annulus temperatures (FIG. 288 and FIG. 289) it produces a slight delay in the temperature increase after the pump coastdown compared to the experimental data and to the other sensitivity cases. It is interesting to note that a certain delay in the temperature increase could be detected in the experimental data of the coolant outlet and thimble annulus temperatures of instrumented subassembly XX10. Taking into account that the power to flow ratio of subassembly XX09 is much higher than that of subassembly XX10, it might be that for a non-fueled subassembly (i.e. subassembly XX10,) gamma heating is more relevant.

8.4. POLITECNICO DI TORINO (ITALY)

8.4.1. SHRT-17

The uncertainty analysis in SHRT-17 involved the mass flow rate to be prescribed as a boundary condition at the inlet of each subassembly in the thermal hydraulic module of the FRENETIC code. Due to the lack of experimental data for individual subassemblies, the boundary conditions were provided by RELAP5-3D[©] simulations performed by ENEA in the framework of this international benchmark. In view of the strong dependence of the computed results on the prescribed mass flow rate in each subassembly, and due to the uncertainties in the experimental data and the differences between data and results of the RELAP5-3D[©]

simulations, a parametric analysis on this set of values was performed, and the results reported and described in Section 7.9.5.1.

8.4.2. SHRT-45R

To confirm that the point-kinetic method is sufficient for the temporal integration of the neutronics equations, the initial part of the SHRT-45R transient was studied by both the quasi-static method and the point-kinetic method, in order that the results could be compared. As a reference case, the neutronics equations were integrated according to the predictor-corrector quasi-static method, using a shape timestep of 10^{-3} s and a reactivity timestep equal to that of the shape timestep; the convergence criterion imposed on the solution of the neutron flux at each shape timestep was a relative error of 10^{-5} (identical to that imposed for steady state conditions). A comparison of these results was made to those obtained with the point-kinetic method using a reactivity timestep equal to the neutronic/thermal hydraulic coupling timestep ($5 \cdot 10^{-3}$ s) and maintaining constant the parameters used to discretize the thermal hydraulic equations; representative results for some integral parameters are presented in TABLE 43. It is observed that the results are in agreement to within the imposed accuracy, which motivates the use of the point-kinetic method to analyze the transient on longer time scales.

Notwithstanding the foregoing results, it should be noted that the concordance of the quasi-static solution and the point-kinetic solution during the first 50 s may be correlated to other modelling assumptions. In particular, the hypothesis that the coolant flow through the core only decreases in magnitude but does not redistribute in the xy -plane possibly contributes to the observed point-like behaviour of the solution. In addition, the absence of certain feedback models in the FRENETIC code implies that some potential localized feedback effects are neglected, which also contributes to the observed point-like behaviour of the solution. Finally, it is assumed that the agreement of the results computed by the quasi-static and the point-kinetic methods, which is verified for the first 50 s of the transient, is true for the extrapolation over the entire 900 s of the transient.

TABLE 43. COMPARISON OF RESULTS BETWEEN THE PREDICTOR-CORRECTOR QUASI-STATIC METHOD AND THE POINT-KINETIC METHOD

t [s]	predictor-corrector quasi-static ($\Delta t_\phi=1 \cdot 10^{-3}$ s, $\Delta t_\rho=1 \cdot 10^{-3}$ s)				point-kinetic ($\Delta t_\rho=5 \cdot 10^{-3}$ s)			
	p(t) [W]	$\rho(t)$ [pcm]	$T_{c,max}(t)$ [K]	$T_{f,max}(t)$ [K]	p(t) [W]	$\rho(t)$ [pcm]	$T_{c,max}(t)$ [K]	$T_{f,max}(t)$ [K]
0.00	6.000×10^7	+0.000	751.6	814.1	6.000×10^7	+0.000	751.6	814.1
0.10	6.000×10^7	+0.05263	751.6	814.1	6.000×10^7	+0.05272	751.6	814.1
1.00	5.987×10^7	-1.449	753.3	814.9	5.987×10^7	-1.450	753.3	814.9
10.0	4.406×10^7	-128.9	877.9	915.7	4.404×10^7	-129.0	878.0	915.8
50.0	1.619×10^7	-259.2	966.2	979.2	1.618×10^7	-259.3	966.0	979.0

Δt_ϕ : shape timestep; Δt_ρ : reactivity timestep; t: time; p(t): total power; $\rho(t)$: net reactivity; $T_{c,max}(t)$: peak coolant temperature; $T_{f,max}(t)$: peak fuel centreline temperature.

8.5. UNIVERSITY OF FUKUI (JAPAN)

8.5.1. Comparison between system codes

The NETFLOW++ results were cross-checked by running a second simulation of the SHRT-45R test using the RELAP5-3D code. Details of the two simulations are summarized in [129]. FIG. 290 to FIG. 295 show a comparison of the pump flow rate, IHX temperatures, Z-Pipe inlet temperature and temperature at the top of the XX09 SA. As illustrated in these figures, both codes calculate the SHRT-45R transient similarly. The IHX calculated temperatures at the inlet of the primary and the outlet of the secondary overpredict the measured temperatures. Therefore, it is clear that overprediction of these temperatures is not code dependent. In terms of the temperature in the steel SA XX10, NETFLOW++ overpredicts the peak outlet temperature, while RELAP5 underpredicts the temperature.

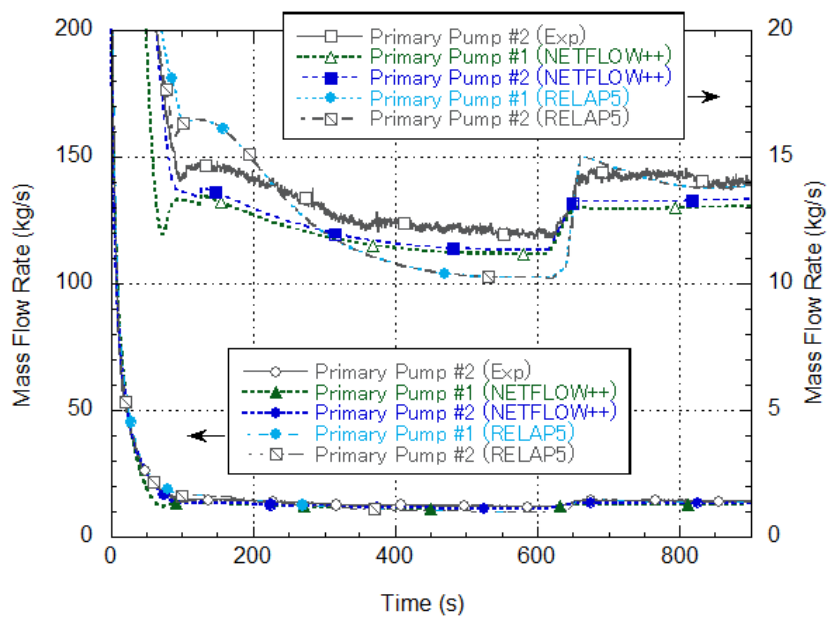


FIG. 290. Pump flow rate comparison among NETFLOW++, RELAP5 and measured data.

8.5.2. Analysis of uncertainty due to cross-section covariances.

During the generation of the ECCO nuclear data libraries, covariance matrices were produced for those isotopes for which this information is available in the evaluated nuclear data libraries. Covariance data is processed with the ERRORR module of NJOY and subsequently reformatted to the AMERE format for use in ERANOS. 33 energy groups were used for the covariance data. More details can be found in [130]. The uncertainty of k_{eff} due to cross-section covariances was analyzed with first-order perturbation theory; for the uncertainty of reactivity differences (Doppler effect, void effect), extended generalized perturbation theory was used. The standard routines in ERANOS v2.0 were used for all analyses. Forward and adjoint fluxes were calculated with diffusion theory in a 3-D hexagonal-Z geometry with 33 energy groups.

It should be pointed out that for this analysis, the spatial model of the “reference” and “perturbed” cores must be identical. Thus, it is not possible to analyze the uncertainty of the expansion feedback effects, since the spatial models differ between the reference and the expanded core.

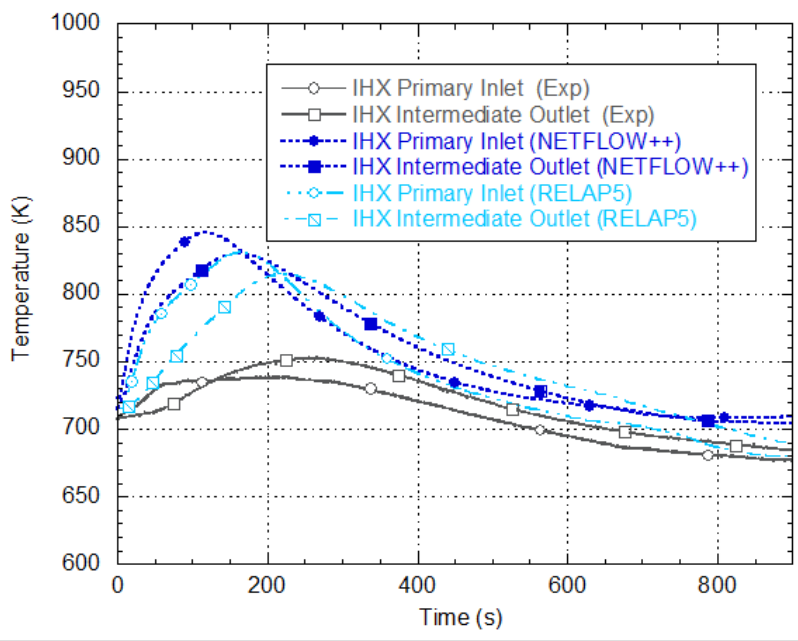


FIG. 291. IHX temperatures comparison among NETFLOW++, RELAP5 and measured data.

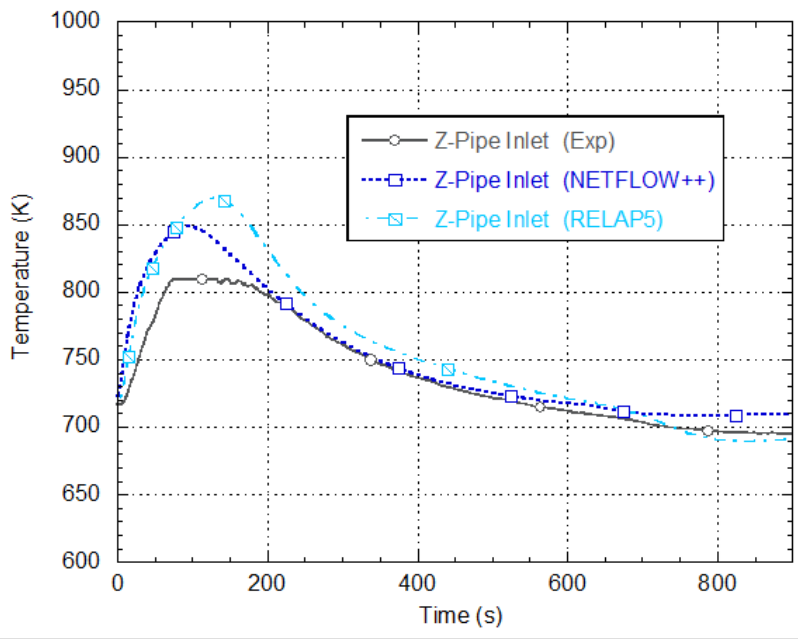


FIG. 292. Z-Pipe inlet temperature comparison among NETFLOW++, RELAP5 and measured data.

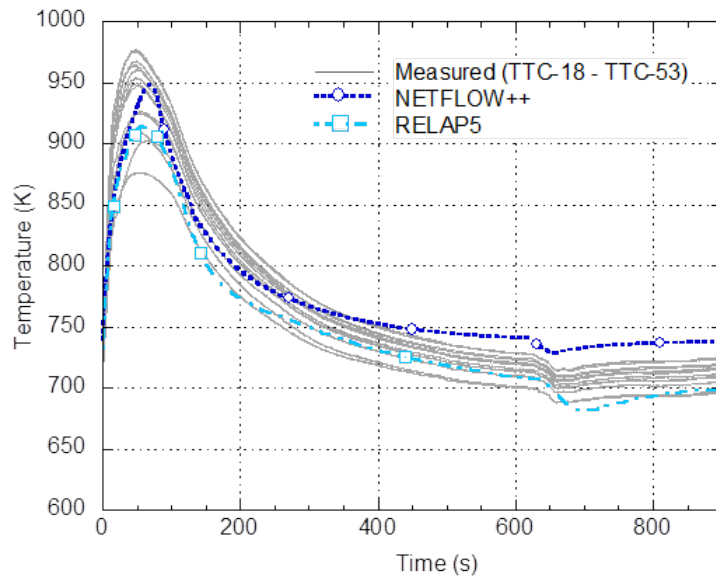


FIG. 293. XX09 temperature comparison among NETFLOW++, RELAP5 and measured data.

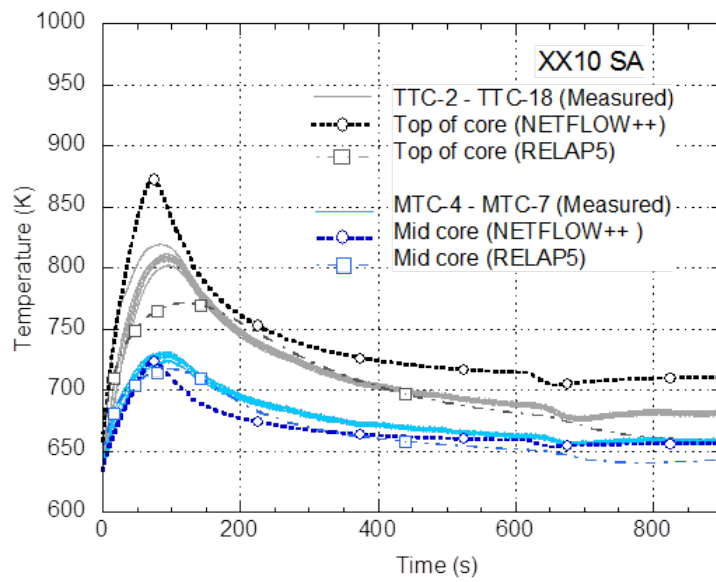


FIG. 294. XX10 temperatures comparison among NETFLOW++, RELAP5 and measured data.

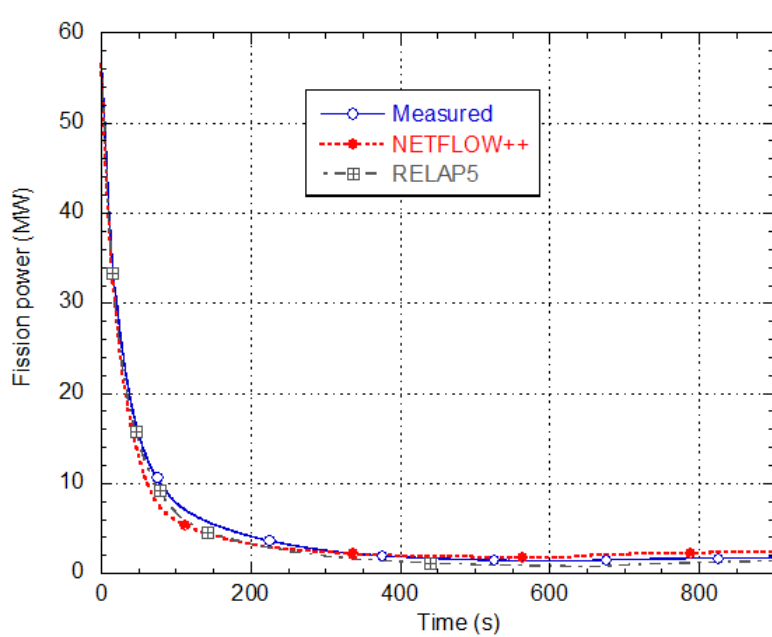


FIG. 295. Fission power comparison among NETFLOW++, RELAP5 and measured data.

8.6. KOREA ATOMIC ENERGY RESEARCH INSTITUTE (REPUBLIC OF KOREA)

8.6.1. MARS-LMR

In order to improve the calculation results in MARS-LMR, sensitivity tests for several parameters were conducted. These parameters were selected among the dependent parameters. The parameters in the sensitivity test are summarized in TABLE 23 in Section 7.12.5.3. The parameters with the greatest impact on the results will be described in this section.

To match the pump 2 flow, the minor loss coefficient, K was changed to be a function of Reynolds number during the transient.

The inter-subassembly heat transfer was considered in XX09 and XX10. FIG. 296 shows the actual arrangement of the instrumented SAs and their surrounding SAs for SHRT-17. In the modelling, a stagnant sodium gap between the instrumented SA and surrounding SAs was added. Moreover, it was assumed that all surrounding SAs were driver fuel subassemblies.



FIG. 296. The XX09 and XX10 instrumented subassemblies and their neighbouring subassemblies during SHRT-17.

In addition, sensitivity tests for heat transfer through the inner wall of the subassembly duct and in the thimble region were carried out with weighted heat transfer coefficients. These parameters directly affect the inter-subassembly heat transfer. In XX09, when the heat transfer through both the inner wall and the thimble region was decreased, the peak coolant temperature increased due to reduction of heat loss. In XX10, when the heat transfer through the inner wall of the subassembly duct was decreased, the peak coolant temperature decreased due to reduction of heat addition. The sensitivity study found that heat transfer in the thimble region is not an influential parameter. In conclusion, the coolant temperature in XX09 and XX10 can be modified by adjusting the inter-subassembly heat transfer, which is governed by heat transfers through both the duct and the thimble. Inter-subassembly heat transfer is especially influential in XX10, as shown in FIG. 297. This trend was also observed in SHRT-45R.

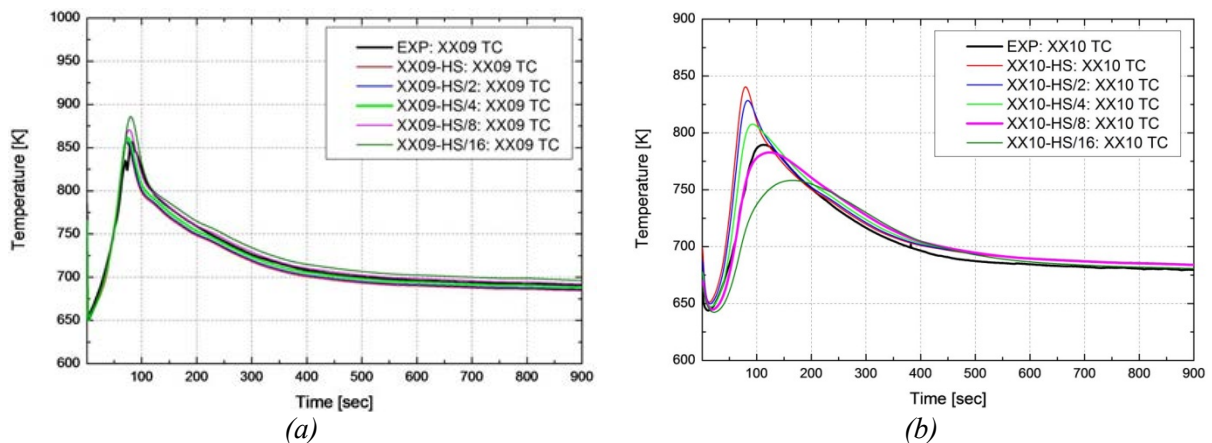


FIG. 297. Results of sensitivity analysis for heat transfer through the inner wall of the duct of (a) XX09 and (b) XX10.

Internal heat structures such as the IHX shroud, Z-Pipe walls and reactor shield were added in the final calculation. When these heat structures were added, the IHX temperatures became close to the experimental results, as shown in FIG. 298. As legends in FIG. 298 indicate, the individual structure effect was analyzed and the legend “All” indicates the case where all heat structures were applied. In addition, a sensitivity test for each structure was conducted with a weighted heat transfer area. The highest sensitivity was observed in the Z-Pipe, as shown in FIG. 298(c). Some deviation from the experimental results was still observed.

All decay heat models that are available in MARS-LMR: ANS73, ANS79 and ANS94, were compared for the SHRT-45R analysis. The lowest decay heat was observed using ANS94. However, the initial fission power was still underestimated by 16%, so a correction factor of 0.84 was applied to the decay heat model of ANS94.

A sensitivity analysis for reactivity feedback models was performed. The most sensitive feedback model was the axial expansion model. When the axial expansion feedback was reduced, the predicted fission power increased initially, then decreased later in the transient, as shown in FIG. 299. The fission power still deviated from the experimental results after about 300 seconds.

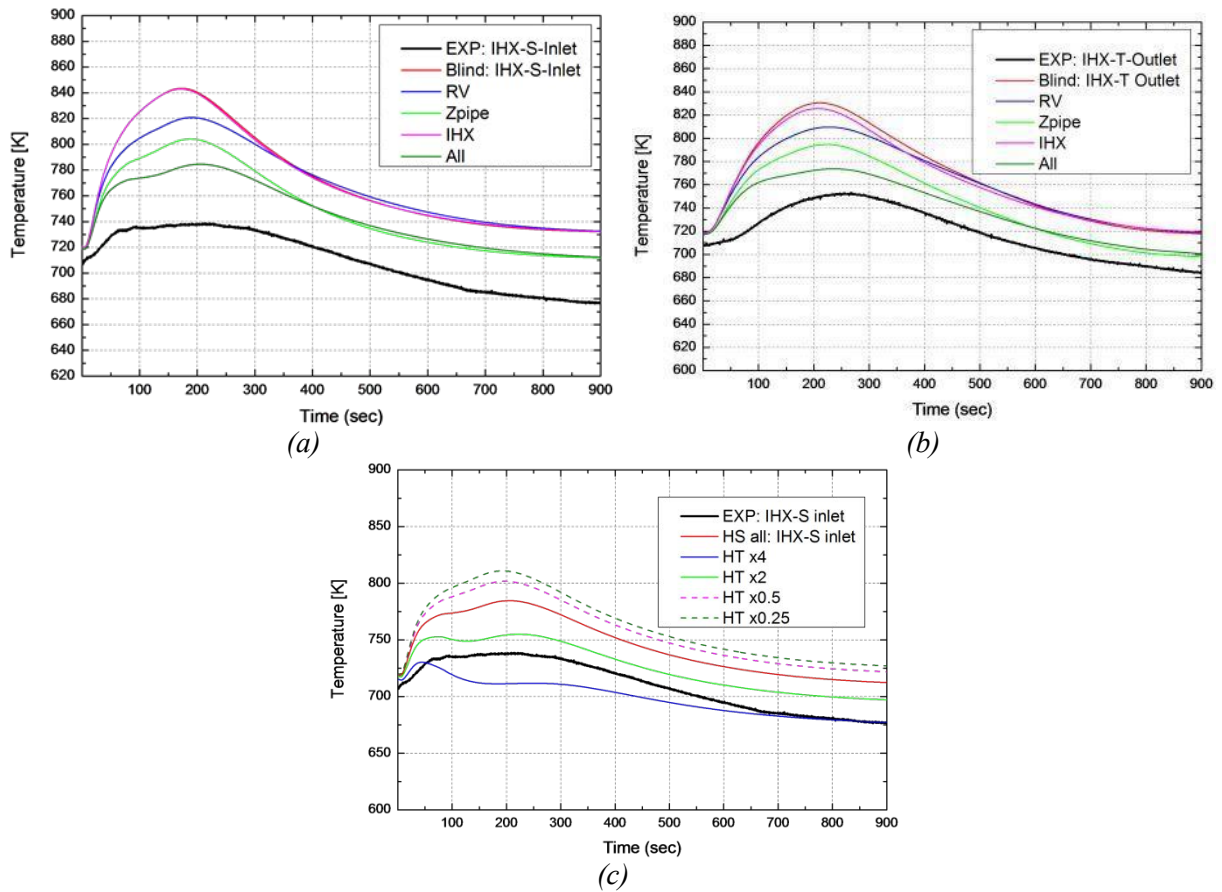


FIG. 298. Internal heat structure effect on temperatures during SHRT-45R.

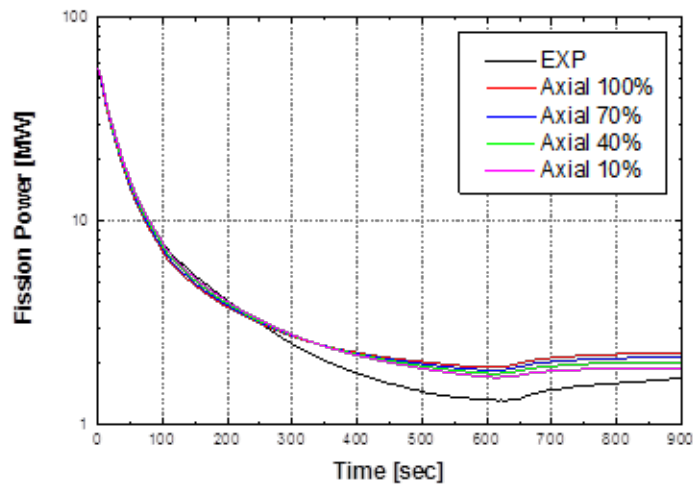


FIG. 299. Sensitivity analysis of fission power on axial expansion reactivity.

8.7. KOREA INSTITUTE OF NUCLEAR SAFETY (REPUBLIC OF KOREA)

8.7.1. Parametric study of instrumented subassembly steady state temperatures

Simulation results for the coolant temperatures within the instrumented subassemblies (XX09, XX10) are influenced by parameters related to the power, flow and heat transfer. The thimble flow, subassembly power, inlet nozzle power (gamma heating), outer hexcan heat transfer

coefficient, and axial power shape were selected as the major parameters to investigate and determine their impact on the instrumented subassembly steady state temperatures at the FM2-T, MTC, TTC, TC, OTC and ATC axial locations.

For the thimble flow, the value was varied from zero to the value from the benchmark specification. For gamma heating at the inlet nozzle and for the outer hexcan heat transfer, the value was varied from zero to the value that approximately produced the temperature recorded at that location. The subassembly power was varied $\pm 10\%$ from the value given in the benchmark specification. The ranges of the parameters are listed in TABLE 44. The effect of parameter variation on the XX10 temperatures at the various axial locations is shown in FIG. 300.

TABLE 44. PARAMETER CASES FOR THE ESTIMATION OF TEMPERATURES FOR XX10

Parameter cases	Thimble flow (kg/s)	Subassembly power as a fraction of the benchmark specification value	Inlet nozzle power as a fraction of the subassembly power	Outer hexcan heat transfer (surface area fraction)	Axial power shape (cumulative power fraction at MTC location)
Reference value	0.2535	1	0	1	0.501 (flat power shape)
Case 1	0	0.9	0	0	0.501
Case 2	0.132	0.93	0.145	0.17	0.719
Case 3	0.2535	1	0.2	0.2	0.780
Case 4	-	1.1	-	-	-
Axial locations affected	MTC to ATC	MTC to ATC	Uniform temperature curve shift, FM2-T to ATC	TC to ATC	MTC to TC

The parametric study results showed that Case 2 best matched the XX10 initial temperature data, as shown in FIG. 300. A similar parametric study was done to investigate the XX09 steady state temperatures.

8.7.2. Effect of wire-wrapped fuel bundle correlations on the XX09 temperatures

For the phase 2 calculations, the form loss coefficient in the laminar region of the CTS correlation was increased by a factor of 2.5 for the wire-wrapped fuel bundles. The effect of increased pressure drop during SHRT-17 was investigated by varying the multiplication factor on the form loss coefficient for the laminar region of the CTS correlation between 1 and 5.

As the multiplication factor was increased, the predicted flows through pump 2 and XX09 decreased, but the predicted flows through XX10 and through the XX09 thimble increased during the natural circulation portion of the transient, as shown in FIG. 301. The XX09 temperature at the TTC location was influenced by the reduction of the XX09 flow. Therefore

the XX09 temperature peak at the TTC location increased as the multiplication factor increased, as shown in FIG. 302.

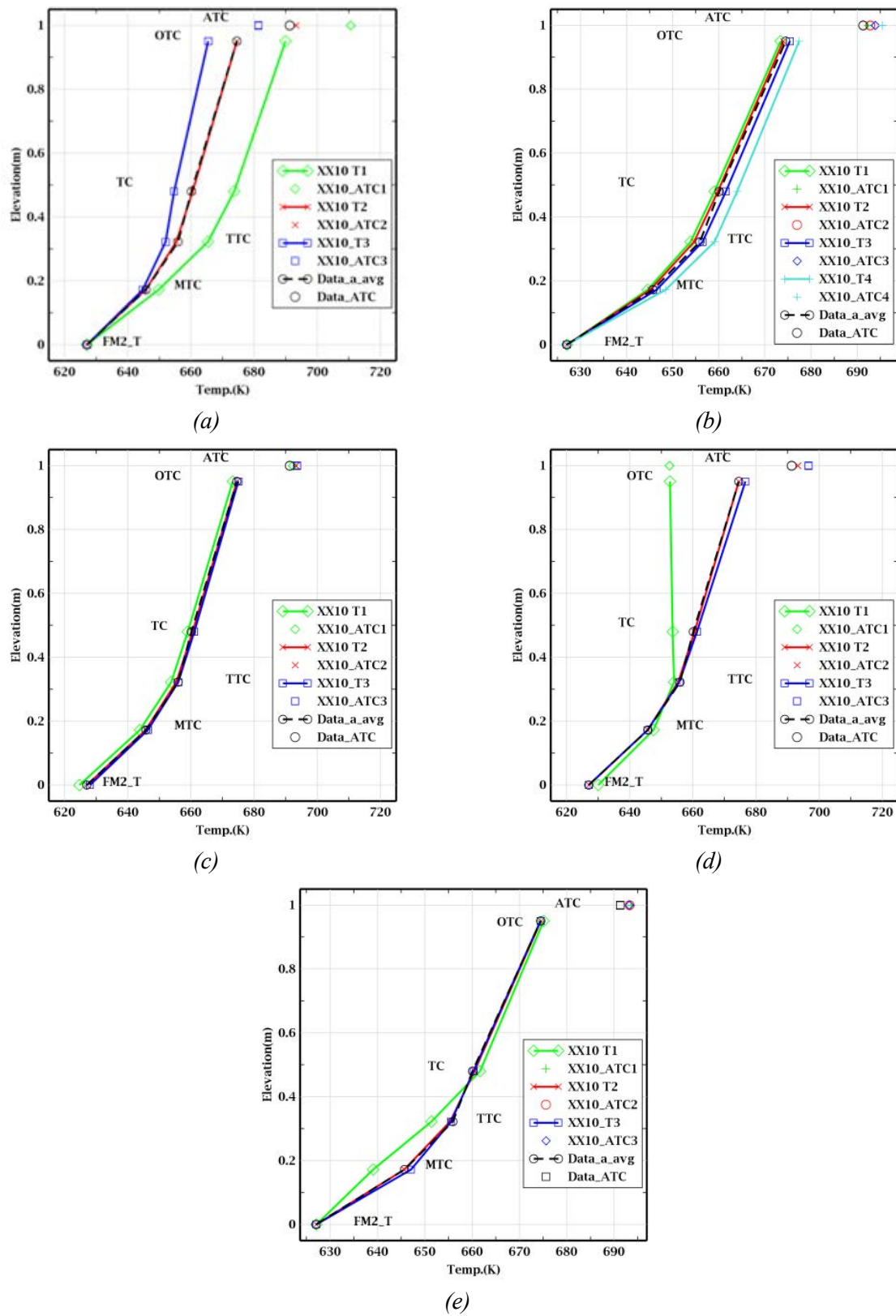


FIG. 300. Effect on the initial XX10 temperatures of (a) thimble flow, (b) subassembly power, (c) inlet nozzle power fraction, (d) outer hexcan heat transfer, and (e) axial power shape.

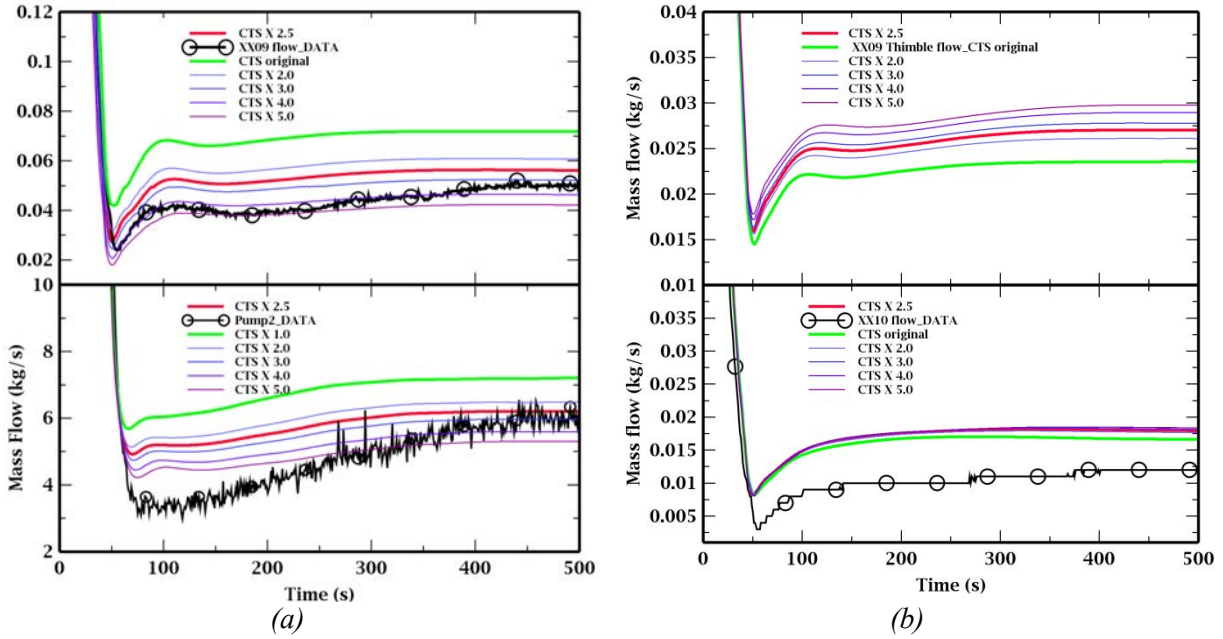


FIG. 301. Effect of the CTS correlation laminar region form loss coefficient multiplication factor on (a) pump #2 and XX09 flows and (b) XX09 thimble flow and XX10 flow.

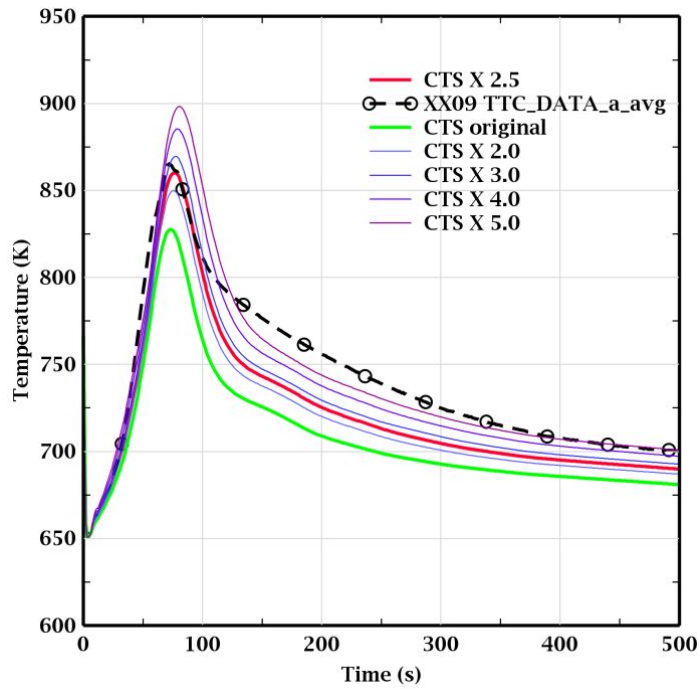


FIG. 302. Effect of the form loss coefficient multiplication factor on XX09 top of core temperature.

8.8. NRG (NETHERLANDS)

The following sensitivity calculations were performed for both SHRT-17 and SHRT-45R during the blind phase:

- (a) Sensitivity on heat transfer correlations. In the base case, the Mikityuk correlation [72] was used for tube bundles (Section 7.14.2). A sensitivity run was performed with the Ushakov correlation [118]. Results were very similar, which means that the results are not very sensitive to the choice of the heat transfer correlation;
- (b) Sensitivity on porosity and fuel swelling. In the base case, a gas porosity of 15% and sodium porosity of 10% were used. A sensitivity run was performed with the solid material (both porosities equal to zero). Results showed that the choices of porosity and fuel swelling have a noticeable effect on maximum fuel temperature;
- (c) Sensitivity on definition of Doppler coefficient (SHRT-45R only). The base case was performed assuming logarithmic Doppler feedback. A sensitivity run was performed assuming linear Doppler feedback (temperature independent reactivity feedback). Results were very similar;
- (d) Sensitivity on reactivity feedback from a Control Assembly (SHRT-45R only). In the base model calculations the CA reactivity was assumed to be -5.534×10^{-4} \$/K, following [106]. An independent estimation was made using alternative data which led to a CA reactivity coefficient of $-1.63E \times 10^{-4}$ \$/K. The minimum value of the CA reactivity was -0.06 \$ with the first value and -0.02 \$ with the second value. The overall results remained very similar, which shows that the CA makes a very small contribution to the total reactivity in this case;
- (e) Sensitivity on decay heat and fission power definition. For the base case the group constants for the 11-group decay heat producers were tuned following the data shown in [106]. For the sensitivity run the default group constants were assumed. Differences in the fission and decay power were noticeable, but other results were very similar;
- (f) Sensitivity on auxiliary EM pump characteristics. Somewhat different values were found concerning the nominal parameters of the EM pump. The base calculation was performed with $V_N = 0.0315$ m³/s and $\Delta P_N = 1724$ Pa, following [106]. A sensitivity run was performed for SHRT-45R with $V_N = 0.0462$ m³/s and $\Delta P_N = 1750$ Pa, following [131]. Results were very similar.

8.9. IBRAE-RAN (RUSSIAN FEDERATION)

To investigate the influence on calculation results of parameters in the EBR-II model developed and implemented using SOCRAT-BN models, a sensitivity analysis was performed. For both SHRT-17 and SHRT-45R, 100 calculations were performed for each parameter selected, where the model parameters were randomly varied within fixed ranges. The parameters selected and the ranges are presented in TABLE 45 below. A normal distribution of the parameters in a given range was chosen.

The sensitivity of the MCP №2 mass flow rate, the peak cladding temperature and the XX09 sodium outlet temperature to values of the model input parameters was investigated. Sensitivity of the total core power was also investigated for the SHRT-45R transient. Results for SHRT-17 are presented in FIG. 303 and for SHRT-45R in FIG. 304. For each plot, three curves are presented – for maximum values, minimum values and base values.

The difference between maximum and minimum values for MCP-2 mass flow rates in SHRT-17 was about 0.8 kg/s. The difference in the maximum and minimum peak cladding temperature was about 20 K. The same is true for the sodium outlet temperature in XX09.

TABLE 45. PARAMETERS AND RANGES CHOSEN FOR SENSITIVITY ANALYSES

Parameter	SHRT-17	SHRT-45R
Thermal power	[0.97;1.03]	-
MCP head	[0.95;1.05]	-
Heat transfer coefficient in a core	[0.85;1.15]	-
IHX heat transfer in primary side	[0.85;1.15]	-
IHX heat transfer in a secondary side	[0.9;1.1]	-
Outlet cladding diameter	[0.99;1.01]	-
Secondary side mass flow rate	[0.97;1.03]	-
Natural convection heat transfer	[0.9;1.1]	-
Secondary side sodium inlet temperature	[0.995;1.005]	-
In-core sodium reactivity feedback	-	[0.9;1.1]
Core radial expansion	-	[0.9;1.1]
Core axial expansion	-	[0.9;1.1]
Fuel Doppler effect	-	[0.9;1.1]
Decay heat	-	[0.9;1.1]

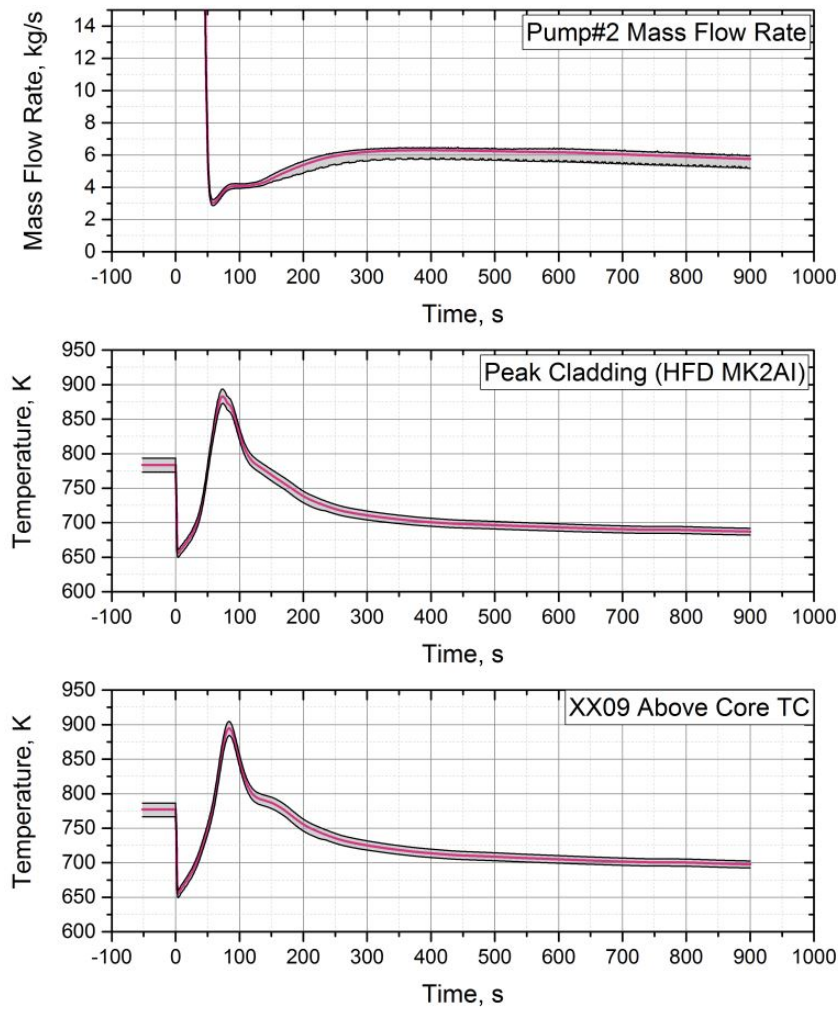


FIG. 303. SHRT-17 sensitivity analysis results.

The maximum calculated value for the total core power at the end of the SHRT-45R transient was 5.9%, minimum value – 5.5%. At time 100s, the difference between maximum and minimum peak cladding temperature was about 30 K. The same is true for the XX09 sodium outlet temperature.

The maximum influence on the peak cladding temperature was from the primary pump head parameter.

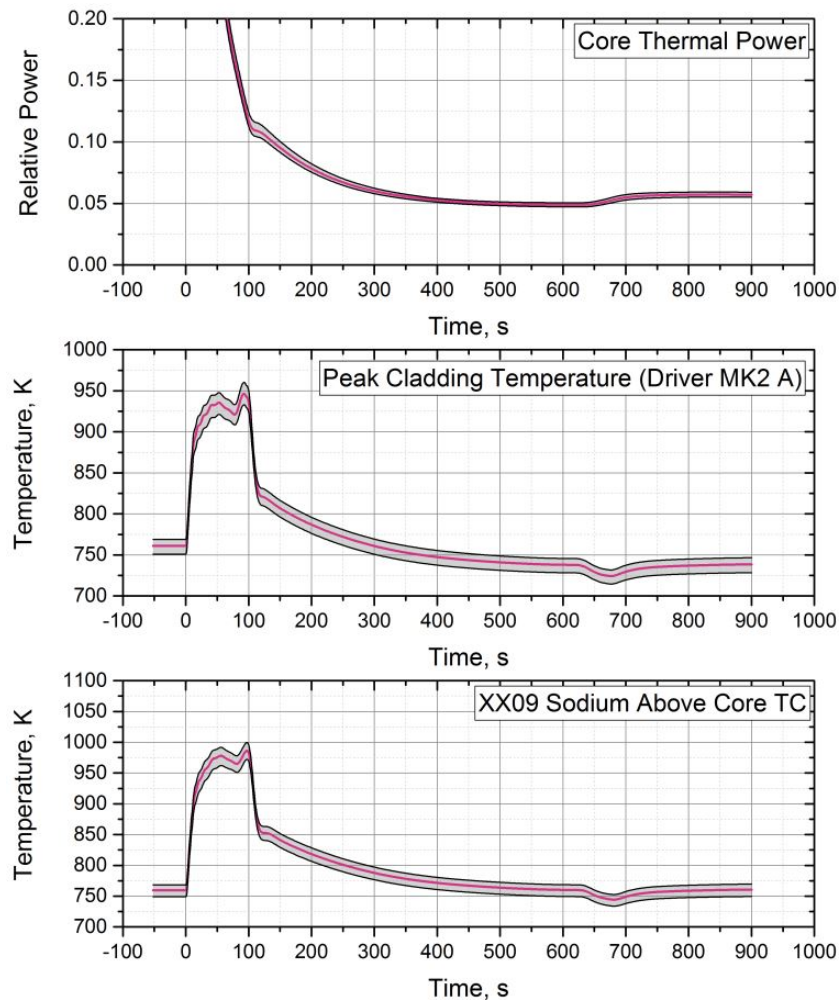


FIG. 304. SHRT-45R sensitivity analysis results.

8.10. PAUL SCHERRER INSTITUTE (SWITZERLAND)

The major contributors of uncertainties in the PSI TRACE calculations are simplifications in the geometrical model and also statistical errors in the Serpent Monte Carlo calculations. The impacts from the geometrical model simplifications have been discussed Section 7.16.2.1, with a recommendation that future development of the model include 3-D representation of the cold pool. This section will focus on the impact of statistical errors of safety-related neutronic parameters obtained from Serpent on the TRACE calculation results.

Due to the huge negative reactivity insertion incurred by the reactor SCRAM protection action after the initiation of the SHRT-17 transient, impacts from statistical errors in the safety-related neutronic parameters listed above were calculated to be negligible compared to those caused by simplifications in the geometrical model of TRACE. However, for the

unprotected SHRT-45R transient, the reactivity responses were not masked by the large negative reactivity insertion from the control rods. Therefore, sensitivity studies for SHRT-45R were performed.

As seen from FIG. 305, impacts from uncertainties in all reactivity parameters individually on the maximum coolant temperature at the core outlet are negligibly small (less than 2 K), which confirms that the transient simulations using safety coefficients obtained from Monte Carlo calculations were comparable in accuracy to the ones using safety coefficients obtained from deterministic calculations, as done by Argonne. Differences between the TRACE transient simulation results and the results from Argonne are mainly due to simplifications of hydraulic components (such as pumps, hot/cold pool) in the TRACE model and limitations of the codes.

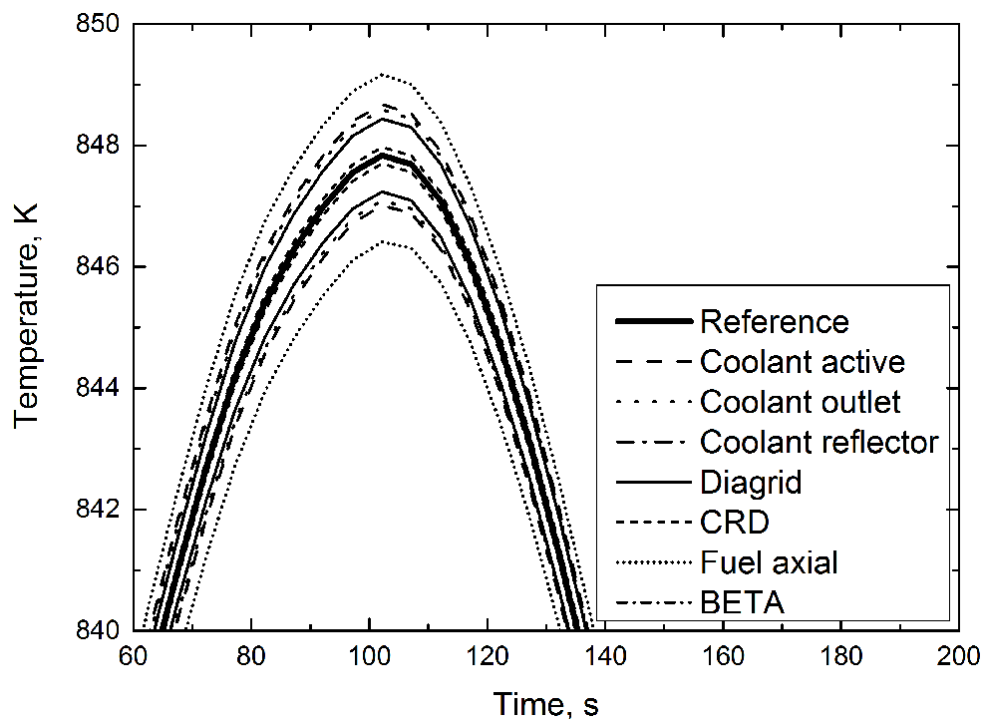


FIG. 305. Impact of statistical uncertainty of core safety-related parameters on the core outlet coolant temperature during the SHRT-45R transient.

8.11. TERRAPOWER (USA)

8.11.1. Sensitivity to heat transfer correlations

The applied heat transfer correlation was varied among those shown in TABLE 34 (Section 7.17.2.2). The choice of heat transfer correlation has a negligible impact on reactivity feedback (as measured by change in % error in predicting fission power). This is demonstrated in FIG. 306.

The variation of heat transfer correlation affected peak cladding and peak fuel temperatures by only 2°C, as shown in FIG. 307.

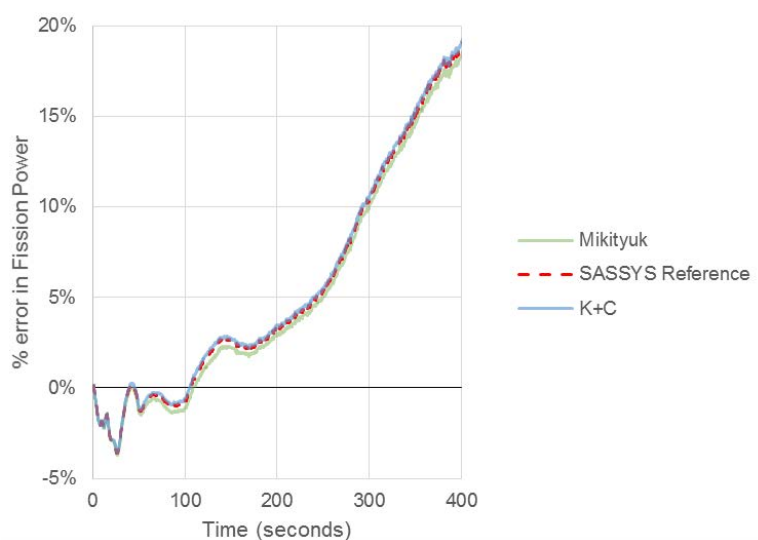


FIG. 306. Accuracy of fission power as a function of heat transfer correlation.

8.11.2. Sensitivity to pressure drop correlations

TABLE 46 summarizes the three modelling assumptions for pressure drop correlations that were investigated.

TABLE 46. SUMMARY OF HYDRAULIC SENSITIVITY RUNS

Name of sensitivity run	Correlation in wire-wrapped bundles (Channels 1,2,5,6,7, 8,9,10)	Correlation in non-wire-wrapped bundles (Channels 3,4,11,12,13)
Reference (Blasius)	Blasius	Blasius
CTP	CTP	CTP
CTP Wire	CTP	Blasius

The effect of varying the hydraulic correlations can be summarized as follows:

- (a) Severity of flow reversal in channel 13 (outer reflector) is affected by the choice of correlation. The largest flow reversal occurs in the reference case, where Blasius is applied;
- (b) The flow redistribution between driver channels 1 and 10 is significant (7% maximum difference in normalized flow, when compared to the previous model which grouped these subassemblies and, by definition, assumed their flow was identical);
- (c) Flow redistribution between channel 1 and 11 is even more significant and affected by the choice of hydraulic correlation. The reference case produces the most severe relative flow redistribution. This is shown in FIG. 308;
- (d) In addition to the previously discussed issues with XX09 flow rate data, a significant disparity (23%) exists between the XX10 experimental flow rate (0.296 kg/s) and the benchmark prescribed value (0.372 kg/s). Variations in hydraulic correlations are insufficient to explain the discrepancy between the SAS4A/SASSYS-1 flow rate for XX10 and the experimental measurement. Without being able to use either of these flow rates, it is difficult to specifically validate the choice of hydraulic correlations.

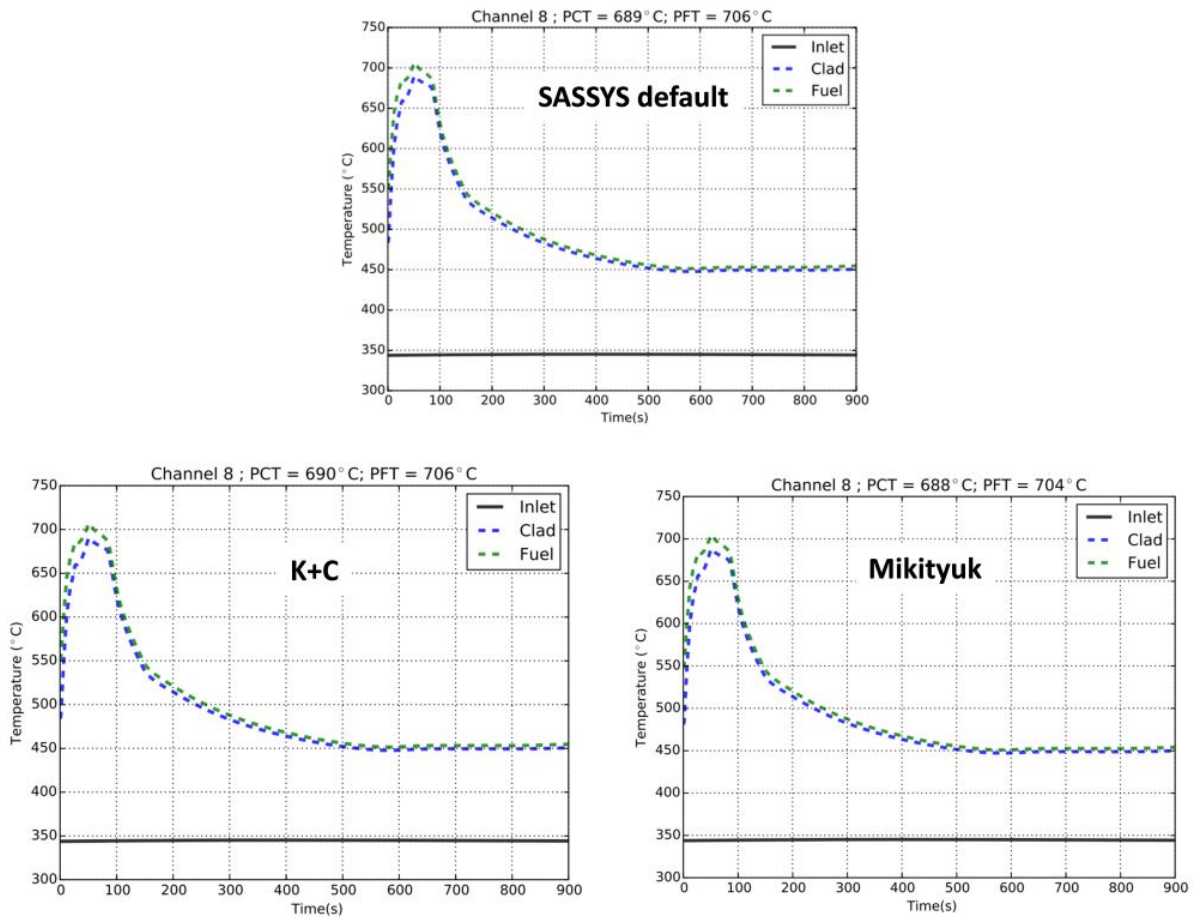


FIG. 307. Peak cladding and fuel temperatures for three heat transfer correlations.

The flow redistribution towards the inner drivers can be explained by the fact that the reflector subassembly enters the laminar flow region at ~ 30 seconds, where the friction factors are much higher than those in the turbulent region (which the driver experiences). The choice of correlation can affect the initial orifice coefficient selected for each channel, which also affects the severity of the flow redistribution.

8.11.3. Sensitivity to assumed fuel properties

A sensitivity run was completed to investigate the effect of using the phase 1 axial expansion material properties (shown in Section 7.17.2.1, TABLE 32). The largest change in material property is the increase in the Young's modulus of the fuel from 2.8 GPa to 150 GPa (the value recommended in the SAS4A/SASSYS-1 manual) and the increase of the fuel expansion coefficient to 2.83×10^{-5} 1/K. The phase 1 properties produce a much less "stiff" (i.e., more pliable) fuel, so axial reactivity feedback is dominated by cladding expansion, coolant temperatures and the power to flow ratio of the channel. In contrast, the relatively stronger and more rapidly expanding fuel in phase 2 causes axial expansion feedback to be dominated by fuel temperatures and pin power. The results are shown in FIG. 309, where "reference" refers to the phase 2 results and the other results are obtained using an identical input deck with phase 1 fuel properties.

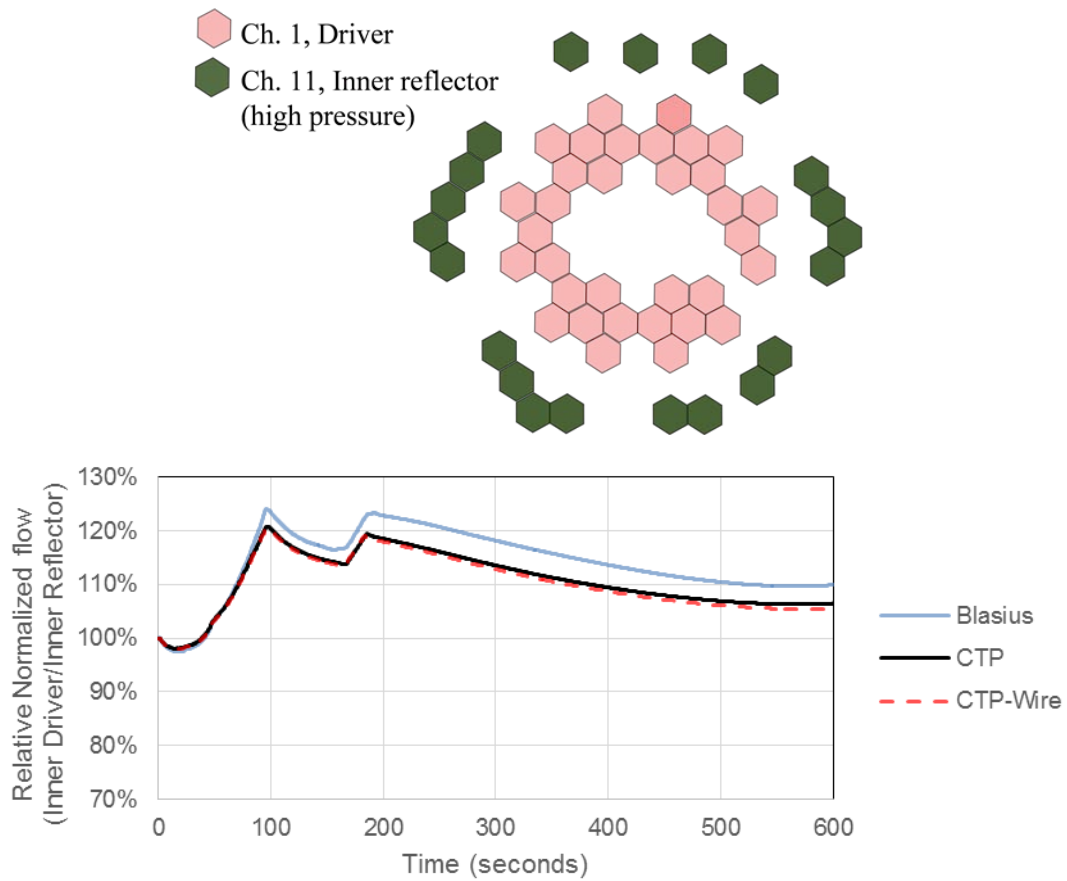


FIG. 308. Relative normalized flow between channel 1 and channel 11.

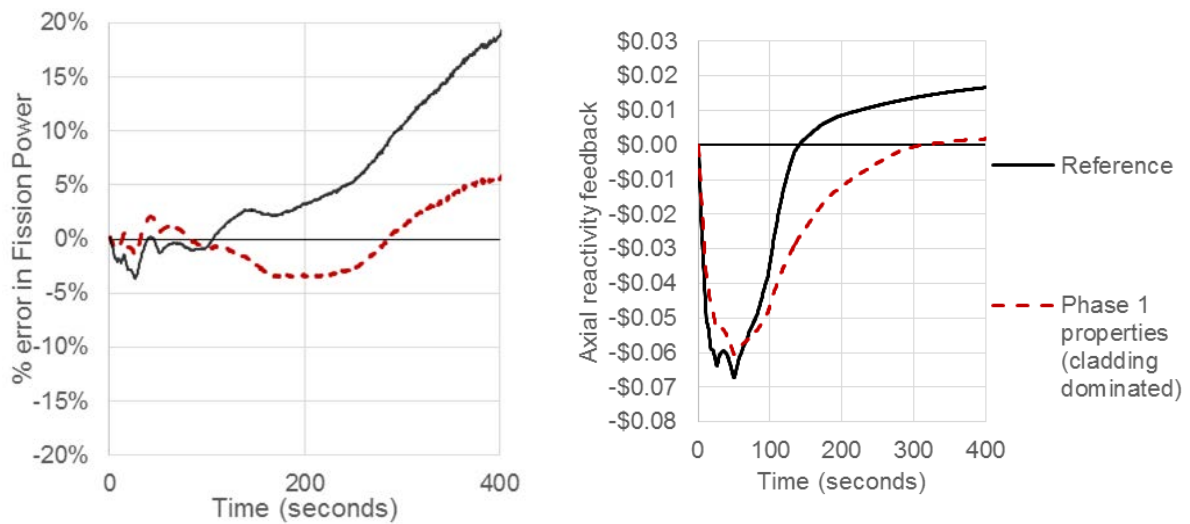


FIG. 309. Error (%) in fission power prediction (left) and axial reactivity feedback (right) for two sets of fuel and cladding mechanical assumptions.

Inspection of the reactivity feedback components shows that when using the phase 2 mechanical properties, the feedback from axial expansion is actually positive after ~130 seconds. The results demonstrate how fuel mechanical properties such as strength are important to the progression of unprotected loss of flow transients. High-strength fuel results in positive reactivity feedback at the end of the transient as power decreases and is detrimental. Use of the phase 1 fuel properties results in better agreement with the fission

power data, but this alone is insufficient to justify superior validity of the phase 1 fuel properties.

Overall, this sensitivity study shows that – at least in terms of predicting power and flow- this study has essentially reached a point of conclusion where the remaining residual error is small (on the order of a few cents of reactivity) and practically irreducible. The lack of detailed knowledge on some of the inputs (e.g., fuel properties), incomplete data set (e.g., missing/faulty flow rates), and error bounds on the experimental data make it very difficult to justify strong conclusions on whether one particular arbitrary input choice or modelling method is more valid than another.

8.12. ARGONNE NATIONAL LABORATORY (USA)

After the blind phase of the benchmark was concluded and the measured test data were released to the participants, Argonne performed a series of parametric and sensitivity studies on the SAS4A/SASSYS-1 model input parameters to determine where better agreement with the measured data could be achieved. One of the sensitivity studies focused on improving the reactivity feedback modelling for the SHRT-45R transient. Although the power prediction for SHRT-45R was close to the reference power level in absolute terms, in relative terms the SAS4A/SASSYS-1 model overpredicted power by as much as 60% towards the end of the transient. A reactivity feedback sensitivity study was performed to investigate the effect of the reactivity feedback input parameters on the SHRT-45R power prediction and to determine whether or not the differences were caused by user input or various modelling and experimental uncertainties.

In order to eliminate, or at least significantly reduce, the uncertainties beyond the reactivity feedbacks, a SHRT-45R SAS4A/SASSYS-1 model based on a simplified treatment of the primary circuit (PRIMAR-1) was created. In this simplified treatment, the coolant boundary conditions at the core inlet were specified by the user. This change alone reduced the power prediction difference from 60% to about 33% near the end of the transient, thus confirming that at least part of the original difference was not caused by the reactivity feedback modelling.

The results of the reactivity input sensitivity study with the PRIMAR-1 model show that significant changes would be needed in order to match the measured reactor power by modifying only the reactivity feedback user input parameters. Only the coolant density and the core radial expansion feedbacks are strong enough feedback effects to be able to compensate for the difference, and even these would require significant modifications. If the coolant density feedback alone were modified, it would need to be decreased by a factor of four to obtain very good agreement with the transient power. For the core radial expansion feedback, which is believed to be the most uncertain feedback effect in the simulation due to effects such as subassembly bowing, power is well matched if both the grid plate expansion is the only contributor to the radial expansion feedback effect (i.e., no load pads expansion) and the magnitude of the feedback is increased by a factor of five.

Other reactivity feedback modifications that were tested include variations for the fuel axial expansion reactivity feedback effect and updates to account for control rod driveline expansion in the cold pool. These did not produce any noticeable improvement in the power prediction. Therefore, based on the results of the reactivity input sensitivity study, it was concluded that, although uncertainties in the reactivity input for the SHRT-45R simulation remain, these uncertainties are relatively small and cannot be solely responsible for the

disagreement between the predicted and transient power levels. Other modelling and measurement uncertainties are likely responsible for the discrepancy.

After the reactivity feedback sensitivity studies, a series of parametric analyses were performed on several primary heat transport system model parameters to improve agreement with measured temperatures and flow rates. The first parameter that was examined was the pump locked rotor loss coefficient, an orifice coefficient for calculating the pressure drop through a stopped pump. A value of 1.0 was used initially, which led to well predicted SHRT-45R flow rates but overpredicted SHRT-17 flow rates due to insufficient flow resistance through the pump.

During the second phase of the benchmark, a parametric analysis was performed to determine what locked rotor loss coefficient was necessary to achieve good agreement with the measured SHRT-17 flow rates. With a coefficient of 3.6 instead of 1.0, agreement between the measured and predicted SHRT-17 flow rates was significantly improved. Additional investigations suggested that the pumps did not lock for SHRT-45R so the increased locked rotor resistance did not affect the SHRT-45R flow rates. See Section 7.18.5.3 for more details.

Next, sensitivity studies were performed for parameters related to upper plenum wall heat transfer, specifically the wall mass and sodium-to-wall heat transfer coefficient. These parameters were analyzed to determine if better agreement with the Z-Pipe inlet temperature could be obtained. The wall mass was sufficiently large that an unrealistically large or small value is necessary to affect the Z-Pipe inlet temperature; the wall mass was not changed. Sensitivity studies were performed on the upper plenum heat transfer coefficient with the reference SHRT-45R power level enforced as a boundary condition. Because of the complicated flow patterns, estimating the appropriate coefficient is difficult. A value of $700 \frac{W}{m^2-K}$ produced the best agreement with the measured data, and the model was changed accordingly. FIG. 310 illustrates the Z-Pipe inlet temperature for various upper plenum heat transfer coefficients.

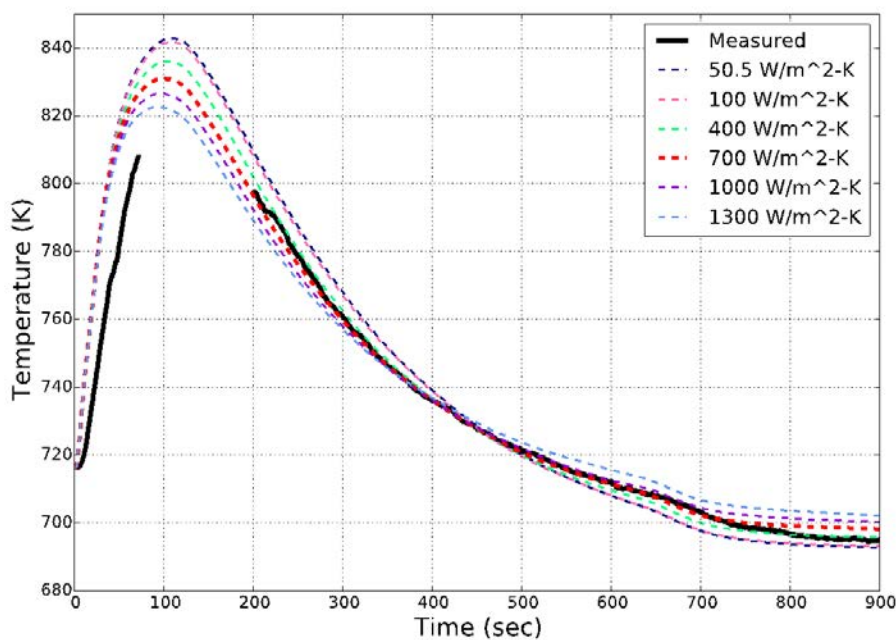


FIG. 310. Z-Pipe inlet temperature sensitivity studies.

Finally, a series of sensitivity studies were performed for parameters related to Z-Pipe wall heat transfer in order to improve agreement with the measured IHX inlet temperature, for which the shape was quite different from the measured Z-Pipe inlet temperature. None of the parameters that were changed led to improved agreement; the predicted IHX inlet temperature could be shifted up or down depending on how the parameters were changed, but the shape of the measured data could never be matched. Additionally, the Z-Pipe is a simple component, so unreasonable large changes could not be made to the values of those input parameters. FIG. 311 illustrates the IHX inlet temperature for various Z-Pipe heat transfer coefficients.

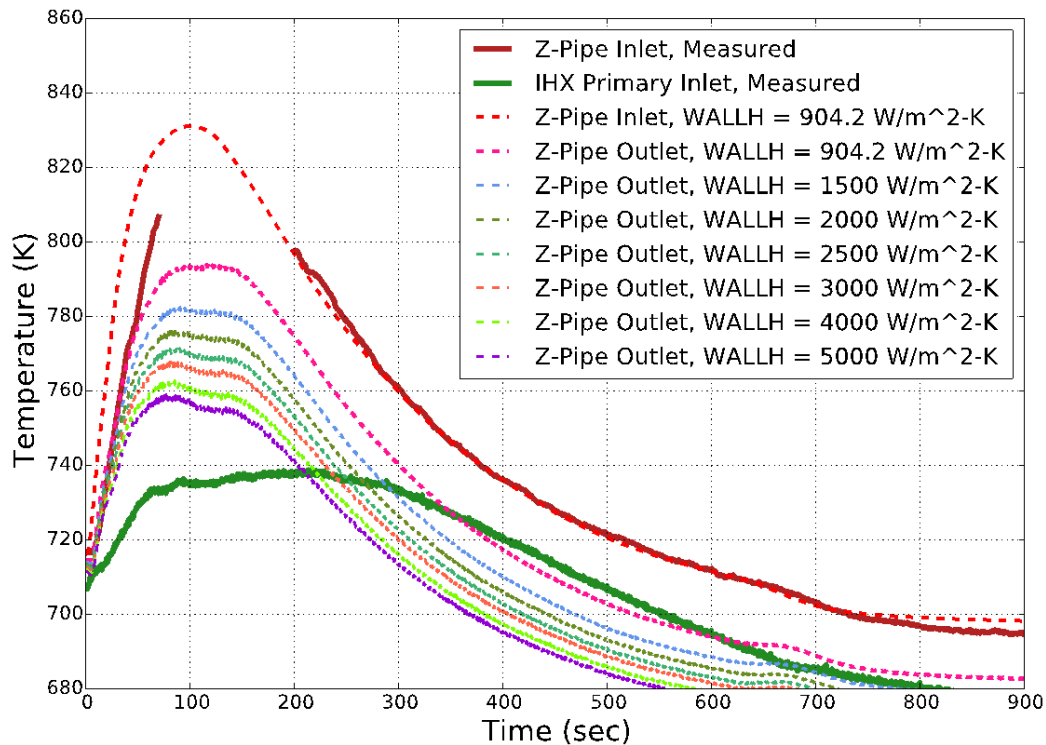


FIG. 311. IHX inlet temperature sensitivity studies.

9. QUALIFICATION PROCESS

9.1. THE SCCRED METHODOLOGY

A key feature of the activities performed in nuclear reactor safety technology is driven by the necessity to demonstrate the qualification level of each tool adopted within an assigned process and of each step of the process. Therefore, the qualification of best estimate codes, models, “best modelling practices” and uncertainty methods must be considered of great importance in order to ensure the validity of BEPU (Best Estimate Plus Uncertainty) analyses. A consistent code assessment supported by a qualified experimental database is an important step for developing a solid ground for the uncertainty evaluation in the frame of the BEPU approach. Thus, the SCCRED methodology [132] has been developed to generate a series of documents and tools to set-up a qualified experimental and calculated database for verification and validation (V&V) purposes for BEPU applications, i.e. best estimate computational codes and associated uncertainty methodologies.

A detailed description of the SCCRED methodology and the process for its application is given in Appendix III.

9.2. RESULTS OF THE QUALIFICATION PROCEDURE

9.2.1. The methodology

In the framework of this benchmark, a reduced version of the qualification process has been adopted, selecting a smaller set of parameters for performing the geometrical fidelity and the demonstration of achieving a steady state. In addition, only a quantitative analysis by the FFTBM (Fast Fourier Transport Based Method) was carried out, without performing the qualitative analysis (which is a mandatory step for a full application of the qualification process).

The main goal of the quantitative evaluation, as well as the analysis carried out, is to support the interpretation of the results calculated by the CRP participants, i.e. to provide quantitative measures of the discrepancies between the assumptions made by the participants and reference specification data. These quantitative measures support an understanding of the reasons for differences between the participants' results and the experimental data. It is important to specify that the applied process has no objective of providing a ranking among participants.

During the third RCM in March 2015, a preliminary list was presented of data to be requested from the participants in order to perform the analysis. After a discussion among the participants, some changes were implemented and a final list of the selected parameters was developed. After the meeting, N.IN.E. and Argonne started to extract the necessary reference values from the geometric information and steady state parameters for the SHRT-17 transient of the EBR-II benchmark. This phase required considerable effort and ongoing communication between N.IN.E. and Argonne to develop the proper reference values. After various revisions, a final template about the data to be requested for the qualification process was delivered to the participants at the end of 2015. The list includes different kinds of data for performing the different steps of the qualification process.

As a first step, the participants were asked to provide some details about their nodalization (e.g. number of heat structures (or mesh points) and hydraulic volumes used to model the EBR-II), as summarized in

TABLE 47.

Explanations were provided to the participants in order to promote a common understanding about the adopted definitions. In particular:

The term 'Hydraulic Volumes' indicates the points where fluid (mass and energy) balance equations are solved (see also definition in item #1 in

TABLE 47).

- (a) Thus the 'number of volumes for a generic component or part of the reactor' means the number of volumes into which this component or part of the reactor has been subdivided and simulated by the code and where the fluid balance equations of mass and energy are solved;
- (b) The term 'Hydraulic Component' refers to a set of 'Volumes' which are simulated by the code through a particular Hydrodynamic Component (e.g. a fuel channel can be represented in the RELAP5 code by a PIPE Hydrodynamic Component which is subdivided into 20 axial volumes).

The term ‘Mesh Points’ indicates the points where the heat conduction equations are solved (see also the definition of item #2) in

TABLE 47).

- (a) Thus the ‘number of meshes’ refers to a not-fluid domain, for instance the concrete or the metallic wall of the reactor;
- (b) The term ‘Heat Structure’ refers to a set of ‘Mesh Points’ (axially and radially) which the code uses to discretize a particular Heat Structure Component (e.g. the fuel rods inside a fuel channel can be represented in the RELAP5 code by a Heat Structure Component that has 20 axial meshes and 10 radial meshes).

TABLE 47. NODALIZATION FEATURES

#	Parameter
1	Total number of Hydraulic Volumes (i.e. points where balance equations are solved)
2	Total number of Mesh Points (i.e. points where heat conduction equations are solved)
4	Number of Hydraulic Volumes for modelling the primary side (without the pool)
5	Number of Hydraulic Volumes for modelling the intermediate side
6	Number of Hydraulic Volumes for modelling the pool
7	Number of Hydraulic Components for the whole core (from the top of the Upper Grid Plate to the bottom of the Upper Plenum)
8	Number of Hydraulic Volumes for the whole core (from the top of the Upper Grid Plate to the bottom of the Upper Plenum)
9	Number of Hydraulic Volumes per each Driver subassembly
10	Number of Hydraulic Volumes per each Partial Driver subassembly
11	Number of Hydraulic Volumes per High Flow Driver subassembly
12	Number of Hydraulic Volumes for the two Instrumented subassemblies (XX09 and XX10)
13	Number of Heat Structures for the whole core (from the top of the Upper Grid Plate to the bottom of the Upper Plenum)
14	Number of Mesh Points for the whole core (from the top of the Upper Grid Plate to the bottom of the Upper Plenum)
15	Number of Heat Structures for all Driver subassemblies
16	Number of Heat Structures for all Partial Driver subassemblies
17	Number of Heat Structures for all High Flow Driver subassemblies
18	Number of Heat Structures for the two Instrumented subassemblies (XX09 and XX10)

Regarding the demonstration of the geometrical fidelity, three different tables were developed and provided to the participants. These tables also included the reference values calculated by

Argonne and N.I.N.E. In particular, TABLE 48 and TABLE 49 contain the geometrical data for EBR-II including:

- (a) Hydraulic Volume, such as:
 - (i) Liquid volumes → 17 parameters
 - (ii) Flow areas → 4 parameters
 - (iii) Hydraulic diameters → 5 parameters
 - (iv) Lengths → 3 parameters
- (b) Heat structures, such as:
 - (i) Volumes or masses → 19 parameters
 - (ii) Surface areas → 5 parameters
 - (iii) Heated diameters → 1 parameter

TABLE 48. GEOMETRICAL FIDELITY OF THE NODALIZATION – HYDRAULIC VOLUMES

#	Parameter	Unit	Reference Value Y _E
1	Pool liquid volume		329.724
2	Primary circuit liquid volume (without pool)		10.96302
3	High pressure Inlet Plenum liquid volume		0.72120
4	Low pressure Inlet Plenum liquid volume		1.13086
5	Liquid volume in-core, Drivers		0.07927
6	Liquid volume in-core, Partial Drivers		0.02387
7	Liquid volume in-Core, High Flow Drivers		0.04098
8	Liquid volume in-Core, Experimental Subassemblies	m ³	0.03057
9	Liquid volume in-Core, XX09 and XX10		0.00641
10	Liquid volume in-Core, Steel/Dummy Subassemblies		0.01182
11	Liquid volume in-Core, Reflector Subassemblies		0.20081
12	Liquid volume in-Core, Blanket Subassemblies		0.34485
14	Upper plenum liquid volume		2.88817
15	Z-Pipe liquid volume		1.07548
16	IHX primary side liquid volume		1.99569
17	IHX intermediate side liquid volume		3.20209
18	High pressure pipe flow area	m ²	0.0730
19	Low pressure pipe min/max flow area		0.0082/0.0186
20	Z-Pipe flow area		0.0923
21	IHX primary side flow area		0.6362
22	Hydraulic diameter of core (at elevation of active part), Drivers, High Flow Drivers and Partial Drivers	m	0.00269
23	Hydraulic diameter of core (at elevation of active part), Dummy sub.		0.00265
24	Hydraulic diameter of core (at elevation of active part), Reflectors		0.00353
25	Hydraulic diameter of core (at elevation of active part), Blanket sub.		0.00165
26	High pressure pipe length		17.932
27	Low pressure pipe length		31.236
28	Z-Pipe length		11.652

#	Parameter	Unit	Reference Value Y _E
29	Hydraulic diameter of the intermediate side of the IHX		0.0134

In TABLE 50, each participant was asked to indicate the density at steady state conditions of the different materials that constitute the heat structures in order to properly calculate the values of the volume or mass of the respective heat structures.

TABLE 51 contains the volume of fluid within the primary and intermediate loops below selected elevations. Participants were asked to provide these values from their code model in order to build the two curves of volume versus elevation for both loops.

TABLE 49. GEOMETRICAL FIDELITY OF THE NODALIZATION - HEAT STRUCTURES

#	Parameter	Unit	Reference Value Y _E	
			Volume	Mass
Heat structure volume/mass in-Core (Drivers, High Flow Drivers and Partial Drivers):				
30	- Stainless Steel 316		0.03926	314.087
31	- Stainless Steel 304		0.12306	972.153
32	- Fuel Alloy, U-5Fs		0.01528	278.141
33	- Plenum Gas (Helium)		0.01241	0.00206
34	- Stagnant Sodium		0.00612	5.2719
Heat structure volume/mass in-Core (Experimental, Instrumented, Steel, Reflector and Blanket Subassemblies):				
35	- Stainless Steel 316		0.01468	117.474
36	- Stainless Steel 304		1.35443	10700.0
37	- Fuel Alloy, U-5Fs		0.00537	97.754
38	- Plenum Gas (Helium)		0.08799	0.01464
39	- Stagnant Sodium		0.10880	93.761
40	- Depleted Uranium		0.90926	17366.9
41	IHX heat structure volume/mass (tubes and intermediate inlet pipe) between Primary & Intermediate system	m ³	0.56125	4433.88
42	IHX Well Casing heat structure volume/mass	or	2.16394	17095.1
43	Inlet Plena heat structure volume/mass	kg	1.18646	9373.04
44	High and Low Pressure Piping heat structures volume/mass		0.23637	1867.3
Z-Pipe heat structure volume/mass:				
45	- Stainless Steel 304		0.18598	1469.25
46	- Stagnant Sodium		0.65093	560.999
47	Pumps heat structure volume/mass		1.76006	13904.5
48	Reactor Vessel (Neutron Shield and Reactor Cover) heat structure volume/mass		30.7625	66511.9
49	Active heat structure surface area in-Core (Drivers, High Flow Drivers and Partial drivers)	m ²	30.5699	
50	Active Heat structure surface area in-Core (Experimental, Instrumented, Steel, Reflector and Blanket Subassemblies)		10.7449	

#	Parameter	Unit	Reference Value Y _E
51	Passive heat structure surface area in-core (Drivers, High Flow Drivers and Partial Drivers)		50.4641
52	Passive heat structure surface area in-core (Experimental, Instrumented, Steel, Reflector and Blanket Subassemblies)		733.3572
53	IHX heat structure surface area (tubes and intermediate inlet pipe) between primary and intermediate system		476.7627
54	Heated diameter of the intermediate side of IHX	m	0.0134

Regarding verifying that a steady state had been achieved, a set of parameters was identified for comparison against the measured experimental data. These parameters are shown in TABLE 52 and consist of:

- (a) Powers → 2 parameters;
- (b) Pressures → 8 parameters;
- (c) Velocities → 2 parameters;
- (d) Volumetric flow rates → 7 parameters;
- (e) Temperatures → 12 parameters;
- (f) Volumetric inventories → 2 parameters;
- (g) Heat losses → 4 parameters.

TABLE 50. MATERIAL DENSITIES AT STEADY STATE CONDITION

Material	Unit	Density
Stainless Steel 316		
Stainless Steel 304		
Fuel Alloy, U-5Fs		
Plenum Gas (Helium)		
Depleted Uranium	kg/m ³	
Graphite		
Sodium (at steady state condition)		
Sodium (at 800 °F)		
Sodium (at 582 °F)		

TABLE 51. VOLUME OF FLUID VERSUS ELEVATION

#	Position	Elevation [m]	Reference Value	
			Volume of Primary Circuit [m ³]	Volume of Intermediate Circuit [m ³]
1	Bottom of shield	-1.551	0.0	0.0
2	Bottom of lower grid plate	-1.106	1.215	0.0
3	Top of upper grid plate	-0.624	2.765	0.0
4	Bottom of reactor core	0.000	3.092	0.0
5	Top of reactor core	0.361	3.272	0.0
6	Axis of Z-Pipe inlet	1.182	4.624	0.0*
7	IHX lower tube sheet	2.232	7.206	0.812

8	Pump outlet	3.446	8.354	1.423
9	IHX upper tube sheet	5.369	10.962	2.390
10	Bottom of primary tank cover	5.827	10.962	3.202

* This value corresponds to the elevation of the bottom of the IHX, 1.559 m.

For those items for which reference values are not available, only comparisons among the participants' values are performed. Based on the methodology, the calculated values were to be taken when stable conditions had been reached during the "null transient" steady state calculation, i.e. when the inherent drift of each parameter is less than 1% over the last 100 seconds of the steady state calculation (acceptance criterion-SS).

TABLE 52. STEADY STATE PARAMETERS

#	Parameter	Unit	Reference Value Y _E
1	Primary circuit power balance	MW	57.29
2	Secondary circuit power balance		57.29
3	Pump 1 Discharge Pressure	kPa	295.79
4	Pump 2 Discharge Pressure		288.89
5	Low pressure inlet plenum pressure		not available
6	High pressure inlet plenum pressure		not available
7	Upper plenum pressure		43.850
8	Z-Pipe inlet pressure		not available
9	IHX inlet pressure		not available
10	IHX outlet pressure	not available	
11	Pump 1 velocity	rpm	799.03
12	Pump 2 velocity		764.92
13	Pump 1 volumetric flow	m ³ /s	0.275 @ 800 ⁰ F (4352.6 gpm)
14	Pump 2 volumetric flow		0.274 @ 800 ⁰ F (4346.5 gpm)
15	Low pressure inlet volumetric flow		not available
16	High pressure inlet volumetric flow		not available
17	Core outlet volumetric flow		0.5363 @ 800 ⁰ F (8500 gpm)
18	Z-Pipe volumetric flow		0.532 @ 800 ⁰ F (8438.5 gpm)
19	IHX intermediate side volumetric flow		0.354 @ 582 ⁰ F (5614.6 gpm)
20	Low pressure inlet plenum temperature		623.7
21	High pressure inlet plenum temperature		624.7
22	Average core inlet temperature	624.56	
	Upper Plenum temperature at the following elevations ⁽¹⁾ :		
23	- Close to 1.182 m above the bottom of the core	K	not available
24	- Close to 1.40 m above the bottom of the core		not available
25	- Close to 1.57 m above the bottom of the core		not available
26	Z-Pipe inlet temperature		not available
27	IHX primary inlet temperature		710.0
28	IHX primary outlet temperature		628.5
29	IHX intermediate inlet temperature		574.15
30	IHX intermediate outlet temperature		714.2
31	Rod surface temperature (hottest subassembly)		not available
32	Total sodium volumetric inventory in primary system	m ³	340.69 (90 000 gal)
33	Total sodium volumetric inventory in intermediate system		48.36 (12,775 gal)
34	Z-Pipe heat losses	kW	not available

35	IHX heat losses	not available
36	High/low pressure piping heat losses	not available
37	Reactor cover vessel heat losses	not available

In addition, per TABLE 53, the participants were requested to provide the values of the calculated pressure at different positions in order to build the pressure drops versus length curve for both high pressure and low pressure paths. If no pressure measurements or reference ΔP values were available, a code-to-code comparison was performed for these parameters.

Finally, for the quantitative accuracy evaluation performed by the FFTBM, a list of 49 parameters (see

TABLE 54) was requested from the participants, including:

- (a) Powers \rightarrow 2 parameters;
- (b) Pressures \rightarrow 8 parameters;
- (c) Velocities \rightarrow 2 parameters;
- (d) Mass flow rates \rightarrow 6 parameters;
- (e) Temperatures \rightarrow 25 parameters;
- (f) Pressure drops \rightarrow 5 parameters;
- (g) Mass inventories \rightarrow 4 parameters.

Among all these parameters, only those for which the experimental results are available were selected to perform the FFTBM, for a total of 26 parameters, including 3 mass flow rates and 23 temperatures (both coolant and cladding temperatures).

TABLE 53. PRESSURE VERSUS LENGTH

#	Position	Length [m]	Calculated Pressure [MPa]
Low Pressure Path			
1	Top of the pool	0.000	
2	Pump-1 inlet	2.133	
3	Pump-1 outlet	2.381	
4	Low pressure inlet plenum (topmost position)	20.944	
5	Upper plenum (topmost position)	23.536	
6	Z-Pipe inlet	25.080	
7	Z-Pipe outlet	36.732	
8	IHX primary side inlet	37.058	
9	IHX primary side outlet	39.758	
10	Pool outside of IHX primary side outlet	39.836	
High Pressure Path			
1	Top of the pool	0.000	
2	Pump-1 inlet	2.133	
3	Pump-1 outlet	2.381	
4	High pressure inlet plenum (topmost position)	12.073	
5	Upper plenum (topmost position)	14.665	
6	Z-Pipe inlet	16.209	

7	Z-Pipe outlet	27.861
8	IHX primary side inlet	28.187
9	IHX primary side outlet	30.886
10	Pool outside of IHX primary side outlet	30.965

TABLE 54. LIST OF PARAMETERS FOR THE ‘ON-TRANSIENT’ QUALIFICATION BY FFTBM

#	Parameter	Type of Data	Unit	
1	Core Power	Calculated only	MW	
2	IHX Power Exchanged	No reference available		
3	Pump 1 Outlet Pressure	No reference available	MPa	
4	Pump 2 Outlet Pressure	No reference available		
5	Low Pressure Inlet Plenum Pressure	No reference available		
6	High Pressure Inlet Plenum Pressure	No reference available		
7	Upper Plenum Pressure	No reference available		
8	Z-Pipe Inlet Pressure	No reference available		
9	IHX Inlet Pressure	No reference available		
10	IHX Outlet Pressure	No reference available		
11	Pump 1 Velocity	Measured value		rpm
12	Pump 2 Velocity	Measured value		
13	Pump 1 Mass Flow Rate	No reference available	kg/s	
14	Pump 2 Mass Flow Rate	Measured value		
15	Core Coolant Mass Flow Rate	No reference available		
16	Z-Pipe Mass Flow Rate	No reference available		
17	XX09 Subassembly Mass Flow Rate	Measured value		
18	XX10 Subassembly Mass Flow Rate	Measured value		
19	Low Pressure Inlet Plenum Temperature	Measured value		
20	High Pressure Inlet Plenum Temperature	Measured value		
21	Upper Plenum Temperature	Measured value		
22	IHX Primary Inlet Temperature	Poor		
23	IHX Primary Outlet Temperature	Measured value		
24	IHX Intermediate Inlet Temperature	Measured value		
25	IHX Intermediate Outlet Temperature	Measured value		
26	Rod Surface Temperature (Hottest Driver)	No reference available		
	XX09 Subassembly Temperatures:		K	
27	- Temperature at Flowmeter (FM-1TC)	Measured value		
28	- Mid-Core Temperature (MTC-20)	Measured value		
29	- Top of Core Temperature (TTC-8)	Measured value		
30	- Above Core Temperature (14TC-37)	Measured value		
31	- Core Outlet Temperature (OTC-01)	Measured value		
	XX10 Subassembly Temperatures:		K	
32	- Temperature at Flowmeter (FM-1TC)	Measured value		
33	- Mid-Core Temperature (MTC-4)	Measured value		
34	- Top of Core Temperature (TTC-2)	Measured value		
35	- Above Core Temperature (14TC-3)	Measured value		
36	- Core Outlet Temperature (OTC-01)	Measured value		
	Subassembly Outlet Temperatures:		K	
37	- Partial Driver (1A1)	Measured value		
38	- Driver (3B1)	Measured value		
39	- Driver (4F1)	Measured value		

#	Parameter	Type of Data	Unit
40	- Driver next to XX10 (5C2)	Measured value	
41	- High Flow Driver (6C4)	Measured value	
42	- Reflector (9E4)	Measured value	
43	- Blanket (12E6)	Measured value	
44	Pressure Drop between Pump Outlet and Low Pressure Inlet Plenum	No reference available	
45	Pressure Drop between Pump Outlet and High Pressure Inlet Plenum	No reference available	
46	Pressure Drop between Low Pressure Inlet Plenum and Upper Plenum	No reference available	kPa
47	Pressure Drop between High Pressure Inlet Plenum and Upper Plenum	No reference available	
48	Pressure Drop between Z-Pipe Inlet and Z-Pipe Outlet	No reference available	
49	Total Primary Sodium Mass Inventory	Design value	kg

Among the selected parameters, two of them (the upper plenum temperature and the IHX primary side outlet temperature) have data recorded at multiple locations. Since each simulation result has to be compared with one experimental parameter, these two parameters were used more than once while performing the FFTBM. In particular:

- (a) For the upper plenum temperature, experimental data at eight positions within the upper plenum were available, so each of these has been compared with the upper plenum temperatures calculated by the participants;
- (b) For the IHX primary side outlet temperature, experimental data at four positions within the IHX outlet region were available, so each of these has been compared with the IHX primary side outlet temperatures calculated by the participants.

Because of this, a total of 36 experimental and calculated parameters were used to perform the quantitative accuracy evaluation by the FFTBM. TABLE 55 lists the participants who provided their results to perform the analysis. Due to limited time and resources, and also because of restrictions on the features and capabilities of the individual codes, some participants did not provide some of the data requested for the various steps of the analysis.

TABLE 55. LIST OF PARTICIPANTS IN THE QUALIFICATION PROCESS AND DATA PROVIDED

Name	Organization	Country	Nodalization features	Geom. fidelity	SS Achievement	FFTBM
T. Sumner	ANL	USA	None	Partial	Partial	Partial
A. Del Nevo, E. Martelli	ENEA	Italy	Partial	Partial	Partial	Full
N. Rtishchev	IBRAE	Russian Fed.	Full	Full	Partial	Partial
H. Ohira	JAEA	Japan	Full	Partial	Full	Full
C. Choi	KAERI	Rep. of Korea	Full	Partial	Full	Full
A. Shin	KINS	Rep. of Korea	Full	Partial	Partial	Partial
D. Sui	NCEPU	China	Partial	Partial	Partial	Partial
A. Petruzzi, D. De Luca	N.IN.E.	Italy	Full	Partial	Full	Full
H. Mochizuki	U. of Fukui	Japan	Partial	Partial	Partial	Full

G. H. Su, N. Yue	XJTU	China	Full	Partial	Partial	Full
Full – Full data provided						
Partial – Partial data provided						
None – No data provided						

9.2.2. Participants' results

9.2.2.1. Nodalization features

The first comparison among the codes used by the participants is related to the nodalization features. TABLE 56 summarizes the data provided by the participants about the hydraulic volumes and mesh points or heat structures used in the nodalizations.

TABLE 56. NODALIZATION FEATURES PROVIDED BY PARTICIPANTS

#	Parameter	ANL	ENEA	IBRAE	JAEA	KAERI	KINS	NCEPU	N.IN.E.	U_Fukui	XJTU
1	Total number of Hydraulic Volumes	--	3992	914	664	456	426	19297	4516	324	231
2	Total number of Mesh Points	--	31236	10863	5096	1861	1171	20998	>100000	1911	650
3	Hydraulic Volumes of the primary side	--	3661	865	662	398	313	289	4051	321	170
4	Hydraulic Volumes of the intermediate side	--	25	49	1	52	23	42	45	23	56
5	Hydraulic Volumes of the pool	--	306	25	1	6	90	19008	423	3	5
6	Hydraulic Components for the whole core	--	217	70	637	25	16	9	100	-	24
7	Hydraulic Volumes for the whole core	--	3071	507	637	232	196	234	3600	240	85
8	Hydraulic Volumes per each Driver sub.	--	15	30	1	16	11	26	36	24	15
9	Hydraulic Volumes per each Partial Driver sub.	--	15	30	1	16	11	26	36	24	15
10	Hydraulic Volumes per each High Flow Driver sub.	--	15	30	1	16	11	26	36	24	15
11	Hydraulic Volumes for the two Instrumented sub.	--	58	112	2	104	16	26	144	24	30
12	Heat Structures for the whole core	--	215	50	637	27	17	234	459	80	42
13	Mesh Points for the whole core	--	--	8281	208936	1210	658	1872	97602	240	504
14	Heat Structures for all Driver sub.	--	1400	4	32	75	2	--	160	--	10
15	Heat Structures for all Partial Driver sub.	--	840	5	10	111	2	--	60	--	10
16	Heat Structures for all High Flow Driver sub.	--	3192	4	18	<i>Added to Drivers^a</i>	2	--	90	--	10
17	Heat Structures for the two Instrumented sub.	--	112	8	2	524	8	52	14	14	15

-- Data not provided

^a The driver and high flow driver subassemblies are modelled with the same channel.

The total number of hydraulic volumes and mesh points used for the whole nodalization of EBR-II and those used to model only the core region are shown in FIG. 312 and FIG. 313, respectively. FIG. 314 depicts separately the hydraulic volumes used to model the primary side, the intermediate side and the pool.

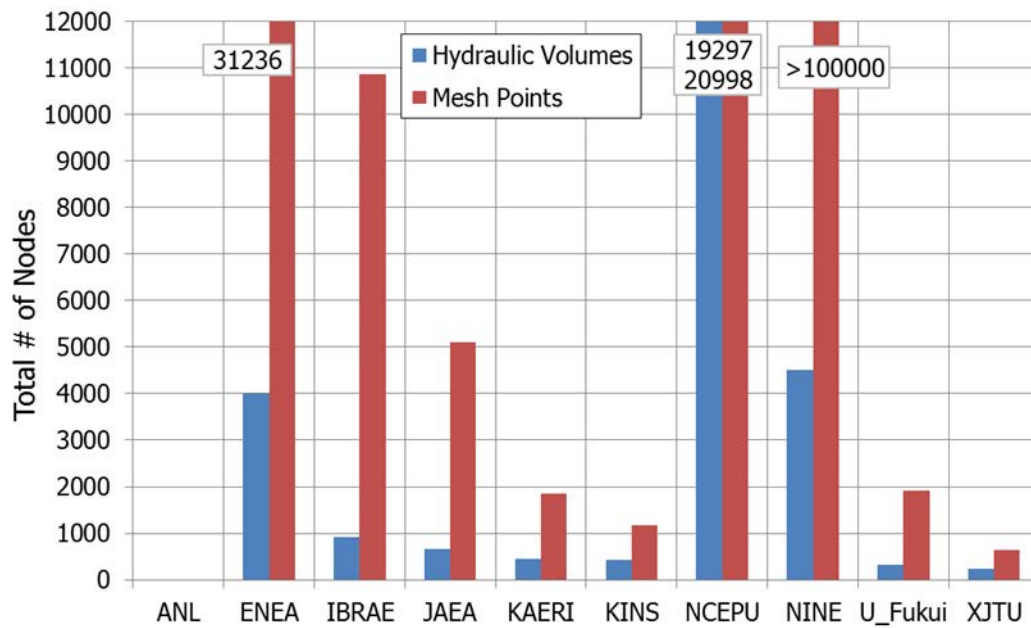


FIG. 312. Nodalization features, hydraulic volumes and mesh points for the whole EBR-II nodalization.

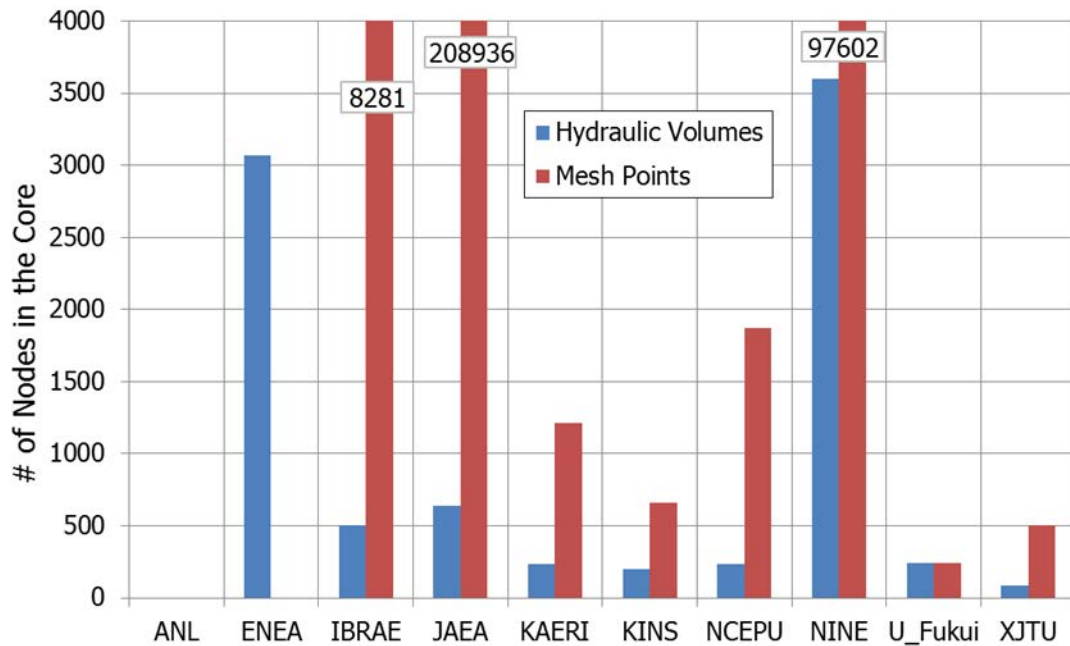


FIG. 313. Nodalization features, hydraulic volumes and mesh points in the core region.

9.2.2.2. Geometrical fidelity

This step is related to demonstration of the geometrical fidelity of the nodalization models that were developed. In addition, FIG. 315 and FIG. 316 depict the comparison between the EBR-II elevations and the curves of the primary circuit volume and intermediate circuit volume, respectively. It should be noted that the reference elevation (0.0 m) is at the bottom of the reactor core.

Additional details about the demonstration of the geometrical fidelity are shown in FIG. 317 through FIG. 322.

TABLE 57 and TABLE 58 show the percentage error between the reference values (calculated by Argonne and N.I.N.E. and discussed in Appendix III) and the data provided by the participants. The percentage error (E%) is calculated with the following formula:

$$E\% = 100 \cdot (Y_E - Y_C) / Y_E,$$

where:

Y_E = Reference value

Y_C = Participants' result

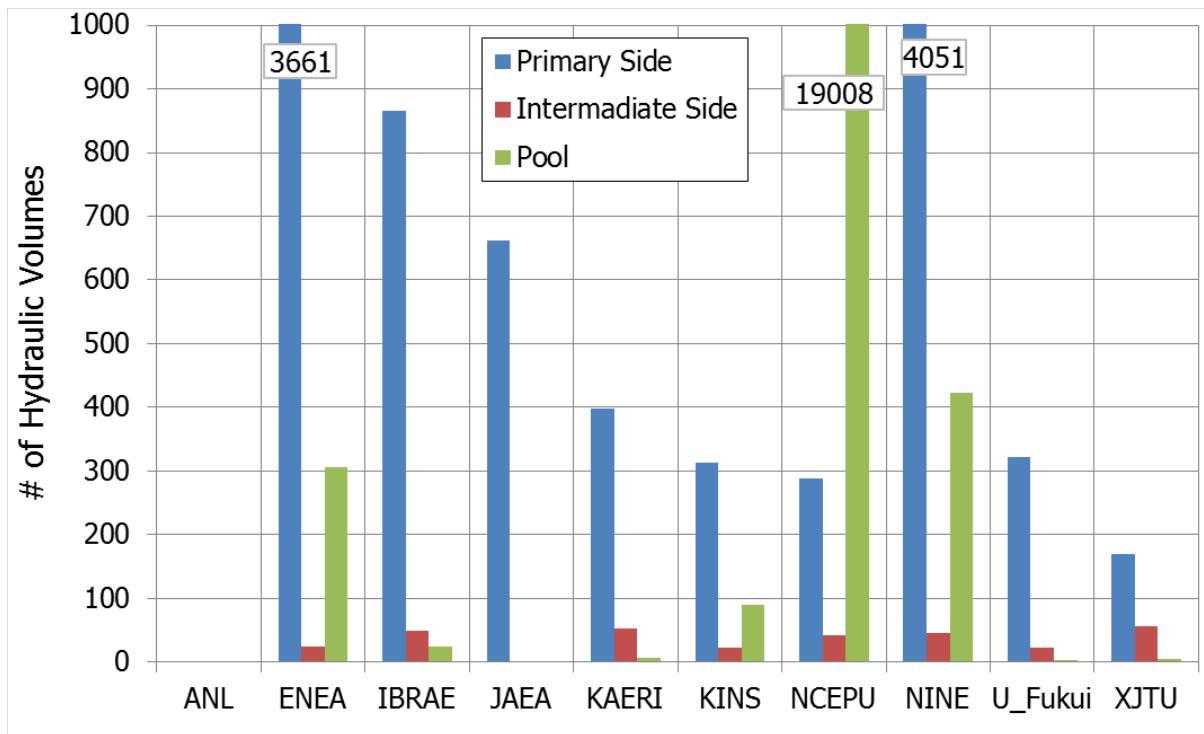


FIG. 314. Nodalization features, hydraulic volumes in the primary side, intermediate side and pool.

In addition, FIG. 315 and FIG. 316 depict the comparison between the EBR-II elevations and the curves of the primary circuit volume and intermediate circuit volume, respectively. It should be noted that the reference elevation (0.0 m) is at the bottom of the reactor core.

Additional details about the demonstration of the geometrical fidelity are shown in FIG. 317 through FIG. 322.

TABLE 57. GEOMETRICAL FIDELITY OF THE EBR-II NODALIZATION: PARAMETERS 1-29 (% ERROR)

#	Parameter	ANL	ENEA	IBRAE	JAEA	KAERI	KINS	NCEPU	N.IN.E.	U. Fukui	XJTU
1	Pool liquid volume	-0.14	1.67	4.82	5.93	4.54	12.62	11.14	-0.35	18.08	2.04
2	Primary circuit liquid volume (without pool)	5.59	0.49	-18.59	-2.24	3.03	2.38	28.85	0.60	-39.45	2.10
3	High pressure Inlet Plenum liquid volume	0.37	4.41	-68.33 ^a	-0.67	-25.30	-6.10	-9.61 ^b	3.86	-8.26	-3.71
4	Low pressure Inlet Plenum liquid volume	0.00	2.66	0.24	0.10	25.47	-6.16	--	-2.41	-10.00	0.07
5	Liquid volume in-core, Drivers	7.25	-4.65	20.51	20.94	-134.62 ^c	1.88	-11.14	1.07	-5.08	-1.47
6	Liquid volume in-core, Partial Drivers	23.40	-8.59	17.51	17.93	-18.81	22.41	--	0.44	-9.05	6.79

#	Parameter	ANL	ENEA	IBRAE	JAEA	KAERI	KINS	NCEPU	N.IN.E.	U. Fukui	XJTU	
7	Liquid volume in-Core, High Flow Drivers	3.88	-4.61	13.98	13.98	<i>Added to Drivers^c</i>		18.67	--	1.41	-14.35	3.95
8	Liquid volume in-Core, Experimental Sub.	22.89	-0.65	16.26	22.67	56.44 ^d	9.13	--	-1.06	-10.70	--	
9	Liquid volume in-Core, XX09, XX10	18.07	2.65	37.75	61.62	3.84	15.13	80.05	-0.90	1.25	41.16	
10	Liquid volume in-Core, Steel/Dummy Sub.	56.60	0.59	46.87	-44.42	<i>Added to Exper.^d</i>		31.73	--	2.69	-4.08	13.13
11	Liquid volume in-Core, Reflector Sub.	13.57	2.94	10.11	46.44	-26.78	-1.01	--	1.55	33.61	3.39	
12	Liquid volume in-Core, Blanket Sub.	14.68	-6.91	15.12	56.09	-67.26	18.50	--	1.12	14.85	-28.19	
14	Upper plenum liquid volume	7.71	-2.26	3.05	-86.08	-6.88	7.73	--	3.85	7.71	7.64	
15	Z -Pipe liquid volume	-5.48	-3.53	3.61	-0.05	-4.79	0.18	--	-0.07	0.37	-7.60	
16	IHX primary side liquid volume	5.72	-4.73	0.15	0.34	0.13	0.00	7.30	0.00	-47.41	18.72	
17	IHX intermediate side liquid volume	64.86	48.42	-21.05	1.59	-5.98	0.33	7.25	1.89	37.05	12.46	
18	High pressure pipe flow area	1.10	0.00	3.16	1.10	1.08	0.04	12.88	1.11	0.96	0.05	
19	Low pressure pipe min flow area	-0.12	0.00	3.66	0.00	-0.16	1.13	--	-0.12	0.00	1.13	
	Low pressure pipe max flow area	0.00	0.00	4.84	--	-0.21	1.93	0.54	-0.27	0.00	1.94	
20	Z-Pipe flow area	0.00	0.00	-0.05	-0.11	-4.72	-0.05	--	0.00	-0.11	-7.58	
21	IHX primary side flow area	0.00	0.00	0.14	0.35	0.13	0.00	0.03	0.00	-47.41	18.72	
22	Hydraulic diameter of core, Driver, HFD, PD	0.04	-0.78	-0.37	0.00	-0.19	-0.37	27.03	-0.19	0.00	6.48	
23	Hydraulic diameter of core, Dummy Sub.	-0.14	0.00	0.00	-3.55	-0.34	-1.89	25.92	-0.12	-1.51	5.07	
24	Hydraulic diameter of core, Reflector Sub.	-1.73	0.00	0.00	-9.07	-6.46	0.00	-0.14	1.98	0.00	-6.52	
25	Hydraulic diameter of core, Blanket Sub.	-0.10	0.52	0.00	31.52	-50.79	0.00	7.33	0.00	0.00	-19.39	
26	High pressure piping length	8.30	-2.57	7.83	3.93	10.36	6.47	--	0.90	11.59	1.35	
27	Low pressure piping length	3.61	3.58	3.42	3.73	-41.22	4.38	--	1.52	-3.41	0.51	

#	Parameter	ANL	ENEA	IBRAE	JAEA	KAERI	KINS	NCEPU	N.IN.E.	U. Fukui	XJTU
28	Z-Pipe length	-5.48	0.11	3.66	0.00	-0.06	0.00	--	-0.07	0.48	0.00
29	Hyd. Diam., IHX int. side	0.00	0.00	0.00	0.00	0.00	0.00	6.72	0.00	0.00	0.00

-- Data not provided

^a The lower adapter region of the subassemblies is included in the high pressure inlet plenum.

^b The percentage error refers to the sum of the liquid volume in both high pressure and low pressure inlet plena.

^c Also includes the liquid volume of the High Flow Drivers.

^d Also includes the liquid volume of the Steel/Dummy Subassemblies.

FIG. 317 indicates the results related to the pool and the primary circuit liquid volume, and FIG. 318 shows the comparison of the IHX primary side and intermediate side liquid volumes. It can be seen from FIG. 318 that the percentage errors are slightly higher for the liquid volume on the intermediate side of the IHX because the benchmark specifications have not defined the intermediate system in as much detail and therefore participants have made some arbitrary assumptions in their models. For instance, ANL developed a simple loop model to represent the intermediate system (keeping the correct geometry for the primary side of the IHX), while ENEA did not take into account the liquid volume in the upper plenum of the intermediate side because they did not consider it relevant for the analysis.

In other zones of the primary side, the percentage errors are relatively small, except for a few participants, as can be seen from FIG. 319, where the liquid volumes of the high pressure and low pressure inlet plena are considered, and FIG. 320, where the data related to the upper plenum and Z-Pipe liquid volume are shown. Regarding the upper plenum liquid volume, the percentage error is affected by the approximation made in calculating the reference value. Practically, the volume between the subassembly outlets and the bottom of the upper plenum was evaluated as if it contained no structures (i.e. completely full of liquid), and it was included in the upper plenum liquid volume (taking into account this volume, the difference in the reference value of the upper plenum liquid volume is about 7.7%). Regarding the core region, the percentage error of the liquid volume in the driver, partial driver, high flow driver and instrumented subassemblies are shown in FIG. 321.

TABLE 58. GEOMETRICAL FIDELITY OF THE EBR-II NODALIZATION: PARAMETERS 30–54 (% ERROR)

#	Parameter	ANL	ENEA	IBRAE	JAEA	KAERI	KINS	NCEPU	N.IN.E.	U. Fukui	XJTU
Volume/mass in-Core (D, HFD, PD):											
30	Stainless Steel 316	--	2.70	-5.07	17.27	-253.08 ^a	80.59	--	0.00	--	-11.73
31	Stainless Steel 304	--	-4.95	22.40	--	SS-316	91.85	--	0.00	--	-38.87
32	Fuel Alloy, U-5Fs	--	0.33	0.00	-9.03	-58.44	18.26	--	-0.02	--	-0.69
33	Plenum Gas (Helium)	--	--	0.00	0.56	-41.58	--	--	0.02	--	-36.70
34	Stagnant Sodium	--	--	29.74	-103.59	--	--	--	0.05	--	1.19
Volume/mass in-Core (others):											
35	Stainless Steel 316	--	4.09	28.47	-486.85	-7918.3 ^a	81.47	--	-2.59	--	--

#	Parameter	ANL	ENEA	IBRAE	JAEA	KAERI	KINS	NCEPU	N.IN.E.	U. Fukui	XJTU
36	Stainless Steel 304	--	-7.40	-16.68	77.60	SS-316	-19.61	--	-0.57	--	--
37	Fuel Alloy, U-5Fs	--	0.19	-5.21	43.95	54.84	14.53	--	-0.02	--	--
38	Plenum Gas (Helium)	--	--	-2.70	7.14	2.69	--	--	--	--	--
39	Stagnant Sodium	--	--	-20.00	-104.72	--	--	--	--	--	--
40	Depleted Uranium	--	-1.94	0.00	0.27	-9.36	-2.18	--	2.92	--	--
41	IHX volume/mass (between P & I)	--	-3.07	0.00	-5.34	3.54	-0.92	--	0.00	--	-0.07
42	IHX Well Casing volume/mass	--	--	34.74	10.88	5.85	--	--	--	--	3.16
43	Inlet Plena volume/mass	--	--	8.30	1.77	--	68.41	--	--	--	--
44	HPP and LPP Piping volume/mass	--	-1.87	0.12	--	--	28.74	--	-3.95	--	--
Z-Pipe volume/mass:											
45	Stainless Steel 304	--	0.12	3.66	20.99	0.11	-15.58	--	-0.07	--	-0.34
46	Stagnant Sodium	--	0.11	3.66	-3.39	0.11	-15.58	--	-0.07	--	-3.38
Other											
47	Pumps volume/mass	--	86.48	--	--	--	--	--	--	--	--
48	Reactor Vessel volume/mass	--	-4.54	1.22	--	-0.44	--	--	5.02	--	--
49	Active surface area in-Core (D, HFD, PD)	--	0.26	0.00	1.88	3.53	39.46	--	0.76	0.76	-1.41
50	Active surface area in-Core (others)	--	10.95	-5.17	1255.99	73.01	54.71	--	25.08	25.08	--
51	Passive surface area in-core (D, HFD, PD)	--	-9.23	-7.19	30.62	57.97	34.92	--	10.37	10.37	-2.58
52	Passive surface area in-core (others)	--	--	7.27	69.59	14.30	20.83	--	34.76	34.76	1.31
53	IHX surface area (between P & I)	--	1.04	0.03	0.00	0.67	-0.09	--	0.67	0.67	0.13
54	Heated diameter of IHX tubes	--	0.00	0.00	0.00	0.00	0.00	6.72	0.00	0.00	0.00

-- Data not provided

^a Also includes the heat structure volume/mass of the SS-304.

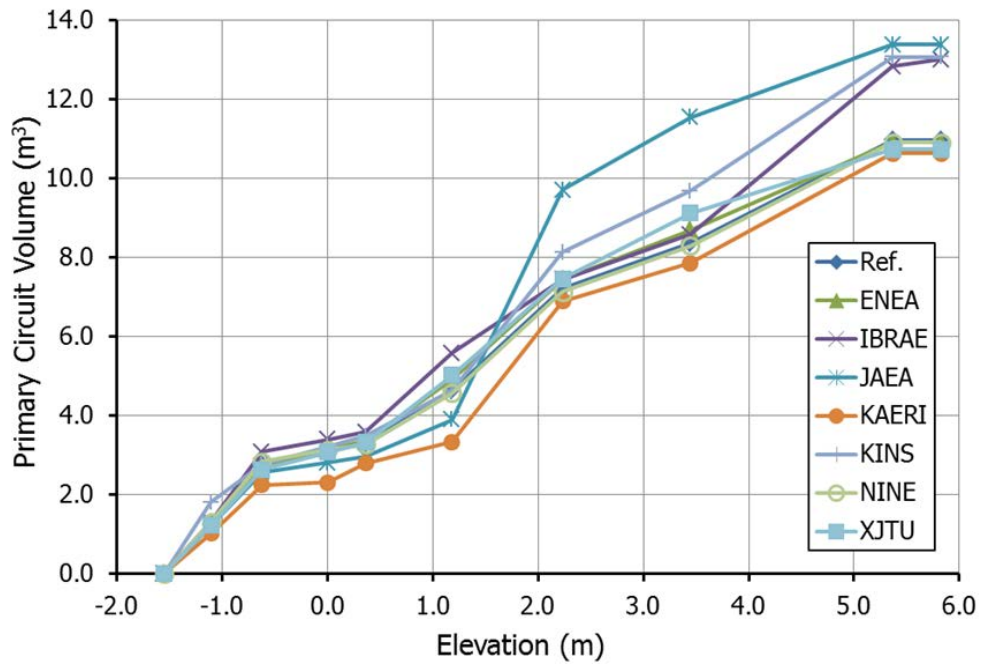


FIG. 315. Geometrical fidelity, primary circuit volume versus elevation curve.

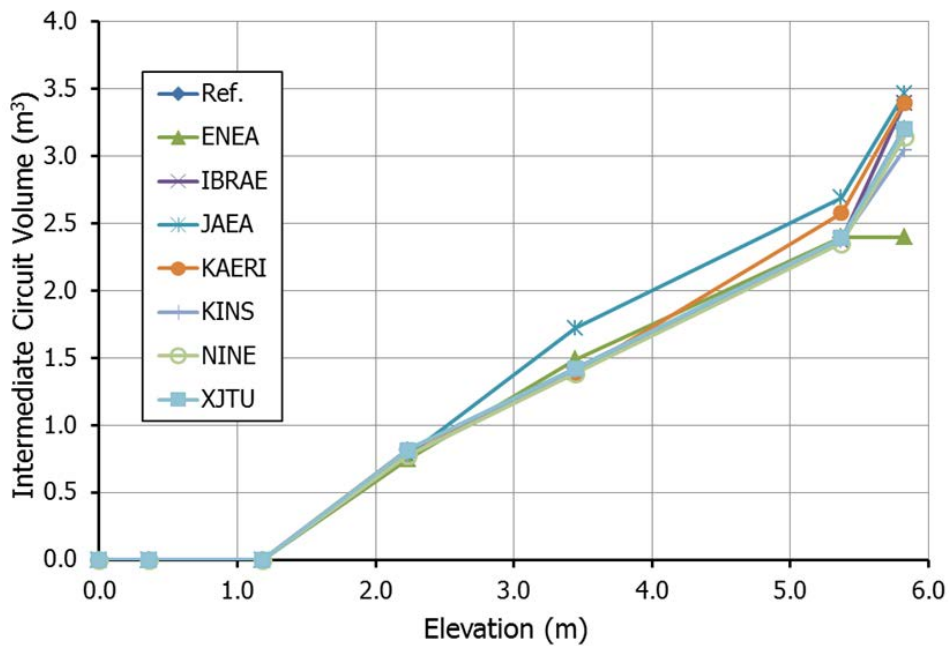


FIG. 316. Geometrical fidelity, intermediate circuit volume versus elevation curve.

FIG. 322 depicts the discrepancies related to the heat structures volume (or mass) of the driver, partial driver and high flow driver subassemblies. For some participants, the percentage error is affected by the modelling assumption of grouping together different types of subassemblies or including the lower adapter liquid volume in the inlet plena.

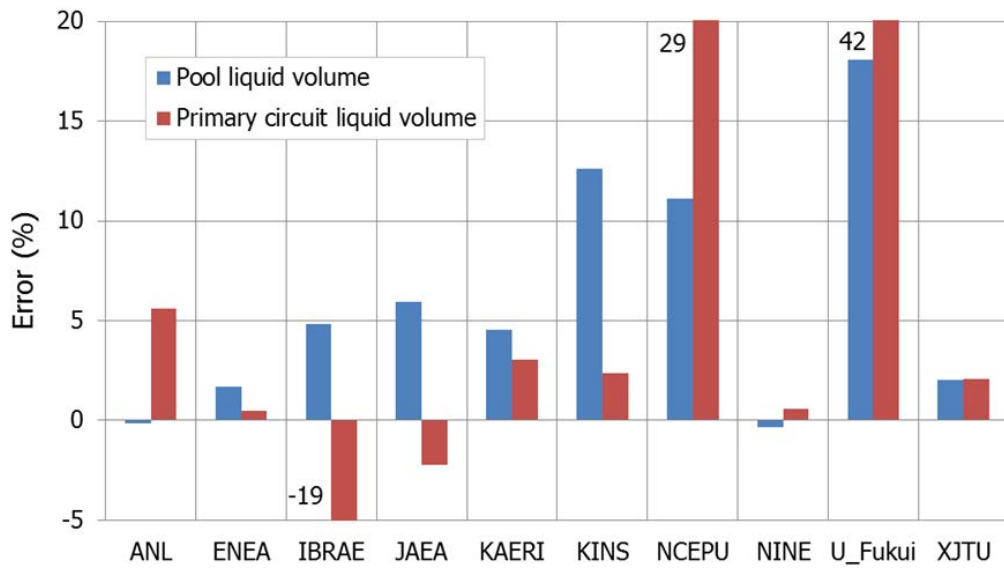


FIG. 317. Geometrical fidelity, pool and primary circuit liquid volume.

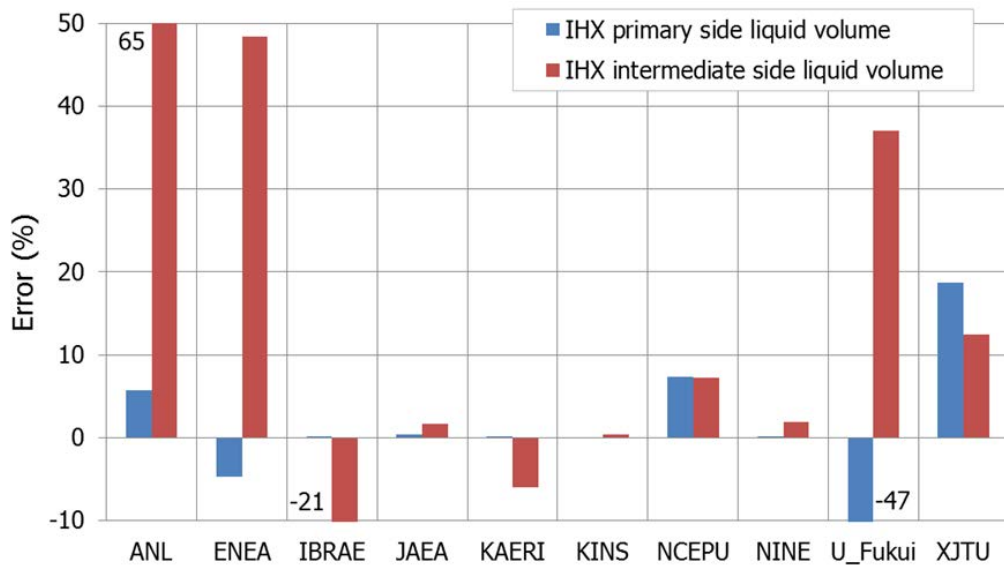


FIG. 318. Geometrical fidelity, IHX primary and intermediate side liquid volume.

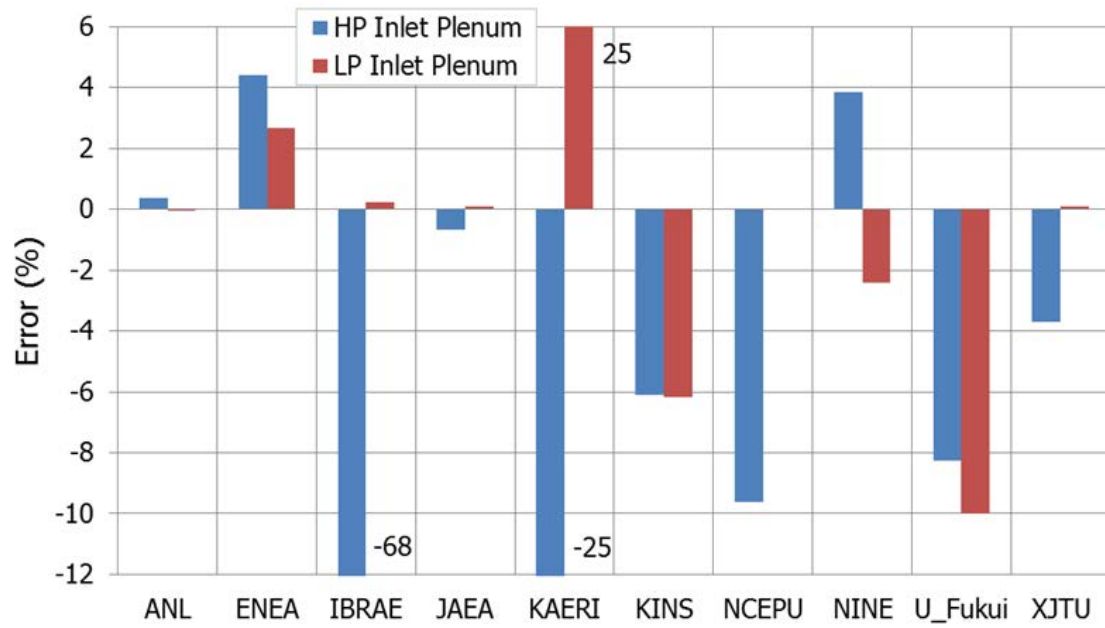


FIG. 319. Geometrical fidelity, high pressure and low pressure liquid volume.

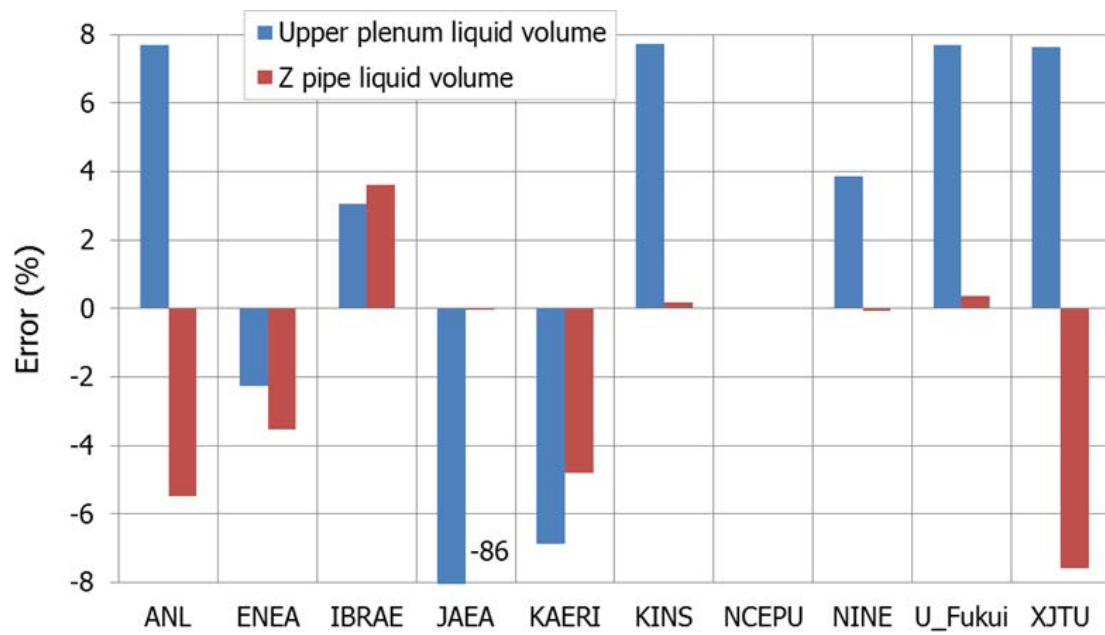


FIG. 320. Geometrical fidelity, upper plenum and Z-Pipe liquid volume.

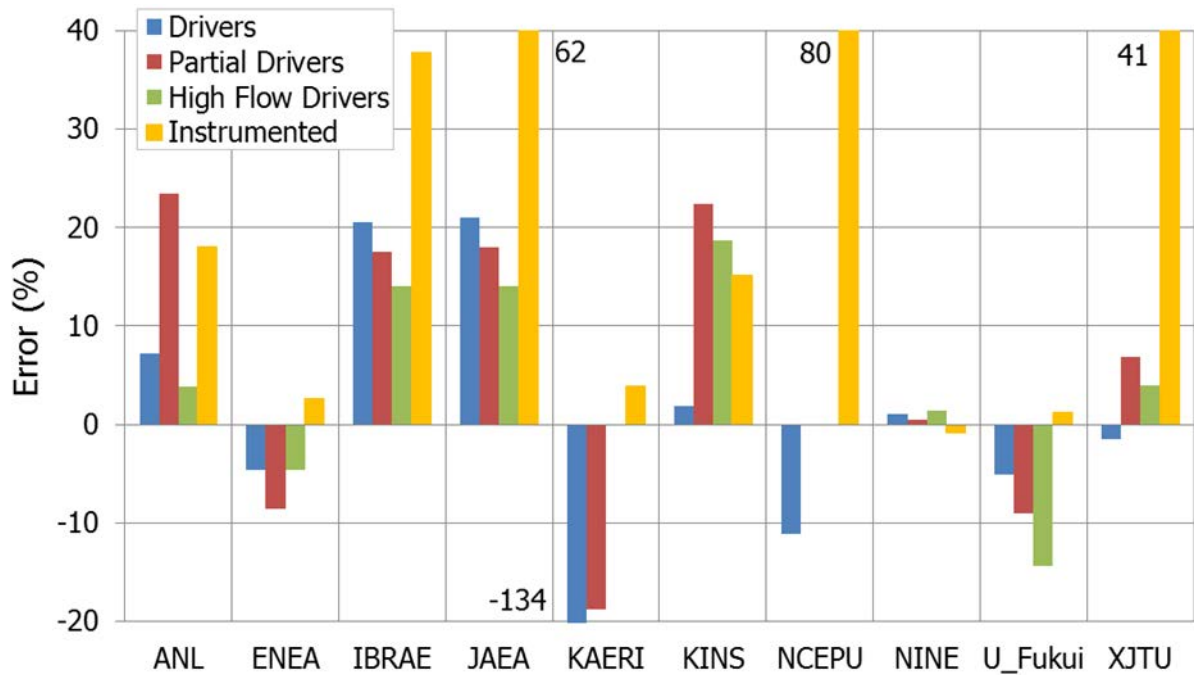


FIG. 321. Geometrical fidelity, liquid volume in driver, partial driver, high flow driver and instrumented subassemblies.

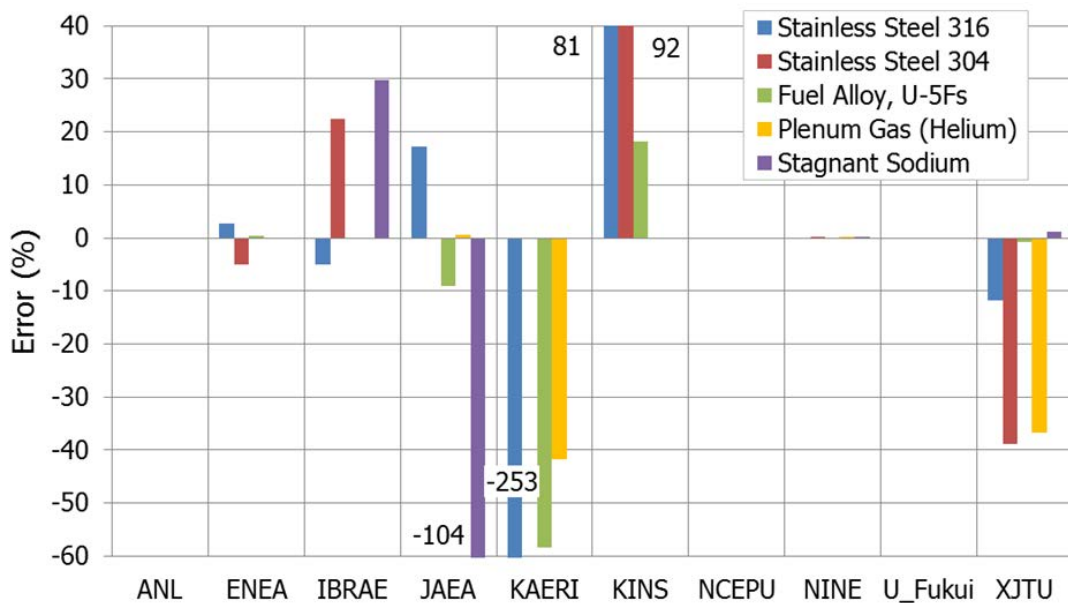


FIG. 322. Geometrical fidelity, heat structure volume (or mass) in driver, partial driver and high flow driver subassemblies.

9.2.2.3. Demonstration of establishing a Steady state

This step of the qualification process deals with demonstrating establishment of a steady state. In this phase, two separate tables were developed:

- (a) TABLE 59 contains the parameters (21) for which a reference value was provided with the benchmark specifications. In this table, the percentage error between the reference value and the participants' results is calculated following the formula shown in the previous section;
- (b) TABLE 60 lists the parameters (16) that do not have a reference value. The table shows the absolute values in order at least to perform a comparison among the participants' results.

TABLE 59. PERCENTAGE ERRORS AT STEADY STATE

#	Parameter	ANL	ENEA	IBRAE	JAEA	KAERI	KINS	NCEPU	N.IN.E.	U. Fukui	XJTU
1	Primary circuit power balance	-0.02	-0.02	0.23	2.18	-0.02	-0.02	-0.02	0.00	0.00	-0.02
2	Secondary circuit power balance ^a	-0.02	4.56	0.23	2.18	-0.02	3.28	-0.02	4.26	0.00	-0.02
3	Pump 1 discharge pressure ^b	--	-59.97	--	3.18	12.65	0.51	8.53	-32.06	-18.84	-2.35
4	Pump 2 discharge pressure ^b	--	-63.80	--	1.70	10.56	7.09	6.35	-35.24	-21.76	5.83
7	Upper plenum pressure ^b	-275.94	-376.62	--	-26.06	-298.87	0.00	-19.73	-383.54	-157.01	-0.34
11	Pump 1 velocity	-0.42	-5.08	0.00	0.00	0.00	0.00	9.44	0.87	-2.27	-0.03
12	Pump 2 velocity	-0.42	-9.76	0.00	0.00	0.00	0.13	5.40	-3.55	-6.88	0.00
13	Pump 1 vol. Flow, @ 800 ^o F	-0.66	2.18	5.82	-3.64	0.18	0.00	0.07	1.52	1.09	2.64
14	Pump 2 vol. Flow, @ 800 ^o F	-0.88	1.75	-0.36	-0.36	-0.18	0.00	-0.29	0.49	0.73	2.31
17	Core outlet vol. flow, @ 800 ^o F	0.04	-0.65	0.43	-2.18	-0.02	0.00	-2.46	-2.32	-0.50	0.25
18	Z-Pipe vol. flow, @ 800 ^o F	-0.66	-0.83	-0.38	-2.44	0.08	-0.08	-3.29	-2.48	-0.56	-0.55
19	IHX intermediate. Side vol. flow, @ 582 ^o F	-0.06	0.00	0.00	-0.28	-3.56	-4.27	50.28	-0.77	-2.32	-0.05
20	LPP temperature	-0.33	-0.38	-0.30	-0.21	0.10	-0.13	-1.17	-0.28	-0.22	-0.63
21	HPP temperature	-0.16	-0.27	-0.16	-0.05	0.26	0.04	-1.01	-0.16	-0.09	-0.38
22	Average core inlet temperature	-0.18	-0.21	-0.18	-0.07	0.24	0.02	-1.03	-0.17	-0.12	-0.42
27	IHX primary inlet temperature	-1.55	-1.48	-1.03	-1.10	-1.51	-0.62	-1.39	-1.98	-1.71	-1.75
28	IHX primary outlet temperature	1.06	0.40	0.43	0.62	0.94	0.60	-0.40	0.01	0.63	0.36
29	IHX inter. Inlet temperature	0.53	-0.01	0.00	-0.03	-0.02	-0.02	-1.59	0.00	-0.02	-0.03
30	IHX inter. Outlet temperature	-0.19	0.57	-0.28	0.32	-0.57	0.55	-0.33	-1.41	0.03	-0.38
32	Sodium vol. inventory in primary circuit	0.04	1.58	4.24	4.91	4.49	12.30	--	-0.32	16.12	2.04

#	Parameter	ANL	ENEA	IBRAE	JAEA	KAERI	KINS	NCEPU	N.IN.E. U. Fukui	XJTU	
33	Sodium vol. inventory in intermediate circuit ^c	-363.80	--	92.00	92.95	92.88	--	--	93.44	95.54	--

-- Data not provided

^a The reference value does not take into account the heat losses (value equal to the primary circuit power balance).

^b The reference values are not absolute pressures, and these parameters are not considered in the comparison.

^c The specification for the sodium inventory in the intermediate side was not detailed.

It must be remembered that the calculated values correspond to the point at which stable conditions were reached during the steady state calculation.

FIG. 323 and FIG. 324 show the pressure drop versus length curves built by the participants for the high pressure and low pressure flow paths, respectively. Note that the starting point (0.0 m) is at the top of the pool and that all the curves have been shifted in order to have a value of 0.0 kPa at this position.

Additionally, comparisons among the participants of the percentage error of some steady state parameters are provided in the next figures. FIG. 325 presents the pumps and Z-Pipe volumetric flow rates (items #13, #14, and #18 in TABLE 59), while FIG. 326 displays the percentage error of the pump velocities (items #11 and #12 in TABLE 59). It can be seen that the errors in the pump volumetric flow rates and the pump velocities are not consistent with each other, reflecting the fact that different pump models or form loss coefficients were used by various participants. In FIG. 327 the percentage errors of the low pressure and high pressure inlet plena temperatures (items #20 and #21 in TABLE 59) are shown: small discrepancies with respect to the reference values exist. Similarly, low percentage errors (less than 2% for all the participants) can be noted in FIG. 328, where the IHX inlet and outlet temperatures of the primary and intermediate side (see items #27 to #30 in TABLE 59) are compared.

For the steady state parameters for which a reference value is not available, a comparison between the absolute values of the participants' results has been performed:

- (a) FIG. 329 represents the steady state values of the high pressure and low pressure volumetric flow rates (items #15 and #16 of TABLE 60). It can be seen that the discrepancies among the participants are very low;
- (b) FIG. 330 shows the upper plenum and Z-Pipe inlet temperatures (items #23 to #26 in TABLE 60). Regarding the upper plenum temperature, ENEA provides the minimum and maximum values (among 60 values) at two different elevations (see items #23 and #25 of TABLE 60), while in the figure, only the average value is displayed. It should be noted that the participant results are inside the range of values obtained by ENEA, except for one participant (XJTU).

TABLE 60. STEADY STATE PARAMETER VALUES, NO DATA AVAILABLE

#	Parameter	ANL	ENEA	IBRAE	JAEA	KAERI	KINS	NCEPU	N.IN.E. U. Fukui	XJTU	
5	LPP pressure ^a	424.0	468.3	--	238.9	206.2	419.9	292.7	377.1	206.3	63.5

6 HPP pressure ^a	190.8	504.0	--	295.2	431.3	365.7	292.7	410.5	434.3	267.0
8 Z-Pipe inlet pressure ^a	164.9	194.7	--	54.1	159.7	159.8	58.7	199.9	182.2	43.1
9 IHX inlet pressure ^a	--	143.3	--	3.3	114.9	122.3	--	157.7	120.5	10.7
10 IHX outlet pressure ^a	--	167.2	--	11.8	127.5	126.6	--	179.6	143.3	30.9
15 LPP inlet volumetric flow	0.077	0.077	0.077	0.088	0.079	0.080	--	0.081	0.075	0.077
16 HPP inlet volumetric flow	0.474	0.461	0.457	0.482	0.470	0.460	--	0.461	0.468	0.458
Upper Plenum temperature at the following elevations:										
23 - Close to 1.182 m above the bottom of core	722.7	712-734	724.0	--	721.9	723.7	--	732.3	--	627.3
24 - Close to 1.40 m above the bottom of core	722.7	--	724.0	--	721.9	723.7	--	732.3	--	627.3
25 - Close to 1.57 m above the bottom of core	722.7	718-729	724.0	--	721.9	--	--	732.3	--	627.3
Other temperatures, heat losses										
26 Z-Pipe inlet temperature	722.7	720.9	724.0	718.8	721.9	723.1	698.4	732.3	722.2	725.3
31 Rod surface temperature (hottest sub.)	787.7	781.8	782.9	--	764.9	767.1	--	793.8	--	815.0
34 Z-Pipe heat losses	959.5	--	308.0	596.5	639.2	3.2	--	337.0	11.6	1288.2
35 IHX heat losses	178.3	--	54.5	--	134.4	--	--	--	--	--
36 High/low pressure piping heat losses	--	--	6.0	--	--	171.0	--	--	15.5	--
37 Reactor cover vessel heat losses	--	--	--	--	-0.7	--	--	--	--	--

-- Data not provided

^a These parameters are not considered in the comparison because of the different units used by participants.

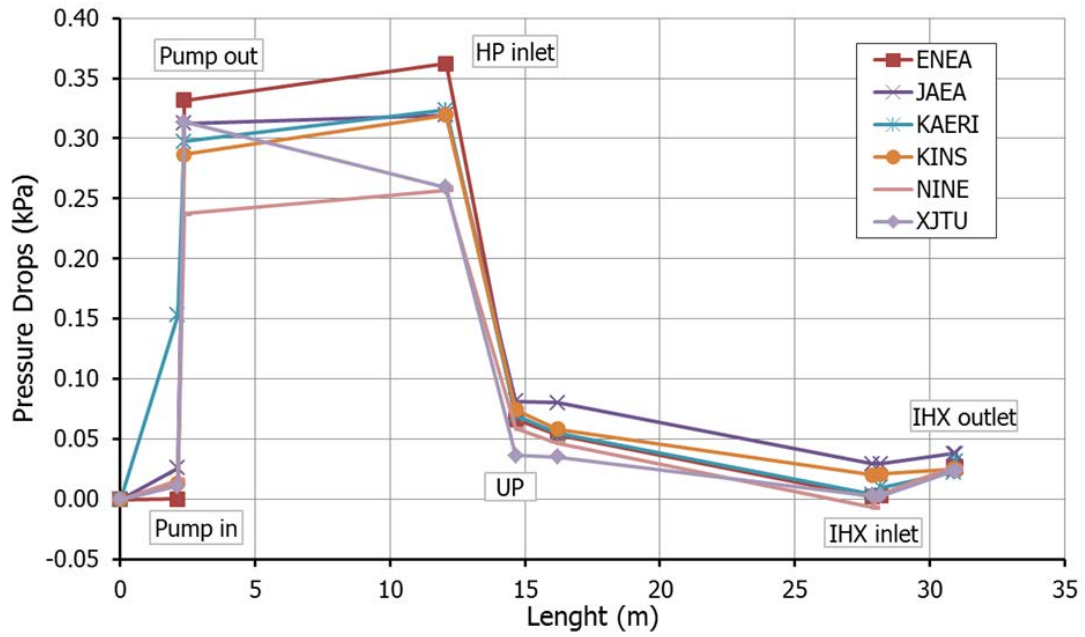


FIG. 323. Pressure drop versus length curve, high pressure path

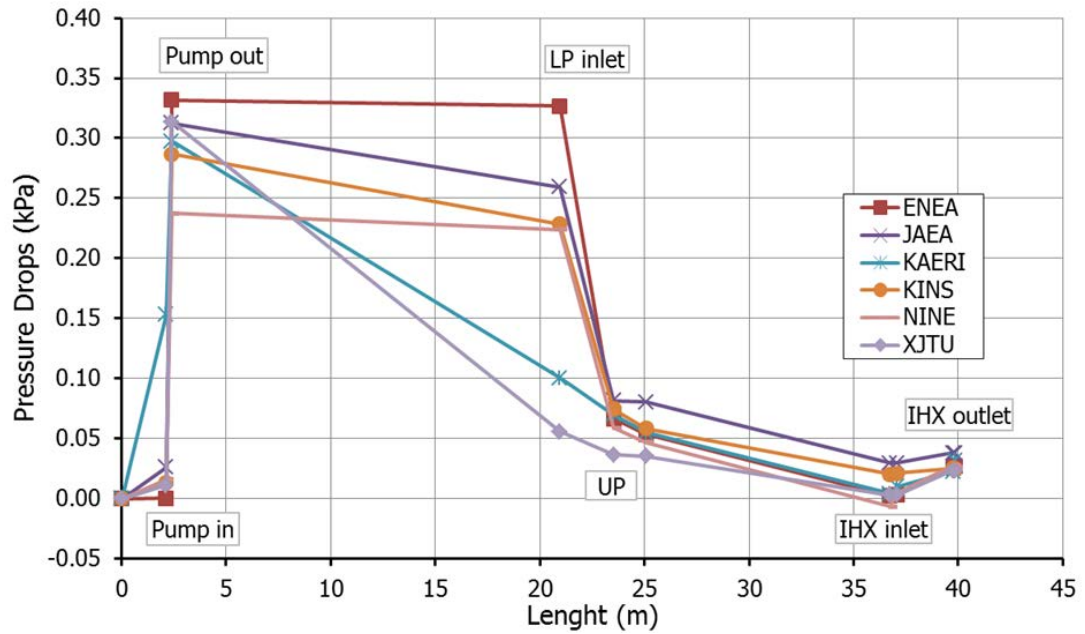


FIG. 324. Pressure drop versus length curve, low pressure path.

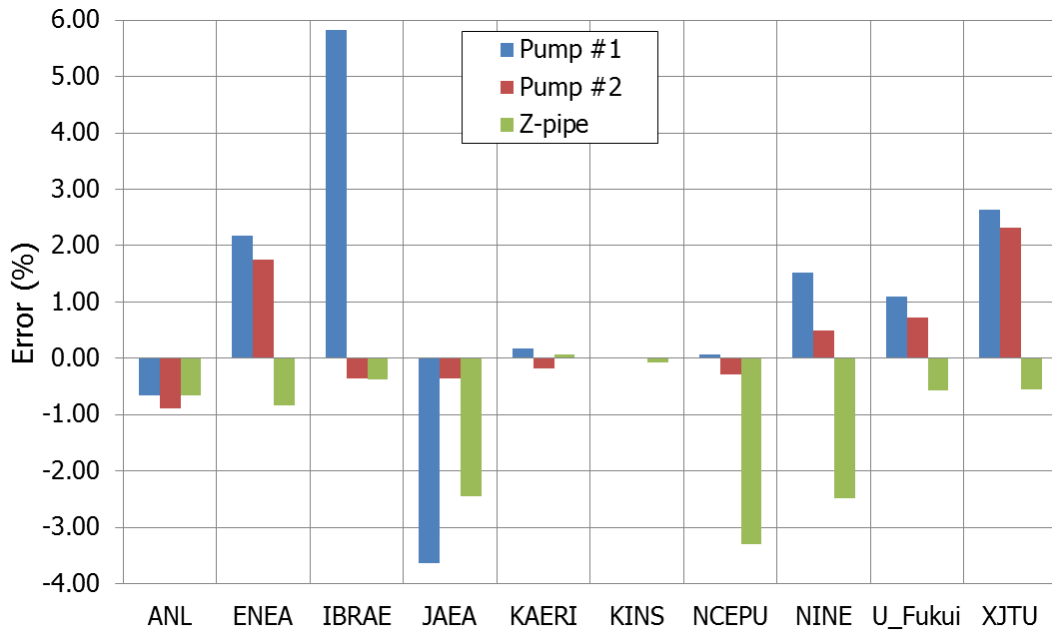


FIG. 325. Achieving a steady state: pump and Z-Pipe volumetric flow rates.

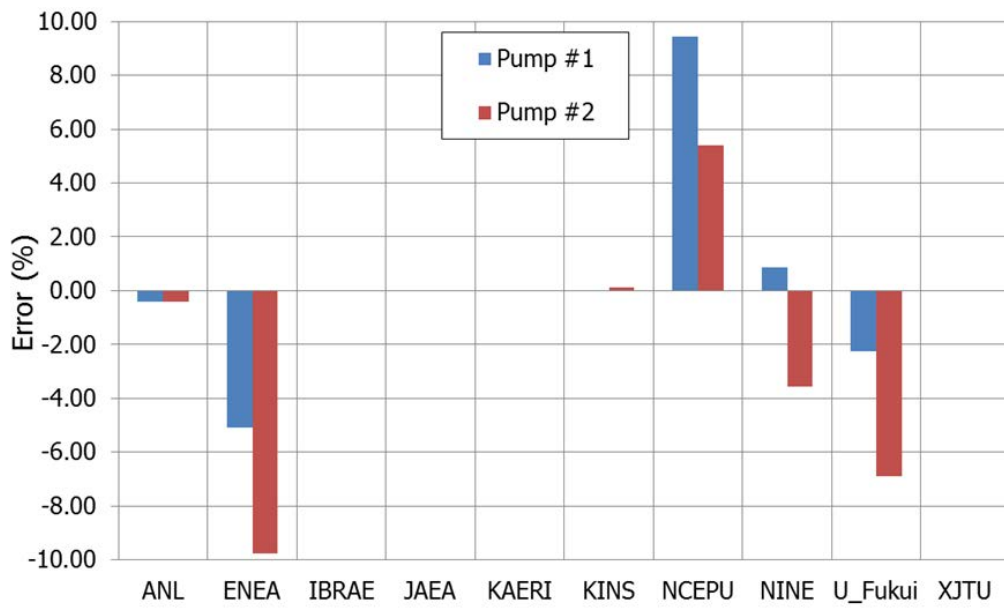


FIG. 326. Achieving a steady state: pump velocities.

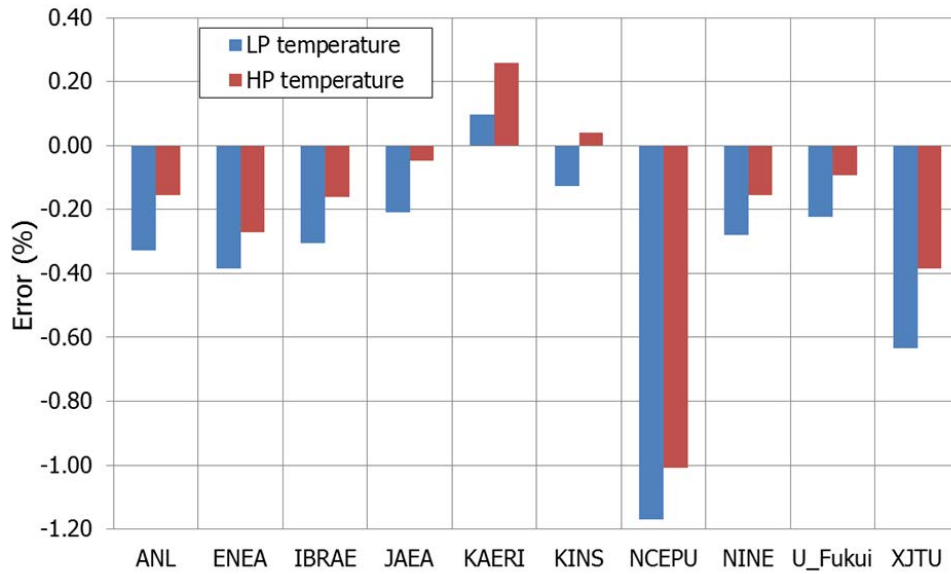


FIG. 327. Achieving a steady state: low pressure and high pressure inlet plena temperatures.

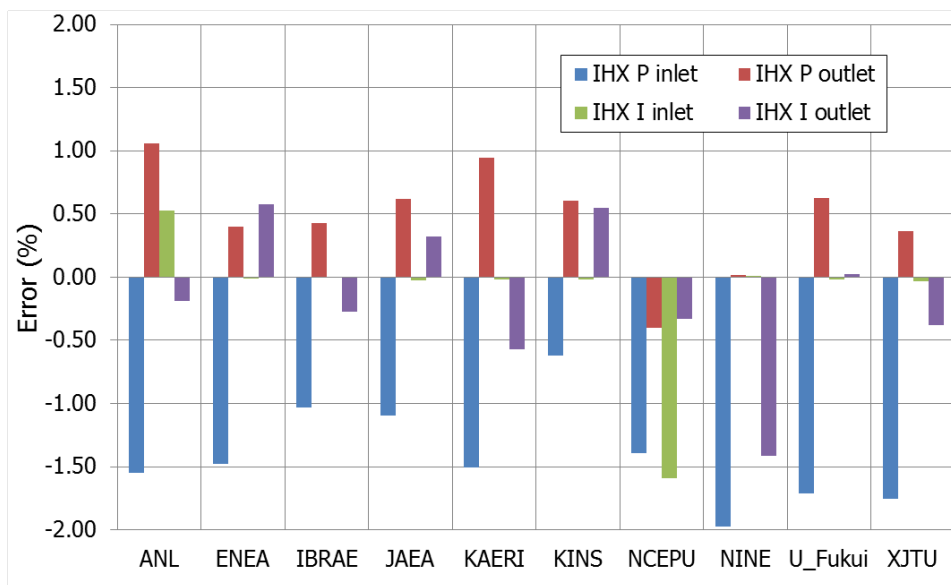


FIG. 328. Achieving a steady state: IHX inlet and outlet temperatures of primary and intermediate side.

9.2.2.4. Quantitative accuracy evaluation

This is the last step of the adopted methodology which deals with the quantitative accuracy evaluation performed utilizing the FFTBM. TABLE 61 lists the Average Accuracy (AA) values for the 26 selected parameters for each participant. Note that for the upper plenum temperature (item #21) and for the outlet temperature of the IHX primary side (item #23), two AA values were selected for each participant. This is due to the fact that, as specified before, several experimental measurements are available for these two parameters and only the

maximum (item #21a and item #23a respectively) and minimum (item #21b and item #23b respectively) AA values are reported in the table. The AA values derived from the comparison between the calculation results and the remaining experimental data vary inside these ranges for each participant.

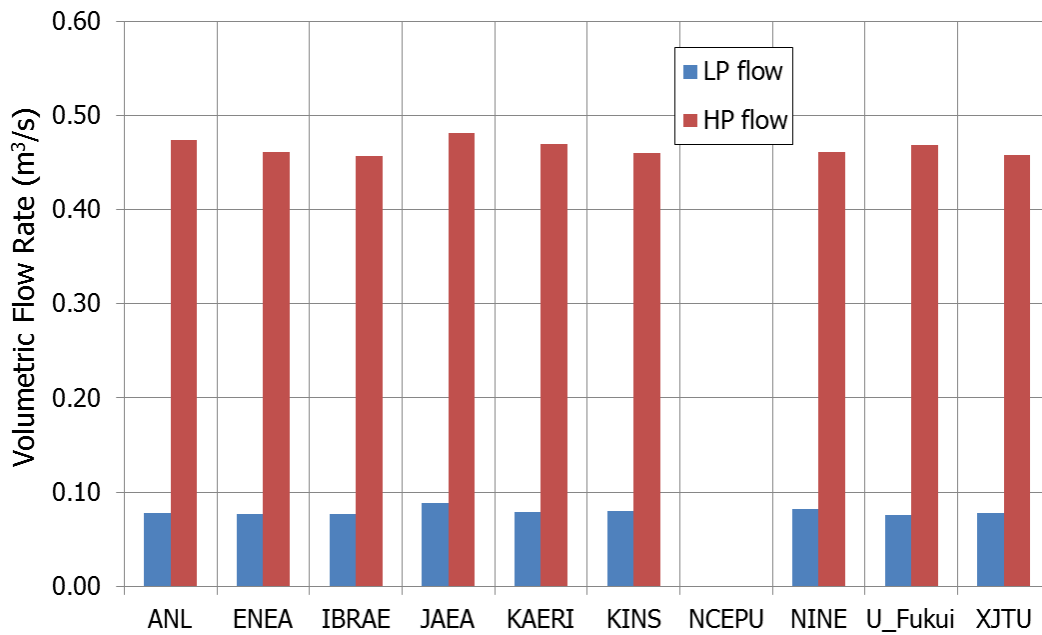


FIG. 329. Achieving a steady state: high pressure and low pressure volumetric flow rates.

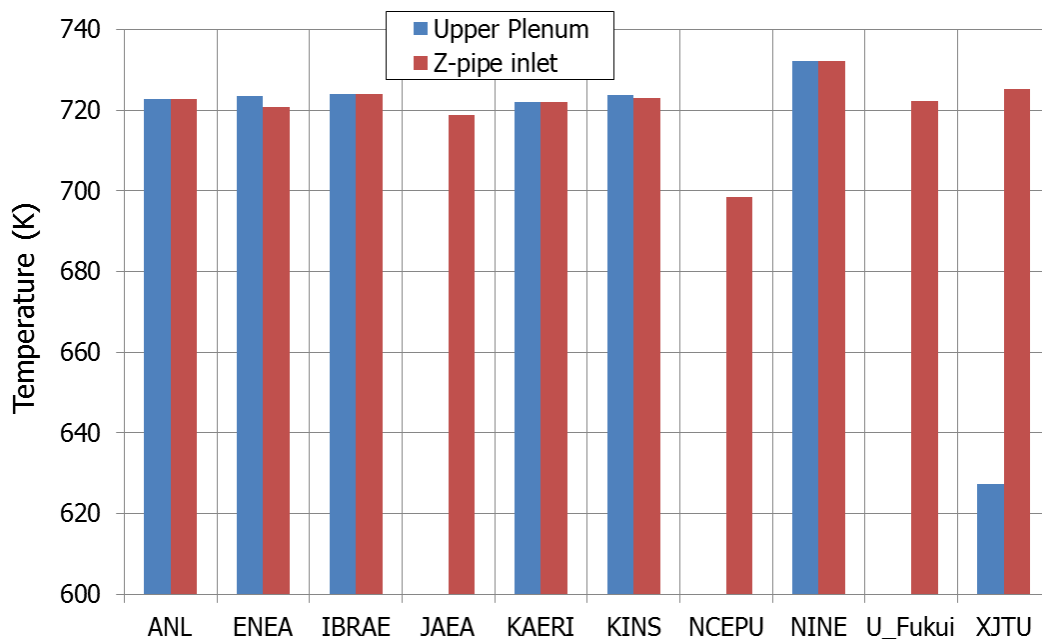


FIG. 330. Achieving a steady state: upper plenum and Z-Pipe inlet temperatures.

In FIG. 331 the AA values of the mass flow rate of pump 2 and of the two instrumented subassemblies are reported. It can be seen that:

- (a) the pump 2 mass flow rate is in good agreement with the experimental data over the entire transient. This is indicated by the fact that the AA values vary from 0.0864 to 0.1226;
- (b) wider AA value ranges are predicted for the mass flow rates of subassemblies XX09 (from 0.0519 to 0.2155) and XX10 (from 0.0824 to 0.2821).

For these three parameters, the NCEPU AA values were not included in the AA ranges, as including them would produce ranges that are not representative of the rest of the results.

TABLE 61. FFTBM AA RESULTS FOR THE DIFFERENT PARTICIPANTS

#	Parameter	ANL	ENEA	IBRAE	JAEA	KAERI	KINS	NCEPU	N.IN.E.	U. Fukui	XJTU
14	Pump 2 MFR	0.0864	0.1226	0.0947	0.102	0.0946	0.1063	--	0.0866	0.1054	0.0906
17	XX09 MFR	0.1311	0.0965	0.0519	0.0849	0.0728	0.096	0.7153	0.178	0.2155	0.1698
18	XX10 MFR	0.1819	0.1466	0.2821	0.0824	0.1076	0.1027	0.4432	0.2298	0.0931	0.165
19	LPP T	0.053	0.0496	0.0503	0.0498	0.0526	0.0476	--	0.0511	0.0476	0.053
20	HPP T	0.0494	0.0502	0.0489	0.0489	0.0498	0.0507	0.0573	0.0495	0.0486	0.0487
21a	UP T _{max}	0.0688	0.1187	0.0956	0.1017	0.0929	0.1604	--	0.0925	0.2349	0.101
21b	UP T _{min}	0.0511	0.0476	0.0359	0.0747	0.0522	0.1337	--	0.0676	0.2152	0.0756
22	IHX P In T	0.2539	0.2624	0.0665	0.2373	0.2537	0.1054	0.1493	0.1291	0.2785	0.1987
23a	IHX P Out T _{max}	0.3107	0.295	0.0572	0.2896	0.0467	0.1014	0.286	0.293	0.2759	0.2562
23b	IHX P Out T _{min}	0.2915	0.275	0.039	0.2697	0.0238	0.0847	0.2734	0.2736	0.2566	0.2375
25	IHX I Out T	0.1006	0.0501	0.0309	0.0473	0.0463	0.0577	0.0915	0.0714	0.0652	0.0494
27	XX09 FM T	0.0261	0.0256	0.0259	0.0276	0.0293	0.0264	--	0.0236	0.0264	0.0266
28	XX09 MTC T	0.1405	0.0725	0.071	0.074	0.0663	0.0678	0.2486	0.0849	0.3113	0.0903
29	XX09 TTC T	0.085	0.0693	0.096	0.0741	0.0551	0.0923	0.2844	0.0766	0.1014	0.0843
30	XX09 ATC T	0.0809	0.1444	0.1215	0.0994	0.0718	0.112	--	0.1404	0.1301	0.0779
31	XX09 OCT T	0.0452	0.0634	0.1413	0.0809	0.0862	0.0974	0.2041	0.1214	0.2522	0.1284
32	XX10 FM T	0.0203	0.0204	--	0.0231	0.0235	0.0212	--	0.0202	0.0208	0.0223
33	XX10 MTC T	0.0818	0.049	--	0.0927	0.0418	0.033	0.2682	0.0575	0.1827	0.1129
34	XX10 TTC T	0.0707	0.0676	--	0.0944	0.035	0.0344	0.3338	0.0679	0.1046	0.1076
35	XX10 ATC T	0.0815	0.118	--	0.2076	0.0589	0.0623	--	0.1163	0.1383	0.1069
36	XX10 OCT T	0.0538	0.0635	--	0.1207	0.0602	0.0415	0.2962	0.148	0.1773	0.1328
37	PD 1A1 T	0.1488	0.0705	0.151	0.0661	0.1471	--	--	0.1227	0.1742	0.1053
38	Driver 3B1 T	0.1718	0.192	0.2066	0.1757	0.1757	--	--	0.1629	0.2486	0.1871
39	Driver 4F1 T	0.1533	0.1257	0.1976	0.1161	0.1509	--	--	0.1541	0.1799	0.195
40	Driver 5C2 T	--	0.1759	0.2428	0.1184	0.1951	--	--	0.1581	0.2155	0.2269
41	HFD 6C4 T	0.1307	0.0849	0.1483	0.0587	0.1377	0.3022	--	0.1144	0.1794	0.1931
42	Refl. 9E4 T	0.072	0.0666	--	0.0444	0.0805	--	--	0.0841	0.0788	0.0937
43	Blanket 12E6 T	0.1258	0.1654	--	0.149	0.1552	--	--	0.1502	0.148	0.1866

FIG. 332 shows the AA values for the temperature in the low pressure and high pressure inlet plena and in the upper plenum. Regarding the inlet plena temperatures, the comparison between the reference data and the simulation results provides low AA values (around 0.05) for all the participants. However, the AA values for the upper plenum temperature are

characterized by a wider range: the AA values for the maximum temperature vary from 0.069 to 0.235, while the range for the minimum temperature is between 0.036 and 0.215.

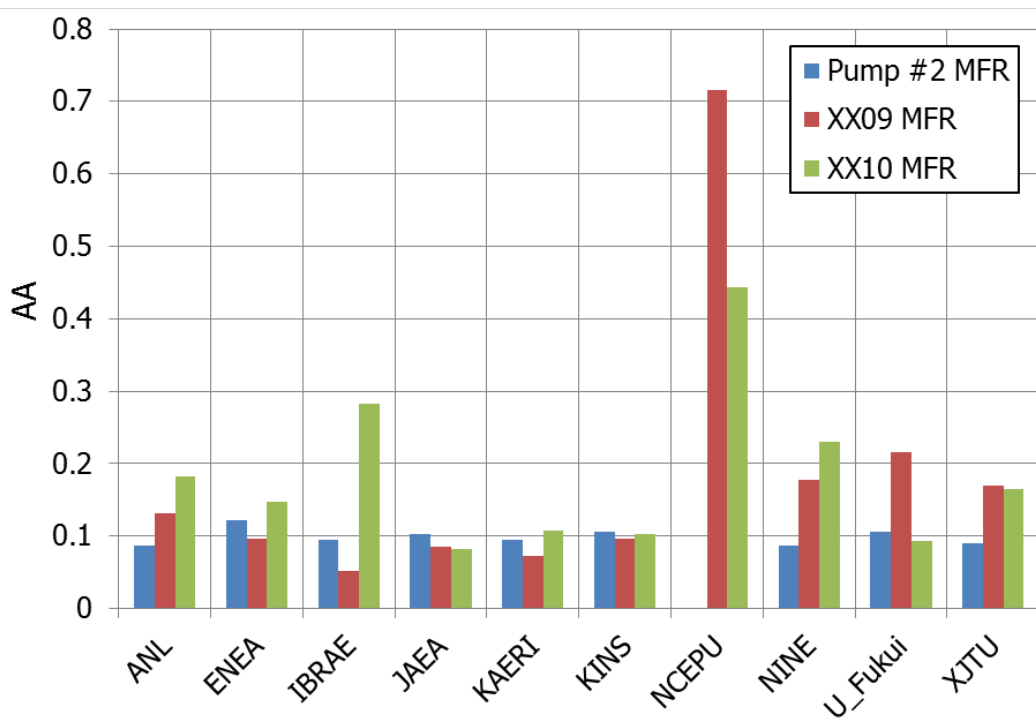


FIG. 331. FFTBM results, mass flow rates for pump 2 and the two instrumented subassemblies (XX09 and XX10).

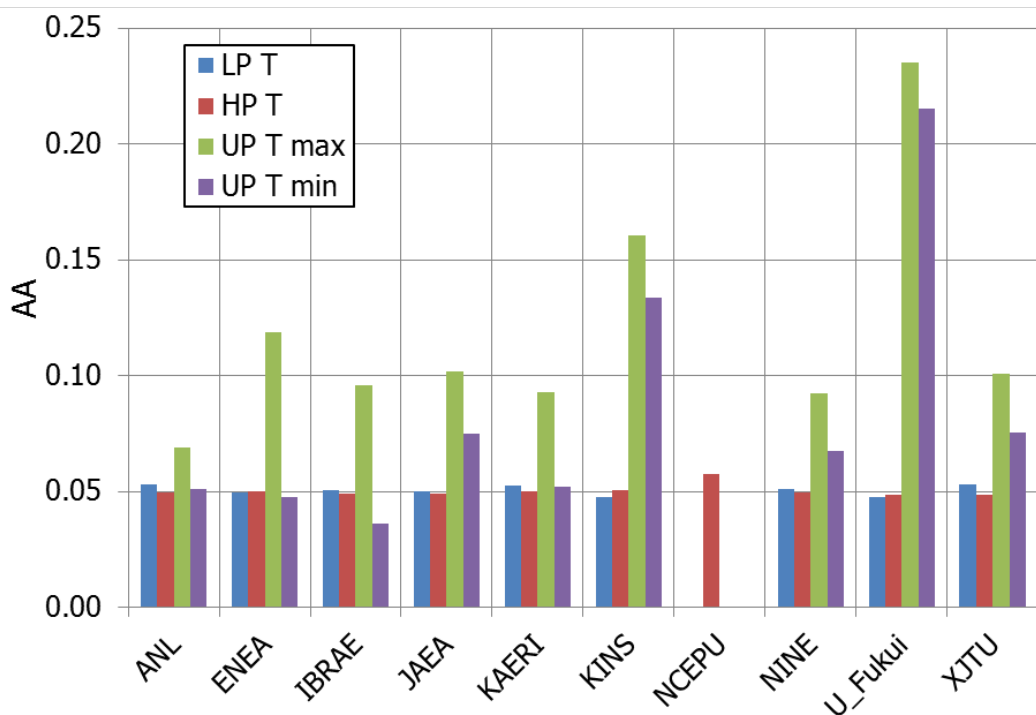


FIG. 332. FFTBM results, low pressure and high pressure inlet plena and upper plenum temperatures.

FIG. 333 presents AA values for the IHX primary side inlet and outlet temperatures, as well as for the IHX intermediate side outlet temperature. The following considerations apply:

- The comparison between the experimental data and participant results for the IHX primary side temperatures shows higher AA values and wider ranges compared to the data for the intermediate side;
- For the IHX primary side inlet temperature, the AA values vary from 0.066 to 0.279;
- For the IHX primary side outlet temperature, the AA values are higher than for the IHX primary side inlet temperature for almost all the participants. The minimum AA values varying from 0.039 to 0.292, while the maximum AA values are between 0.047 and 0.311;
- The simulation results for the IHX intermediate side outlet temperature are in good agreement with the experimental data, as shown by the fact that the maximum AA value is about 0.1.

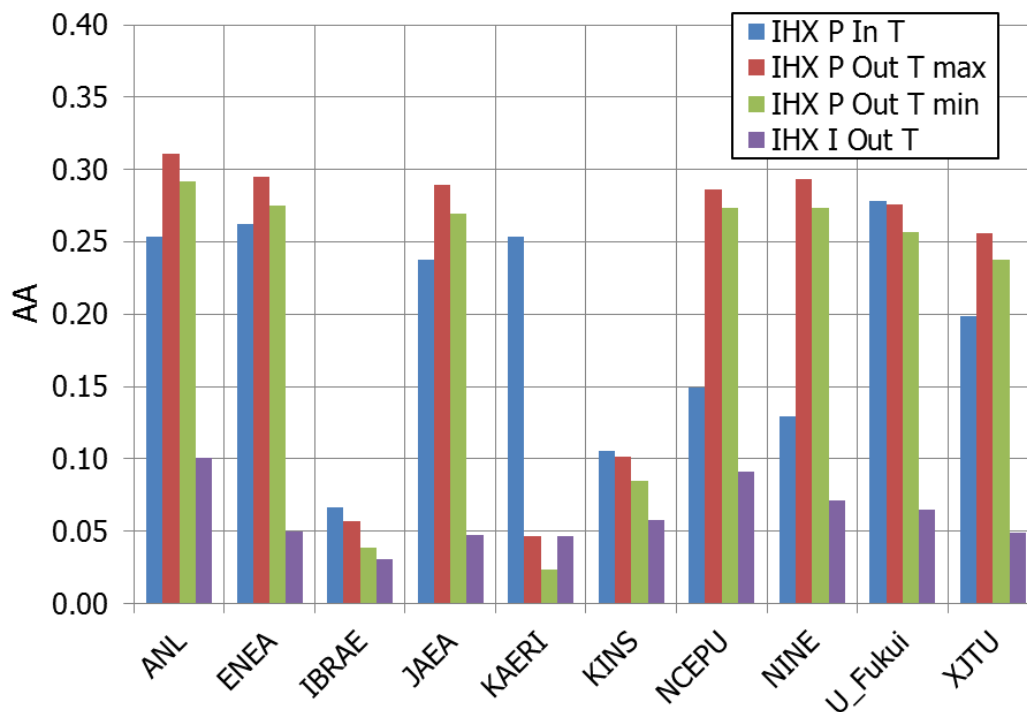


FIG. 333. FFTBM results, IHX primary side inlet and outlet temperatures and intermediate side outlet temperature.

Turning now to the instrumented subassemblies, the AA values show good agreement between the experimental data and the simulation results of all participants for the flowmeter temperatures in both XX09 and XX10, as shown in FIG. 334 and FIG. 335, respectively. The AA values for these temperatures are less than 0.03 for all the participants. However, larger discrepancies and wider ranges can be seen for the coolant and cladding temperatures along the two instrumented subassemblies. The results for these parameters do not fall within a well-defined rule. Generally, lower AA values are obtained for the cladding temperature along the active part of the subassemblies, while higher AA values are observed for the coolant temperatures above the core region. In particular, for XX09, the AA values related to the coolant and cladding temperatures vary between 0.045 and 0.311 (see FIG. 334), while for XX10, the AA values of the different temperatures range from 0.033 to 0.334 (see FIG. 335).

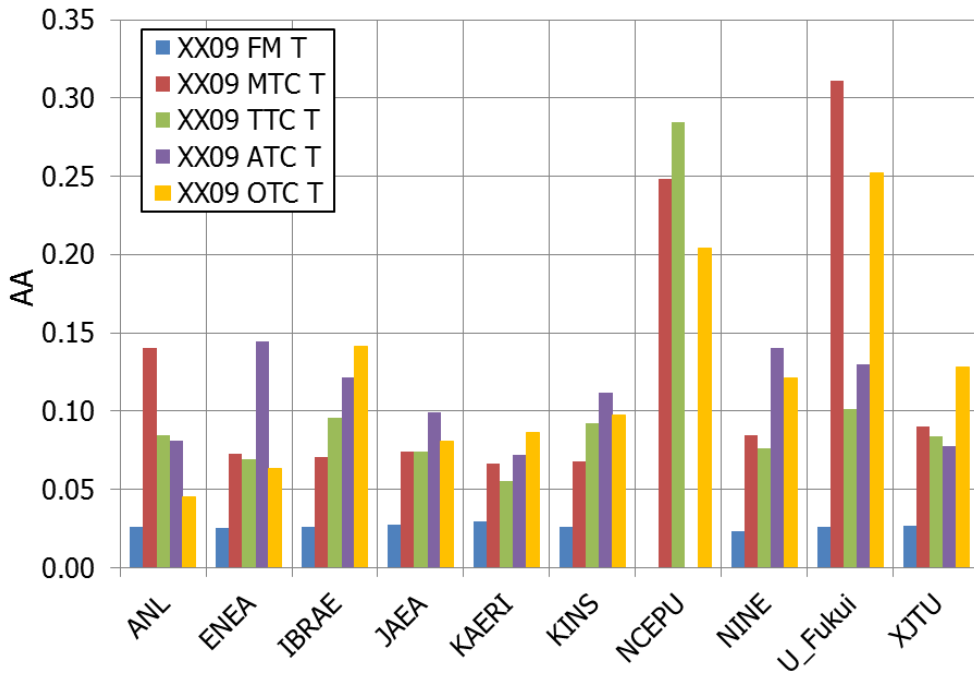


FIG. 334. FFTBM results, XX09 subassembly coolant and cladding temperatures.

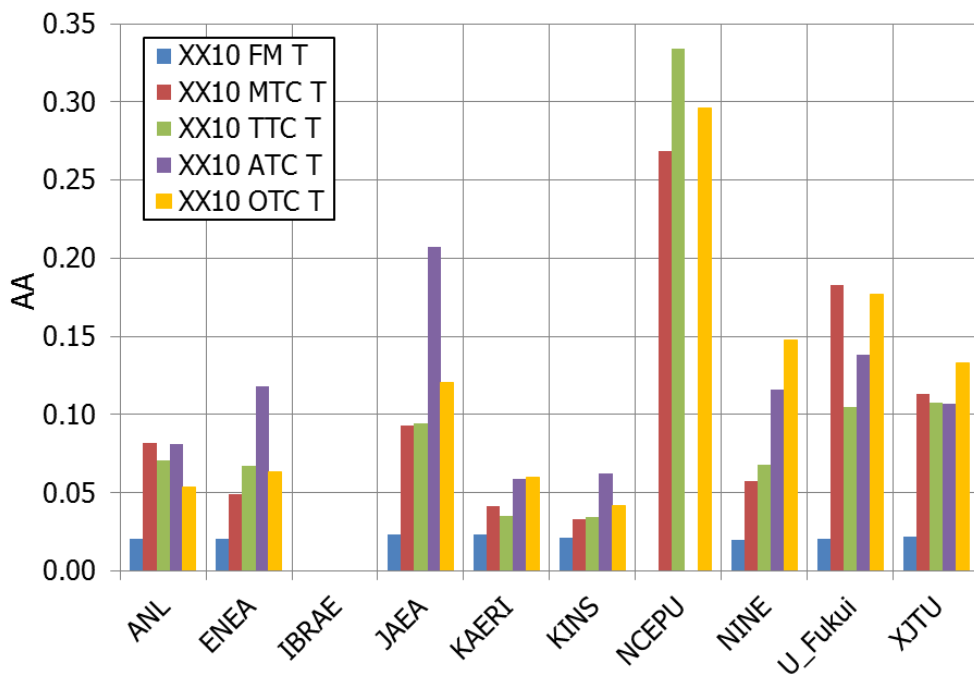


FIG. 335. FFTBM results, XX10 subassembly coolant and cladding temperatures.

9.3. MAIN OUTCOMES FROM THE ANALYSIS

The primary goal of the qualification analysis described above was to support interpretation of the results submitted by the CRP participants through providing quantitative measures of the discrepancies between the models developed by the participants and the reference specification data. These measures are intended to support better understanding of the reasons for the differences between the calculated results and the experimental data. It is important to emphasize that the process was not intended to provide a ranking among the results.

It should be noted that this is the first time that the SCCRED methodology has been applied to a system other than a light water reactor system, so the results of this analysis have also provided a learning experience in broadening the SCCRED methodology to a wider class of reactor systems.

9.3.1. Summary of the results

The summary in Section 9.2.2.1 on nodalization features shows the varying level of detail of the models and the different assumptions and user choices made by the participants. For instance, the total number of hydraulic volumes used to model the entire EBR-II reactor varies from several hundred up to 20 000, while the mesh points selected for all the heat structures vary from about 1000 to 100 000.

From the analysis of the geometrical fidelity data it can be seen that most of the parameters are inside the error band of 10% and only few of them exceed the error range of 20%. The higher error values are found in the liquid and stainless steel volumes of the outer core region (experimental, steel, reflector and blanket subassemblies). In addition, most of the liquid volume versus elevation curves are in good agreement with the reference values for both the primary and the intermediate loops (see FIG. 315 and FIG. 316).

The steady state values are generally predicted well by all the participants. The parameters characterized by the lowest errors are the temperatures in the high pressure and low pressure inlet plena (all of them below 0.4% except for one participant). The highest discrepancies are found for the IHX primary side inlet temperature (without considering the sodium inventory in the primary and intermediate circuits), where almost all the errors vary between 1% and 2% (see FIG. 328).

Regarding the FFTBM results, it can be seen that the higher AA values occur for both inlet and outlet temperatures on the IHX primary side, for which almost all participants have a value higher than 0.25. This can be due to the particular geometry of the IHX (i.e. the baffle plate at the primary side inlet) and to the positions where the thermocouples are located. Better agreement is found between the experimental data and the simulation results for the low pressure and high pressure inlet plena, where the AA values for all the participants are around 0.05. It should be noted that the same conclusions are obtained from comparison of the recorded and predicted steady state parameters, that is, the inlet plena temperatures are globally well predicted by the participants, while the results of the IHX primary side temperatures show some discrepancies with the experimental data.

9.3.2. Lessons learned

Application of the proposed qualification methodology to the benchmark was certainly a worthwhile effort and was helpful for obtaining more insights about interpretation of the participants' results. In particular, the methodology made it possible to identify the relative

importance of the different kinds of discrepancies or errors (discrepancies in developing the models, in achieving a steady state, and in predicting the time behaviour of selected responses of interest). As such, application of the methodology is recommended for future CRPs. Note: it is extremely important to implement application of this methodology at the very beginning of the project. The data requested by the methodology should be identified in the benchmark specifications, and an entire phase of the benchmark project should be devoted to preparing the information needed for application of the methodology.

One of the main challenges in applying the qualification methodology to this benchmark was to adopt a suitable terminology applicable to all the different computer codes used by the participants. Another challenge was applying the methodology to a different kind of reactor system than those (i.e. light water reactors) for which the methodology had already been successfully applied in the past. This is a very important step in understanding exactly which data should be requested from the participants so as to allow for performing a meaningful comparison analysis.

Regarding the application of the methodology to the benchmark, the following are noted:

- (a) The experimental or reference data were mostly related only to temperature or mass flow rates measurements. This fact limits a full interpretation of the reasons for the discrepancies among the participants' results;
- (b) The qualitative analysis of the transients (i.e. the derivation of phenomenological windows and of relevant thermal hydraulics aspects) was not performed due to limited resources and time;
- (c) The quantitative accuracy evaluation performed by the FFTBM is limited only to the derivation of single AAs. The global average amplitude (AA_{tot}) was not derived due to the following reasons:
 - (i) Experimental or reference data are related only to temperature or mass flow rate measurements, and thus they do not characterize the global behaviour of the system;
 - (ii) The weighting factors to calculate AA_{tot} are available only for light water reactors. A new derivation of these factors based on experimental evidence is needed for application to sodium cooled fast reactors.

10. OBSERVATIONS AND TRENDS WITHIN THE COLLECTIVE SET OF PARTICIPANT RESULTS

10.1. GENERAL OBSERVATIONS

As expected, participant results improved in phase 2 over the phase 1 (blind) results, and phase 2 results were more consistent among the participants than were the phase 1 results. Participants generally predicted overall trends in the recorded data successfully.

Some aspects of the analysis were beyond the capabilities of systems analysis codes, e.g., prediction of the IHX primary side inlet temperature. During the CRP, the conclusion was reached that the recorded IHX inlet temperature data were not representative of the average inlet temperature, and so the average Z-Pipe outlet temperature/IHX inlet temperature predictions of the systems analysis codes could not match the recorded data. This conclusion is consistent with the phase 2 results of two of the participants. One of these analyses was

performed using coupled systems thermal hydraulic/computational fluid dynamics codes, which produced temperatures at multiple locations in the IHX primary side inlet, and one of the IHX upper node temperatures gave a good comparison against the recorded data at the IHX inlet. The other used two dimensional heat structures, including in the IHX inlet plenum, and in this case produced very good agreement with one of the IHX upper node temperatures over more than half of the elapsed time for both transients.

The remainder of this section highlights several trends in the collective results. The full set of collective results plots for both phase 1 and phase 2 can be found in Appendix IV.

10.2. SHRT-17

10.2.1. Primary pump flowrate

As mentioned in Sections 3.3.1 and 3.3.2, analysis performed during the CRP indicated that both primary pumps locked during SHRT-17; incorporating this knowledge into the modelling brought primary pump flowrate predictions of most of the simulations into close alignment with the recorded data, as can be seen in FIG. 336.

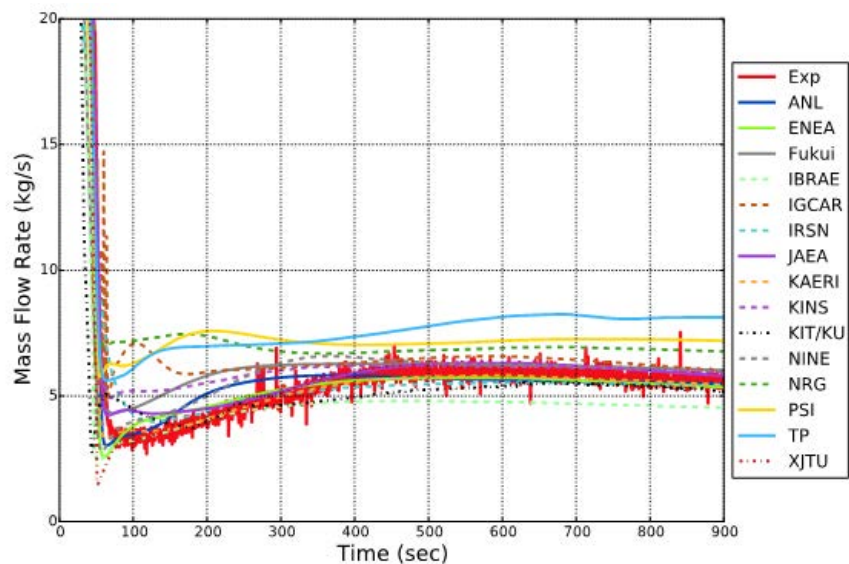


FIG. 336. SHRT-17 phase 2 primary flow rate predictions vs. measured data.

All the simulations model the rapid loss of flow following the loss of power to the pumps at time $t=0$ s. and predict the qualitative behaviour of the flow as it stabilizes upon establishment of natural circulation. The region where the simulations differ from one another the most is from about 75 to 300 seconds, which is the transition to natural circulation. The differences in nodalization, pump models, locked rotor coefficient values, etc. among the models all impact the predicted values in this region.

This behaviour of the flow rate predictions drives similar behaviour in the results for peak fuel and coolant temperature, as can be seen in FIG. 337, where again, the coolant temperature results differ from one another the most between approximately 75 and 300 seconds.

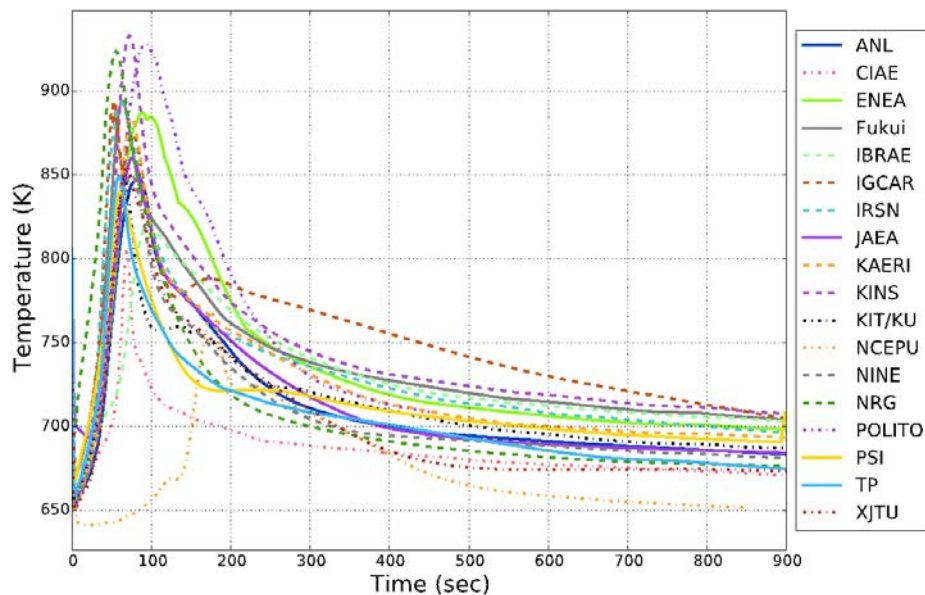


FIG. 337. SHRT-17 phase 2 peak in-core coolant temperature predictions.

10.2.2. XX09 temperatures

Participant models of the instrumented subassemblies varied considerably. Most included radial heat transfer; some used subchannel modelling to produce radial temperature distributions across the subassembly, while others calculated an average outer cladding temperature at each axial node. A few accounted for gamma heating. Comparisons of temperature predictions against recorded data within XX09 indicate that accounting for radial heat transfer with neighbouring subassemblies and good prediction of primary pump flow rate were the most important factors in obtaining good XX09 temperature predictions.

10.2.3. XX10 temperatures

Good results for primary pump flow were again important in predicting temperatures within XX10. The expectation was that accounting for gamma heating in the modelling would improve agreement with the recorded data, since XX10 consisted of steel pins, not fuel and gamma heating is a significant contributor to pin temperatures. However, this was not the case; models that included gamma heating did no better, and sometimes not as well, as models that did not. Again, modelling radial heat transfer from neighbouring subassemblies and accurately predicting primary pump flow rate were the most important factors in agreement between predicted and measured XX10 temperatures.

The impact of model assumptions for power generation in XX10 during SHRT-17 was investigated by the NRG participant. Three cases were considered for power drop in XX10 following scram: 1) power drop is the same as in a fueled subassembly, 2) power drop reflects gamma heating due to fission product decay, and 3) power drops to zero and remains zero throughout the transient, which corresponds to neglecting gamma heating in the model. The results showed that these three different assumptions produce only small differences in the calculated XX10 temperatures, due to the size of the power transferred from neighbouring subassemblies and also to a balancing effect caused by a reduction in radial power transfer as the power generated within XX10 increases (case 2). A detailed explanation of the analysis is presented in Appendix V.

10.3. SHRT-45R

10.3.1. Primary pump flowrate and fission power

SHRT-45R analysis has the added challenge of needing to accurately predict power as well as primary pump flow in order to perform a good simulation of the temperature behaviour throughout the plant. In addition, accuracy of the mass flow rate prediction is affected by the accuracy of the power prediction.

Looking first at the modelling of reactor power, most participants who evaluated SHRT-45R chose point-kinetics to calculate reactivity feedbacks. The resulting fission power values exceeded the recorded data from about 300 seconds forward for all participants, as shown in the plots in FIG. 338. There was also quite a spread among the participants in the power values predicted for SHRT-45R. This spread in power results produced peak fuel and coolant temperature predictions with significant spread, as is clear from the plots of peak coolant temperature in FIG. 339.

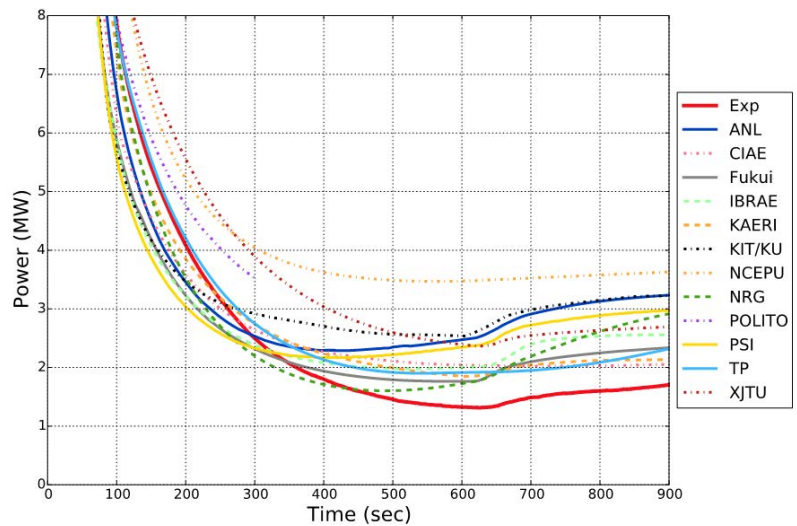


FIG. 338. SHRT-45R phase 2 fission power predictions vs. measured data.

The differences between predicted and measured fission power did have an effect on the flow predictions, but overall, the modelling captured the flow behaviour better than the power behaviour. As shown in FIG. 340, several participants matched the recorded flow data very closely, and most captured the shape of the data curve and were within 20% of the data values. This spread in flow curves is due at least in part to the spread in predicted power values shown in FIG. 338.

10.3.2. Z-Pipe inlet temperature

The power and flow predictions described in Section 10.3.1 resulted, for most models, in a predicted power/flow ratio during the last 600 s. of the transient that was higher than the ratio calculated from the measured values. Therefore, the average temperature of the sodium leaving the core during the last 600 s. was overpredicted. This meant that the temperature of the sodium entering the outlet plenum and eventually entering the Z-Pipe was also predicted to be too high by most simulations. This is clearly seen in the plots of the Z-Pipe inlet temperature presented in FIG. 341; these plots indicate that most simulations overpredicted the inlet temperature during the last half of the transient.

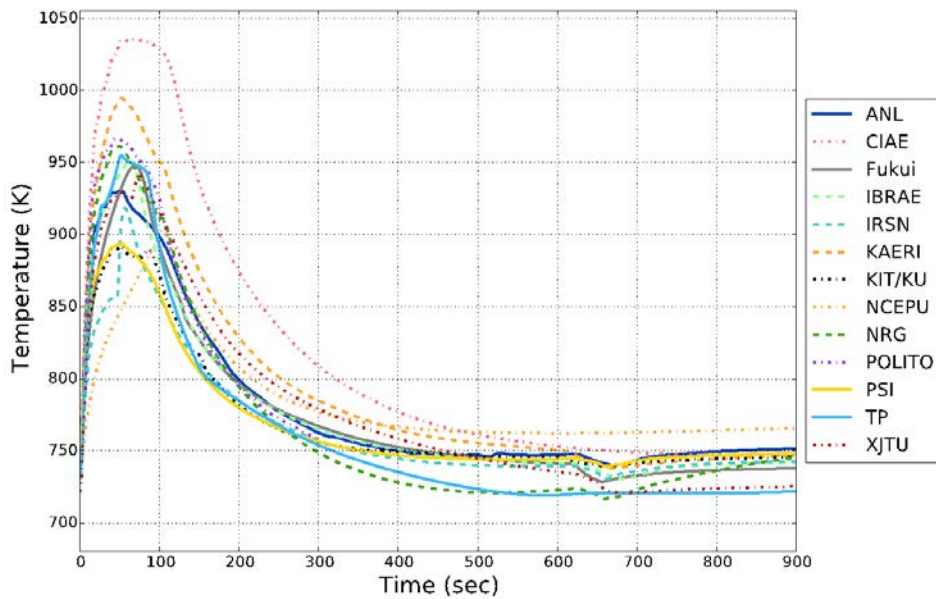


FIG. 339. SHRT-45R phase 2 peak in-core coolant temperature predictions.

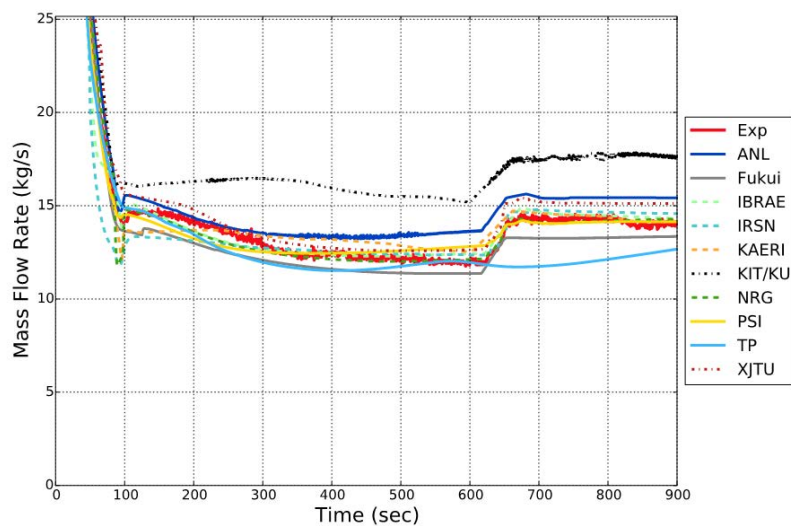


FIG. 340. SHRT-45R phase 2 primary flow rate predictions vs. measured data.

The challenge posed by predicting the power during SHRT-45R is demonstrated by the upper plenum wall heat transfer sensitivity study performed by Argonne and discussed in Section 8.12. Instead of using the calculated power, Argonne’s study enforced the measured SHRT-45R power level as a boundary condition, while using the code-generated values for the primary pump mass flow rate. As shown in FIG. 310, when the model was modified to force the power to follow the recorded data, the Z-Pipe inlet temperature predictions matched the Z-Pipe inlet temperature data measurements very well from about 200 s. onward, regardless of the value used for the heat transfer coefficient. One focus of future work should be improving calculations of the SHRT-45R transient power levels.

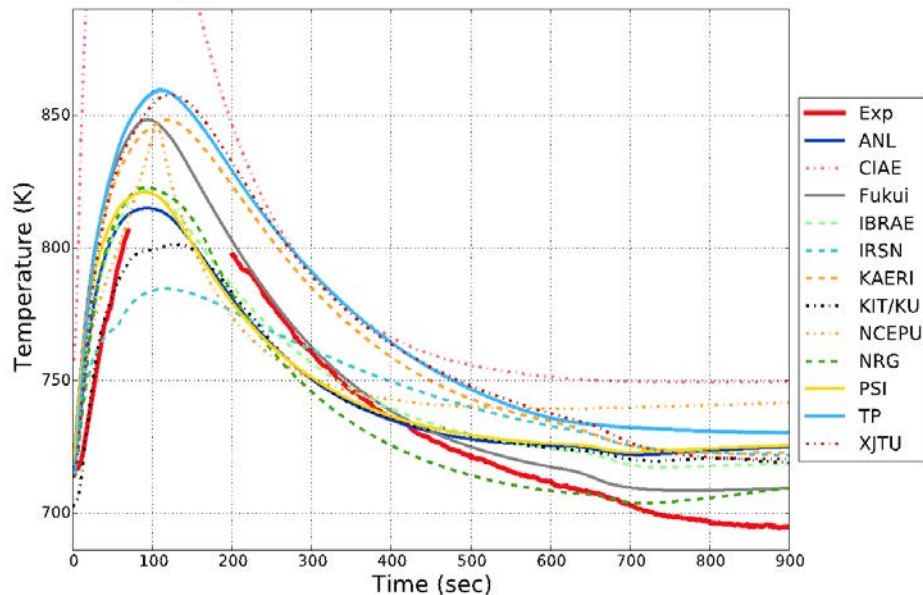


FIG. 341. SHRT-45R phase 2 Z-Pipe inlet temperature predictions vs. measured data.

10.3.3. XX09 and XX10 temperatures

Final temperature results for both instrumented subassemblies generally overpredict the measured data in the last half of the transient. This is consistent with the simulation results for power discussed in Section 10.3.1.

11. CONCLUSIONS AND RECOMMENDATIONS

11.1. CONCLUSIONS FROM THE EBR-II BENCHMARKS STUDY

Both the thermal hydraulic and neutronic simulations performed for the CRP were challenging to produce. The EBR-II reactor had a complex geometry, particularly in the upper and lower plena regions and in the instrumented subassemblies. Also, some plant details that would have been helpful for the modelling simply were not available. A large body of recorded data was provided for both transients but was limited by having been taken with 1980's technology and by the fact that several key instruments that had been installed when EBR-II was built had failed by the time the SHRT tests were run and could not be accessed to be replaced.

Operating within these limitations, the CRP participants collectively showed significant modelling progress over the course of the CRP and were able to predict most plant parameters with acceptable accuracy, as discussed in detail in Sections 7 and 10. Most participants also achieved reasonably good predictions for temperatures in the instrumented subassemblies, a significant achievement, given the complicated geometries of these two subassemblies.

The least satisfactory outcome of the simulations was the inability of most models to predict the IHX primary side inlet temperature. However, investigating this modelling obstacle led to the realization that the recorded data at this location did not represent an average temperature in the region and therefore could not be predicted accurately by a standard systems analysis code approach. This conclusion was confirmed by two participants who took modified

modelling approaches that produced results that matched the recorded data much more satisfactorily.

While the fuel used in EBR-II at the time of the SHRT tests was U-5Fs, future safety analyses of metal-fueled fast reactors will focus on reactors fueled with U-Pu-Zr ternary alloy. Such analyses will include severe accident cases that will require thermodynamic properties not only for solid fuel but also for molten fuel and fuel vapour. However, these properties are not readily available at present. The participant team at Kyushu University, which developed the U-5Fs properties used by KIT in their joint CRP analyses, has also developed a consistent set of thermodynamic properties for U-Pu-Zr as an extension of their work on the CRP. These properties have been implemented in SIMMER-III and are discussed in some detail in Appendix VI.

The CRP also provided an opportunity to experiment for the first time with applying the SCCRED qualification process to a fast reactor system. As described in Section 9, this was a valuable learning experience that provided an alternative look at the collective results of the CRP simulations and produced quantitative measures of the discrepancies between the simulation results and the recorded data. The exercise of applying this approach, which had been developed for light water reactors, also brought out factors that need to be re-derived for future application of this process to simulations of sodium cooled fast reactors.

This was the largest fast reactor CRP ever conducted by the IAEA, with 19 participant groups representing 11 countries. Overall, the participants found the CRP to be an effective approach for testing modelling in fast reactor systems analysis codes and for adding new modelling options. Including a separate neutronics benchmark for SHRT-45R was found to be a valuable aspect of the CRP and one that has not often been included in past CRP's. The CRP was also found to be an effective way to transfer knowledge to the next generation of researchers. In addition to a number of early career staff who contributed to the CRP, the participant groups collectively included five summer interns, seven Master's students and eight PhD students, as well as several postdocs.

11.2. LESSONS LEARNED FROM THE EBR-II BENCHMARKS STUDY

At the final RCM, the CRP participants discussed what lessons had been learned over the four-year course of the project. These focused primarily on the benchmark specifications, conduct of the CRP, improvements in how future test programmes might be conducted, benefits and drawbacks of the CRP as a method for benchmark analyses, etc. The lessons learned that were identified by the participants can be summarized as follows:

Regarding conduct of future CRPs:

- (a) Plan to issue a revision to the original benchmark specification early in the CRP. Formally set aside a period of time (4–6 months) following the first RCM for refinement of the benchmark specifications as the participants begin to develop their models and provide questions and feedback to the institution that developed the specification. This was done with the EBR-II benchmarks CRP and resulted in revision 1 of both specifications being issued about seven months after the first RCM. Revision 1 contained clarifications, a few corrections and some additional information about the EBR-II plant;

- (b) Initiate uncertainty analysis and results qualification analysis at the start of the CRP. Identify the parameters that will be needed for the analyses in the benchmark specification, and schedule a phase of the project to be devoted to preparing the information needed for the analyses;
- (c) The CRP was a valuable driver for adding new models to systems codes and contributed, for many participants, to code validation and added confidence in model generation;
- (d) The CRP was very beneficial for engaging early career researchers, giving them exposure to a range of modelling approaches, codes and experiments. It also gave them the opportunity to be involved in an international project and communicate with an international community of experienced researchers. And for some, it was an opportunity to expand their expertise beyond light water reactors to include fast reactors;
- (e) It was valuable to include a separate neutronics benchmark for an unprotected transient like SHRT-45R;
- (f) The large size of this CRP (19 participants) was, in general, quite manageable. However, future CRPs with such a large number of participants should consider forming subgroups to address specific modelling challenges;
- (g) It would be beneficial to pair up participants at the beginning of the CRP to peer review each other throughout the course of the project. This would also encourage more decentralized communications among the CRP participants;
- (h) For CRPs with a large number of participants, consider using a project management tool to manage project timelines and participant progress. Have the IAEA facilitate communications between RCMs by creating a forum for group communications and to encourage communications by all participants, not just the CRP organizers;
- (i) At several times during the blind analysis phase (approximately the first 18–20 months of the CRP), evaluate progress by all participants in creating models and performing the steady state initialization.

Regarding data collection for whole plant tests and plant operation:

- (a) The CRP analyses provided insight into improved instrumentation variety and location for future prototype reactors, also on the importance of being able to change out failed instrumentation;
- (b) Before conducting a test series such as the SHRT series, run some trial transients on a primary loop mock-up and record data in the same locations as in the actual reactor. Perform simulations of these transients and compare the results against the recorded data. This will identify instrument locations and configurations that are recording data that are not consistent with the capabilities of the computer models.

Appendix I

FRICITION AND HEAT TRANSFER CORRELATIONS

Due to the large variety of codes used by the benchmark participants, many different correlations were incorporated into the models of EBR-II for the CRP. For some codes, specific correlations were hard-coded in, while in other codes, users selected from several options. The correlations selected for modelling these transients played an important role in determining the transient simulation progression, and therefore also in how well the simulation predictions agreed with the data measurements.

A series of correlations used by the benchmark participants has been collected and is provided in the tables below. The friction factor and heat transfer correlations selected to simulate SHRT-17 and SHRT-45R were provided by each organization for three important component types: pin bundles, pipes and the primary side of the intermediate heat exchanger. Friction factor correlations were provided because of their effect on natural circulation flow rates. Heat transfer correlations were provided because of their effect on temperatures, which were the most common measurement type used for comparison against simulation results. The friction and heat transfer correlations are listed below to provide additional insight into the differences among the simulation tools and models selected by each organization.

Unless specified otherwise, pressure drop is related to friction factor as

$$\Delta P = f \frac{w^2}{2 \rho A^2 D_h} L$$

Commonly used variables:

- f = Friction factor
- w = Mass flow rate
- ρ = Density
- A = Flow area
- u = Velocity
- D_h = Hydraulic diameter
- L = Length
- Re = Reynolds number
- Pe = Peclet number
- Nu = Nusselt number
- Gr = Grashof number
- Pr = Prandtl number
- ϵ = Roughness
- $\frac{P}{D}$ = Pitch-to-diameter ratio
- H = Spacer wire pitch
- ΔP = Pressure drop

TABLE 62. PIN BUNDLE CORRELATIONS

	Pin Bundle Friction Factor Correlations	Pin Bundle Heat Transfer Correlations
CIAE	$f = \begin{cases} 0.15/\text{Re}^{0.18} & \text{Re} \geq 1800 \\ 83/\text{Re} & \text{Re} < 1800 \end{cases}$	$\text{Nu} = 5.0 + 0.025 \text{Pe}^{0.8}$
NCEPU	$f = \begin{cases} 1.029 + \frac{2837}{\text{Re}^{1.24}} & \text{Re} \geq 800 \\ 64/\text{Re} & \text{Re} < 800 \end{cases}$	$\text{Nu} = \left[-16.15 + 24.96 \left(\frac{P}{D}\right) 8.55 \left(\frac{P}{D}\right)^2 \right] (a + b \text{Pe}^c)$ <p>where $a = 0, b = 1, \text{ and } c = 0.3$ for $\text{Pe} \geq 150$ $a = 4.496, b = 0, \text{ and } c = 0.3$ for $\text{Pe} \geq 150$</p>
XJTU	$f = \frac{\frac{32}{\sqrt{H}} \left(\frac{P}{D}\right)^{1.5}}{\text{Re}} (1 - \varphi)^{\frac{1}{2}} + \frac{0.48}{\text{Re}^{0.25}} \varphi^{\frac{1}{2}}$ <p>where</p> $\varphi = \begin{cases} 0 & \text{Re} \leq 400 \\ \frac{\text{Re} - 400}{4600} & 400 < \text{Re} < 5000 \\ 1 & \text{Re} \geq 5000 \end{cases}$	$\text{Nu} = 4.496 \left[-16.15 + 24.96 \left(\frac{P}{D}\right) - 8.55 \left(\frac{P}{D}\right)^2 \right]$
IRSN	$\Delta P = \frac{\Lambda_0 \left(\frac{L}{D_h}\right) \rho U^2}{2 f(\alpha)}$ <p>where</p> $\Lambda_0 = \left(-2 \log_{10} \left[\frac{\epsilon/3.7}{D_h} + \left(\frac{6.81}{\text{Re}}\right)^{0.9} \right] \right)^{-2}$ $f(\alpha) = e \left[1 + 4.6 \left(\frac{P}{D} - 1\right) \right] \text{tg}(\alpha)$ $\text{tg}(\alpha) = \frac{\pi d}{h}$	$\text{Nu} = 4.82 + 0.0185 (\text{Re Pr})^{0.827}$
KIT & Kyushu University	$f = \begin{cases} 0.046/\text{Re}^{0.2} & \text{Re} > 2000 \\ 16/\text{Re} & \text{Re} \leq 2000 \end{cases}$	$\text{Nu} = 0.025 (\text{Re Pr})^{0.8}$

Pin Bundle Friction Factor Correlations

Pin Bundle Heat Transfer Correlations

$$f = \begin{cases} C_T / \text{Re}^{0.18} & \text{Re} \geq \text{Re}_T \\ \left(\frac{C_T}{\text{Re}^{0.18}} \right) \psi^{1/3} + \left(\frac{C_L}{\text{Re}} \right) (1 - \psi)^{1/3} & \text{Re}_L < \text{Re} < \text{Re}_T \\ C_L / \text{Re} & \text{Re} \leq \text{Re}_L \end{cases}$$

where

$$\psi = \log \left(\frac{\text{Re}}{\text{Re}_L} \right) / \log \left(\frac{\text{Re}_T}{\text{Re}_L} \right)$$

$$C_L = \left(-974.6 + 1612 \left(\frac{P}{D} \right) - 598.5 \left(\frac{P}{D} \right)^2 \right) \times \left(\frac{H}{D} \right)^{0.06 - 0.085 \left(\frac{P}{D} \right)}$$

$$C_T = \left(0.8063 - 0.9022 \log \left(\frac{H}{D} \right) + 0.3526 \left(\log \left(\frac{H}{D} \right) \right)^2 \right) \times \left(\frac{P}{D} \right)^{9.7} \left(\frac{H}{D} \right)^{1.78 - 2.0 \left(\frac{P}{D} \right)}$$

$$\text{Re}_L = 10^{(1.7 \frac{P}{D} + 0.777)}$$

$$\text{Re}_T = 10^{(0.7 \frac{P}{D} + 3.3)}$$

$$\text{Nu} = 4.0 + 0.33 \left(\frac{P}{D} \right)^{3.8} \left(\frac{Pe}{100} \right)^{0.86} + 0.16 \left(\frac{P}{D} \right)^{5.0}$$

IGCAR

$$f = \begin{cases} C_T / \text{Re}^{0.18} & \text{Re} \geq 3000 \\ \text{Interpolate between } f(\text{Re}_T) \text{ \& } f(\text{Re}_L) & 2200 < \text{Re} < 3000 \\ C_L / \text{Re} & \text{Re} \leq 2200 \end{cases}$$

where

$$C_T = 0.203$$

$$C_L = 64 / \Phi$$

$$\text{Re}_T = 3000$$

$$\text{Re}_L = 2200$$

$$\Phi = 0.69$$

$$\text{Nu} = 4.0 + 0.33 \left(\frac{P}{D} \right)^{3.8} \left(\frac{Pe}{100} \right)^{0.86} + 0.16 \left(\frac{P}{D} \right)^{5.0}$$

ENEA

$$f = \begin{cases} \left(-2 \log \left\{ \frac{\epsilon}{3.7D} + \frac{2.51}{\text{Re}} \times \left[1.14 - 2 \log \left(\frac{\epsilon}{D} + \frac{21.25}{\text{Re}^{0.9}} \right) \right] \right\} \right)^{-2} & \text{Re} \geq 3000 \\ \left(3.75 - \frac{8250}{\text{Re}} \right) \times \frac{(f_{T,3000} - f_{L,2200}) + f_{L,2200}}{64 / \text{Re}} & 2200 < \text{Re} < 3000 \\ 64 / \text{Re} & \text{Re} \leq 2200 \end{cases}$$

$$\text{Nu} = 5.0 + 0.025 \text{Pe}^{0.8}$$

where

$$\epsilon = 1.0 \times 10^{-5} \text{ m}$$

N.I.N.E

$$f = \begin{cases} C_T / \text{Re}^{0.18} & \text{Re} \geq \text{Re}_T \\ \left(\frac{C_T}{\text{Re}^{0.18}} \right) \psi^{1/3} + \left(\frac{C_L}{\text{Re}} \right) (1 - \psi)^{1/3} & \text{Re}_L < \text{Re} < \text{Re}_T \\ C_L / \text{Re} & \text{Re} \leq \text{Re}_L \end{cases}$$

where

$$\psi = \log \left(\frac{\text{Re}}{\text{Re}_L} \right) / \log \left(\frac{\text{Re}_T}{\text{Re}_L} \right)$$

POLITO

$$C_L = \left(-974.6 + 1612 \left(\frac{P}{D} \right) - 598.5 \left(\frac{P}{D} \right)^2 \right) \times \left(\frac{H}{D} \right)^{0.06 - 0.085 \left(\frac{P}{D} \right)}$$

$$\text{Nu} = 4.0 + 0.33 \left(\frac{P}{D} \right)^{3.8} \left(\frac{\text{Pe}}{100} \right)^{0.86} + 0.16 \left(\frac{P}{D} \right)^{5.0}$$

$$C_T = \left(0.8063 - 0.9022 \log \left(\frac{H}{D} \right) + 0.3526 \left(\log \left(\frac{H}{D} \right) \right)^2 \right) \times \left(\frac{P}{D} \right)^{9.7} \left(\frac{H}{D} \right)^{1.78 - 2.0 \left(\frac{P}{D} \right)}$$

$$\text{Re}_L = 10^{(1.7 \frac{P}{D} + 0.777)}$$

$$\text{Re}_T = 10^{(0.7 \frac{P}{D} + 3.3)}$$

$$f = \begin{cases} C_T / \text{Re}^{0.18} & \text{Re} \geq \text{Re}_T \\ \left(\frac{C_T}{\text{Re}^{0.18}} \right) \psi^{1/3} + \left(\frac{C_L}{\text{Re}} \right) (1 - \psi)^{1/3} & \text{Re}_L < \text{Re} < \text{Re}_T \\ C_L / \text{Re} & \text{Re} \leq \text{Re}_L \end{cases}$$

where

$$\psi = \log \left(\frac{\text{Re}}{\text{Re}_L} \right) / \log \left(\frac{\text{Re}_T}{\text{Re}_L} \right)$$

JAEA

$$C_L = \left(-974.6 + 1612 \left(\frac{P}{D} \right) - 598.5 \left(\frac{P}{D} \right)^2 \right) \times \left(\frac{H}{D} \right)^{0.06 - 0.085 \left(\frac{P}{D} \right)}$$

$$\text{Nu} = 7.0 + 0.025 (0.5 \text{ Re Pr})^{0.8}$$

$$C_T = \left(0.8063 - 0.9022 \log \left(\frac{H}{D} \right) + 0.3526 \left(\log \left(\frac{H}{D} \right) \right)^2 \right) \times \left(\frac{P}{D} \right)^{9.7} \left(\frac{H}{D} \right)^{1.78 - 2.0 \left(\frac{P}{D} \right)}$$

$$\text{Re}_L = 10^{(1.7 \frac{P}{D} + 0.777)}$$

$$\text{Re}_T = 10^{(0.7 \frac{P}{D} + 3.3)}$$

$$\Delta P = f \frac{L \rho u^k}{2D}$$

where

k is a constant between 1.9 and 2.1

$$f = \begin{cases} (0.094 R^{0.223} + 0.53R) + 88.0 R^{0.44} \text{Re}^{-1.62} R^{0.134} & \text{Re} \geq \text{Re}_T \\ \text{Interpolate between } f(\text{Re}_T) \text{ \& } f(\text{Re}_L) & \text{Re}_L < \text{Re} < \text{Re}_T \\ 64/\text{Re} & \text{Re} \leq \text{Re}_L \end{cases} \quad \text{Nu} = 5.0 + 0.025 \text{Pe}^{0.8}$$

University of Fukui

where

$$R = \frac{\epsilon}{D_h}$$

$$\text{Re}_T = 3000$$

$$\text{Re}_L = 2100$$

$$f = \begin{cases} C_T / \text{Re}^{0.18} & \text{Re} \geq \text{Re}_T \\ \left(\frac{C_T}{\text{Re}^{0.18}} \right) \psi^{\frac{1}{3}} + \left(\frac{C_L}{\text{Re}} \right) (1 - \psi)^{\frac{1}{3}} & \text{Re}_L < \text{Re} < \text{Re}_T \\ C_L / \text{Re} & \text{Re} \leq \text{Re}_L \end{cases}$$

where

$$\psi = \log \left(\frac{\text{Re}}{\text{Re}_L} \right) / \log \left(\frac{\text{Re}_T}{\text{Re}_L} \right)$$

$$C_L = \left(-974.6 + 1612 \left(\frac{P}{D} \right) - 598.5 \left(\frac{P}{D} \right)^2 \right)$$

$$\times \left(\frac{H}{D} \right)^{0.06 - 0.085 \left(\frac{P}{D} \right)}$$

$$C_T = \left(0.8063 - 0.9022 \log \left(\frac{H}{D} \right) + 0.3526 \left(\log \left(\frac{H}{D} \right) \right)^2 \right)$$

$$\times \left(\frac{P}{D} \right)^{9.7} \left(\frac{H}{D} \right)^{1.78 - 2.0 \left(\frac{P}{D} \right)}$$

$$\text{Re}_L = 10^{(1.7 \frac{P}{D} + 0.777)}$$

$$\text{Re}_T = 10^{(0.7 \frac{P}{D} + 3.3)}$$

KAERI

For $\text{Pe} \leq 150$:

$$\text{Nu} = 4.496 \left(-16.16 + 24.96 \left(\frac{P}{D} \right) - 8.55 \left(\frac{P}{D} \right)^2 \right)$$

For $150 < \text{Pe} < 1000$:

$$\text{Nu} = \left(-16.15 + 24.96 \left(\frac{P}{D} \right) - 8.55 \left(\frac{P}{D} \right)^2 \right) \text{Pe}^{0.8}$$

	Pin Bundle Friction Factor Correlations	Pin Bundle Heat Transfer Correlations
	$f = \begin{cases} C_T / \text{Re}^{0.18} & \text{Re} \geq \text{Re}_T \\ \left(\frac{C_T}{\text{Re}^{0.18}} \right) \psi^{1/3} + \left(\frac{C_L}{\text{Re}} \right) (1 - \psi)^{1/3} & \text{Re}_L < \text{Re} < \text{Re}_T \\ C_L / \text{Re} & \text{Re} \leq \text{Re}_L \end{cases}$	
	where	
	$\psi = \log \left(\frac{\text{Re}}{\text{Re}_L} \right) / \log \left(\frac{\text{Re}_T}{\text{Re}_L} \right)$	
KINS	$C_L = \left(-974.6 + 1612 \left(\frac{P}{D} \right) - 598.5 \left(\frac{P}{D} \right)^2 \right) \times \left(\frac{H}{D} \right)^{0.06 - 0.085 \left(\frac{P}{D} \right)}$	$\text{Nu} = 5.0 + 0.025 (\text{Pe})^{0.8}$
	$C_T = \left(0.8063 - 0.9022 \log \left(\frac{H}{D} \right) + 0.3526 \left(\log \left(\frac{H}{D} \right) \right)^2 \right) \times \left(\frac{P}{D} \right)^{9.7} \left(\frac{H}{D} \right)^{1.78 - 2.0 \left(\frac{P}{D} \right)}$	
	$\text{Re}_L = 10^{(1.7 \frac{P}{D} + 0.777)}$	
	$\text{Re}_T = 10^{(0.7 \frac{P}{D} + 3.3)}$	
	<hr/>	
	$f = \begin{cases} \left[2 \log_{10} \left(\frac{2.51}{\text{Re} \sqrt{f}} + \frac{R}{3.7} \right) \right]^{-2} & \text{Turbulent} \\ \frac{4.4}{\text{Re}^{0.595}} \exp \left(-\frac{0.00275}{R_1} \right) & \text{Transition} \\ \frac{64 C_{Lam}}{\text{Re}} & \text{Laminar} \end{cases}$	
NRG	where	$\text{Nu} = 0.047 \left\{ 1 - \exp \left(-3.8 \left(\frac{P}{D} - 1 \right) \right) \right\} (\text{Pe}^{0.77} + 250)$
	$R = \frac{\epsilon}{D_h}$	
	$\epsilon = 1.0 \times 10^{-6} \text{ m}$	
	$R_1 = \max(R, 0.007)$	
	$C_{Lam} = 0.96 \left(\frac{P}{D} \right) + 0.63$	
	<hr/>	
	$f = \begin{cases} \frac{0.21}{\text{Re}^{0.25}} \left(1 + \frac{124}{(H/d_r)^{1.65}} [1.78 + 1.485 \left((s/d_r) - 1 \right)] \left((s/d_r) - 1 \right) \right) & \text{Turbulent} \\ \frac{64}{\text{Re}} \left(0.407 + 2.0 \sqrt{(s/d_r) - 1} \times \left[1 + \frac{17.0 \left((s/d_r) - 1 \right)}{H/d_r} \right] \right) & \text{Laminar} \end{cases}$	$\text{Nu} = \text{Nu}_i + \frac{0.041 \text{Pe}^A}{x^2} \left(1 - \frac{1}{\frac{x^{30} - 1}{6} + \sqrt{1.15 + 1.24 \epsilon}} \right)$
IBRAE	where	$\text{Nu}_i = \left(7.55 x - \frac{6.3}{x^B} \right) \left(1 - \frac{3.6}{x^{20} (1 + 2.5 \epsilon_c^{0.86}) + 3.2} \right)$
		$A = 0.56 + 0.19x - \frac{0.1}{x^{80}}$
		$B = 17x (x - 0.81)$
		$\epsilon = \frac{k_w}{k_f}$
		$x = \frac{s}{d_r}$
		$k_w = \text{wall thermal conductivity}$
		$k_f = \text{sodium thermal conductivity}$
		$\epsilon_c = \text{approximate criterion of thermal similarity of the fuel rods in triangular assembly}$

	Pin Bundle Friction Factor Correlations	Pin Bundle Heat Transfer Correlations
	$f = 8 \left[\left(\frac{8}{\text{Re}} \right)^{12} + \frac{1}{(a+b)^{1.5}} \right]^{\frac{1}{12}}$ <p>where</p> $a = \left[2.457 \ln \left(\frac{1}{\left(\frac{7}{\text{Re}} \right)^{0.9} + 0.27 \left(\frac{\epsilon}{D_h} \right)} \right) \right]^{16}$ $b = \left(\frac{37530}{\text{Re}} \right)^{16}$	$\text{Nu} = 0.047 \left\{ 1 - \exp \left(-3.8 \left(\frac{P}{D} - 1 \right) \right) \right\} (\text{Pe}^{0.77} + 250)$
Argonne	$f = \begin{cases} 0.1875/\text{Re}^{0.2} & \text{Re} \geq 2050 \\ 76.5/\text{Re} & \text{Re} < 2050 \end{cases}$	$\text{Nu} = 5.0 + 0.025 \text{Pe}^{0.8}$
TerraPower	$f = \begin{cases} 0.33211/\text{Re}^{0.25} & \text{Re} \geq 2400 \\ 64/\text{Re} & \text{Re} < 2400 \end{cases}$	$\text{Nu} = 7.71 + 0.039 \text{Pe}^{0.77}$

TABLE 63. PIPE CORRELATIONS

	Pipe Friction Factor Correlations	Pipe Heat Transfer Correlations
CIAE	$f = \begin{cases} 0.0055 \left[1 + \left(20,000 \frac{\epsilon}{D_h} + \frac{10^6}{Re} \right)^{1/3} \right] & Re \geq 1082 \\ 64/Re & Re < 1082 \end{cases}$ <p>where $\epsilon = 1.0 \times 10^{-5}$ m</p>	$Nu = 5.0 + 0.025 Pe^{0.8}$
NCEPU	$f = \begin{cases} 0.0055 + 0.55/Re^{1/3} & \text{Turbulent} \\ 64/Re & \text{Laminar} \end{cases}$	$Nu = 6 + 0.025(\varphi Pe)^{0.8}$ <p>where</p> $\varphi = \frac{0.014(1 - e^{-71.8x})}{x}$ $x = \frac{1}{Re^{0.45} Pr^{0.2}}$
XJTU	$f = \begin{cases} 0.3164/Re^{0.25} & Re \geq Re_T \\ \text{Interpolate between} & Re_L < Re < Re_T \\ f(Re_T) \text{ \& } f(Re_L) & \\ 64/Re & Re \leq Re_L \end{cases}$ <p>where $Re_T = 3000$ $Re_L = 2000$</p>	$Nu = 4.82 + 0.0185 Pe^{0.827}$
IRSN	$\Delta P = \frac{\Lambda \left(\frac{L}{D_h} \right) \rho U^2}{2}$ <p>where</p> $\Lambda = \max \left(\frac{64}{Re}, 0.316 Re^{-0.25}, 0.012 \right)$	$Nu = 4.82 + 0.0185 (Re Pr)^{0.827}$
KIT & Kyushu University	No pipe friction modeled	No pipe heat transfer modeled
IGCAR	$f = \begin{cases} \text{given by } \frac{1}{\sqrt{f}} = -2 \log \left(\frac{\epsilon}{3.7 D_h} + \frac{2.51}{Re \sqrt{f}} \right) & \text{Turbulent} \\ 64/Re & \text{Laminar} \end{cases}$	$Nu = 5.0 + 0.025 Pe^{0.8}$

	Pipe Friction Factor Correlations	Pipe Heat Transfer Correlations
ENE A	$f = \begin{cases} \text{given by } \frac{1}{\sqrt{f}} = -2 \log \left(\frac{\epsilon}{3.7 D_h} + \frac{2.51}{Re} \left[1.14 - 2 \log \left(\frac{\epsilon}{D_h} + \frac{21.5}{Re^{0.9}} \right) \right] \right) & Re \geq Re_T \\ \text{Interpolate between } f(Re_T) \text{ \& } f(Re_L) & Re_L < Re < Re_T \\ 64/Re & Re \leq Re_L \end{cases}$	$Nu = 5.0 + 0.025 Pe^{0.8}$
	<p>where</p> $Re_T = 3000$ $Re_L = 2200$	
N.I.N.E	$f = \begin{cases} \left(-2 \log \left\{ \frac{\epsilon}{3.7 D} + \frac{2.51}{Re} \times \left[1.14 - 2 \log \left(\frac{\epsilon}{D} + \frac{21.25}{Re^{0.9}} \right) \right] \right\} \right)^{-2} & Re \geq 3000 \\ \left(3.75 - \frac{8250}{Re} \right) \times (f_{T,3000} - f_{L,2200}) + f_{L,2200} & 2200 < Re < 3000 \\ 64/Re & Re \leq 2200 \end{cases}$	$Nu = 4.0 + 0.33 \left(\frac{D}{D_0} \right)^{3.8} \left(\frac{Pe}{100} \right)^{0.86} + 0.16 \left(\frac{D}{D_0} \right)^{5.0}$
	<p>where</p> $\epsilon = 1.0 \times 10^{-5} \text{ m}$	
POLITO	No pipe friction modeled	No pipe heat transfer modeled
JAEA	$\Delta P = \Delta P_0 \left(\frac{W}{W_0} \right)^n$ <p>where</p> $\Delta P_0 = 18701.2 \text{ Pa}$ $W_0 = 452.4 \text{ kg/s}$ $n = 1.973$	$Nu = \max(Nu_1, Nu_2)$ <p>where</p> $Nu_1 = 5.0 + 0.025 (0.5 Re Pr)^{0.8}$ $Nu_2 = 0.0302 Gr^{2/5} \frac{Pr^{7/15}}{(1 + 0.494 Pr^{2/3})^{2/5}}$

$$\Delta P = f \frac{L \rho u^k}{2 D}$$

where

k is a constant between 1.9 and 2.1

$$f = \begin{cases} (0.094 R^{0.223} + 0.53R) + 88.0 R^{0.44} \text{Re}^{-1.62} R^{0.134} & \text{Re} \geq \text{Re}_T \\ \text{Interpolate between } f(\text{Re}_T) \text{ \& } f(\text{Re}_L) & \text{Re}_L < \text{Re} < \text{Re}_T \\ 64/\text{Re} & \text{Re} \leq \text{Re}_L \end{cases} \quad \text{Nu} = 5.0 + 0.025 \text{Pe}^{0.8}$$

University of Fukui

where

$$R = \frac{\epsilon}{D_h}$$

$$\text{Re}_T = 3000$$

$$\text{Re}_L = 2100$$

$$f = \begin{cases} 0.0055 + 0.55/\text{Re}^{1/3} & \text{Turbulent} \\ 64/\text{Re} & \text{Laminar} \end{cases} \quad \text{Nu} = 6 + 0.025 \{0.014 \text{Re}^{1.45} \text{Pr}^{1.2} (1 - e^{-71.8 \text{Re}^{-0.45} \text{Pr}^{-0.2}})\}$$

KAERI

$$f = 8 \left[\left(\frac{8}{\text{Re}} \right)^{12} + \frac{1}{(a+b)^{3/2}} \right]^{1/12}$$

where

$$a = \left[2.457 \ln \left(\frac{1}{\left(\frac{7}{\text{Re}} \right)^{0.9} + 0.27 \left(\frac{\epsilon}{D_h} \right)} \right) \right]^{16}$$

$$b = \left(\frac{3.753 \times 10^4}{\text{Re}} \right)^{16}$$

$$\epsilon = 1.5 \times 10^{-6} \text{ m}$$

$$\text{Nu} = 5.0 + 0.025 (\text{Pe})^{0.8}$$

KINS

$$f = \begin{cases} \left[2 \log_{10} \left(\frac{2.51}{\text{Re} \sqrt{f}} + \frac{R}{3.7} \right) \right]^{-2} & \text{Turbulent} \\ \frac{4.4}{\text{Re}^{0.595}} \exp \left(-\frac{0.00275}{R_1} \right) & \text{Transition} \\ \frac{64 C_{Lam}}{\text{Re}} & \text{Laminar} \end{cases} \quad \text{Nu} = 5.0 + 0.025 \text{Pe}^{0.8}$$

NRG

where

$$R = \frac{\epsilon}{D_h}$$

$$\epsilon = 1.0 \times 10^{-6} \text{ m}$$

$$R_1 = \max(R, 0.007)$$

$$C_{Lam} = 1.0$$

$$f = \begin{cases} 0.11 \left(\frac{\Delta}{d_r} + \frac{68}{\text{Re}} \right)^{0.25} & \text{Turbulent} \\ 64/\text{Re} & \text{Laminar} \end{cases} \quad \text{Nu} = \begin{cases} 5 + 0.025 \text{Pe}^{0.8} & \text{Turbulent} \\ 4.36 & \text{Laminar} \end{cases}$$

IBRAE

	Pipe Friction Factor Correlations	Pipe Heat Transfer Correlations
	$f = 8 \left[\left(\frac{8}{\text{Re}} \right)^{12} + \frac{1}{(a+b)^{1.5}} \right]^{\frac{1}{12}}$	
	where	
PSI	$a = \left[2.457 \ln \left(\frac{1}{\left(\frac{7}{\text{Re}} \right)^{0.9} + 0.27 \left(\frac{\epsilon}{D_h} \right)} \right) \right]^{16}$ $b = \left(\frac{37530}{\text{Re}} \right)^{16}$	$\text{Nu} = 8.4 + 0.034 \text{Pe}^{0.77}$
Argonne	$f = \begin{cases} 0.0055 \left[1 + \left(20,000 \frac{\epsilon}{D_h} + \frac{10^6}{\text{Re}} \right)^{1/3} \right] & \text{Re} \geq 1082 \\ 64/\text{Re} & \text{Re} < 1082 \end{cases}$	$\text{Nu} = 4.8 + 0.025 \text{Pe}^{0.8}$
	where	
	$\epsilon = 1.0 \times 10^{-5} \text{ m}$	
TerraPower	$f = \begin{cases} 0.0055 \left[1 + \left(20,000 \frac{\epsilon}{D_h} + \frac{10^6}{\text{Re}} \right)^{1/3} \right] & \text{Re} \geq 1082 \\ 64/\text{Re} & \text{Re} < 1082 \end{cases}$	$\text{Nu} = 4.8 + 0.025 \text{Pe}^{0.8}$
	where	
	$\epsilon = 4.5 \times 10^{-5} \text{ m}$ for primary pipes	
	$\epsilon = 1.0 \times 10^{-5} \text{ m}$ for intermediate pipes	

TABLE 64. INTERMEDIATE HEAT EXCHANGER CORRELATIONS

	IHX Primary-Side Friction Factor Correlations	IHX Primary-Side Heat Transfer Correlations
CIAE	$f = \begin{cases} 0.0055 \left[1 + \left(20,000 \frac{\epsilon}{D_h} + \frac{10^6}{Re} \right)^{1/3} \right] & Re \geq 1082 \\ 64/Re & Re < 1082 \end{cases}$ <p>where $\epsilon = 1.0 \times 10^{-5} \text{ m}$</p>	$Nu = 5.0 + 0.025 Pe^{0.8}$
NCEPU	$f = 0.0055 \left[1 + \left(20,000 \frac{\epsilon}{D_h} + \frac{10^6}{Re} \right)^{1/3} \right]$	$Nu = A + B Pe^C$ <p>where</p> $A = 0.25 + 6.2 \left(\frac{P}{D} \right)$ $B = -0.007 + 0.032 \left(\frac{P}{D} \right)$ $C = 0.8 - 0.024 \left(\frac{P}{D} \right)$
XJTU	$f = \begin{cases} 0.3164/Re^{0.25} & Re \geq Re_T \\ \text{Interpolate between} & Re_L < Re < Re_T \\ f(Re_T) \text{ \& } f(Re_L) & \\ 64/Re & Re \leq Re_L \end{cases}$ <p>where $Re_T = 3000$ $Re_L = 2000$</p>	$Nu = 4.496 \left[-16.15 + 24.96 \left(\frac{P}{D} \right) - 8.55 \left(\frac{P}{D} \right)^2 \right]$
IRSN	$\Delta P = \frac{\Lambda \left(\frac{L}{D_h} \right) \rho U^2}{2}$ <p>where</p> $\Lambda = \max \left(\frac{64}{Re}, 0.316 Re^{-0.25}, 0.012 \right)$	$Nu = 6 + 0.006 (Re Pr)^{0.827}$
KIT & Kyushu University	No IHX friction modeled	Infinite heat sink
IGCAR	$f = \begin{cases} \text{given by } \frac{1}{\sqrt{f}} = -2 \log \left(\frac{\epsilon}{3.7 D_h} + \frac{2.51}{Re \sqrt{f}} \right) & \text{Turbulent} \\ 64/Re & \text{Laminar} \end{cases}$	$Nu = 6 + 0.006 Pe$

	IHX Primary-Side Friction Factor Correlations	IHX Primary-Side Heat Transfer Correlations
ENEAC	$f = \begin{cases} \text{given by } \frac{1}{\sqrt{f}} = -2 \log \left(\frac{\epsilon}{3.7 D_h} + \frac{2.51}{Re} \left[1.14 - 2 \log \left(\frac{\epsilon}{D_h} + \frac{21.5}{Re^{0.9}} \right) \right] \right) & Re \geq Re_T \\ \text{Interpolate between } f(Re_T) \text{ \& } f(Re_L) & Re_L < Re < Re_T \\ 64/Re & Re \leq Re_L \end{cases}$	$Nu = 4.0 + 0.33 \left(\frac{P}{D} \right)^{3.8} \left(\frac{Pe}{100} \right)^{0.86} + 0.16 \left(\frac{P}{D} \right)^{5.0}$
	<p>where</p> $Re_T = 3000$ $Re_L = 2200$	
N.I.N.E	$f = \begin{cases} \left(-2 \log \left\{ \frac{\epsilon}{3.7 D} + \frac{2.51}{Re} \times [1.14 - 2 \log \left(\frac{\epsilon}{D} + \frac{21.25}{Re^{0.9}} \right)] \right\} \right)^{-2} & Re \geq 3000 \\ \left(3.75 - \frac{8250}{Re} \right) \times (f_{T,3000} - f_{L,2200}) + f_{L,2200} & 2200 < Re < 3000 \\ 64/Re & Re \leq 2200 \end{cases}$	$Nu = 5.0 + 0.025 Pe^{0.8}$
	<p>where</p> $\epsilon = 1.0 \times 10^{-5} \text{ m}$	
POLITO	No IHX friction modeled	No IHX heat transfer modeled
IAEA	$\Delta P = \Delta P_0 \left(\frac{W}{W_0} \right)^n$ <p>where</p> $\Delta P_0 = 12869.2 \text{ Pa}$ $W_0 = 451.5 \text{ kg/s}$ $n = 1.917$	$Nu = 0.625 Pe^{0.4}$

	IHX Primary-Side Friction Factor Correlations	IHX Primary-Side Heat Transfer Correlations
University of Fukui	$\Delta P = f \frac{L \rho u^k}{2 D}$ <p>where</p> <p>k is a constant between 1.9 and 2.1</p> $f = \begin{cases} (0.094 R^{0.223} + 0.53R) + 88.0 R^{0.44} Re^{-1.62 R^{0.134}} & Re \geq Re_T \\ \text{Interpolate between } f(Re_T) \text{ \& } f(Re_L) & Re_L < Re < Re_T \\ 64/Re & Re \leq Re_L \end{cases}$	$Nu = 5.0 + 0.025 Pe^{0.8}$
	<p>where</p> $R = \frac{\epsilon}{D_h}$ $Re_T = 3000$ $Re_L = 2100$	
KAERI	$f = \begin{cases} 0.0055 + 0.55/Re^{1/3} & \text{Turbulent} \\ 64/Re & \text{Laminar} \end{cases}$	$Nu = A + B Pe^C$ <p>where</p> $A = 0.25 + 6.2 \left(\frac{P}{D}\right)$ $B = -0.007 + 0.032 \left(\frac{P}{D}\right)$ $C = 0.8 - 0.024 \left(\frac{P}{D}\right)$
	$f = 8 \left[\left(\frac{8}{Re}\right)^{12} + \frac{1}{(a+b)^{3/2}} \right]^{1/12}$ <p>where</p> $a = \left[2.457 \ln \left(\frac{1}{\left(\frac{7}{Re}\right)^{0.9} + 0.27 \left(\frac{\epsilon}{D_h}\right)} \right) \right]^{16}$ $b = \left(\frac{3.753 \times 10^4}{Re} \right)^{16}$ $\epsilon = 1.5 \times 10^{-6} \text{ m}$	$Nu = 5.0 + 0.025 (Pe)^{0.8}$
NRG	$f = \begin{cases} \left[2 \log_{10} \left(\frac{2.51}{Re \sqrt{f}} + \frac{R}{3.7} \right) \right]^{-2} & \text{Turbulent} \\ \frac{4.4}{Re^{0.595}} \exp \left(-\frac{0.00275}{R_1} \right) & \text{Transition} \\ \frac{64 C_{Lam}}{Re} & \text{Laminar} \end{cases}$	$Nu = 0.047 \left\{ 1 - \exp \left(-3.8 \left(\frac{P}{D} - 1 \right) \right) \right\} (Pe^{0.77} + 250)$
	<p>where</p> $R = \frac{\epsilon}{D_h}$ $\epsilon = 1.0 \times 10^{-6} \text{ m}$ $R_1 = \max(R, 0.007)$ $C_{Lam} = 0.96 \left(\frac{P}{D}\right) + 0.63$	

	IHX Primary-Side Friction Factor Correlations	IHX Primary-Side Heat Transfer Correlations
IBRAE	$f = \begin{cases} \frac{0.21}{\text{Re}^{0.25}} \left(1 + \left(\frac{s}{d_r} - 1 \right)^{0.32} \right) & \text{Turbulent} \\ \frac{64}{\text{Re}} K_l & \text{Laminar} \end{cases}$ <p>where</p> $K_l = 0.41 + 1.9 \left(\frac{s}{d_r} - 1 \right)^{1/3}$ <p>s = lattice pitch d_r = rod diameter</p>	$\text{Nu} = \text{Nu}_l + \frac{0.041 \text{Pe}^A}{x^2} \left(1 - \frac{1}{\frac{x^{30} - 1}{6} + \sqrt{1.15 + 1.24 \epsilon}} \right)$ <p>where</p> $\text{Nu}_l = \left(7.55 x - \frac{6.3}{x^B} \right) \left(1 - \frac{3.6}{x^{20} (1 + 2.5 \epsilon_c^{0.86}) + 3.2} \right)$ $A = 0.56 + 0.19x - \frac{0.1}{x^{80}}$ $B = 17x (x - 0.81)$ $\epsilon = \frac{k_w}{k_f}$ $x = \frac{s}{d_r}$ <p>k_w = wall thermal conductivity k_f = sodium thermal conductivity ϵ_c = approximate criterion of thermal similarity of the fuel rods in triangular assembly</p>
PSI	$f = 8 \left[\left(\frac{8}{\text{Re}} \right)^{12} + \frac{1}{(a+b)^{1.5}} \right]^{\frac{1}{12}}$ <p>where</p> $a = \left[2.457 \ln \left(\frac{1}{\left(\frac{7}{\text{Re}} \right)^{0.9} + 0.27 \left(\frac{\epsilon}{D_h} \right)} \right) \right]^{16}$ $b = \left(\frac{37530}{\text{Re}} \right)^{16}$	$\text{Nu} = 0.047 \left\{ 1 - \exp \left(-3.8 \left(\frac{P}{D} - 1 \right) \right) \right\} (\text{Pe}^{0.77} + 250)$
Argonne	$f = \begin{cases} 0.0055 \left[1 + \left(20,000 \frac{\epsilon}{D_h} + \frac{10^6}{\text{Re}} \right)^{1/3} \right] & \text{Re} \geq 1082 \\ 64/\text{Re} & \text{Re} < 1082 \end{cases}$ <p>where $\epsilon = 1.0 \times 10^{-5}$ m</p>	$\text{Nu} = 4.8 + 0.025 \text{Pe}^{0.8}$
TerraPower	$f = \begin{cases} 0.0055 \left[1 + \left(20,000 \frac{\epsilon}{D_h} + \frac{10^6}{\text{Re}} \right)^{1/3} \right] & \text{Re} \geq 1082 \\ 64/\text{Re} & \text{Re} < 1082 \end{cases}$ <p>where $\epsilon = 4.5 \times 10^{-5}$ m for primary side $\epsilon = 1.0 \times 10^{-5}$ m for intermediate side</p>	$\text{Nu} = 4.8 + 0.025 \text{Pe}^{0.8}$

Appendix II

SUMMARY OF BENCHMARK MODELLING CHOICES

In addition to the correlations available to each organization based on their chosen codes, the results they obtained varied based on their modelling choices and which aspects of the CRP they chose to participate in. The tables below summarize each organization's modelling choices. TABLE 65 identifies which organizations contributed to each aspect of the CRP. TABLE 66 summarizes how each organization divided the EBR-II subassemblies into channels. TABLE 67 identifies which reactivity feedback effects each organization considered for SHRT-45R. TABLE 68 summarizes how each participant modelled the primary pumps, auxiliary EM pump and IHX. TABLE 69 summarizes how each participant represented the inlet plena, outlet plenum and cold pool in their models.

TABLE 65. SUMMARY OF BENCHMARK PARTICIPATION

	SHRT-17 T/H	SHRT-45R T/H	Subchannel Analysis	CFD	SHRT-45R Neutronics	Geometrical Fidelity and Steady-State Qualification	FFTBM Process
CIAE	✓	✓				✓	
NCEPU	✓	✓				✓	✓
XJTU	✓	✓		✓ ^A		✓	✓
IRSN	✓	✓					
KIT/Kyushu	✓	✓			✓		
IGCAR	✓			✓ ^B		✓	✓
ENEA	✓			✓ ^B	✓	✓	✓
NINE	✓					✓	✓
POLITO	✓	✓			✓		
JAEA	✓		✓			✓	✓
U. Fukui	✓	✓	✓	✓ ^C	✓	✓	✓
KAERI	✓	✓				✓	✓
KINS	✓					✓	✓
NRG	✓	✓	✓	✓ ^C			
IBRAE	✓	✓				✓	✓
PSI	✓	✓			✓		
Argonne	✓	✓	✓		✓	✓	✓
TerraPower		✓	✓				

^A – CFD analysis of Interwrapper Flow

^B – CFD analysis of XX09

^C – CFD analysis of Cold Pool

TABLE 66. CORE MODELLING CHOICES

	Channel Basis ^A	# Channels, SHRT-17		Interwrapper Channels SHRT-17	# Channels, SHRT-45R		Interwrapper Channels SHRT-45R
		Rows 1-7	Rows 8-16		Rows 1-7	Rows 8-16	
CIAE	P/F Ratio, SA Type	7	5	Not modelled	8	5	Not modelled
NCEPU	SA Type	4	5	Not modelled	4	5	Not modelled
XJTU	SA Type	4	2	CFD Model	4	2	CFD
IRSN	SA Type	4	2	Not modelled	4	2	Not modelled
KIT/Kyushu	P/F Ratio, SA Type	14	4	2	17	17	3
IGCAR	P/F Ratio, SA Type	9	1	Not modelled	-	-	-
ENEA	Rows 1-7: 1-to-1 Rows 8-16: Type	127	24	60	-	-	-
NINE	Rows 1-6: 1-to-1 Rows 7-16: Row, Type	83	17	Heat Conduction Model	-	-	-
POLITO	1:1 for all SA	127	0	Heat Conduction Model	127	510	Heat Conduction Model
JAEA	1:1 for all SA	127	510	3822	-	-	-
U. Fukui	SA Type	8	2	Heat Conduction Model	8	2	Heat Conduction Model
KAERI	P/F Ratio, SA Type	9	2	Heat Conduction Model	9	2	Heat Conduction Model
KINS	Flow, Type	10	1	2	-	-	-
NRG	SA Type	10	2	Heat Conduction Model for XX09/XX10	10	2	Heat Conduction Model for XX09/XX10
IBRAE	SA Type	11	2	1	13	2	1
PSI	P/F Ratio, SA Type	4	3	Not modelled	4	3	Not modelled
Argonne	P/F Ratio, SA Type	14	8	1	13	9	1
TerraPower	P/F Ratio, SA Type, ρ	-	-	-	10	3	Not modelled

^A – Basis for dividing the core subassemblies among channels representing one or more subassemblies:

P/F Ratio: Power to flow ratio

SA Type: Subassembly type

1-to-1: 1 subassembly per channel

Row: Which row of the core the subassembly was loaded into

Flow: Mass flow rate for the subassembly

ρ : Reactivity feedback coefficients for the subassembly

TABLE 67. SHRT-45R REACTIVITY FEEDBACK MODELLING CHOICES

	Doppler	Sodium Density	Radial Core Expansion	Axial Fuel Expansion	Axial Clad Expansion	Control Rod Driveline Expansion
CIAE	✓	✓	✓	✓	✓	
NCEPU	✓	✓	✓	✓		
XJTU	✓	✓	✓	✓	✓	✓
IRSN	✓	✓	✓	✓	✓	✓
KIT/Kyushu ^A	✓	✓	✓	✓	✓	
IGCAR			Did not model SHRT-45R			
ENEA			Did not model SHRT-45R			
NINE			Did not model SHRT-45R			
POLITO ^A	✓	✓				
JAEA			Did not model SHRT-45R			
U. Fukui	✓	✓	✓	✓	✓	
KAERI	✓	✓	✓	✓	✓	✓
KINS			Did not model SHRT-45R			
NRG	✓	✓	✓	✓	✓	✓
IBRAE	✓	✓	✓	✓		
PSI	✓	✓	✓	✓		✓
Argonne	✓	✓	✓	✓	✓	✓
TerraPower	✓	✓	✓	✓	✓	✓

^A – Used spatial kinetics. Remaining organizations modeling SHRT-45R used point kinetics.

TABLE 68. PRIMARY SODIUM SYSTEM PUMP AND IHX MODELLING CHOICES

	Primary Pump Model	# Primary Pumps ^A	Auxiliary EM Pump	IHX Model
CIAE		Did not model primary sodium system		
NCEPU	Homologous	1	Simplified	Shell and Tube
XJTU	Homologous	2	Simplified	Shell and Tube
IRSN	Homologous	2	Flow Rate Proportional To Voltage	Shell and Tube
KIT/Kyushu	Time-Dependent Pressure Boundary Condition	1	Simplified	Simplified
IGCAR	Homologous	2	Not modeled	Shell and Tube
ENEA	Homologous	2	Not modeled	Shell and Tube
NINE	Homologous	2	Not modeled	Shell and Tube
POLITO		Did not model primary sodium system		
JAEA	Simplified	2	Not modeled	Shell and Tube
U. Fukui	Homologous	2	Simplified	Shell and Tube
KAERI	Homologous	2	Simplified	Shell and Tube
KINS	Homologous	2	Not modeled	Shell and Tube
NRG	Pump Head vs. Flow	2	Pump Current vs. Time	Shell and Tube
IBRAE	Homologous	2	EM Pump Model	Shell and Tube
PSI	Homologous	2	Simplified	Shell and Tube
Argonne	Homologous	2	EM Pump Model	Shell and Tube
TerraPower	Homologous	2	EM Pump Model ^B	Shell and Tube

^A – Does not include auxiliary EM pump

^B – Modeled but did not use EM pump

TABLE 69. PRIMARY SODIUM SYSTEM VOLUME AND LEAKAGE MODELLING CHOICES

	Number of Inlet Plena Volumes	Number of Upper Plenum Volumes	Number of Cold Pool Volumes/Meshes	Leakage Flow Paths Modeled
CIAE		Did not model primary sodium system		
NCEPU	2	17×15	22×32×27	Not modeled
XJTU	2	1	3 Layers	Not modeled
IRSN	2	1	1	Not modeled
KIT/Kyushu	36×3	3×37	Two 2-D Regions: 10×52 and 37×4	Not modeled
IGCAR	1 ^A	1	1	✓
ENEA	High-Pressure Plenum: 5×12×1 Low-Pressure Plenum: 2×12×1	5×12×4	2×8×19	✓
NINE	12	6	3×2×72	✓
POLITO		Did not model primary sodium system		
JAEA	2	2	1	✓
U. Fukui	2	1	Systems: 2 ^B CFD: 800,000	✓
KAERI	6	2	6×1	✓
KINS	4	5	2×6×10	✓
NRG	2	3	CFD: 392,254 ^C	✓
IBRAE	4	1	26×1	Not modeled
PSI	2	1	8	✓
Argonne	2	1	2	✓
TerraPower	2	1	1	✓

^A – Subassemblies in Rows 8-16 assumed to draw sodium directly from pump outlet

^B – Cold pool modeled as two 0-D volumes for system modeling, CFD analysis performed separately

^C – CFD model coupled to systems model

The links among the RDS, the input deck, the QR and the EH are highlighted in FIG. 342. The solid lines indicate the time sequence of the activities, the dotted lines constitute the feedback for the review and the dashed lines are the necessary input to develop the input deck and the EH. The whole process is based on continuous iterative review and exchange of information among the different analysts involved in the activities. An independent review of each step is guaranteed by the fact that the developer of the EH is different from the input deck developer, and the input deck developer is different from the person who works on the RDS.

Block A in FIG. 342 is related to the collection of relevant drawings and reports of the selected facility. This documentation constitutes the basis for writing down the RDS (block B). The writing of the RDS is also the first step of the review process, when each document is checked for consistency against other sources of information, which results in the establishment of a final documentation set for the particular facility.

The next block in the chart (block C) is related to the creation of a RDS for the selected test to be analyzed. The RDS of the test will contain the definition of the test conditions, the set points and the boundary conditions. The RDS of the facility and of the test are the basis of the code input development.

The development of an input (block D) must follow a preconfigured set of nodalization strategies described in a dedicated document (block E) that consists of a collection of the nodalization strategies, user choices and model selections to be used for the development of any other input. The development of the code input is supported by calculation notes (block F) which are produced by the input developer in order to document in a systematic and traceable way how the data in the RDS are converted into the numbers constituting the input.

A review of the RDS takes place at this phase: the input developer uses the RDS to extract the necessary information for the input preparation, together with the availability of the original documentation already collected. Potential errors and misinterpretations may be identified and corrected in the RDS. The writing down of the RDS-test also constitutes a review of the RDS-facility.

One of the reasons for needing an RDS is connected to the duration of the experimental campaign performed at each facility (typically from five to ten years). During those years, different modifications can be made to the facility configuration in order to improve the fidelity of the facility with respect to the reference plant, to reduce the heat losses, to install a more sophisticated instrumentation apparatus, etc. Such information and modifications are obviously not part of the original documentation and, in general, could be only partially reflected in separate reports and documents. Thus, the goal of the RDS is to analyze the amount of available documentation and to resolve possible contradictions coming out from different reports in order to produce a consistent and homogenous set of data for the facility.

Once the code input file has been produced and the code calculation run, the qualification of the code results has to be performed following appropriate procedures. The code analyst generates the Qualification Report (QR, block G), which collects the results of the qualification process of the code calculation that was performed.

The Engineering Handbook (EH, block H) constitutes the final step for the set-up of a qualified database useful for the V&V of BEPU methodologies. The IAEA Safety Reports Series No 52 states that a “document containing a full description of how the database has been converted into an input data deck for a specific computer code” should be available.

Based on the above definition, the EH not only describes the code input file and the calculation notes made available by the input developer for simulating the facility through the nodalization, but it also provides the engineering justifications of the code user choices and the explanation of any differences with respect to the general nodalization strategies.

At this step, a final review of the three sets of documents is also performed: every entry in the input deck is checked between the calculation notes and the RDS of the facility, errors or inconsistencies found in the input are tracked and reported and appropriate corrections are made and then finally documented in the EH. In order to ensure the independence of the review process, it is of the utmost importance that the engineer in charge of the EH be different from the input deck developer (the latter should be involved in the preparation of the EH only to provide the description of the “nodalization rationale” and of the “user choices”).

To summarize, the SCCRED methodology has been developed in such a way as to allow for the collection, organization, use and preservation of an exhaustive set of geometrical data, experimental results and code calculation responses, ensuring finally:

- (a) an exhaustive consolidated set of information;
- (b) the traceability of the information, including the decisions taken during the activity;
- (c) the standardization of the format by which the information is collected;
- (d) the availability of a database of experimental and associated calculated results for the assessment process of Best Estimate codes;
- (e) the availability of a database of error or accuracy (derived from the differences between experiment and calculation results) for the V&V of the uncertainty methods.

More details about the qualification procedure step (which is the objective of the present report) of the SCCRED methodology are provided in the next section.

III.2. QUALIFICATION PROCEDURE FOR SYSTEM THERMAL HYDRAULIC CODE CALCULATIONS

Simulations using thermal hydraulic system codes are performed to evaluate Nuclear Power Plant (NPP) behaviour during a postulated transient (safety analysis, licensing calculations, scoping calculations, etc.) or to evaluate code capability (code assessment). The calculation analysis constitutes a process that involves the code itself, the data of the reference plant, the data about the transient, the nodalization and the code user. All these elements interact with each other and affect the results.

Computer code applications require preparation of a mathematical model consisting of the code itself and of a set of input data grouped in a file (the nodalization) describing the plant or the facility within the limits and assumptions of the code capability. The preparation of this model constitutes the largest source of errors and uncertainty when using best estimate (BE) codes.

A major issue in the use of a mathematical model is the capability of the model to reproduce the plant or facility behaviour under steady state and transient conditions. These aspects constitute two main checks that must be passed in the qualification process. The first of them is related to the implementation of a nodalization-schematization of the reference plant or

facility; the second one is related to the ability to reproduce and analyze the transient behaviour to derive the needed information.

In the following, it is assumed that the code has fulfilled the validation and qualification processes and a “frozen” version of the code has been made available to the final code user. In other words, this means that the code user does not have any possibility of modifying or changing the physical and numerical models of the code (only the options described in the user manual are available to the code user).

The procedure developed and applied at N.IN.E. to qualify the nodalization, i.e. to demonstrate that the code results (obtained by the application of the code using the developed nodalization) constitute a realistic approximation of the reference plant behaviour (a full size NPP or a facility), is described below following the SCCRED methodology. The qualification procedure is applicable in all cases when a qualified nodalization is required (e.g. investigation of the behaviour of a NPP during a transient is a typical activity requiring a qualification procedure).

The qualification of the nodalization is a mandatory process for taking into account the effect of many different sources of approximations:

- (a) The data of the reference plant or facility available to the code user are typically insufficient to produce a perfect nodalization-schematization of the reference plant;
- (b) The code user derives, from the available data, an approximated nodalization-schematization of the plant or facility, reducing the level of detail of the simulated hardware;
- (c) The limits on the capability of the code to reproduce the hardware, the plant systems and the actuation logic of the systems further reduce the level of detail of the nodalization-schematization.

The need for qualifying both the code capability and the nodalization features in order to perform the transient analysis derives from the following statements:

- (a) The code options must be adequate;
- (b) The nodalization-schematization solutions must be adequate;
- (c) The simulation of some systems can be tested only under transient conditions (e.g. performance of the Emergency Core Cooling System (ECCS), which is not involved in normal plant operation, i.e. during steady state code conditions);
- (d) The capability of the “code-nodalization” of the system to reproduce relevant thermal hydraulic phenomena expected in the transient must be tested.

A qualification procedure has been developed that include a) the necessary checks for the different aspects mentioned above and b) the criteria adopted to produce a judgement about the acceptability of the code analysis results.

The goal of the qualification procedure is to develop and obtain a qualified nodalization considering comparison with the hardware data, the boundary and initial conditions, and the time trends of relevant quantities. The procedure distinguishes between two main processes: the “steady state” and the “transient” level of qualification [136], [137], [138]. Criteria for selecting relevant quantities are mentioned in the following discussion. A layout of the

procedure can be seen in FIG. 343, where the two processes are represented by the two steps “f” and “j” which constitute two checkpoints of the procedure. If the two checkpoints are not satisfied (paths “g” and “k”), the nodalization must be improved (step “c”). It must be pointed out that many cycles “c-d-e-f-g” could be necessary to reach step “h”. Similarly, every time path “k” is activated, the process goes again from “c” to “f” and then from “h” up to “j” (the path “c-d-e-f-h-i-j-k-c” could be actuated more than one time). The last step “l” is reached at the end of the procedure, and this implies the qualification of the developed nodalization.

The steps shown in FIG. 343 are described in detail in the remaining part of this section (where additional general considerations are provided) and in the following two sub-sections dealing with the “Steady State” and the “On-Transient” level of qualification, respectively (where specific considerations are given).

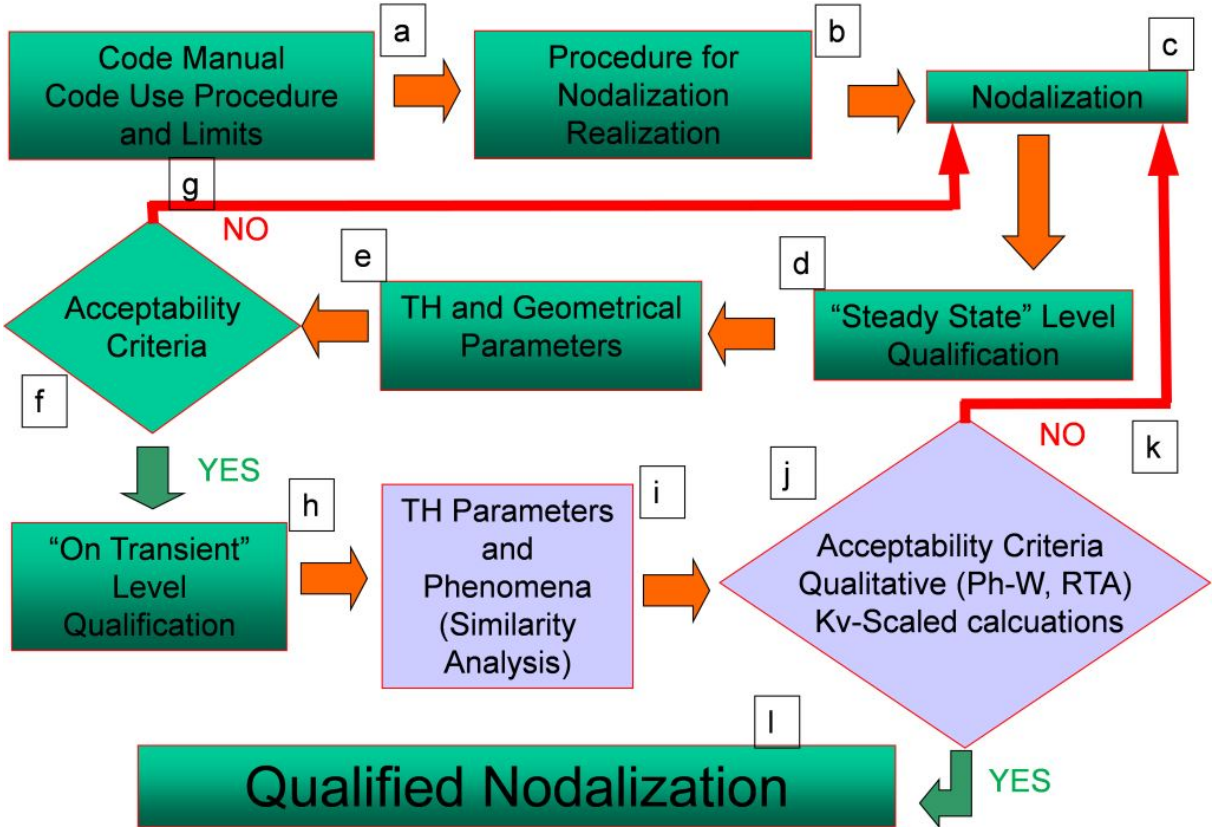


FIG. 343. Flowsheet of the qualification procedure.

Step “a” (the code)

An internationally recognized code version (“frozen” code) must be available. The consistency of the code installation on the computer must be checked. No special deficiencies shall have been detected in predicting the phenomena to be considered.

This step also considers the information that is available in the code user manuals and in the guidelines for the use of the code. This type of information takes into account the specific limits and assumptions of the code (specifics of the code adopted for the analysis) and provides guidelines about the way to achieve the best nodalizations.

From a generic point of view, the following statements should be considered:

- (a) Homogeneous nodalization (i.e. nodalization developed adopting the same set of criteria and following the same set of guidelines);
- (b) Strict observation of the user guidelines;
- (c) Standard use of the code (and model) options.

Step “b” (the procedures for the nodalization development)

Code user experience and recommendations by the code developers are useful for setting up procedures to be applied for a better nodalization. These special procedures are related to the specific code adopted for the analysis. For instance, in relation to the use of the RELAP5 code, the following rules, among many others, are generally adopted during the development of the nodalization:

- (a) The ratio between the length and the diameter of a node shall be larger than 1;
- (b) The ratio between the volumes of two adjacent nodes shall be between 0.5 and 2;
- (c) The ratio between the lengths of two adjacent nodes shall be between 0.5 and 2;
- (d) Use a standard set of code options;
- (e) Use more than nine mesh points for simulating the heat structures of the fuel bundles;
- (f) Adopt special techniques like the “slice” nodalization to improve the capability of the code to simulate phases of the transient involving natural circulation phenomena.

However special cases can be identified where the rules in the above list cannot be followed.

Step “c” (the nodalization)

The development of the nodalization depends on several aspects such as: availability of data, code user capability and experience, and code capability. Data must be qualified, and this implies that the data shall derive from:

- (a) A qualified facility (if the analysis is performed for a facility);
- (b) A qualified test design;
- (c) Qualified test data.

The database for the implementation of the nodalization shall be derived from official documents, and traceability of each reference shall be maintained. Three different types of data sources can be identified:

- (a) Qualified data from official sources;
- (b) Data deriving from non-official sources. This type of data can be derived from similar plant data or other qualified nodalization for the same type of plant. The use of these data can introduce potential errors, and the effect on the calculation results must be carefully evaluated;
- (c) Data assumed by the code user. This type of data constitutes assumptions by the code user (based on experience or on similitude with other similar plants), and its

use should be avoided. Any special assumptions adopted by the code user or special solutions in the nodalization must be recorded and documented.

The nodalization must reproduce all the relevant parts of the reference plant, including geometrical and materials fidelity and the reproduction of the systems and of the related logic. A nodalization representing an actual system (ITF or NPP) is qualified when:

- (a) It represents geometrical fidelity with the system to be analyzed (see Section III.3);
- (b) It reproduces the measured nominal steady state condition of the system (see Section III.3);
- (c) It shows satisfactory behaviour under time-dependent conditions (see Section III.3).

III.3. QUALIFICATION AT THE STEADY STATE LEVEL

The step dealing with the “steady state qualification” includes two qualification checkpoints: the first is related to the evaluation and comparison of the geometrical data of the hardware with respect to the estimated numerical values implemented in the nodalization (i.e. demonstration of the geometrical fidelity of the nodalization with respect to the system to be analyzed); the second is related to the capability of the nodalization to reproduce the steady state qualified conditions of the system.

Hardware and modelled geometrical values are compared, as are recorded and calculated steady state parameters, in order to satisfy the acceptability criteria. TABLE 70 lists ten categories of geometrical parameters to be checked against acceptable criteria. TABLE 71 lists fifteen categories of thermal hydraulic parameters to be checked against acceptable criteria. For each item in TABLE 70 and TABLE 71, acceptable errors (AE) have been set-up and listed in the right column of each table. It shall be considered that experimental measurements are typically available with an error band that must be considered when performing the comparison against the calculated results. No error is assigned if the calculated value is inside the experimental uncertainty bands. In general, the error E^2 between a measured value Y_E and calculated value Y_C can be calculated by the following formulas, where U_E is the measurement uncertainty

$$\text{if } Y_E - U_E \leq Y_C \leq Y_E + U_E \quad \rightarrow \quad E = 0$$

$$\text{if } Y_C < Y_E - U_E \quad \rightarrow \quad E = (Y_E - U_E - Y_C) / Y_E$$

$$\text{if } Y_C > Y_E + U_E \quad \rightarrow \quad E = (Y_C - Y_E - U_E) / Y_E$$

III.3.1. Demonstration of Geometrical Fidelity

Steps “e” (geometrical parameters) and “f” (acceptance criteria)

² If the calculated datapoint lies within the experimental uncertainty band, there is no possibility of performing a better calculation and thus, consistent with the SCCRED qualification methodology and the “acceptable errors”, the associated error is zero.

This qualification checkpoint should be performed by a user different from the code user who has developed the nodalization. The relevant geometrical values (e.g. volume, heat transfer area, elevations, etc.) of the hardware are identified (step “e”) and compared with the values implemented in the nodalization.

TABLE 70. STEADY STATE QUALIFICATION - DEMONSTRATION OF GEOMETRICAL FIDELITY: ACCEPTABLE ERRORS

#	Category of geometrical parameters	Acceptable error ^a
1	Primary circuit volume	1%
2	Secondary circuit volume	2%
3	Non-active structure heat transfer area (overall)	10%
4	Active structure heat transfer area (overall)	0.1%
5	Non-active structure heat transfer volume (overall)	14%
6	Active structure heat transfer volume (overall)	0.2%
7	Volume vs height curve (i.e. “local” volume per each circuit)	10%
8	Component relative elevation	0.01 m
9	Flow area of components like valves, pumps, orifices	1%
10	Generic flow area	10%

^a The % error is defined as the ratio: $|\text{system hardware value} - \text{code model value}| / |\text{system hardware value}|$

TABLE 71. STEADY STATE QUALIFICATION - ACCEPTABLE ERRORS TO ACHIEVE A STEADY STATE

#	Category of thermal hydraulic parameters ^a	Acceptable error ^b
1	Primary Circuit Power	2%
2	Secondary Circuit Power	2%
3	Absolute pressure (PRZ, SG, ACC)	0.1%
4	Fluid temperature	0.5% ^c
5	Rod surface temperature	10 K
6	Pump velocity	1%
7	Heat losses	10%
8	Local pressure drops	10% ^d
9	Mass inventory in primary circuit	2% ^e
10	Mass inventory in secondary circuit	5% ^e
11	Flow rates (primary and secondary circuit)	2%
12	Bypass mass flow rates	10%
13	Pressurizer level (collapsed)	0.05 m
14	Secondary side or downcomer level	0.1 m ^e
15	Axial and radial power distribution	1%

^a With reference to each parameter, the solution must be stable, with an inherent drift $< 1\% / 100 \text{ s}$ (acceptance criterion-SS).

^b The % error is defined as the ratio: $|\text{reference or measured value} - \text{calculated value}| / |\text{reference or measured value}|$. The “dimensional error” is the numerator of this expression.

^c The acceptable error shall be consistent with the power error.

^d 10% of the difference between the maximum and minimum pressures in the loop.

^e The acceptable error shall be consistent with the other errors.

Several parameters in TABLE 70 can be identified per category in relation to the level of qualification the user wishes to apply (e.g. category #5, “Non-active structure heat transfer volume” can include only one parameter – the total volume in the whole facility – or as many parameters as there are different structures in the facility – core barrel, RPV wall, primary piping etc.). Category #7, “Volume vs height curve (i.e. “local” volume per each circuit)”, requires building curves for both the real system and for the modelled one that represent the amount of geometrical volume of each circuit (e.g. primary and secondary circuits) below a certain elevation. The criterion imposes a maximum difference of 10% between the two curves (real system and modelled one) at any elevation except for the topmost position, where items 1 and 2 in TABLE 70 impose a maximum difference of 1% and 2% for the primary and secondary circuit, respectively. An example of these curves is given in FIG. 344.

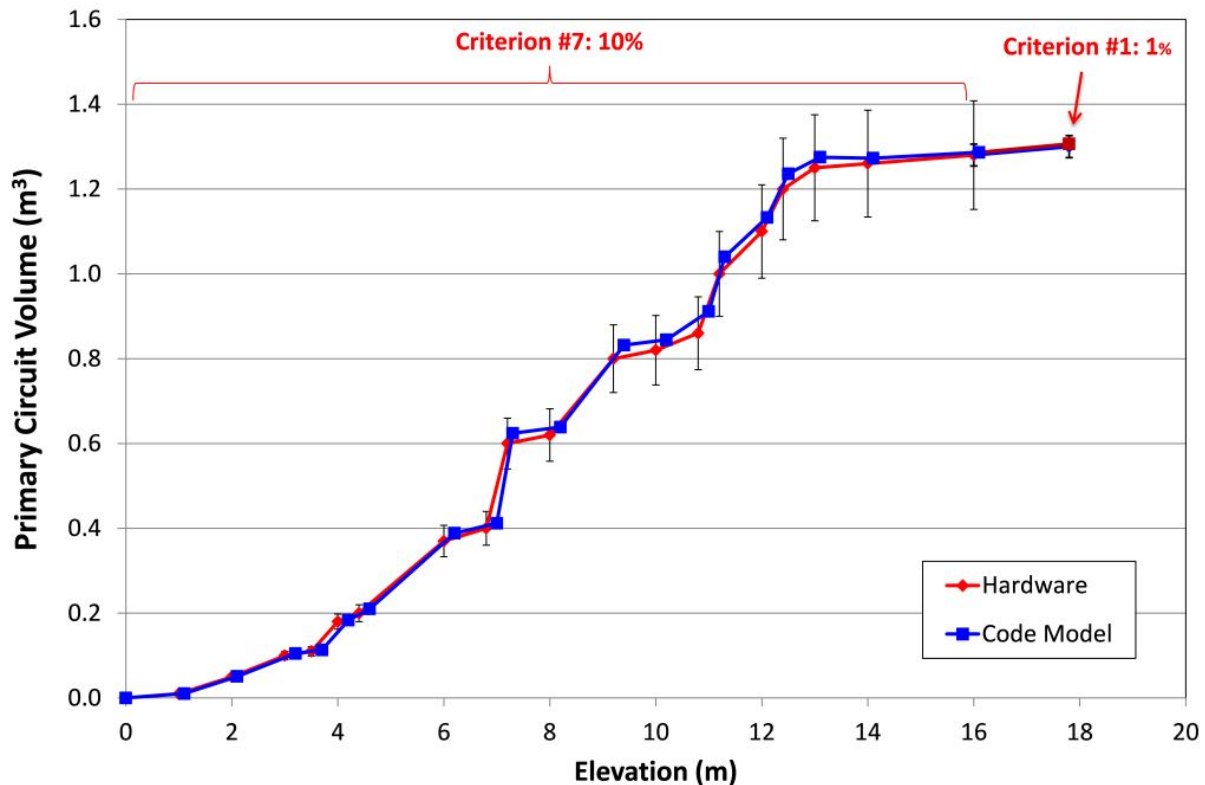


FIG. 344. Example of a primary side volume versus elevation curve.

Step “g” (geometrical fidelity - improvement loop)

If one or more of the acceptability criteria in step “f” of the geometrical fidelity is not fulfilled (i.e. $E_i > AE_i$ where ‘i’ is a generic parameter) a review of the nodalization (step “c”) must be performed. This process can request more detailed data, improvement of the nodalization-schematization, different user and code model choices, etc. Path “g” must be repeated until all acceptability criteria in TABLE 70 are satisfied (i.e. all $E_i \leq AE_i$ where ‘i’ is a generic parameter).

III.3.2. Demonstration of Establishing a Steady State

Steps “e” (thermal hydraulic parameters) and “f” (acceptance criteria)

This qualification checkpoint requires performing a “steady state” calculation. This activity depends on the different code peculiarities. As an example, for the RELAP5 code, the steady state calculation is performed by a “null transient” calculation, which implies adopting the “transient” option without triggering any event (e.g. valve opening, pump switching off, etc.) that can create a transient (i.e. time-dependent) state of the system.

The relevant thermal hydraulic parameters of the steady state conditions have to be identified. A thermal hydraulic parameter is considered as relevant when it is of major relevance to determining the plant behaviour and can be reliably measured. The selected relevant parameters are then extracted from the results of the steady state calculation (step “e”) for comparison against experimental parameters.

TABLE 71 lists fifteen categories of thermal hydraulic parameters to be checked against acceptable criteria. For each parameter of the categories in TABLE 71, acceptable errors have been set-up and listed in the right column. Several parameters can be identified per each category in relation to the level of qualification the user wishes to apply (e.g. category #4 “Fluid temperature” can include the hot leg, the cold leg, the steam generator inlet and outlet liquid temperatures, etc.). Category #8, “Local pressure drops”, requires building curves for both the experimental measurements and the calculated results that represent the pressure drop (ΔP) distribution versus the length of each circuit (e.g. primary and secondary circuits). The criterion imposes a maximum difference of 10% of the difference between the maximum and minimum measured pressures in each circuit at any position along the loop. An example of these curves is given in FIG. 345 (no measurement uncertainties have been considered in this example).

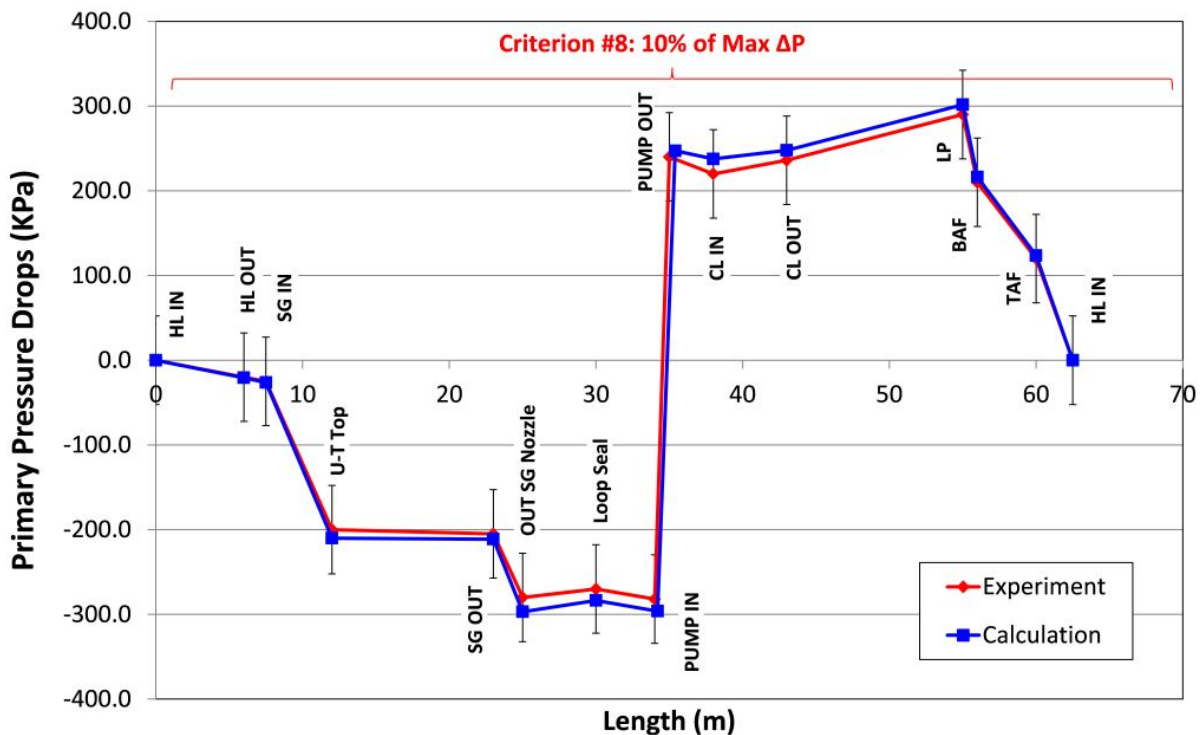


FIG. 345. Example of pressure drop distribution versus loop length.

The values of the thermal hydraulic parameters listed in TABLE 71 to be compared against the experimental measurements are determined from the end of the steady state calculation, which consists of a null transient simulation if, for example, the RELAP5 code is used. In this case, the convergence of the steady state calculation shall be checked and an additional acceptance criterion established (acceptance criterion-SS): the inherent drift of each parameter time trend shall be less than 1% over the last 100 seconds of the steady state calculation (see footnote (a) below TABLE 71, plus the plot in FIG. 346 of convergence of a null transient run; no measurement uncertainties have been considered in this example).

Step “g” (steady state achievement - improvement loop)

If one or more of the acceptability criteria in step “f” of the steady state run is not fulfilled (i.e. $E_i > AE_i$ where ‘i’ is a generic parameter), a review of the nodalization (step “c”) must be performed. This process can request more detailed data, improvement of the nodalization-schematization, different user and code model choices, etc. Path “g” must be repeated until all acceptability criteria in TABLE 71 are satisfied (i.e. all $E_i \leq AE_i$ where ‘i’ is a generic parameter).

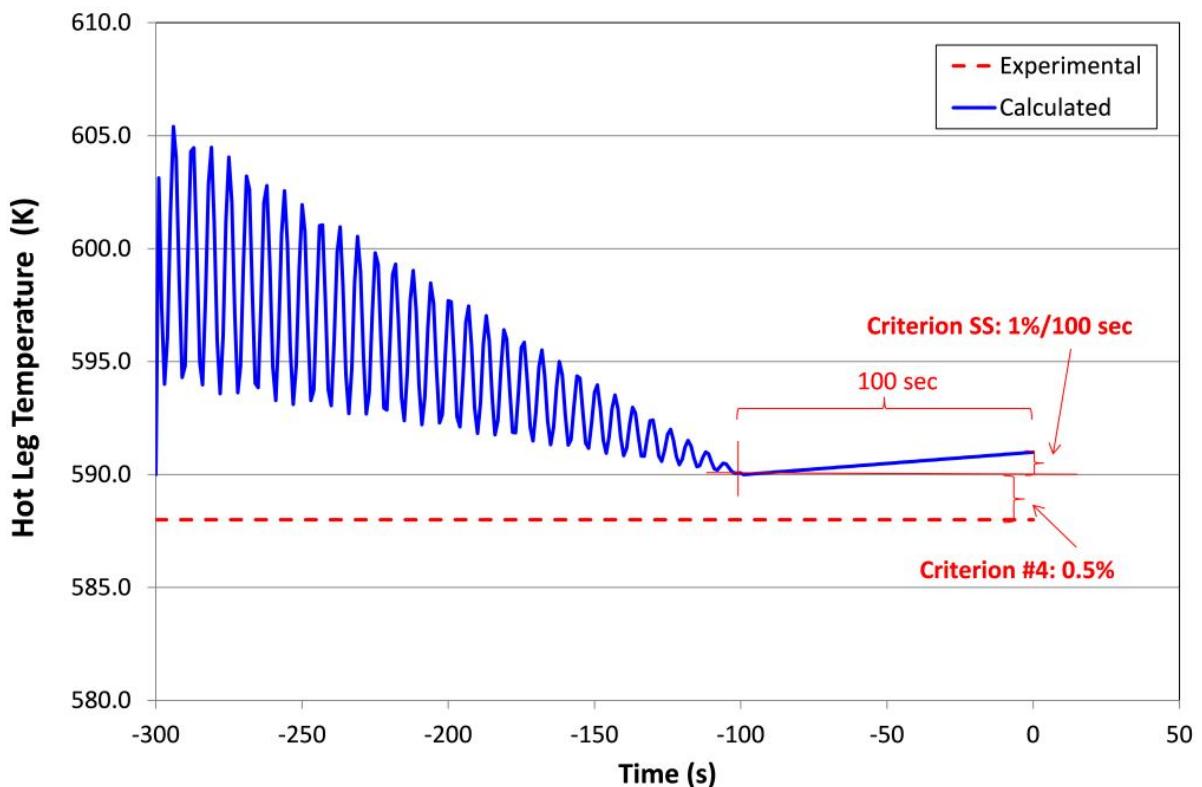


FIG. 346. Example of steady state for hot leg fluid temperature.

III.4. THE ‘ON-TRANSIENT’ QUALIFICATION

After the steady state qualification is completed, the on-transient level qualification must be performed following steps h), i) and j) in FIG. 343. Path “k” must be activated if the on-transient qualification is not successful.

Step “h” (the on-transient qualification)

This step constitutes the “On-Transient” level qualification. This activity is necessary to demonstrate the capability of the code and of the nodalization to reproduce the relevant thermal hydraulic phenomena expected during the transient. This step also makes it possible to verify that the implementation in the code model of some systems operating only during transient events (e.g. the ECCS performance) is correct. Two different situations can be identified:

- (1) The objective of the code calculation is the analysis of a transient in a test facility. The nodalization represents the schematization of the facility, and the code calculation is used for code assessment purposes. In this case, it is necessary to prove the capability of the code and of the nodalization scheme to simulate the transient test: i.e. the code options selected by the user, the schematization solutions and the logic of some systems (i.e. ECCS) are checked during this phase. The on-transient qualification requires performing several sub-steps, and in each of them, a comparison between experimental measurements and calculated results is carried out;
- (2) The object of the code calculation is the analysis of a transient in a NPP. The nodalization represents the schematization of the NPP, and the code calculation can be used for NPP safety analysis purposes. In this case, it is necessary to check the capability of the nodalization to reproduce the expected thermal hydraulic phenomena occurring during the transient, the selected code options, the solutions adopted by the user for the plant schematization and the logic of systems not involved in the steady state calculation but called into operation during the transient. The on-transient qualification requires performing several sub-steps, and it is rarely possible to perform a comparison between calculated results and measurement data due to the absence of NPP transient data. In order to overcome this limitation, a similar transient test must be performed in a facility which is a prototype of the NPP under consideration and the recorded data adopted to perform a “Kv-scaled analysis” (see also item (1) below).

In case of availability of NPP measured data for the analysis of the selected transient, the ‘On-Transient’ qualification of the NPP nodalization follows the same steps and criteria as for the ITF nodalization. In the following, steps i) and j) refer to this situation.

However, in general, no data exist for the selected NPP transients or tests to be simulated, thus the qualification of the NPP nodalization can be obtained through ‘similarity analysis’. Three different levels of similarity analysis can be performed, depending on the availability of data. In order of decreasing reliability of the analysis, they are:

- (1) Qualification of the NPP nodalization through the use of similar experimental tests performed in facilities that are possible prototypes of the considered NPP and through the so-called “Kv-scaled” calculation. The “Kv-scaled” calculation consists of using the developed NPP nodalization for calculation of the same type of transient performed in a facility. The NPP nodalization is prepared for a “Kv-scaled” calculation by properly scaling the boundary and initial conditions adopted in the facility. It generally means that power, mass flow rates and ECCS capacities are scaled, adopting as a scaling factor the ratio between the volume of the facility and the volume of the NPP. The capability of the NPP scaled nodalization to reproduce qualitatively the transient evolution and the relevant thermal hydraulic phenomena occurring in the selected ITF experiment is the criterion to be fulfilled for completing the “On-Transient” qualification level;

- | | |
|---|---|
| <ul style="list-style-type: none"> + Occurring o Partially occurring - Not occurring | <ul style="list-style-type: none"> + Suitable for code assessment o Limited suitability - Not suitable |
|---|---|

Test type versus test facility

- + Performed
- o Performed but of limited use
- Not performed or planned

Phenomena versus L2-5 test

- + Occurring
- O Partially occurring
- Not occurring

Phenomena versus calculation

- E Excellent
 - R Reasonable
 - M Minimal
 - U Unqualified
 - Not applicable
-

TABLE 72 shows how the CSNI phenomena identification can be used to evaluate the relevance of the phenomena with respect with to the selected test and facility.

Step “j” (‘on-transient’ acceptability criteria)

Qualitative and quantitative accuracy evaluations are carried out to evaluate the acceptability of the calculation at the “transient level”.

Qualitative Accuracy Evaluation

The qualitative accuracy evaluation must be completed before any meaningful attempt to perform the quantitative evaluation and shall address topics like:

- (a) Facility (ITF) validity;
- (b) Test validity;
- (c) Calculation validity.

The following sub-steps are involved during the qualitative accuracy evaluation:

- (1) **Visual observation:** visual comparisons are performed between experimental and calculated relevant parameters throughout the transient;
- (2) **Resulting Time Sequence of Events:** the list of calculated significant events with the corresponding calculated time of occurrences is compared with the experimental events and values (see sample in TABLE 73);
- (3) **Use of the Phenomena specified in the CSNI Validation Matrix** (see TABLE 72). The relevant phenomena suitable for the code assessment, plus the relevance of the phenomena in the selected facility and in the selected test, can be derived from the CSNI matrix. A judgement can be made, taking into account the characteristics of the facility, the test peculiarities and the code results;
- (4) **Use of the Phenomenological Windows (PhW), Key Phenomena and Relevant Thermal hydraulic Aspects (RTA).** Each test scenario (measured or calculated) shall be divided into phenomenological windows (i.e., time spans in which a unique relevant physical process mainly occurs and a limited set of parameters controls the scenario). In each PhW, key phenomena and RTA must be identified. Key phenomena are attributed to a class of experiments. The lists prepared by the

Organization for Economic Cooperation and Development (OECD)/CSNI are used in the process [132], [140]. RTAs (see TABLE 74) are defined as the characterization of the key phenomena for the specific transient and selected facility and are characterized by numerical values of significant parameters:

- (i) Single Valued Parameters (e.g., minimum level in the core);
- (ii) Non Dimensional Parameters (e.g., Froude numbering the hot leg at the beginning of reflux condensation);
- (iii) Time Sequence of Events (e.g., time when dryout occurs);
- (iv) Integral Parameters (e.g., integral of break flow rate during subcooled blowdown);
- (v) Derivative Parameters (e.g. derivative of primary and secondary pressure).

TABLE 73. EXAMPLE OF RESULTING TIME SEQUENCE OF EVENTS (LOFT FACILITY - TEST L2-5)

Event	Time (s)		
	Exp	Err	Calc
Experiment L2-5 initiated	0.0	-	0.0
Subcooled blowdown ended	0.043	±0.01	0.032
Reactor scrammed	0.24	±0.01	0.24
Cladding temperature initially deviated from saturation	0.91	±0.2	0.3
Primary coolant pumps tripped	0.94	±0.01	0.94
Subcooled break flow ended (cold leg)	3.4	±0.5	0.1
Partial rewet initiated	12.1	±1.0	8.2
Pressurizer emptied	15.4	±1.0	15.3
Accumulator A injection initiated	16.8	±0.1	15.1
Partial rewet ended	22.7	±1.0	15.1
HPIS injection initiated	23.9	±0.02	23.9
Maximum cladding temperature reached	28.47	±0.02	5.2
LPIS injection initiated	37.32	±0.02	37.32
Accumulator emptied	49.6	±0.1	52.0
Core cladding quenched	65.0	±2	65.5
BST maximum pressure reached	72.5	±1.0	-
LPIS injection terminated	107.1	±0.4	-

TABLE 74. EXAMPLE OF RTAS SUITABLE FOR QUALITATIVE ACCURACY EVALUATION (LOFT FACILITY- TEST L2-5)

		Unit	Exp.	Calc.	Judgement
RTA: Critical Flow					
TSE	Time of Maximum break flow rate	s	0.1	0.1	E
	Upper plenum in saturation conditions	s	0.18	0.2	E
IPA	Integral break flow rate at dryout time	kg	595.0	435.	R
	Integral break flow rate at ACC injection time	kg	3790.0	4680.	R
	Integral break flow rate at core quenching time	kg	4804.0	5857.	R
	Integral break flow rate at 100 s	kg	5280.0	6150.	R

		Unit	Exp.	Calc.	Judgement
RTA: Pressurizer Behaviour					
TSE	Time of minimum PRZ level (emptying time)	s	15.4	15.3	E
NDP	PRZ pressure/primary pressure at 5 s	-	1.93	1.78	R
	PRZ pressure/primary pressure at 10 s	-	2.01	1.94	E
	PRZ pressure / primary pressure at emptying time	-	1.87	1.85	E
TSE	Time of PRZ – primary pressure equalization	s	38.0	40.0	E
RTA: Core Power Behaviour					
TSE	Cladding temp. initially deviated from saturation	s	0.91	0.6	R
	Time of early quenching (start)	s	12.26	8.2	E
	Time of early quenching (end)	s	22.7	15.1	R
	Time of maximum cladding temperature	s	28.47	5.2	R
SVP	Peak cladding temperature	°C	1078.0	1114.0	E
TSE	Time of core cladding fully quenched	s	65.1 ± 2	65.5	E
RTA: Primary System Behaviour					
SVP	Pressure at dry out time	MPa	9.65	10.6	M
	Pressure at 10 s	MPa	5.69	5.69	E
	Pressure at 20 s	MPa	2.95	2.75	E
	Pressure at core quenching time	MPa	0.45	0.47	E
	Pressure at 100 s	MPa	0.40	0.4	E
RTA: Accumulator Behaviour					
TSE	ACC intervention time	s	16.8	15.1	R
SVP	ACC pressure 10 s after injection initiation	MPa	2.68	2.57	E
	ACC pressure 20 s after injection initiation	MPa	1.78	1.712	E
	ACC pressure at core quenching time	MPa	0.98	0.63	R
IPA	Integral ACC flowrate at core quenching time	kg	1504.0	1570.	E
	Integral ACC flowrate at 100 s	kg	1506.0	1584.	E
TSE	Time of accumulator emptied	s	49.6	52.	E
RTA. HPIS Behaviour					
TSE	HPIS intervention time	s	23.9	23.7	-
SVP	HPIS flowrate at core quenching time	kg/s	0.74	0.79	E
	HPIS flowrate at 100 s	kg/s	0.75	0.79	E
IPA	Integral HPIS flowrate at core quenching time	kg	33.3	30.24	E
	Integral HPIS flowrate at 100s	kg	59.5	60.36	E
RTA: LPIS Behaviour					
TSE	LPIS intervention time	s	37.32	37.1	-
SVP	LPIS flowrate at core quenching time	kg/s	5.67	5.71	E
	LPIS flowrate at 100 s	kg/s	7.21	6.1	R
IPA	Integral LPIS flowrate at core quenching time	kg	146.80	173.0	R
	Integral LPIS flowrate at 100 s	kg	379.66	310.	R

Around 20 RTAs, characterized by more than 40 values of significant parameters, must be selected for the qualitative evaluation of a database. Key phenomena and RTAs are used for the following purposes:

- (1) to judge the relevance with respect to the scaling and the quality of a test facility (key phenomena);
- (2) to judge the relevance with respect to the scaling and the quality of a test design (key phenomena);
- (3) to judge the relevance of an experimental database (key phenomena and RTAs);
- (4) to judge the calculation performance (RTAs);
- (5) to assess the success of a similarity study and of the nodalization qualification process (RTAs);
- (6) to assess the similarity of different experimental databases (RTAs).

The qualitative analysis is finally synthetized by the use of five subjective judgement marks, which are applied to the matrix of phenomena, to the visual observation of the time trends, and to the list of RTAs:

- (a) The code predicts the parameter qualitatively and quantitatively (**Excellent** - the calculation falls within the experimental data uncertainty bands);
- (b) The code predicts the parameter qualitatively, but not quantitatively (**Reasonable** - the calculation shows only correct behaviour and trends);
- (c) The code does not predict the parameter, but the reason is understood and predictable (**Minimal** - the calculation does not lie within the experimental data uncertainty bands and does not have correct trends);
- (d) The code does not predict the parameter and the reason is not understood (**Unqualified** - calculations do not show the correct trend and behaviour, and reasons are unknown and unpredictable);
- (e) Not applicable (-).

A successful application of the qualitative process is the first step of the “on-transient qualification” process and constitutes a prerequisite to the second and last step of the process: the application of the quantitative analysis.

Quantitative Accuracy Evaluation

If the qualitative accuracy evaluation step has been successful, the accuracy of the code calculations can be quantified utilizing the Fast Fourier Transform Based Method (FFTBM). This tool produces from each comparison between calculated and measured time trends one pair of values in the frequency domain: 1) the so-called “Average Accuracy” (AA) and 2) the “Weighted Frequency” (WF). The transformation from time to the frequency domain avoids the dependence of the error on the transient duration. Weight factors are attributed to each time trend to make possible the summing up of the AA of each parameter and the achievement of a unique threshold for accepting a calculation (AA_{TOT}). A quantitative accuracy evaluation must be carried out following demonstration that the calculation is qualitatively acceptable. The same time trends selected for the qualitative analysis are utilized as input to the FFTBM software. Acceptability criteria have been set-up and a full description of the FFTBM is given in [141] and [142].

Step “k” (on-transient qualification - improvement loop)

This path is actuated if one or more checks (qualitative and/or quantitative) of the on-transient qualification are not fulfilled. The nodalization is improved (step “c”) by changing schematization solutions, adopting different user and code model choices or increasing the level of detail using new data. Every time the nodalization is modified, a new process must be performed through the loop “c-d-e-f-h-i-j”, which implies establishment of a new steady state and a new on-transient qualification.

Step “I” (achievement of a qualified nodalization)

This is the last step of the procedure. The nodalization obtained is called the Analytical Simulation Model (ASM) and consists of a qualified plant (or facility) nodalization running in a qualified code by a qualified user. The ASM can be used to predict plant scenarios characterized by the same phenomenological windows and key phenomena as the assigned transient.

It must be pointed that a modification of the nodalization (which can be requested, for instance, to better reproduce the experimental results) requires a new qualification process for both “at steady state” and “on-transient” levels.

Once the qualification process has been successfully concluded, the Qualification Report (QR) in block G of the SCCRED methodology (FIG. 342) shall be assembled. The QR is a document necessary to demonstrate that the code results are qualitatively and quantitatively acceptable with respect to established acceptance criteria which are part of the qualification process described above.

Based on the qualification procedures, the minimum amount of information which shall be contained in a QR is:

- (a) The demonstration of the geometrical fidelity (block e in FIG. 343) of the model with respect to the facility, i.e. the verification of the items listed in TABLE 70;
- (b) The qualification at the steady state level (blocks d and e in FIG. 343), i.e. the demonstration of the capability of the model to reproduce the steady state qualified condition of the test, achieved by verification of the items listed in TABLE 71;
- (c) The qualification at transient level (block h in FIG. 343), i.e. the demonstration of the capability of the code nodalization to reproduce the relevant thermal hydraulic phenomena expected during the transient and, in particular, the verification of the qualitative and quantitative accuracy steps.

III.5. THE FFTBM ACCURACY EVALUATION FOR QUALIFICATION PURPOSES

Within the qualification procedure described above, the quantification of the accuracy of code calculations is performed, using the amplitude of the Fourier Transform of the experimental signal and of the difference between this and the calculated results. The accuracy of a code calculation can be evaluated through these values by representing the discrepancies between the calculation and the experimental data with a dimensionless Average Amplitude (AA) that represents the relative magnitude of these discrepancies [138], [143]. The Fast Fourier Transform Based Method (FFTBM) tool has been validated and applied in numerous international benchmarks [144], [145]. The mathematical background of FFTBM is provided below.

Several approaches have been proposed to quantify the accuracy of a given code calculation [137], [143], [146], [147]. Even though these methods were able to give some information about the accuracy, they were not considered satisfactory because they involved some empiricism and were lacking a precise mathematical meaning. In addition, subjective engineering judgement at various levels is an integral part of these proposed methods.

Generally, the starting point of each method is an error function by means of which the accuracy is evaluated. Some requirements were fixed which an objective error function should satisfy:

- (a) At any time during the transient, this function should remember the previous history;
- (b) Engineering judgement should be avoided or reduced;
- (c) The mathematical formulation should be simple;
- (d) The function should be non-dimensional;
- (e) It should be independent of the transient duration;
- (f) Compensating errors should be taken into account (or pointed out);
- (g) the function values should be normalized.

The simplest formulation about the accuracy of a given code calculation $F_{calc}(t)$, with reference to the experimental measured data $F_{exp}(t)$, is obtained by the difference function $\Delta F(t)$:

$$\Delta F(t) = F_{calc}(t) - F_{exp}(t) \quad (17)$$

The information contained in this time-dependent function, continuously varying, should be condensed to give a limited number of values which could be taken as indexes for quantifying accuracy. This is allowed because the complete set of instantaneous values of $\Delta F(t)$ is not necessary to draw an overall judgement about accuracy. Integral approaches satisfy this requirement, since they produce a single value on the basis of the instantaneous values of a given function of time. On the other hand, in searching for functions expressing all the information through a single value, some interesting details could be lost. Therefore, it would be preferable to define methodologies leading to more than one value in order to characterize the code calculation accuracy. Information that comes from the time dependence of a certain parameter, either a physical or a derivate one, may not be sufficient for a deep comprehension of the phenomenon of concern; in such a case, it may be useful to study the same phenomenon from other points of view, free of time dependence. In this context, the complete behaviour of a system in periodic regime conditions (periodic conditions due to instability phenomena are explicitly excluded) can be shown by the harmonic response function that describes it in the frequency domain. Furthermore, the harmonic analysis of a phenomenon can point out the presence of perturbations otherwise hidden in the time domain.

III.6. THE FFTBM ALGORITHM DEVELOPMENT

It is well-known that the Fourier transform is essentially a powerful problem solving technique. Its importance is based on the fundamental property that one can analyse any relationship from a completely different viewpoint, with no lack of information with respect to the original one. The Fourier transform can translate a given time function $g(t)$, into a corresponding complex function $\tilde{g}(f)$ defined, in the frequency domain f , by the relationship:

$$\tilde{g}(f) = \int_{-\infty}^{+\infty} g(t) e^{-j2\pi ft} dt \quad (18)$$

The graphical display of a transformed signal is obtained through the two spectral coordinates, frequency and amplitude, which respectively substitute for time and the quantity value in the time domain representation.

Afterwards, it is assumed that the experimental and calculated results, to which the Fourier transform is applied, satisfy the analytical conditions required by the Fourier transform application theory; i.e., it is assumed that they are continuous (or generally continuous)³ over the time intervals under consideration, along with their first derivatives, and absolutely integrable in the interval $(-\infty, +\infty)$ ⁴. This last requirement can be easily satisfied in case of the CRP analyses, since the functions of interest assume values different from zero only in the interval $(0, T)$. Therefore:

$$\tilde{g}(f) = \int_0^T g(t) e^{-j2\pi ft} dt \quad (19)$$

The Fourier integral Eq. 19 is not suitable for machine computation because an infinity of samples of $g(t)$ is required. Thus, it is necessary to truncate the sampled function $g(t)$ so that only a finite number of points are considered, or in other words, the discrete Fourier transform is evaluated. Truncation introduces a modification of the original Fourier transform (the Fourier transform of the truncated $g(t)$ has a rippling); this effect can be reduced by choosing the length of the truncation function to be as long as possible.

By analogy with the Fourier transform for a continuous function $g(t)$, the Fourier transform for a discrete set of $g_k = g(t_k)$ with $k = 0, 1, 2, \dots, N-1$ may be defined as below:

$$\tilde{g}(f_n) = \int_0^{T_d} g(t) e^{-i2\pi f_n t} dt \approx \frac{1}{N} \sum_{k=0}^{N-1} g_k e^{-i2\pi f_n t_k} \Delta t = \Delta t \frac{1}{N} \sum_{k=0}^{N-1} g_k e^{-i2\pi f_n t_k} \quad (20)$$

where, T_d is the transient time duration of the sampled signal. When using functions sampled in digital form, the Fast Fourier Transform (FFT) can be used. The FFT is an algorithm that can compute more rapidly than the discrete Fourier transform. To apply the FFT algorithm, functions must be identified in digital form by discrete values, and the number of values must be a power of 2. Thus, if the number of points defining the function in the time domain T_d is $N = 2^{m+1}$ then according to the sampling theorem, the sampling frequency f_s is given by Eq. 21,

$$\frac{1}{\Delta t} = f_s = 2f_{max} = \frac{N}{T_d} = \frac{2^{m+1}}{T_d} \quad (21)$$

where f_{max} is the highest (maximum) frequency component of the signal. The sampling theorem does not hold beyond f_{max} ; from the relation in (5), it is seen that selection of the number of points is strictly connected to the sampling frequency. The FFT algorithm determines the number of points, equally spaced, which is a power with base 2 (N ranges from 2^9 to 2^{12}). Generally, an interpolation is necessary to satisfy this requirement. Taking into account that the available subroutine packages evaluate the FFT normalized to the time duration T_d from Eq. 19 and Eq. 21, it can easily be seen that $|\tilde{g}(0)|$ represents the mean value

³ i.e. discontinuous only at a finite number of points. The existence of the Fourier Transform is guaranteed if $g(t)$ is summable according to Lebesgue on the real axis.

⁴ i.e. $\int_{-\infty}^{+\infty} |g(t)| dt < \infty$

of the function $g(t)$ in the interval $(0, T_d)$ while $|\tilde{g}(f_n)|$ represents the amplitude of the n -th term of the Fourier polynomial expansion of $g(t)$.

The method developed for the code accuracy quantification of an individual calculation is based on the amplitude of the FFT of the experimental signal and of the difference between this signal and the calculated result. In particular, the method introduces the definition of two figures of merit: the Average Amplitude (AA) given in Eq. 22 and the Weighted Frequency (WF) in Eq. 23, which provide a synthesis of the information about the error function from Eq. 17:

$$AA = \frac{\sum_{n=0}^{2^m} |\tilde{\Delta F}(f_n)|}{\sum_{n=0}^{2^m} |\tilde{F}_{\text{exp}}(f_n)|} \quad (22)$$

$$WF = \frac{\sum_{n=0}^{2^m} |\tilde{\Delta F}(f_n)| \cdot f_n}{\sum_{n=0}^{2^m} |\tilde{\Delta F}(f_n)|} \quad (23)$$

The Average Amplitude represents the relative magnitude of the discrepancy between the calculation results of interest and the corresponding experimental data: the lower the AA, the better the agreement between the experiment and the calculation. The Weighted Frequency factor characterizes the kind of error, because its value emphasizes if the error has more relevance at low or high frequencies. Depending upon the transient, high frequency errors can be more acceptable than low frequency ones. In other words, better accuracy is achieved by low AA values at high WF values.

Obtaining an overall picture of the accuracy of a given calculation requires combining the information obtained for the individual parameters into average indexes of performance. This is obtained by defining the following quantities: the Global Average Amplitude AA_{tot} given in Eq. 24 and the Global Weighted Frequency WF_{tot} in Eq. 25:

$$(AA)_{\text{tot}} = \sum_{i=1}^{N_{\text{var}}} (AA)_i (w_f)_i \quad (24)$$

$$(WF)_{\text{tot}} = \sum_{i=1}^{N_{\text{var}}} (WF)_i (w_f)_i \quad (25)$$

with

$$\sum_{i=1}^{N_{\text{var}}} (w_f)_i = 1 \quad (26)$$

where N_{var} is the number of parameters analysed and $(w_f)_i$ are weighting factors that take into account the unique importance of each parameter from the viewpoint of safety analyses. This introduces some degree of engineering judgement that has been fixed by a proper and unique definition of the weighting factors. This is necessary to account for the different relevance,

from the point of view of safety and reliability of the measurement, of the various quantities being considered.

III.7. THE FFTBM RELEVANT PARAMETERS

To apply the FFTBM described in the previous section, it is necessary to set the following parameters:

- (a) Sampling frequency;
- (b) Number of points;
- (c) Cut frequency;
- (d) Weighting factors.

In order to evaluate the discrete Fourier transform, it is necessary, first of all, to sample the signals to be analysed. The choice of the sampling frequency depends on the transient and the kind of parameter to be investigated (i.e. pressure, flow rate, clad temperature, etc.). The fulfilment of the sampling theorem is required to avoid distortion of sampled signals due to occurrence of aliasing. Aliasing occurs until the frequency sampling is increased to f_c , where f_c is the highest frequency component of the Fourier transform characterizing the spectrum of the continuous function $g(t)$:

$$T_d = \frac{1}{2f_c} \quad (27)$$

Therefore, experimental data acquisition should be characterized by a sampling frequency greater than $2f_c$ (normally from 3 to 5 times f_c is used); a similar frequency should be applied to the corresponding calculated results. In addition, analysis of these data requires that the lowest value of f_c (between the experimental and calculated ones) should be taken as the limiting value. A typical value of f_c related to parameters of interest in thermal hydraulic transients is 1 Hz; however, specific responses like break flow rates or pressure drop measurements may require higher values.

Since the FFT algorithm requires that functions be identified by a number of values, equally spaced and the number being a power of 2, interpolation is necessary to satisfy this requirement. However, comparison of experimental signals and calculated results, and the evaluation of their difference function $\Delta F(t)$, requires that they have the same timescale. Furthermore, after selecting the number of points N , the maximum frequency of functions transformed by the FFT is given by:

$$f_{\max} = \frac{2^m}{T_d} = \frac{f_c}{2} \quad (28)$$

Thus, the number of points is strictly associated with the adopted sampling frequencies; it is meaningless to choose a number of points corresponding to a frequency⁵ greater than the f_{\max} achievable using a certain f_c .

⁵ Beyond $f_c/2$ the sampling theorem does not hold, and there is no further information about these frequencies.

Conversely, during the interpolation step, some information could be lost by choosing too low a number of points. Also, the interpolation introduces an additional effect on the signals, i.e. each interpolation, using a linear method, adds a slope. It has been verified that this effect is negligible because the only impact is the addition of some spurious frequencies in the original signal spectrum having values greater than the typical frequencies of thermal hydraulic parameters. Since most thermal hydraulic quantities are characterized by low frequencies, then high frequency errors (therefore, these spurious contributions, too) can be totally avoided by considering proper filtering techniques.

To filter any spurious contribution, a cut frequency has been introduced. This cut frequency characterizes the higher frequency value which has to be considered for the evaluation of AA and WF, as defined by Eq. 22 and Eq. 23. Typical thermal hydraulic parameter curves (for different kinds of transients) have been analyzed [148], aiming at defining a unique suitable value of cut frequency in such a way as to avoid partial loss of information. A cut frequency value of 1 Hz is generally suitable to analyze time dependence of thermal hydraulic parameters; only flow rates and densities require cut frequency values up to 2 Hz.

In order to give an overall picture of the accuracy of the calculation, the FFTBM accounts for the accuracy evaluated for each parameter, and by defining some weighting factors $(w_f)_i$, global indexes of code performance are evaluated (see Eq. 24 and Eq. 25). The need to define $(w_f)_i$ derives from the fact that the selected parameters are characterized, among other things, by different importance and reliability of measurement. Thus, each $(w_f)_i$ takes into account:

- (a) ‘*Experimental accuracy*’: experimental measures of thermal hydraulic parameters are characterized by a more or less sensitive uncertainty due to:
 - (i) Intrinsic characteristics of the instrumentation;
 - (ii) Assumptions formulated in getting the measurement;
 - (iii) Unavoidable discrepancies existing between experimental measurements and the code-calculated quantities (mean values evaluated over cross-sections, at volume centres or across junctions, etc.);
- (b) ‘*Safety relevance*’: particular importance is given to the accuracy quantification of calculations concerned with those parameters (e.g. clad temperature, from which peak cladding temperature values are derived) which are relevant for safety and design.

Last, a further contribution is included in the weighting factors definition; this is a component aimed at accounting for the physical correlations governing most of the thermal hydraulic quantities. Taking as the reference parameter the primary pressure (its measurement can be considered highly reliable), a normalization of the AA values calculated for other parameters with respect to the AA value calculated for the primary side pressure is carried out.

The weighting factor for the generic j -th parameter, is defined as:

$$(w_f)_j = \frac{(W_{exp})_j \cdot (W_{saf})_j \cdot (W_{norm})_j}{\sum_{j=1}^{N_{var}} (W_{exp})_j \cdot (W_{saf})_j \cdot (W_{norm})_j} \quad (29)$$

where

N_{var} is the number of parameters to which the method is applied;
 $(W_{exp})_j$ is the contribution related to the experimental accuracy;

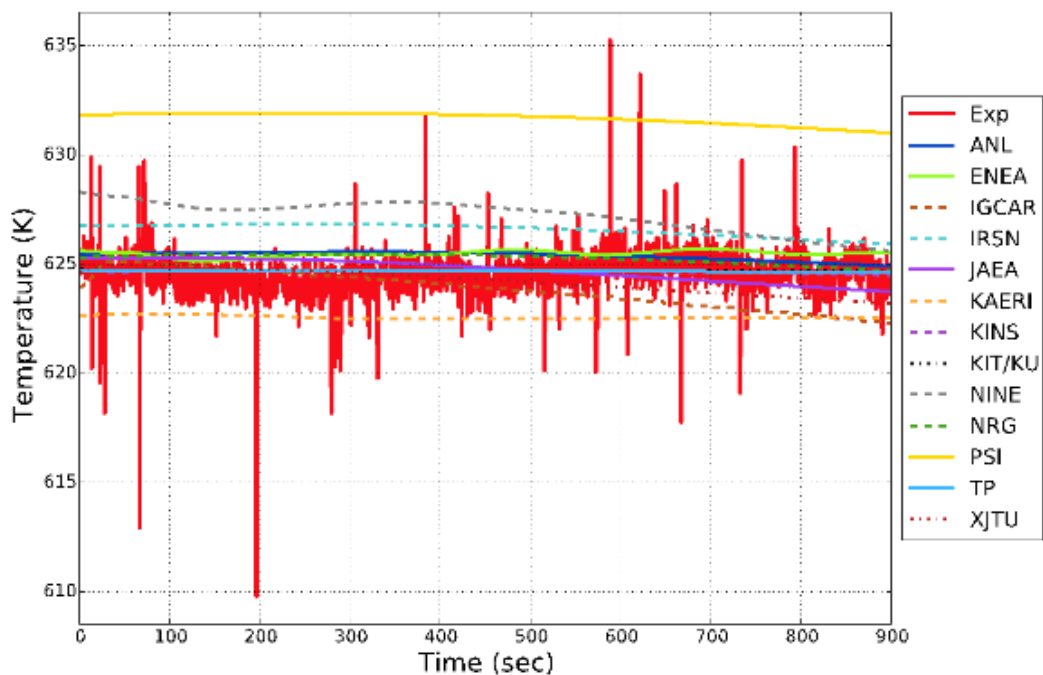
$(W_{\text{saf}})_j$ is the contribution expressing the safety relevance of the parameter;
 $(W_{\text{norm}})_j$ is the component of the normalization vector with reference to the AA evaluated for the primary side pressure.

This introduces a degree of engineering judgement that has been fixed by a proper and unique definition of the weighting factors as discussed in [141].

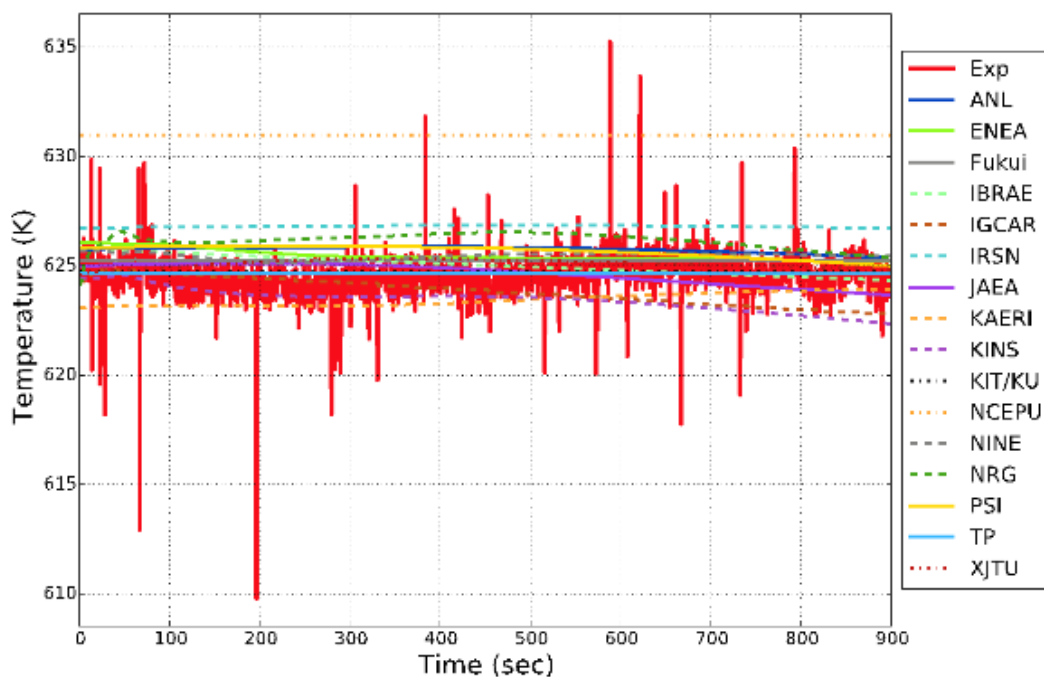
Appendix IV

COLLECTIVE RESULTS PLOTS

SHRT-17

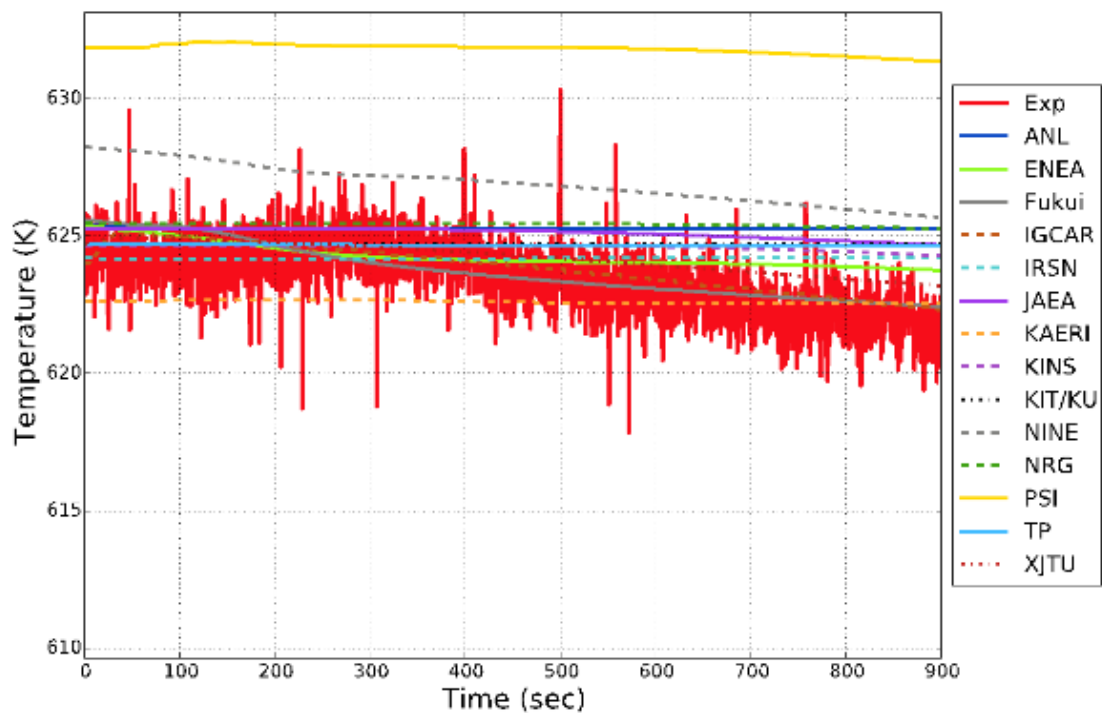


(a) blind results

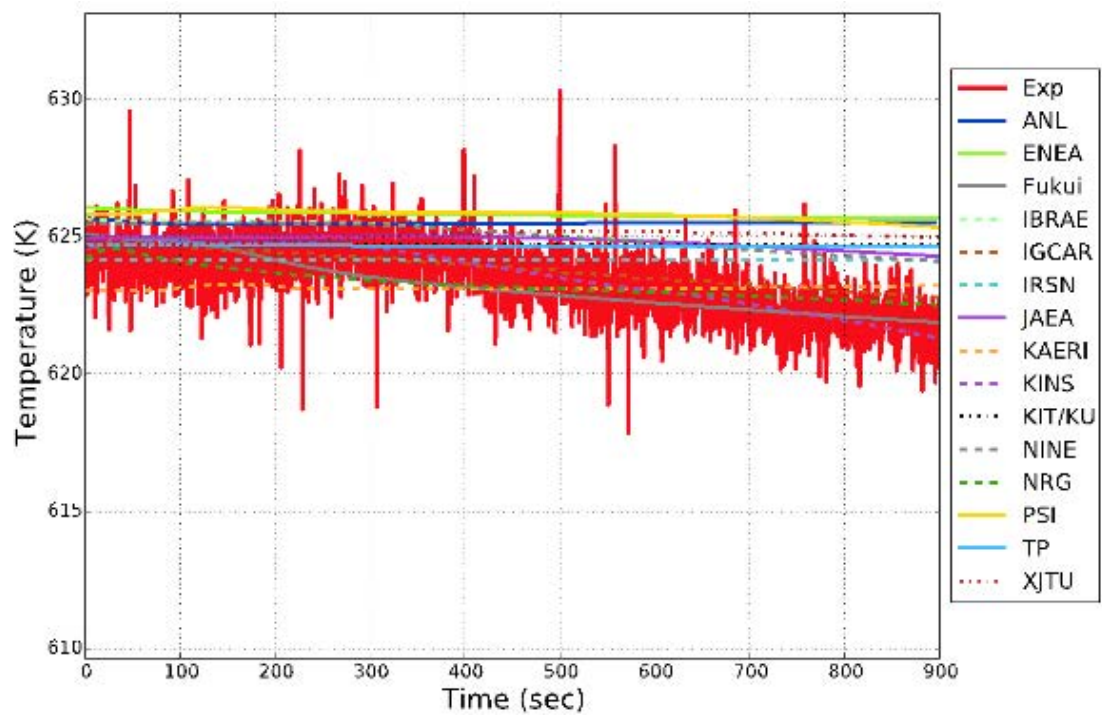


(b) final results

FIG. 347. SHRT-17 high pressure plenum inlet temperature.

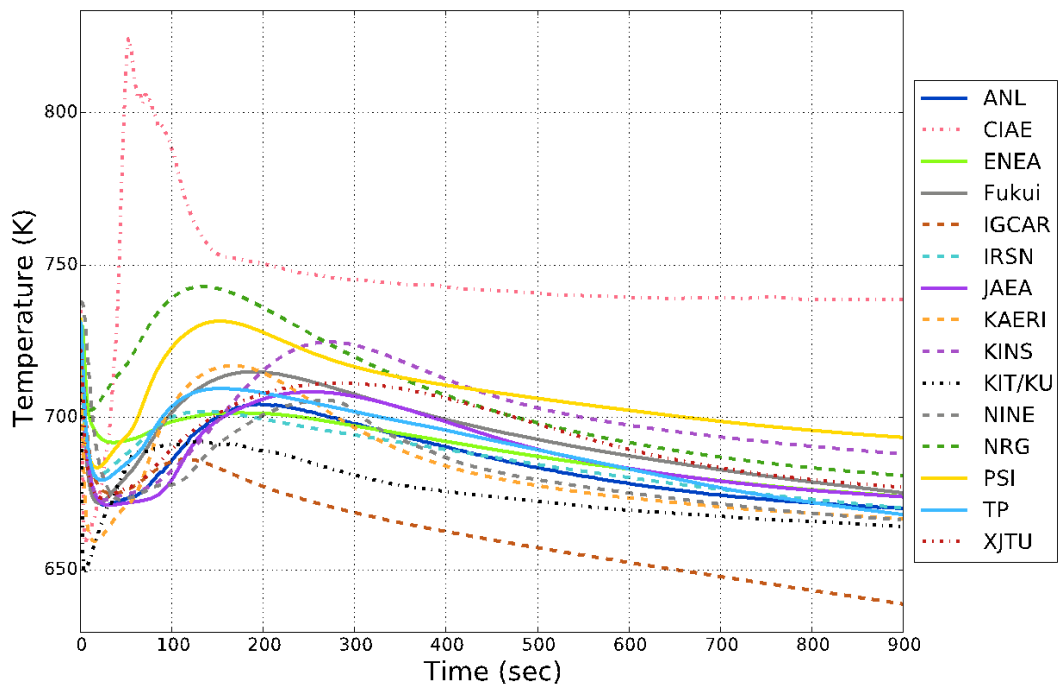


(a) blind results

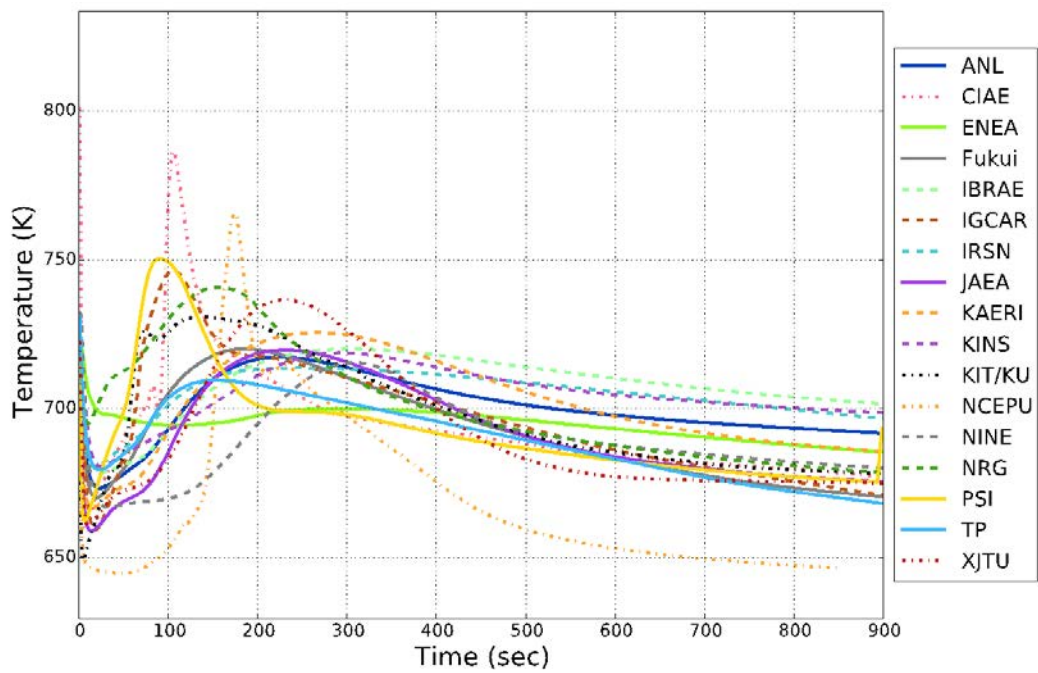


(b) final results

FIG. 348. SHRT-17 low pressure plenum inlet temperature.

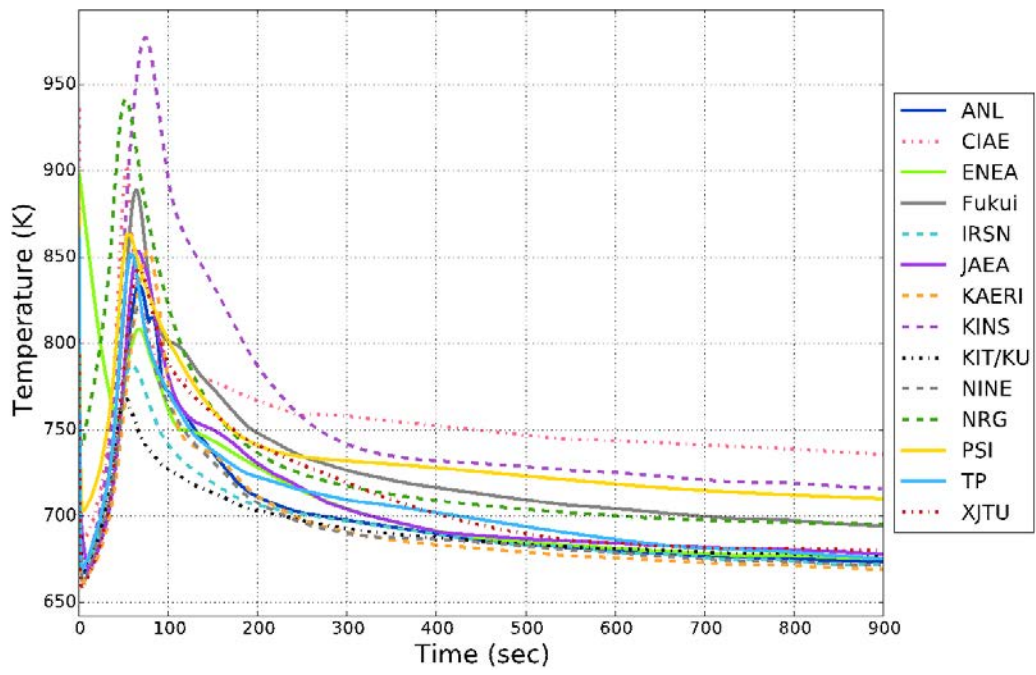


(a) blind results

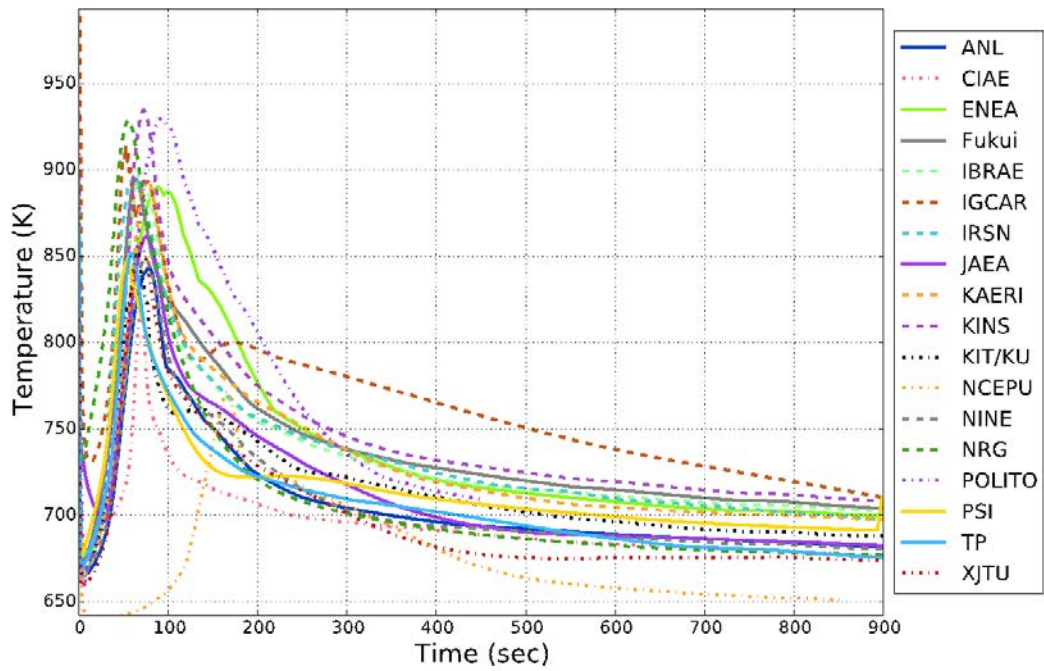


(b) final results

FIG. 349. SHRT-17 Z-Pipe inlet temperature (no recorded data).

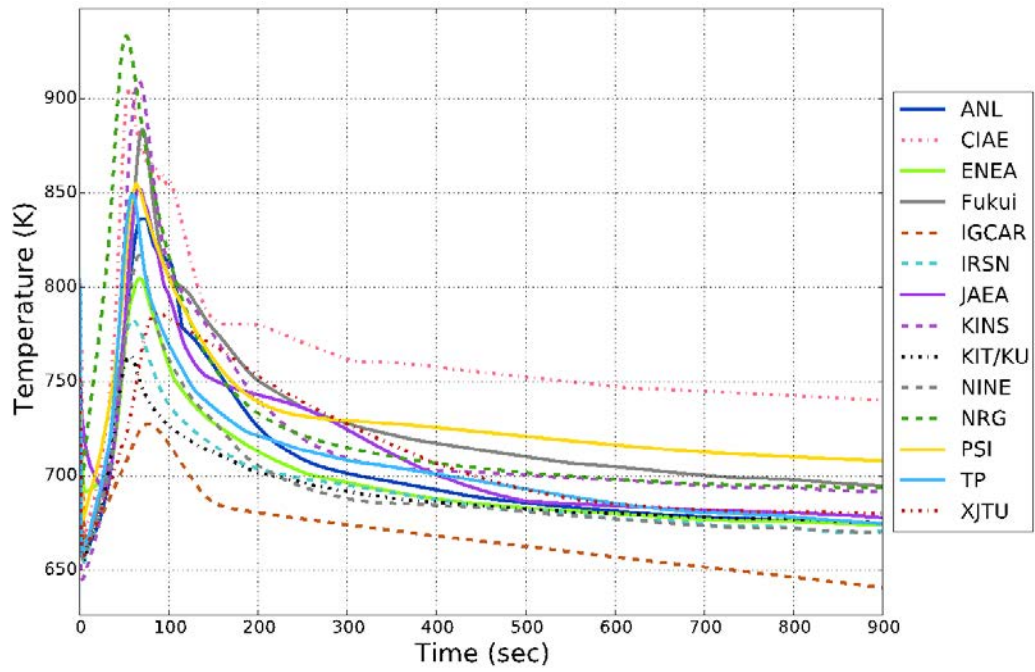


(a) blind results

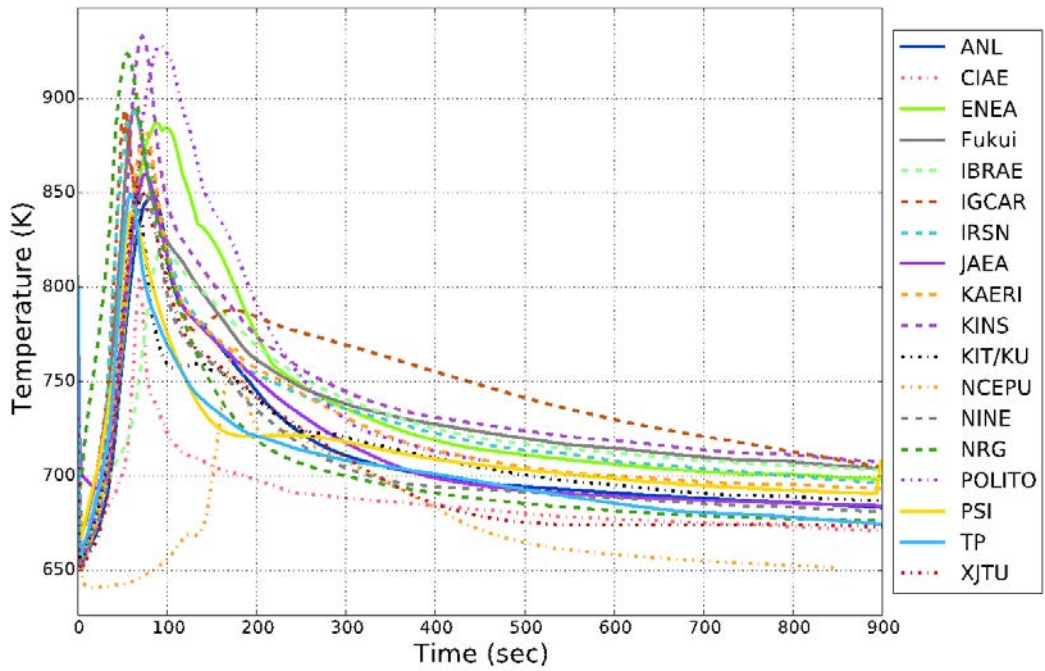


(b) final results

FIG. 350. SHRT-17 peak fuel temperature (no experimental data).

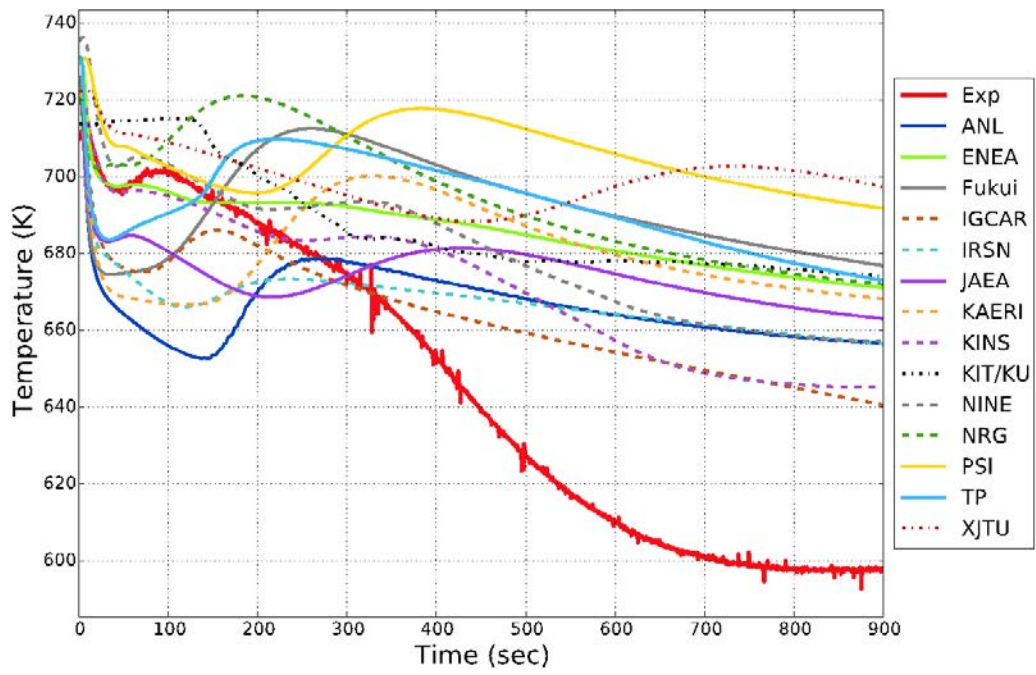


(a) blind results

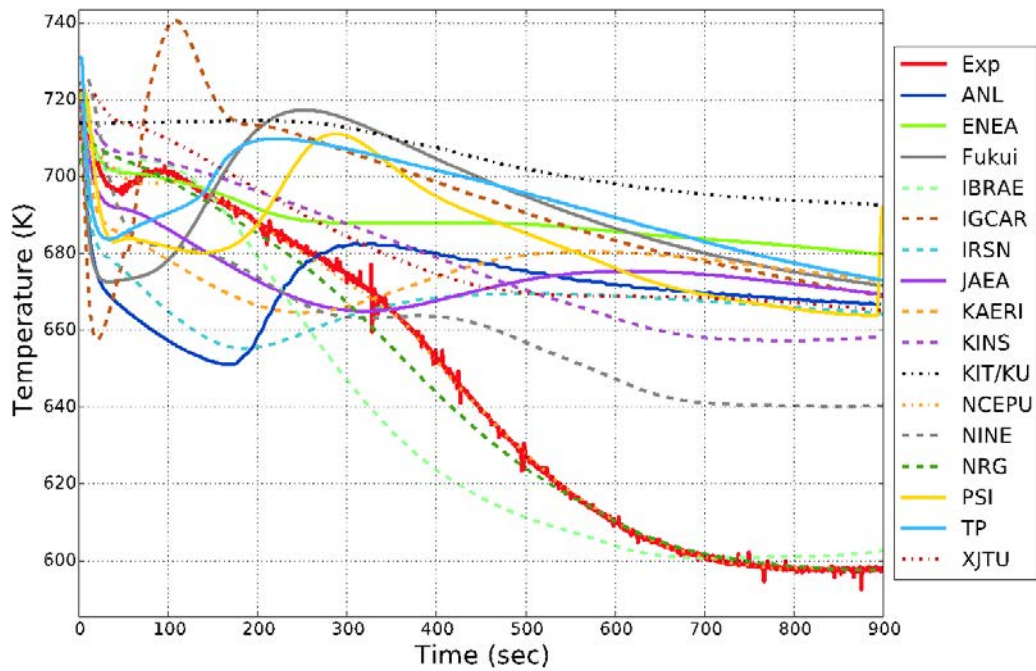


(b) final results

FIG. 351. SHRT-17 Peak coolant temperature (no experimental data).

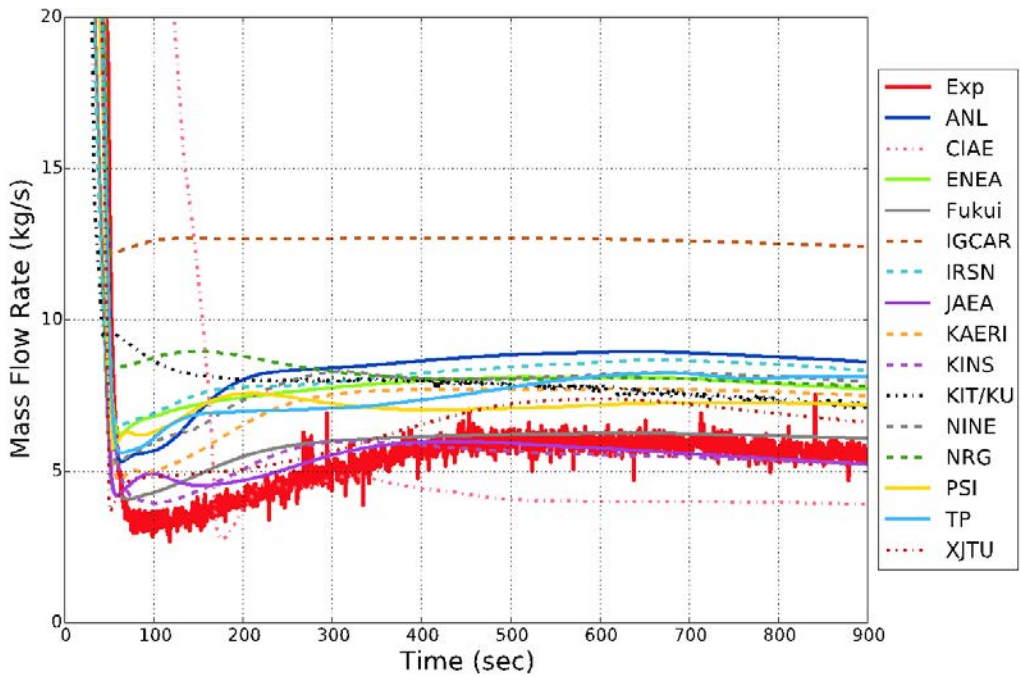


(a) blind results

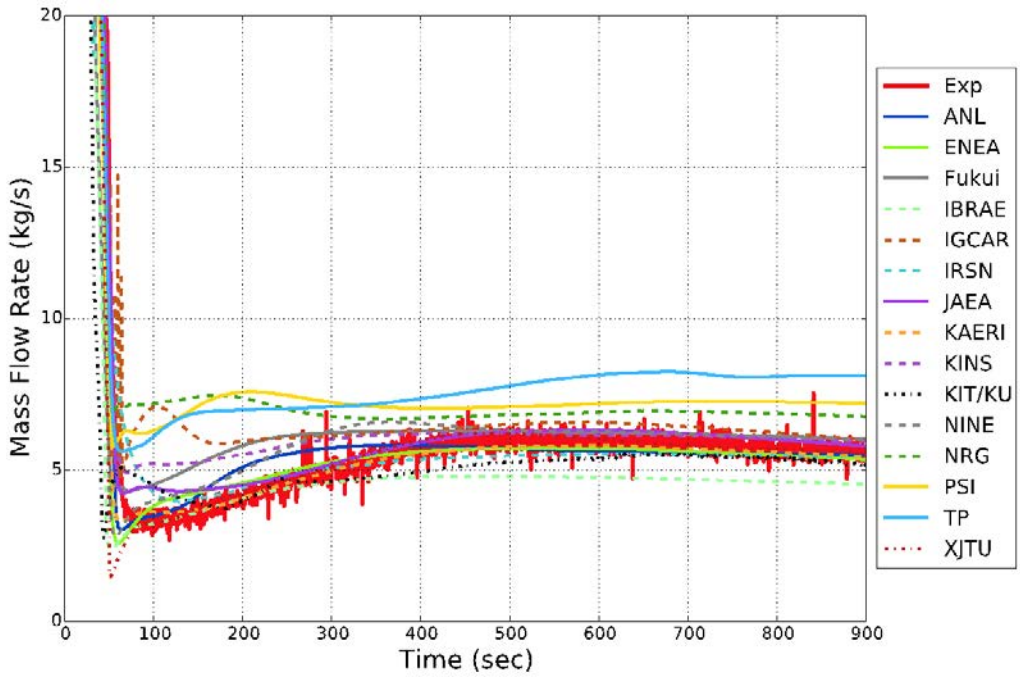


(b) final results

FIG. 352. SHRT-17 IHX primary inlet temperature.

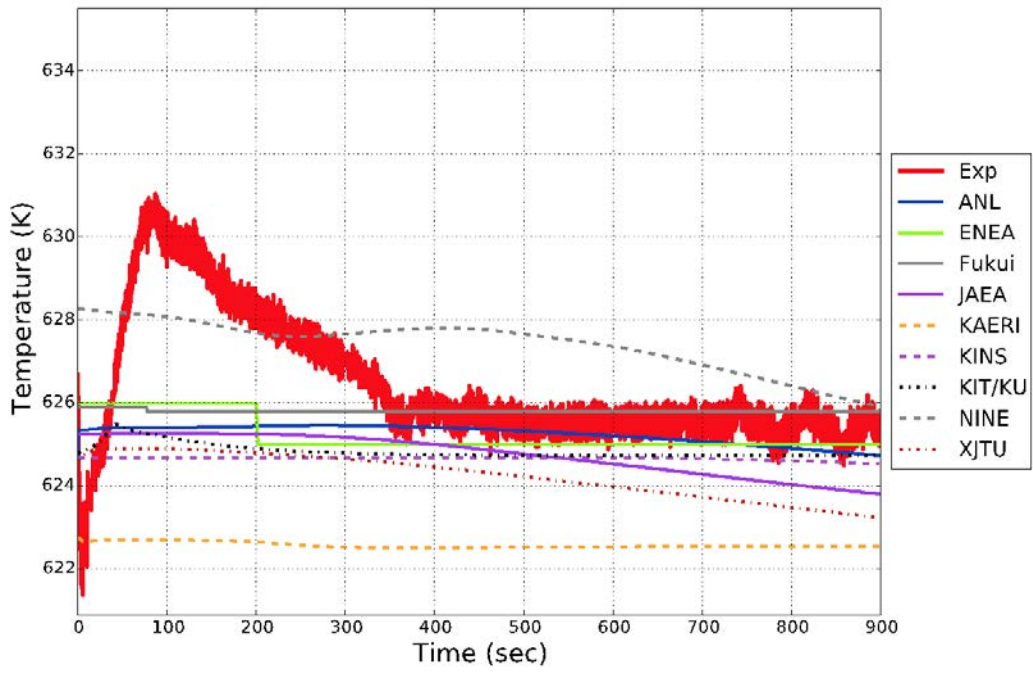


(a) blind results

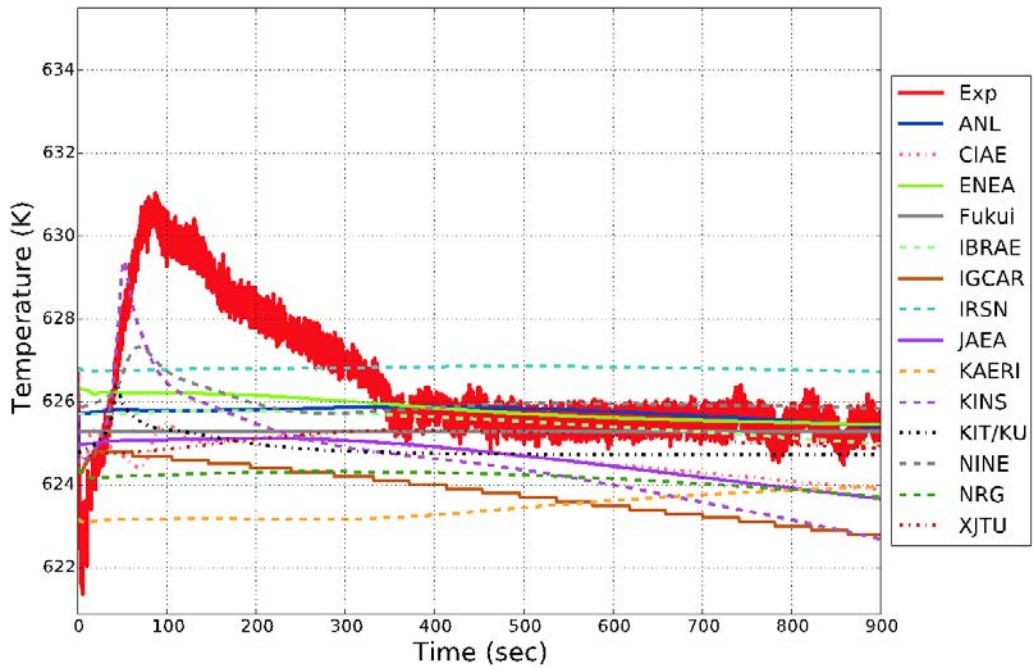


(b) final results

FIG. 353. SHRT-17 pump #2 mass flow rate.

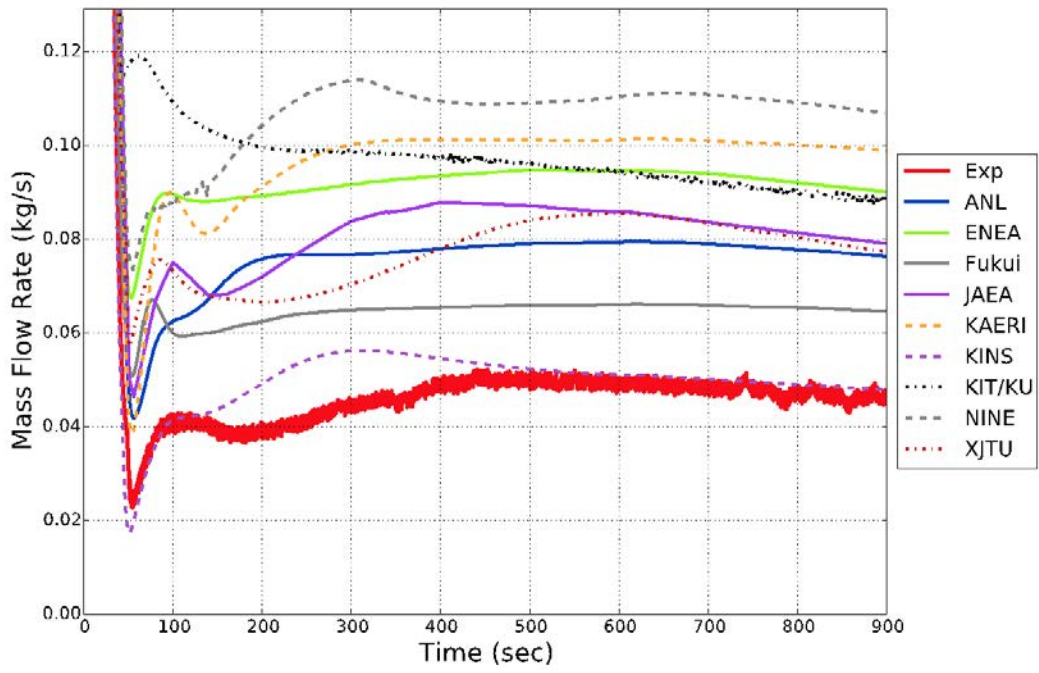


(a) blind results

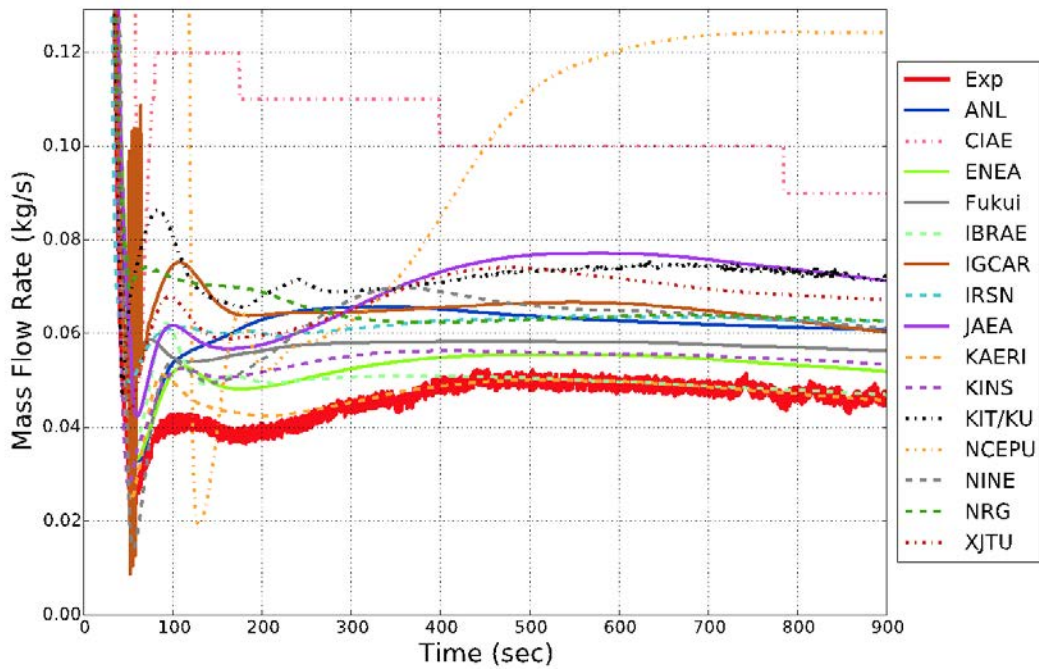


(b) final results

FIG. 354. SHRT-17 XX09 lower flowmeter temperature (FM-1TC).

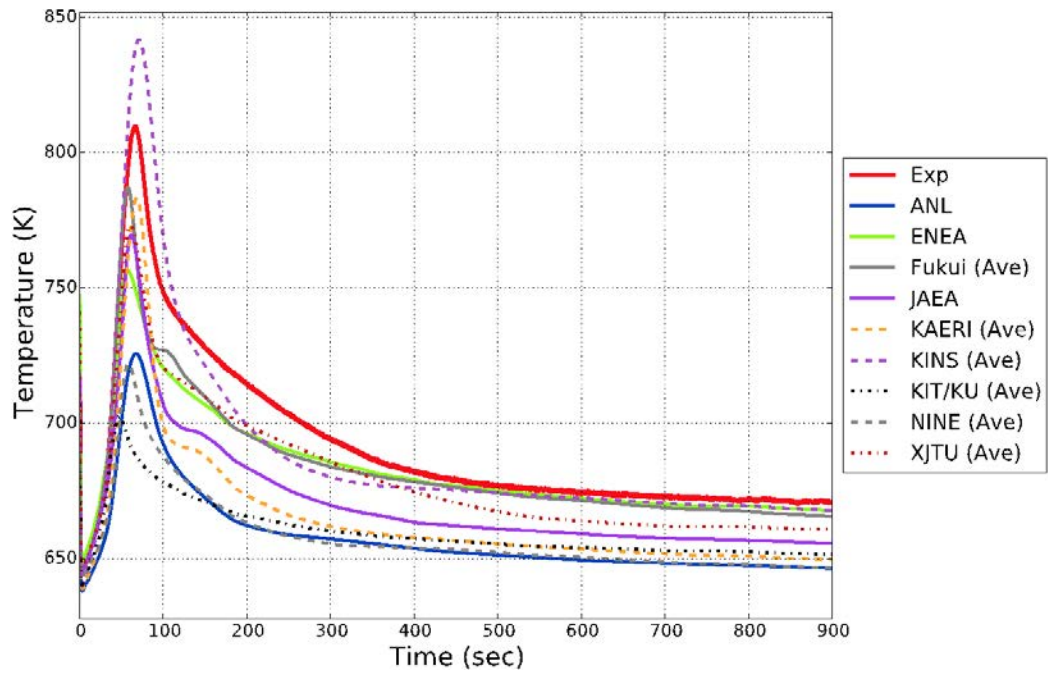


(a) blind results

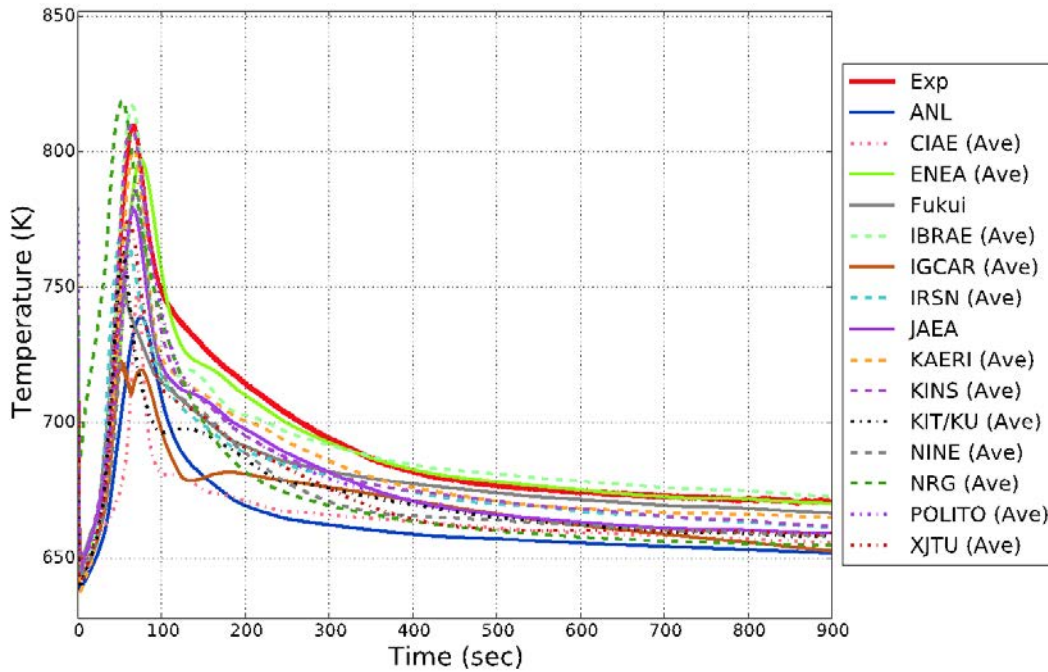


(b) final results

FIG. 355. SHRT-17 XX09 mass flow rate.

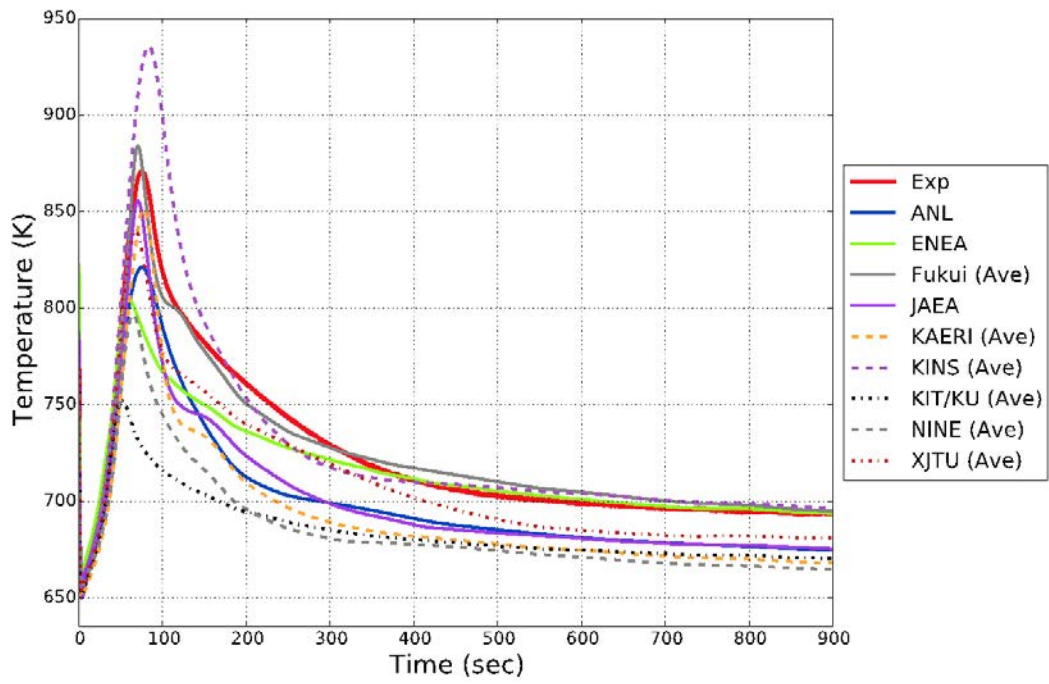


(a) blind results

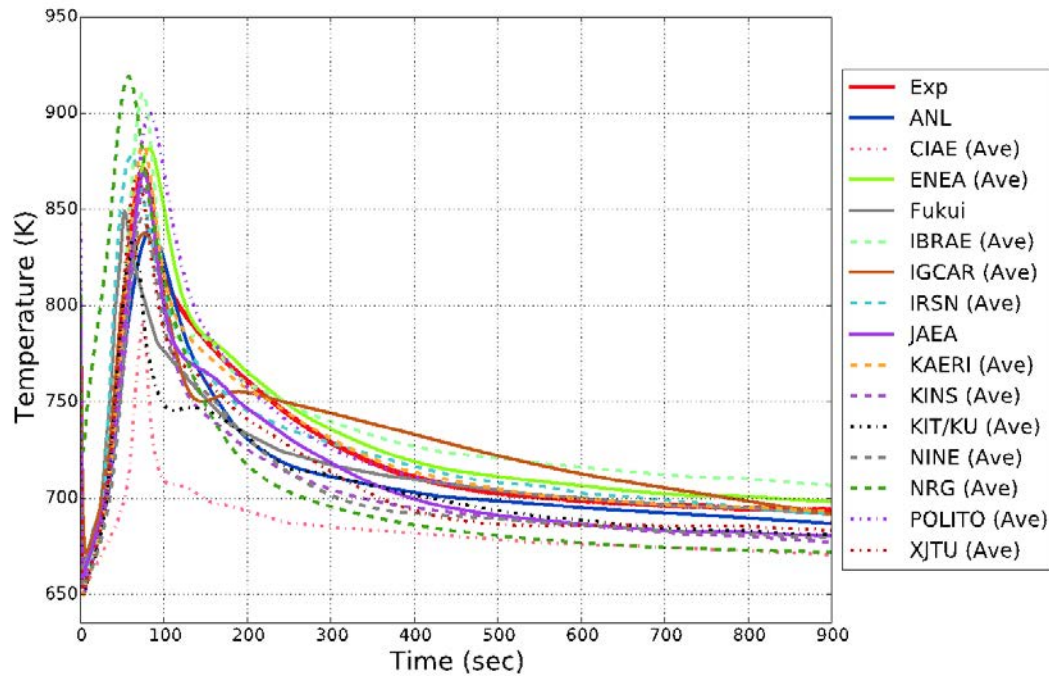


(b) final results

FIG. 356. SHRT-17 XX09 sample midcore temperature (MTC-20).



(a) blind results



(b) final results

FIG. 357. SHRT-17 XX09 sample top of core temperature (TTC-8).

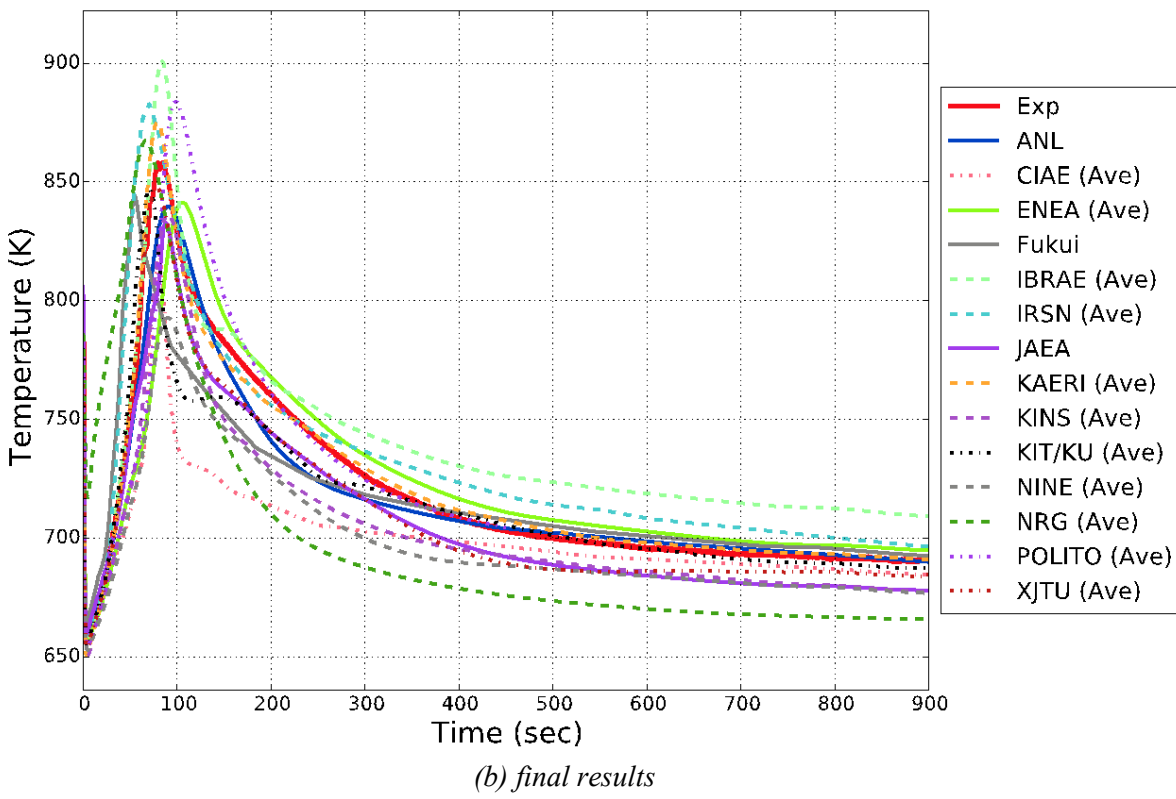
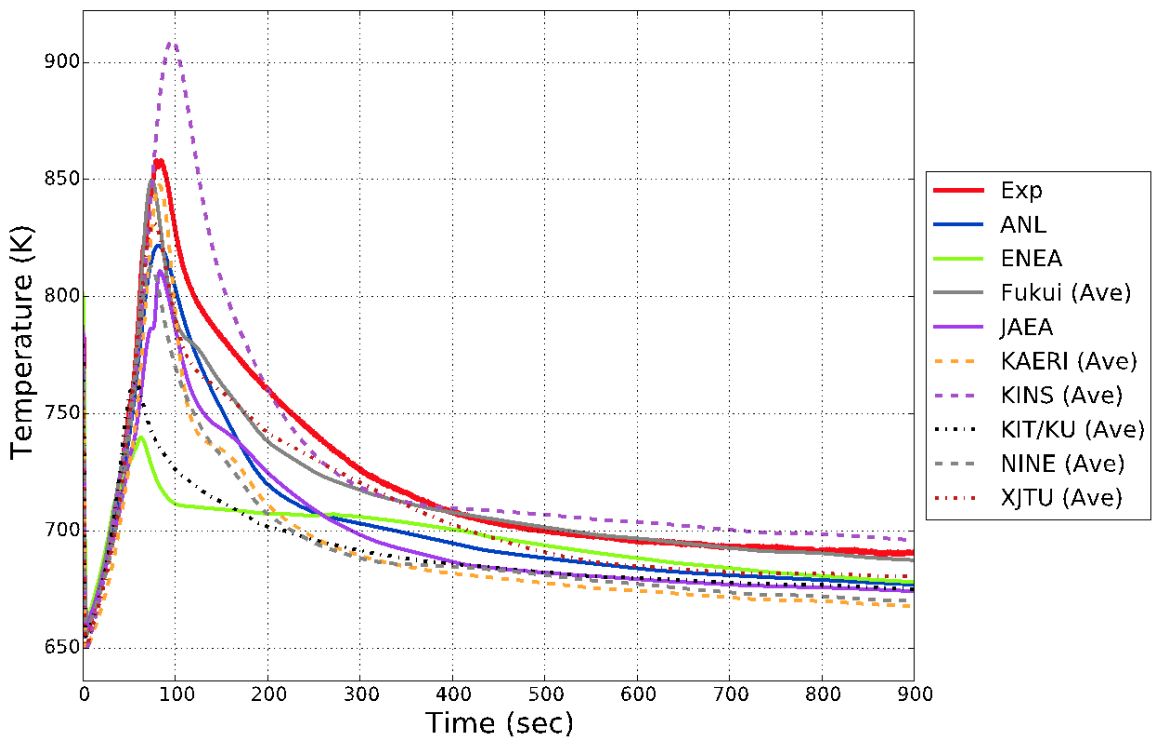
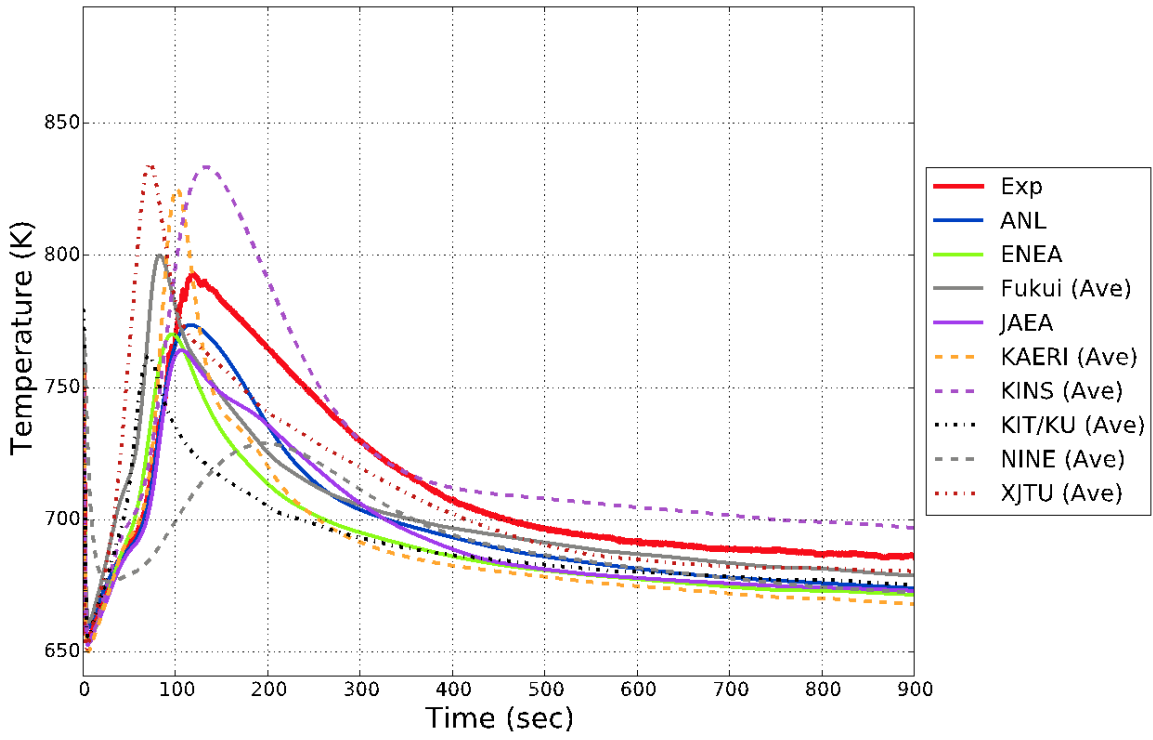
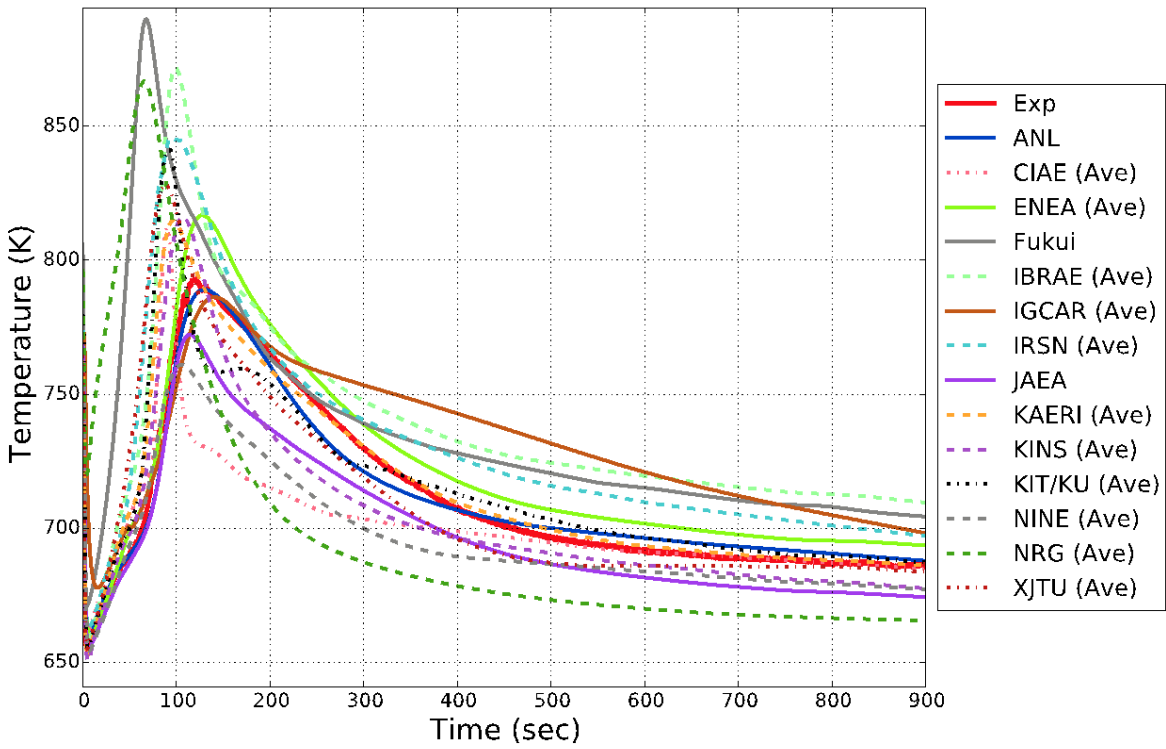


FIG. 358. SHRT-17 XX09 sample above core temperature (14TC-37).

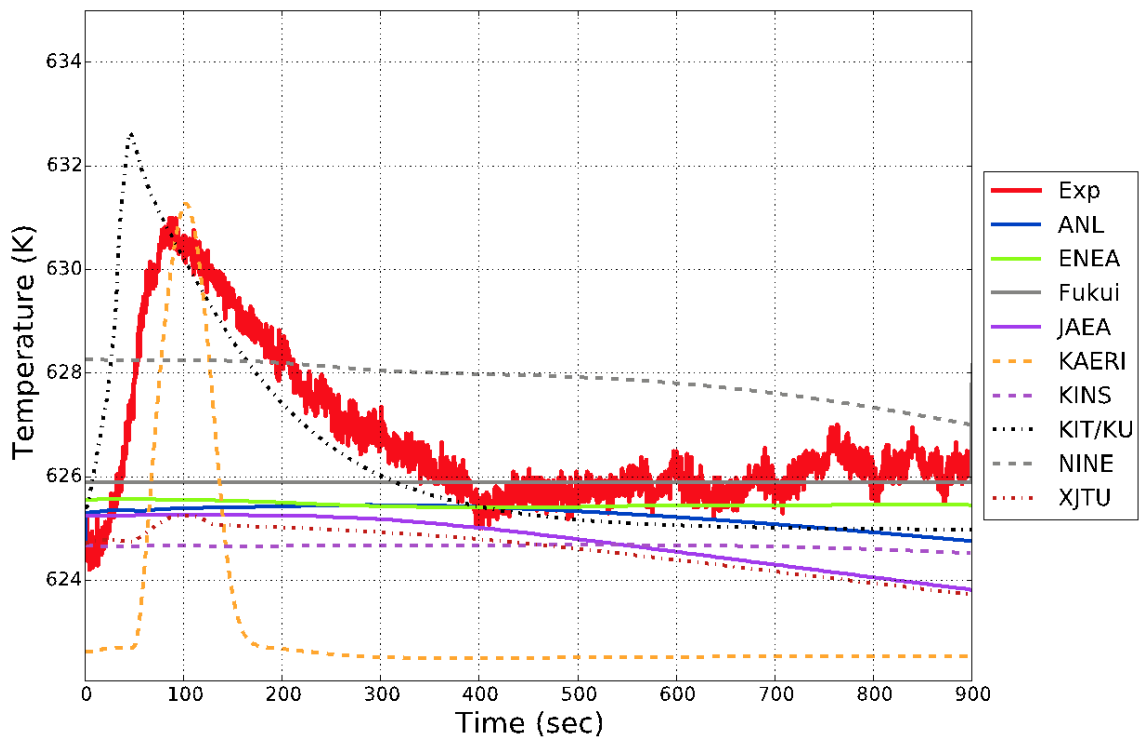


(a) blind results

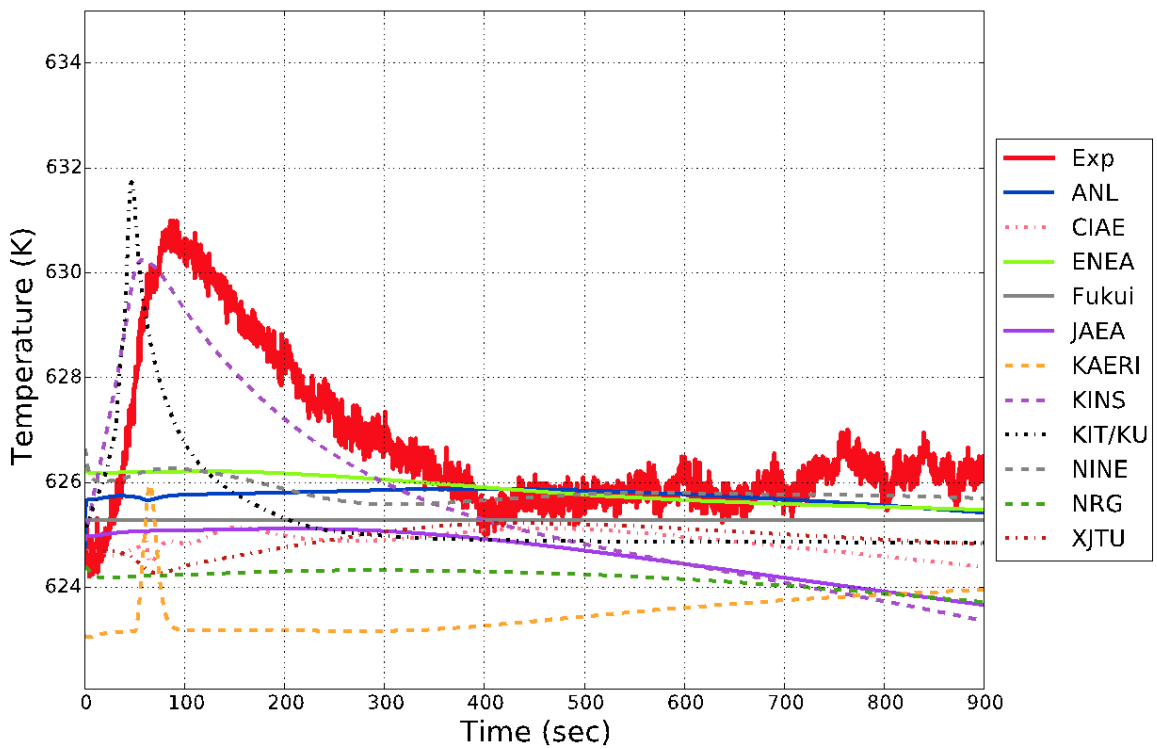


(b) final results

FIG. 359. SHRT-17 XX09 sample core outlet temperature (OTC-01).

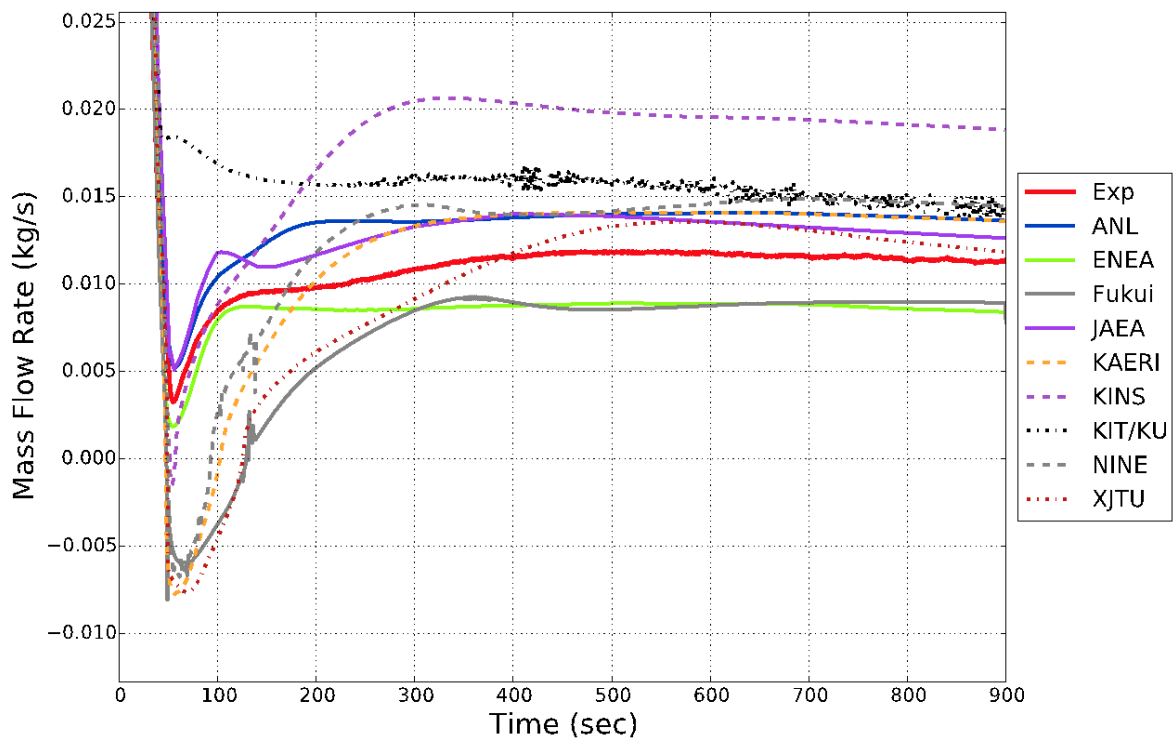


(a) blind results

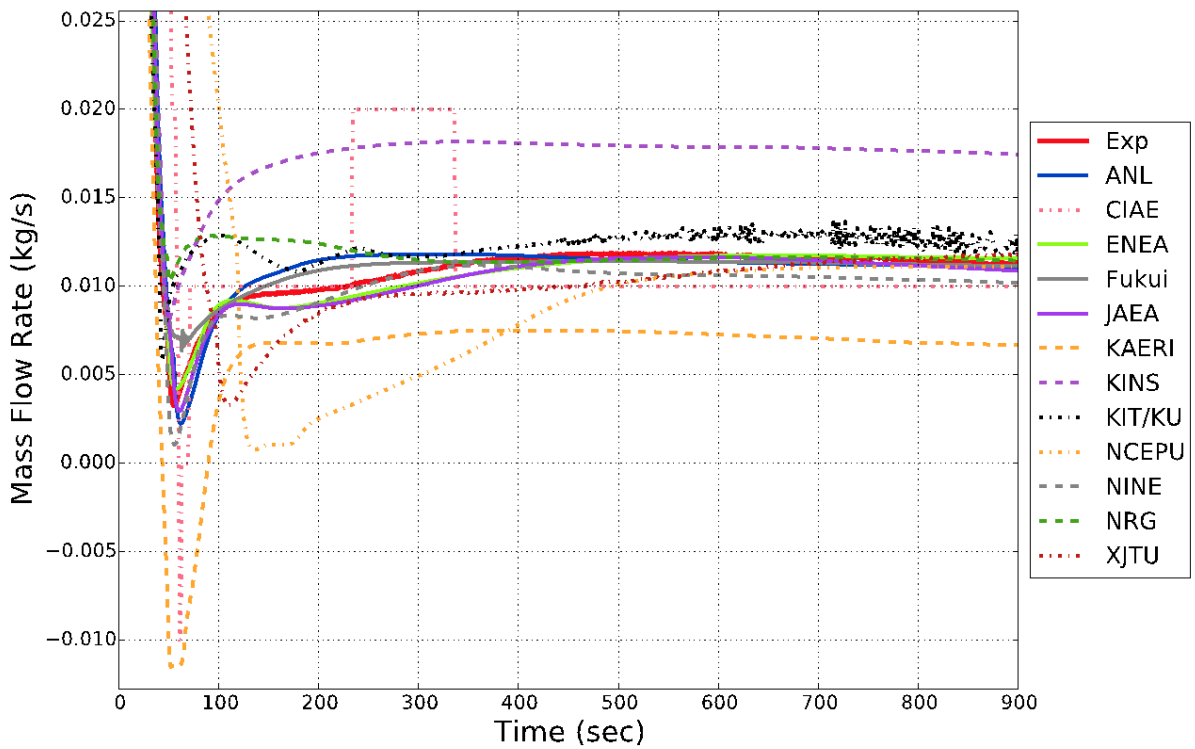


(b) final results

FIG. 360. SHRT-17 XX10 lower flowmeter temperature (FM-1TC)

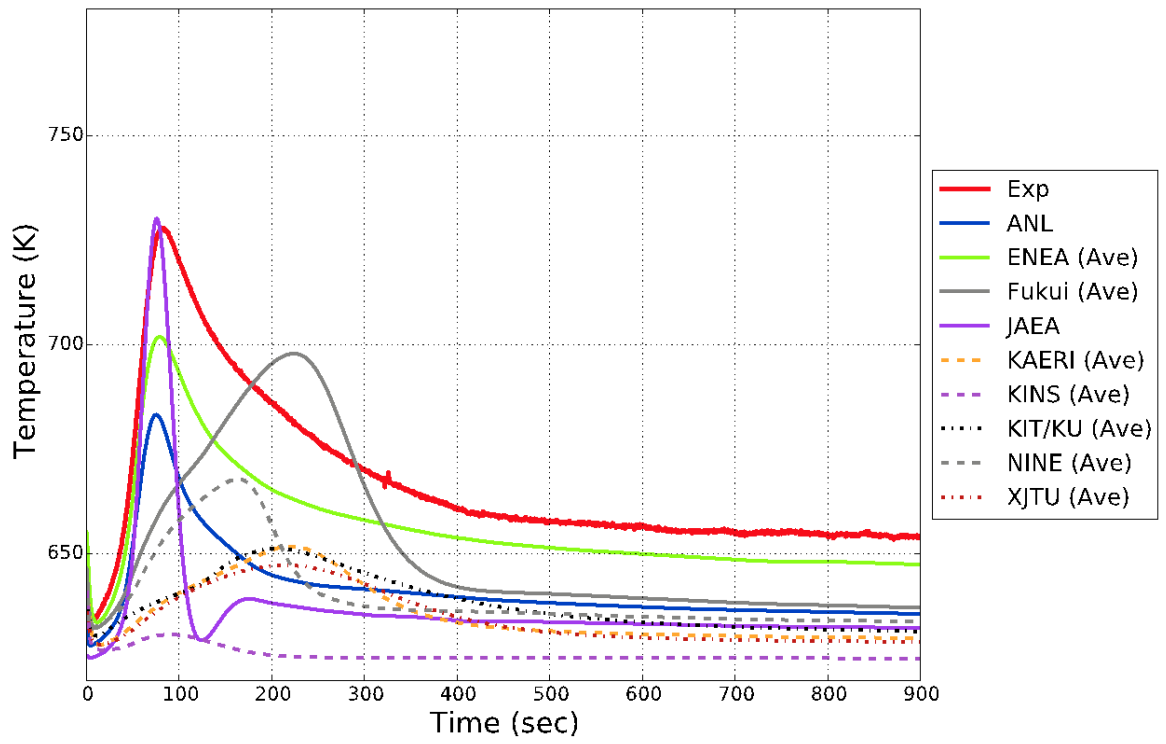


(a) blind results

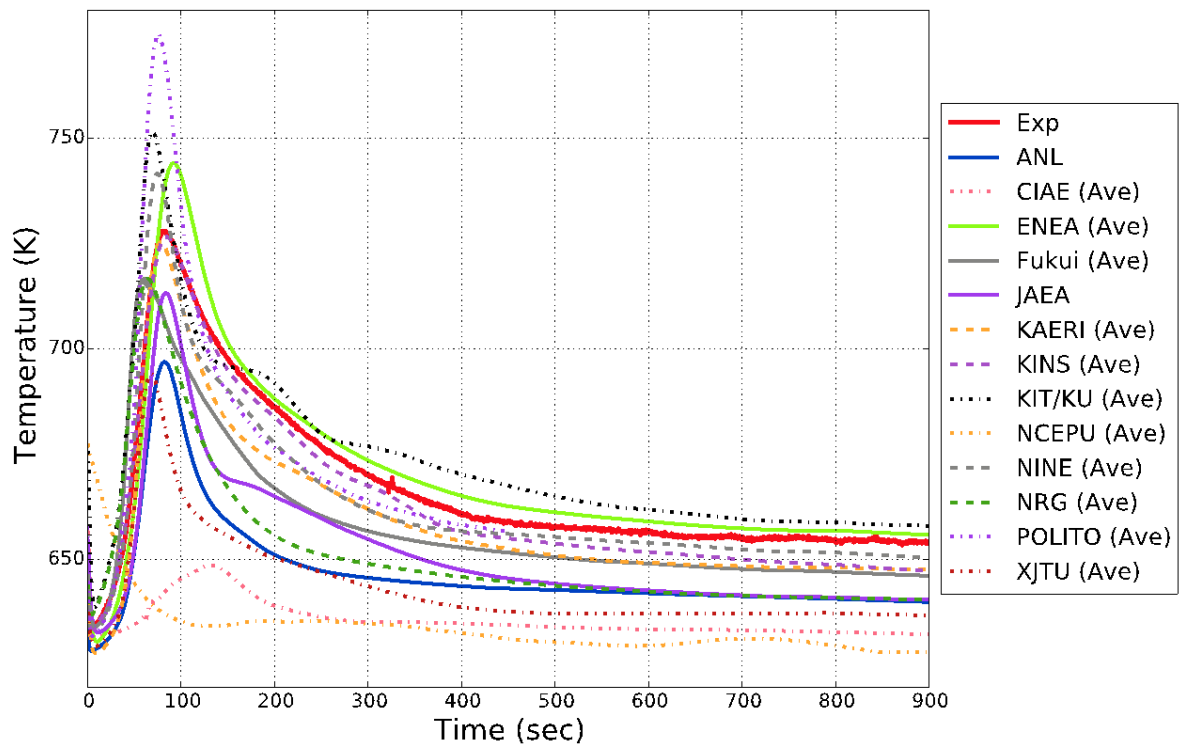


(b) final results

FIG. 361. SHRT-17 XX10 mass flow rate.

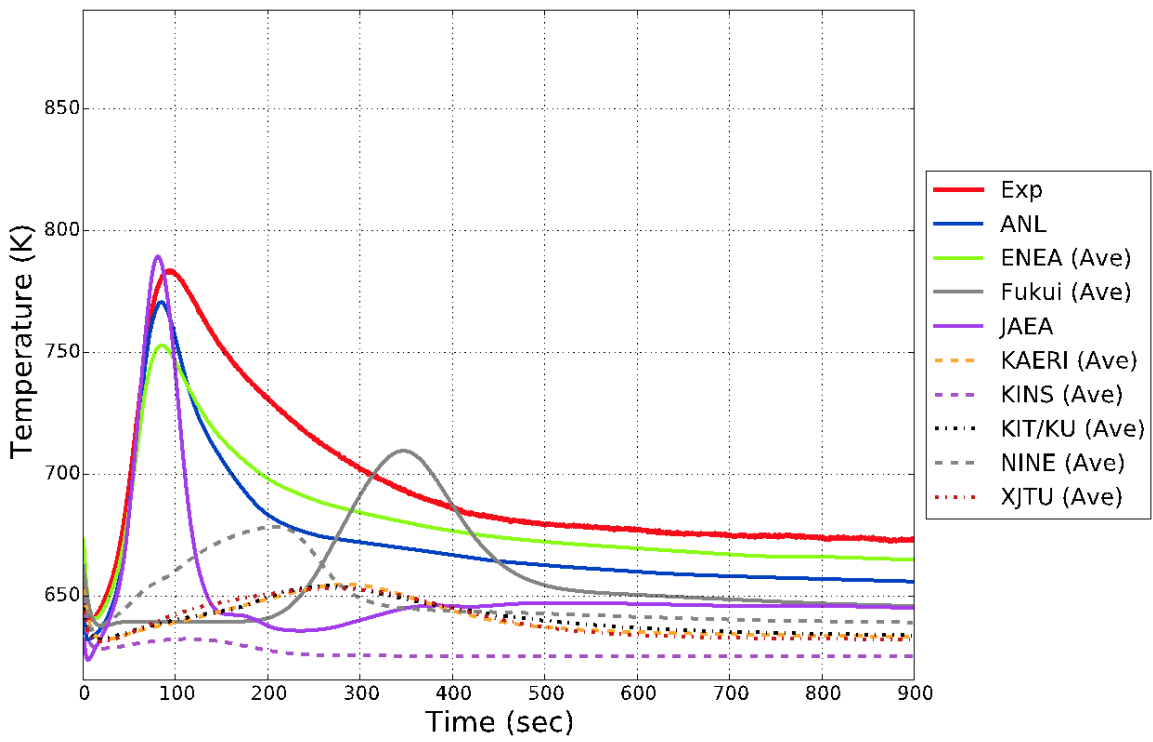


(a) blind results

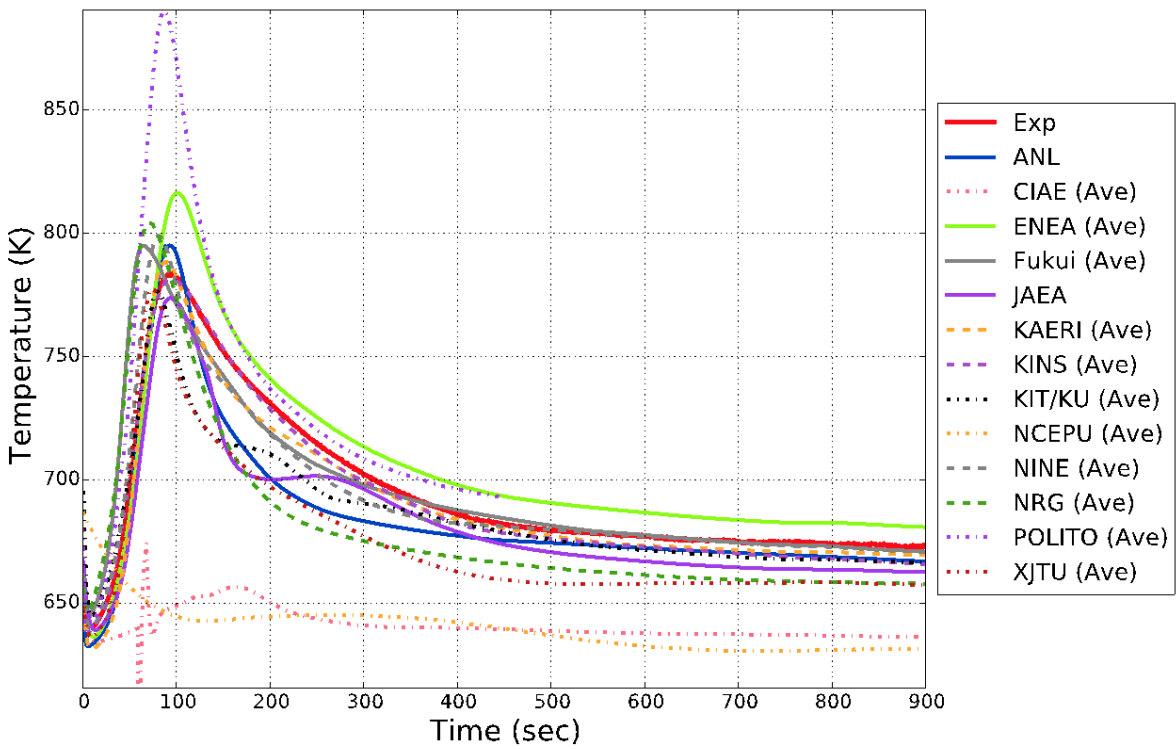


(b) final results

FIG. 362. SHRT-17 XX10 sample midcore temperature (MTC-4).

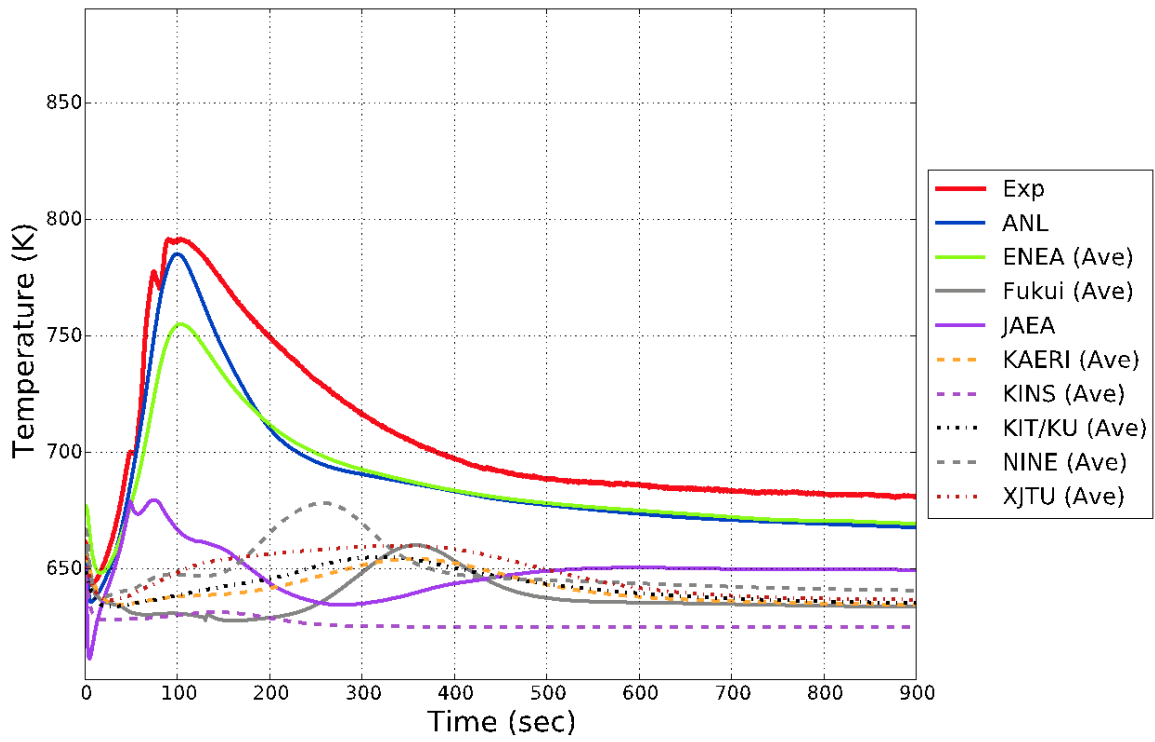


(a) blind results

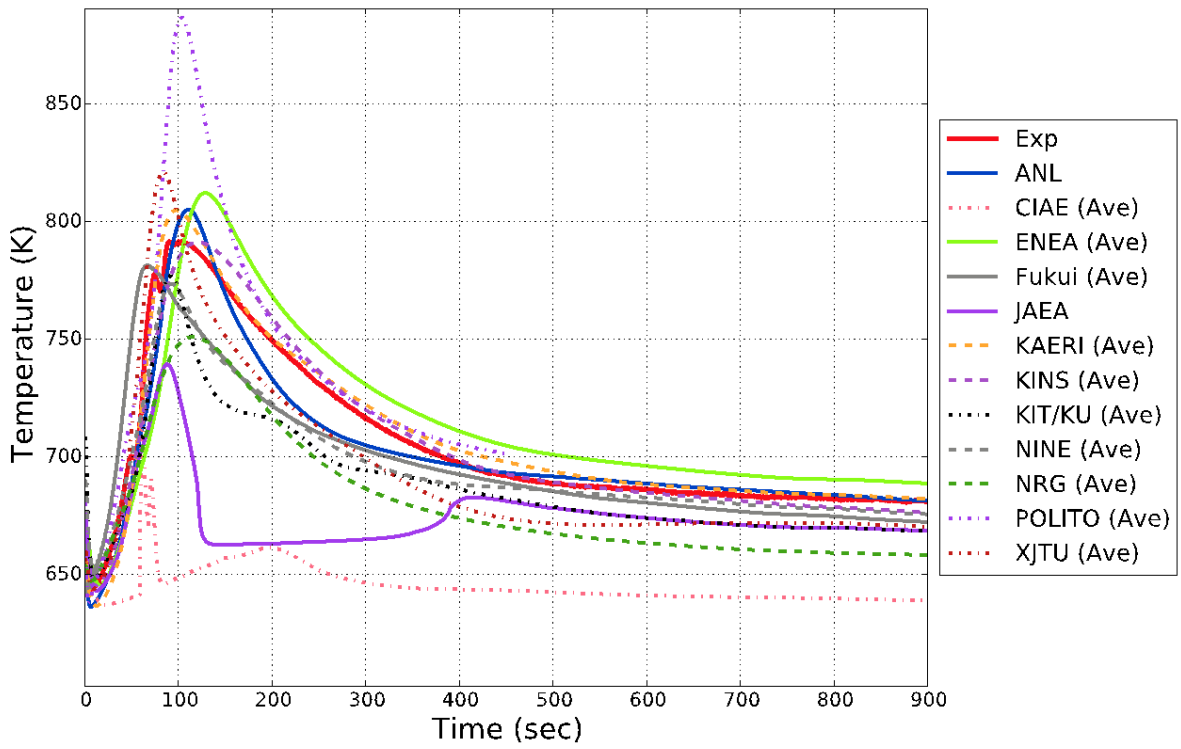


(b) final results

FIG. 363. SHRT-17 XX10 sample top of core temperature (TTC-2).

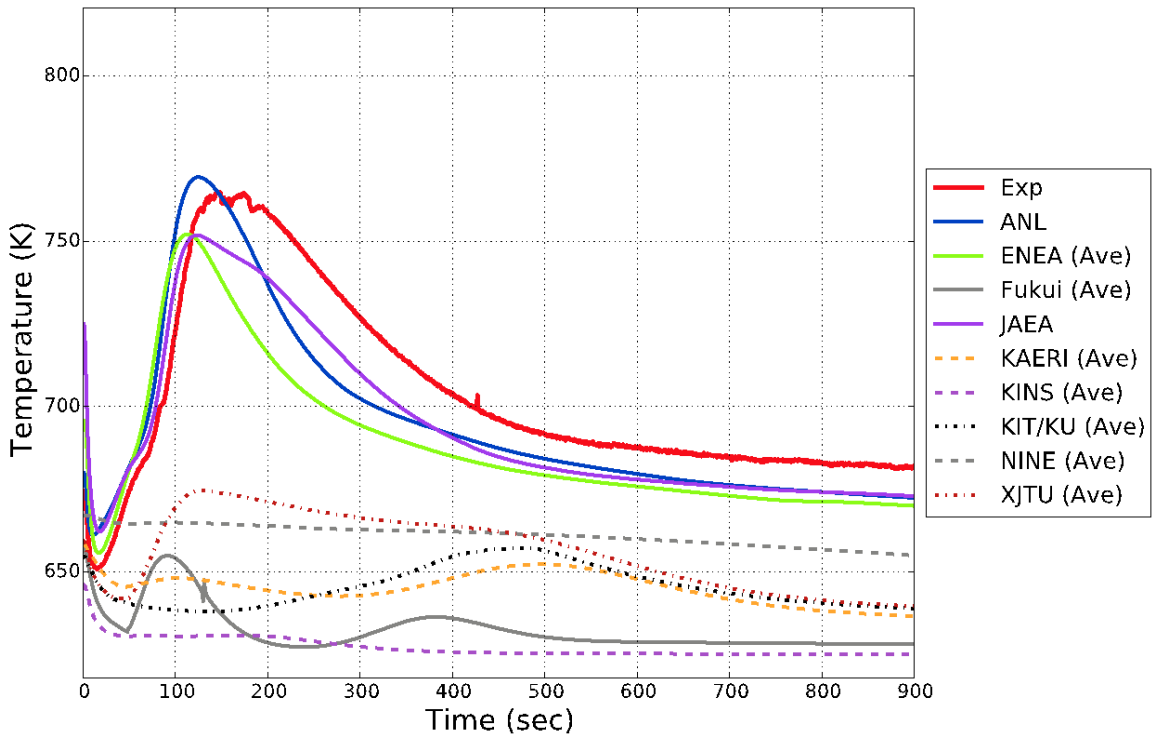


(a) blind results

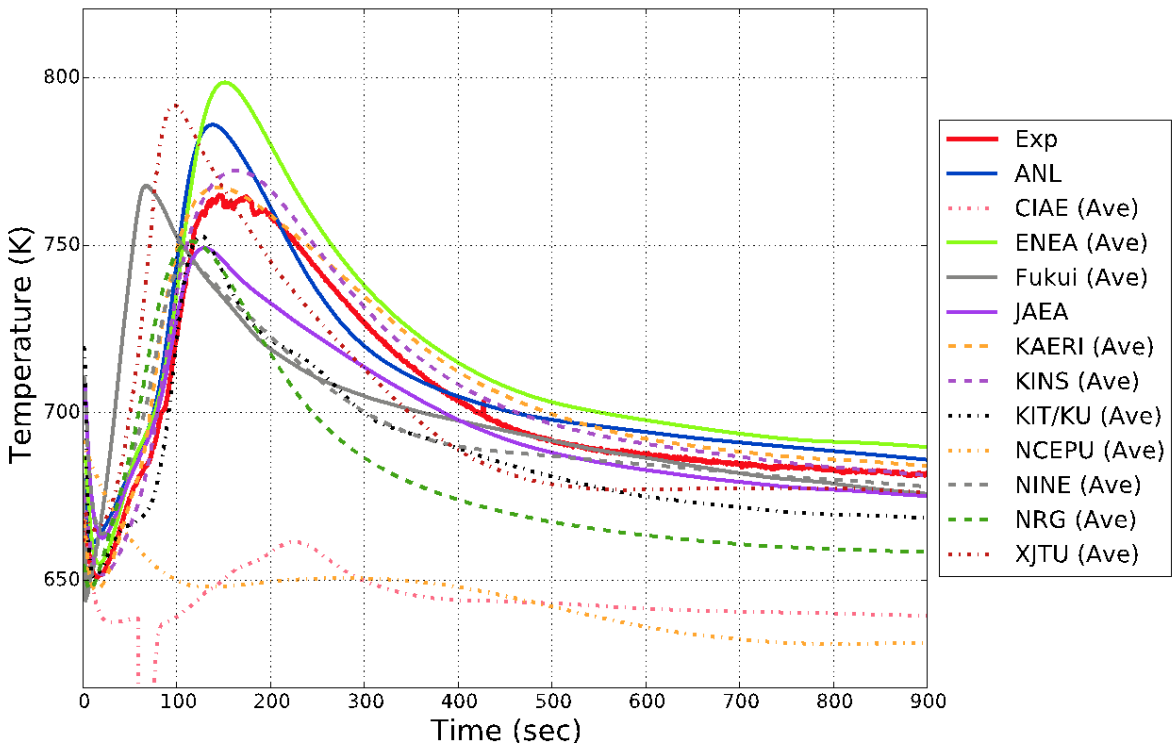


(b) final results

FIG. 364. SHRT-17 XX10 sample above core temperature (14TC-3).



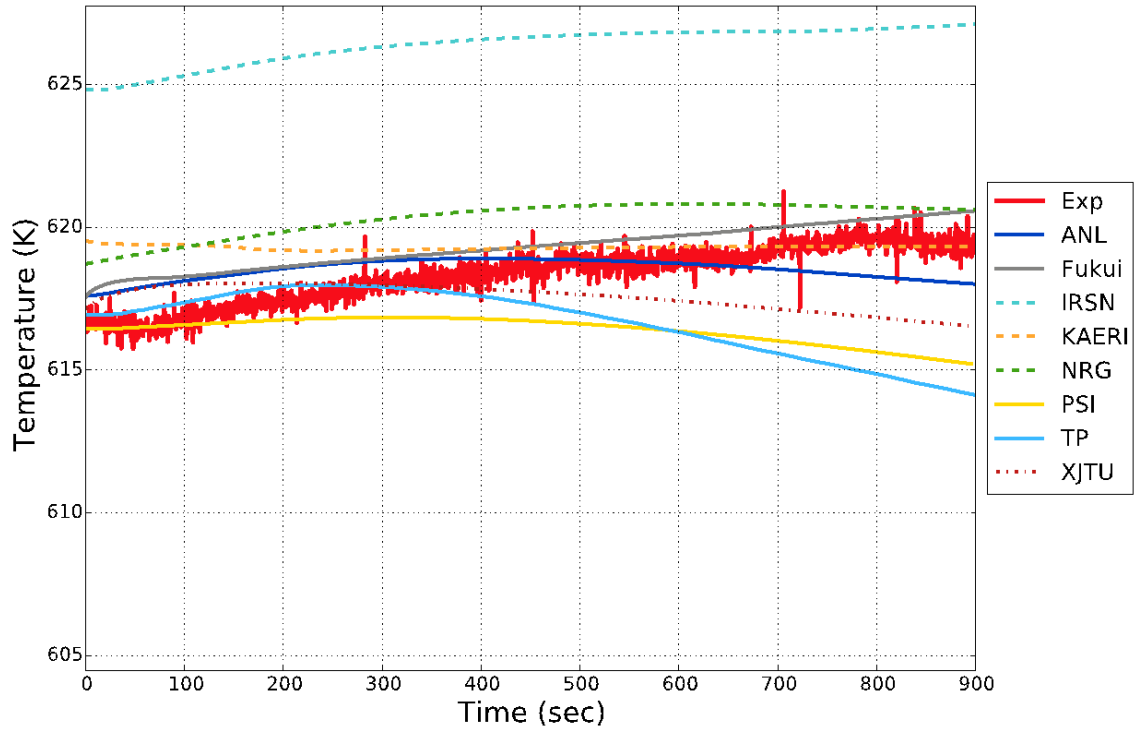
(a) blind results



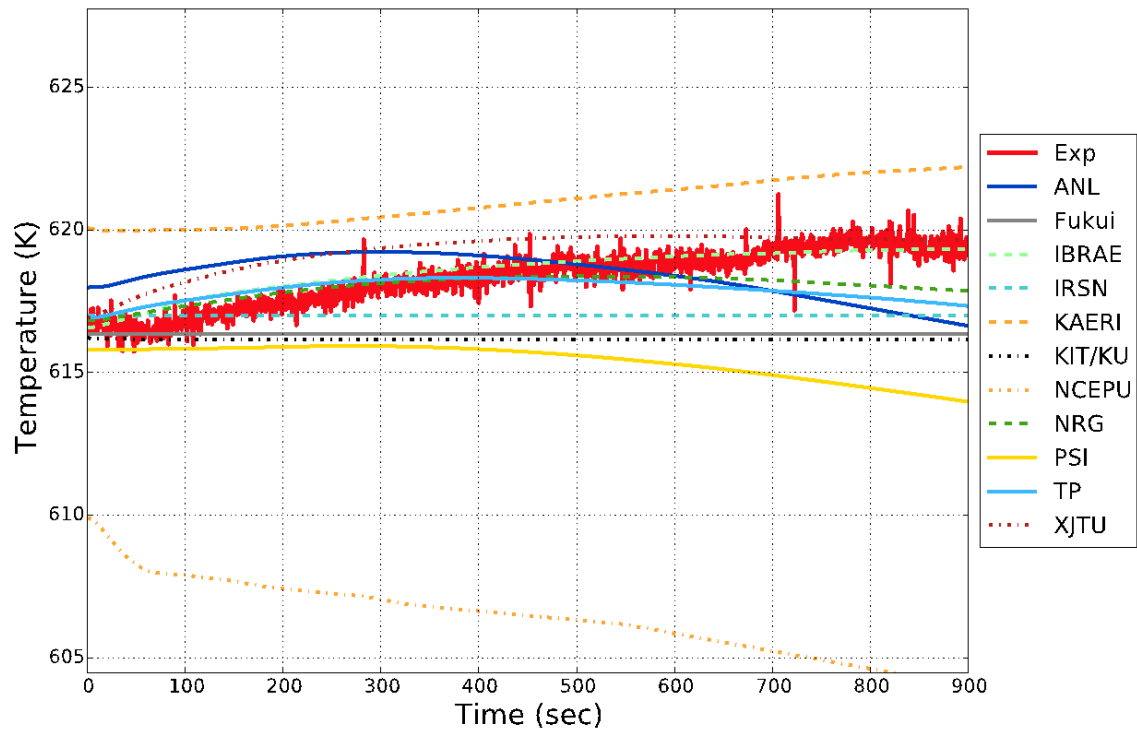
(b) final results

FIG. 365. SHRT-17 XX10 sample core outlet temperature (OTC-01).

SHRT-45R



(a) blind results



(b) final results

FIG. 366. SHRT-45R high pressure plenum inlet temperature.

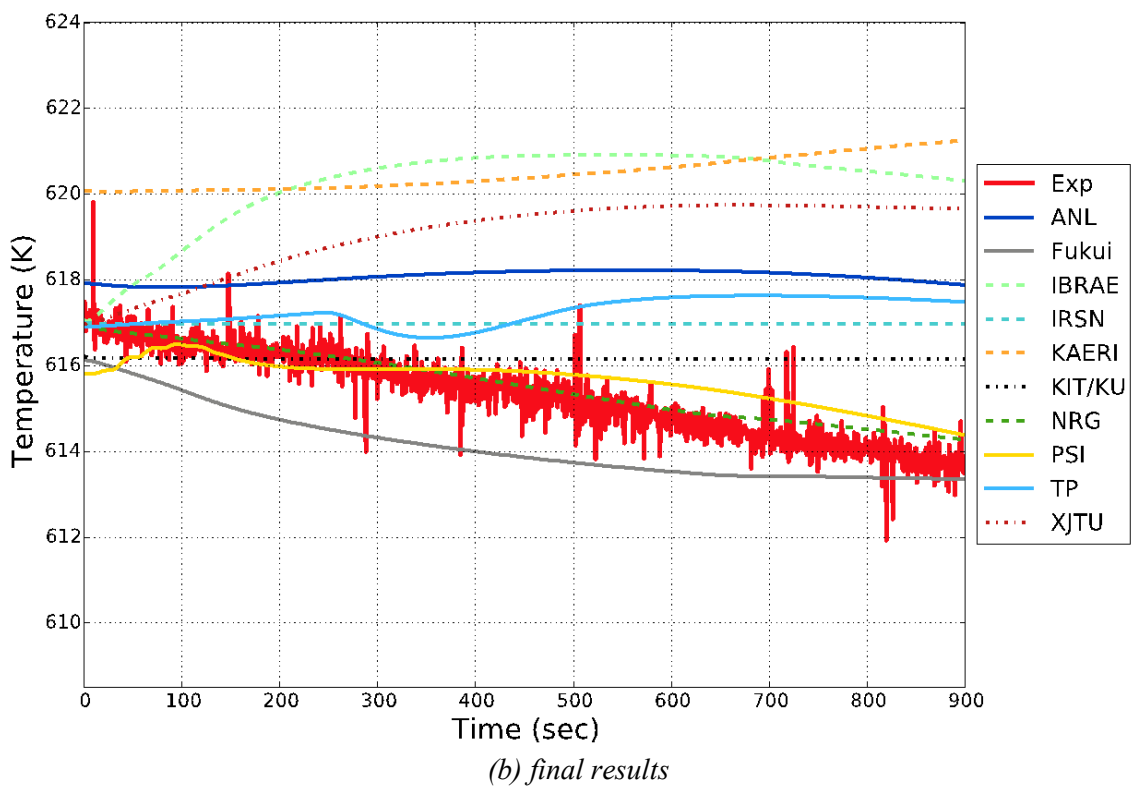
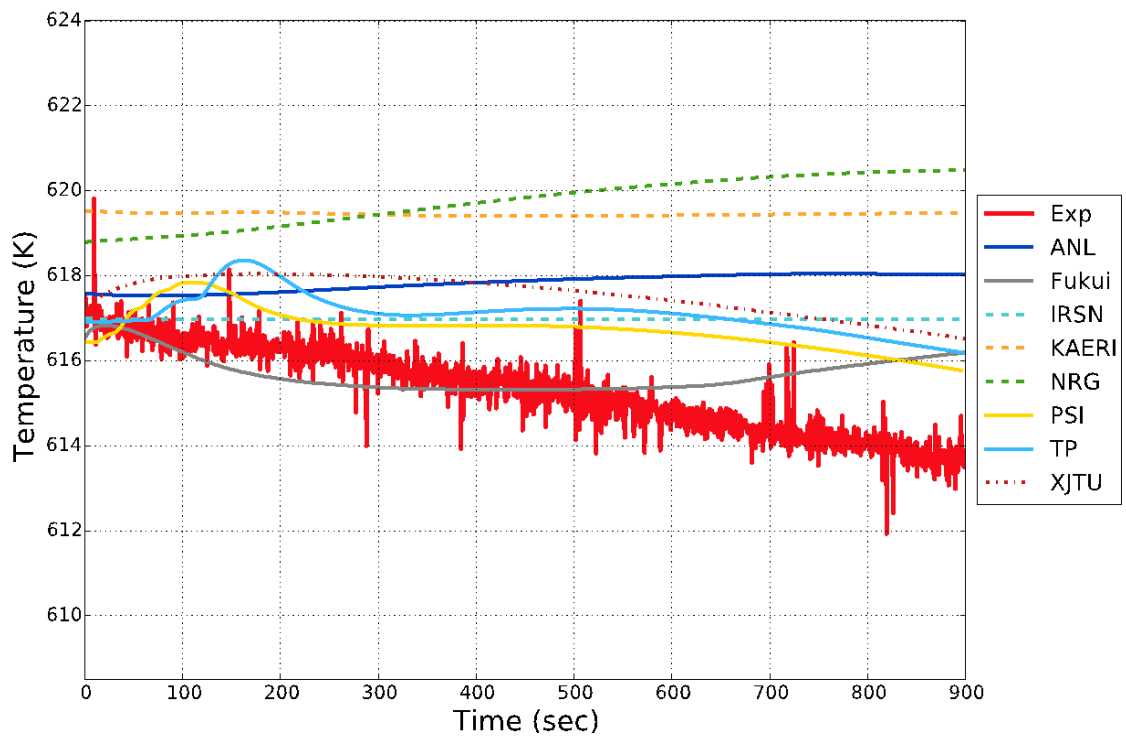
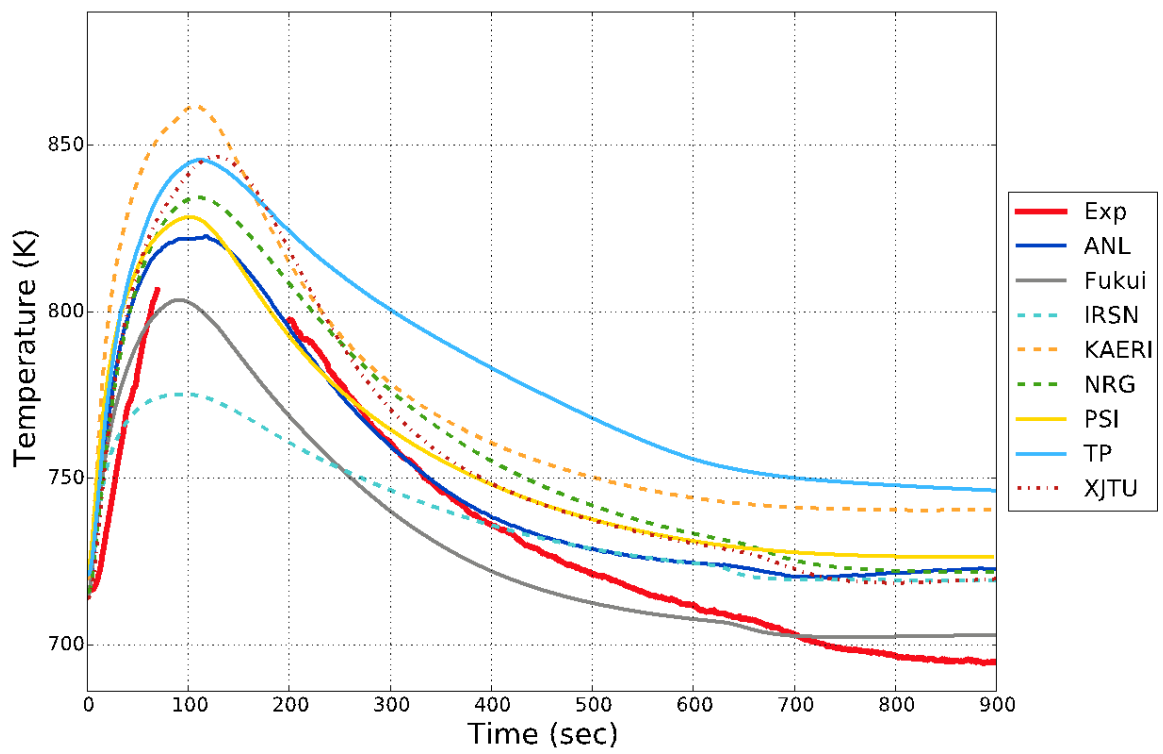
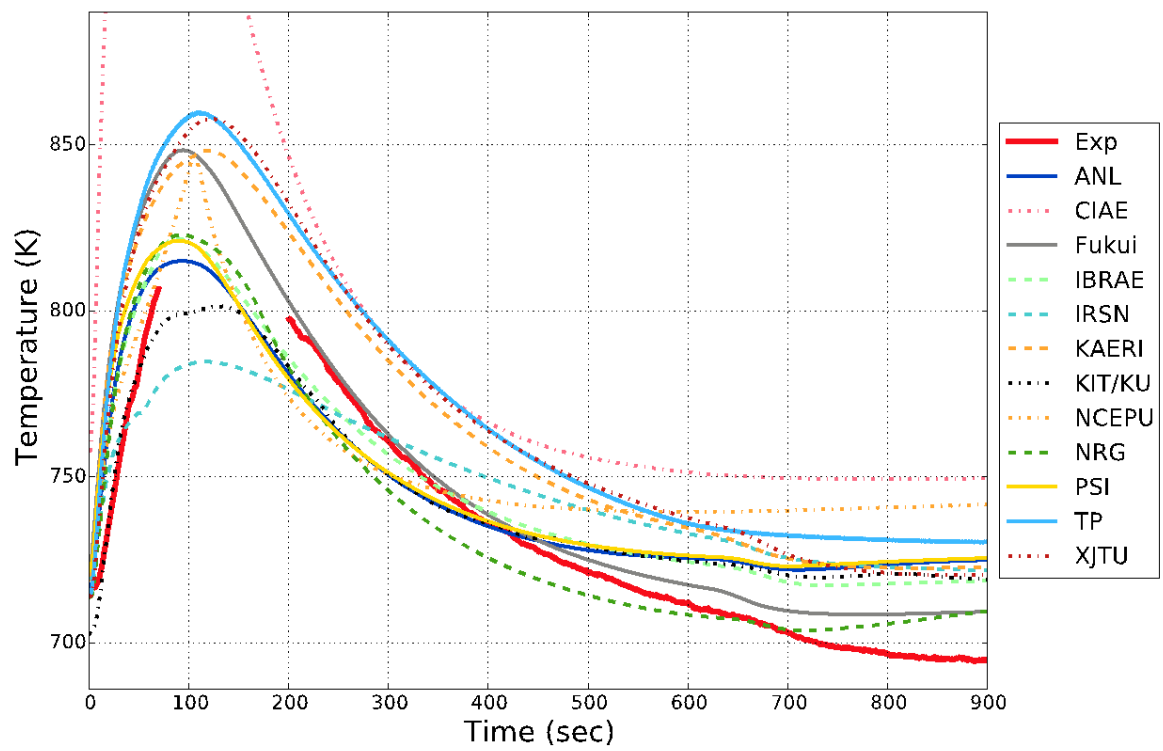


FIG. 367. SHRT-45R low pressure plenum inlet temperature.



(a) blind results



(b) final results

FIG. 368. SHRT-45R Z-Pipe inlet temperature.

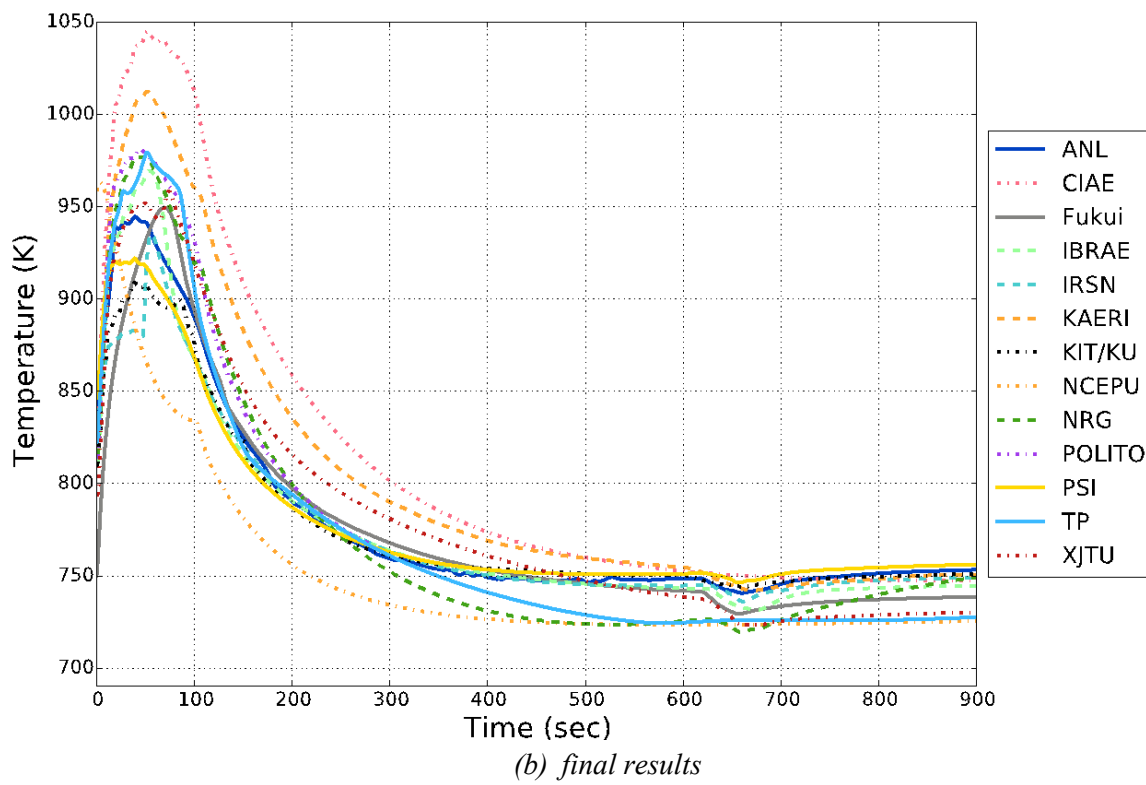
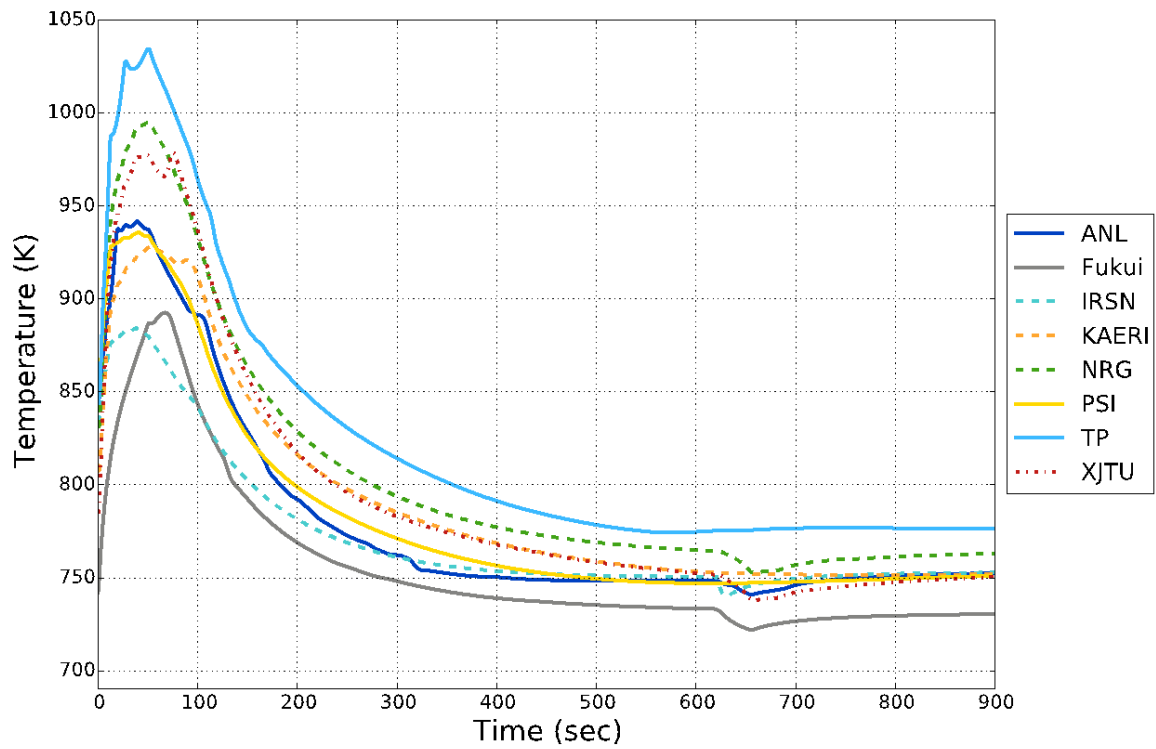


FIG. 369. SHRT-45R peak fuel temperature.

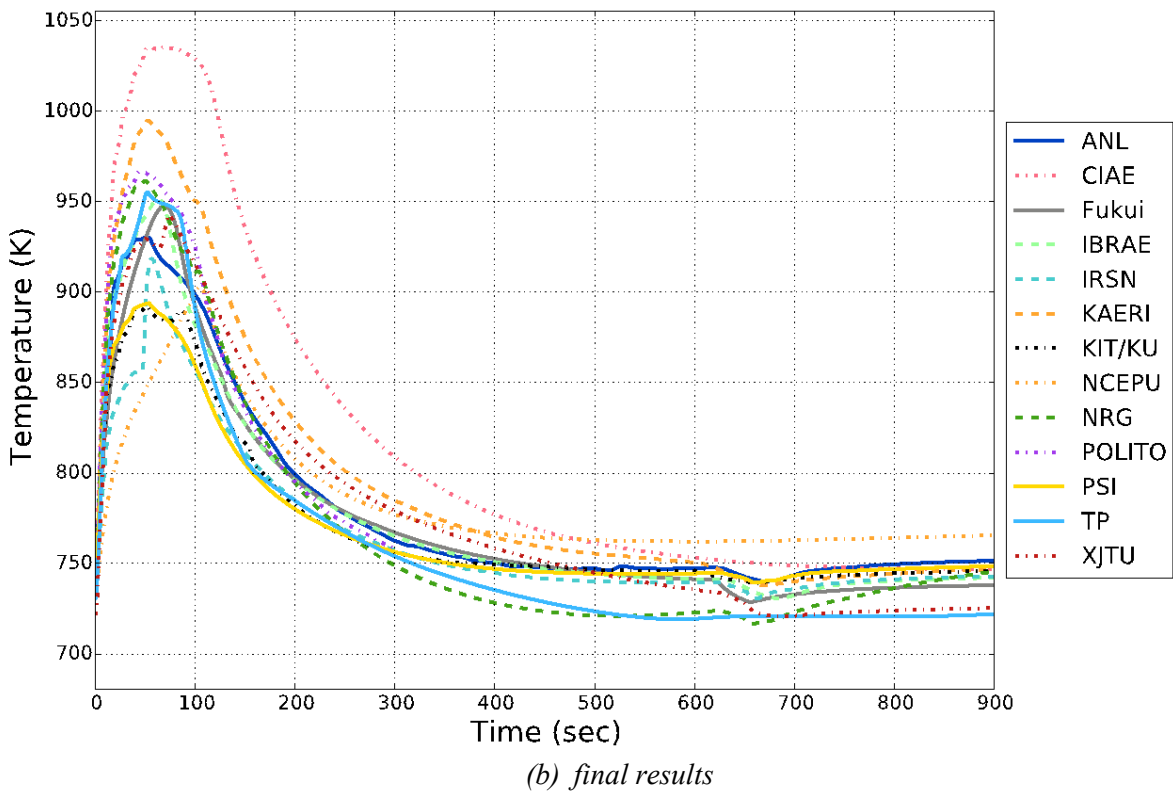
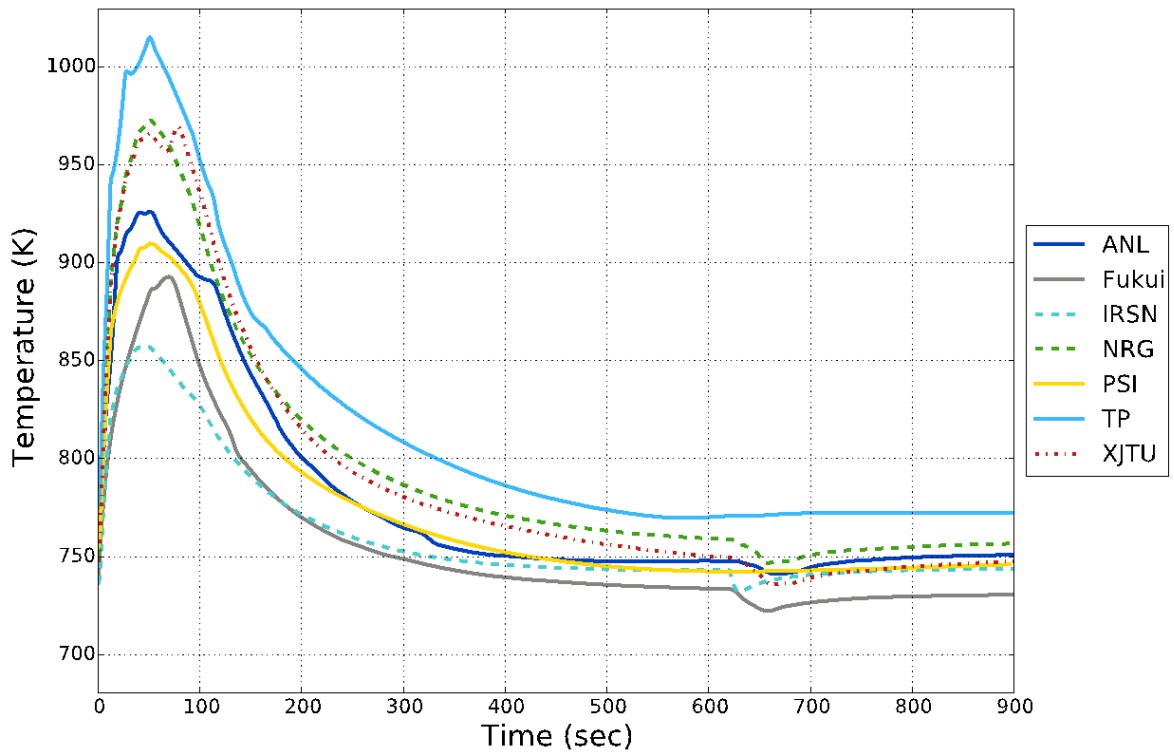
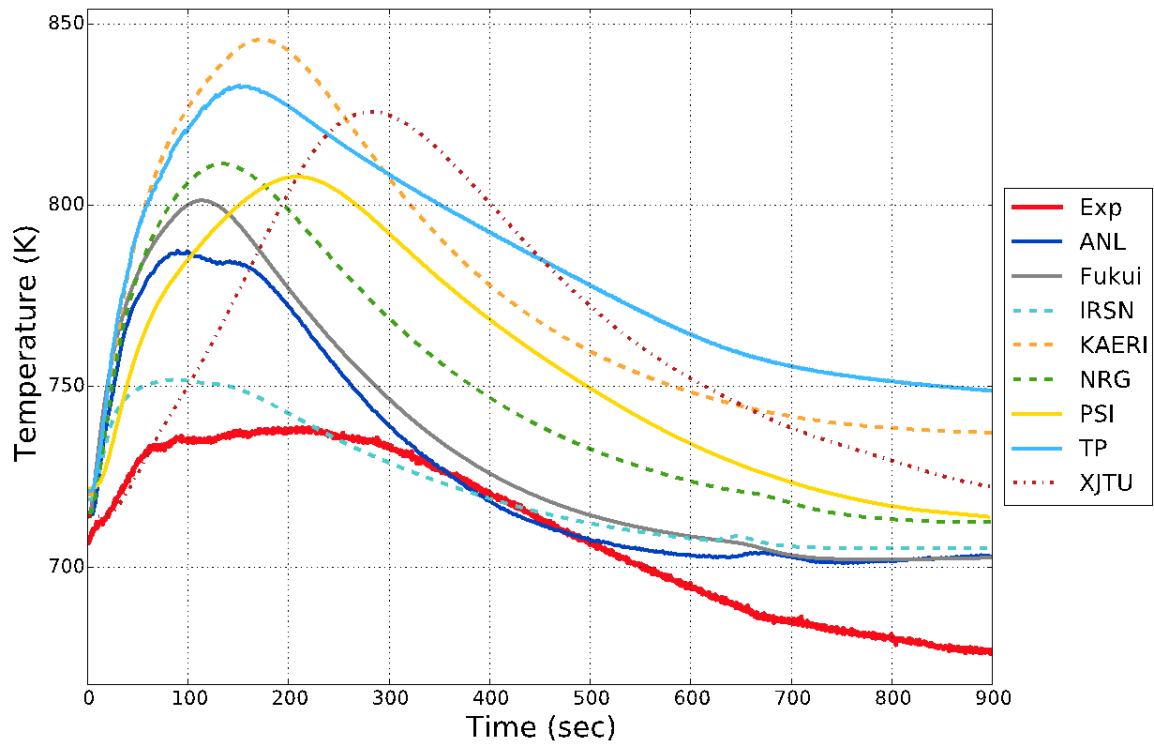
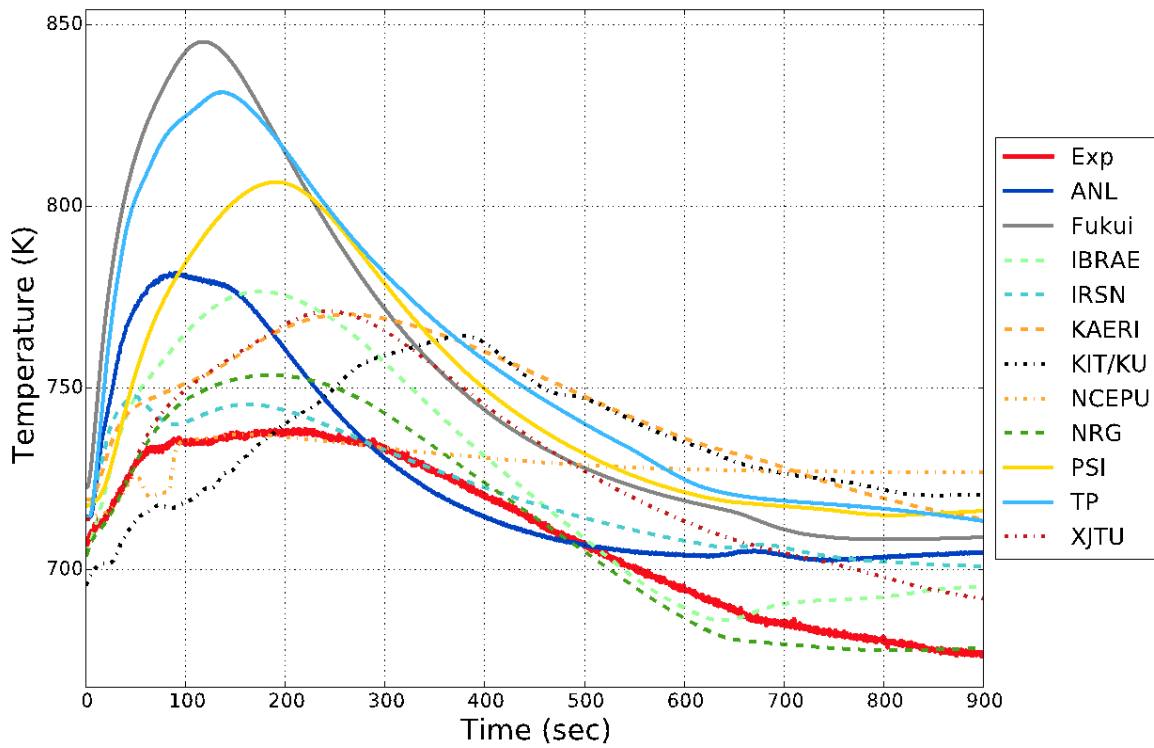


FIG. 370. SHRT-45R peak coolant temperature.



(a) blind results



(b) final results

FIG. 371. SHRT-45R IHX primary inlet temperature.

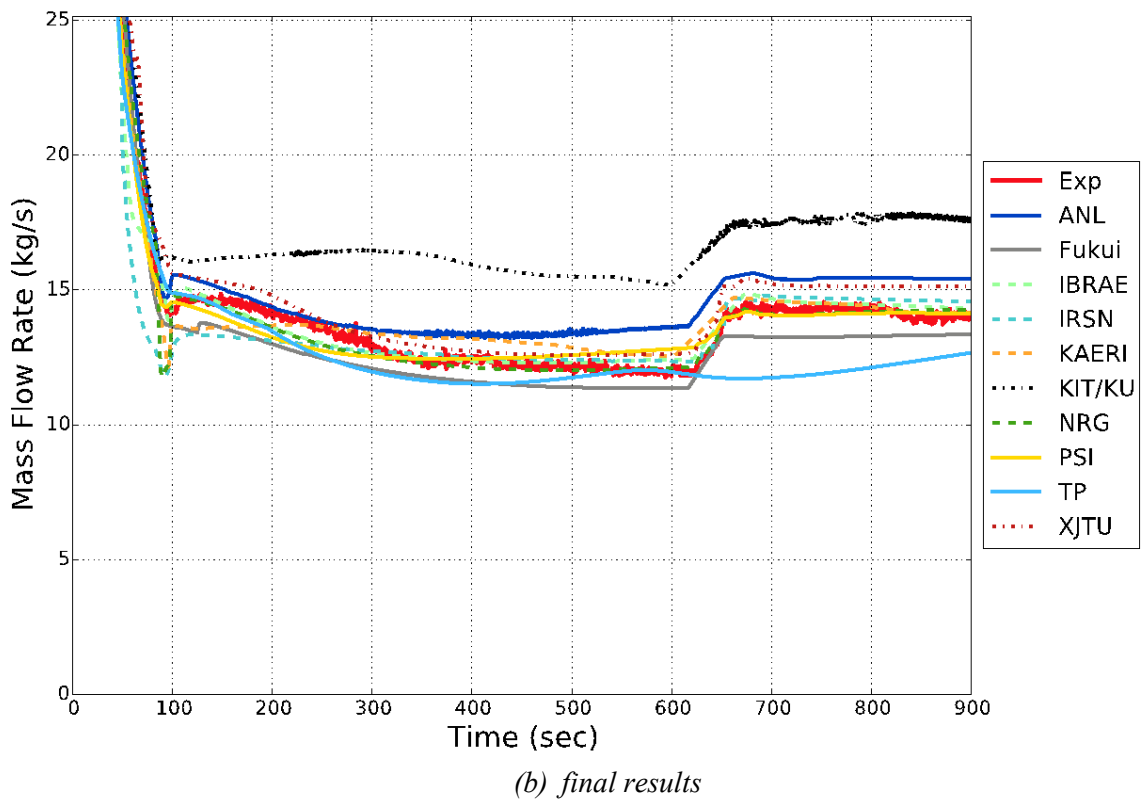
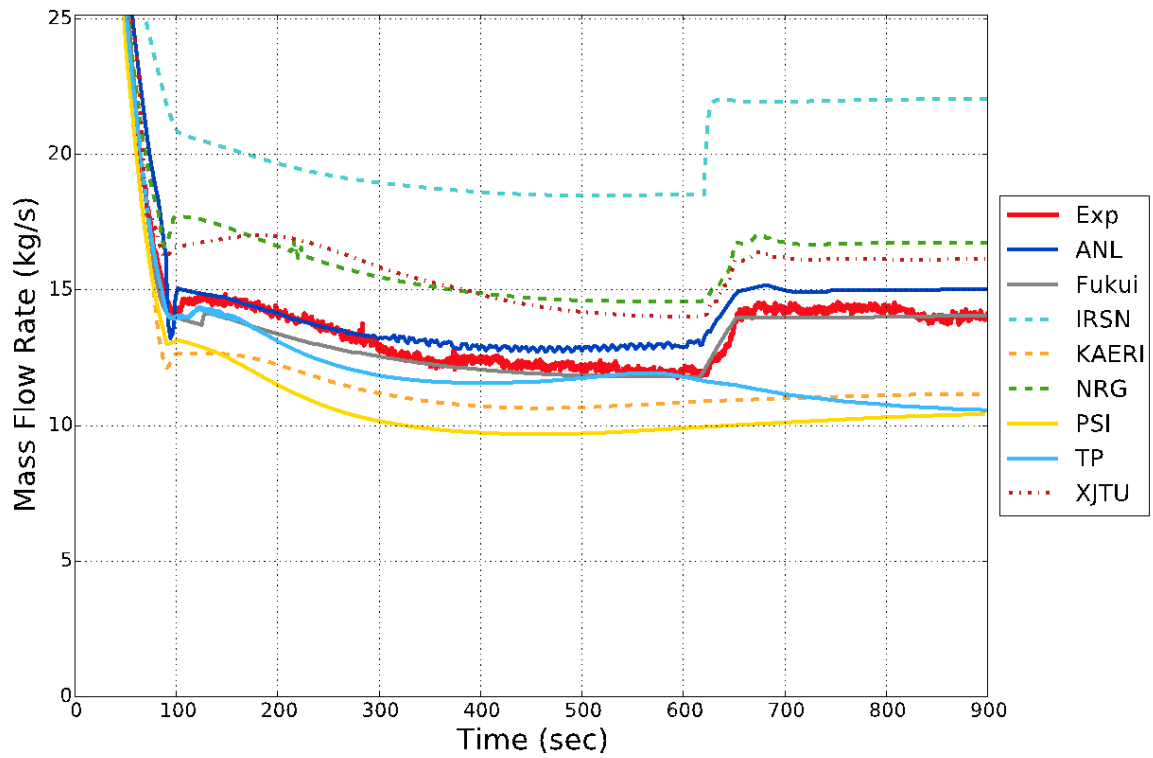
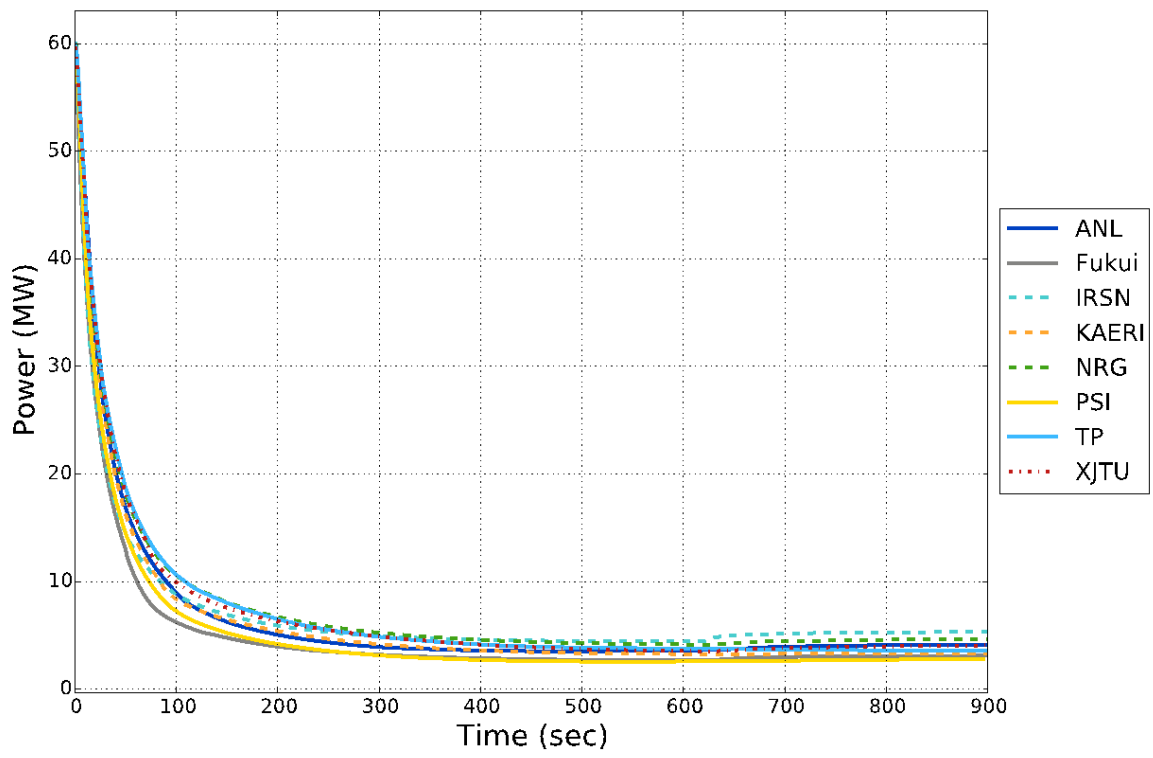
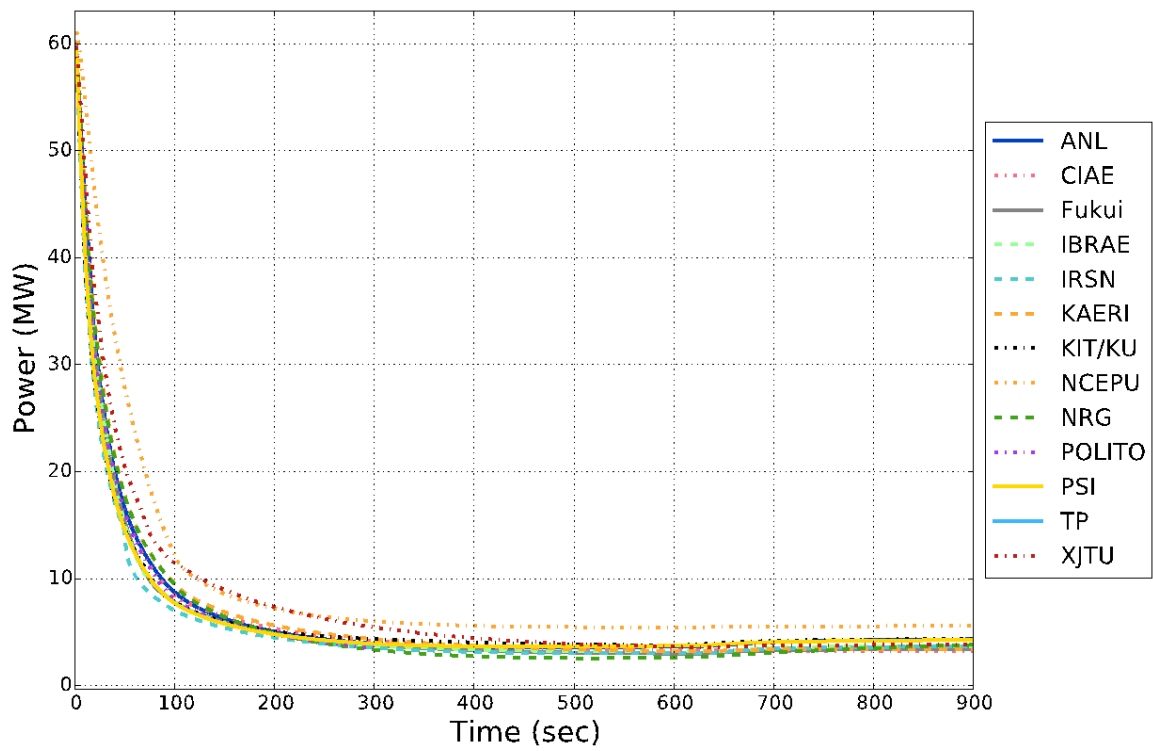


FIG. 372. SHRT-45R pump #2 mass flow rate.

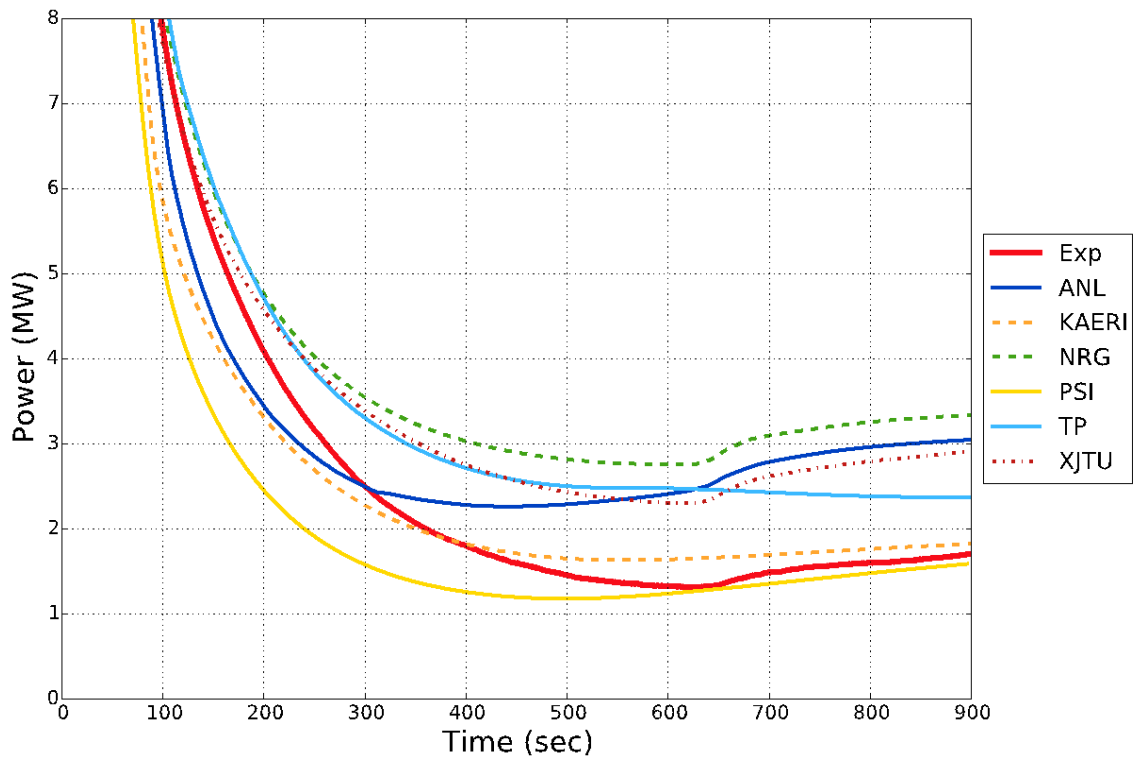


(a) blind results

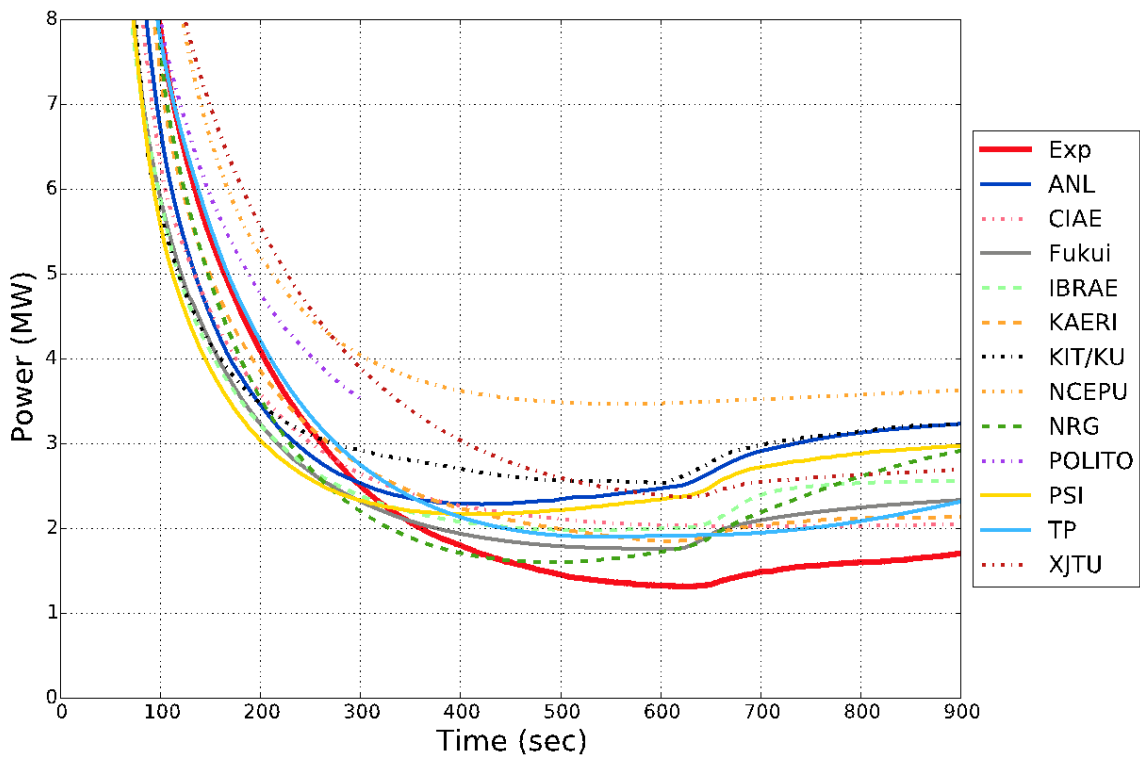


(b) final results

FIG. 373. SHRT-45R total power (full range).

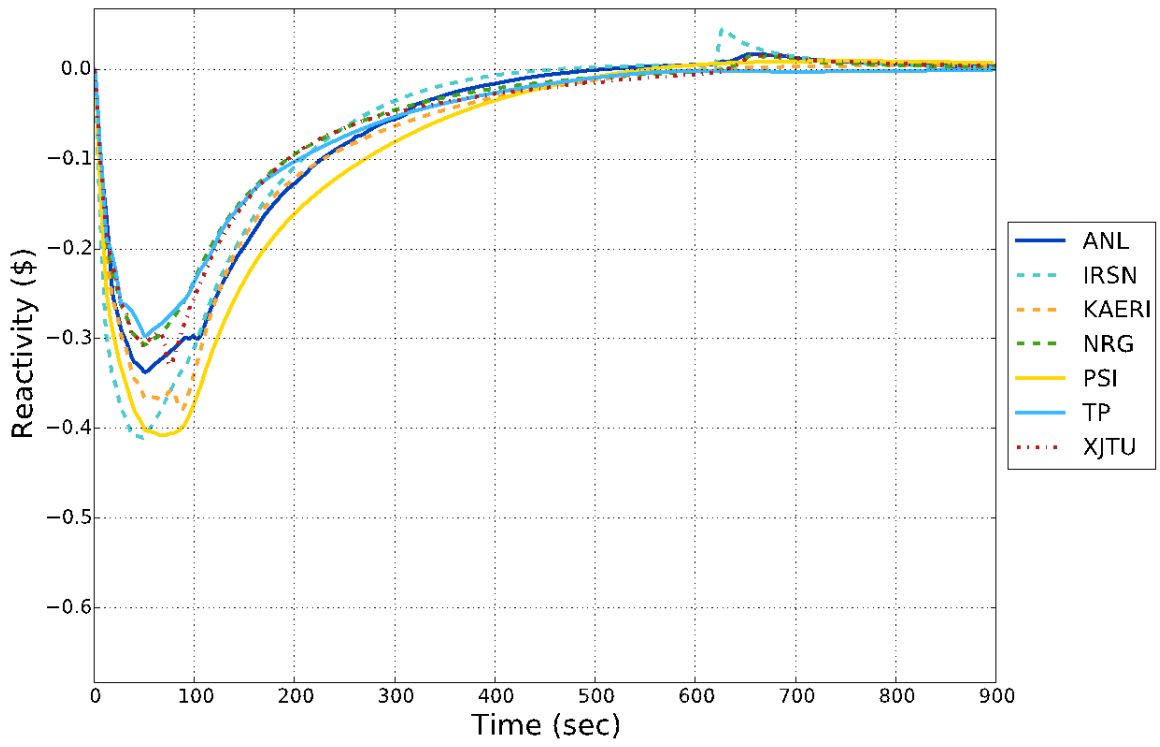


(a) blind results

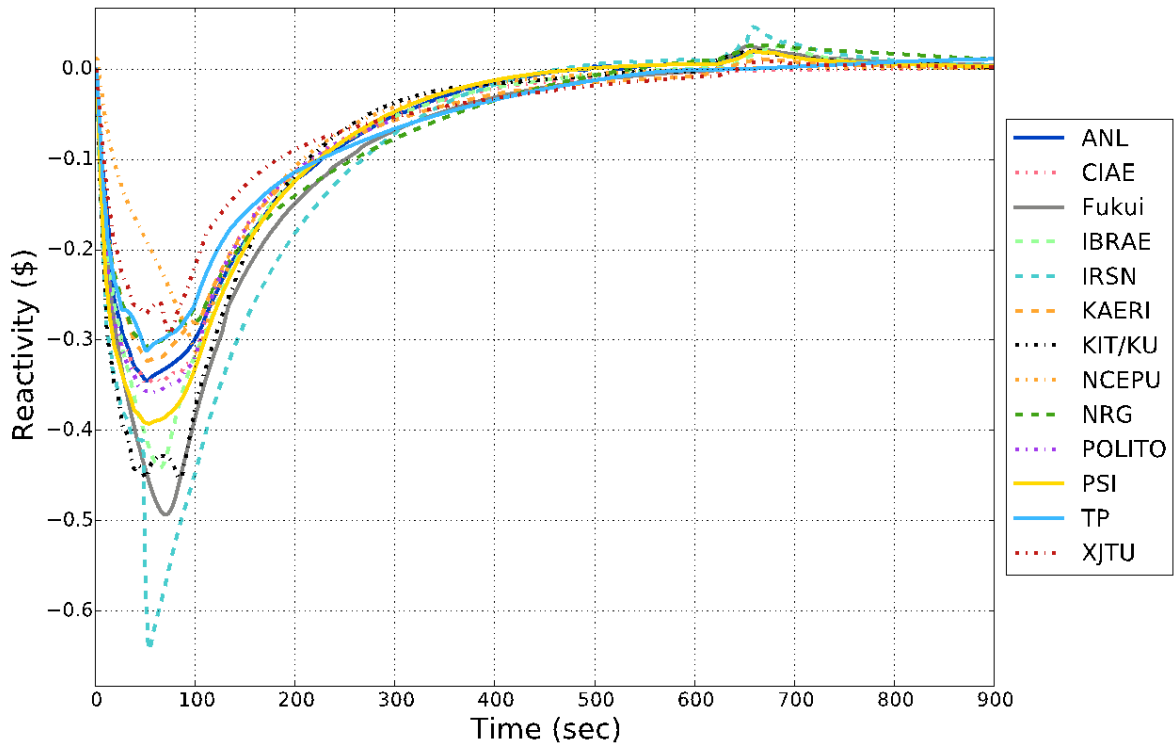


(b) final results

FIG. 374. SHRT-45R fission power (low range).

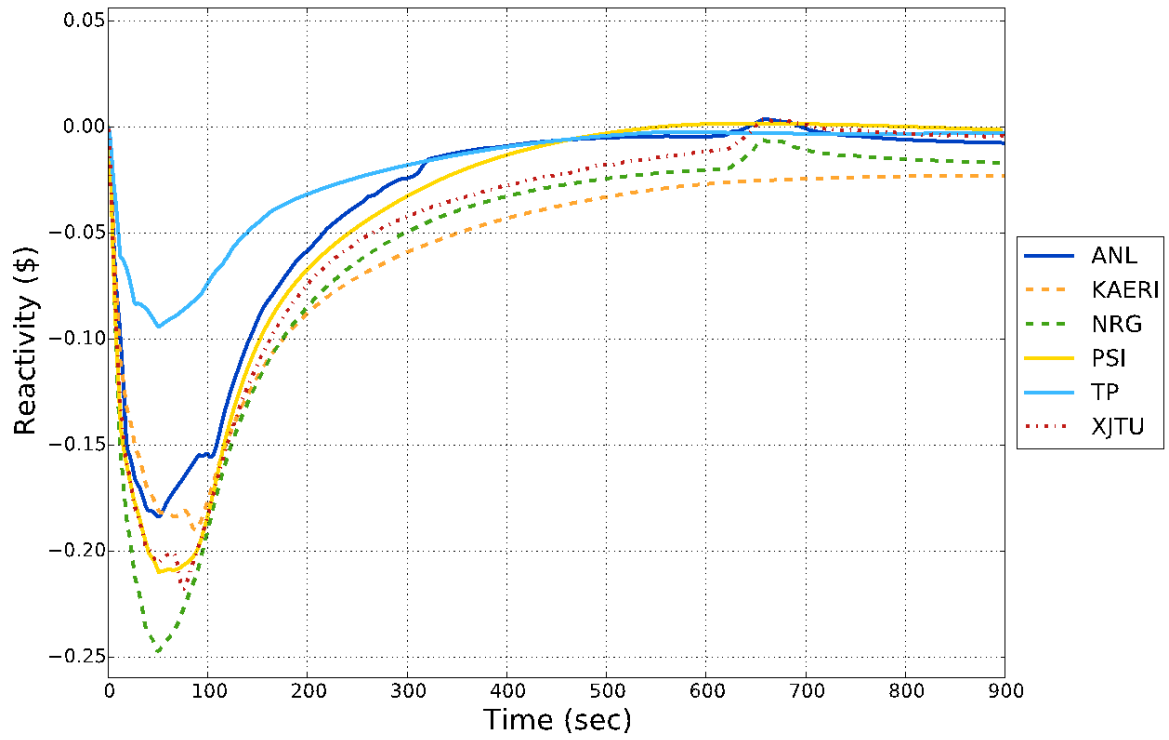


(a) blind results

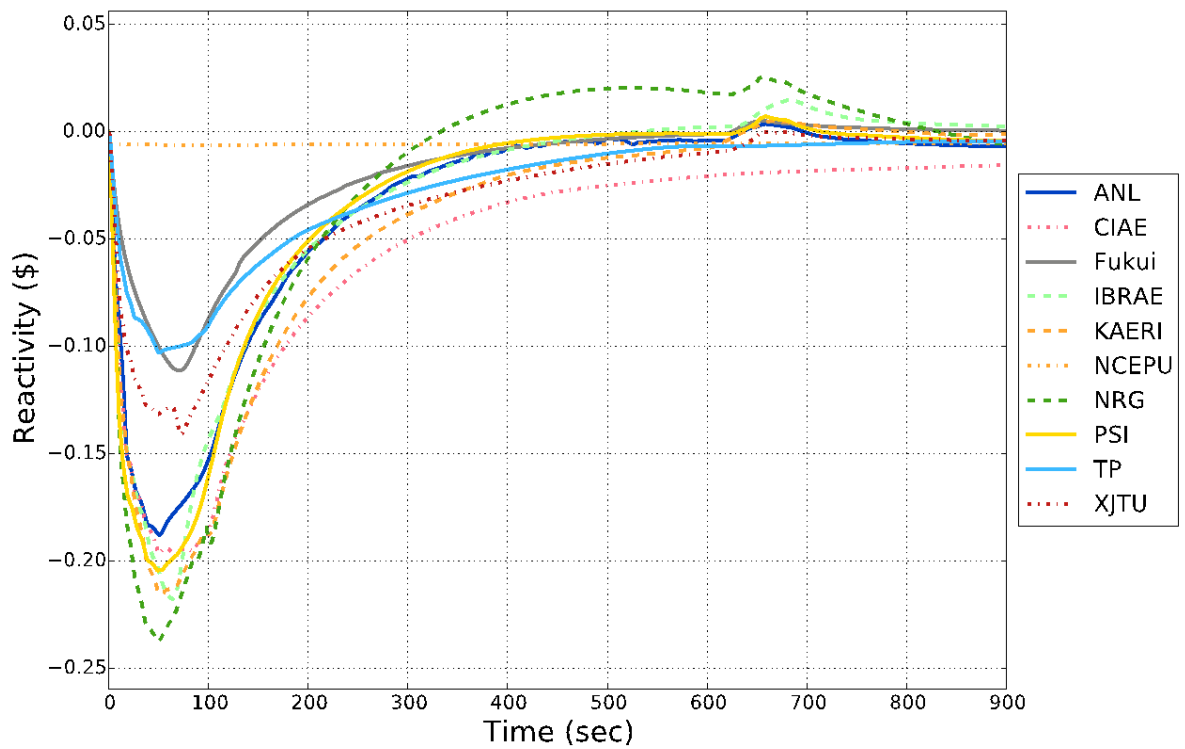


(b) final results

FIG. 375. SHRT-45R net reactivity.



(a) blind results



(b) final results

FIG. 376. SHRT-45R coolant density reactivity feedback.

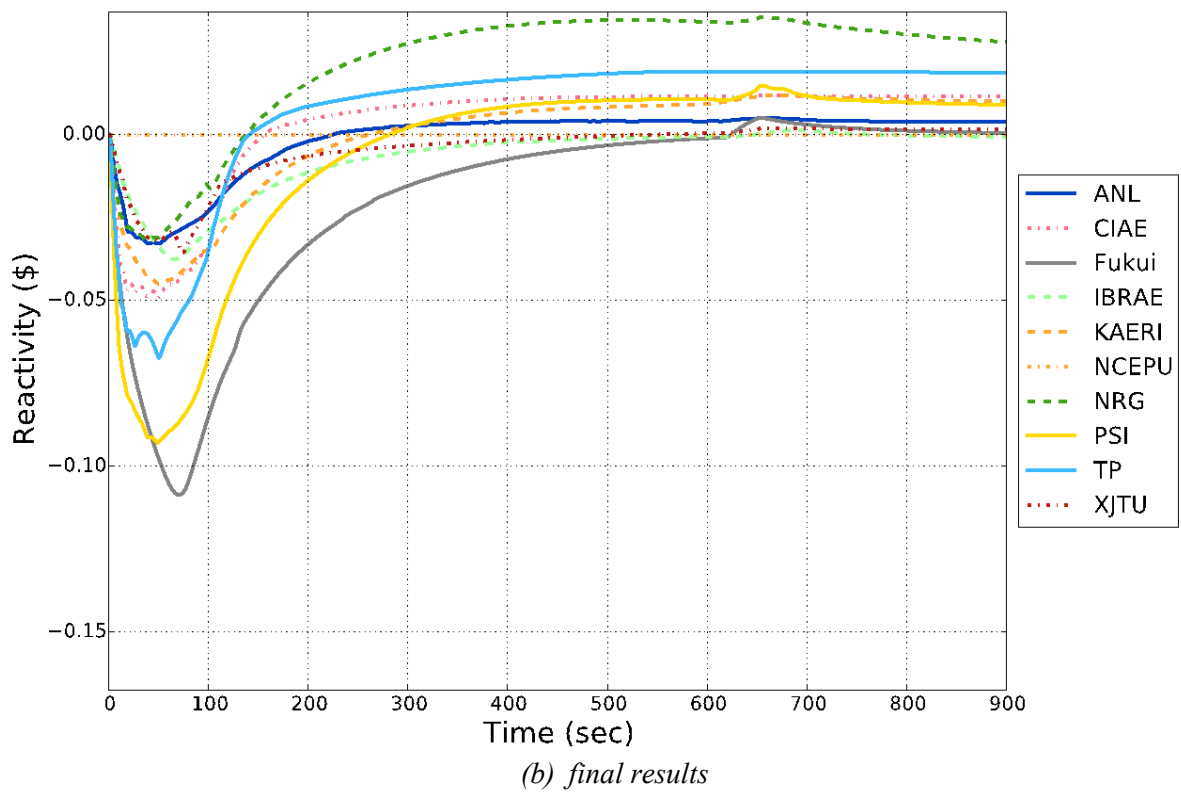
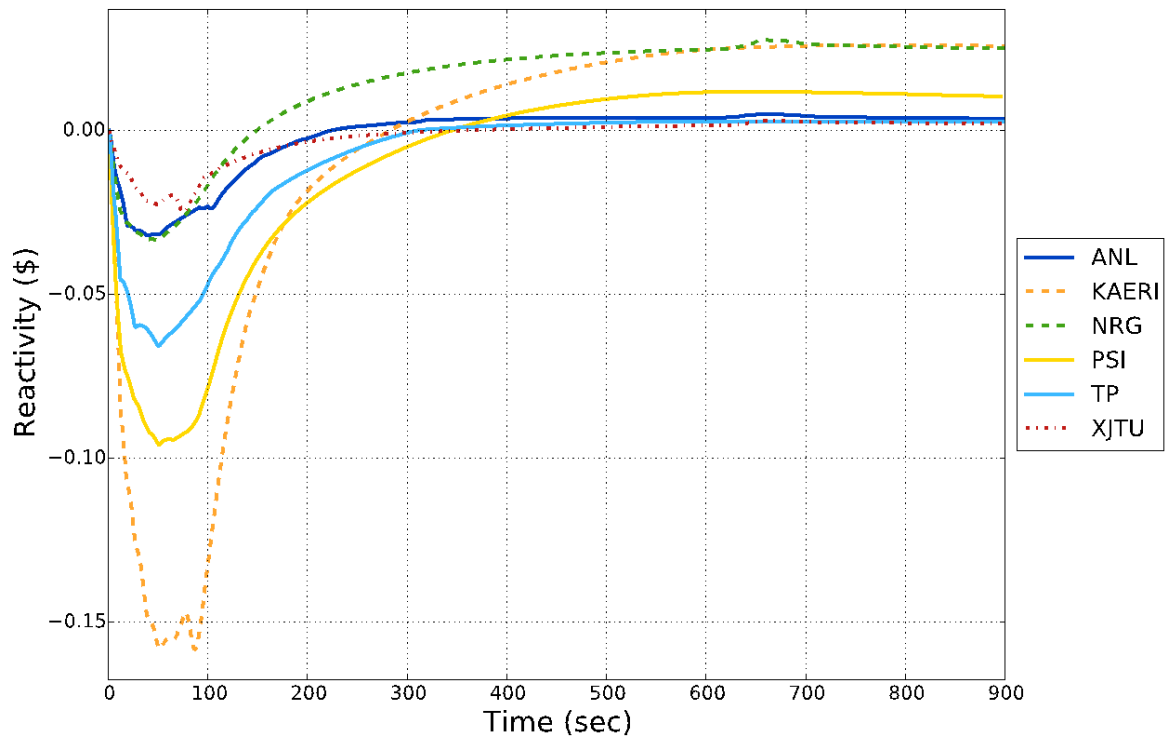
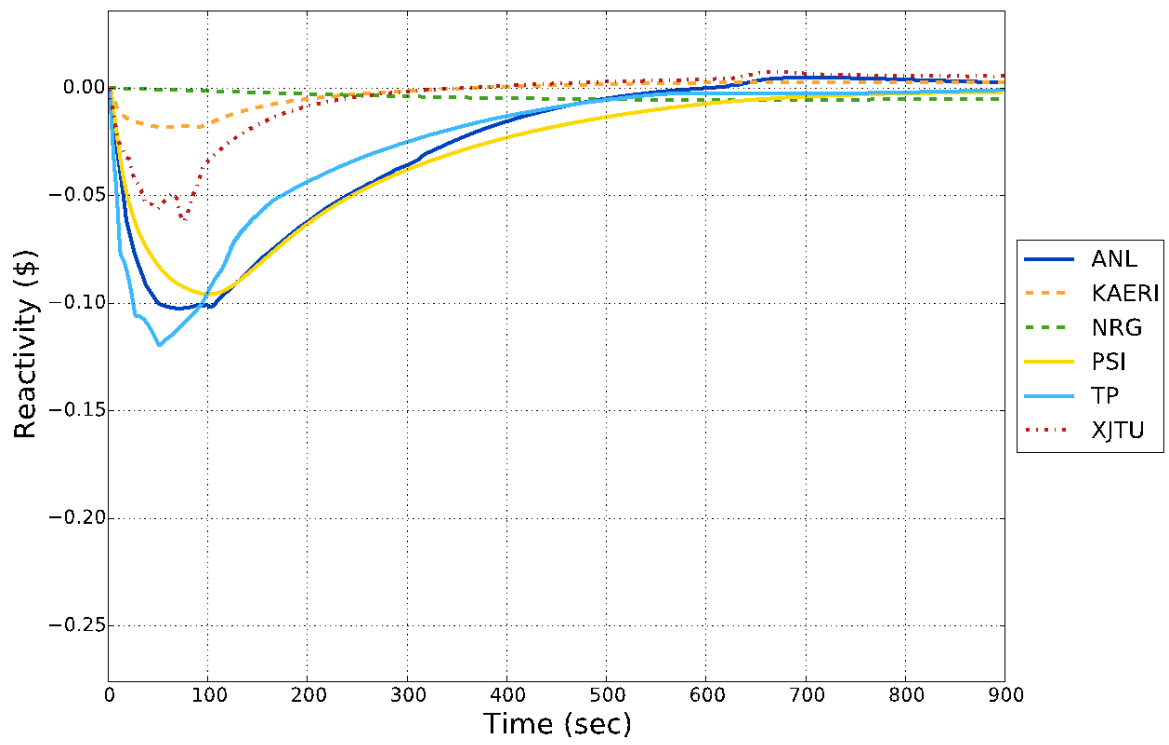
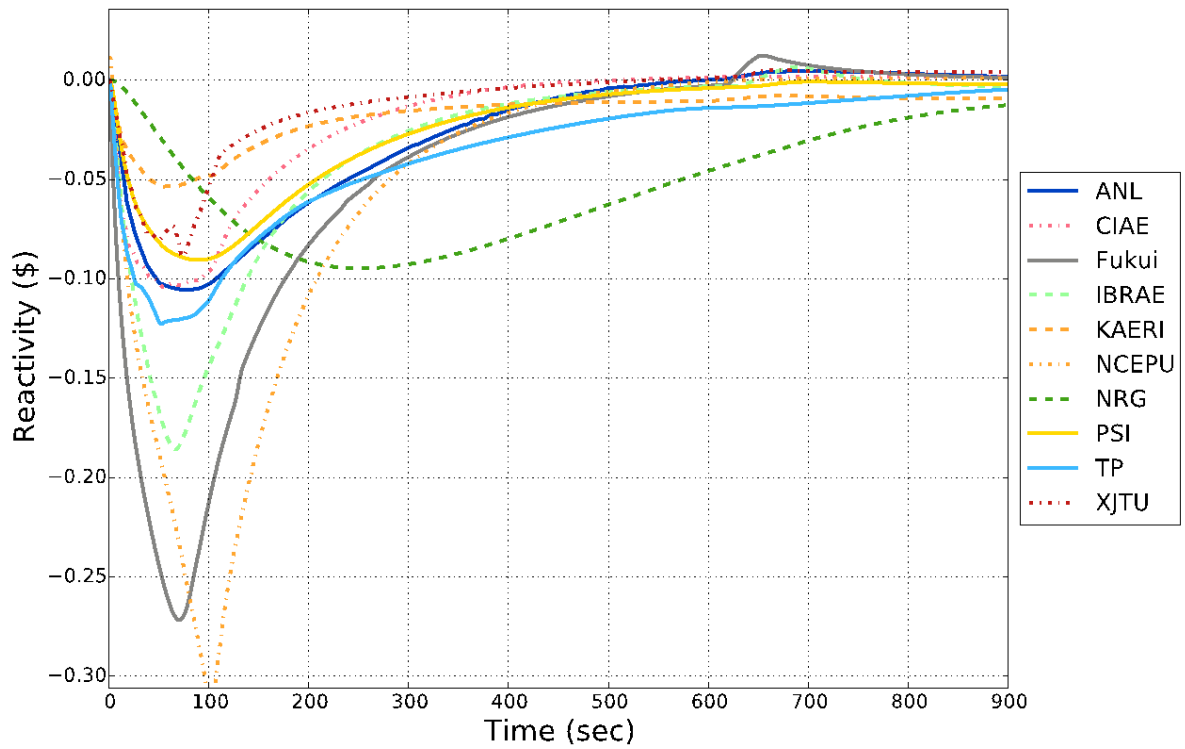


FIG. 377. SHRT-45R axial expansion reactivity feedback.

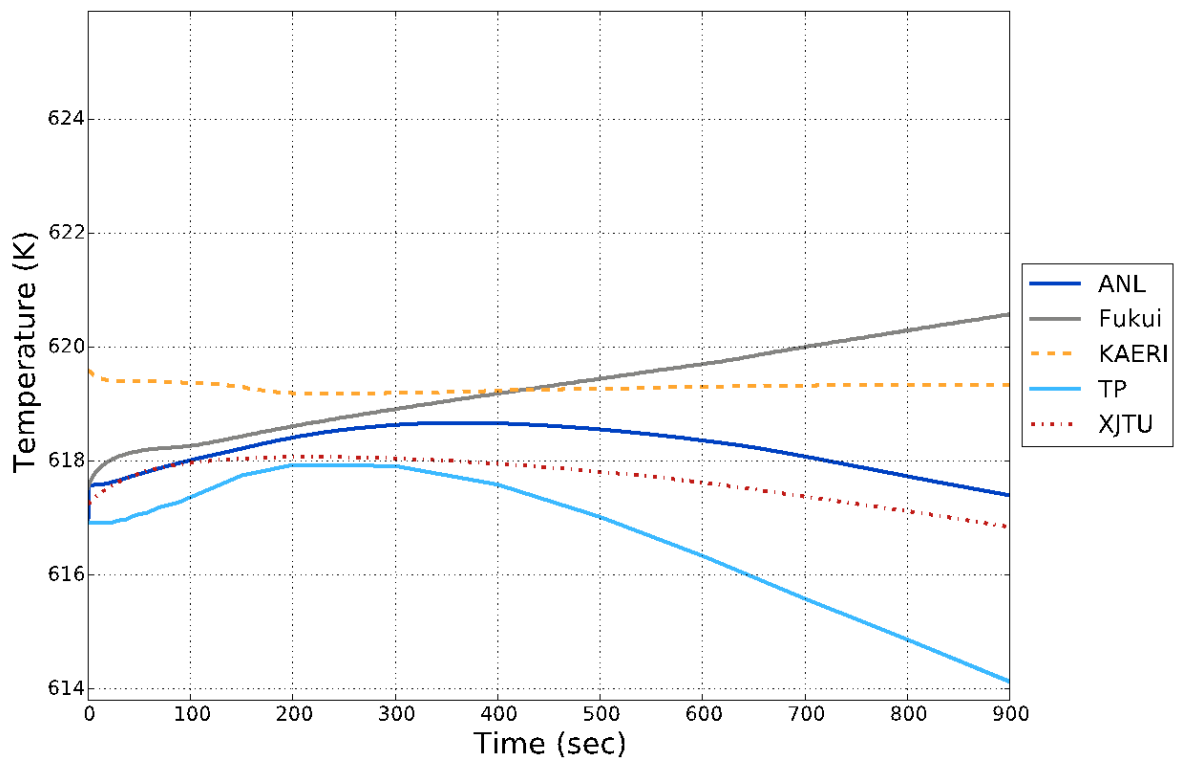


(a) blind results

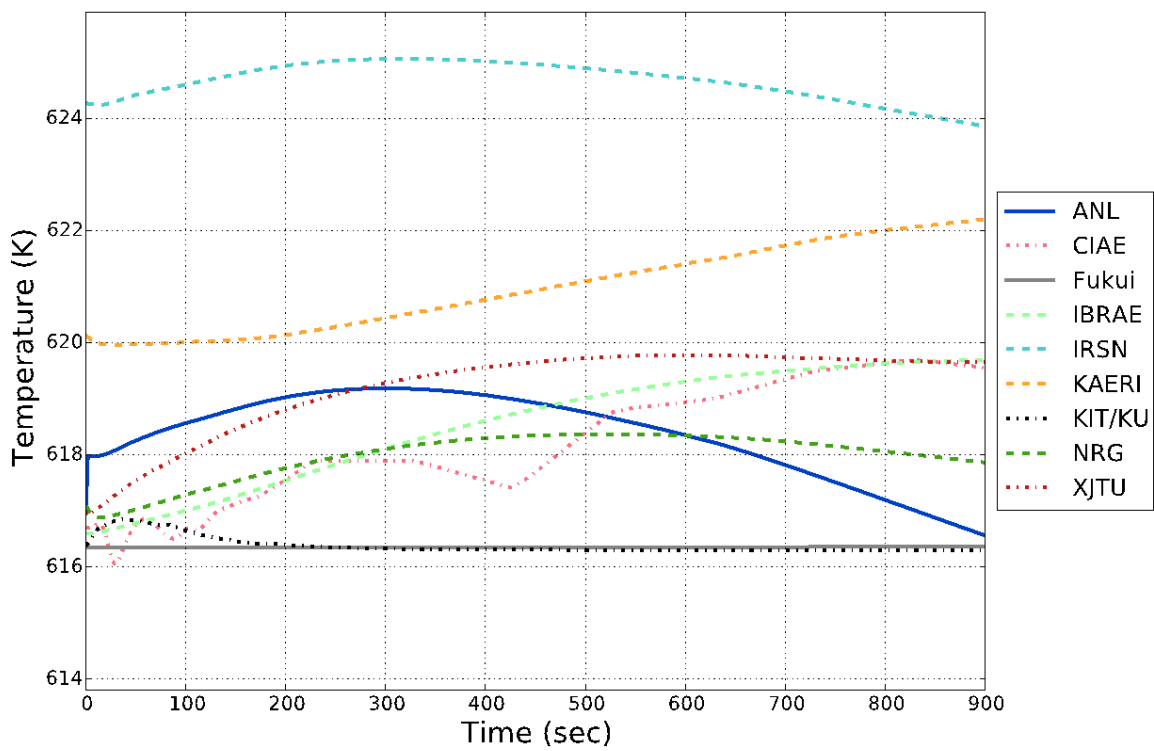


(b) final results

FIG. 378. SHRT-45R radial core expansion reactivity feedback.



(a) blind results



(b) final results

FIG. 379. SHRT-45R XX09 lower flowmeter temperature (FM-ITC) (no recorded data).

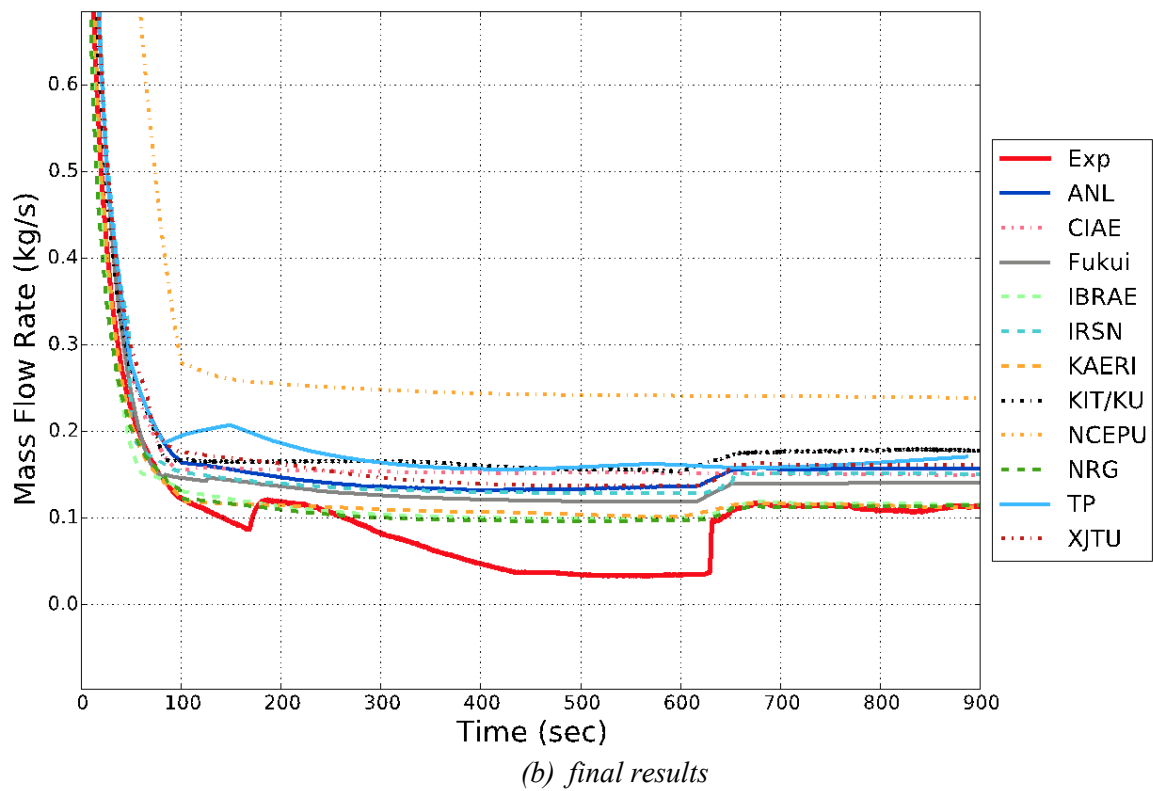
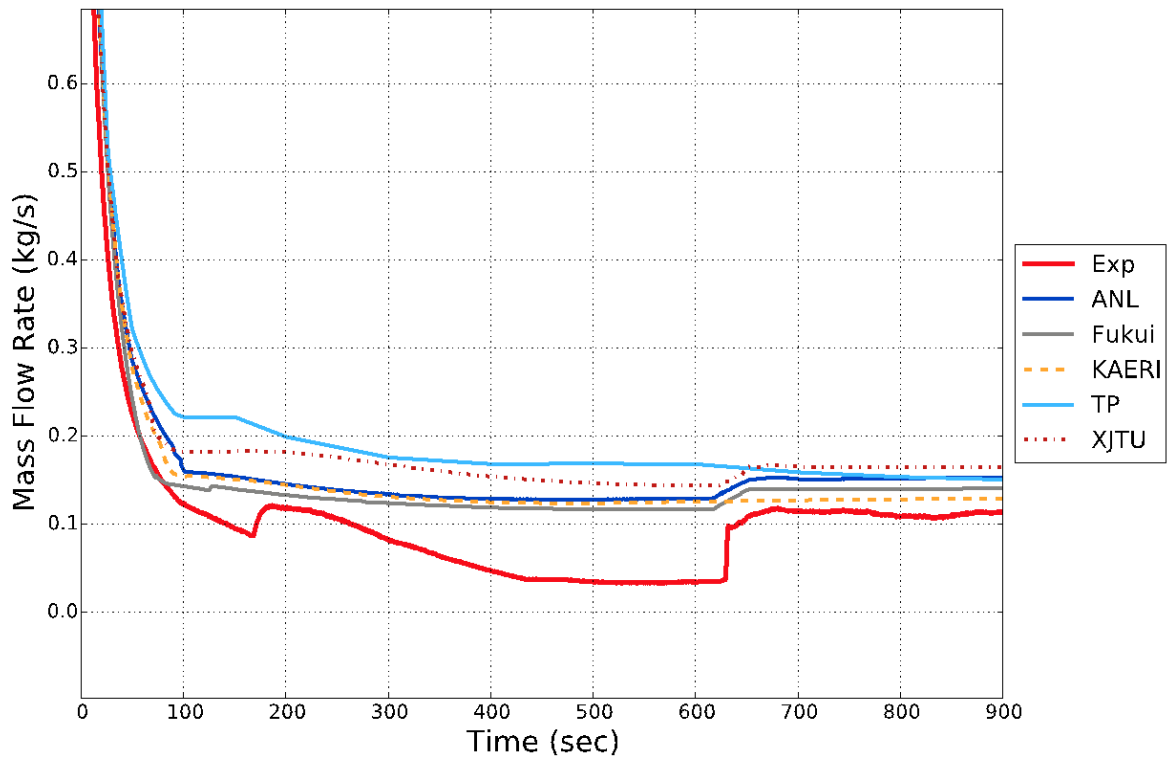


FIG. 380. SHRT-45R XX09 mass flow rate, mid-range.

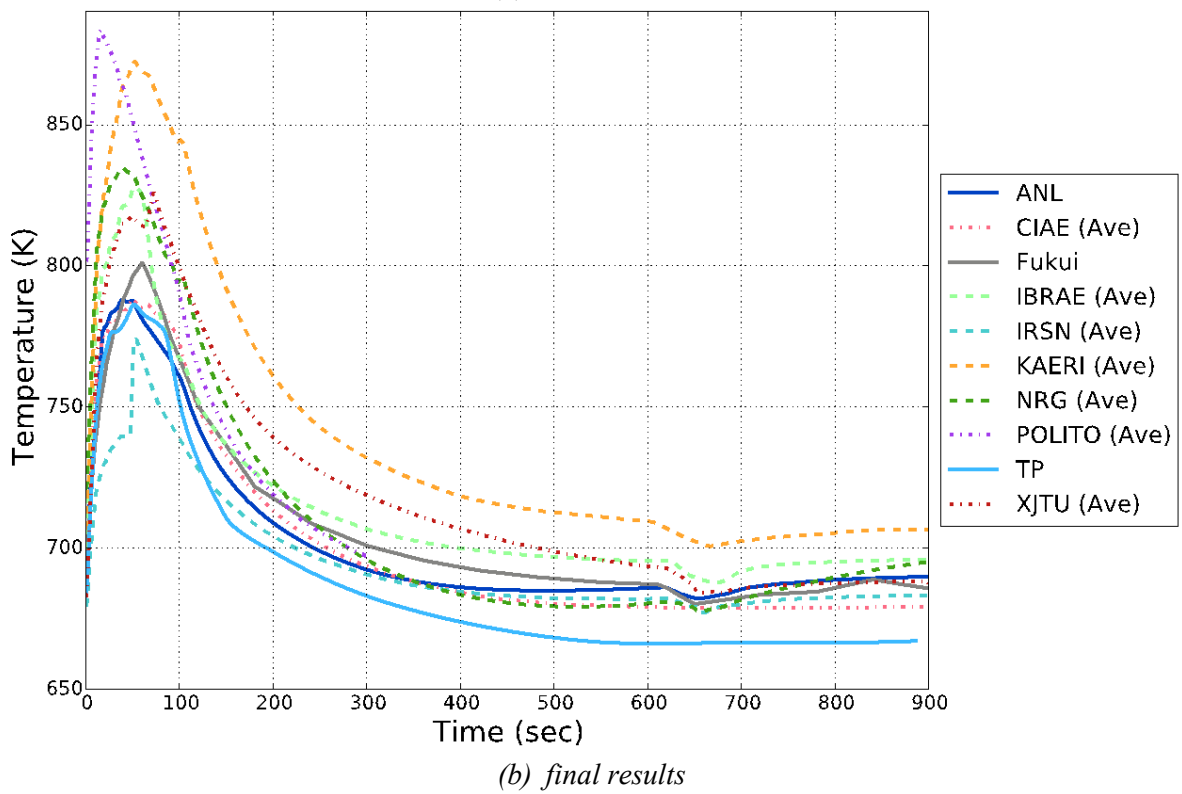
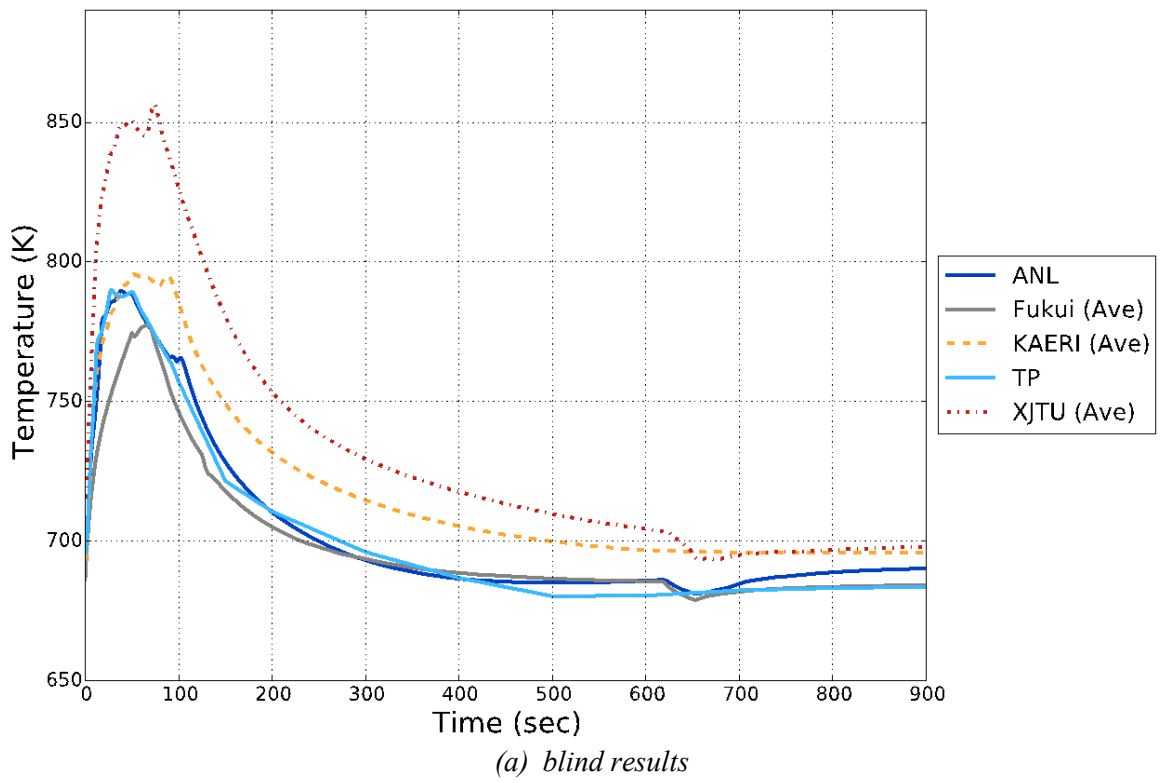


FIG. 381. SHRT-45R XX09 sample midcore temperature (MTC-20), no measured data.

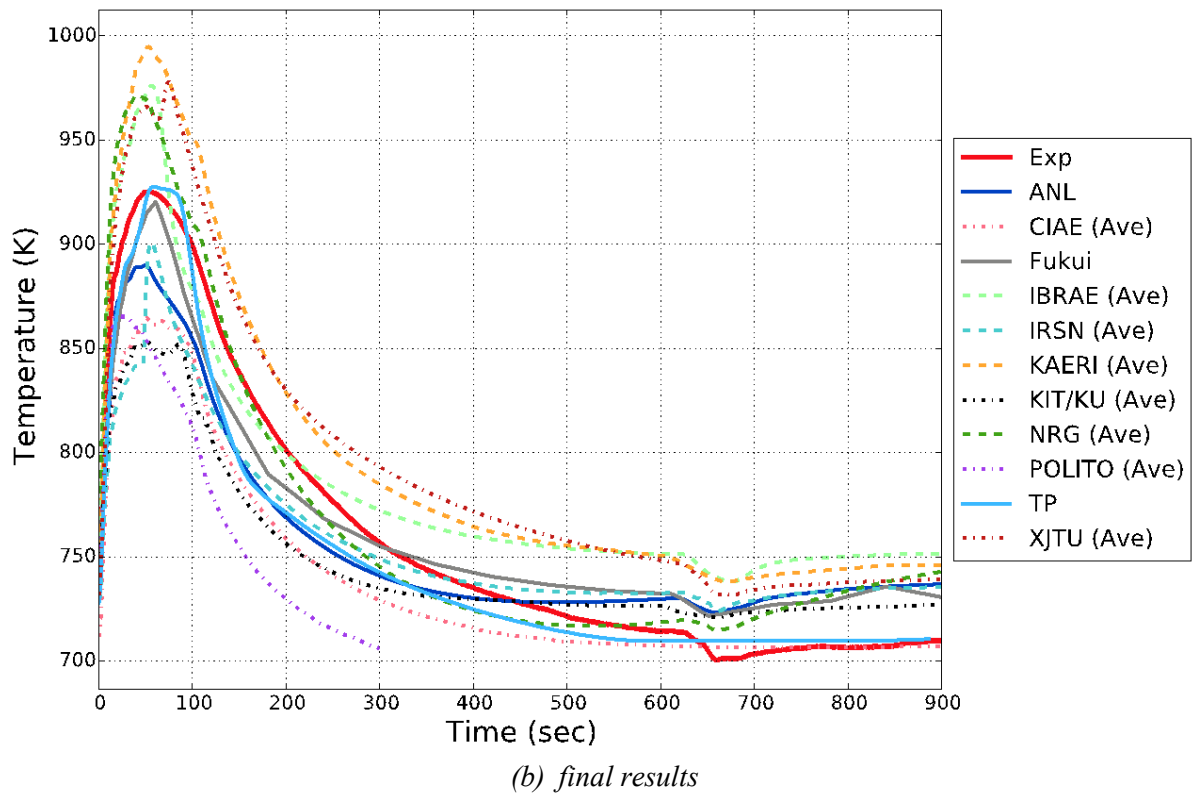
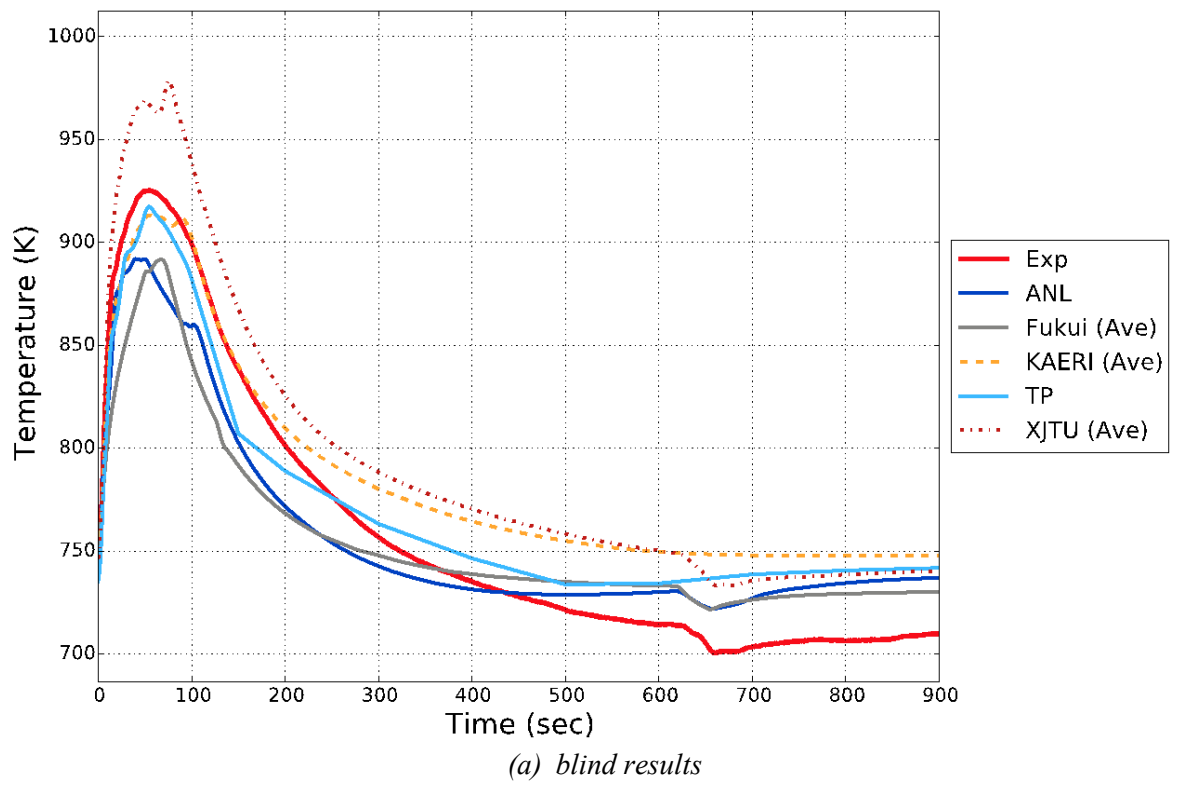
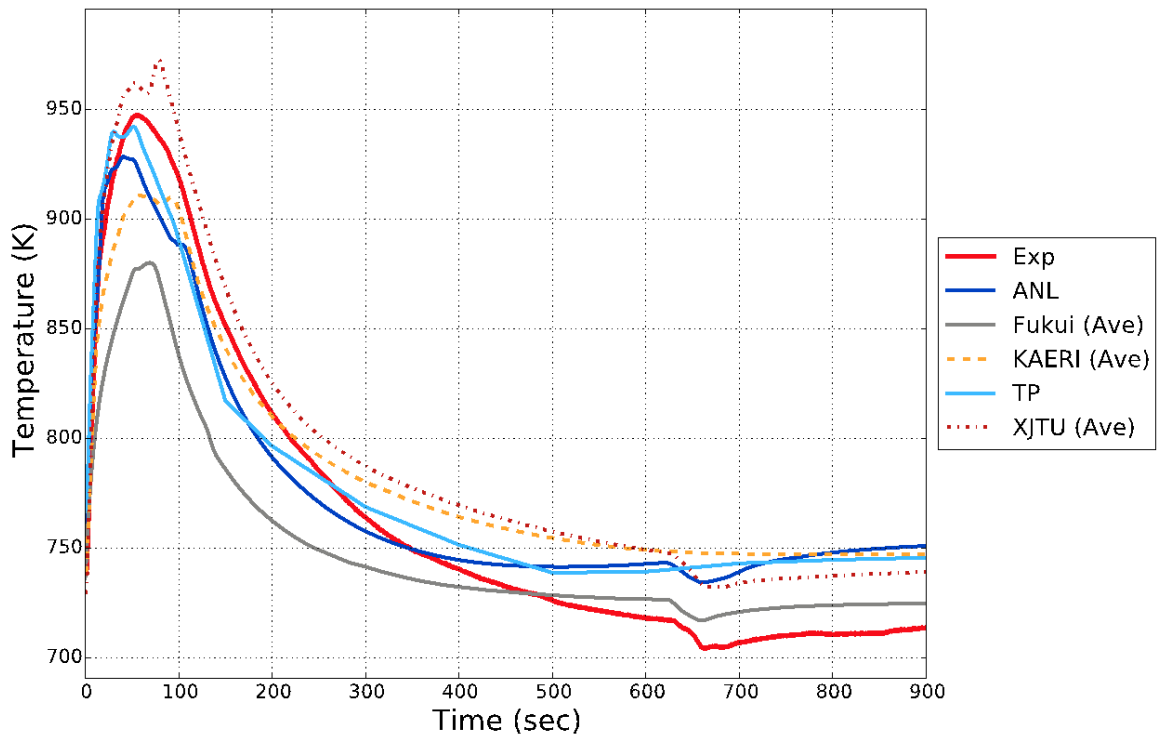
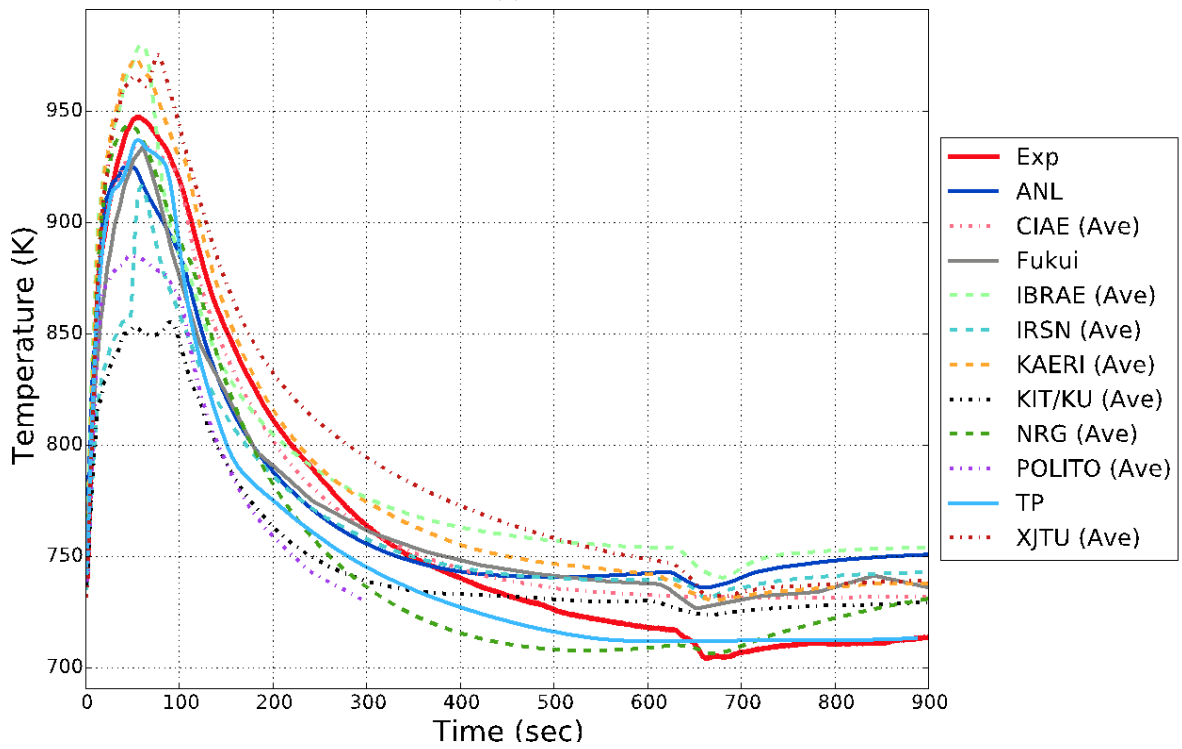


FIG. 382. XX09 sample top of core temperature (TTC-8).



(a) blind results



(b) final results

FIG. 383. SHRT-45R XX09 sample above core temperature (14TC-37).

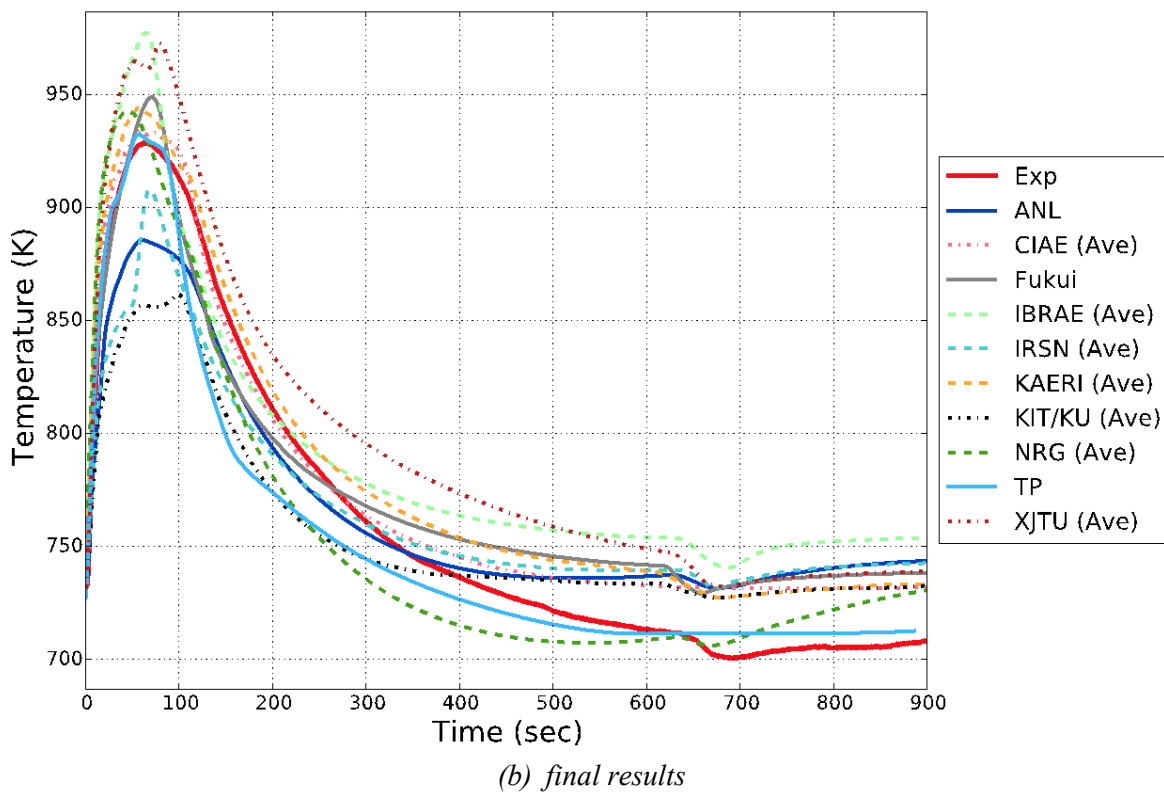
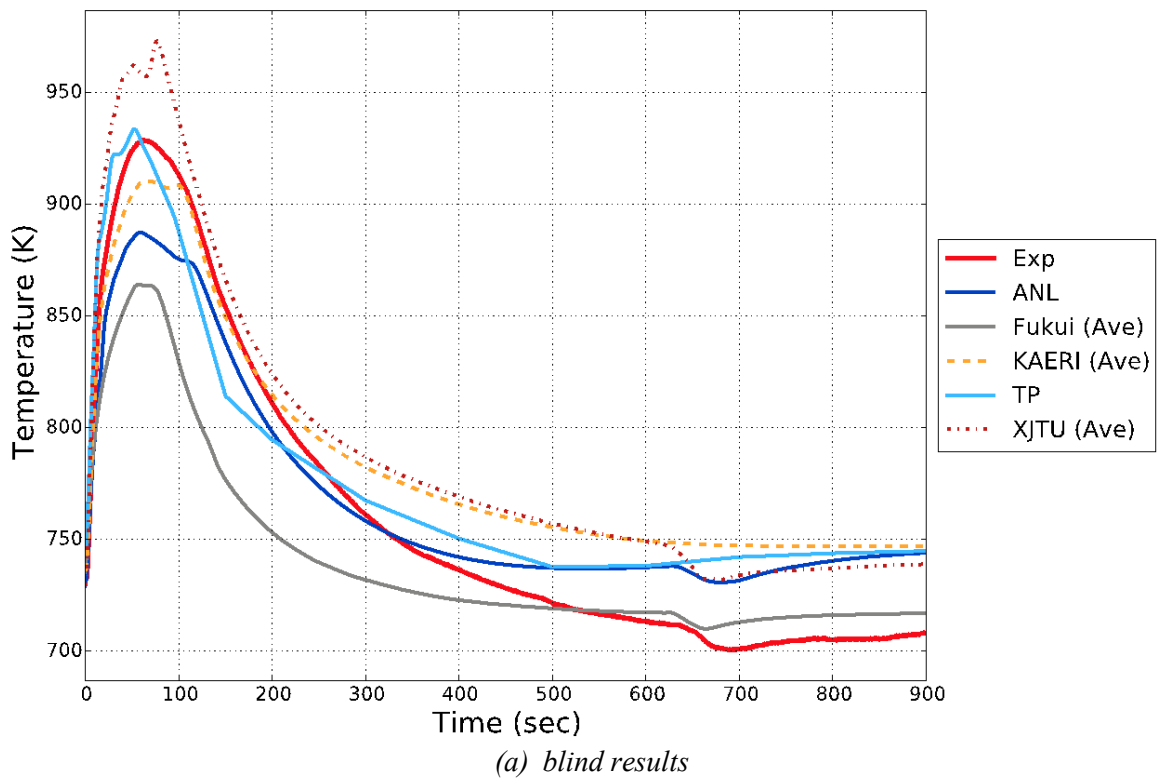


FIG. 384. SHRT-45R XX09 sample core outlet temperature (OTC-01).

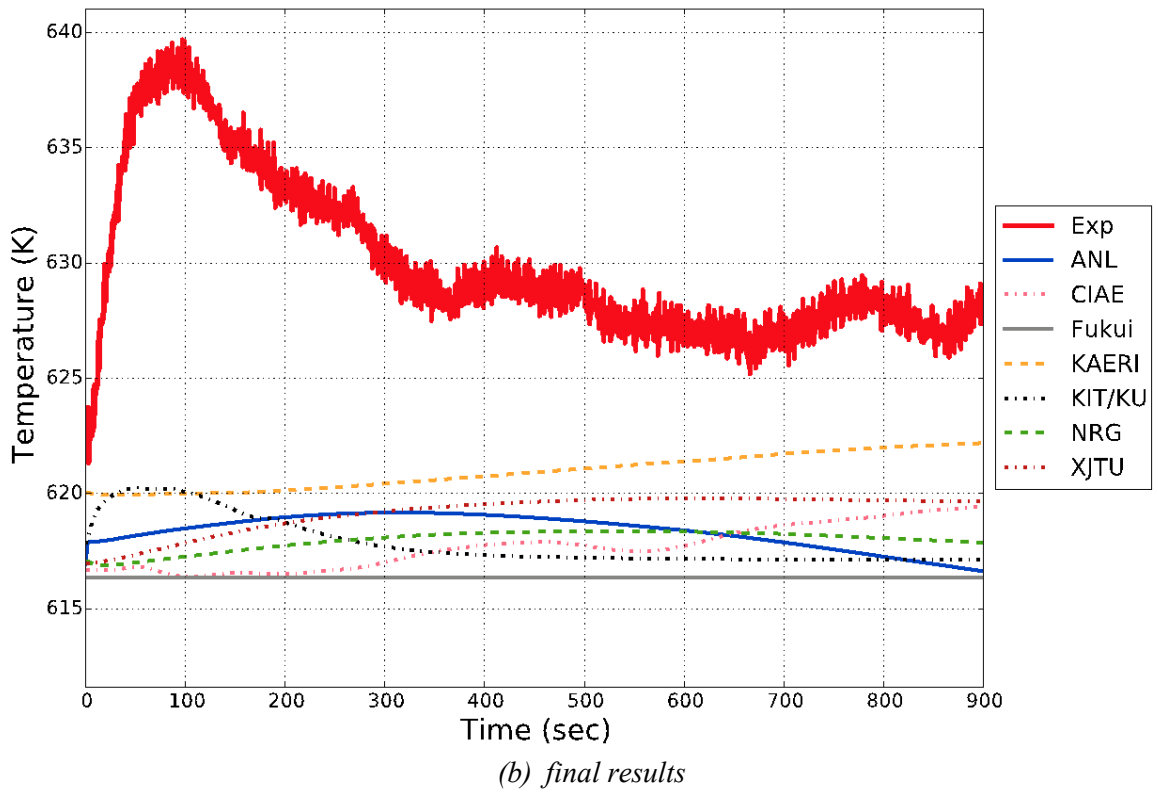
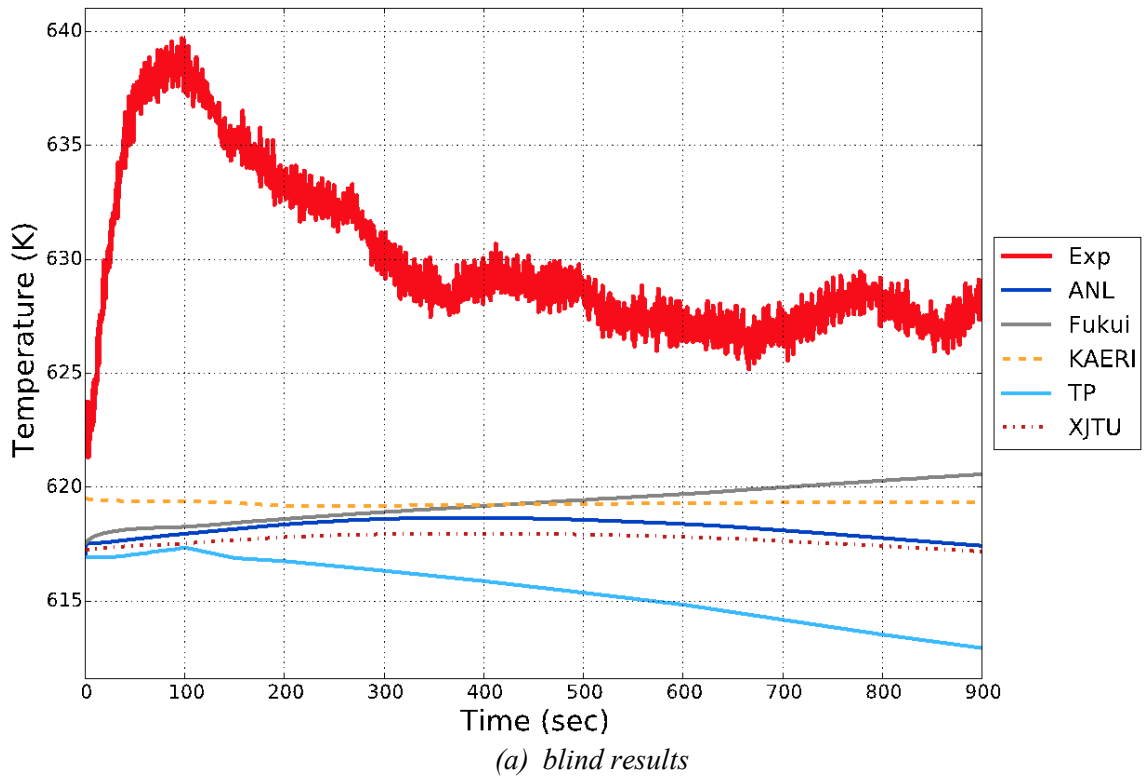


FIG. 385. SHRT-45R XX10 lower flowmeter temperature (FM-1TC).

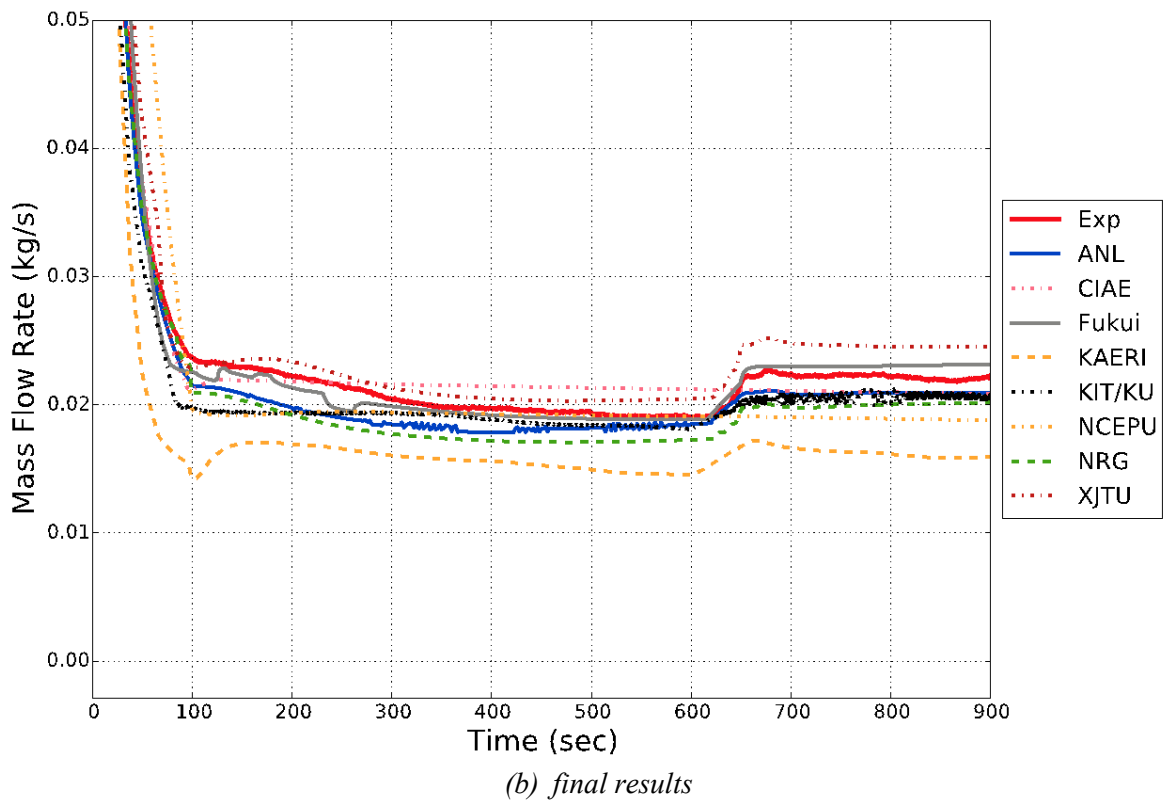
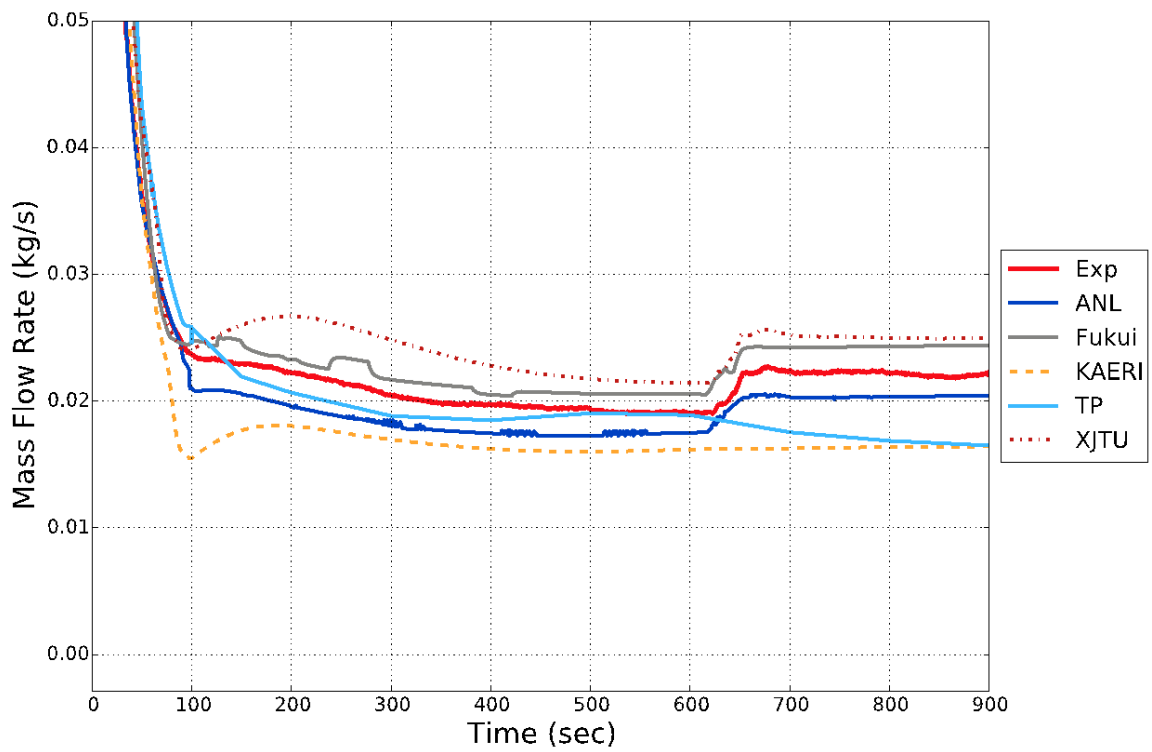
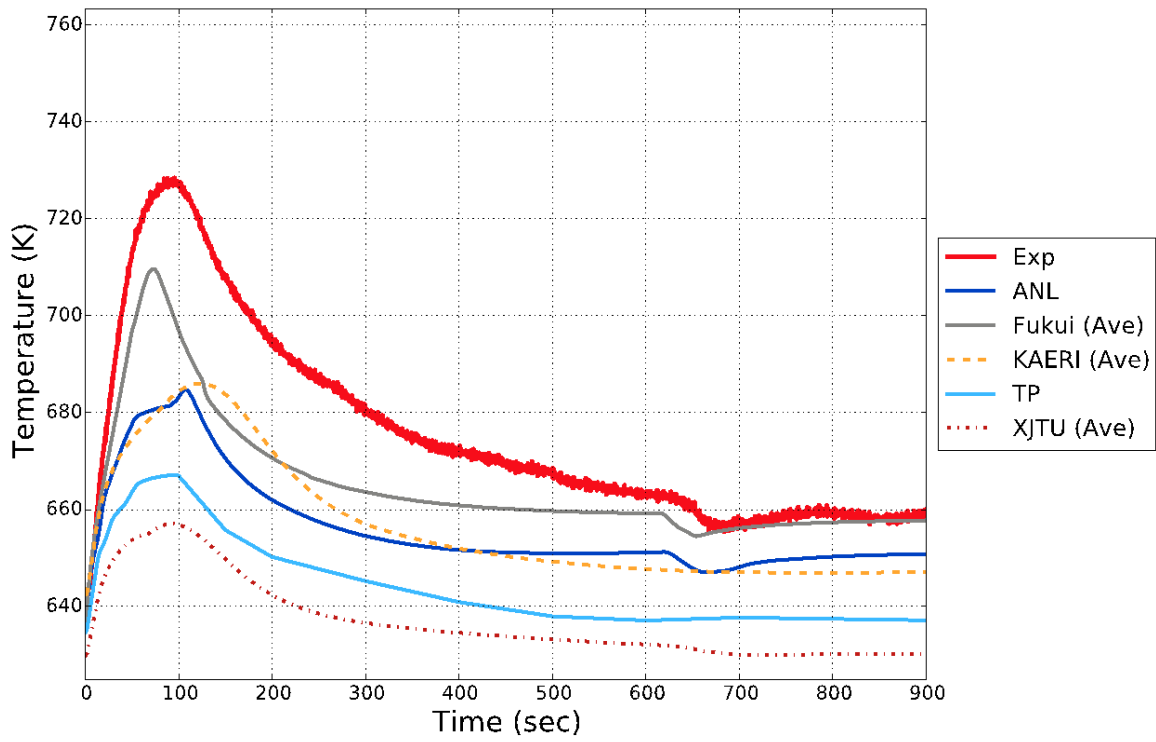
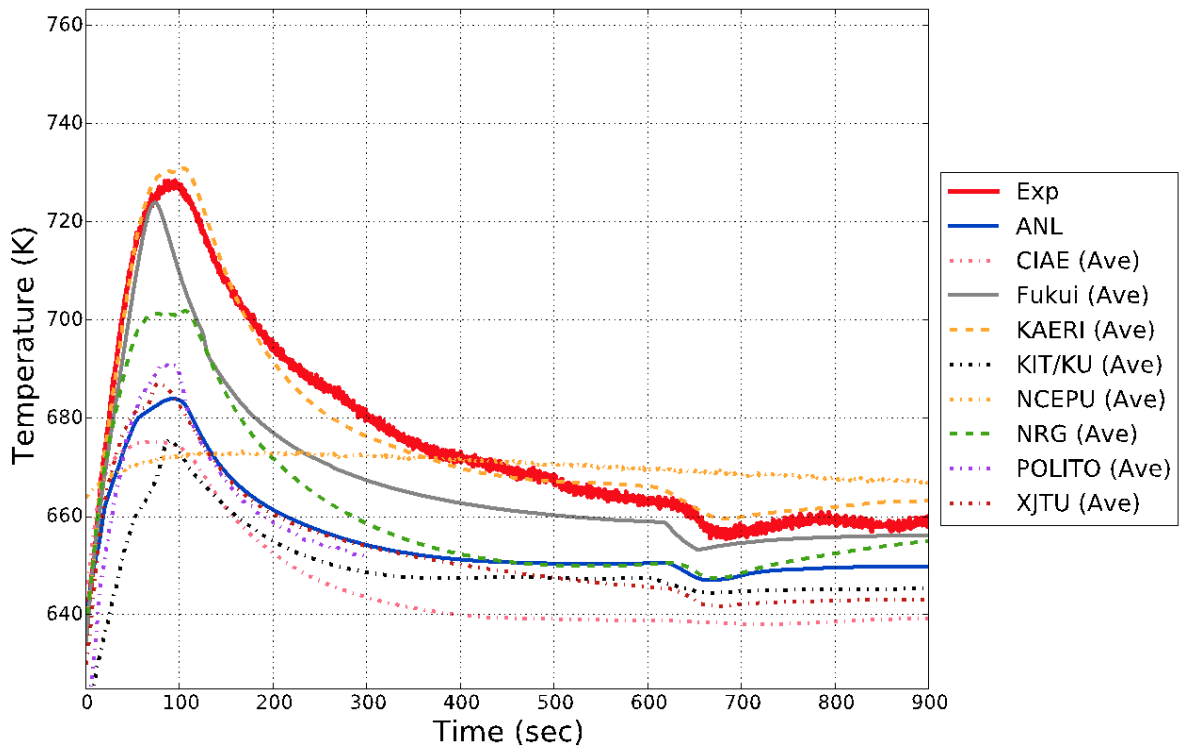


FIG. 386. SHRT-45R XX10 mass flow rate, mid-range.



(a) blind results



(b) final results

FIG. 387. SHRT-45R XX10 sample midcore temperature (MTC-4).

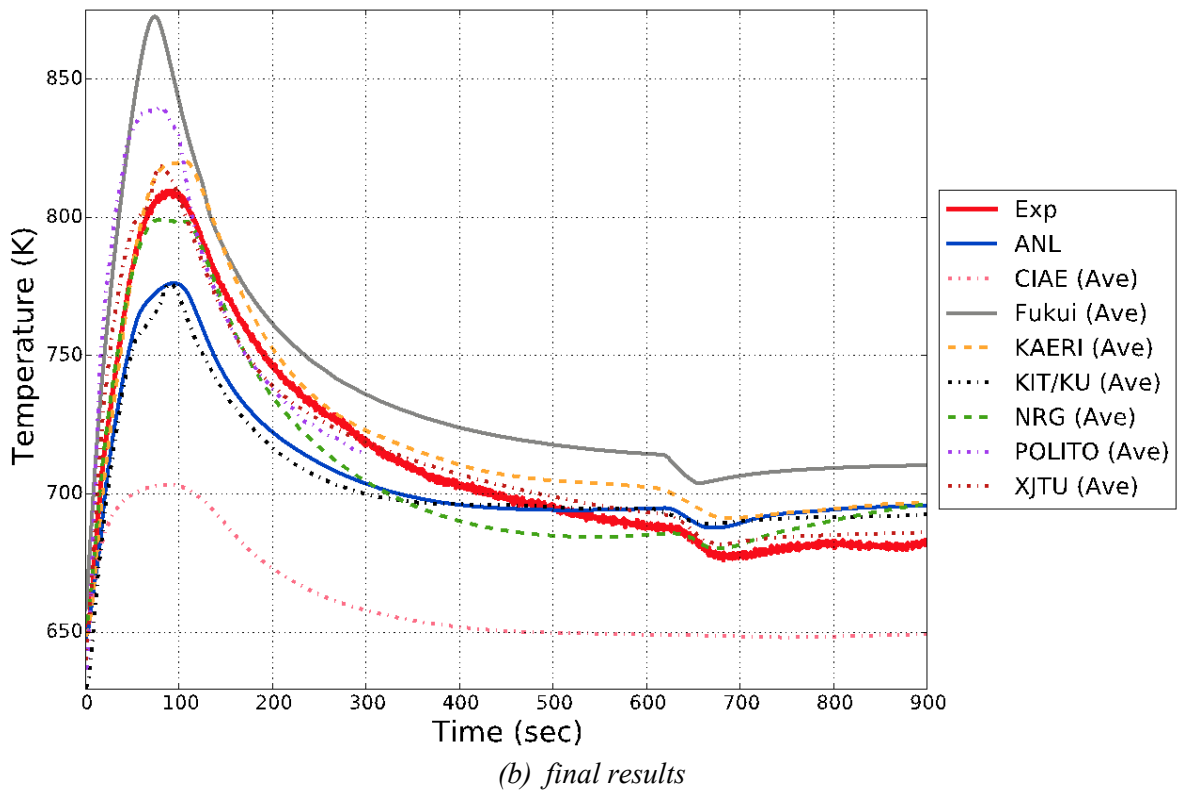
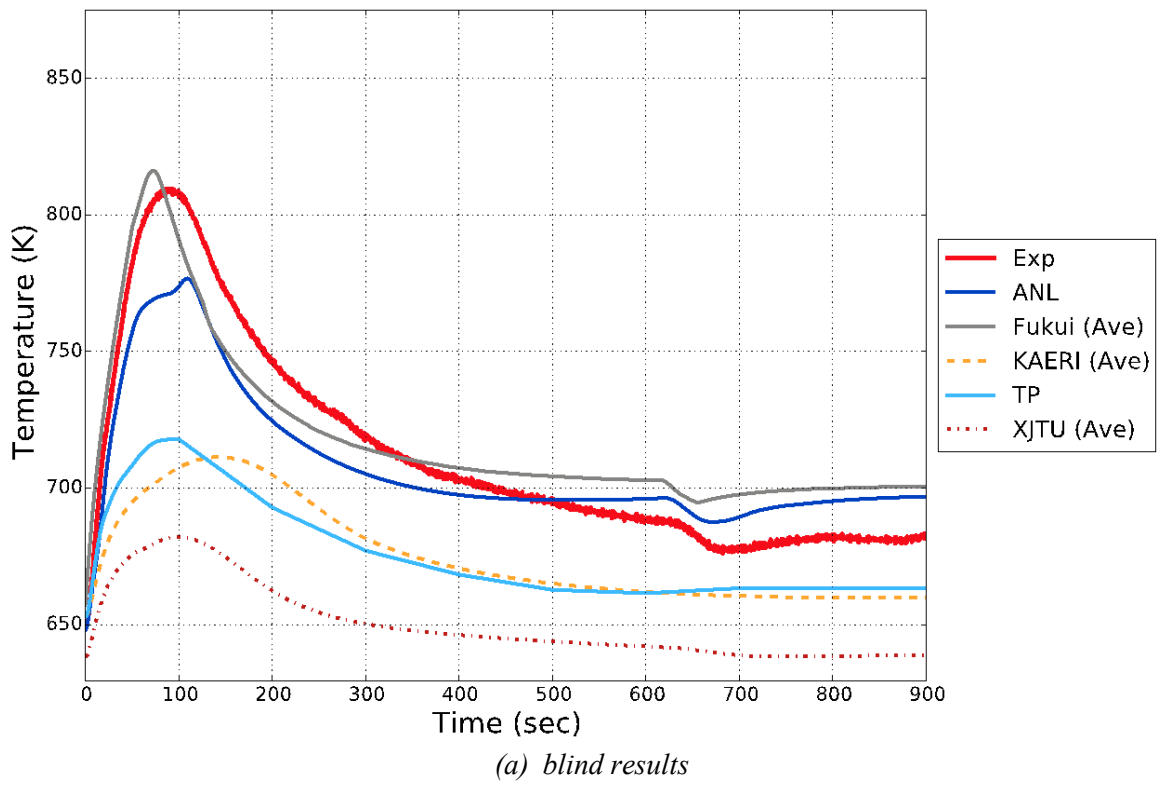


FIG. 388. SHRT-45R XX10 sample top of core temperature (TTC-2).

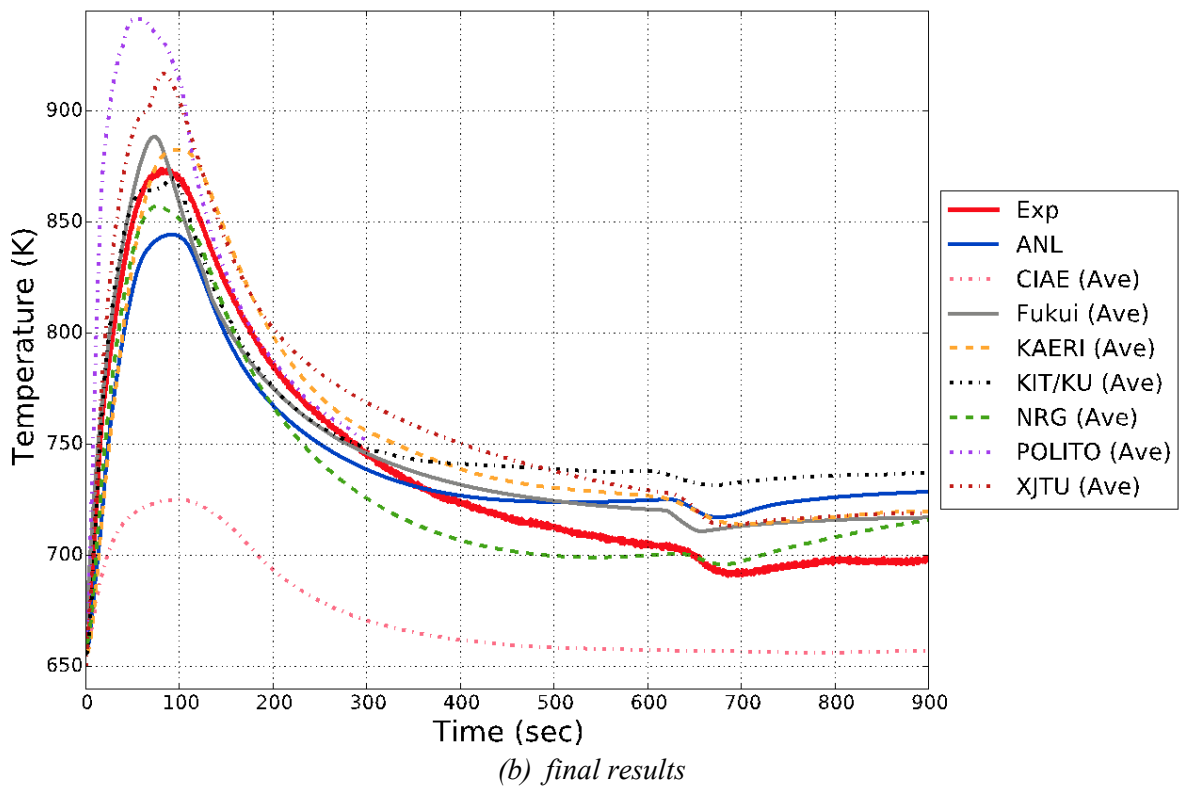
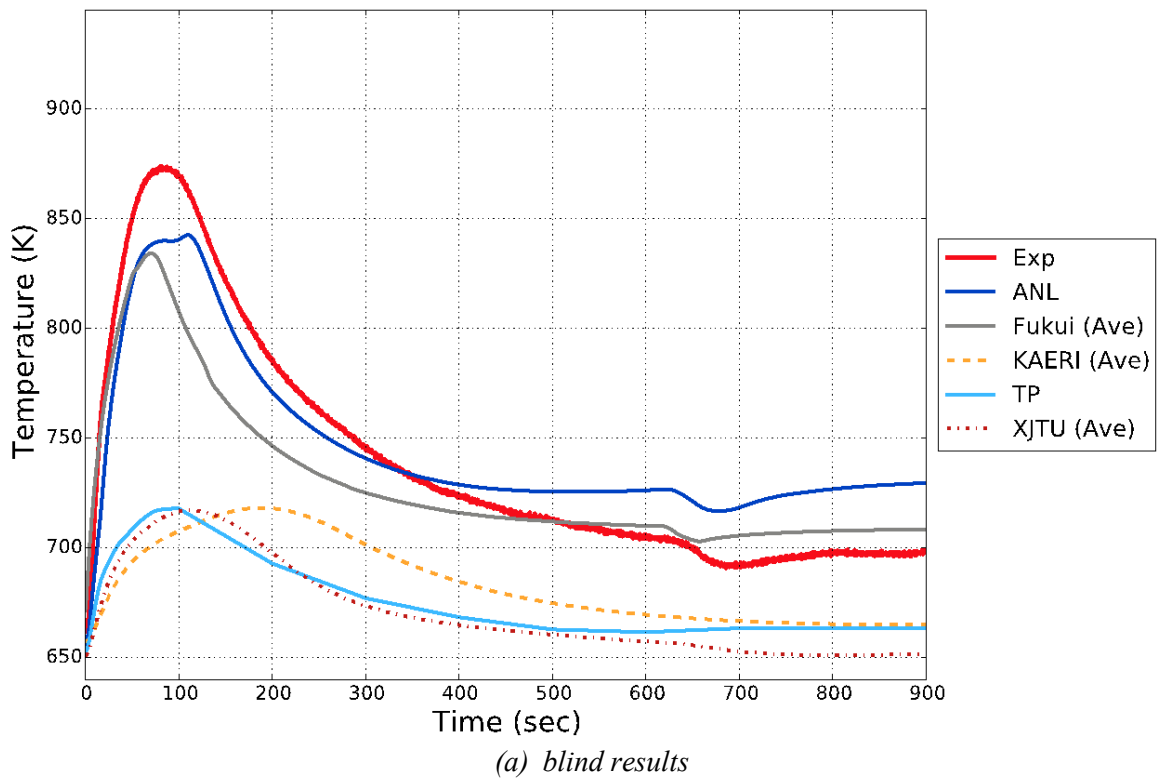
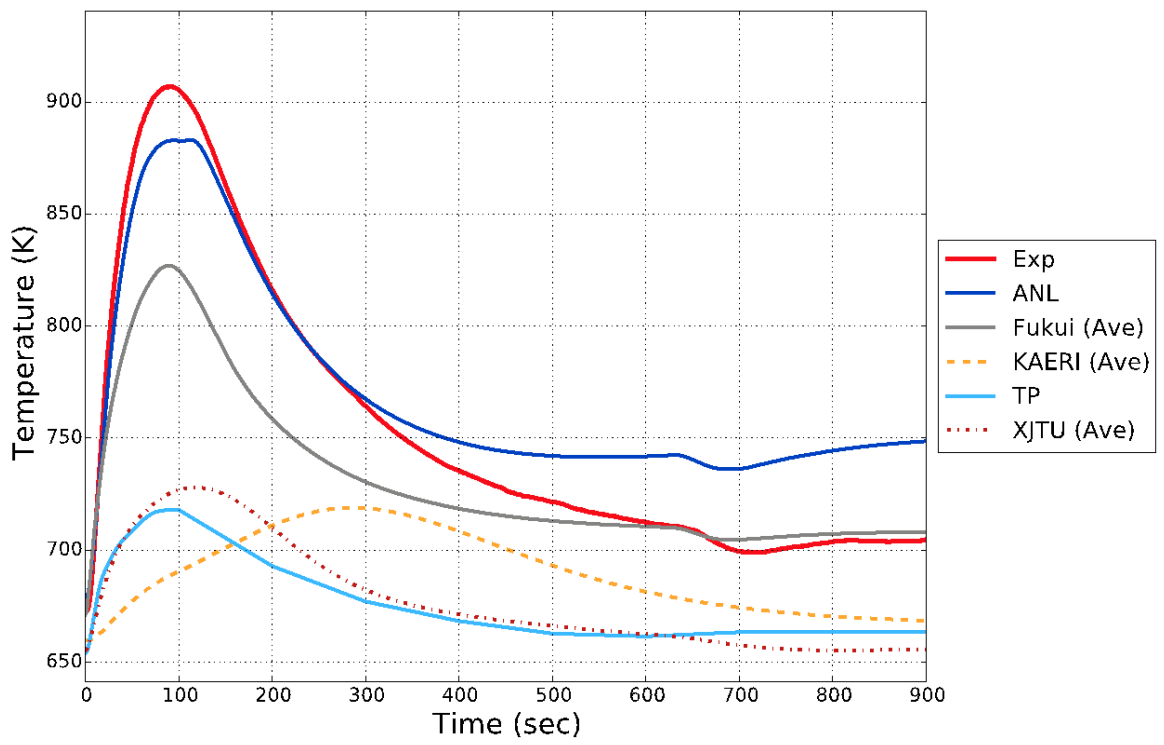
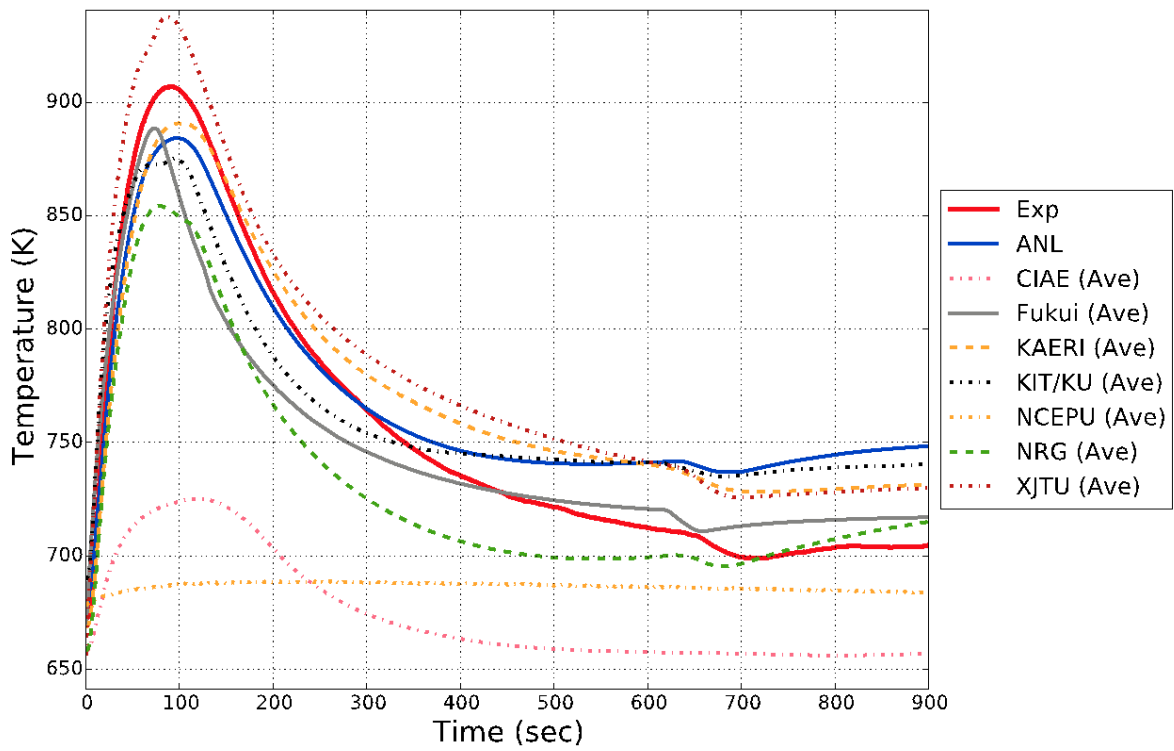


FIG. 389. SHRT-45R XX10 sample above core temperature (14TC-3).



(a) blind results



(b) final results

FIG. 390. SHRT-45R XX10 sample core outlet temperature (OTC-01).

Appendix V

EVALUATION OF ASSUMPTIONS FOR POWER GENERATION IN XX10 DURING SHRT-17 – NRG (THE NETHERLANDS)

V.1. INTRODUCTION

In a fueled subassembly, the relative power after scram follows a typical decay heat curve [4], where the relative power is about 6% immediately after scram and decreases slowly thereafter. In case of a non-fueled subassembly, such as for example XX10, the situation is different: although the absolute power of such a subassembly is relatively low, the relative power after scram may be much higher (~40%), as will be shown in Section V.2.

Most participants in the EBR-II benchmarks CRP used a single decay curve for all subassemblies. This means that for example, in the case of SHRT-17, the relative power generated in XX10 was approximately 6% while it should have been approximately 40%. The present analysis was done to check the effect of different assumptions concerning power generation in non-fueled subassemblies on the overall results.

V.2. HEAT GENERATION IN IRRADIATED MATERIAL

In the case of fuel, at the moment of reactor scram, the power decreases to the decay heat level of ~6% of the operating power and then follows the decay curve. However, for subassemblies that generate power due to gamma heating, for example samples irradiated in research reactors, a rough estimation shows that the relative power reduction will be much smaller. Estimation of the heat generation in a gamma-heated material after scram is shown below.

Nuclear engineering handbooks, for example [149], show distribution of the energy generated per fission. Out of the total energy generated (about 200 MeV/fission), the gamma energies are:

prompt gamma:	5 - 6 MeV
gamma due to fission product decay:	6 MeV

Define the following parameters:

Total radiation heating due to gamma and neutrons:	X , [W/kg]
Radiation heating due to gamma only:	Y , [W/kg]

Analyses performed for fuel for a research reactor (HFR, the High Flux Reactor in Petten, The Netherlands) showed that X is only slightly higher than Y , $X \approx Y$. After reactor scram the neutron heating and the prompt gamma heating disappear. What remains is the gamma from fission product decay. The total gamma heating during normal operation is X [W/kg]. Per fission, 6 MeV is produced from prompt gammas and 6 MeV from decay of fission products. This means that if the fission process stops, the fraction of gamma energy left will be $6/(6+6)$ compared to normal operation. Therefore, the fraction of initial heating may be estimated as: $Y/X \times 6/(6+6)$. Since $X \approx Y$, the value is ≈ 0.5 , or 50% of the normal operating power. More exact calculations performed for HFR show that $Y/X \approx 0.8$, which means that the power will decrease to 0.4 or 40% following reactor scram. In general, it is expected that Y/X will be

significantly smaller than 1.0 only in strong neutron absorbers, such as for example control rod poison materials. For other materials one would expect $Y/X \sim 1.0$.

In the time that follows the scram, the generated heat will decrease following the decay heat curve. For example, after 100 s, the decay power will be $\sim 3\%$, about half of the decay power directly after scram. The power in the irradiated material will therefore be about 20% of the power generated during reactor operation, as summarized in TABLE 75. Values at times throughout SHRT-17 are shown in TABLE 76 below. In summary, the relative heat generation in the irradiated materials is much higher than in the fuel.

TABLE 75. HEAT GENERATION IN FUEL AND IRRADIATED MATERIAL

	Fissile material	Irradiated material
Normal operation	100%	100%
Just after scram	$\sim 6\%$	$\sim 40\%$
100 s after scram	$\sim 3\%$	$\sim 20\%$

TABLE 76. EBR-II SHRT-17, FISSION POWER AND DECAY POWER [106]

Time (s)	Power (MW)			Relative power		
	Fission, Q_{fis}	Decay, Q_{dec}	Total, Q_{tot}	Fission, q_{fis}	Decay, q_{dec}	Total, q_{tot}
0.00	53.93	3.36	57.29	0.941	0.059	1.000
1.00	8.24	3.12	11.36	0.144	0.054	0.198
2.00	6.86	2.95	9.81	0.120	0.051	0.171
3.50	5.61	2.77	8.38	0.098	0.048	0.146
5.00	4.76	2.63	7.39	0.083	0.046	0.129
7.50	3.82	2.46	6.29	0.067	0.043	0.110
10.00	3.23	2.33	5.56	0.056	0.041	0.097
15.00	2.47	2.15	4.62	0.043	0.038	0.081
22.50	1.85	1.95	3.80	0.032	0.034	0.066
30.00	1.46	1.82	3.28	0.025	0.032	0.057
40.00	1.10	1.70	2.79	0.019	0.030	0.049
50.00	0.84	1.60	2.44	0.015	0.028	0.043
60.00	0.66	1.52	2.19	0.012	0.027	0.038
90.00	0.38	1.35	1.73	0.007	0.024	0.030
120.00	0.25	1.24	1.49	0.004	0.022	0.026
180.00	0.13	1.09	1.22	0.002	0.019	0.021
240.00	0.10	1.00	1.10	0.002	0.017	0.019
300.00	0.09	0.93	1.02	0.002	0.016	0.018
360.00	0.08	0.88	0.96	0.001	0.015	0.017
420.00	0.08	0.83	0.92	0.001	0.014	0.016
480.00	0.08	0.80	0.88	0.001	0.014	0.015
540.00	0.08	0.77	0.84	0.001	0.013	0.015
600.00	0.08	0.74	0.82	0.001	0.013	0.014
660.00	0.08	0.71	0.79	0.001	0.012	0.014
720.00	0.08	0.69	0.76	0.001	0.012	0.013
780.00	0.07	0.67	0.75	0.001	0.012	0.013
840.00	0.07	0.65	0.72	0.001	0.011	0.013
900.00	0.07	0.63	0.70	0.001	0.011	0.012

V.3. CASES THAT WERE INVESTIGATED

Three cases were analyzed, representing three choices for modelling power in XX10 during SHRT-17:

- (1) Case 1 (typically used in calculations): XX10 relative power versus time is the same as the in the fuel:

$$Q_{XX10}(t) = Q_0 \times (q_{fis} + q_{dec})$$

Here Q_0 is the initial power of XX10 (equal to 17.2 kW), q_{fis} and q_{dec} are the relative fission power and decay power, as in TABLE 76.

- (2) Case 2 (best estimate power): XX10 relative power follows the irradiated material – TABLE 75:

$$Q_{XX10}(t) = Q_0 \times (q_{fis} \times 0.647 + q_{dec} \times 6.667)$$

The multiplier on decay heat is equal to the ratio of relative power of irradiated material and fuel, equal to $40/6 = 6.667$ (TABLE 75). The multiplier on the fission power, 0.647, was set to result in an initial power of 100%.

- (3) Case 3 (comparison case): Heat generation in XX10 after scram is completely ignored; in other words, the XX10 power is 100% during steady state and 0% during the transient.

$$Q_{XX10}(t) = \begin{cases} 100\% & \text{if } t < 0 \\ 0\% & \text{if } t > 0 \end{cases}$$

Case 3 represents models that do not account for gamma heating.

V.4. RESULTS

Results are shown in FIG. 391 through FIG. 396 FIG. 391 shows the stationary state situation at the start of SHRT-17. The figure shows the XX10 subassembly and the main data for the six neighbouring subassemblies, at the mid-core and the core top elevations. It is seen that the non-fueled subassembly XX10 has relatively low power to flow ratio: $Q/W = 42.7 \text{ kW}/(\text{kg/s})$, while in the neighbours, the ratio is clearly higher than 100. Consequently, a significant amount of heat is transferred from the neighbouring subassemblies to XX10. In the present analysis the heat transfer from the neighbouring subassemblies was calculated assuming that the gap between subassemblies was filled with stagnant sodium.

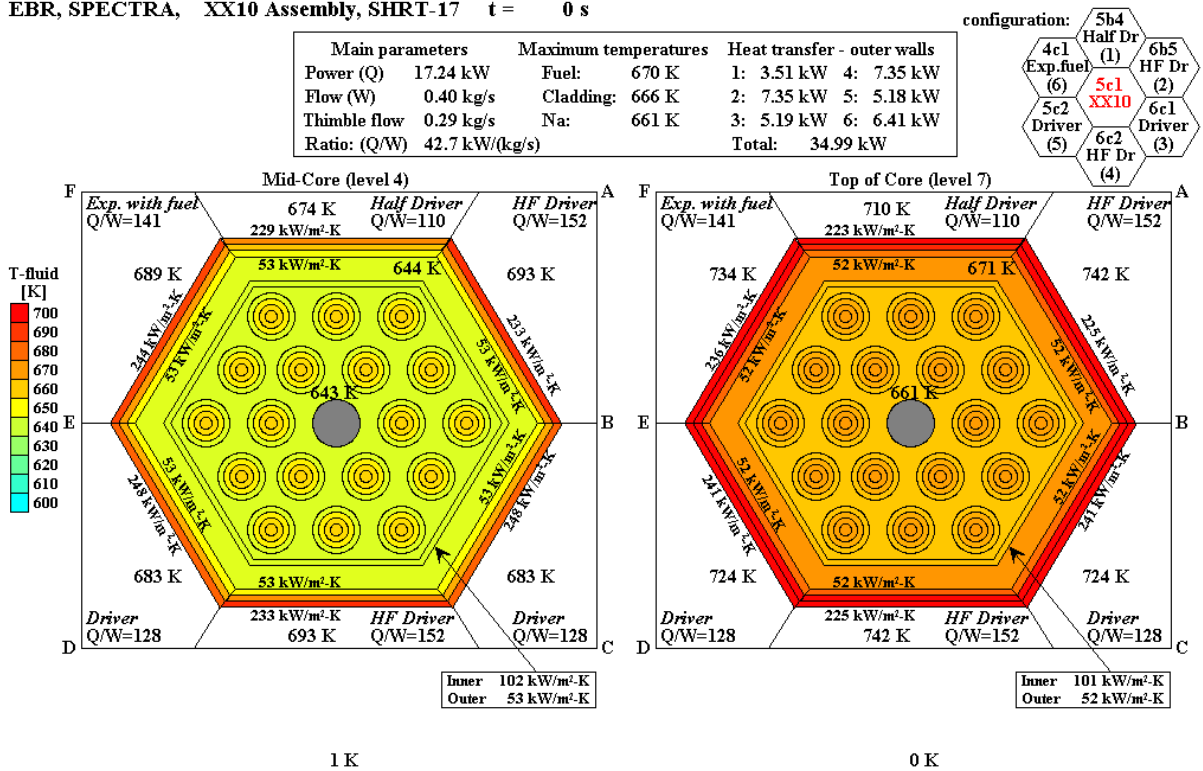


FIG. 391. SHRT-17, XX10, steady state; left: mid-core, right: core top.

FIG. 392 shows the XX10 power contributors for Case 1, including:

- (a) power generated in XX10;
- (b) power transferred from the XX10 rods to the XX10 fluid;
- (c) power transferred from the neighbouring subassemblies to the thimble fluid, and;
- (d) power transferred from the thimble wall to the XX10 fluid.

It is seen that a significant amount of power (peak at about 8 kW) is transferred from the neighbouring subassemblies during the first ~70 seconds.

Figure 393 shows the same values for Case 2. It is seen that the power generated inside XX10 is significantly higher than in the previous case. However, the power transferred from the neighbouring subassemblies is clearly smaller than in Case 1.

Figure 394 shows the same values for Case 3. In this case the power generation in XX10 is assumed to be zero at the time of the scram. As a consequence, the power transfer from the neighbouring subassemblies is very similar to that of Case 1.

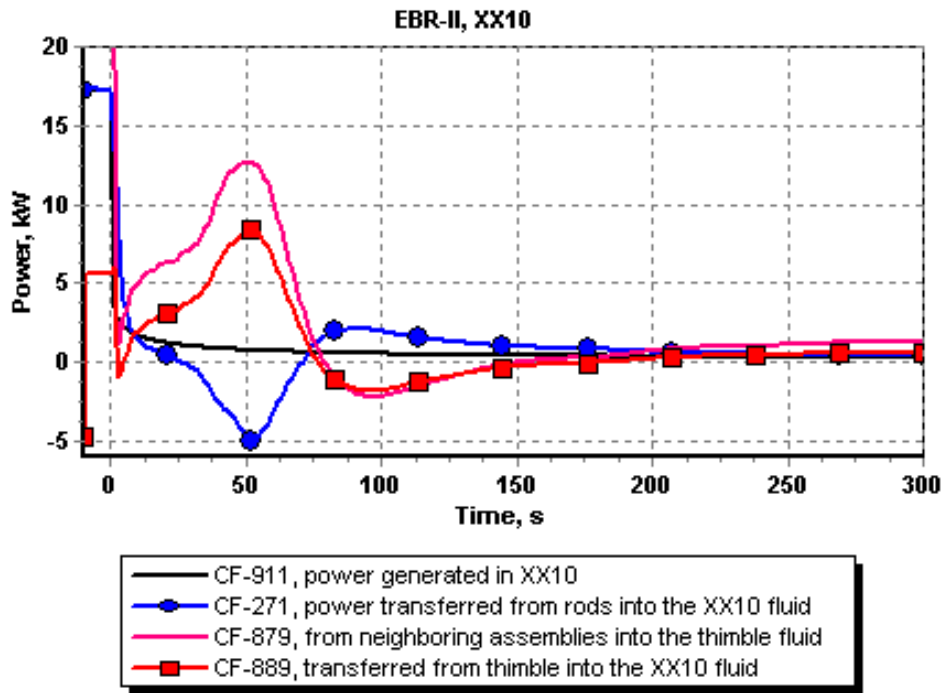


FIG. 392. SHRT-17, XX10 power, Case 1.

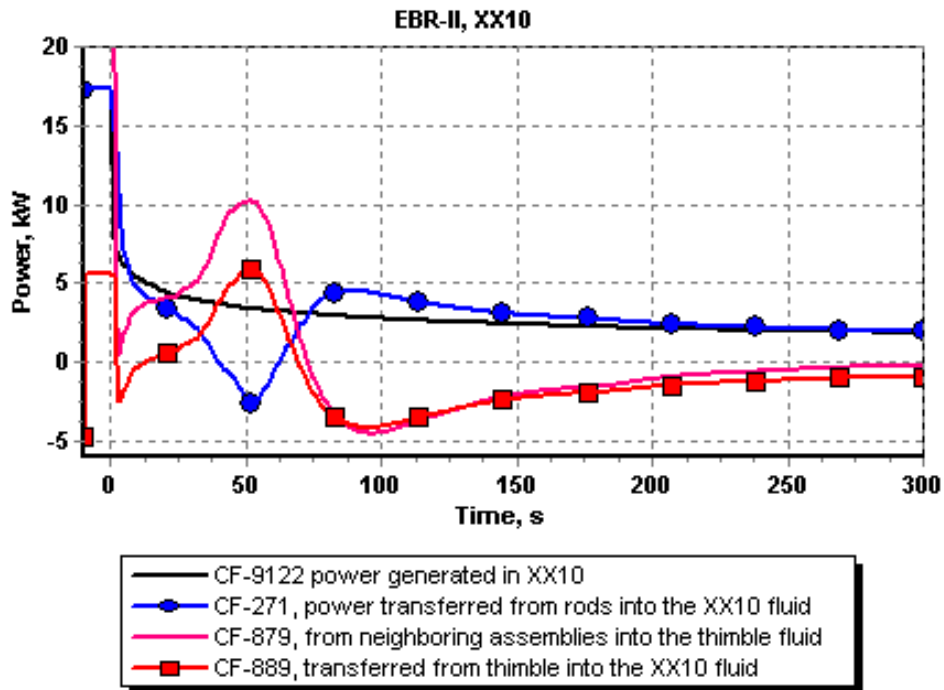


FIG. 393. SHRT-17, XX10 power, Case 2.

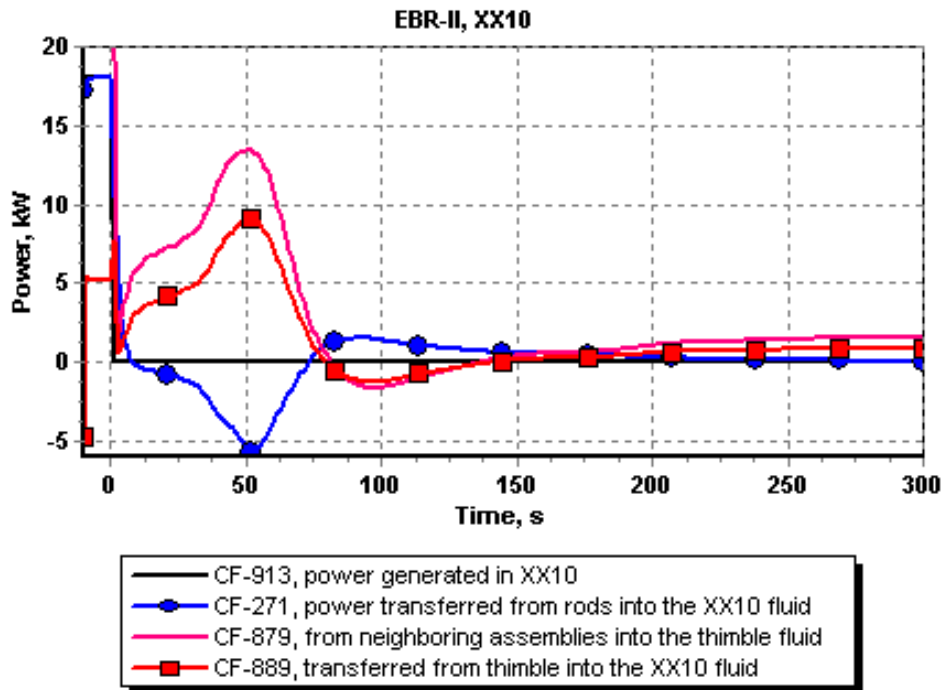


FIG. 394. SHRT-17, XX10 power, Case 3.

Summarizing, if the power generated in XX10 is changed, the power transfer from the neighbours is also altered, and the final result, such as the maximum fluid temperature, is not very different. FIG. 395 and FIG. 396 show the maximum temperatures in the mid-core and at the top of the core. The maximum temperatures at the top of the core are 798 K (Case 1), 805 K (Case 2), and 788 K (Case 3).

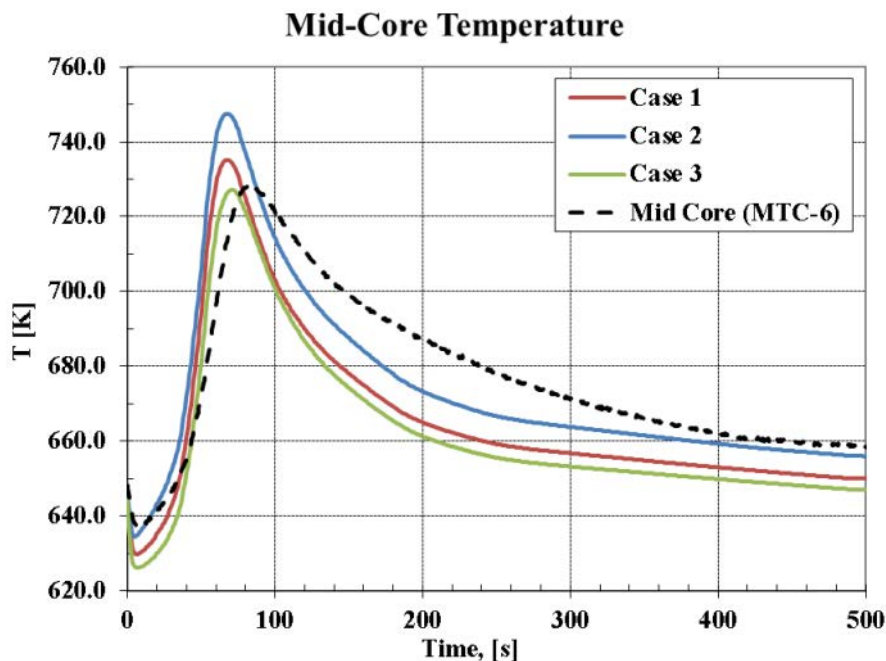


FIG. 395. SHRT-17, XX10 mid-core temperatures.

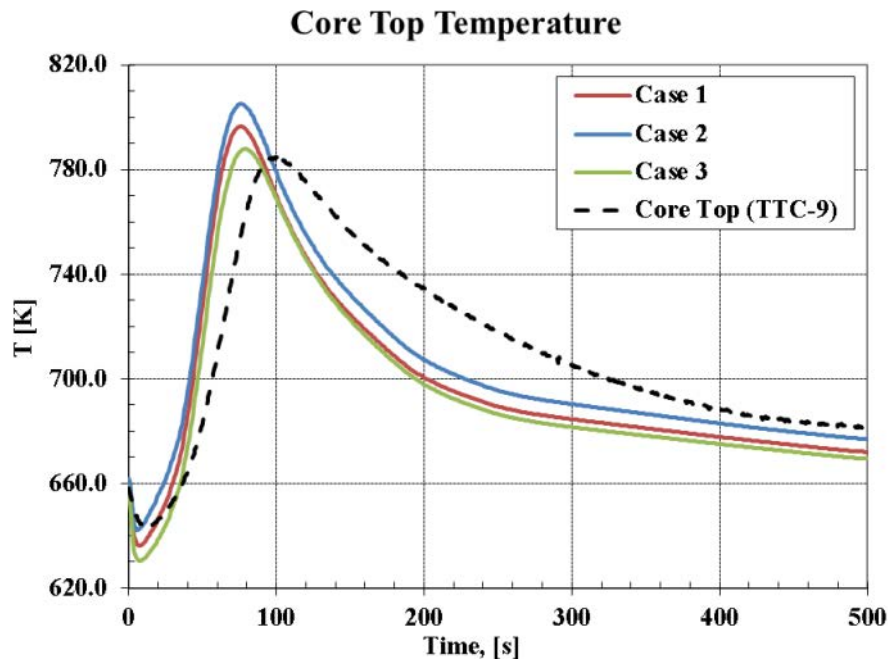


FIG. 396. SHRT-17, XX10 core top temperatures.

V.5. CONCLUSIONS

The calculations performed for cases 1, 2, and 3 showed that different assumptions concerning power generation after scram have a rather small effect on the calculated temperatures. This is because the power transferred from the neighbouring subassemblies is quite large and, furthermore, the system of XX10 and its six neighbours has a self-stabilizing property: if more power is assumed to be generated within XX10, less power is transferred from the neighbours and the final temperatures in XX10 are quite similar.

**RECOMMENDED DATA FOR METAL FUEL PROPERTIES FOR FUTURE
SEVERE TRANSIENT ANALYSES – KYUSHU UNIVERSITY (JAPAN)**

Numerical simulations of severe accident sequences in nuclear reactors require that the thermodynamic as well as transport properties of reactor core materials be evaluated over wide temperature and pressure ranges. However, experimental data with respect to metal fuels are rather scarce, especially in the high temperature region, and few theoretically-based recommendations have been made relating to matters necessary for reactor safety analysis. Here, based on an analytic equation of state (EOS) model [83] implemented in the accident analysis code SIMMER-III [150], a consistent set of thermodynamic properties of U-Pu-Zr ternary alloy with a typical composition (70 weight % U, 20 weight % Pu and 10 weight % Zr) is provided for use in safety analyses of metal-fueled reactors.

Lacking properties of solid U-Pu-Zr alloy such as specific enthalpy, the solidus and liquidus temperatures and heat of fusion can be evaluated using the phase diagram based on the CALPHAD (Calculation of Phase Diagram) approach [68] with the thermodynamic database of actinide alloys developed by CRIEPI, Japan [151]. The CALPHAD results indicate that the solidus and liquidus temperatures for (U-70, Pu-20, Zr-10 wt.%) alloy are $T_{\text{sol}} = 1,372$ K and $T_{\text{liq}} = 1,596$ K, respectively and that two major phase transition points exist at 857 K and 928 K, where the specific enthalpy changes significantly, as shown in FIG. 397.

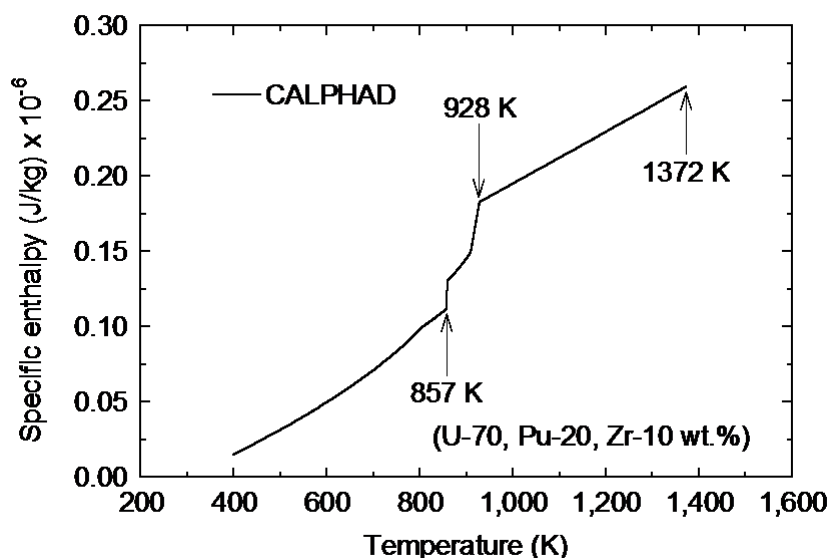


FIG. 397. Specific enthalpy of solid ternary alloy (CALPHAD results).

Available experimental data [152] are used to evaluate the temperature dependent density of the solid U-Pu-Zr alloy with phase transitions up to the solidus point. Near the melting point, the density of a liquid metal generally shows an almost linear dependence on temperature. The temperature gradient for the U-Pu-Zr liquid density can be evaluated by the additivity rule for the volumetric expansion coefficient at the liquidus temperature using the temperature dependent data for U, Pu and Zr ([153], [154], [155]).

Although no vapour pressure data for U-Pu-Zr fuel have been measured, Joseph *et al.* [156] evaluated the vapour pressure of (U-70, Pu-20, Zr-10 wt.%) alloy based on the Principle of

Corresponding State (PCS). The recalculated vapour pressure was fit to the following four-term vapour pressure equation:

$$\ln p^+ = 40.506 + 1.2910 \times 10^{-4}T - \frac{53033}{T} - 1.8237 \ln(T),$$

where p^+ is the saturation vapour pressure in Pa and T is the temperature in K. The above equation yields a normal boiling point of 3,660 K.

The critical parameters can also be estimated based on the PCS method, for consistency with the evaluation of the vapour pressure. The result gives the critical temperature $T_c = 9,160$ K, the critical pressure $p_c = 238$ MPa and the critical density $\rho_c = 3,210$ kg/m³ for (U-70, Pu-20, Zr-10 wt.%) alloy. This yields a critical compressibility of 0.20, which seems to be a reasonable estimate for a metallic material. In FIG. 398, the above equation is compared with the available vapour pressure data for U, Pu and Zr ([157], [158]).

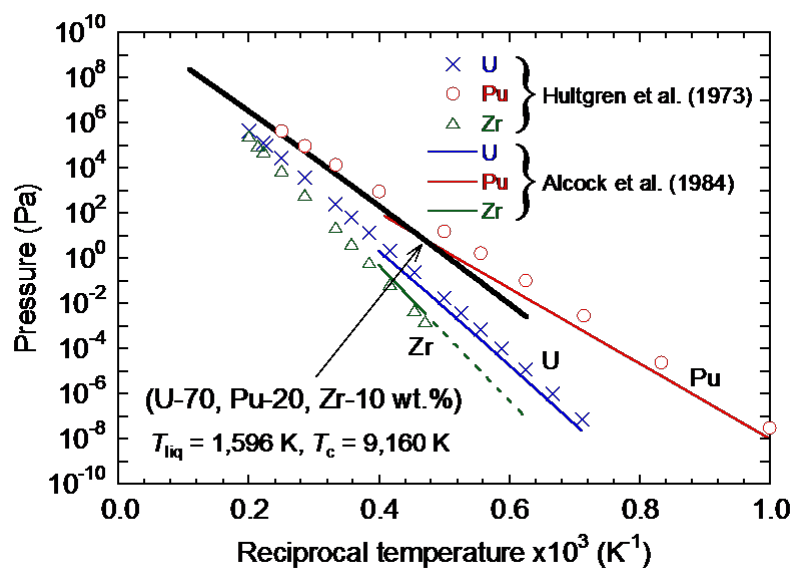


FIG. 398. Ternary alloy vapour pressure curve.

In the SIMMER-III EOS model [83], the modified Redlich-Kwong (MRK) equation is used to describe vapour thermodynamic states. FIG. 399 shows the vapour isotherm shapes of (U-70, Pu-20, Zr-10 wt.%) alloy on a p - v diagram calculated by the MRK equation. The spinodal line and the saturation curve are also indicated in the figure. Here, we take $p_c = 231.9$ MPa instead of 238 MPa for numerical consistency.

FIG. 400 shows the specific enthalpy of (U-70, Pu-20, Zr-10 wt.%) alloy in the liquid phase along the saturation curve up to 4 000 K, as well as in the solid phase. Here, the liquid enthalpy was evaluated based on the MRK equation and thermodynamic relationships. A comparison of the SIMMER EOS liquid enthalpy against the values calculated using the Neumann-Kopp rule with heat capacity data for U, Pu and Zr [157], as well as against the values predicted by CALPHAD, indicates good agreement. These results support that the present SIMMER-III evaluation of liquid and vapour thermodynamic properties is applicable to U-Pu-Zr fuel and reasonably describes its integral quantities such as enthalpy.

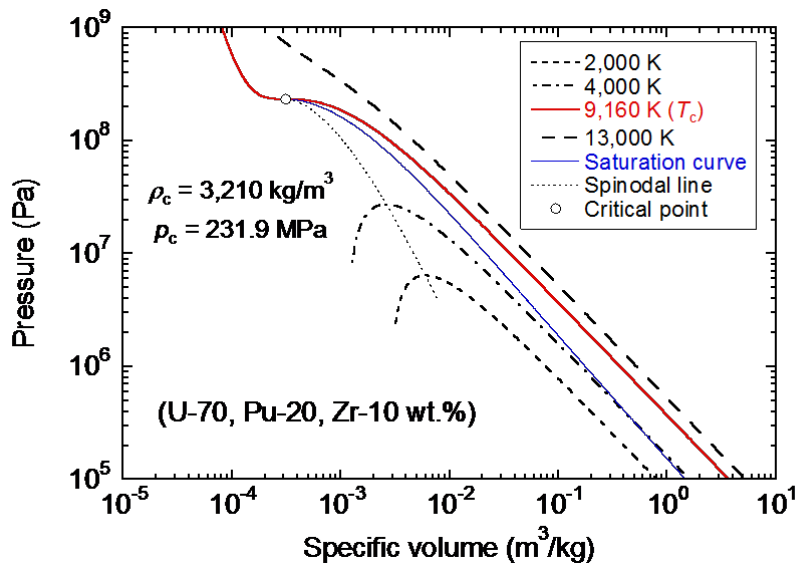


FIG. 399. Vapour isotherm shapes on p - v diagram.

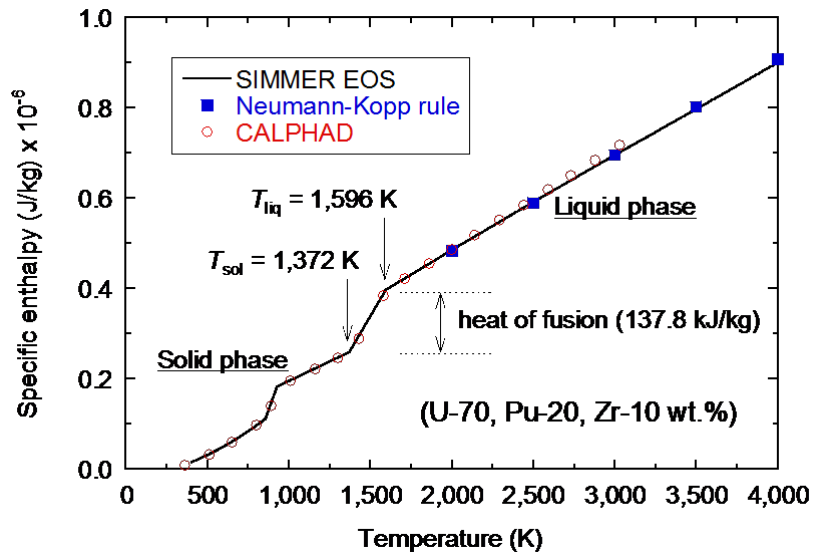


FIG. 400. Specific enthalpies of solid and liquid phases.

REFERENCES

- [1] INTERNATIONAL ATOMIC ENERGY AGENCY, Status of Fast Reactor Research and Technology Development, IAEA-TECDOC-1691, IAEA, Vienna (2012).
- [2] PLANCHON, H. P., *et al.*, Implication of the EBR-II inherent safety demonstration tests, Nuclear Engineering and Design **101** (1987) 75-90.
- [3] SACKETT, J. I., "Approaches to Measurement of Thermal-Hydraulic Parameters in Liquid-Metal-Cooled Fast Breeder Reactors", Advanced Course in Measurement Techniques in Power Engineering, Proc. International Centre for Heat and Mass Transfer CONF-830930-1 Dubrovnik, Yugoslavia (1983).
- [4] AMERICAN NUCLEAR SOCIETY, Decay Heat Power in Light Water Reactors, ANSI/ANS-5.1-2005 (2005).
- [5] FANNING, T. H., ed., "The SAS4A/SASSYS-1 Safety Analysis Code System", ANL/NE-12/4, Nuclear Engineering Division, Argonne National Laboratory, (2012) https://wiki.anl.gov/sas/Code_Manual.
- [6] TENCHINE, D., *et al.*, Status of CATHARE code for sodium cooled fast reactors, Nuclear Engineering and Design **245** (2012) 140-152.
- [7] International Atomic Energy Agency, Benchmark analyses on the natural circulation test performed during the PHENIX end-of-life experiments, IAEA-TECDOC-1703, IAEA, Vienna (2013).
- [8] MAAS, L., "Calculation of the PHENIX end-of-life test in natural circulation with the CATHARE code", Proceedings of ICAPP 2012, Chicago, USA (2012).
- [9] NATESAN, K., *et al.*, Thermal hydraulic investigations of primary coolant pipe rupture in an LMFBR, Nuclear Engineering and Design **236** (2006) 1165–1178.
- [10] SARATHY, U. P., *et al.*, Primary circuit temperature evolution during off-site power failure event in PFBR, Indian Chemical Engineer Journal, Section A **42** 2 (2000) 94-102.
- [11] BONIFETTO, R., *et al.*, A full-core coupled neutronic/thermal-hydraulic code for the modeling of lead-cooled nuclear fast reactors, Nucl. Eng. and Design **261** (2013) 85-94.
- [12] CARON, D., DULLA, S., and RAVETTO, P., New aspects in the implementation of the quasi-static method for the solution of neutron diffusion problems in the framework of a nodal method, Annals of Nuclear Energy **87** (2016) 34-48.
- [13] MARS Code Manual, KAERI/TR-2812/2004 (2004).
- [14] JEONG, H. Y. *et al.*, "Thermal-hydraulic models in MARS-LMR code", KAERI/TR-4297/2011 (2011).
- [15] Ha, K. S. *et al.*, "Validation of the reactivity feedback models in MARS-LMR", KAERI/TR-4395/2011, 2011.
- [16] CHOI, C. *et al.*, "New control rod drive-line/reactor vessel (CRDL/RV) expansion reactivity feedback model in MARS-LMR", SFR-960-DS-486-002Rev.1 (2014).
- [17] CHOI, C. *et al.*, "New fuel axial expansion reactivity feedback model in MARS-LMR", SFR-960-DS-486-004Rev.0 (2015).
- [18] MOCHIZUKI, H., Development of the plant dynamics analysis code NETFLOW++, Nuclear Engineering and Design **240** (2010) 577-587.
- [19] MOCHIZUKI, H., Verification of NETFLOW code using plant data of sodium cooled reactor and facility, Nuclear Engineering and Design **237** (2007) 87-93.
- [20] MOCHIZUKI, H., Inter-subassembly heat transfer of sodium cooled fast reactors: validation of the NETFLOW code, Nuclear Engineering and Design **237** (2007) 2040-2053.

- [21] MOCHIZUKI, H., KIKUCHI, N., and LI, S., Computation of natural convection test at Phenix reactor using the NETFLOW++ code, Nuclear Engineering and Design **262** (2013) 1-11.
- [22] TENCHINE, D., *et al.*, International benchmark on the natural convection test in PHENIX reactor, Nuclear Engineering and Design, **258** (2013) 189 – 198.
- [23] RELAP5-3D[®] Code Manual Volume II: User's Guide and Input Requirements, INEEL-EXT-98-00834, Revision 4.0, June 2012.
- [24] RELAP5-3D[®] Code Manual Volume I: Code Structure, System Models and Solution Methods, INEEL-EXT-98-00834, Revision 4.0 (2012).
- [25] RELAP5-3D[®] Code Manual Volume II: Appendix A Input Requirements, INEEL-EXT-98-00834, Revision 4.0 (2012).
- [26] RELAP5-3D[®] Code Manual Volume IV: Models and Correlations, INEEL-EXT-98-00834, Revision 4.0 (2012).
- [27] LU, D. *et al.*, Development of system analysis code for pool-type fast reactor under steady state operation, Atom. Energy Sci. and Technol. **46** 4 (2012) 422-428.
- [28] SUI, D. *et al.*, Development of three-dimensional hot pool model in a system analysis code for pool-type FBR, Nucl. Eng. and Design **256** (2013) 264-273.
- [29] FLAD, M. *et al.*, "ESFR severe accident analyses with SIMMER-III", International Conference on Fast Reactors and Related Fuel Cycles: Safe Technologies and Sustainable Scenarios (FR13), Paris, France (2013).
- [30] KONDO, S. *et al.*, "SIMMER-III: A Computer Program for LMFR Core Disruptive Accident Analysis", JNC-TN—9400-2001-002 2000.
- [31] YAMANO, H. *et al.*, "SIMMER-IV: A Three-Dimensional Computer Program for LMFR Core Disruptive Accident Analysis", JNC-TN—9400-2003-070 (2003).
- [32] VINOGRADOVA, J.U., *et al.*, "Validation of SOCRAT-BN code on rod bundle experiments", Proceedings of the 10th International Topical Meeting on Nuclear Thermal-Hydraulics, Operation and Safety (NUTHOS-10), paper 1356, Okinawa, Japan (2014).
- [33] RTISHCHEV, N.A., *et al.*, "Validation of SOCRAT-BN code on the base of reactor experiments", Proceedings of the 10th International Topical Meeting on Nuclear Thermal-Hydraulics, Operation and Safety (NUTHOS-10), paper 1356, Okinawa, Japan (2014).
- [34] RTISHCHEV, N.A., *et al.*, "Validation of SOCRAT-BN code against the experimental data gained during the PHENIX natural circulation end of life experiments", Innovations in Atomic Energy: Proceedings of the Conference (in Russian) Moscow (2015).
- [35] SPECTRA Sophisticated Plant Evaluation Code for Thermal-Hydraulic Response Assessment, Version 3.61, Volume 1 – Program Description, Volume 2 – User's Guide, Volume 3 – Subroutine Description, Volume 4 - Verification and Validation", NRG report K6202/MSt-150930 (2015).
- [36] MA, Z., *et al.*, Basic verification of THACS for sodium cooled fast reactor system analysis, Annals of Nuclear Energy **76** (2015) 1-11.
- [37] YUE, N., *et al.*, Thermal-hydraulic analysis of EBR-II shutdown heat removal tests SHRT-17 and SHRT-45R, Progress in Nuclear Energy **85** (2015) 682-693.
- [38] U. S. NUCLEAR REGULATORY COMMISSION, "TRACE V5.840 User's Manual, Volume 1: Input Specification, Volume 2: Modelling Guidelines", USNRC, Washington, D. C. USA (2014).

- [39] U. S. NUCLEAR REGULATORY COMMISSION, Office for Nuclear Regulatory Research, "TRACE V5.0 Theory Manual – Field Equations, Solution Methods, and Physical Models", Washington, D. C. USA (2013) <http://pbadupws.nrc.gov/docs/ML0710/ML071000097.pdf>
- [40] SPORE, J. W., SADASIVAN, P., and LILES, D. R., "Accelerator Transmutation of Waste Updates for TRAC-M", Los Alamos National Laboratory LA-UR-01-3660 (2001).
- [41] DOWNAR, T., *et al.*, "PARCS v3.0 – U.S. NRC Core Neutronics Simulator – User Manual", University of Michigan, Ann Arbor, Michigan (2009).
- [42] DERSTINE, K.L., "DIF3D: A Code to solve One-, Two- and Three-Dimensional Finite-Difference Diffusion Theory Problems," ANL-82-64, Argonne National Laboratory (1984).
- [43] RIMPAULT, G. *et al.* "The ERANOS code and data system for fast reactor neutronic analyses", Proc. Int. Conf. PHYSOR2002, Seoul, Korea (2002).
- [44] RIMPAULT, G., "Algorithmic features of the ECCO cell code for treating heterogeneous fast reactor subassemblies," International Conference on Mathematics and Computations, Reactor Physics, and Environmental Analyses, Portland, OR, USA (1995) 802-812.
- [45] RIMPAULT, G., "Physics documentation of ERANOS: the ECCO cell code", Rapport Technique H0-5010-430-5420, CEA, France (1997).
- [46] LEE, C.H. and YANG, W.S., "MC²-3: Multigroup Cross Section Generation DIFn Code for Fast Reactor Analysis," ANL/NE-11-41 Rev. 1, Argonne National Laboratory (2011).
- [47] GOORLEY, J. T., *et al.*, "Initial MCNP6 Release Overview – MCNP version 1.0", LA-UR-13-22394, 2013.
- [48] MACFARLANE, R.E. *et al.*, "The NJOY Nuclear Data Processing System, Version 2012", LA-UR-12-27079, 2012.
- [49] ALCOUFFE, R.E. and BAKER, R.S., "PARTISN: A Time-Dependent, Parallel Neutral Particle Transport Code System", LA-UR-08-07258. Revised March 2009.
- [50] ALCOUFFE, R.E. *et al.*, "DANTSYS: A Diffusion Accelerated Neutral Particle Code System", LA-12969-M, Los Alamos National Laboratory (1995).
- [51] BUCKEL, G., *et al.*, "A new SIMMER-III Version with Improved Neutronics Solution Algorithms", FZKA 6290, June 1999.
- [52] RABITI, C., ALFONSI, A., and EPINEY, A., "New Simulation Schemes and Capabilities for the PHISCS/RELAP5-3D Coupled Suite", *Nuclear Science and Engineering*, Vol. 182, pp. 104-118 (2016), [dx.doi.org/10.13182/NSE14-143](https://doi.org/10.13182/NSE14-143).
- [53] BOWMAN, S. M., "SCALE 6: comprehensive nuclear safety analysis code system", Nuclear Technology, Special Issue on the SCALE Nuclear Analysis Code System/Reactor Safety 174 [dx.doi.org/10.13182/NT10-163](https://doi.org/10.13182/NT10-163) (2011).
- [54] LEPPÄNEN, J., "Serpent – a continuous energy Monte Carlo reactor physics burnup calculation code", VTT Technical Research Centre of Finland (2013) <http://montecarlo.vtt.fi>
- [55] LEPPÄNEN, J., *et al.*, The Serpent Monte Carlo code: status, development and applications in 2013, *Annals of Nuclear Energy* **82** (2015) 142-150.
- [56] LEPPÄNEN, J., Performance of Woodcock delta-tracking in lattice physics applications using the Serpent Monte Carlo reactor physics burnup calculation code, *Annals of Nuclear Energy* **37** (2010) 715–722.
- [57] LEPPÄNEN, J., Two practical methods for unionized energy grid construction in continuous-energy Monte Carlo neutron transport calculation, *Annals of Nuclear Energy* **36** (2009) 878–885.

- [58] RINEISKI, A., Decay heat production in a TRU burner, *Progress in Nuclear Energy* **50** (2008) 377–381.
- [59] RINESKI, A., SINITSA, V., and MASCHEK, W., “C₄P, a Multigroup Nuclear CCCC Data Processing System for Reactor Safety and Scenario Studies”, Annual Meeting of Nuclear Technology /JK2005/, Nurenberg, Germany, May 10 - 12, 2005.
- [60] SMITH, M. A., ADAMS, C., YANG, W. S., and LEWIS, E. E., VARI3D & “PERSENT: Perturbation and Sensitivity Analysis”, Argonne National Laboratory, ANL/NE-13/8 (2013).
- [61] ANSYS CFX Release 15.0 User Manual, ANSYS, Inc. (2013).
- [62] WHEELER, C.L., et al., “COBRA4i Code System to Calculate Rod-bundle and Core Thermal-Hydraulics”, BNWL-1962, Battelle Pacific Northwest Laboratories, Richland, WA, USA (1976).
- [63] FRICANO, J. and BUONGIORNO, J., “COBRA4i-MIT: an Updated Subchannel Analysis Code for Sodium Fast Reactor Design,” in International Congress on Advances in Nuclear Power Plants (ICAPP), Nice, France (2011).
- [64] DONOVAN, T.E., GEORGE, T.L., and WHEELER, C.L., “COBRA-IV Wire Wrap Data Comparisons”, Pacific Northwest Laboratory, PNL-2938 (1979).
- [65] INTERNATIONAL ATOMIC ENERGY AGENCY, LMFR Core and Heat Exchanger Thermohydraulic Design: Former USSR and Present Russian Approaches, IAEA-TECDOC-1060, IAEA, Vienna (1999).
- [66] STAR-CD, version 3.26, Computational Dynamics, Ltd., New York, USA, 2005.
- [67] Thermo-Calc Software, www.thermocalc.com.
- [68] CALPHAD (CALculation of PHase Diagrams) Project, <http://www.calphad.org>.
- [69] KURATA, M., NAKAMURA, K., and OGATA, T., Thermodynamic evaluation of the quaternary U-Pu-Zr-Fe system – assessment of cladding temperature limits of metallic fuel in a fast reactor, *Journal of Nuclear Materials* **294** (2001) 123-129.
- [70] HUH, B., KIM, S., and CHUNG, C., The turbulent Prandtl number for temperature analysis in rod bundle subchannels, *Journal of Nuclear Science and Technology* **42** 2 (2005) 183-190.
- [71] GRABER, H. and RIEGER, M., Experimentelle Untersuchung des Wärmeübergangs an Flüssigmetall (NaK) in parallel durchstromten Rohrbündeln bei konstanter und exponentieller Warmeflussdichteverteilung, *Atomkernenergie* **19** (1972) 23-30.
- [72] MIKITYUK, K., Heat transfer to liquid metal: review of data and correlations for tube bundles, *Nuclear Engineering and Design* **239** 4 (2009) 680-687.
- [73] MOCHIZUKI, H. and TAKANO, M., Heat transfer in heat exchangers of sodium cooled fast reactor systems, *Nuclear Engineering and Design* **239** (2009) 295-307.
- [74] AGARWAL, A. K. and KHATIB RAHBAR, M., Dynamic simulation of LMFBR systems, *Atom. Energy Rev.* **18** 2 (1980) 329-552.
- [75] FINK, J. K. and LEIBOWITZ, L., “Thermodynamic and Transport Properties of Sodium Liquid and Vapor”, ANL/RE-95/2, Argonne Natl Lab, IL (1995).
- [76] CHANG, W. P., et al., Model development for analysis of the Korea advanced liquid metal reactor, *Nuclear Engineering and Design* **217** (2002) 63-80.
- [77] BLASIUS, H., Das Aehnlichkeitsgesetz bei Reibungsvorgängen in Flüssigkeiten, *Forsch. Arb. Ing.* **131** (1913) 1-41.
- [78] ENGEL, F. C., MARKLEY, R. A., and BISHOP, A. A., Laminar, transition, and turbulent parallel flow pressure drop across wire-wrap-spaced rod bundles, *Nuclear Science and Engineering* **69** 2 (1979) 290-296.
- [79] KAZIMI, M. S. and CARELLI, M. D., “Heat Transfer Correlation for Analysis of CRBRP Assemblies”, CRBRP-ARD-0034, Westinghouse (1976).

- [80] TENCHINE, D., *et al.*, Status of CATHARE code for sodium cooled fast reactors, *Nuclear Engineering and Design* **245** (2012) 140-152.
- [81] IDEL'CIK, I. E., *Mémento des pertes de charges*, Eyrolles (Electricité de France) (1986).
- [82] KONDO, S., *et al.*, "Current status and validation of the SIMMER-III LMFR safety analysis code," Proc. 7th Int. Conf. on Nucl. Eng. ICONE-7, Tokyo, Japan (1999).
- [83] MORITA, K. and FISCHER, E. A., Thermodynamic properties and equations of state for fast reactor safety analysis part 1: analytic equation-of-state model, *Nucl. Eng. And Des.* **183** 3 (1998) 177-191.
- [84] MORITA, K., *et al.*, "SIMMER-III Analytic Equation-of-State Model", JNC TN9400 2000-005 (1999).
- [85] SORAN, P. D., "Neutronics rebalance algorithms for SIMMER", LA-6152-MS, Los Alamos Scientific Laboratory (1975).
- [86] SRINIVASAN, G., *et al.*, The fast breeder test reactor – design and operating experiences, *Nuclear Engineering and Design*, **236** 7-8 (2006) 796-811.
- [87] VEZZONI, B., *et al.*, "SIMMER/PARTISN Analyses of the EBR-II shutdown heat removal tests", Proc. Int. Conf. PHSOR 2016, Sun Valley, ID, USA (2016).
- [88] MARCHETTI, M., GABRIELLI, F., RINEISKI, A., and MASCHEK, W., "The SIMMER/PARTISN capability for transient analysis", Proc. Int. Conf. PHYSOR 2014, Kyoto, Japan (2014).
- [89] KIEFHABER, E., "Updating of an 11-groups nuclear cross section set for transmutation applications", FZKA-6480 Germany (2000) 582.
- [90] ANDRIOLO, L., *et al.*, "Extension of the SIMMER code for the assessment of core thermal expansion feedbacks for transient analysis", Proc. Int. Conf. ICAPP 2015, Nice, France (2015).
- [91] ANDRIOLO, L., *et al.*, "An innovative methodology for evaluating core thermal expansion feedbacks in transient analyses", Proc. Int. Conf. ICAPP 2015, Nice, France (2015).
- [92] ANDRIOLO, L., "Impact des combustibles sphere-pac innovants sur les performances de sûreté des réacteurs à neutrons rapides refroidis au sodium", Université Grenoble Alpes, Ph.D. Thesis defended on 19 August 2015.
- [93] TOBITA, Y., *et al.*, "Interfacial area modeling for a multi-phase, multi-component fluid-dynamics code", International Conference on Multiphase Flows, Tsukuba, Japan (1991).
- [94] VEZZONI, B., *et al.*, Safety-related optimization and analyses of an innovative fast reactor concept, *Sustainability* **4** (2012) 1274–1291.
- [95] FEI, T., *et al.*, "Neutronics benchmark for EBR-II shutdown heat removal test SHRT-45R", Proc. Int. Conf. PHYSOR 2016, Sun Valley, Idaho, USA, (2016).
- [96] KONING, A. *et al.* (Eds.), *The JEFF-3.1 Nuclear Data Library*, JEFF Report 21, ISBN 92-64-02314-3, NEA/OECD, Paris, France (2006).
- [97] VEZZONI, B., *et al.*, "IAEA EBR-II neutronics benchmark: impact of modeling options on KIT results", Proc. Int. Conf. PHYSOR 2016, Sun Valley, Idaho, USA, (2016).
- [98] MENEGHETTI, D. AND KUCERA, D. A., Calculation of temperature coefficients of reactivity for EBR-II kinetic analyses, *Ann. Nucl. Energy* **14** 12 (1987) 663-671.
- [99] CROFF, A. G., ORIGEN2: a versatile computer code for calculating the nuclide compositions and characteristics of nuclear materials, *Nucl. Tech.* **62** 3 (1983) 335-352.

- [100] BORISHANSKII, V. M., GOTOVSKII, M. A., and FIRSOVA, É. V., Heat transfer to liquid metal flowing longitudinally in wetted bundles of rods, *Sov. At. Energy* **27** 6 (1969) 1347-1350.
- [101] SKUPINSKI, E., TORTEL, J., and VAUTRY, L., Determination of convection of sodium potassium alloys in circular tubes, *Int. J. Heat Mass Transfer* **8** (1965) 937.
- [102] COLEBROOK, C. F., Turbulent flow in pipes, with particular reference to the transition region between smooth and rough pipe laws, *Journal of the Institution of Civil Engineers* **11** London (1939) 133-156.
- [103] DAVIS, C. B., "Applicability of RELAP5-3D for Thermal-Hydraulic Analyses of a Sodium cooled Actinide Burner Test Reactor", INL/EXT-06-11518 Idaho National Laboratory (2006).
- [104] DAVIS, C. B., "Evaluation of the Use of Existing RELAP5-3D Models to Represent the Actinide Burner Test Reactor", INL/EXT-07-12228 Idaho National Laboratory (2007).
- [105] DEL NEVO, A. AND MARTELLI, E., Validation of a three-dimensional model of EBR-II and assessment of RELAP5-3D based on SHRT-17 test, *Nuc. Tech.* **193** (2016) 1–14.
- [106] SUMNER, T. and WEI, T., "Benchmark Specifications and Data Requirements for EBR-II Shutdown Heat Removal Tests SHRT-17 and SHRT-45R", ANL-ARC-226, Rev. 1, Argonne National Laboratory, Argonne, Illinois (2012).
- [107] TODREAS, N. and KAZIMI, M., *Nuclear Systems, Hemisphere*, New York (1990).
- [108] KELLETT, M. A., BERSILLON, O., and MILLS, R. W., "The JEFF-3.1/-3.1.1 radioactive decay data and fission yields sub-libraries", JEFF Report 20, ISBN 978-92-64-99087-6, OECD Nuclear Energy Agency, Paris, France (2009).
- [109] SANTAMARINA, A., *et al.*, "The JEFF-3.1.1 Nuclear Data Library", JEFF Report 22, ISBN 978-92-64-99074-6, OECD Nuclear Energy Agency, Paris, France (2009).
- [110] CHENG, S. K. and TODREAS, N. E., Hydrodynamic models and correlations for bare and wire-wrapped hexagonal rod bundles – bundle friction factors, subchannel friction factors, and mixing parameters, *Nucl. Eng. Design* **92** (1986) 227-251.
- [111] LYON, R. N., Liquid metal heat transfer coefficients, *Chem. Eng. Pror.* **47** 2 (1951) 75-79.
- [112] SEBAN, R. A. and SHIMAZAKI, T. T., Heat transfer to a fluid flowing turbulently in a smooth pipe with walls at constant temperature, *Trans. Am. Soc. Mech. Engrs.* **73** (1951) 803.
- [113] GARLAND, W. J., "Decay Heat Estimates for MNR", Technical Report 1998-03 McMaster University (1999).
- [114] CHEN, S. K., PETROSKI, R., and TODREAS, N. E., Numerical implementation of the Cheng and Todreas correlation for wire wrapped bundle friction factors – desirable improvements in the transition flow regime, *Nuclear Engineering and Design* **263** (2013) 406-410.
- [115] AOKI, S., Current liquid-metal heat transfer research in Japan, *Prog. Heat Mass Transfer* **7** (1973) 569-587.
- [116] CHURCHILL, S. W. and BERNSTEIN, M., A correlating equation for forced convection from gases and liquids to a circular cylinder in crossflow, *Journal of Heat Transfer* **99** 2 (1977) 300-306.
- [117] TOSHIBA, "Validation of 4S Safety Analysis Code SAEMKON for Loss of Offsite Power Event", ML12278A087, Tokyo, Japan (2012).

- [118] USHAKOV, P. A., ZHUKOV, A. V., and MATYUKHIN, M. M., Heat transfer to liquid metals in regular arrays of fuel elements, *High Temperature* **15** (1977) 868-873.
- [119] ZHANG, Y. and MIKITYUK, K., “Validation of the Serpent and TRACE codes using the SHRT-17 and SHRT-45R loss of flow tests performed in the EBR-II reactor”, Proceedings of Int. Conf. ICAPP 2015, Nice France, (2015) Paper 15229.
- [120] KUDASHOV, I. G., *et al.*, Heat-exchange models in the SOCRAT-BN code for calculating sodium boiling in geometrically different channels, *Atomic Energy* **117** 5 (2015) 323-328.
- [121] KIRILLOV, P. L., *et al.*, “Thermal Hydraulic Calculations Handbook (in Russian)”, IzdAt, Moscow, Russian Federation (2010).
- [122] SUBBOTIN, V. I., *et al.*, A study of heat transfer to molten sodium in tubes, *Soviet Atomic Energy* **13** 4 (1963) 991-994.
- [123] BATES, E., *et al.*, “Phase 2 of the EBR-II SHRT-45R benchmark study – TerraPower’s COBRA-4i-MIT results”, International Congress on Advances in Nuclear Power Plants (ICAPP) San Francisco (2016).
- [124] KAGANOVE, J. J., “Numerical Solution of the One-Group Space-Independent Reactor Kinetics Equations for Neutron Density Given the Excess Reactivity”, ANL-6132, Argonne National Laboratory, Argonne, Illinois USA (1960).
- [125] FULLER, E. L., “The Point Kinetics Algorithm for FX2, ANL-7910”, Argonne National Laboratory, Argonne, Illinois USA (1972) 503-508.
- [126] ARGONNE NATIONAL LABORATORY, “Properties for LMFBR Safety Analysis”, ANL-CEN-RSD-76-1 (1976).
- [127] RINEISKI, A., “KIN3D: module de cinétique spatiale et de perturbations pour TGV2”, Note Technique, CEA-Cadarache, SPRC/LEPH (1997) 97-203.
- [128] MARCHETTI, M. *et al.*, Neutron deterministic models of the EBR-II SHRT-45R core configuration, *Transactions of the ANS* **111** Anaheim, CA, USA (2014) 1188-1190.
- [129] VAN ROOIJEN, W. F. G. and MOCHIZUKI, H., Analysis of the EBR-II SHRT-45R unprotected loss of flow experiment with ERANOS and RELAP, *Science and Technology of Nuclear Installations* **2015** Article ID 832721 (2015) 1-14.
- [130] VAN ROOIJEN, W. F. G., Analysis of the MZA/MZB benchmarks with modern nuclear data sets, *Annals of Nuclear Energy* **62** (2013) 504-525.
- [131] ARGONNE NATIONAL LABORATORY, “Auxiliary EM Pump Model - SAS4A/SASSYS-1 EBR-II Benchmarks Analyses”, private communication, Argonne National Laboratory (2013).
- [132] PETRUZZI, A. and D’AURIA, F., Standardized Consolidated Calculated and Reference Experimental Database (SCCRED): a supporting tool for V&V and uncertainty evaluation of best-estimate system codes for licensing applications, *Nuclear Science and Engineering* **182** 1 (2016) 13-53.
- [133] OECD/CSNI, “Integral Test Facility Validation Matrix for the Assessment of Thermal-Hydraulic Codes for LWR LOCA and Transients”, OECD/GD(97)12, NEA/CSNI/R(96)17 (1996).
- [134] OECD/CSNI, “Separate Effects Test Matrix for Thermal-Hydraulic Code Validation Volume I, Phenomena Characterization and Selection of Facilities and Tests”, OECD/GD(94)82 (1994).
- [135] OECD/CSNI, “Separate Effects Test Matrix for Thermal-Hydraulic Code Validation Volume II, Facilities and Experiment Characteristics”, OECD/GD(94)83 (1994).

- [136] BAJIS, T. *et al.*, “On-Transient Qualification of LOBI/MOD2, SPES, LSTF, BETHSY and Krsko Plant Nodalizations for RELAP5/MOD2 Code”, University of Pisa, Report DCMN - NT 185, Pisa, Italy (1991).
- [137] D'AURIA, F., LEOPARDI, M., and POCHARD, R., “Methodology for the evaluation of thermal-hydraulic codes accuracy”, Proc. Int. Conf. on New Trends in Nuclear System Thermal-hydraulics, Pisa, Italy (1994) 467-477.
- [138] AMBROSINI, W., BOVALINI, R., and D'AURIA, F., Evaluation of accuracy of thermal-hydraulic code calculations, *Energia Nucl.* **7** (1990) 5-16.
- [139] AKSAN, N., BESSETTE, D., BRITAIN, I. *et al.*, “Code Validation Matrix of Thermal-hydraulic Codes for LWR LOCA and Transients”, OECD/CSNI 132 (1987).
- [140] ANNUNZIATO, A., GLAESER, H., LILLINGTON, J. N. *et al.*, “CSNI Code validation matrix of Thermal-hydraulic Codes for LWR LOCA and Transients”, OECD/CSNI 132, Rev. 1 (1996).
- [141] BOVALINI, R., D'AURIA, F., and LEOPARDI, M., “Qualification of the Fast Fourier Transform Based Methodology for the quantification of thermal-hydraulic code accuracy”, University of Pisa Report, DCMN - NT 194(92), Pisa, Italy (1992).
- [142] PETRUZZI, A. and D'AURIA, F., “Accuracy Quantification: Description of the Fast Fourier Transform Based Method (FFTBM)”, University of Pisa Report, DIMNP- NT 556(05), Pisa, Italy (1992).
- [143] LEONARDI, M., D'AURIA, F., and POCHARD, R., “The FFT based method in the frame of the UMAE”, Spec. Workshop on Uncertainty Analysis Methods, London (March 1994).
- [144] WICKETT, T. *et al.*, “Report of the Uncertainty Method Study for Advanced Best Estimate Thermal-hydraulic Code Applications”, OECD/NEA/CSNI R (97) 35, I and II (1998).
- [145] PETRUZZI, A. (lead author, 1 of 2): “BEMUSE PHASE II REPORT: Re-Analysis of the ISP-13 Exercise, Post Test Analysis of the LOFT L2-5 Test Calculation”, OECD/CSNI Report NEA/CSNI/R(2006)2 – Issued June 19, 2006, JT03210882, Paris (F), © OECD (2006) 625.
- [146] RIEBOLD, W., “Minutes of the OECD/CSNI SACTE Task Group Meeting”, Paris (December 1987).
- [147] POCHARD, R. and PORRACCHIA, A., “Assessment closure proposal”, OECD/CSNI SACTE Task Group Meeting, Paris (December 1986).
- [148] USNRC and OECD/CSNI, Proceedings of the OECD/CSNI Workshop on Transient Thermal-Hydraulic and Neutronic Codes Requirements, Annapolis, Maryland, USA, USNRC NUREG/CP-0159 and OECD/CSNI NEA/CSNI/R(97)4 (1997).
- [149] HOOGENBOOM, J.E. and VAN DAM, H., Kernreactorkunde, Technische Universiteit Delft, July 1991.
- [150] TOBITA, Y., *et al.*, “The development of SIMMER-III, an advanced computer program for LMFR safety analysis, and its application to sodium experiments”, *Nuclear Technology* **153** 3 (2006) 245-255.
- [151] KURATA, M., Thermodynamic assessment of the Pu-U, Pu-Zr and Pu-U-Zr systems, *Calphad* **23** No. 3-4 (1999) 305-337.
- [152] JANNEY, D.E. and PAPESCH, C.A., “FCRD Transmutation Fuels Handbook 2015”, INL/EXT-15-36520, Idaho National Laboratory (2015).
- [153] DROTNING, W.D., Density and thermal expansion of liquid U-Nb alloys, *High Temperatures – High Pressures* **14** (1982) 253-258.

- [154] JONES, L.V., et al., The viscosity and density of molten plutonium metal and a plutonium-cerium-cobalt eutectic alloy, American Society of Metals Transactions Quarterly **55** (1962) 819-825.
- [155] PARADIS, P-F. and RHIM, W-K, Thermophysical properties of zirconium at high temperature, Journal of Materials Research **14** 9 (1999) 3713-3719.
- [156] JOSEPH, M., SIVAKUMAR, N., and MANORAVI, P., Studies on equation of state of high temperature nuclear materials, Annals of Nuclear Energy **31** 10 (2004) 1163-1175.
- [157] HULTGREN, R., et al., "Selected Values of the Thermodynamic Properties of the Elements", American Society for Metals (1973).
- [158] ALCOCK, C.B., ITKIN, V.P., and HERRIGAN, M.K., Vapour pressure equations for the metallic elements: 298-2500K, Canadian Metallurgical Quarterly **23** 3 (1984) 309-313.

ACRONYMS AND ABBREVIATIONS

0-D	zero dimensional
1-D	one dimensional
2-D	two dimensional
3-D	three dimensional
AA	average accuracy
AE	acceptable error
ANL	Argonne National Laboratory
ANS	American Nuclear Society
ASM	analytical simulation model
ATC	annulus thimble thermocouple
BC	boundary condition
BE	best estimate
BEPU	best estimate plus uncertainty
BWR	boiling water reactor
CA	control assembly
CALPHAD	CALculation of PHAse Diagram
CFD	computational fluid dynamics
CIAE	China Institute of Atomic Energy
CRDL	control rod drive line
CRIEPI	Central Research Institute of Electric Power Institute
CRP	coordinated research project
CSNI	Committee on the Safety of Nuclear Installations
CTP	Chen-Todreas-Petroski
CTS	Cheng and Todreas correlation (simplified model)
CV	compressible volume
CZP	cold zero power
DNB	departure from nucleate boiling
EBR-II	Experimental Breeder Reactor II
ECCS	emergency core cooling system
EH	engineering handbook
EM	ElectroMagnetic
ENEA	Italian National Agency for New Technologies, Energy and Sustainable Economic Development
EOS	equation of state
FDD	finite difference diffusion
FFT	fast fourier transform
FFTBM	fast fourier transform based method
FM	FlowMeter
HFD	high flow driver
HFP	hot full power
HFR	high flux reactor
HPP	high pressure plenum
HTC	heat transfer coefficient

HW-CR	high-worth control rod
IAEA	International Atomic Energy Agency
IBRAE	Nuclear Safety Institute of the Russian Academy of Sciences
IFA	Interfacial-Area
IGCAR	Indira Gandhi Centre for Atomic Research
IHX	intermediate heat exchanger
IRSN	Institute for Radiological Protection and Nuclear Safety
ITF	Integral Test Facility
JAEA	Japan Atomic Energy Agency
KAERI	Korea Atomic Energy Research Institute
KERMA	Kinetic Energy Released in MATter
KINS	Korea Institute of Nuclear Safety
KIT	Karlsruhe Institute of Technology
KU	Kyushu University
LMR	liquid metal reactor
LOCA	loss of coolant accident
LPP	low pressure plenum
MCP	modular centrifugal pump
MFR	mass flow rate
M-G	motor generator
MRK	Modified Redlich-Kwong
MTC	Midplane ThermoCouple
N.IN.E.	Nuclear and Industrial Engineering
NCEPU	North China Electric Power University
NK	neutron kinetic
NPP	nuclear power plant
NRG	Nuclear Research and Consultancy Group
OECD	Organization for Economic Cooperation and Development
OTC	Outlet coolant ThermoCouple
PCS	principle of corresponding state
PCT	peak cladding temperature
PD	parital driver
PFT	peak fuel temperature
PHTS	primary heat transport system
PhW	Phenomenological Windows
Polito	Politecnico di Torino
PSI	Paul Scherrer Institute
PWR	pressurized water reactor
QR	qualification report
RBMK	high power channel-type reactor
RCM	research coordination meeting
RDS	reference data set
RTA	relevant thermal hydraulic aspects
RV	reactor vessel

SA	Subassembly
SCCRED	standardized and consolidated calculated & reference experimental database
SHRT	shutdown heat removal test
SS	stainless steel
STH	system thermal hydraulic
TTC	top of core thermocouple
UP	upper plenum
V&V	validation and verification
VVER	water-water energetic reactor
WF	weighted frequency
XJTU	Xi'an Jiaotong University
XS	cross-section

CONTRIBUTORS TO DRAFTING AND REVIEW

Arima, T.	Kyushu University, Japan
Balestra, P.	Italian National Agency for New Technologies, Energy and Sustainable Economic Development (ENEA) /University of Rome, Italy
Bates, E.	TerraPower, USA
Batra, C.	International Atomic Energy Agency
Bonifetto, R.	Politecnico di Torino, Italy
Briggs, L. L.	Argonne National Laboratory (ANL), USA
Caron, D.	Politecnico di Torino, Italy
Chen, X.-N.	Karlsruhe Institute of Technology (KIT), Germany
Cherubini, M.	Nuclear and Industrial Engineering (N.I.N.E.), Italy
Choi, C.	Korea Atomic Energy Research Institute (KAERI), Republic of Korea
De Luca, D.	Nuclear and Industrial Engineering (N.I.N.E.), Italy
Del Nevo, A.	Italian National Agency for New Technologies, Energy and Sustainable Economic Development (ENEA), Italy
DiPiazza, I.	Italian National Agency for New Technologies, Energy and Sustainable Economic Development (ENEA), Italy
Doda, N.	Japan Atomic Energy Agency (JAEA), Japan
Dulla, S.	Politecnico di Torino, Italy
Fei, T.	Argonne National Laboratory (ANL), USA
Gabrielli, F.	Karlsruhe Institute of Technology (KIT), Germany
Hu, W.	China Institute of Atomic Energy (CIAE), China
Kriventsev, V.	International Atomic Energy Agency
Maas, L.	Institut de Radioprotection et de Sûreté Nucléaire (IRSN), France
Marinari, R.	Italian National Agency for New Technologies, Energy and Sustainable Economic Development (ENEA), Italy
Marchetti, M.	Karlsruhe Institute of Technology (KIT), Germany
Martelli, E.	Italian National Agency for New Technologies, Energy and Sustainable Economic Development (ENEA)/University of Rome, Italy
Maschek, W.	Karlsruhe Institute of Technology (KIT), Germany
Mikityuk, K.	Paul Scherrer Institute (PSI), Switzerland
Mochizuki, H.	University of Fukui, Japan
Mohammed, A.	Argonne National Laboratory (ANL), USA
Moisseytsev, A.	Argonne National Laboratory (ANL), USA
Monti, S.	International Atomic Energy Agency
Morita, K.	Kyushu University, Japan
Ohira, H.	Japan Atomic Energy Agency (JAEA), Japan

Parisi, C.	Italian National Agency for New Technologies, Energy and Sustainable Economic Development (ENEA), Italy
Petruzzi, A.	Nuclear and Industrial Engineering (N.I.N.E.), Italy
Qiao, P.	China Institute of Atomic Energy (CIAE), China
Rineiski, A.	Karlsruhe Institute of Technology (KIT), Germany
Rtishchev, N.	Nuclear Safety Institute of the Russian Academy of Sciences (IBRAE-RAN), Russian Federation
Shin, A.	Korea Institute of Nuclear Safety (KINS), Republic of Korea
Sofu, T.	Argonne National Laboratory (ANL), USA
Stempniewicz, M.	Nuclear Research and Consultancy Group (NRG), Netherlands
Su, G. H.	Xi'an Jiaotong University, China
Sui, D.	North China Electric Power University (NCEPU), China
Sumner, T.	Argonne National Laboratory (ANL), USA
Tarasov, A.	Nuclear Safety Institute of the Russian Academy of Sciences (IBRAE-RAN), Russian Federation
Truong, B.	TerraPower, USA
Uppala, P. S.	Indira Ghandi Centre for Atomic Research (IGCAR), India
van Rooijen, W.	University of Fukui, Japan
Vezzoni, B.	Karlsruhe Institute of Technology (KIT), Germany
Wei, T. Y. C.	Argonne National Laboratory (ANL), USA
Yue, N.	Xi'an Jiaotong University, China
Zanino, R.	Politecnico di Torino, Italy
Zhang, D.	Xi'an Jiaotong University, China
Zhang, Y.	Paul Scherrer Institute (PSI), Switzerland

Research Coordination Meetings

Argonne, Illinois: USA: 18–19 June 2012

Vienna, Austria: 5–7 November 2013

Bologna, Italy: 23–27 March 2015

Vienna, Austria: 26–29 April 2016

International Atomic Energy Agency
Vienna
ISBN 978-92-0-105517-0
ISSN 1011-4289